

Spectroscopic Studies of the Physiological Speciation of Ruthenium(III) Anticancer Complexes

by

Michael Ian Webb

B.Sc. (Honours), Mount Allison University, 2008

Thesis Submitted In Partial Fulfillment of the
Requirements for the Degree of
Doctor of Philosophy

in the
Department of Chemistry
Faculty of Science

**© Michael Ian Webb 2013
SIMON FRASER UNIVERSITY
Summer 2013**

All rights reserved.

However, in accordance with the *Copyright Act of Canada*, this work may
be reproduced, without authorization, under the conditions for
“Fair Dealing.” Therefore, limited reproduction of this work for the
purposes of private study, research, criticism, review and news reporting
is likely to be in accordance with the law, particularly if cited appropriately.



Library and Archives
Canada

Published Heritage
Branch

395 Wellington Street
Ottawa ON K1A 0N4
Canada

Bibliothèque et
Archives Canada

Direction du
Patrimoine de l'édition

395, rue Wellington
Ottawa ON K1A 0N4
Canada

Your file Votre référence

ISBN: 978-0-499-23925-9

Our file Notre référence

ISBN: 978-0-499-23925-9

NOTICE:

The author has granted a non-exclusive license allowing Library and Archives Canada to reproduce, publish, archive, preserve, conserve, communicate to the public by telecommunication or on the Internet, loan, distribute and sell theses worldwide, for commercial or non-commercial purposes, in microform, paper, electronic and/or any other formats.

The author retains copyright ownership and moral rights in this thesis. Neither the thesis nor substantial extracts from it may be printed or otherwise reproduced without the author's permission.

In compliance with the Canadian Privacy Act some supporting forms may have been removed from this thesis.

While these forms may be included in the document page count, their removal does not represent any loss of content from the thesis.

AVIS:

L'auteur a accordé une licence non exclusive permettant à la Bibliothèque et Archives Canada de reproduire, publier, archiver, sauvegarder, conserver, transmettre au public par télécommunication ou par l'Internet, prêter, distribuer et vendre des thèses partout dans le monde, à des fins commerciales ou autres, sur support microforme, papier, électronique et/ou autres formats.

L'auteur conserve la propriété du droit d'auteur et des droits moraux qui protège cette thèse. Ni la thèse ni des extraits substantiels de celle-ci ne doivent être imprimés ou autrement reproduits sans son autorisation.

Conformément à la loi canadienne sur la protection de la vie privée, quelques formulaires secondaires ont été enlevés de cette thèse.

Bien que ces formulaires aient inclus dans la pagination, il n'y aura aucun contenu manquant.

Canada

Approval

Name: **Michael Ian Webb**
Degree: **Doctor of Philosophy (Chemistry)**
Title of Thesis: ***Spectroscopic Studies of the Physiological Speciation
of Ruthenium(III) Anticancer Complexes***
Examining Committee: **Chair:** Firstname Surname
Position

Dr. Charles Walsby
Senior Supervisor
Associate Professor

Dr. Paul Percival
Supervisor
Professor

Dr. Tim Storr
Supervisor
Assistant Professor

Firstname Surname
Supervisor
Assistant/Associate/Professor

Firstname Surname
Internal Examiner
Assistant/Associate/Professor
School/Department or Faculty

Firstname Surname
External Examiner
Assistant/Associate/Professor,
Department
University

Date Defended/Approved: August 12, 2013

Partial Copyright Licence



The author, whose copyright is declared on the title page of this work, has granted to Simon Fraser University the right to lend this thesis, project or extended essay to users of the Simon Fraser University Library, and to make partial or single copies only for such users or in response to a request from the library of any other university, or other educational institution, on its own behalf or for one of its users.

The author has further granted permission to Simon Fraser University to keep or make a digital copy for use in its circulating collection (currently available to the public at the "Institutional Repository" link of the SFU Library website (www.lib.sfu.ca) at <http://summit.sfu.ca> and, without changing the content, to translate the thesis/project or extended essays, if technically possible, to any medium or format for the purpose of preservation of the digital work.

The author has further agreed that permission for multiple copying of this work for scholarly purposes may be granted by either the author or the Dean of Graduate Studies.

It is understood that copying or publication of this work for financial gain shall not be allowed without the author's written permission.

Permission for public performance, or limited permission for private scholarly use, of any multimedia materials forming part of this work, may have been granted by the author. This information may be found on the separately catalogued multimedia material and in the signed Partial Copyright Licence.

While licensing SFU to permit the above uses, the author retains copyright in the thesis, project or extended essays, including the right to change the work for subsequent purposes, including editing and publishing the work in whole or in part, and licensing other parties, as the author may desire.

The original Partial Copyright Licence attesting to these terms, and signed by this author, may be found in the original bound copy of this work, retained in the Simon Fraser University Archive.

Simon Fraser University Library
Burnaby, British Columbia, Canada

revised Fall 2011

Abstract

Ruthenium(III) complexes have been described as the next generation of metal-based anticancer compounds. Two of the most promising clinical candidates are imidazolium [*trans*-RuCl₄(1*H*-imidazole)(DMSO-S)] (NAMI-A) and indazolium [*trans*-RuCl₄(1*H*-indazole)₂] (KP1019). The proposed mode of action of these compounds involves ligand substitution, protein-mediated delivery, and reduction from Ru(III) to Ru(II), either within the hypoxic environment of tumour cells or by biological reducing agents. Electron paramagnetic resonance spectroscopy (EPR) was used to demonstrate the importance of protein binding for these complexes, specifically to human serum albumin (hsA), and the effect this has on their speciation and redox stability. Electron nuclear double resonance spectroscopy (ENDOR) has helped identify the nature of coordinate hsA interactions. Inspired by these results, several derivatives of both complexes were synthesized, targeting hydrophobic interactions with hsA. By increasing the hydrophobicity of the axial ligands, these complexes bind non-covalently to hsA with greater affinity and stability. This stabilization can allow for the delivery of the unsubstituted complexes to tumour cells, potentially enhancing their anticancer activity. Additional *in vitro* EPR studies on both NAMI-A and KP1019 have helped probe the potential biological targets of both complexes, since NAMI-A interacts predominantly with cell walls, while KP1019 readily enters eukaryotic cells and binds with the mitochondria and cytoplasmic protein components.

Keywords: Ru(III) Anticancer Compounds; Electron Paramagnetic Resonance; Human Serum Albumin.

Acknowledgements

There have been many people who have helped in one way or another in the completion of this thesis. I have tried to mention these individuals specifically; however this is not an exhaustive list. Without the help, guidance, and advice of all of the people listed below I would not be where I am today, and I am very grateful and humbled by all of the support I have received over the years.

The story of my academic research career begins back at Mount Allison University. Here I made the decision to ultimately pursue an Honours degree in Chemistry, not truly realizing what that entailed. I am very grateful for Dr. Stephen Duffy for being beyond accommodating, to teach Chem. 4521 – Environmental Chemistry in his office to me one on one, and for suggesting that I should strive to do an honours research project with Dr. Steve Westcott. Lucky for me, Old Man Westcott was willing to take a chance on a 3rd year student who was still trying to figure his life out. In his “Wild Toads” research group I truly discovered the passion that I have for research, and how rewarding teaching others can be from the Saturday Toads. I was fortunate to also perform a special topics research project with Dr. Adrian Culf. Both these experiences made me realize that graduate school was a definite possibility. I am also grateful for the other members of not only the Chemistry department at Mount Allison, but also the biochemistry and biology department for their help, guidance, and expertise throughout my undergraduate career. I will never forget these experiences and always look back with fondness at my time spent at Mount A.

To begin my graduate career, I began by contacting professors in Canada who were doing research that was interesting to me. Luckily, my first choice, Dr. Charles Walsby, was willing to give the kid from a small East Coast town a chance. Coming from Sackville, New Brunswick to Burnaby, British Columbia was a culture shock to say the least, but with the help of Dr. Walsby and his research group the transition was seamless. Over the next 5 years, not only did a very productive partnership form, but also a

friendship. I am extremely grateful to Charles for accepting me into his group and giving me the opportunity to succeed. I was also fortunate during my time at SFU to make several lasting friendships with not only members of the Walsby group, but within the Chemistry department and even outside the university. Beginning with the Walsby group, I would like to thank Naniye Cetinbas who was extremely helpful in guiding me during my first few months at SFU, Qi He (Tommy) who was a pleasure to be around both in and out of the lab, Changhua Mu for all the helpful discussions and for staying late the occasional night to take my samples out of the incubator (you were a life saver!), and Stephanie Chang for your helpful critiques and questions in preparing me for my thesis defence. I also would like to thank the undergraduate students who have helped me over the years on a variety of projects, in chronological order: Jonathan Jiang, Jackie Williams, Haley Mitchell, Ryan Chard, Yaser Al-Jobory, Boris Wu, Thalia Jang, and Micah Brush. They were instrumental in completing many of the projects that were made into publications, and for that I am very grateful. In the Chemistry department there are several good friendships that I was fortunate to make, primarily with members in the Centre of Excellence in Inorganic Chemistry, commonly known as the Leznoff and Storr groups. I would like to thank, Dr. Edwin Wong for having the patience to teach me how to solve an X-ray crystal structure, and also Dr. Michael Katz for helping me (and Edwin) solve the most troublesome structures. I would like to thank Michael Jones for helping run and work-up cyclic voltammograms for several of my compounds, and Frank Haftbaradaran for running countless elemental analysis samples for me. Additionally, I would also like to thank all the members of the Chemistry department at SFU for helping me as a student, teaching assistant, and president of the graduate caucus. Outside of the university, I was fortunate to be a member of a 3 on 3 hockey team, the “Fighting Irish” where I have made several lasting friendships, and was able to escape the confines of the lab for a few hours every week. Everyone listed above were all positive influences in my life, and their support was greatly appreciated and will not be forgotten.

In preparing for my thesis submission, I am very thankful to my committee members Dr. Paul Percival and Dr. Tim Storr. Their expertise, experience, and guidance

have helped me develop into the scientist that I am today. For my thesis defence I am also grateful for my internal and external examiners, Dr. Dipankar Sen and Dr. Jürgen Gailer respectively. For them, in addition to my committee members, to take time out of their day to read my thesis and offer helpful suggestions on ways to improve it, I am very grateful.

Last, but certainly not least, I am extremely grateful for my family and all of their love and support. It begins at home, and it is safe to say that no one has been more unconditionally supportive of me in everything that I do than my loving wife Adrienne. Coming home to her and the dogs (Kao and Baylen) has been the highlight of several of my days, and helped me get through the tough times, in particular, writing this very thesis. Without them in my life I would not be as happy as I am now. At my home away from home, now in Ottawa, Ontario, my mother and father have also been highly supportive of me, both emotionally and financially. To my siblings, Matthew, Deanna, Mark, Denise, and Rory, I am thankful for your support, and curiosity as to what I was doing at SFU through the years. Also, to my new family, Dr. Ron, Jutta, and Erin Skitch, I am thankful for their love and support through the years. I am also grateful to members of my extended family for all of their support, encouragement, and prayers.

Table of Contents

Approval	ii
Partial Copyright Licence	iii
Abstract	iv
Acknowledgements.....	v
Table of Contents	viii
List of Tables	xii
List of Figures	xiii
List of Acronyms	xix

1. Introduction – Ruthenium Anticancer Agents.....	1
1.1. From Platinum to Ruthenium	1
1.2. Ruthenium Anticancer Agents.....	2
1.2.1. Octahedral Geometry	2
1.2.2. Ligand Exchange	3
1.2.3. Oxidation State.....	4
1.2.4. Transport Protein Interactions.....	4
1.3. Serum Proteins.....	5
1.3.1. Human Serum Transferrin	5
1.3.2. Human Serum Albumin	6
1.4. Ru(II) Anticancer Agents.....	7
1.5. Ru(III) Anticancer Agents	9
1.5.1. “Keppler-type” Family of Ru(III) Complexes.....	10
1.5.2. “NAMI-A-type” Family of Ru(III) Complexes.....	11
1.5.3. Mechanism of Action.....	12
1.6. Electron Paramagnetic Resonance Spectroscopy	15
1.6.1. Basic Principles of EPR	16
1.6.2. “Powder-Pattern” EPR.....	19
1.7. Simulation of EPR Spectra	21
1.8. Research Goals	22
2. The Solution and Protein Binding Behaviour of the Promising “Keppler-type” Ruthenium(III) Anticancer Agents KP1019 and KP418.....	24
2.1. Introduction.....	24
2.2. Experimental.....	25
2.2.1. Synthesis	25
2.2.2. Preparation of Protein Solutions	25
2.2.3. Preparation of EPR Samples	25
2.2.4. EPR Measurements and Simulations	27
2.2.5. EPR Experimental Conditions	27
2.3. Results and Discussion	28
2.3.1. Aqueous Solution EPR Prior to Ligand Exchange	28
2.3.2. Solution Behaviour of KP418.....	32

2.3.3. Solution Behaviour of KP1019	35
2.3.4. Interactions of the Complexes with Serum Proteins	35
2.3.5. Interactions with hsA	36
2.3.6. Interactions with hsTf	40
2.3.7. Interactions of the Complexes with Whole Human Serum	42
2.4. Conclusion	45
3. Interactions of the Antimetastatic Ru(III) Complex NAMI-A with Human Serum Albumin	49
3.1. Introduction.....	49
3.2. Experimental	50
3.2.1. Synthesis	50
3.2.2. Preparation of EPR Samples	50
3.2.3. EPR Measurements and Simulation.....	51
3.2.4. EPR Experimental Conditions	51
3.3. Results and Discussion	52
3.3.1. Ligand Exchange Processes in Phosphate Buffer	52
3.3.2. Interaction of NAMI-A with Human Serum Albumin	58
3.3.3. Behaviour of NAMI-A in Whole Human Serum.....	63
3.3.4. Reduction of NAMI-A by Ascorbic Acid.....	64
3.3.5. Effect of hsA Interactions on Reduction of NAMI-A	65
3.4. Conclusions.....	68
4. Pyridine-based Analogues of the Antimetastatic Ru(III) Complex NAMI-A: Targeting Non-Coordinate Interactions with Albumin.....	69
4.1. Introduction.....	69
4.2. Experimental	71
4.2.1. Synthesis	71
4.2.2. Crystallographic Structure Determination	75
4.2.3. Electrochemical Measurements	75
4.2.4. Optical Measurements	75
4.2.5. Preparation of EPR Samples.....	76
4.2.6. EPR Measurements and Simulation.....	77
4.2.7. EPR Experimental Conditions	77
4.3. Results and Discussion	77
4.3.1. Synthesis	77
4.3.2. Crystal Structures.....	78
4.3.3. Aqueous Solution Behaviour - EPR	81
4.3.4. Aqueous solution Behaviour - UV-Vis.....	85
4.3.5. Interactions of the Complexes with hSA - EPR	87
4.3.6. Interactions of the Complexes with hSA – UV-Vis	93
4.3.7. Effect of Protein Binding on Reductive Stability	94
4.4. Conclusions.....	98

5. Pyridine-based Analogues of the Antineoplastic Ru(III) Complex KP1019: Using Non-coordinate Interactions with Albumin to Increase Bioavailability.....	100
5.1. Introduction.....	100
5.2. Experimental.....	101
5.2.1. Synthesis	101
5.2.2. Crystallographic Structure Determination	105
5.2.3. Optical Measurements	105
5.2.4. Preparation of EPR Samples.....	106
5.2.5. EPR Measurements and Simulation.....	106
5.2.6. EPR Experimental Conditions	106
5.2.7. Anticancer Activity Testing.....	106
5.3. Results and Discussion	107
5.3.1. Synthesis	107
5.3.2. Crystal Structures.....	107
5.3.3. Aqueous Solution Behaviour – EPR.....	109
5.3.4. Aqueous Solution Behaviour – UV-Vis	114
5.3.5. Interactions of Complexes with hsA – EPR	115
5.3.6. Optical Measurement of hsA Binding	121
5.3.7. Biological Activity.....	123
5.4. Conclusions.....	126
6. Using <i>in vitro</i> EPR to Probe the Mechanism of Action of Ruthenium(III) Anticancer Agents.....	128
6.1. Introduction.....	128
6.2. Experimental.....	129
6.2.1. Cell Growth and Isolation of Cell Fractions	129
6.2.2. Preparation of EPR Samples	130
6.2.3. EPR Measurements and Simulation.....	131
6.2.4. EPR Experimental Conditions	131
6.3. Results and Discussion	131
6.3.1. EPR of Interactions with Isolated Cellular Components	131
6.3.2. EPR of Whole Cell Interactions.....	137
6.3.3. Temperature Dependence	141
6.3.4. Concentrations of Detected Ru(III) Species	142
6.4. Conclusions.....	143
7. Probing the Mechanism of Action of Ru(III) Anticancer Agents Using ENDOR Spectroscopy	145
7.1. Introduction.....	145
7.2. Principles of ENDOR Spectroscopy.....	146
7.2.1. Introduction to ENDOR	146
7.2.2. ENDOR Theory	148
7.3. Experimental	151

7.3.1. Synthesis	151
7.3.2. Preparation of ENDOR Samples	151
7.3.3. EPR Measurements and Simulation.....	153
7.3.4. EPR Experimental Conditions	153
7.3.5. ENDOR Experimental Conditions.....	153
7.4. Results and Discussion	153
7.4.1. Aqueous Solution Behaviour	153
7.4.2. Ligand Exchange Studies.....	164
7.4.3. Interactions with hsA.	166
7.4.4. Interactions with Individual Amino Acids.....	170
7.5. Conclusion	174
8. Future Directions	175
8.1. EPR of Ruthenium(III) Anticancer Agents in Biological Media	175
8.2. Relating the Binding Constants of Ru(III) Complexes to Antimetastatic Activity	176
8.3. Determining the Binding Constants of Ru(III) Anticancer Agents to hsTf.....	176
8.4. Synthesis of Further Hydrophobic Ru(III) Complexes.....	177
8.5. EPR of Other Paramagnetic Anticancer Metal Complexes	178
8.6. Concluding Statements	179
References	181
Appendices.....	198
Appendix A. Supplementary Information for Chapter 2.	199
Appendix B. Supplementary Information for Chapter 3.	210
Appendix C. Supplementary Information for Chapter 4.	220
Appendix D. Supplementary Information for Chapter 5.	273
Appendix E. Supplementary Information for Chapter 6.....	316
Appendix F. Supplementary Information for Chapter 7.....	333

List of Tables

Table 4-1 Crystal data and details of data collection and refinement for compounds 1a,b , 2a,b , 3a , 4b , and 5a,b	80
Table 4-2 Reduction potentials of compounds 1a,b – 5a,b vs. NHE; peak-to-peak differences in parentheses ($ E_{pc} - E_{pa} $).....	95
Table 5-1 Crystal data and details of data collection and refinement for compounds 1a , 2a , 3b , 4a , and 5a	109
Table 7-1 ENDOR-active nuclei studied in this work.	154

List of Figures

Figure 1-1	The development of platinum anticancer agents currently used in cancer therapy.....	2
Figure 1-2	A logarithmic presentation of the relative kinetics of aqueous ligand exchange for a variety of metal ions. (Figure based on references 30 and 40.) ^{33,44}	3
Figure 1-3	The human serum proteins albumin (hsA) and transferrin (hsTf).	6
Figure 1-4	Promising Ru(II)-arene anticancer agents.	8
Figure 1-5	The development of Ru(III) anticancer agents undergoing clinical evaluation.....	10
Figure 1-6	The proposed <i>in vivo</i> behaviour of Ru(III) anticancer agents.....	13
Figure 1-7	The energy level splitting diagram of an unpaired electron in an applied magnetic field.....	17
Figure 1-8	Energy levels of a system with $S = \frac{1}{2}$ and $I = \frac{1}{2}$. When resonance is achieved, two transitions are allowed (solid arrows) and are observed in the EPR spectra as two separate peaks.....	18
Figure 1-9	Typical EPR spectral shapes from different local symmetries around paramagnetic metal centres ($S = \frac{1}{2}$), shown in both the absorption and derivative modes.	20
Figure 1-10	Procedure for the simulation of a complex Ru(III) EPR spectrum from distinct species.	22
Figure 2-1	Experimental frozen-solution EPR spectra of a) KP418 (20 mM) and b) KP1019 (10 mM) immediately following dissolution in HEPES buffer, and deconvolution into rhombic and axial spectral components via simulation. For experimental conditions see 2.2.5.	29
Figure 2-2	Dispersion mode EPR spectrum of a) KP418 and b) KP1019, \dagger = principle g values of the axial spectral components, * = principle g values of the rhombic spectral components. For EPR experimental conditions see 2.2.5.....	30

Figure 2-3	EPR spectra from KP418 after incubation in HEPES buffer at 37 °C, A) experimental EPR spectra, B) deconvolution of the 6 hour spectrum by simulation. Simulation parameters: intact KP418 (\diamond); <i>KP418-H₂O</i> (\circ); <i>KP418-(H₂O)₂-trans</i> (\blacksquare); <i>KP418-(H₂O)₂-cis</i> (\blacktriangle), C) time dependence of signal intensities, determined by simulation as described in the text. For EPR experimental conditions see 2.2.5.....	33
Figure 2-4	EPR spectra of KP418 after incubation at 37 °C with A) hsA and B) whole human serum. Upper panels: individual simulated spectral components; g values and linewidths in main text and Appendix A – Table A-1. Lower panels: experimental EPR spectra and simulations constructed from weighted sums of spectral components. For EPR experimental conditions see 2.2.5.....	37
Figure 2-5	EPR spectra of KP1019 after incubation at 37 °C with A) hsTf, B) apo-hsA, and C) whole human serum. Upper panels: individual simulated spectral components; g values and linewidths in main text and Appendix A – Table A-1. Lower panels: experimental EPR spectra and simulations constructed from weighted sums of spectral components. For EPR experimental conditions see 2.2.5.	39
Figure 2-6	EPR spectra from KP418 interacting with apo-hsTf with incubation in HEPES buffer at 37 °C. a) Experimental EPR spectra, b) deconvolution of 6 hour spectrum by simulation, c) time dependence of signal intensities, determined by simulation as described in text. † – signal from trace amounts of iron-bound hsTf. For EPR experimental conditions see 2.2.5.....	41
Figure 2-7	Summary of the major reaction pathways for KP418 and KP1019 in the presence of serum proteins, as determined from EPR studies.....	47
Figure 3-1	EPR spectra of frozen solutions of NAMI-A after incubation in buffer at 37 °C. a) EPR spectra after incubation times of 0 – 24 hours. b) Deconvolution of 6 hour spectrum by simulation. c) Change in EPR signal intensity for species generated, as determined by spectral simulation. Legend: ♦ (blue) NAMI-A, \diamond (red) <i>NAMI-A-H₂O-A</i> , \blacksquare (green) <i>NAMI-A-H₂O-E</i> , \square (black) <i>NAMI-A-(H₂O)₂</i> , \blacktriangle (aqua) <i>NAMI-A-(H₂O)₃-fac</i> , \triangle (orange) <i>NAMI-A-(H₂O)₃-mer</i> , ● (purple) <i>NAMI-A-(H₂O)₄</i>	54
Figure 3-2	Speciation of NAMI-A in buffer at pH 7.4 determined from EPR measurements.....	58

Figure 3-3	EPR spectra from frozen solutions of NAMI-A after incubation in buffer with hsA at 37 °C. a) EPR spectra following incubation times of 0 – 24 hours. b) Deconvolution of 20 minute spectrum by simulation. c) Change in EPR signal intensity for species generated, as determined by spectral simulation. Legend: ◇ (red) NAMI-A, ◇ (blue) <i>NAMI-A-H₂O-A</i> , ■ (green) <i>NAMI-A-H₂O-E</i> , □ (black) <i>NAMI-A-hsA-1</i> , ▲ (aqua) <i>NAMI-A-hsA-2</i> , △ (orange) <i>NAMI-A-hsA-3</i>	60
Figure 3-4	Predominant NAMI-A ligand exchange processes with hsA, leading to three distinct protein coordinated species with characteristic EPR spectra.....	62
Figure 3-5	EPR spectra from frozen solutions of NAMI-A after incubation in whole human serum at 37 °C. a) EPR spectra following incubation times of 0 – 24 hours. b) Deconvolution of 0 minute spectrum by simulation, c) Deconvolution of 30 minute spectrum by simulation. For simulation parameters (g values and linewidths) see main text	64
Figure 3-6	EPR spectra from NAMI-A frozen solutions after incubation at 37 °C with: (a) ascorbic acid (85 µM), (b) hsA, followed by addition of ascorbic acid, (c) hsA and ascorbic acid.....	66
Figure 4-1	The promising antimetastatic agents, NAMI and NAMI-A, and the pyridine-based analogues whose synthesis is described in this chapter.....	70
Figure 4-2	Crystal structures of compounds 1a,b , 2a,b , 3a , 4b , and 5a,b	79
Figure 4-3	EPR measurements of a) 1a and b) 4b incubated in physiological buffer at 37 °C, and deconvolution of spectra collected after 10 minutes of incubation. For EPR experimental conditions see 2.2.5. For parameters used in each simulation see Appendix C – Table C-1	82
Figure 4-4	UV-Vis spectra for complexes 1a and 4a in physiological buffer, with incubation at 37 °C for up to 2 hours.....	86
Figure 4-5	EPR spectra of a) 1a and b) 4a incubated with hsA in physiological buffer at 37 °C, and spectral deconvolution of spectra collected after 30 minutes of incubation	89
Figure 4-6	Relative fractions of coordinate (gold) and non-coordinate (red) hsA bound Ru(III) complexes following 0, 10, and 60 minutes of incubation at 37 °C, as determined from integrated EPR signal intensity.....	92

Figure 4-7	UV-Vis spectrum of complex 4b in physiological buffer with hsA over 2 hours.....	93
Figure 4-8	EPR measurement of 1a and 4a after initial incubation with hsA in physiological buffer at 37 °C for the times shown; followed by the addition of ascorbic acid. For EPR experimental conditions see 2.2.5. For EPR spectra of analogous experiments with the remaining complexes see Appendix C – Figure C-25	98
Figure 5-1	The promising Ru(III) “Keppler-type” anticancer compounds KP1019 and KP1339 and their pyridine-based analogues whose synthesis is described in this chapter.	101
Figure 5-2	Crystal structures of complexes 1a , 2a , 3b , 4a , and 5a	108
Figure 5-3	EPR measurements of a) 1b and b) 4a incubated in PBS buffer at 37 °C, and spectral deconvolution of spectra collected after 120 and 30 minutes respectively. For EPR experimental conditions see 2.2.5. For spectral parameters used in each simulation see Appendix D – Table D-1	111
Figure 5-4	UV-Vis spectra for complex 1a incubated in PBS for 2 hours at 37 °C.	115
Figure 5-5	EPR measurement of complexes a) 1a , b) 3a , and c) 5a incubated in PBS buffer (1 mM, and 4% DMSO for complexes 3a and 5a) with hsA (0.5 mM) at 37 °C, and spectral deconvolution of all spectra collected (shown in red) from individual components (shown in blue). For EPR experimental conditions see 2.2.5. For spectral parameters used in each simulation see Appendix D – Table D-2	117
Figure 5-6	Relative fractions of coordinate (yellow) and non-coordinately (red) hsA bound Ru(III) complexes following 0, 2, and 24 hours of incubation at 37 °C, as determined by simulation of the EPR spectra.	120
Figure 5-7	UV-Vis spectra for complex 1a incubated with hsA in PBS buffer for 24 hours at 37 °C.	122
Figure 5-8	MTS assay results for all sodium compensated complexes following incubation with the cells for 24 hours, where: ■ = free complex in solution and ◆ = complex pre-incubated with hsA.	125

Figure 6-1	Experimental EPR and spectral simulations for NAMI-A incubated with isolated <i>S. Cerevisiae</i> cell components: (a) cell walls, (b) mitochondria, (c) cytoplasmic protein fraction, and (d) nuclear fraction. Upper panels: individual simulated spectral components; g values and linewidths in main text and Appendix E – Table E-1 . Lower panels: experimental EPR spectra and simulations constructed from weighted sums of spectral components. For EPR experimental conditions see 6.2.4.....	134
Figure 6-2	Experimental EPR and spectral simulations for KP1019 incubated with isolated <i>S. Cerevisiae</i> cell components: (a) cell walls, (b) mitochondria, (c) cytoplasmic protein fraction, and (d) nuclear fraction. Upper panels: individual simulated spectral components; g values and linewidths in main text and Appendix E – Table E-1 . Lower panels: experimental EPR spectra and simulations constructed from weighted sums of spectral components. For EPR experimental conditions see 6.2.4.....	136
Figure 6-3	EPR spectra and simulations of NAMI-A incubated with whole cells of <i>S. Cerevisiae</i> . Left panel: Spectra after different incubation time periods. A: Simulation of the EPR spectrum after 2 hours of incubation. B: Simulation of the EPR spectrum after 24 hours of incubation. For EPR experimental conditions see 6.2.4.....	138
Figure 6-4	EPR spectra and simulations of KP1019 incubated with whole cells of <i>S. Cerevisiae</i> . Left panel: Spectra after different incubation time periods. A: Simulation of the EPR spectrum after 30 minutes of incubation. B: Simulation of the EPR spectrum after 24 hours of incubation. For EPR experimental conditions see 6.2.4.....	140
Figure 7-1	Isotopically labelled i) bis-DMSO and ii) NAMI-A complexes synthesized and studied using ENDOR. (D = ^2H in each deuterium labelled compound and Im = imidazole).	146
Figure 7-2	A pictorial comparison between EPR and ENDOR spectroscopy (figure adapted from reference 298). ³²³	147
Figure 7-3	Energy level diagram for an $S = \frac{1}{2}$, $I = \frac{1}{2}$ system, (i) EPR with hyperfine interactions, and (ii) ENDOR transitions.	150
Figure 7-4	Two possible ENDOR line splitting patterns for systems where $S = \frac{1}{2}$, $I = \frac{1}{2}$	150
Figure 7-5	Solution EPR and ENDOR spectrum of KP1019 in 1:1 DMSO:glycerol, with the static field set at g_{\perp} for KP1019-Uniaxial.....	155

Figure 7-6	Frozen solution behaviour of the <i>bis</i> -DMSO complex: a) EPR spectra measured over 60 minutes of incubation at 37 °C, b) simulation of the EPR spectrum after 0 minutes of incubation, c) deconvolution of the EPR spectrum following 30 minutes of incubation.....	157
Figure 7-7	^1H ENDOR spectra of a) the unlabelled Ru(III) <i>bis</i> -DMSO complex, and its D ₆ -DMSO-labelled derivatives in b) PBS, and c) D ₂ O, centred at the ^1H Larmor frequency.....	159
Figure 7-8	^1H ENDOR of NAMI-A and its deuterated derivatives, centred at the proton Larmor frequency, where * = exchangeable.	162
Figure 7-9	ENDOR of NAMI-A and its ^{15}N -imidazole derivative.	163
Figure 7-10	ENDOR spectra of a) NAMI-A and b) D ₆ -DMSO-NAMI-A after 0 and 20 minutes of incubation at 37 °C, pH 7.4 measured with the field set at g_\perp	166
Figure 7-11	ENDOR of a) NAMI-A and the b) <i>bis</i> -DMSO complex following incubation with hsA for 30 minutes at 37 °C, pH 7.4.....	169
Figure 7-12	ENDOR spectra of a) NAMI-A following incubation with histidine and b) the resulting ENDOR spectrum of the 120 minute sample showing the full spectrum and centred at the proton Larmor frequency.....	173
Figure 8-1	Scheme to synthesize further Ru(III) compounds for potential anticancer activity.....	178

List of Acronyms

bis-DMSO	$[(\text{DMSO})_2\text{H}][\text{trans-RuCl}_4(\text{DMSO}-S)_2]$
cisplatin	<i>cis</i> -diamminedichloroplatinum(II)
DNA	deoxyribonucleic acid
EDTA	ethylenediaminetetraacetic acid
ENDOR	electron nuclear double resonance
EPR	electron paramagnetic resonance
HEPES	(4-(2-hydroxyethyl)-1-piperazineethanesulfonic acid)
hsA	human serum albumin
hsTf	human serum transferrin
kDa	kilodalton
KP418	imidazolium [<i>trans</i> -RuCl ₄ (1 <i>H</i> -imidazole) ₂]
KP1019	indazolium [<i>trans</i> -RuCl ₄ (1 <i>H</i> -indazole) ₂]
KP1339	sodium [<i>trans</i> -RuCl ₄ (1 <i>H</i> -indazole) ₂]
LW	linewidth
NAMI	sodium [<i>trans</i> -RuCl ₄ (1 <i>H</i> -imidazole)(DMSO- <i>S</i>)]
NAMI-A	imidazolium [<i>trans</i> -RuCl ₄ (1 <i>H</i> -imidazole)(DMSO- <i>S</i>)]
NTA	nitrilotriacetic acid
PBS	phosphate buffered saline
RF	radiofrequency

1. Introduction – Ruthenium Anticancer Agents

1.1. From Platinum to Ruthenium

The landmark discovery in 1965 of the antitumour properties of *cis*-diamminedichloroplatinum(II) (cisplatin) heralded a new era of anticancer research using metallopharmaceuticals.^{1,2} Currently, platinum-based anticancer agents are used in greater than 50% of clinical cancer treatments.^{3,4} Cisplatin (**Figure 1-1**) is particularly effective against solid tumour types, such as testicular, ovarian, head, and neck cancers.⁵ Despite its clinical success, the quest for alternatives to cisplatin remains important, since Pt-based anticancer drugs have two significant disadvantages: high intrinsic toxicity,⁶ and resistance (either acquired or intrinsic) from various cancer types.^{6,7} The first drawback is the most problematic since the primary target of Pt-based anticancer drugs, DNA, is present in all cells.⁸ This results in a low specificity of cisplatin for tumour cells, while several cell lines have even developed resistance to cisplatin,^{9,10,11} thereby motivating the derivatization of cisplatin through the incorporation of various amine and anionic ligands.^{7,12} Such studies resulted in the second generation platinum drug carboplatin ($[\text{Pt}(\text{C}_6\text{H}_6\text{O}_4)(\text{NH}_3)_2]$) (**Figure 1-1**), which is used in the treatment of ovarian cancer.¹³ Further developments have produced several promising and currently administered clinical candidates, such as the third generation compound oxaliplatin, which is effective in colon cancer treatment (**Figure 1-1**).¹⁴⁻¹⁶ Both carboplatin and oxaliplatin display diminished side effects when compared with their predecessor cisplatin,¹⁷ however their primary target remains DNA, which has been problematic when dealing with the issue of acquired resistance.^{18,19} To overcome these issues, thousands of platinum-based analogues have been synthesized,^{6,12,20-22} including the incorporation of other metals.^{23,24} To date, numerous metals have been utilized in the development of anticancer agents, these include: bismuth, copper, gallium, gold, molybdenum, osmium, ruthenium, tin, titanium, and zinc.²⁵ The focus of this research has been on ruthenium anticancer agents, specifically those with Ru in the 3+ oxidation state.

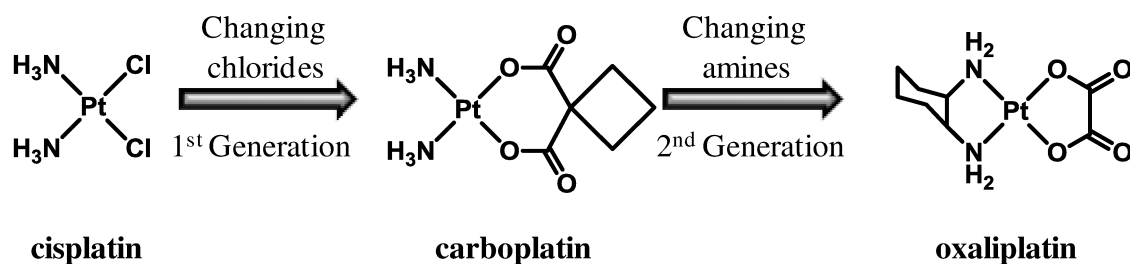


Figure 1-1 The development of platinum anticancer agents currently used in cancer therapy.

1.2. Ruthenium Anticancer Agents

The use of ruthenium complexes as anticancer agents began with the discovery that the complex *fac*-[RuCl₃(NH₃)₃] inhibited cell division of *Escherichia coli* cells at a comparable concentration to cisplatin.²⁶ This was further developed in the early 1980s by Clarke *et al.* with a report that the related Ru(II) complex *cis*-Ru(NH₃)₄Cl₂ displayed anticancer activity.²⁷ Aqueous solubility was an issue for such complexes,²⁸ inhibiting further clinical evaluation, which motivated the synthesis of new Ru complexes and led to the emergence of several promising Ru(II) and Ru(III) anticancer drug candidates.²⁹⁻³¹

Complexes containing Ru exhibit a variety of appealing characteristics, such as: i) octahedral geometry allowing for the possibility of up to 30 stereoisomers,³² ii) slow ligand exchange kinetics,³³ iii) a range of available oxidation states (II-IV) under physiological conditions,³⁴ and iv) interactions with transport proteins which allows for the potential selective delivery of the complexes to tumour sites.³ Each property will be discussed in further detail below.

1.2.1. Octahedral Geometry

Ru anticancer complexes are predominately hexacoordinate with octahedral geometry, as opposed to the square planar geometry of Pt(II) anticancer agents.³⁰ This structural difference led to the early proposal for an alternative mode of action of Ru complexes,³⁵ as compared to the DNA targeting of square planar Pt(II) anticancer agents.^{33,36} By exploiting the ability of Ru to coordinate six ligands, the synthesis of enantiomeric Ru(II) half-sandwich complexes which mimic enzyme inhibitors was

achieved.³² These complexes have recently drawn attention for their respective anticancer activity,^{30,37-40} displaying the possibilities that exist in the design of novel bioactive organometallic species.

1.2.2. Ligand Exchange

For metal-based drugs, ligand exchange has a significant impact on their biological activity since few drugs reach their biological target prior to being modified. For ruthenium complexes, the rate of Ru(II) and Ru(III) ligand exchange is similar to that of Pt(II) complexes. These exchange rates are slow, on the order of minutes to days, as shown in **Figure 1-2** for aqueous ligand exchange.⁴¹ This is a highly desirable quality since these rates are on the order of cell division processes,⁶ meaning the therapeutic agents can reach their biological target prior to being biologically altered.⁴² Although it is generally accepted that Ru(II) complexes are more labile than Ru(III),^{41,43} the kinetics of ligand exchange for such complexes is dependent on the nature of the chelating ligands and the overall charge on the complex.²⁵ Such changes can have a dramatic effect on the crystal field splitting, which in turn can impact the activation energy for aquation.

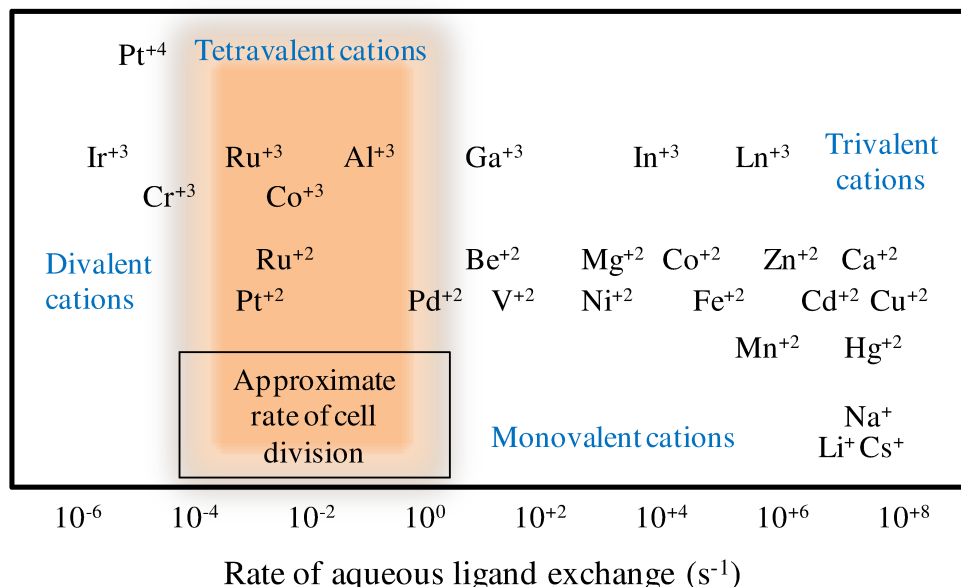


Figure 1-2 A logarithmic presentation of the relative kinetics of aqueous ligand exchange for a variety of metal ions. (Figure based on references 30 and 40.)^{33,44}

1.2.3. Oxidation State

Ruthenium is unique among the platinum metals in that several oxidation states are accessible under physiological conditions.³⁴ Furthermore, the redox potential of Ru complexes can be tuned by varying the ligands around the metal centre.^{45,46} In biological systems, reducing agents such as glutathione (up to 10 mM in blood)⁴⁷ and ascorbic acid (11-79 µM in blood)⁴⁸ have been postulated to play an important role in the speciation of Ru anticancer compounds, leading to the “activation by reduction” hypothesis for Ru(III) anticancer compounds.^{28,49} This postulates that the conversion from Ru(III) to Ru(II) is achieved *in vivo* either by biological reducing agents or within tumour cells. The rapid cell division of many cancer cells leads to high oxygen and nutrient requirements.⁵⁰ However, the development of blood vessels is slow compared to tumour growth, leading to a lower than normal O₂ level in cancer cells (hypoxia).^{34,51} This can also lead to alternative energy processes in tumour cells resulting, for example, in a decrease in the cellular pH from 7.4 to 5.8.⁵² These differences between normal and tumour cell metabolism should favour the selective reduction of Ru(III) to Ru(II) within tumours.^{49,53} This then activates the compounds towards ligand substitution and increases their propensity for binding to biomolecules.⁴⁶ With a similar coordination environment, Ru(II) complexes are more actively substituted than Ru(III) in the absence of π-bonding effects.⁴¹ Reduction from Ru(III) to Ru(II) results in a filled t_{2g} orbital set, meaning that π-donor ligands that were coordinated firmly to the Ru(III) metal centre become less strongly bound to the Ru(II) metal centre.⁴⁹ This has been proposed as a prodrug targeting strategy for Ru(III) complexes, since they could be preferentially reduced in the hypoxic environments frequently found in tumours.^{46,54-56}

1.2.4. Transport Protein Interactions

Iron mimicking has been suggested to be a key feature in the selective delivery of Ru anticancer agents to tumour cells.⁵⁷ As mentioned previously, rapidly dividing tumour cells have increased nutrient requirements. One possible consequence of this is the upregulation of transferrin receptors on their cell surface, resulting in the sequestering of

more iron-loaded transferrin.⁵⁸ Previous *in vivo* studies have shown a 2- to 12-fold increase in Ru concentration in cancer cells compared to healthy cells, depending on the cell type.⁵⁹ Such selective delivery of Ru anticancer complexes has been implicated in a dramatic decrease in off-target activities when compared to their platinum predecessors.^{4,34,35,60,61} This is believed to be due to the ability of Ru to bind to the serum transport proteins albumin (hsA) and transferrin (hsTf).^{49,62} A central focus of the work in this thesis concerns the interactions of Ru(III) anticancer complexes with serum proteins, specifically hsTf and hsA.

1.3. Serum Proteins

1.3.1. Human Serum Transferrin

hsTf is a monomeric glycoprotein which binds iron reversibly (**Figure 1-3**).⁶³ This iron-transport protein is capable of binding up to two Fe³⁺ ions in solution, with Fe³⁺ selected preferentially to Fe²⁺. Fe(III) binding sites are located within the C- and N-terminal lobes of the protein, with both lobes being highly homologous.⁶⁴ Within each lobe, the Fe ion exists in an octahedral binding site, consisting of two tyrosines, a histidine, an asparagine, and a synergistic bidentate carbonate anion.⁶⁵ All forms of transferrin (apo – no Fe, mono – 1 Fe, and diferric – 2 Fe) are recognized by the transferrin receptor protein on the cell surface, however diferric transferrin has the highest affinity.⁵⁸ Once bound to cell-surface receptors, hsTf is encapsulated in a membrane bound vesicle (endosome). Inside the endosome the pH is lowered from 7.4 to 5.5, which leads to release of the iron ions from transferrin.⁶⁶ The newly formed iron-free apotransferrin remains bound to its receptor with a high affinity at low pH. It is then recycled back to the cell surface and liberated at extracellular, physiological pH.^{58,67}

With a blood concentration of ~35 μM,⁶⁸ hsTF (molecular weight 80 kDa) is approximately 30% saturated with Fe³⁺, thereby allowing for the transportation of other species, including endogenous metal ions into cells.^{69,70} This property of hsTf has been the inspiration for novel drug design strategies, exploiting the natural function of this protein.⁷¹⁻⁷³ As mentioned previously, in several cancers the expression of transferrin

receptors on the tumour-cell surface is upregulated, leading to an increase in the number of receptors on the cell surface.⁶⁶ This has been the basis for a focus on hsTf as a system for targeted delivery of metal-based drugs into cancer cells, while leaving normal cells relatively unaffected, and consequently, minimizing side effects.³⁴ It has been shown that ruthenium can be transported into cancer cells via both transferrin-dependent and transferrin-independent mechanisms.⁷⁴

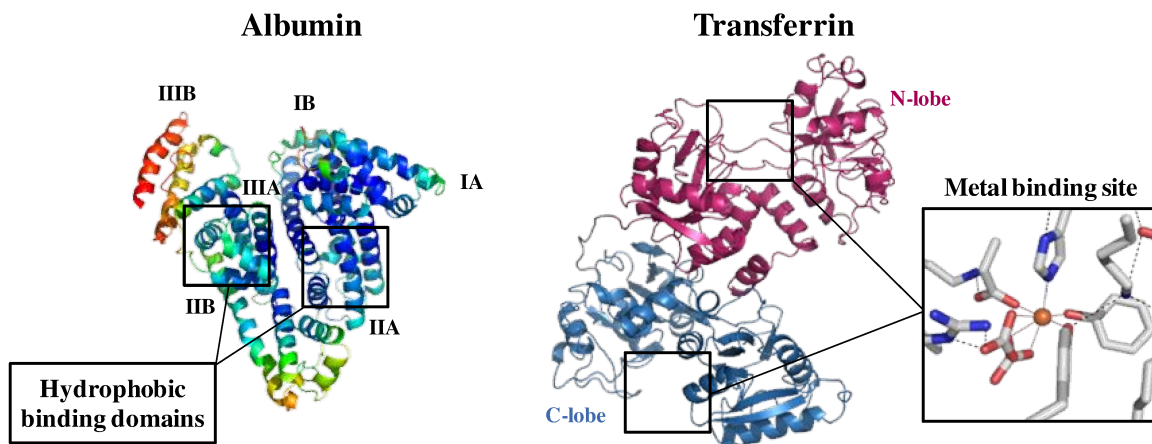


Figure 1-3 The human serum proteins albumin (hsA) and transferrin (hsTf).

1.3.2. Human Serum Albumin

Albumin (**Figure 1-3**) is an abundant multifunctional protein in the human circulatory system. This small (66 kDa) monomeric protein contains 585 amino acids, subdivided into 3 homologous α -helical domains, numbered I, II, and III.^{75,76} Each domain can be further subdivided, with subdomains IIA and IIIA containing the well-established hydrophobic binding pockets of various pharmaceuticals and other molecules.⁷⁷⁻⁷⁹ The first binding site, known as Sudlow's site I,^{80,81} is within subdomain IIA. Here the wall of the pocket is formed by hydrophobic amino acid side chains, while entrance to the pocket is guarded by positively charged amino acid residues, such as lysine, arginine, and histidine.^{82,83} The second drug binding site, Sudlow's site II,^{84,85} is located within subdomain IIIA. The wall of this pocket is again lined with hydrophobic side chains, with an arginine residue (Arg-410) located at the entrance, while the hydroxyl moiety of a tyrosine residue (Tyr-411) faces the inside of the pocket.^{82,83}

With a physiological concentration of ~0.60 mM,^{68,75} hsA is the most abundant protein in the circulatory system. At physiological pH, hsA adopts a helical conformation (67% α -helical content), and its amino acid sequence contains 17 disulphide bridges, with a single free cysteine (Cys-34), and one tryptophan residue (Trp-214) which sits in Sudlow's site I.^{75,86} Albumin has been found to bind a variety of compounds such as fatty acids, bilirubin, metal ions, steroid hormones, vitamins, and pharmaceuticals.^{77,86,87} Serum albumin performs a variety of physiologically important functions such as control of osmotic blood pressure, radical deactivation, and delivery of amino acids after hydrolysis for the synthesis of proteins, in addition to the transport, metabolism, and distribution of various compounds (including drugs) within the body.^{57,75,76}

1.4. Ru(II) Anticancer Agents

The field of Ru(II) anticancer agents is dominated by Ru(II)-arene complexes,⁸⁸ pioneered by the work of both Dyson and Sadler.^{89,90} Both groups used the same half-sandwich, “piano-stool” Ru(II) scaffold as shown in **Figure 1-4a**, where the arene forms the seat of the piano stool and the ligands resemble the legs. Linking the ligands Y and Z to form a bidentate chelating ligand (L) appears to be advantageous towards anticancer activity.⁹¹ The structure of Ru(II)-arene complexes allows for the facile modification of the three main building blocks, the monodentate ligand X, the bidentate ligand L, and the arene, each of which can be modified to improve the pharmaceutical properties of the complex.⁹² Previous studies have shown that the nature of the chelating ligand can help control the stability and ligand-exchange kinetics of the complex, while the nature of the arene ligand can help influence cell uptake and interactions with biological targets.^{93,94} “Half-sandwich” Ru(II) mono-arene complexes often possess good aqueous solubility, which is an advantage for clinical use.⁹⁵ Additionally, the arene ligand is relatively inert towards displacement under physiological conditions.⁹⁶ The leaving group, which is typically a chloride, occupies the biomolecule binding site on the metal centre, and can be of importance to control the timing of activation of these complexes.^{96,97}

One important class of Ru(II) anticancer complexes is arene diamine compounds which have the cation $[(\eta^6\text{-biphenyl})\text{Ru}(N,N\text{-}1,2\text{-ethylenediamine})\text{Cl}]^+$, as shown in

Figure 1-4b.⁹⁸ One promising candidate of this type, RM175, which has a compensating hexafluorophosphate (PF_6^-) anion, displays promising anticancer activity *in vitro* against colorectal cancer cells, with DNA as the primary target.^{99,100} Substitution of the anion of RM175 for chloride led to another promising anticancer complex, ONCO4417. This compound displayed high antineoplastic activity *in vivo*, with comparable efficacy to platinum anticancer complexes against a number of tumour cell lines.¹⁰¹

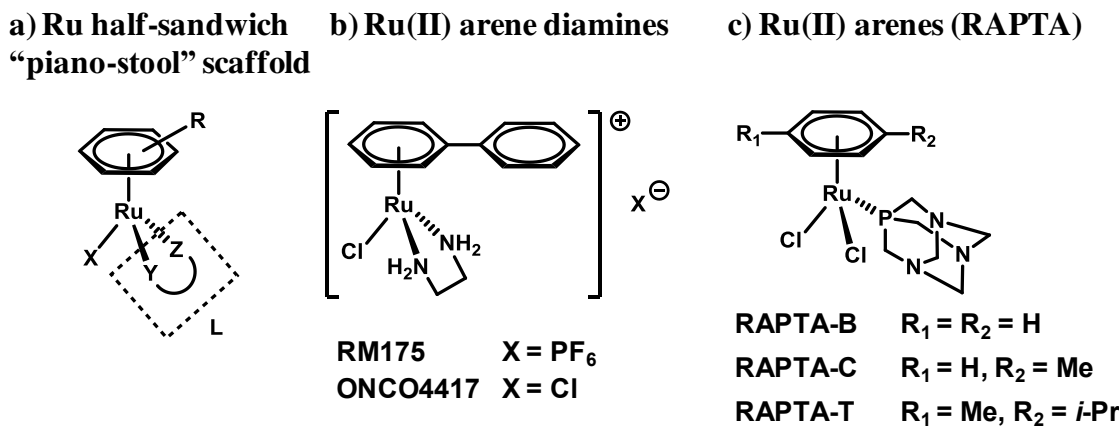


Figure 1-4 Promising Ru(II)-arene anticancer agents.

A second class of Ru(II) arenes are known as the “RAPTA” family of compounds, and contain a coordinating phosphoadamantane ligand (Figure 1-4c).^{102,103} The first clinical candidate, RAPTA-B, was found to be weakly cytotoxic against tumour cells while displaying minimal toxicity towards healthy cells.^{93,94} This led to the next generation RAPTA-C (η^6 -*p*-MeC₆H₄Prⁱ)Ru(*P*-pta)Cl₂ and RAPTA-T complexes (η^6 -*p*-MeC₆H₄Prⁱ)Ru(*P*-pta)Cl₂, where (*pta* = 1,3,5-triaza-7-phospha-tricyclo-[3.3.1.1]decane).¹⁰⁴ RAPTA-C inhibited cell growth significantly, triggering apoptosis in Ehrlich ascites carcinoma cell lines,¹⁰⁵ while RAPTA-T showed antimetastatic activity in breast cancer cell lines.¹⁰⁶ RAPTA-T is currently undergoing further preclinical evaluation.⁵⁴

1.5. Ru(III) Anticancer Agents

The most promising ruthenium(III) drug candidates are generally negatively charged octahedral complexes containing axial heterocyclic nitrogen donor ligands and four equatorial chlorides completing the coordination sphere, while charge compensation is typically provided by protonated nitrogen heterocycles or sodium ions.^{3,31,49,107,108} The most prominent examples of these compounds are imidazolium [*trans*-RuCl₄(1*H*-imidazole)(DMSO-*S*)] (NAMI-A), with a single axial heterocyclic nitrogen ligand and DMSO at the other axial position, and indazolium [*trans*-RuCl₄(1*H*-indazole)₂] (KP1019) (**Figure 1-5**), both of which have completed phase-I clinical trials successfully.¹⁰⁸⁻¹¹¹ NAMI-A, currently undergoing phase I/II clinical trials, is being evaluated for the use in second line combination drug therapy for the treatment of Lewis lung carcinoma.⁵⁴ Further clinical evaluation of KP1019 led to failure in phase II trials due to poor solubility,¹¹² leading to the use of its sodium compensated analogue, KP1339, which has significantly improved (35-fold) increase in aqueous solubility.^{107,113} The clinical success of these two complexes has led to further incorporation of additional heterocyclic ligands (2nd generation)¹¹⁴⁻¹¹⁷ and additional metals, forming bi-metallic Ru(III) anticancer complexes (3rd generation)¹¹⁸⁻¹²¹ (**Figure 1-5**). This thesis will focus primarily on the KP1019 and NAMI-A families of compounds.

NAMI-A and KP1019 share several important chemical features: (i) Ru(III) oxidation states, (ii) octahedral geometry, (iii) kinetically inert axial heterocyclic ligands, (iv) exchangeable ligands (Cl⁻, or DMSO), and (v) an overall -1 charge and corresponding counterions. Despite these similarities, each complex shows quite different anticancer activity, with KP1019 exhibiting significant antineoplastic activity in contrast to NAMI-A, which is comparatively non-cytotoxic but shows excellent antimetastatic properties.^{49,53,57,107-109,122-128}

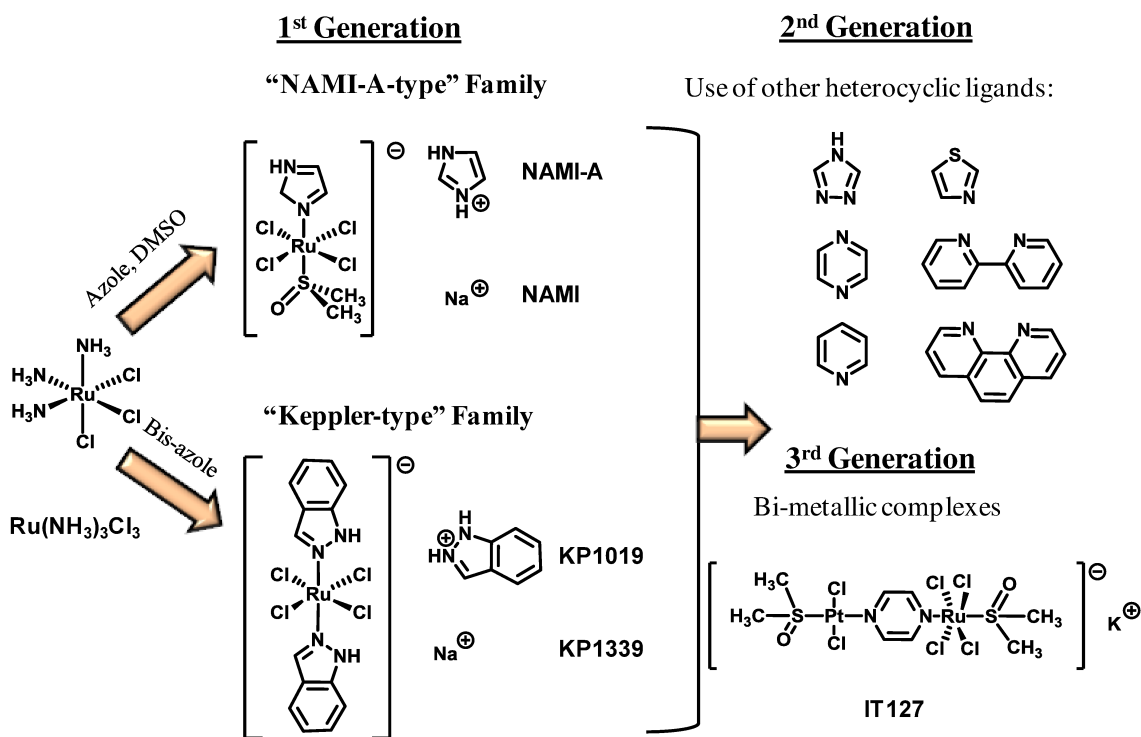


Figure 1-5 The development of Ru(III) anticancer agents undergoing clinical evaluation.

1.5.1. “Keppler-type” Family of Ru(III) Complexes

The “Keppler-type” family of Ru(III) anticancer compounds consists of Ru(III) complexes having the general formula [RuCl₄L₂]⁻HL/Na⁺, where the heterocyclic nitrogen ligands (L) are arranged in a *trans* configuration. These types of Ru(III) compounds were first reported in the late 1980s, beginning with the synthesis of imidazolium [*trans*-RuCl₄(1*H*-imidazole)₂] (KP418).¹²⁹ Subsequently, several derivatives have been synthesized,^{45,130,131} the most promising of which are the bis-indazole complex KP1019 and its sodium analogue KP1339 (**Figure 1-5**).^{132,133} Despite their structural similarities, the observed activities of KP418 and KP1019/KP1339 are dramatically different. Preliminary screening of KP1019 showed promising activity against over 50 tumour cell lines,¹³⁴⁻¹³⁷ suggesting its potential as a broad-spectrum anticancer agent. The highest activity was observed in the human colon carcinoma cell lines HT29 and SW480,¹³⁸ where the induction of apoptosis was via the intrinsic mitochondrial

pathway.¹³⁷ Interestingly, only a low degree of acquired resistance was observed in KB-3-1 epithelial cells following treatment with KP1019 for over one year, suggest a mechanism of action that is different from cisplatin.¹³⁹ Additionally, the observation of reactive oxygen species and DNA strand breaks provided preliminary evidence for the complexity of the mechanism of action for this complex.¹³⁶ *In vitro* testing of KP418 demonstrated comparable antiproliferative activity against human colon cancer cell lines,^{134,140} but it exhibited significantly higher long-term side effects.^{140,141}

KP1019 entered phase I clinical trials in 2004, and was found to be effective on 5 of the 6 patients tested.^{107,109} Following treatment with KP1019, mild toxicity was observed, however this was confounded by the relative insolubility of the complex, leading to the use of its more soluble sodium analogue KP1339 which has progressed further in clinical trials.¹⁴² Interestingly, the activity of KP1339 is somewhat diminished when compared to KP1019, most significantly when tested against the SW480 human colorectal cancer cell line,¹⁴³ against which KP1019 has a well established activity profile.^{136,137} Understanding the source of activity of KP1019 when compared to both KP418 and KP1339 remains highly important, particularly for future drug design.

1.5.2. “NAMI-A-type” Family of Ru(III) Complexes

The “NAMI-A-type” family of Ru(III) complexes are structurally similar to the “Keppler-type”, except that they have a DMSO ligand in one of the axial coordination sites. As mentioned earlier, Ruthenium-DMSO complexes were first described in the early 1980s as potential cancer therapeutics.^{27,144} The rationale behind using DMSO as a ligand are several, as it is an ambidentate ligand, capable of coordinating through the sulphur or oxygen atoms, a property which is governed by sterics and electronics.¹⁴⁵ Additionally, DMSO can impart desirable pharmaceutical properties such as water solubility and its intrinsic capacity to diffuse through phospholipid membranes.¹⁴⁶ This led to the synthesis of a *bis*-DMSO complex: hydrogen *trans*-[*bis*(dimethyl sulfoxide)tetrachlororuthenate(III)] in the early 1990s by the group of Gianni Sava.¹⁴⁷ This has been used as the precursor for the azole ligated complexes,^{148,149} including the clinical candidates NAMI-A and its sodium compensated analogue NAMI (**Figure**

1-5).¹⁵⁰ Although modest antimetastatic activity is observed for NAMI,^{151,152} NAMI-A has been observed to display better pharmacological properties and chemical stability.^{153,154} NAMI-A is the most intensively studied ruthenium(III) anticancer complex, and has attracted particular attention because of its ability to prevent the formation of metastases and inhibit their growth.^{127,128,153-165} This complex has shown relatively modest cytotoxic activity in experimental *in vivo* models and has been the focus of ongoing research specifically for its antimetastatic properties.^{128,158,159}

The ability of NAMI-A to selectively target metastases is of significance in the field of cancer therapy. Metastatic cancer is defined as the spread of tumour cells into not only neighbouring healthy tissue, but throughout the body.¹⁶⁶ The dispersive nature of metastases renders them inaccessible to surgery or radiotherapy, leaving chemotherapy as the primary treatment option.¹⁶⁷ However, metastases are often poorly responsive to chemotherapy, and therefore, more often than the primary tumour, represent the leading cause of cancer death.^{165,168} The low cytotoxicity of NAMI-A has been attributed to its high selectivity for metastatic cells over other tumour cells. Since the cell population of a tumour is heterogeneous, only a small fraction possesses metastatic ability. It has been suggested that NAMI-A selectively targets this fraction of the primary tumour, which is subsequently observed as a modest cytotoxicity.^{25,54}

In 1999 NAMI-A became the first ruthenium complex to be clinically evaluated on humans. It successfully completed phase I clinical trials, using 24 patients who showed a good tolerability over a wide range of sub-toxic doses. Upon receiving high doses of NAMI-A, drug related-toxicities such as nausea and vomiting were observed, in addition to mild renal dysfunction which was reversible following treatment.¹⁶⁹ NAMI-A is currently undergoing phase I/II trials, being used in combination therapy with Gemcitabine for the treatment of metastatic non-small-cell lung carcinoma.⁵⁴

1.5.3. Mechanism of Action

It is now well established that compounds such as NAMI-A and KP1019 are prodrugs, where aqueous ligand exchange and protein interactions (**Figure 1-6**) are key

features in their biological speciation.^{57,107,140,170-176} In physiologically relevant aqueous solutions, KP1019 exchanges chloride ligands to give insoluble species.^{170,172,177} Under the same conditions NAMI-A exchanges DMSO and chloride ligands to give several water-soluble mono-nuclear polyqua species, and also forms oligomeric species that eventually predominate in solution.^{128,176,178} For both complexes these exchange processes are highly pH and temperature dependent, leading to their administration by infusion at slightly acidic pH, conditions under which aquation suppressed.^{122,174,176} Fundamentally, the differences in the axial ligands of NAMI-A and KP1019 led to distinct behaviour, both when prepared in buffered saline solutions and *in vivo*.

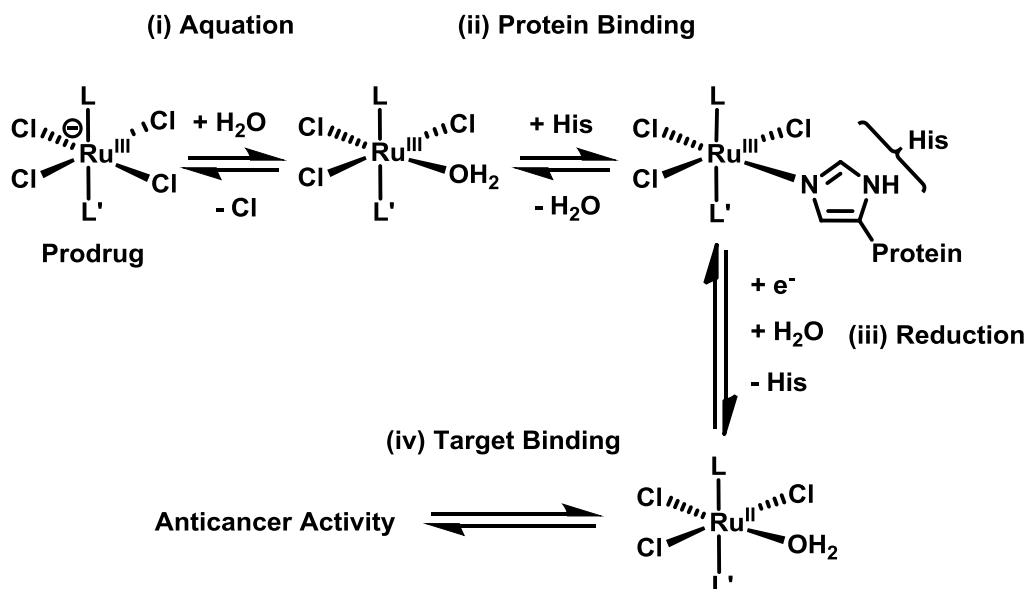


Figure 1-6 The proposed *in vivo* behaviour of Ru(III) anticancer agents.

After infusion, both compounds can interact with various species, and small molecule components of blood, such as chloride and ascorbate likely play important roles in their *in vivo* speciation.^{176,179,180} Serum proteins, particularly hsA and hsTf, have also been identified as key players in the transport and speciation of NAMI-A, KP1019, and other ruthenium complexes.^{122,175,181-184} A number of reports have demonstrated that both these complexes can coordinate to hsA and hsTf to give relatively stable species via ligand exchange with amino acid side chains, most likely from histidine and possibly

cysteine.^{116,171} Within the literature hsTf was initially regarded as the predominant vector for delivery of the Ru(III) species to cancer cells *in vivo*, via a “Trojan Horse” mechanism.^{172,185-187} However, recent studies have shown that albumin binding can dominate *in vivo*,^{111,188,189} which has been exploited in current drug design strategies.¹⁹⁰⁻¹⁹²

Following cell entry, the ultimate biological fate of both KP1019 and NAMI-A is largely unknown. The leading theory is that the complexes are reduced within the hypoxic environment of tumour cells,⁴⁹ however this has not been proven experimentally. Furthermore, the primary biological targets responsible for the observed contrasting modes of activity remain unclear. In contrast to cisplatin, DNA has been suggested to not be the primary target, as both complexes form DNA-crosslinks that are inferior to that of cisplatin.^{193,194} Recent studies have suggested that KP1019 binds with low molecular weight cytoplasmic proteins,^{112,143} and that the environment around the Ru centre consists of sulfur, nitrogen, or oxygen donor groups.^{188,195}

For NAMI-A, the highly selective anti-metastatic nature of this complex has been extensively studied with a particular effort in relating the *in vitro* experimental findings to its observed *in vivo* activity. Several studies have highlighted the diverse nature of the observed antimetastatic activity for NAMI-A, including: (i) NAMI-A stops cell proliferation at the G₂M pre-mitotic phase,¹⁹⁶ (ii) at concentrations of 1 μM – 50 μM, depending on cell line, NAMI-A has been observed to interact with integrins on the cell surface, increasing the tumour adhesion to the culture substrate, thereby preventing cell migration,^{125,163,164} (iii) at doses giving observable anti-metastatic activity, it affects several functions of endothelial cells, thus inhibiting angiogenesis,¹⁹⁷ (iv) NAMI-A acts as a nitric oxide scavenger,¹⁹⁸ and (v) with induction of apoptosis NAMI-A down-regulates the extracellular signal-regulated kinase (ERK1/2), thus inhibiting the mitogen activated protein kinase (MAPK) signaling pathway.^{157,199} Overall the observed biological effects of NAMI-A suggest that this drug acts through a complex mechanism, at both the extracellular and intracellular level.

The chemical and biochemical basis for the activities of both KP1019 and NAMI-A is an active area of research, focusing on: (i) identification of the species formed in

physiological media, (ii) the link between structure and anticancer activity, (iii) interactions with serum proteins, particularly human serum transferrin (hsTf) and human serum albumin (hsA), and (iv) interactions with intracellular molecules, such as nucleotides and glutathione. A variety of analytical techniques have been applied to these areas of research for both families of Ru(III) anticancer complexes, including: spectrophotometric methods,^{174,175,178,200-202} NMR,^{176,178,200,201,203} electrochemistry,^{45,116,204,205} mass spectroscopy,^{113,116,143,203,206} X-ray absorption spectroscopy (XAS),^{188,191,195,207-209} HPLC,^{170,174,210} circular dichroism,^{74,200} and capillary-zone electrophoresis.^{116,211,212} In addition, density functional theory (DFT) calculations on the solvation of both KP1019 and NAMI-A have been reported recently.²¹³⁻²¹⁷ Unfortunately, these studies do not give a coherent or complete picture of the behaviour of these complexes under physiological conditions, information essential for future clinical applications.

One technique that is complementary to these areas of research is electron paramagnetic resonance (EPR) spectroscopy, which has been used extensively in this thesis. Electron paramagnetic resonance spectroscopy (EPR) is uniquely suited to studies of Ru(III) complexes, as this technique can characterize the structure and symmetry of paramagnetic Ru(III) ($4d^5$, low spin $S = \frac{1}{2}$) centres and determine changes to the ligands of complexes and their geometry.^{218,219} This allows for the direct detection of aquation processes and biomolecules interactions. Furthermore, since Ru(II) ($4d^6$, $S = 0$) is diamagnetic and EPR silent, reduction of Ru(III) centres can be followed by loss of EPR signal intensity.

1.6. Electron Paramagnetic Resonance Spectroscopy

This thesis reports the first application of EPR to characterize the behaviour of Ru(III) anticancer complexes in a variety of physiologically relevant environments. Since EPR only detects species with unpaired electrons, it unequivocally differentiates between the Ru(III) and Ru(II) oxidation states of the complexes, allowing detection of reduction processes that may occur under physiological conditions. In addition, EPR is highly

sensitive to changes in the first coordination sphere of paramagnetic centres, and thus is ideal for characterizing ligand-exchange processes for Ru(III).

1.6.1. Basic Principles of EPR

In spectroscopy, energy level differences, ΔE , are probed by radiation with frequency (ν), given by:

$$\Delta E = h\nu \quad (1.1)$$

where h is Plank's constant. In EPR, ΔE results from interactions of the magnetic moments of the electrons with magnetic fields. The magnetic moments (μ_z) of electrons arise from their intrinsic spin angular momentum ($S = \frac{1}{2}$). The interaction between the electron magnetic moment and a magnetic field is known as the Zeeman interaction, with energy given by:

$$E_{\text{Zeeman}} = -\mu_z B_z \quad (1.2)$$

where B_z is the applied magnetic field ($B_z = B_0$), and the magnetic moment of an electron is defined by:

$$\mu_z = -g_e \mu_B m_s \quad (1.3)$$

The first term g_e , is the free electron g value. The second term, μ_B , is the Bohr magneton, which is the natural unit of the electronic magnetic moment, and m_s is the magnetic spin quantum number. By substituting equation 1.3 into 1.2 the Zeeman energy for a free electron placed in a magnetic field is given by:

$$E_{\text{Zeeman}} = g_e \mu_B B_z m_s = \pm \frac{1}{2} g_e \mu_B B_z \quad (1.4)$$

The energy separation between the ground state ($m_s = -\frac{1}{2}$) and the excited state ($m_s = +\frac{1}{2}$) is defined as the Zeeman splitting (**Figure 1-7**) which from equation 1.4 is given by:

$$\Delta E_{\text{Zeeman}} = g_e \mu_B B_0 \quad (1.5)$$

for a free electron, and thus transitions can occur when the resonance condition is satisfied:

$$\Delta E = g_e \mu_B B_0 = h\nu \quad (1.6)$$

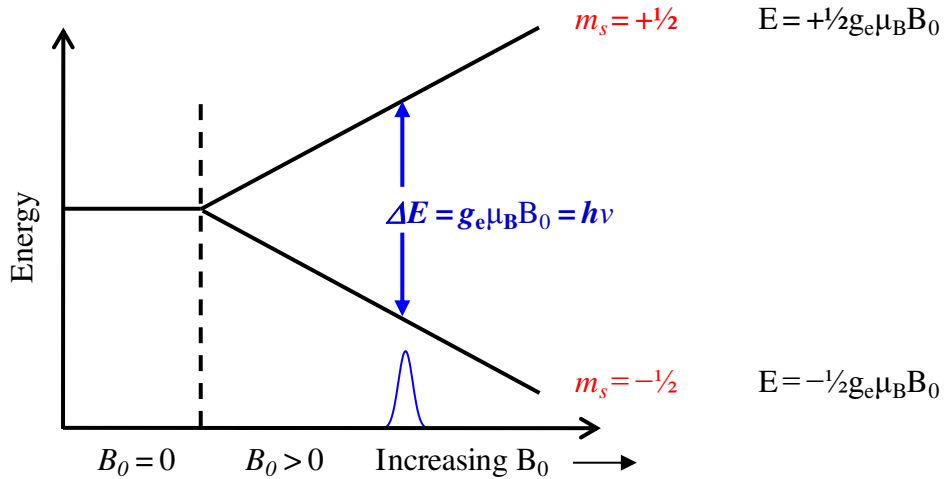


Figure 1-7 The energy level splitting diagram of an unpaired electron in an applied magnetic field.

In a paramagnetic sample, the observed transitions do not usually occur at the free-electron g value. This is primarily due to the effective field experienced by the electrons, which is generated not only by the applied magnetic field, but also from contributions from the local environment. EPR transitions are described by the observed g values, which can be calculated from the resonance condition:

$$g = h\nu / (\mu_B B) \quad (1.7)$$

where B is the experimentally measured transition magnetic field and g is the g value corresponding to the effective field at the electron. B represents the vectorial sum of the local magnetic field and the applied magnetic field. Therefore, the difference between g and g_e indicates how much the local magnetic field around the electron differs from the applied magnetic field.

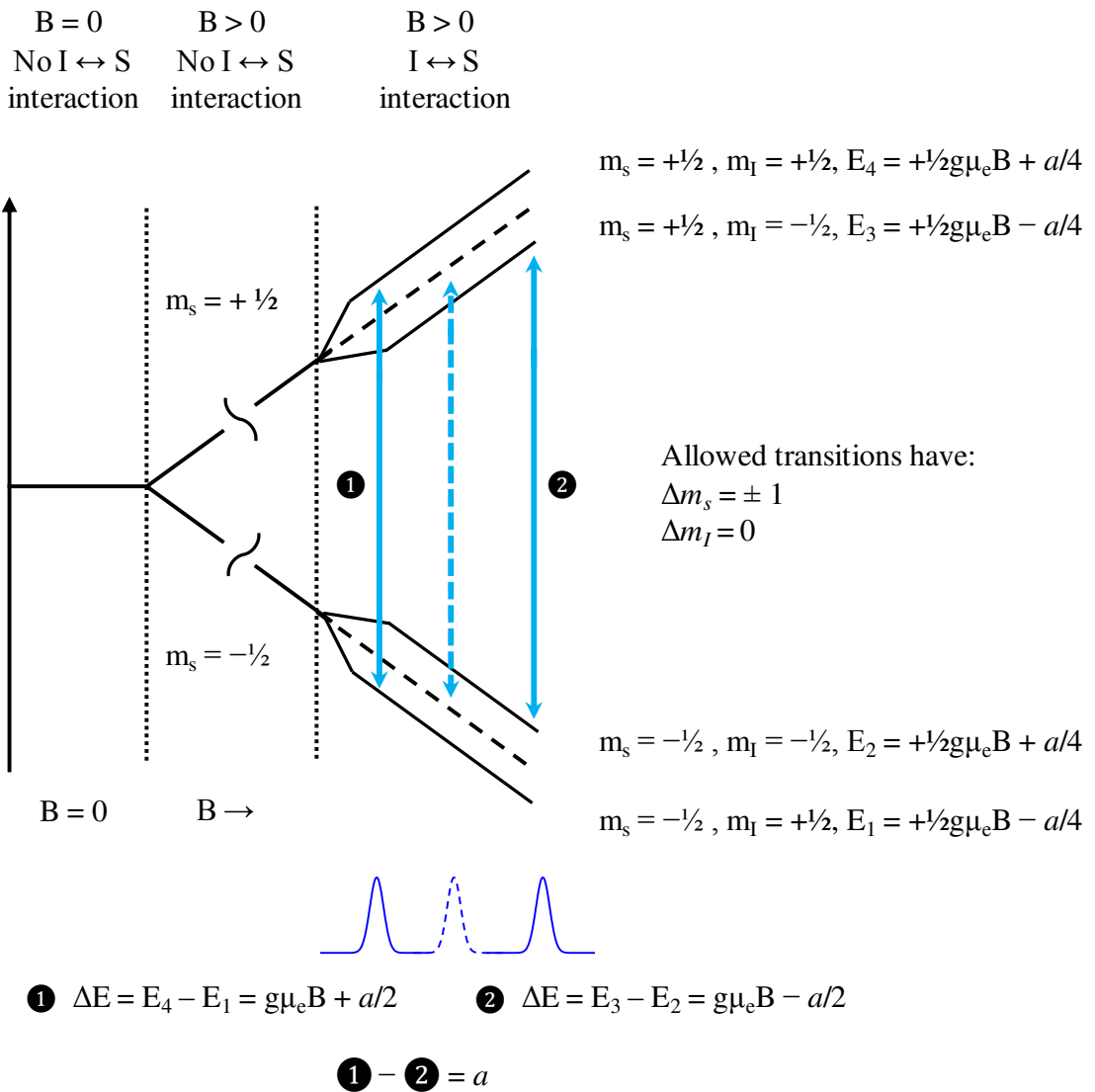


Figure 1-8 Energy levels of a system with $S = \frac{1}{2}$ and $I = \frac{1}{2}$. When resonance is achieved, two transitions are allowed (solid arrows) and are observed in the EPR spectra as two separate peaks.

The nuclei of atoms in paramagnetic species have their own magnetic moments if their nuclear spin $I > 0$, which can interact with magnetic moments of unpaired electrons. The interaction between the unpaired electron and spin-active nuclei is known as the hyperfine (HF) interaction, and can be due to two possible types of interactions: isotropic and anisotropic. The anisotropic hyperfine interaction arises from through-space interactions between the magnetic dipole of the unpaired electron with the magnetic

dipole of a nearby nucleus. This type of hyperfine interaction is orientation dependent with respect to the magnetic field direction and is observed in paramagnetic samples of crystals, powders, and frozen solutions. Conversely, the isotropic hyperfine interaction does not depend on orientation with respect to the magnetic field. This interaction occurs through bonds within the paramagnetic system, relying on the direct Fermi-contact interaction of the electron spin with the nuclear spin and can be observed in liquid solutions and solid samples. In the simplest case for an isotropic system with $S = \frac{1}{2}$ and $I = \frac{1}{2}$, the energy of a HF interaction is given by:

$$E = g\mu_B B_0 m_s + am_s m_I \quad (1.8)$$

Here, a is the hyperfine coupling constant and m_I is the magnetic nuclear spin quantum number. For a spin $\frac{1}{2}$ nucleus ($I = \frac{1}{2}$), the observed EPR signal is split into two signals (**Figure 1-8**), which are separated by the hyperfine coupling a , measured in field units. In this thesis, for all EPR spectra measured no hyperfine interactions were resolved. However, by using the double resonance technique of electron nuclear double resonance (ENDOR), hyperfine interactions can be measured. This technique will be further discussed in Chapter 7.

1.6.2. "Powder-Pattern" EPR

All EPR spectra that will be shown in the following chapters and appendices are "powder-pattern" EPR of frozen solutions. These types of EPR spectra result from ensembles of randomly oriented paramagnetic species which are measured after dissolution in media and frozen. The resulting EPR spectrum is a summation of contributions from microcrystallites with all possible orientations of the molecules frozen in solution. This results in linewidths that are typically broader than the EPR of free radicals in solution and the spectra often exhibit g anisotropy. The anisotropy in the g factor in paramagnetic metal complexes is dependent on the local ligand field and spin-orbit coupling.

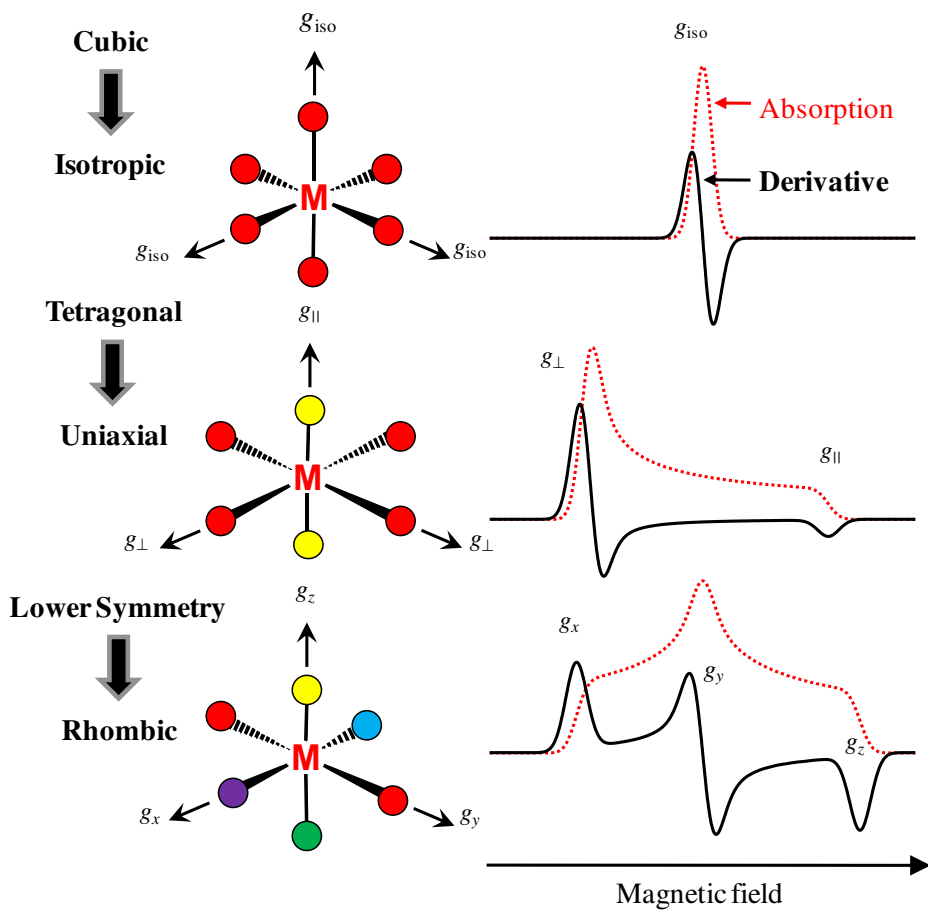


Figure 1-9 Typical EPR spectral shapes from different local symmetries around paramagnetic metal centres ($S = \frac{1}{2}$), shown in both the absorption and derivative modes.

In single-crystal samples, the values of g and a are often dependent on the orientation of the sample relative to the magnetic field. For polycrystalline samples, the orientation of g_x , g_y , and g_z in the molecular axis frame is not known with respect to the lab x , y , and z coordinates. Thus, in a “powder-pattern” spectrum, the principle g values of the g -tensor are simply labelled g_1 , g_2 , and g_3 , in order of increasing magnetic field. In the simplest case, an isotropic g tensor is observed, where $g_1 = g_2 = g_3$ (cubic symmetry), resulting in a single line in the EPR spectrum. Frequently, the symmetry observed around a paramagnetic metal centre is lower, resulting in observed uniaxial ($g_1 = g_2 \neq g_3$, tetragonal symmetry) or rhombic ($g_1 \neq g_2 \neq g_3$, no distinct symmetry elements) EPR signals. Typical EPR powder-patterns for paramagnetic species with $S = \frac{1}{2}$ with no

hyperfine interaction are shown in **Figure 1-9**. For paramagnetic metal ions, the broad lines observed in the EPR spectrum can mask hyperfine interactions between the unpaired electron and neighbouring nuclei; however, this information can be recovered using electron nuclear double resonance (ENDOR) spectroscopy.

1.7. Simulation of EPR Spectra

To interpret and understand all of the EPR data obtained in studies of Ru(III) anticancer compounds, spectral simulations were necessary. In this thesis all EPR spectra were simulated using the program Bruker WinEPR Simfonia, which efficiently produces accurate results for most $S = \frac{1}{2}$ systems. Spectral parameters, g values, and linewidths, were initially determined from the experimental spectra for each species. When multiple species were present, each species was identified individually with its own unique simulation parameters. The resulting spectral parameters were then varied individually until the resulting simulated spectrum observed was as close as possible to the experimental spectrum. To recreate the experimental spectrum the individual simulated EPR spectra were summed with different weighting factors (contributions) and compared to the experimental data.

Most of the species studied here undergo complex ligand-exchange processes under physiological conditions. Consequently the concentrations of the species observed varied with time. Simulation of EPR spectra at different time points using a single set of simulation parameters and only varying the weighting factors ensured a unique solution for several overlapping species. This procedure is summarized below in **Figure 1-10**, and was performed for all EPR spectra reported in this thesis and the accompanying appendices, a total of over 300 spectra.

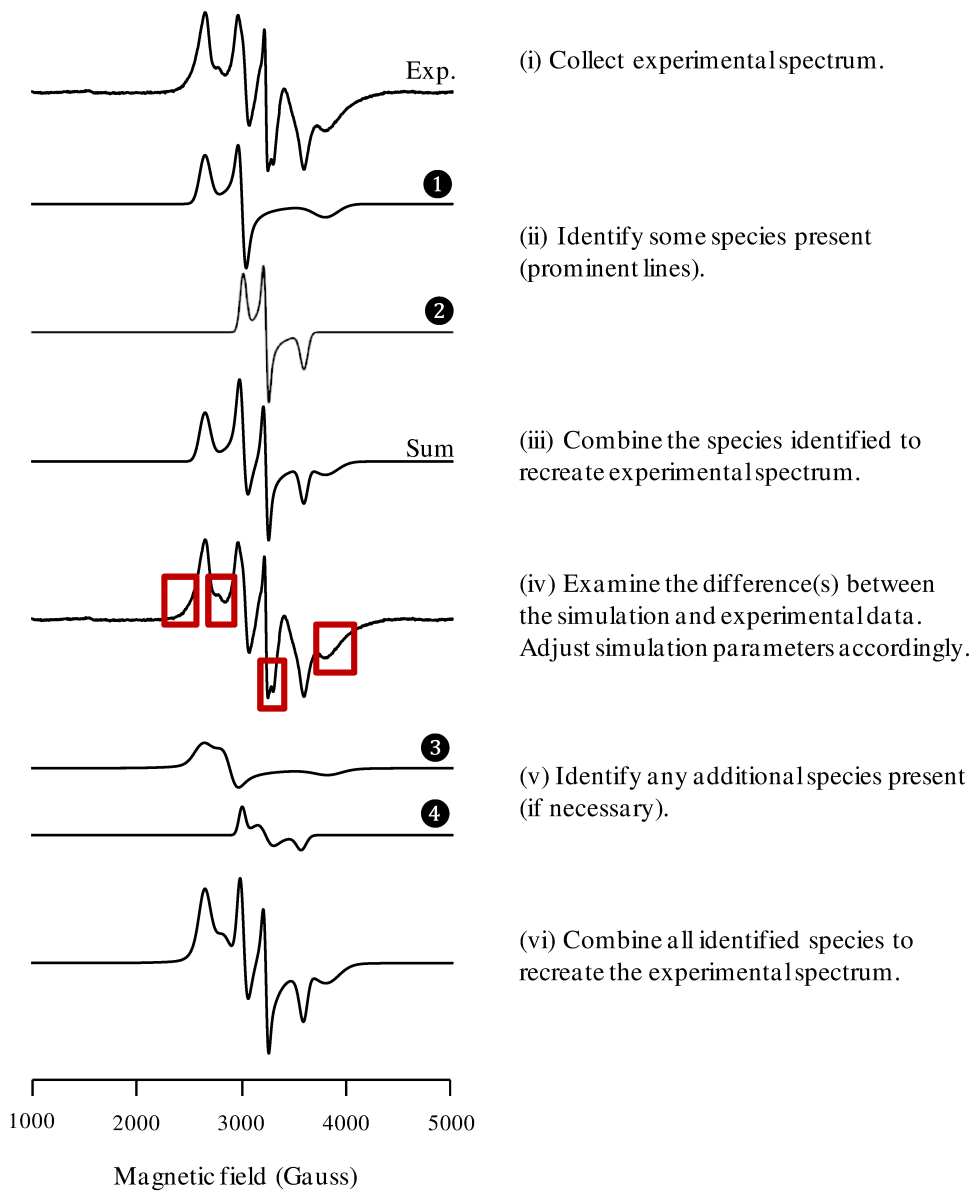


Figure 1-10 Procedure for the simulation of a complex Ru(III) EPR spectrum from distinct species.

1.8. Research Goals

The field of ruthenium anticancer agents has grown rapidly since the discovery of the clinical candidates KP1019 and NAMI-A. However, despite their success the mechanism of action remains a mystery despite substantial investigation by several groups using a variety of analytical techniques. EPR provides a unique perspective on the

physiological speciation of the Ru(III) complexes as the exclusive observation of the metal centre is possible. This led to the initial goal of this thesis, to study the mechanism of action of Ru(III) anticancer agents using EPR. This is the first application of EPR to monitor the ligand-exchange and protein-binding processes that occur under physiological conditions for the Ru(III) complexes KP418, KP1019, and NAMI-A. Further insight into the nature of the ligand-exchanged and protein-bound Ru(III) species was gained using ENDOR, while the biological targets of each complex were investigated using *in vitro* EPR. This led to the final goal, which was to use ligand design to enhance non-coordinate interactions with human serum albumin to enhance drug delivery and activity. This was achieved through the synthesis of pyridine-based Ru(III) complexes with different affinities for non-coordinate protein binding.

2. The Solution and Protein Binding Behaviour of the Promising “Keppler-type” Ruthenium(III) Anticancer Agents KP1019 and KP418^a

2.1. Introduction

An array of analytical approaches have been applied previously to study the interactions of Ru(III) complexes with serum proteins and the effect of biological conditions on the oxidation state of the metal ion.^{74,112,113,143,171,179,189,195,220} However, these studies have not produced a definitive picture of processes occurring *in vitro* or *in vivo* and a number of important issues remain unresolved. Although it has been recognized for some time that magnetic resonance methods are well suited to probe such interactions,²²¹ this chapter reports the first application of electron paramagnetic resonance (EPR) to characterize the behaviour of ruthenium complexes in the presence of serum proteins and in whole human serum. This approach has shown not only the binding of KP418 and KP1019 to serum proteins, both through ligand exchange and through hydrophobic ligand interactions, but also the oxidative stability of these complexes. Furthermore, by performing measurements after different incubation times, EPR provides insight into the different pharmacological properties of KP418 and KP1019 by analysis of changes in the spectral intensity of the various Ru(III) species detected.

[a] This chapter is based on a published paper and reproduces material with permission from: Cetinbas, N.; Webb M. I.; Dubland, J. A; Walsby, C. J. “Serum-protein interactions with anticancer Ru(III) complexes KP1019 and KP418 characterized by EPR” Journal of Biological Inorganic Chemistry 2010, 15 (2), 131-145. Copyright. 2010 Springer.

2.2. Experimental

2.2.1. Synthesis

Both KP1019 and KP418 were synthesized according to literature procedures.^{129,132} Each compound was characterized and checked for purity by ¹H NMR, UV-Vis, and CHN elemental analysis, the results of which are summarized below: KP418 C₉H₁₃N₆Cl₄Ru Calc. C 24.12 H 2.92 N 18.75, Found C 23.93 H 3.15 N 18.37, KP1019 C₂₁H₁₉N₄Cl₄Ru Calc. C 42.14 H 3.20 N 14.05, Found C 41.75 H 3.18 N 13.68.

2.2.2. Preparation of Protein Solutions

As purchased, the commercial apo-hsTf still contained significant amounts of iron, which was removed using a protocol similar to that described by Mason and colleagues.²²² Briefly, lyophilized protein was dissolved in iron-removal buffer (500 mM sodium acetate buffer, pH 4.5, containing 1 mM ethylenediaminetetraacetic acid (EDTA) and 1 mM nitrilotriacetic acid (NTA)). The resulting light pink solution was concentrated to a minimum volume in an Amicon centrifugal filter unit (molecular mass cut-off of 30 kDa). The protein concentrate was re-suspended in the iron-removal buffer and the process was repeated until a colourless protein concentrate was obtained. Sequential dilution and concentration in 100 mM KCl, 100 mM NaClO₄, and lastly 100 mM KCl solutions was performed to ensure the removal of any residual chelating agents (EDTA, NTA) from the protein solution. After final concentration, the protein was exchanged into HEPES buffer (20 mM NaHCO₃, 150 mM NaCl, 50 mM 4-(2-hydroxyethyl)-1-piperazineethanesulfonic acid (HEPES), pH 7.4). Lyophilized commercial hsA was dissolved in HEPES buffer and used without further purification.

2.2.3. Preparation of EPR Samples

KP418 and KP1019 in HEPES Buffer. For high signal-to-noise EPR measurement of the parent compounds, KP418 and KP1019 were dissolved in HEPES buffer to give nominal concentrations of 20 and 10 mM, respectively. These concentrations were significantly higher than those used in protein binding experiments,

to ensure high signal-to-noise in dispersion-mode EPR experiments. Ten percent, by volume, of glycerol (30 μ L) was added to the samples as a glassing agent and they were then placed in EPR tubes and immediately frozen in liquid nitrogen. For studies of the time dependence of KP418 speciation, a 6 mM solution of the complex in HEPES buffer was incubated at 37 °C with 270 μ L aliquots withdrawn after the following time points: 0, 20 minutes, 2, 6, and 24 hours. Each sample was promptly mixed with 30 μ L of glycerol and frozen in liquid nitrogen. Glycerol was used as a glassing agent, as it has been commonly used in the EPR of aqueous solutions,^{223,224} inhibiting the aggregation of the complexes in solution.²²⁵

KP418 and KP1019 with apo-hsTF or hsA. The procedures for preparing individual EPR samples of each protein bound to the respective metal complex were identical, as follows. A 0.75 mM solution of protein dissolved in 600 μ L of HEPES buffer was combined with 600 μ L of a 1.5 mM solution of the respective complexes. This was then diluted to 4 mL using HEPES buffer and the resulting solution was incubated at 37 °C for one of the following time periods: 0, 20 minutes, 2, 6, and 24 hours. Each 4 mL solution was concentrated down to a volume of less than 200 μ L using an Amicon centrifugal filter unit (molecular weight cut-off of 30 kDa) by centrifuging at 8 °C and 4,500 rpm for approximately 30 minutes, or until a volume of less than 200 μ L was attained. The resulting filtered product was then diluted to 270 μ L with HEPES buffer, mixed with 30 μ L of glycerol, and finally transferred to an EPR tube and immediately frozen in liquid nitrogen.

KP418 and KP1019 in Human Serum Solution. Samples (0.11 mM) of each respective ruthenium complex were prepared in HEPES buffer (10 mL), and promptly mixed with human serum (5 mL). Incubation and isolation of the serum-bound complex EPR samples were as described above for studies of the isolated serum proteins, giving a final Ru concentration of ~4 mM for each time point.

2.2.4. EPR Measurements and Simulations

EPR spectra were collected at X-band (9.3 – 9.4 GHz) using a Bruker EMXplus spectrometer with a PremiumX microwave bridge and HS resonator. Low temperature (20 K) measurements were performed using a Bruker ER 4112HV helium temperature-control system and continuous-flow cryostat. In order to compare the intensities of EPR signals from Ru(III) species in each solution after different incubation times, sample preparation and spectroscopic parameters were unchanged for each experiment. EPR samples (300 μ L) for each series of incubation times were drawn from a common stock solution. The design of the Bruker cryostat system, which contains a quartz-insert tube holder, ensures reproducible sample placement within the EPR resonator. Consequently, variation in instrument sensitivity between measurements was minimal, and automatic tuning of the spectrometer gave a Q-factor of $6500 \pm 10\%$. In experiments with hsA, the distinctive EPR signal from a minor Fe(III) human serum transferrin impurity at $g = 4.3$ also provided a reference for normalizing the Ru(III) EPR signal sensitivity.

All spectra were simulated using the program Bruker WinEPR Simfonia which efficiently produces accurate results for most $S = \frac{1}{2}$ systems. A manual iterative fitting procedure was employed to analyze overlapping spectra observed when multiple Ru(III) species were present in a particular sample. Further details can be found in section 1.7.

2.2.5. EPR Experimental Conditions

All of the time-course EPR spectra were measured using the same experimental conditions in order to facilitate comparisons between data sets. The conditions used were: frequency = 9.38 GHz, microwave power = 2.0 mW, time constant = 40.96 msec, modulation amplitude = 6 Gauss, average of five 2-minute scans, measurement temperature = 20 K.

Rapid-passage experimental conditions were also used for both KP1019 and KP418. Here the conditions used were: frequency = 9.38 GHz, microwave power = 4.0 mW, time constant = 81.92 msec, modulation amplitude = 6 Gauss, 15 second single scan, measurement temperature = 4 K.

2.3. Results and Discussion

Since the focus of this chapter was to understand the behaviour of the Ru(III) compounds in clinical applications, conditions that are relevant to their *in vivo* behaviour were used. Time course experiments were conducted with incubation at 37 °C, pH 7.4, using the buffer system described earlier containing concentrations of bicarbonate and NaCl that are typical for human blood, along with HEPES for increased protein stability and buffering capacity.

2.3.1. Aqueous Solution EPR Prior to Ligand Exchange

In aqueous buffer solutions, both KP418 and KP1019 are thought to undergo exchange of chloride ligands for water.^{132,170,177,226} However, at room temperature with a pH of 7.4 this process is relatively slow, allowing for the parent compounds to be prepared and studied spectroscopically. **Figure 2-1** shows first-derivative frozen-solution X-band EPR spectra, measured at 20 K, for samples of each complex after they had been dissolved in HEPES buffer at room temperature and immediately frozen in liquid nitrogen. The spectroscopic conditions used to obtain these spectra are ideal for most of the studies described in this work, since they provide for the maximum resolution of overlapping species. However, the effects of line broadening due to g strain²¹⁹ on these complexes meant that g_3 could not be determined from the derivative-mode spectra since the high-field peaks were too broad to be extracted from the baseline. To overcome this problem, measurements at lower temperatures (4 K) with rapid scans and high microwave power were made to obtain adiabatic rapid-passage conditions with corresponding dispersion line shapes.²²⁷ The resulting spectra (**Figure 2-2**) allowed for the measurement of the g_3 values for each complex.

The spectra of both complexes demonstrate the presence of two components: a predominant species with a uniaxial spectrum, and a less intense signal from a lower-symmetry species. Spectral simulations were used to separate the contributions from each component and precisely determine their g values. As shown in **Figure 2-1**, these simulations accurately match the experimental data and, combined with the dispersion-

mode measurements, gave the g-tensor principal values, in addition to the relative proportions of each species as follows: (1) KP418, axial species $g = [2.58, 2.58, 1.20]$, rhombic species $g = [3.08, 2.30, 0.95]$ intensity ratio of axial to rhombic $0.65 : 0.35$; (2) KP1019, axial species $g = [2.64, 2.64, 1.20]$; rhombic species $g = [2.94, 2.31, 0.95]$, intensity ratio of axial to rhombic $0.85 : 0.15$. At first glance, it may be tempting to assign the spectra of KP418 and KP1019 in **Figure 2-1** to a single rhombic spectrum; however, in each case attempted simulation rapidly reveals that the relative peak intensities and overall spectral shapes cannot be reproduced with such a model. The presence of two species is also required by the observation of corresponding g_3 absorptions in the dispersion-mode spectra (**Figure 2-2**).

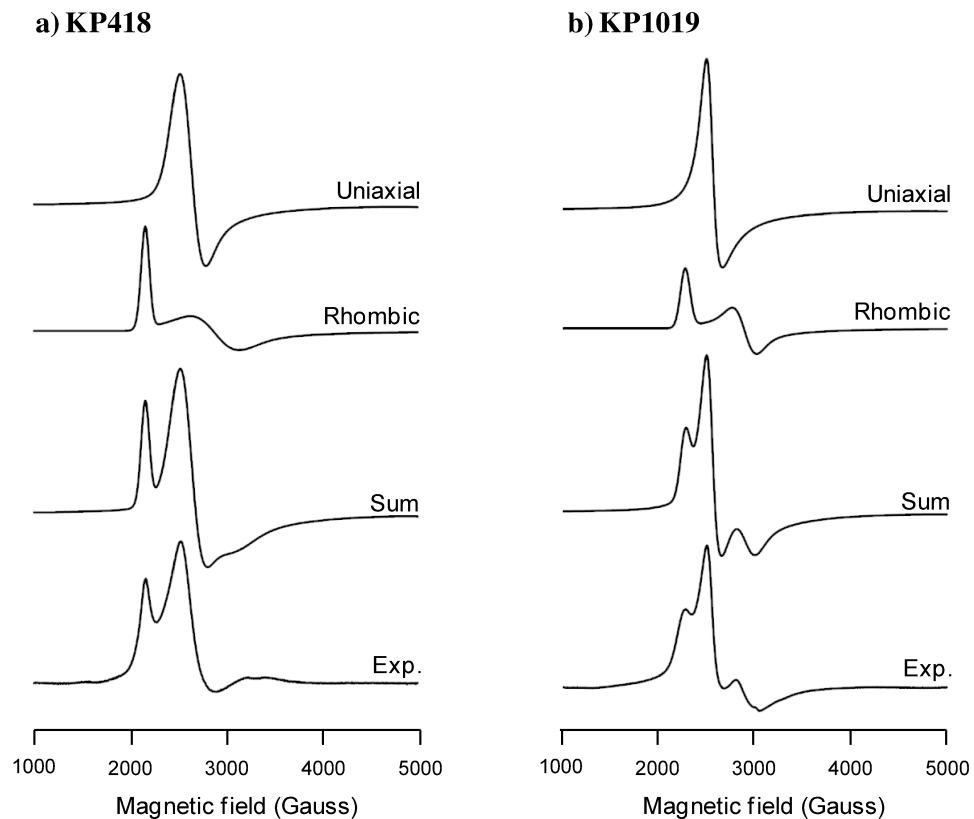


Figure 2-1 Experimental frozen-solution EPR spectra of a) KP418 (20 mM) and b) KP1019 (10 mM) immediately following dissolution in HEPES buffer, and deconvolution into rhombic and axial spectral components via simulation. For experimental conditions see 2.2.5.

A previous report of X-band EPR measurements of KP418 under relevant conditions (10 mM HEPES buffer, 100 mM NaClO₄, pH 7.0) shows a spectrum that is almost identical to that in **Figure 2-1**, with similar reported g values (3.00, 2.34, and 1.2).²²⁶ Although this earlier study interpreted the spectrum in terms of a single rhombic component, it is clear that the same species are present in these measurements and in the same relative concentrations. Accurate interpretation of Ru(III) EPR spectra usually requires spectral simulation, particularly with overlapping spectra.²²⁸ This is especially important here as it allows for the interpretation of the data in terms of two distinct species with confidence, and also enables determination of g values accurately from asymmetric line shapes. That the EPR spectra match those in the earlier report is a critical observation, since it further confirms that the same species are present in solution immediately after dissolution as in other published studies, in particular, those used for *in vitro* experiments.¹³⁷

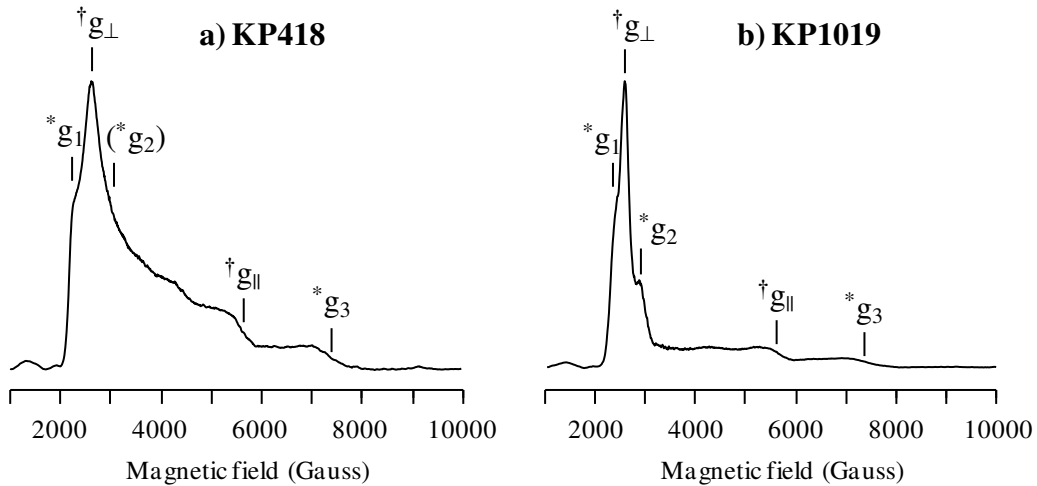


Figure 2-2 Dispersion mode EPR spectrum of a) KP418 and b) KP1019, † = principle g values of the axial spectral components, * = principle g values of the rhombic spectral components. For EPR experimental conditions see 2.2.5.

The EPR spectrum of KP1019 has not been previously reported, possibly owing to the relative insolubility of this complex; in aqueous solution at pH 7.4, KP1019 precipitates within 6 minutes at 37 °C owing to the comparatively rapid formation of the insoluble mono-aqua species.²²⁹ A solution of the non-aquated complex with a

concentration of 10 mM at room temperature was prepared by dissolving the compound as rapidly as possible and then freezing the solution immediately in liquid nitrogen. This frozen solution then gave the EPR spectrum shown in **Figure 2-1**. The presence of two species, the pattern of g values, and the general spectral shape are all reminiscent of KP418, as expected given the chemical and structural similarity of the two complexes.

The observation of two species in the EPR spectra of each complex is surprising given that the analyses described above discount the possibility of significant impurities, and a previous EPR study of KP418 has shown that the EPR spectrum observed is not from the aquated species.²²⁶ Furthermore, all of the EPR spectra are consistent with mononuclear Ru(III) complexes and cannot be from bridged or polymeric species, since spin exchange between adjacent Ru(III) centres would give EPR-silent ($S = 0$) systems in the case of antiferromagnetic coupling, or higher spins in the case of ferromagnetic coupling and corresponding distinct spectra.²¹⁹ Samples of KP418 and KP1019 were also prepared in doubly distilled water and frozen immediately after dissolution as before. The resulting EPR spectra were indistinguishable from those of the complexes in HEPES buffer, demonstrating that ion pairing with different cations from the buffer was not responsible for the distinct species observed spectroscopically. Furthermore, samples of each complex with just HEPES in the buffer were prepared. The observed EPR spectra were identical to those in water, demonstrating that HEPES does not act as a ligand and thus does not influence the experiments, later described, on protein binding.

The two species observed prior to ligand exchange most likely represent either a conformational difference between two populations of complexes or weak intermolecular interactions as a by-product of the freezing process. An unpublished study²³⁰ of these complexes, and other structurally related analogues, in organic solvents (dimethylformamide/toluene, neat dimethylformamide) reports similar heterogeneous EPR, further suggesting that these observations may result from the behaviour of the free complexes upon freezing. This is an interesting phenomenon worthy of future study, but is not overly significant in the context of the work described here.

2.3.2. Solution Behaviour of KP418

There is growing evidence that the therapeutic properties of “Keppler-type” Ru(III) complexes are influenced by ligand exchange processes in solution, prior to interactions with biomolecules.¹⁷² In particular, formation of aquated species through loss of chloride ligands leads to complexes that are activated toward binding of biomolecules due to the lability of bound water ligands.²²⁹ After administration to patients, relatively high blood concentrations of bicarbonate (~20 mM), chloride (~100 mM), and numerous other small-molecule species have the potential to impact on the aquation kinetics and speciation equilibria of Ru(III) complexes, potentially even contributing ligands via exchange. These processes can produce metabolites with different affinities for protein interactions, strongly influencing species that eventually are transported into cancer cells. Therefore, it is critical to characterize these processes to better predict the actual species responsible for the observed anticancer activities of Ru(III)-based chemotherapeutics.

Reports of the time-dependent behaviour of KP418 both in water alone, and in various buffer systems, provide a confusing and often contradictory picture of its speciation behaviour in aqueous solutions. This is due to variation in the buffer components, pH of the solutions used, differences in incubation temperature, and the selective sensitivity of the analytical techniques applied to study the various compounds that potentially can be formed with exchange of ligands from the original complex. The experiments described in this thesis demonstrate that, with incubation at 37 °C in HEPES buffer, KP418 readily undergoes ligand exchange to yield three new species with distinct EPR spectra (**Figure 2-3**). The dominant ligand-exchanged species (*KP418-H₂O*) with g = [2.47, 2.26, 1.79] and LW = [80, 70, 100] Gauss, is assigned to the mono-aqua complex, [RuCl₃(H₂O)(imidazole)₂]⁺, formed by exchange of a single chloride ligand. This is in agreement with several literature reports, which indicates that this species is formed comparatively rapidly after dissolution of KP418 in aqueous solutions.^{170,226,231-233} Subsequent aquation produces the *trans*-diaqua and *cis*-diaqua isomers of [RuCl₂(H₂O)₂(imidazole)₂]⁺, assigned, respectively, to the species *KP418-(H₂O)_{2-trans}*, with g = [2.59, 2.34, 1.72] and LW = [80, 120, 350] Gauss, and *KP418-(H₂O)_{2-cis}*, with g = [2.51, 2.20, 1.73] and LW = [80, 70, 250] Gauss, characterized by these EPR

measurements of KP418 incubated in buffer. Owing to the greater *trans*-directing effect of chloride relative to water, the *cis*-diaqua complex is predicted to be the predominant isomer, and thus is identified by the strongest EPR signal of the two aqua isomers (*KP418-(H₂O)₂-cis*).

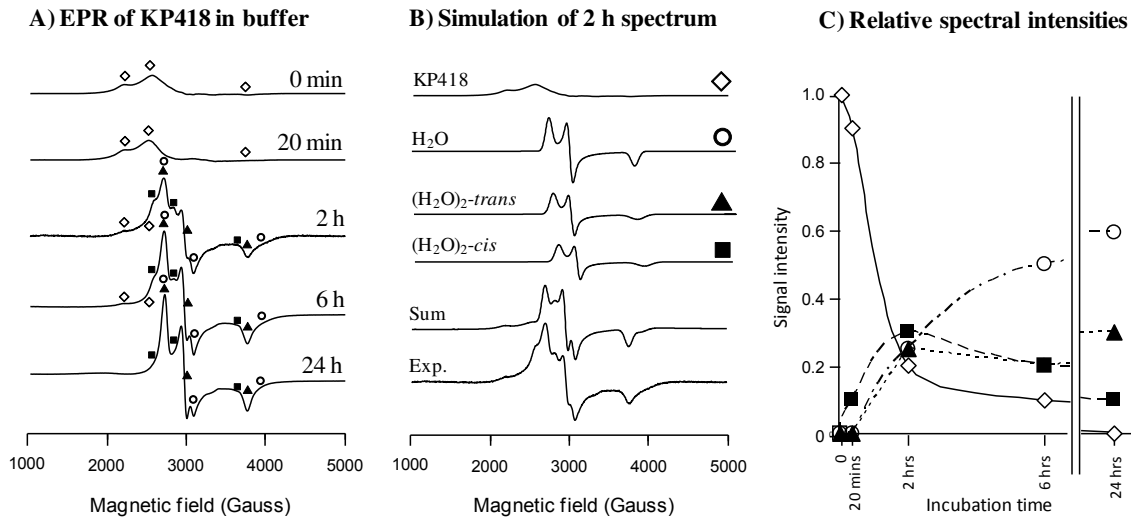


Figure 2-3 EPR spectra from KP418 after incubation in HEPES buffer at 37 °C, A) experimental EPR spectra, B) deconvolution of the 6 hour spectrum by simulation. Simulation parameters: intact KP418 (◊); *KP418-H₂O* (○); *KP418-(H₂O)₂-trans* (■); *KP418-(H₂O)₂-cis* (▲), C) time dependence of signal intensities, determined by simulation as described in the text. For EPR experimental conditions see 2.2.5.

Comparison of the dependence of EPR signal intensity on the incubation time in HEPES buffer (Figure 2-3C) with previous paramagnetic ¹H NMR experiments for KP418 in D₂O shows similar concentration profiles and reaction rates.²²⁶ Here, a shorter half-life for KP418 ($t_{1/2} \approx 2$ h) is observed, as compared with that determined from the ¹H NMR measurements in D₂O with 0.15 mM NaCl at 37 °C ($t_{1/2} \approx 4.6$ h). However, this difference in rate almost certainly arises from the effect of pH, which was not controlled in the earlier experiments and dropped significantly as the ligand-exchange reaction progressed. Overall, there is a very pleasing correlation in the reaction profiles determined by the two methods, and the formation of the three aqua species is the most straightforward interpretation of the EPR data.

In the previously reported EPR study of KP418, a spectrum of the intact complex was presented that agrees with these measurements.²²⁶ However, the effect of incubation at 37 °C resulted in an EPR spectrum that does not correspond to species characterized in these experiments. This may be due to the presence of a relatively high concentration of the perchlorate ion, which in these earlier studies was used as an agent to prevent aggregation of the complexes in solution, a process that leads to line broadening owing to cross-relaxation between paramagnetic centres.²²⁶ A modest amount of glycerol was used in the EPR measurements in this work, which is very effective in this role and is unlikely to react with the species of interest. The effect of different buffer systems, and the presence of 150 mM NaCl in the HEPES buffer, may also be a factor in the different spectra observed after incubation.

Previously reported HPLC measurements of KP418 in physiological saline,¹⁷⁰ and high-performance capillary electrophoresis²³⁴ in phosphate buffer at pH 7.4, have also demonstrated the formation of $[\text{RuCl}_3(\text{H}_2\text{O})(\text{imidazole})_2]$ and $[\text{RuCl}_2(\text{H}_2\text{O})_2(\text{imidazole})_2]^+$. The HPLC experiments additionally indicate that the trisimidazole complex, $[\text{RuCl}_3(\text{imidazole})_3]$, is formed by exchange with the imidazolium counterion. However, as pointed out by other authors, this likely arises from the conditions required for separation of the products, particularly the presence of high concentrations of acetonitrile in the mobile phase.¹⁷⁰

In consideration of other possible species responsible for the EPR measurements reported here, the observation of strong spectra with average g values in the region of $g = 2$ exclude the presence of significant concentrations of bridged or polymeric species. In the case of dimer formation, strong spin exchange across bridging atoms will lead to an EPR-silent ($S = 0$) system in the case of antiferromagnetic coupling, or a spin triplet ($S = 1$) with ferromagnetic coupling.^{41,219} Species such as $[\text{RuCl}_3(\text{OH})(\text{imidazole})_2]^-$, formed by deprotonation of the mono-aqua species $[\text{RuCl}_3(\text{H}_2\text{O})(\text{imidazole})_2]$, along with $[\text{RuCl}_2(\text{H}_2\text{O})(\text{OH})(\text{imidazole})_2]$, from subsequent chloride ligand exchange, may also contribute to the speciation of KP418. It has been suggested that these compounds may form at physiological pH;²³² however, these species have not been detected directly by

experiment. Additionally, there are no reports of exchange of the imidazole ligands of KP418 in aqueous solution, which are kinetically inert under physiological conditions.²³¹

2.3.3. Solution Behaviour of KP1019

Incubation of KP1019 in HEPES buffer at 37 °C leads to rapid precipitation, as observed in these experiments and reported elsewhere.¹⁷² Consequently, EPR studies of speciation in buffer alone were not possible. It is generally accepted that the precipitate observed under physiological conditions is from the insoluble mono-aqua species, formed by chloride ligand exchange,^{132,177} and this compound has been isolated and characterized by X-ray crystallography and spectroscopic methods.²²⁹ The behaviour of KP1019 in solution is strongly dependent on the pH and buffer system,^{170,177} and it has been observed, for example, that bicarbonate increases the hydrolysis rate of the complex.¹⁷⁰ In general, it is clear that despite their structural similarities, KP418 and KP1019 exhibit distinctly different behaviour in physiological solutions that are relevant to their antitumour activity.

2.3.4. Interactions of the Complexes with Serum Proteins

To study the binding to each serum protein, the complexes were incubated in the presence of hsA and apo-hsTf, after which the protein fraction was separated from any free complexes by ultrafiltration, as described in the experimental section. Thus, EPR measurements of the isolated fractions were from Ru(III) species bound to each of the proteins. In the case of KP1019, further evidence for protein binding is provided by the observation that the complex does not precipitate with incubation at 37 °C in the presence of either protein, as observed in pure HEPES buffer. **Figure 2-4, 2-5, and 2-6** show the EPR spectra of the protein-bound fractions of KP418 and KP1019 in the presence of apo-hsTf, hsA, and whole human serum. In each case strong Ru(III) EPR signals are apparent, demonstrating two important properties of both complexes: (1) the oxidation state of the ruthenium centres is not affected significantly by the presence of either the proteins or the serum components, even after 24 hours of incubation at 37 °C, and (2) the majority of the

complexes bind to protein components, although the rate of this process and the mode of interaction varies.

2.3.5. Interactions with hsA

The interactions of each complex with hsA are quite distinct, as shown by the differing EPR signals observed in each case and the overall rate of complex binding determined from the time dependence of the signal intensities. Binding of hydrolyzed KP418 complexes to hsA is slow, with a relatively small fraction of the complexes bound even after 2 hours, and a noticeable increase in binding between 6 and 24 hours (**Figure 2-4A**). Although the overall signal intensity increases with incubation time, the spectral shape is essentially unchanged. Comparison with the complex in buffer alone (**Figure 2-3**) indicates that the predominant species have EPR spectra that are essentially indistinguishable from those of the ligand-exchanged products observed in the absence of the protein. Indeed, the signals from KP418 interacting with hsA can be simulated very well using the g values determined for the free hydrolyzed complexes in solution (**Figure 2-4A**). Therefore, these spectra are assigned to the hydrolyzed complexes bound non-coordinately to hsA. That these signals are not from free complexes in solution is demonstrated by the absence of signals from the parent compound, and the time-dependent increase in overall signal intensity, phenomena inconsistent with observations of KP418 in the HEPES buffer alone (**Figure 2-3**). The ultrafiltration procedure would produce a maximum total concentration of free complexes (if no protein binding occurred) of 0.15 mM, which is near the threshold of detectability for these measurements, and certainly would not produce the strong signals observed after 24 hours of incubation.

To further prove this point, an extra cycle of dilution and ultrafiltration was performed for the samples incubated for 6 and 24 hours, which resulted in identical spectra with a modest reduction in intensity. This additional ultrafiltration cycle produces a further 20-fold reduction in the possible concentration of free complexes, giving a maximum concentration of 8 μ M, which is undetectable by EPR methods. The small reduction in the overall EPR signal that is observed is consistent with the loss of a

fraction of the non-coordinately bound complexes owing to either establishment of equilibrium concentrations with the bulk solution or some protein denaturing.

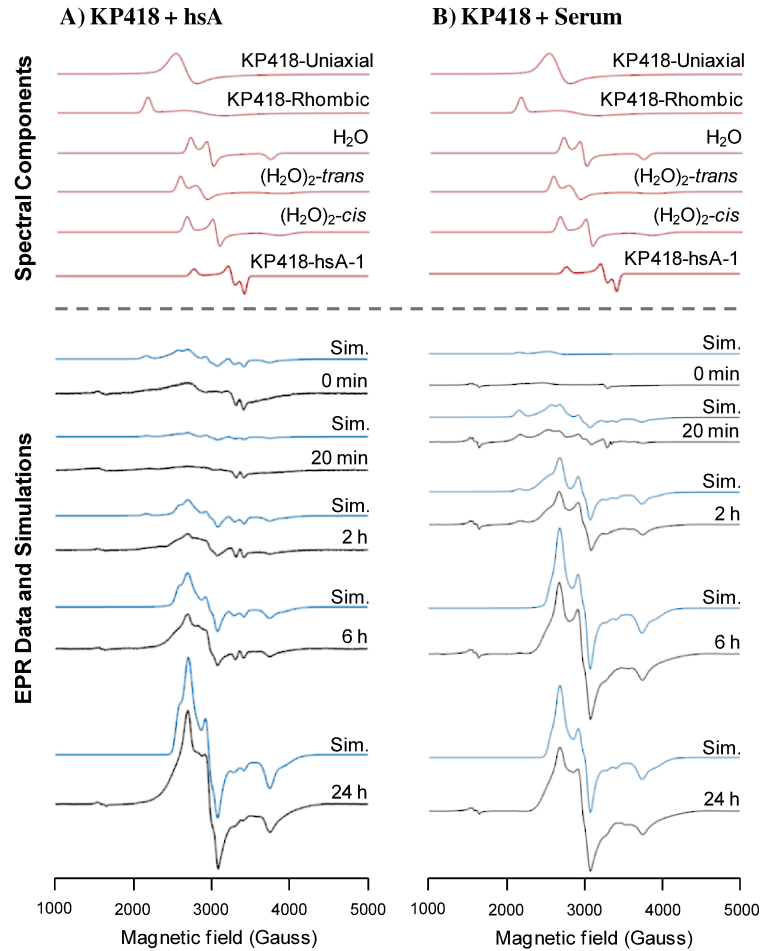


Figure 2-4 EPR spectra of KP418 after incubation at 37 °C with A) hsA and B) whole human serum. Upper panels: individual simulated spectral components; g values and linewidths in main text and Appendix A – Table A-1. Lower panels: experimental EPR spectra and simulations constructed from weighted sums of spectral components. For EPR experimental conditions see 2.2.5.

In these experiments, the EPR spectra show signals from three species with g values and spectral shapes (**Figure 2-4A**) that match those found for the complex incubated in buffer only (**Figure 2-3**). Therefore, it follows that both the mono-aqua and

diaqua complexes bind non-coordinately to hsA, along with the original complex. These binding processes are relatively slow, as can be seen from the overall signal intensities and the time-dependent concentration profiles of the three species (Appendix A – **Figure A-6**). Similar affinities of each aquated complex for hsA are indicated by the intensities of their respective EPR signals, which are essentially equal at all incubation times. The possibility that hydrolytic intermediates of KP418 may be interacting with hsA has been suggested previously,⁴⁹ and the EPR results confirm that this is the major process responsible for metabolites of the complex binding under physiological conditions. The principal molecular binding sites of hsA are the hydrophobic regions in subdomains IIA and IIIA,^{235,236} and are the most probable regions for location of the non-coordinately bound species. It has been suggested in earlier reports that the binding of KP418 to hsA may occur via ligand exchange for histidine imidazoles. However, such coordination would produce characteristic changes to the EPR spectra, so it can be concluded that this is not a major mode of interaction for KP418 with hsA under physiological conditions.

When KP1019 is combined with hsA in HEPES buffer, the separated protein fraction shows strong EPR signals even prior to incubation at 37 °C (**Figure 2-5B**). At the “0 min” time point, the spectrum is dominated by a signal matching that of the parent compound, demonstrating that the majority of KP1019 binds very rapidly in a non-coordinate manner to hsA, in contrast to the behaviour observed for KP418. As the incubation time increases, the signal from the original complex declines in intensity and new species are observed, revealing ligand-exchange processes. The EPR data show production of a major component exhibiting a rhombic EPR signal, *KP1019-hsA-1* ($g = [2.44, 2.24, 1.79]$), with a small contribution from a smaller overlapping axial signal, *KP1019-hsA-2* ($g = [2.32, 2.32, 1.84]$), both of which are visible at longer incubation times. The first hsA-bound species, *KP1019-hsA-1*, is assigned to protein-bound species coordinated to amino acid side chains, most likely through chloride ligand exchange for histidine imidazoles. Deconvolution of the signal from these two species after 24 hours of incubation, which was achieved by summing weighted simulations of the spectra from each component, is shown in Appendix A – **Figure A-4**. Spectra from minor intermediate species are observed after shorter incubation times, but their signal intensities are much

lower than those of the other products, indicating they are not significant to the overall complex binding process.

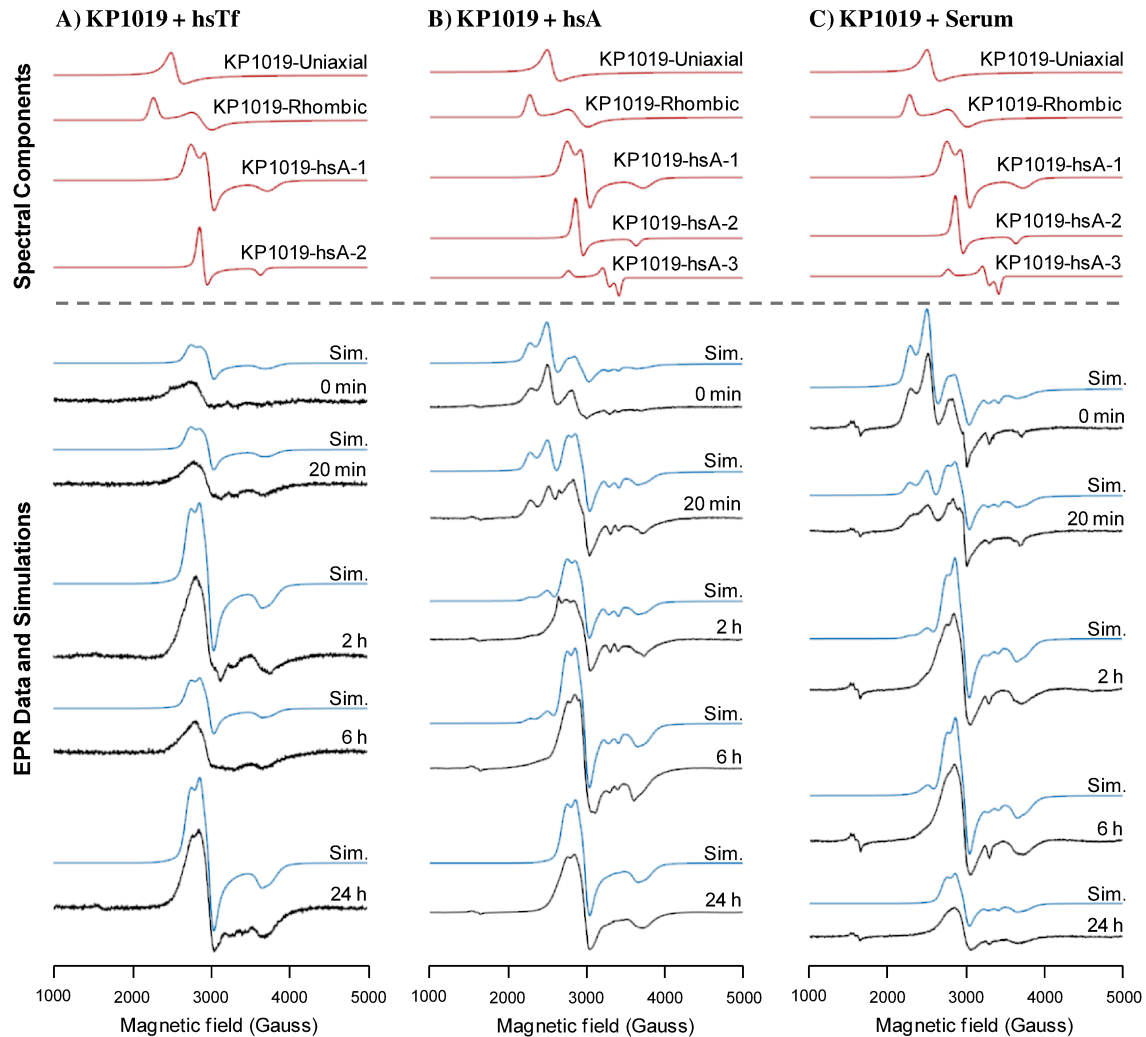


Figure 2-5 EPR spectra of KP1019 after incubation at 37 °C with A) hsTf, B) apo-hsA, and C) whole human serum. Upper panels: individual simulated spectral components; g values and linewidths in main text and Appendix A – Table A-1. Lower panels: experimental EPR spectra and simulations constructed from weighted sums of spectral components. For EPR experimental conditions see 2.2.5.

To determine the time dependence of the contributions from the three main species (*KP1019-Uniaxial/Rhombic*, *KP1019-hsA-1*, and *KP1019-hsA-2*), the EPR spectra at each time point were simulated with weighted sums of the individual

components (**Figure 2-5B**). As described previously for the simulations of the time-dependent spectra of KP418 and its hydrolyzed products, the only parameter varied between the simulations of the spectra at each time point was the contribution from the respective species, with the result being accurate reproductions of the experimental data in each case. The time dependence of the concentrations of the parent complex and the major product (Appendix A – **Figure A-7**) demonstrate that the former is converted, essentially quantitatively, into the latter as the incubation time increases.

For both KP418 and KP1019 an additional coordinate signal, is observed when incubated with hsA (*KP418/KP1019-hsA-3*). This signal has a small g value dispersion, and, comparatively narrow linewidths, suggesting a single well-defined binding site. Human serum albumin contains 35 cysteine residues, 34 of which contribute to the overall tertiary structure through the formation of disulfide bridges.^{75,77} This leaves one free cysteine (Cys-34) which has a reactive thiol available for coordination to exogenous and endogenous species under physiological conditions.^{78,237} Indeed, it is this residue that is frequently cited as an important site of coordinate binding to a variety of drugs.⁷⁹ Therefore, the additional signal was assigned to a species which had undergone coordination to hsA via a cysteine side chain (Cys-34). This signal reached a maximum intensity at the earliest time point for both KP418 and KP1019, and remains relatively unchanged throughout the duration of the experiment.

2.3.6. Interactions with hsTf

In the presence of apo-hsTf, both complexes show behaviour that is quite distinct from their interactions with hsA. In the case of KP418, it is immediately apparent from the EPR spectra that the interaction with apo-hsTf produces new species not observed previously either in buffer alone or with hsA (**Figure 2-6**). Deconvolution of the time-dependent EPR spectra was achieved by noting first that many of the smaller peaks had g values corresponding to the aquated complexes described previously, suggesting that small amounts of these species were also bound non-coordinately to apo-hsTf. However, the EPR data are dominated by a new axial signal, *KP418-hsTf* ($g = [2.38, 2.38, 1.66]$), which determines the overall shape of the spectra and exhibits a well-resolved g_{\parallel} peak.

Excellent simulations of the experimental data were possible using the g values of the aquated complexes determined earlier, the new axial spectrum, and a small contribution from a minority species (unlabelled species in **Figure 2-6**) with very sharp lines and three well-defined g values ($g = [2.40, 2.15, 1.87]$). Simulation of so many overlapping species inevitably raises the question of the uniqueness of the solution, but in this case the analysis is confirmed by: (1) inclusion of essentially only one new species, the broad axial signal from *KP418-hsTf*, (2) the ability to replicate the time-dependent spectra by varying only the relative proportions of each component, and (3) the very close agreement between the simulated and experimental spectra (shown in **Figure 2-6** for the spectrum after 6 hours, and Appendix A – **Figure A-7** for other time points). Observation of the axial spectrum demonstrates a ligand-exchange process has occurred in the presence of apo-hsTf, most likely through interactions with amino acid side chains, such as histidine imidazoles.¹²² Overall, the rate of this process is faster than the protein binding seen through the non-coordinate interactions observed with hsA.

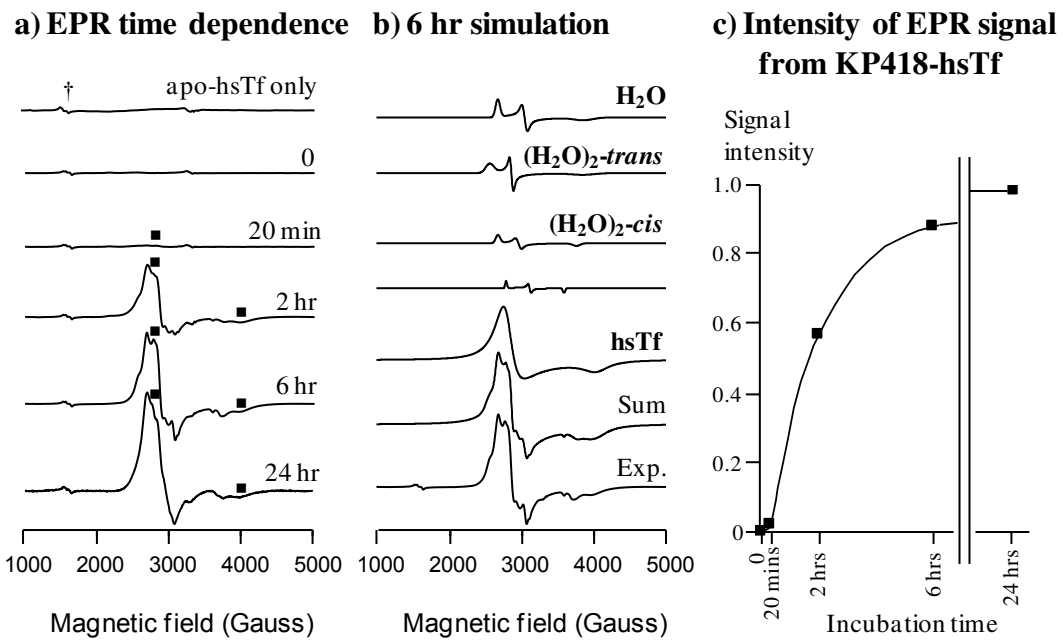


Figure 2-6 EPR spectra from KP418 interacting with apo-hsTf with incubation in HEPES buffer at 37 °C. a) Experimental EPR spectra, b) deconvolution of 6 hour spectrum by simulation, c) time dependence of signal intensities, determined by simulation as described in text. † – signal from trace amounts of iron-bound hsTf. For EPR experimental conditions see 2.2.5.

The absence of non-coordinate binding, as observed with hsA, is not surprising given that hsTf does not have specific hydrophobic binding domains. Whether KP418 binds specifically to the histidines at the binding sites of hsTf (N-lobe, His249; C-lobe, His585), or to other histidine residues throughout the protein, cannot be determined directly from the data. However, the broad linewidth observed in the EPR spectrum suggests an inhomogeneous population of similar species, consistent with several distinct binding sites. Given that coordinate binding is anticipated to be favoured thermodynamically over non-coordinate interactions, it is perhaps surprising that coordinate binding of KP418 to hsA is not observed. It is hypothesized that this is due to kinetic control of the binding process such that even after long incubation times the system remains far from equilibrium, with non-coordinate interactions at the hydrophobic sites dominating.

After long incubation times in the presence of apo-hsTf, KP1019 exhibits EPR spectra (**Figure 2-5A**) indistinguishable from those obtained from comparable experiments with hsA (**Figure 2-5A**). However, the behaviour at earlier time points is quite different, with no evidence of the parent compound, as seen with hsA, demonstrating that binding through non-coordinate interactions does not occur with apo-hsTf. The apparent rate of binding to apo-hsTf is somewhat slower for KP1019 than for KP418, in contrast to earlier reports,^{140,172} possibly reflecting some insolubility of the indazole complex with corresponding loss of EPR signal, a process that would not be readily observable by other methods.

2.3.7. Interactions of the Complexes with Whole Human Serum

Even after incubation in human serum solution at 37 °C for 24 hours, both KP418 and KP1019 show intense EPR spectra, demonstrating that their Ru(III) centres are not reduced significantly to Ru(II) under these conditions. Since the primary goal of this work was to study protein interactions by EPR, the procedure outlined in the experimental section for preparation of the serum samples involved the addition of a dilute solution of the complex in HEPES buffer to pure serum, in a 2:1 volume ratio, followed by ultrafiltration to isolate the protein-bound fractions. This procedure was

found to be optimal for stabilizing the pH and producing final concentrations suitable for EPR experiments. Experiments involving the addition of each complex directly to human serum gave very similar spectra with high signal intensity, demonstrating that dilution of the serum in the first method is not a factor in the observed oxidative stability.

EPR measurements of KP418 (**Figure 2-4B**) and KP1019 (**Figure 2-5C**) after incubation in the serum solution at 37 °C reveal spectra and kinetics in both cases that are very similar to those observed for hsA in the HEPES buffer, consistent with protein interactions being dominated by albumin owing to its comparatively high concentration. The data from KP418 in serum indicate some minor, competing binding interactions, as shown by small signals from the protein-bound parent compound at early time points and peak intensities that cannot be simulated as accurately as in previously described simulations at later time points. In the latter case, a comparison with the data from KP418 with hsA in buffer (**Figure 2-4A**) shows familiar spectral features. At short incubation times, EPR spectra from KP1019 in serum show similar features to those observed after incubation with both hsA and hsTf at 37 °C (**Figure 2-5C**). Spectral simulations of the incubation-time dependent spectra from KP418 (Appendix A – **Figure A-3**) and KP1019 (**Figure 2-5C**) in serum suggest that the dominant species are the same as those observed for hsA in buffer. For both complexes, the additional coordinate hsA signal (*KP418-hsA-1/KP1019-hsA-3*) is again observed in whole human serum. This demonstrates that for both complexes, the coordinate interaction with the surface cysteine is highly favoured, and likely readily occurs *in vivo* given the low pK_a of Cys34 (5.0 – 7.0).²³⁸⁻²⁴⁰

The EPR spectra of KP418 in the serum solution indicate not only that the oxidation state is essentially unaffected by the presence of serum components, but also that the complex binds to hsA under these conditions in the same way as with the protein in buffer. Comparison of spectral shapes and concentration vs. time profiles demonstrates that non-coordinate binding to hsA is the dominant process in serum. Although this might be anticipated given that hsA is the main protein component in human serum, these results suggest that reactions with any of the many small-molecule serum components are comparatively insignificant, and that the majority of the complex is protein-bound. Indeed, it seems likely that binding of the complex to hsA prevents reactions with

common reactive serum components such as ascorbic acid and pyruvate, maintaining the complex in the form of the aquated species with the 3+ oxidation state. These are important observations given that the anticancer activity of Kepler-type complexes has been proposed to revolve around increased proclivity for DNA binding through reduction of the ruthenium centre, and the presence of labile water ligands.^{49,229} It should be noted that the absence of obvious signals from apo-hsTf-bound complexes does not preclude their presence in serum. The serum concentration of hsA (600 μM)⁷⁵ is significantly higher than that of hsTF (35 μM)⁶⁶, and it is likely that EPR spectra from Ru(III) complexes interacting with the more abundant protein obscure those from less abundant interactions.

At longer incubation times, KP1019 in the presence of apo-hsTf, hsA, and serum, exhibits essentially indistinguishable EPR spectra, which are dominated by a single type of species. This demonstrates a similar coordination environment for Ru(III) in each case, derived from a ligand-exchange process with the original complex. As with KP418, the most likely binding mode is through ligand exchange with histidine imidazoles.^{57,122} To exclude other possibilities such as non-coordinate interactions with aquated complexes, the ligand-field parameters of the dominant derivative of KP1019 at longer incubation times (*KP1019-hsA-1*) were compared with those of *KP418-hsTf*, which have previously been identified as KP418 bound coordinately to apo-hsTf. Ligand-field parameters for strong-field d^5 systems, such as those studied here, can be determined directly from experimental g values, as described in detail in Appendix A.^{228,241} These calculations for *KP418-hsTf* and *KP1019-hsA-1* (Appendix A – **Table A-2**) show very similar values of orbital coefficients, tetragonal distortion energy, and covalency. In both cases, greater coordinate bonding character is observed than in the aquated complexes of KP418, consistent with π-type interactions with histidine imidazoles. That *KP418-hsTf* bound to the protein has higher symmetry, as shown by an axial EPR spectrum, than KP1019 (rhombic EPR spectrum) likely arises from the presence of essentially only two ligand types in the former: three chloride ligands and three imidazole ligands, giving approximately trigonal symmetry. As additional evidence of these assignments, both *KP418-hsTf* and *KP1019-hsA-1* exhibit greater linewidths than the aquated KP418

species, consistent with some structural diversity at the several histidine binding sites available in apo-hsTf and hsA.

The concentrations of the complexes used in these experiments are higher than would be found *in vivo* during treatment, but were chosen to give a suitable signal-to-noise ratio in EPR measurements for identification of hydrolyzed and protein-bound compounds. For studies with isolated hsA and apo-hsTf, the molar ratio of complex to protein was 2:1. This was based on existing experimental evidence that several complex molecules bind per protein.⁵⁷ However, the experiments were repeated with complex concentrations equivalent to less than one complex molecule per protein molecule. The resulting spectra, although not as intense, demonstrate the same species and binding trends, but with slightly slower rates, as expected, owing to the lower initial concentration (data not shown). For KP1019 the number of equivalents of Ru bound per protein molecule has been observed to be variable, ranging from 0.5 – 1.5 following prolonged incubation,^{206,234} while for KP418 this value is unknown. In serum experiments, significantly lower complex concentrations were used with a hsA to ruthenium complex molar ratio of approximately 3:1. Therefore, the observed protein binding results are expected to be representative of processes occurring *in vivo*.

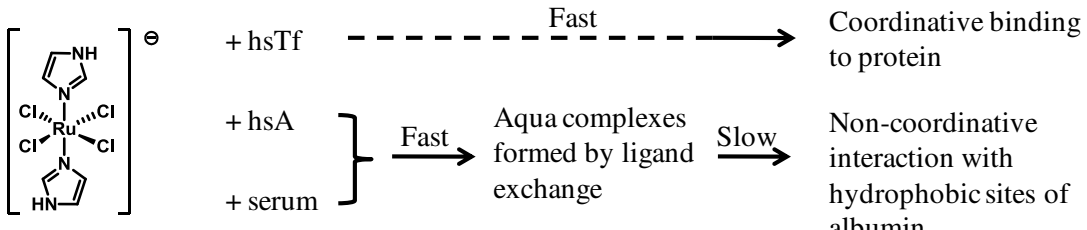
2.4. Conclusion

The successful phase I clinical trial of KP1019 demonstrates that this and other “Keppler-type” complexes are among the leading contenders for new chemotherapeutics.^{107,110} The propensity for these and similar Ru(III) complexes to exchange ligands, particularly in aqueous environments, means it is critical to identify different protein-bound species to gain greater understanding of the origin of their anticancer activity *in vivo*. Through EPR studies, the time-dependent speciation of both KP1019 and the structurally analogous KP418, have been characterized under physiological conditions, identifying serum-protein-bound species derived from each complex. Both complexes show oxidative stability in the presence of serum components.

KP1019 shows behaviour that differs markedly from that of KP418 under physiological conditions. The most striking difference is the very rapid non-coordinate binding of the parent complex to hsA. Strong signals are observed from KP1019 bound to the protein prior to ligand exchange, even before any incubation at 37 °C, demonstrating favourable interactions of the complex with the hydrophobic sites of hsA (**Figure 2-5A**). This behaviour correlates with the greater ability of the indazole ligands of KP1019 to interact with the hydrophobic domains, for example, through π - π stacking interactions with the side chains of phenylalanine and tryptophan residues, than the imidazoles of KP418. This rapid binding of the parent compound is also observed in serum experiments (**Figure 2-5C**), with almost identical EPR spectra and kinetics, indicating that the same hydrophobic interactions are dominant. As with KP418, this implies that interactions of KP1019 with hsA also dominate in serum. The rapid sequestering of KP1019 in serum through this type of interaction suggests that it may be the origin of the lower toxicity of this complex, as compared with KP418, observed *in vivo*. The EPR spectra of KP1019 with apo-hsTf in HEPES buffer show no evidence for non-coordinate binding of the original complex. This is likely due to the absence of hydrophobic binding sites such as those found in hsA.

At longer incubation times the complexes also show distinct behaviour (**Figure 2-5**). KP1019 appears to bind to both proteins via ligand exchange, most likely with histidine imidazoles, a process that is also observed when KP418 interacts with apo-hsTf. However, the dominant interaction of KP418 with hsA is through non-coordinate binding of its aquated products, even after 24 hours. After incubation in serum, interactions with hsA dominate for both complexes, suggesting that the species available for anticancer activity may be quite different for each compound. In general, these EPR experiments show that coordinate binding processes are slow, as would be expected given the relative kinetic inertness of Ru(III) complexes in general.⁴¹ It is hypothesized that after KP1019 initially binds non-coordinately to hsA, it is slowly converted to the coordinately bound species. By contrast, this process does not occur with KP418. This suggests the importance of the effect of ligand exchange on protein affinities, implying that aquation rates should be considered in the design of new anticancer complexes.

KP418



KP1019

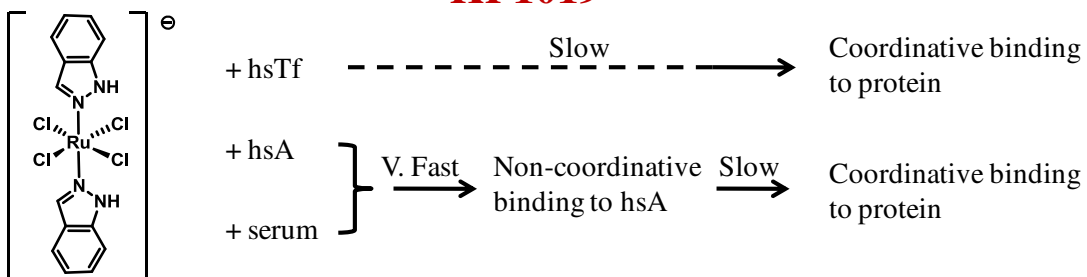


Figure 2-7 Summary of the major reaction pathways for KP418 and KP1019 in the presence of serum proteins, as determined from EPR studies.

A major factor in the success of KP1019 as a cancer treatment is its low nephrotoxicity.¹¹⁰ The EPR measurements described in this chapter suggest that this is due to sequestering of the complex by fast, non-coordinate binding of the parent compound in the hydrophobic binding domains of hsA. By contrast, the comparatively toxic KP418 complex does not exhibit these types of interactions, demonstrating non-coordinate interactions with hsA only after aqueous ligand exchange (**Figure 2-7**). This process is very slow overall, indicating that levels of the free complex will remain high in serum for several hours after administration to patients. Differences in the non-coordinate binding of the intact complexes likely arise from the relative ability of the indazole and imidazole ligands to participate in hydrophobic interactions with hsA. From this, the design of new compounds in this family should include the consideration of hydrophobic axial ligands, possibly containing motifs to optimize π - π stacking with aromatic protein side chains, to facilitate rapid binding to hsA, thereby minimizing side effects.

Overall, these studies demonstrate the complexity and diversity of the behaviour of Ru(III) complexes under physiological conditions. However, rather than hindering further development of these compounds as anticancer drugs, this shows that there is great scope for fine-tuning their properties for targeted treatments and greater efficacy.

3. Interactions of the Antimetastatic Ru(III) Complex NAMI-A with Human Serum Albumin^b

3.1. Introduction

NAMI-A is the most intensively studied of the ruthenium anticancer complexes and has attracted particular attention because of its ability to prevent the formation of metastases and inhibit their growth.^{127,156-158,160-165,242-244} The most commonly cited mechanism for the activity of Ru(III)-based anticancer agents involves ligand exchange with serum components followed by cellular uptake.^{57,175,191} Within hypoxic tumour environments, the Ru(III) centre may be reduced to give more labile Ru(II) species, which are activated towards DNA binding and consequently stimulate apoptosis.⁴⁹ This suggests the possibility of enhanced drug selectivity both through protein mediated transport and by selective generation of activated Ru(II) species within tumours. However, this hypothesis remains controversial and there is growing evidence that variation in the axial ligands of these compounds strongly influences their fundamental mode of action.¹⁰⁸ In the case of NAMI-A, interactions with extracellular matrix components and cell surfaces have been implicated as dominant factors in its observed antimetastatic activity.

By analyzing the speciation of NAMI-A under physiological conditions using EPR spectroscopy, additional insight in the mechanism of this complex was obtained. EPR measurements were used to identify the species generated by aquation and oligomerization in solutions of NAMI-A in buffer. Comparison of these data with spectra from hsA-bound complexes and NAMI-A in whole human serum, has revealed different

[b] This chapter is based on a published paper and reproduces material with permission from: Webb, M.I.; Walsby, C.J. "Control of Ligand Exchange Processes and the Oxidation State of the Antimetastatic Ru(III) Complex NAMI-A Through Interactions with Albumin." Dalton Transactions 2011, 40, 1322-1331. Copyright. 2011 The Royal Society of Chemistry.

protein binding modes. Using ascorbic acid as a reducing agent representative of *in vivo* conditions, it was determined that protein binding also dramatically enhances redox stability.

3.2. Experimental

3.2.1. Synthesis

All reagents and hsA ($\geq 97\%$ purity) were purchased from Sigma-Aldrich. Buffer components were purchased from Bioshops Canada. Pooled normal human serum was purchased from Innovative Research Inc. NAMI-A was synthesized using literature procedures.^{147,245} The elemental purity of NAMI-A synthesized in this work was determined from CHN analysis. C₈H₁₅N₄OSCl₄Ru Calc. C 20.97 H 3.30 N 12.23, Found C 21.16 H 3.29 N 12.08. Lyophilized hsA was dissolved in phosphate buffer (20 mM NaHCO₃, 50 mM NaH₂PO₄ 150 mM NaCl, pH 7.4) and used without further purification.

3.2.2. Preparation of EPR Samples

NAMI-A in Buffer. NAMI-A was dissolved in phosphate buffer to give a concentration of 6 mM, and incubated at 37 °C. Aliquots of 210 µL were withdrawn at the following time points: 0, 10, 20, 30 minutes, 1, 2, 6, and 24 hours. Each sample was promptly mixed with 90 µL of glycerol and frozen in liquid nitrogen.

NAMI-A with hsA. A 0.75 mM solution of hsA in phosphate buffer (600 µL) was added to a 1.5 mM solution of NAMI-A also in phosphate buffer (600 µL). The combined solution was then diluted to 4 mL with phosphate buffer and incubated at 37 °C for one of the following time periods: 0, 10, 20, 30 minutes, 1, 2, 6, and 24 hours. Each 4 mL solution was concentrated down to a volume of less than 200 µL using an Amicon centrifugal filter unit (molecular-weight cut-off 30 kDa) by centrifuging at 8 °C and 4500 rpm for 30 minutes, or until a volume of less than 200 µL was attained. The resulting filtered product was then mixed with 90 µL of glycerol and diluted to a final volume of 300 µL with phosphate buffer, transferred to an EPR tube, and immediately frozen in liquid nitrogen.

NAMI-A with Ascorbic Acid in Buffer. A 670 μ M solution of NAMI-A was prepared in phosphate buffer. Aliquots of an ascorbic acid solution (1.36 mM) were subsequently added to give the following acid concentrations: 0, 6, 85, 170, 256 and 670 μ M. The resulting solution was subjected to: no incubation, incubation at 25 °C and 37 °C respectively. Aliquots of 210 μ L for each acid concentration were mixed with 90 μ L of glycerol, transferred to an EPR tube, and immediately frozen in liquid nitrogen.

NAMI-A with hsA and Ascorbic Acid. (i) Following the same procedure as above, a 1.5 mM solution of NAMI-A was mixed with a 0.75 mM solution of hsA and incubated at 37 °C. After incubation, ascorbic acid (1.36 mM) was added to the mixture, giving an acid concentration of 85 μ M. The resulting solution was filtered and prepared as described above.

(ii) Following the same procedure as (i), ascorbic acid (1.36 mM) was added to the NAMI-A and hsA mixture prior to incubation, with an acid concentration of 85 μ M. The samples were subsequently prepared as described previously.

NAMI-A in Human Serum. NAMI-A was added directly to whole human serum (5 mL) and gently mixed until dissolved. The resulting solution was incubated at 37 °C with 600 μ L aliquots taken and diluted to 1 mL with ultra-pure water after the following incubation time points: 0, 10, 20, 30 minutes, 1, 2, 6, and 24 hours. The protein-bound fractions from each 1 mL solution was prepared as described above for the preparation of NAMI-A with hsA. The filtered product was mixed with 90 μ L of glycerol and diluted to a final volume of 300 μ L with ultra-pure water, then transferred to an EPR tube and immediately frozen in liquid nitrogen.

3.2.3. EPR Measurements and Simulation

See section 2.2.4.

3.2.4. EPR Experimental Conditions

See section 2.2.5.

3.3. Results and Discussion

EPR measurements have allowed for the identification of Ru(III) species formed from NAMI-A under physiological conditions by ligand exchange with water or protein ligands. NAMI-A generally exhibits relatively slow ligand exchange processes, typical for a Ru(III) complex under the chosen experimental conditions (pH 7.4, 37 °C).⁴¹ Changes in the concentrations of various Ru(III) complexes in solution were tracked by first freezing the samples in liquid nitrogen after selected incubation times over a 24-hour period. This essentially constituted a freeze-quench experiment on a long time scale where EPR spectra of the frozen solutions provided a “snap shot” of the species involved and their relative concentrations. The long incubation times used in these studies was chosen based on reports that the half-life for clearance of ruthenium species, following intravenous infusion of NAMI-A, from plasma in human patients is around 50 hours.¹¹¹ In studies of NAMI-A with hsA and in whole human serum, incubation was followed by ultrafiltration, with a molecular-weight cut-off of 30 kDa, to isolate protein-bound fractions. This enabled characterization of both coordinate and non-coordinate interactions of Ru(III) complexes with hsA and excluded signals from unbound complexes in the incubated solutions. The ligand sets and symmetry of the various Ru(III) complexes formed by exchange processes were characterized by specific line positions, defined by g values, and linewidths. When several species were present in solution simultaneously, overlap of their individual spectra required simulation of the experimental data to extract the contribution from each type of complex and their respective signal intensities. The process for the simulation of individual EPR spectra is outlined in section 1.7.

3.3.1. Ligand Exchange Processes in Phosphate Buffer

Ru(III) complexes frequently show complicated ligand-exchange processes in aqueous solutions at physiological pH⁴¹ (see Chapter 2).²⁴⁶ To produce physiologically relevant conditions for aqueous speciation studies of NAMI-A, the complex was incubated in a buffer system containing 50 mM NaH₂PO₄, 150 mM NaCl, and 20 mM NaHCO₃, with a pH of 7.4 at 37 °C. The solution concentration of chloride ions

influences the rates and equilibria of chloride ligand-exchange processes for NAMI-A,¹⁷⁶ and so this buffer solution contains a concentration of Cl^- matching that found in human blood.¹⁷⁸ Immediately after dissolution in buffer, NAMI-A gives a well-resolved and intense uniaxial EPR spectrum (**Figure 3-1**), which is simulated accurately with $g_{\perp} = 2.47$ and $g_{\parallel} = 1.72$ and linewidths of $LW_{\perp} = 105$ and $LW_{\parallel} = 180$ Gauss. This is consistent with a mononuclear low-spin Ru(III) complex with tetragonal symmetry,²¹⁹ as expected for the complex prior to ligand exchange. After 10 minutes at 37 °C, the overall spectral intensity remains essentially unchanged but an additional uniaxial spectrum, with a smaller g value dispersion ($g_{\perp} = 2.32$, $g_{\parallel} = 1.87$, and linewidths $LW_{\perp} = 75$, $LW_{\parallel} = 60$ Gauss) is clearly visible. As for NAMI-A, the observation of a uniaxial EPR signal, which in this case has very narrow linewidths, demonstrates that the new species also has tetragonal symmetry. This requires that one of the axial ligands has been exchanged and, given that the imidazole ligand is known to be kinetically inert under these conditions,¹⁷⁶ must correspond to replacement of DMSO. Therefore this spectrum was assigned to the axially symmetric mono-aqua species, which is formed by exchange of the DMSO with a water ligand from the buffer (*NAMI-A-H₂O-A*).

Simulation of the spectrum obtained after 10 minutes of incubation also reveals a small contribution from a third species, which is produced concurrently but at a significantly slower rate. This species exhibits a rhombic EPR spectrum ($g = [2.40, 2.28, 1.79]$; $LW = [175, 200, 275]$ Gauss; **Figure 3-1b**), indicating lower symmetry, which is consistent with exchange of an equatorial chloride for a water ligand, to give a second mono-aqua species (*NAMI-A-H₂O-E*). It is clear that the tetragonal symmetry complex, *NAMI-A-H₂O-A*, is produced significantly faster than the lower symmetry complex, *NAMI-A-H₂O-E*, during the early stages of aquation. This demonstrates that axial DMSO exchange is significantly faster under physiologically relevant conditions than for equatorial Cl^- ligands.

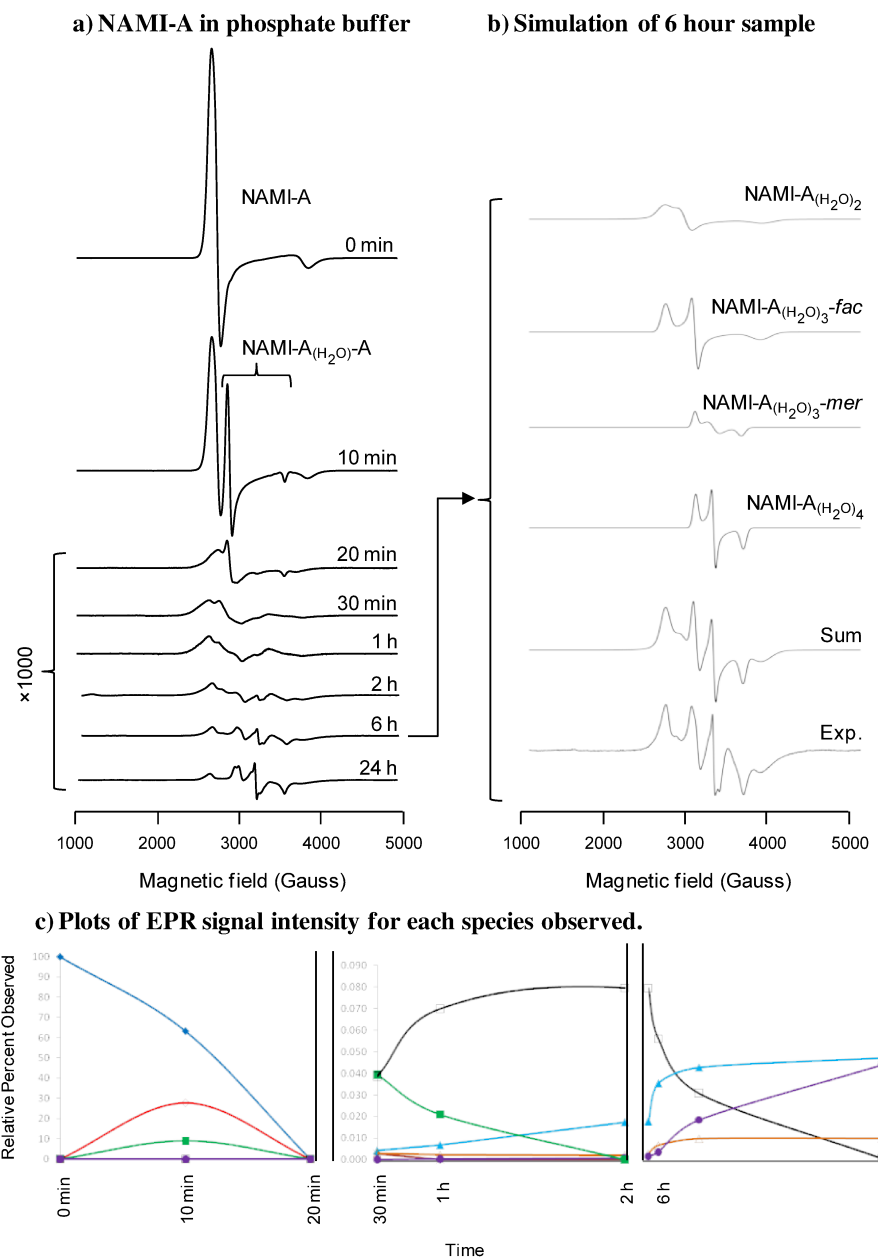


Figure 3-1 EPR spectra of frozen solutions of NAMI-A after incubation in buffer at 37 °C. a) EPR spectra after incubation times of 0 – 24 hours. b) Deconvolution of 6 hour spectrum by simulation. c) Change in EPR signal intensity for species generated, as determined by spectral simulation. Legend: ♦ (blue) NAMI-A, ◇ (red) NAMI-A- H_2O -A, ■ (green) NAMI-A- H_2O -E, □ (black) NAMI-A- $(H_2O)_2$, ▲ (aqua) NAMI-A- $(H_2O)_3$ -fac, △ (orange) NAMI-A- $(H_2O)_3$ -mer, ● (purple) NAMI-A- $(H_2O)_4$.

Bacac *et al.*¹⁷⁶ have described comprehensive ¹H NMR measurements of NAMI-A in buffer at 37 °C and report an overall rate of conversion to aquation products similar to that observed by these EPR studies. These authors also report the formation of the complexes that are assigned here as *NAMI-A-H₂O-E* and *NAMI-A-H₂O-A*, by direct observation of paramagnetic ¹H NMR from coordinated DMSO in the first case, and indirectly for the latter complex from the formation of free DMSO in solution. NMR measurements were not able to detect directly *NAMI-A-H₂O-A*, nor other aquation products. Indeed, *NAMI-A-H₂O-E* is the only aquation product of NAMI-A which has been directly identified prior to the EPR measurements reported here. UV-Vis measurements have also provided evidence of relatively rapid ligand-exchange processes in buffer,^{178,200,203} but these measurements cannot definitively identify the ligand sets of the species involved to distinguish, for example, between *NAMI-A-H₂O-E* and *NAMI-A-H₂O-A*. Recently reported DFT calculations have also sought to characterize these aquation processes. These calculations are limited by the accuracy of solvent models, but specific calculations of chloride ligand exchange have predicted rates in reasonable agreement with experimental reports.^{213,215} In the most recent of these studies²¹⁴ it was reported that the activation free energy of Cl⁻ dissociation from NAMI-A in water is larger than that of DMSO, consistent with the observation that the latter is replaced more rapidly under physiological conditions.

Analysis of EPR spectra collected over 24 hours of incubation at 37 °C identified four additional mononuclear Ru(III) species, which are generated by further aquation of *NAMI-A-H₂O-E* and *NAMI-A-H₂O-A*. One of these, characterized by a rhombic EPR spectrum ($g = [2.53, 2.08, 1.88]$; LW = [160, 125, 250]), is produced relatively rapidly to become the dominant Ru(III) species in solution after 30 minutes of incubation. Concomitant loss of signal intensity from *NAMI-A-H₂O-A* and *NAMI-A-H₂O-E* indicates that both of these species are converted to this product with incubation. Therefore, this species must be the *cis*-diaqua complex, *NAMI-A-(H₂O)₂*, produced either by the exchange of an equatorial chloride from *NAMI-A-H₂O-A*, or loss of the axial DMSO from *NAMI-A-H₂O-E* (**Figure 3-2**). After several hours of further incubation, two additional rhombic signals increasingly dominate the EPR spectra (**Figure 3-1**). These are assigned

to the meridional and facial isomers of the triaqua complexes, which are formed by a further aquation step involving replacement of a Cl^- ligand, either *cis* or *trans* to the equatorial water of *NAMI-A-(H₂O)₂*. The greater *trans* effect of chloride, as compared to water or hydroxide ligands, suggests that the facial isomer will be formed preferentially, with a greater corresponding EPR signal intensity than for the meridional isomer. Consequently, the spectra are identified as follows: *NAMI-A-(H₂O)_{3-fac}* ($g = [2.23, 2.08, 1.88]$; LW = [100, 60, 225] Gauss); and *NAMI-A-(H₂O)_{3-mer}* ($g = [2.22, 2.08, 1.87]$; LW = [60, 120, 90] Gauss). After several hours of incubation, a final aquation step removes a further chloride ligand to give a complex, *NAMI-A-(H₂O)₄*, characterized by a spectrum which can be simulated with $g = [2.23, 2.07, 1.87]$ and LW = [60, 40, 70] Gauss (**Figure 3-1**).

A number of reports have postulated the formation of these types of aquated complexes during the aquation of NAMI-A in buffer solution.^{154,176,213-215} However, the high sensitivity of EPR has allowed for the first direct detection of such species despite the low concentrations present in buffer. Loss of the relatively acidic protons of coordinated water molecules may produce complexes with hydroxide ligands,^{41,154,247} but it was not possible to determine spectroscopically whether this is the case.

A dramatic decrease in the overall EPR signal intensity is observed after only 20 minutes of incubation at 37 °C. Given the absence of significant reducing or oxidizing agents in the buffer solution used, formation of EPR silent Ru(II) or Ru(IV) species can be excluded as the origin of this effect. Oligomerization of Ru(III) NAMI-A aquation products to give oxo- or hydroxo-bridged species can, however, account for these observations since antiferromagnetic coupling between adjacent Ru(III) ($S = \frac{1}{2}$) centres will produce a net spin of $S = 0$. Previous NMR studies on the solution behaviour of NAMI, the sodium salt derivative of NAMI-A, has also suggested that oligomeric species form in solution.²⁴⁷ This process is accompanied by a distinct change in the colour of the NAMI-A solution from yellow to dark brown, in accord with previous observations.^{174,176} Interestingly, the loss of EPR signal intensity is essentially complete after 30 minutes, and even after 24 hours of incubation spectra from mono-nuclear Ru(III) species are readily observed (**Figure 3-1**). This indicates that the polynuclear species are primarily

generated from the aquated complexes produced in the first 30 minutes of incubation, that is: *NAMI-A-H₂O-A*, *NAMI-A-H₂O-E*, and *NAMI-A-(H₂O)₂*. Given that the results indicate *NAMI-A-H₂O-A* is formed rapidly in buffer, dimerization of this complex likely gives the main diamagnetic product. Measurements of signals from *NAMI-A-(H₂O)₂*, *NAMI-A-(H₂O)_{3-mer}*, *NAMI-A-(H₂O)_{3-fac}* and *NAMI-A-(H₂O)₄* after long incubation periods suggests that these species do not oligomerize significantly, and that their formation from the mono-aqua species is competitive with formation of the polynuclear complexes, as outlined in **Figure 3-2**.

Comparison of ligand-exchange processes observed for NAMI-A with the structurally-related complex KP418 (imidazolium [trans-RuCl₄(1*H*-imidazole)₂]), which has two axial imidazole ligands, provides insight into the origin of its solution behaviour. Previous studies, including those described in Chapter 2, have shown that KP418 also undergoes aquation by loss of Cl⁻ ligands to give mono- and diaqua species in physiological buffer solution, with no evidence for loss of the axial imidazole ligands.^{226,231,232,246} There is no indication of significant oligomerization of KP418, since the EPR spectrum after 24 hours of incubation at 37 °C in buffer at pH 7.4 shows no reduction in overall signal intensity.²⁴⁶ Comparison of the NAMI-A and KP418 data demonstrates that the axial ligands modulate intermolecular interactions, and further implicates *NAMI-A-H₂O-A* as the primary source of oligomers.

The EPR measurements reported here highlight the importance of aging in the preparation of NAMI-A solutions for therapy. Previous reports indicate that formation of polynuclear Ru(III) complexes leads to reduced activity.^{176,201} Thus, if mononuclear complexes are desired as the primary active species, then solutions of NAMI-A will need to be prepared immediately prior to treatment.

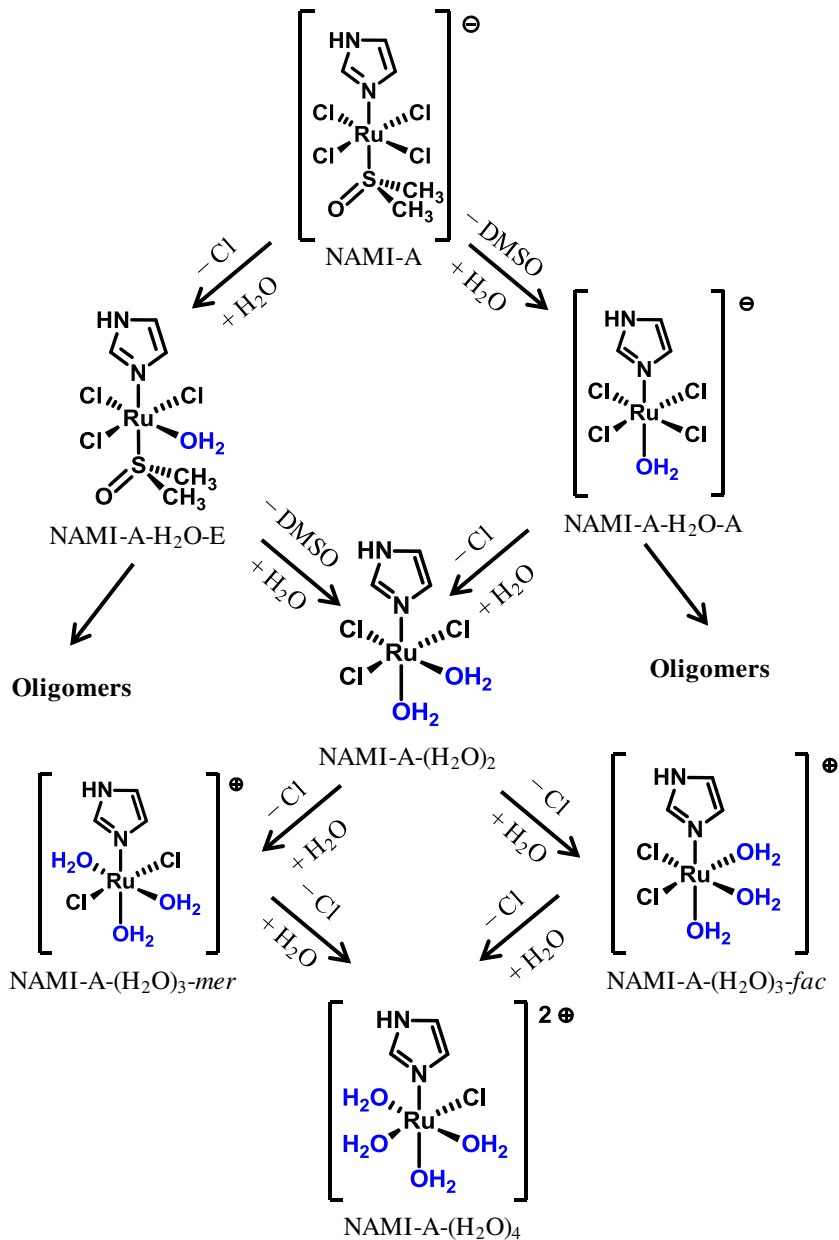


Figure 3-2 Speciation of NAMI-A in buffer at pH 7.4 determined from EPR measurements.

3.3.2. Interaction of NAMI-A with Human Serum Albumin

As the most abundant protein in the circulatory system, hsA plays an important role in the binding, transport, and metabolism of many pharmaceuticals.⁷⁵ NAMI-A has

been observed to bind to hsA,^{57,204} with up to five equivalents of Ru bound per protein molecule.²⁰² However the nature of these interactions remains speculative, with histidine coordination suggested as the preferred binding mode.²⁰⁴

To study these types of interactions for NAMI-A, the complex was incubated with hsA at 37 °C in buffer, after which high molecular weight components were separated by centrifugal ultrafiltration and characterized by EPR spectroscopy. As a result, the spectra shown in **Figure 3-3** report only protein-bound Ru(III) complexes. Within the first 10 minutes of incubation at 37 °C, EPR measurements demonstrate the presence of two dominant species with well-defined uniaxial signals. These spectra have g values and linewidths that are essentially identical to those observed for NAMI-A and *NAMI-A-H₂O-A*, while a small contribution is also observed from *NAMI-A-H₂O-E*. Since these measurements are of protein-bound fractions, this demonstrates that these complexes are able to form non-coordinate interactions with hsA. Similar phenomena have been identified in studies of the structurally similar complexes KP1019 and KP418, and are assigned to interactions with the hydrophobic binding domains of albumin (Chapter 2).²⁴⁶ In the case of KP1019, rapid non-coordinate binding to hsA has been related to its remarkably low levels of side effects observed in human trials^{110,246} and similar behaviour may also account for the relatively low toxicity of NAMI-A.^{183,248} Isolation of high molecular weight components was performed at 8 °C to minimize the rates of ligand-exchange processes during centrifugal ultrafiltration. However, this time period (30 minutes), in addition to 2 minutes at 25 °C required to prepare the NAMI-A solution and mix with hsA in buffer, inevitably led to some contributions from mono-aqua species non-coordinately bound to the protein prior to incubation at 37 °C.

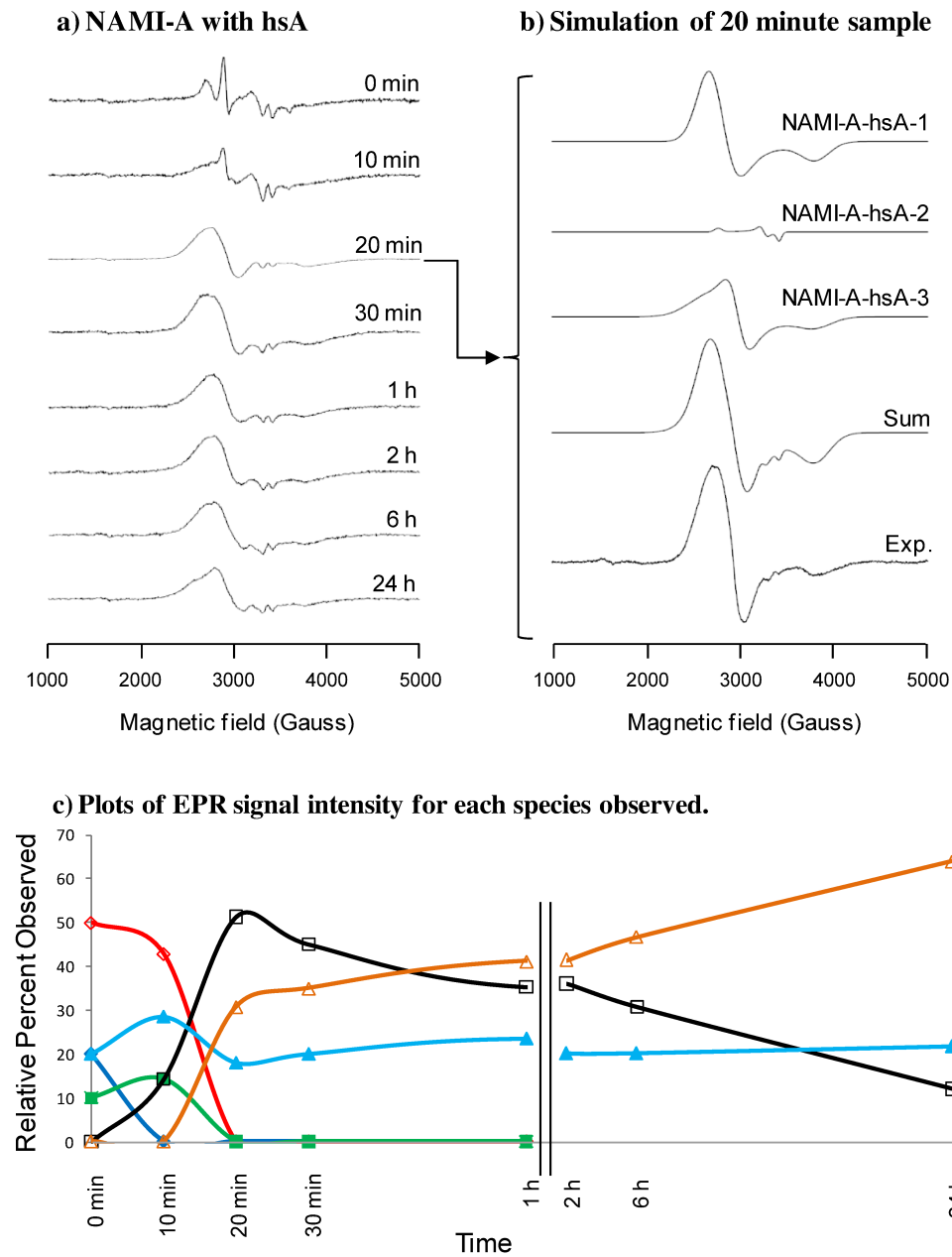


Figure 3-3 EPR spectra from frozen solutions of NAMI-A after incubation in buffer with hsA at 37 °C. a) EPR spectra following incubation times of 0 – 24 hours. b) Deconvolution of 20 minute spectrum by simulation. c) Change in EPR signal intensity for species generated, as determined by spectral simulation. Legend: ◊ (red) NAMI-A, ◇ (blue) NAMI-A-H₂O-A, ■ (green) NAMI-A-H₂O-E, □ (black) NAMI-A-hsA-1, ▲ (aqua) NAMI-A-hsA-2, △ (orange) NAMI-A-hsA-3.

With further incubation the spectrum is increasingly dominated by a uniaxial signal with broad lines which reaches its maximum intensity within 20 minutes (*NAMI-A-hsA-1*: $g_{\perp} = 2.43$, $g_{\parallel} = 1.76$; linewidths, $LW_{\perp} = 300$, $LW_{\parallel} = 300$ Gauss). A second broad rhombic signal is observed with significant intensity after 20 minutes of incubation (*NAMI-A-hsA-2*: $g = [2.54, 2.26, 1.76]$, $LW = [450, 175, 350]$ Gauss) (**Figure 3-3**). Clearly, neither of these species corresponds to any of the aquation products produced in the buffer solution alone, and so they are assigned to Ru(III) complexes that have formed coordinate interactions with the protein via ligand exchange. The g values and broad line shapes observed in the EPR spectra of these species suggest that NAMI-A, similar to KP1019, is coordinated to hsA by ligand exchange with histidine imidazoles. The symmetry of the protein adducts, reflected in their EPR spectra, allows for the identification of their coordination modes. *NAMI-A-hsA-1* exhibits a uniaxial spectrum, demonstrating a tetragonal complex with protein coordination at the axial position occupied by DMSO in the original complex. By contrast, *NAMI-A-hsA-2* is characterized by a distinctly rhombic spectrum, indicating lower symmetry derived from protein coordination at an equatorial position. Analysis of the time-dependent changes in signal intensities from these complexes (**Figure 3-3c**) reveals that *NAMI-A-hsA-1* is formed first with *NAMI-A-hsA-2* reaching a comparable concentration after one hour of incubation. These observations can be explained if the protein adducts are formed by exchange with water ligands of aquated complexes. Exchange of the axial water ligand of *NAMI-A-H₂O-A* to give *NAMI-A-hsA-1*, and equatorial water of *NAMI-A-H₂O-E* to give *NAMI-A-hsA-2* is consistent with both the spectroscopically determined symmetry of these complexes and the time-dependence of their formation, since the relatively slow formation of *NAMI-A-H₂O-E* is rate determining in the production of *NAMI-A-hsA-2*, as outline in **Figure 3-4**.

In addition to these broad signals, a third spectral component with narrow linewidths is observed after incubation of NAMI-A with hsA. This species is characterized by a rhombic EPR spectrum (*NAMI-A-hsA-3*: $g = [2.42, 2.06, 1.96]$; $LW = [80, 70, 55]$ Gauss) (**Figure 3-3**). Although its final intensity is significantly lower than the dominant protein-bound species, *NAMI-A-hsA-1* and *NAMI-A-hsA-2*, it forms more

rapidly, reaching its maximum intensity within 10 minutes of incubation, and remains virtually unchanged with further incubation. The smaller g value dispersion of *NAMI-A-hsA-3*, as compared to the other two coordinately bound species, indicates binding with a different amino-acid side chain. Furthermore, the lower intensity and narrower linewidths of *NAMI-A-hsA-3* indicate a single, ordered ligand environment consistent with a specific protein binding site.

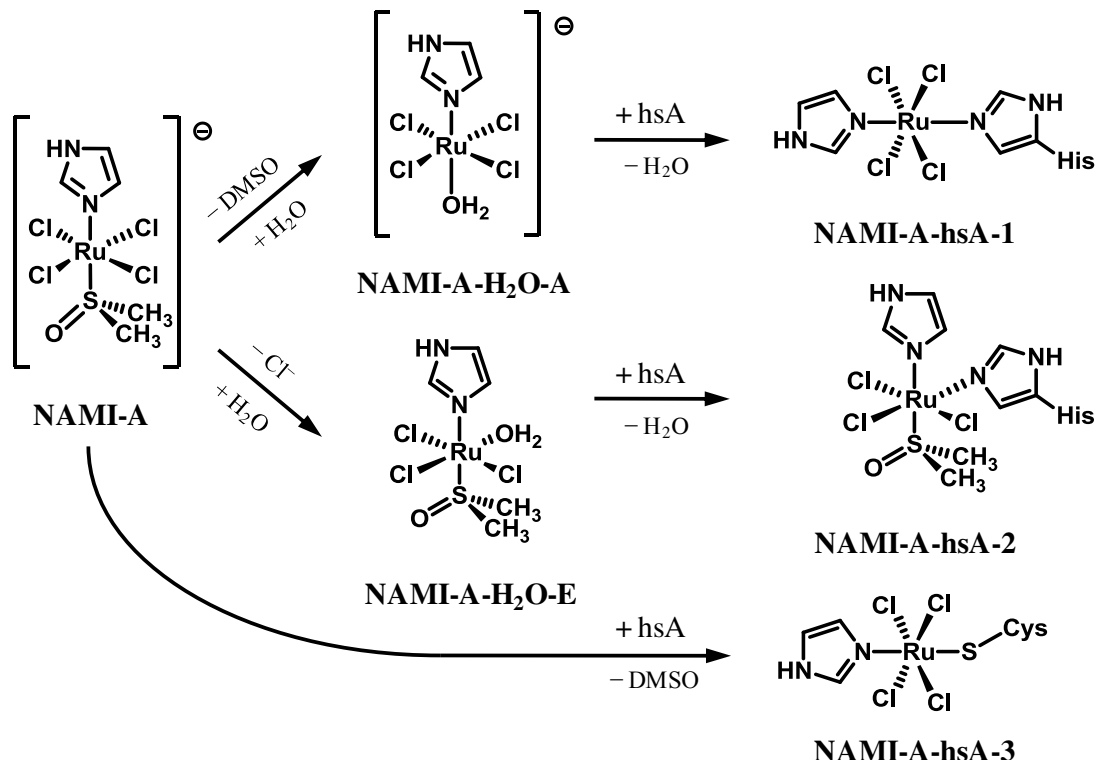


Figure 3-4 Predominant NAMI-A ligand exchange processes with hsA, leading to three distinct protein coordinated species with characteristic EPR spectra.

The broad lines observed for *NAMI-A-hsA-1* and *NAMI-A-hsA-2* are consistent with an ensemble of spectra from slightly different histidine binding sites on the surface of the protein. Observation of an EPR spectrum from a second protein-bound species, *NAMI-A-hsA-3*, with sharp lines and smaller g value dispersion (**Figure 3-3**), indicates a different ligand binding process and a single well-defined binding site. As mentioned in the previous chapter, hsA has one free cysteine (Cys-34) located on the protein surface. Given the presence of a Ru-sulfur bond in NAMI-A, it seems likely that such an

interaction with the thiolate side chain of Cys-34 would be favourable at the labile axial position of NAMI-A or *NAMI-A-H₂O-A* to give *NAMI-A-hsA-3* (**Figure 3-4**). It is notable that interactions of platinum-based drugs with Cys-34 of hsA have been described,^{79,249} further suggesting that this is likely an important mode of protein coordination for ruthenium complexes.

3.3.3. Behaviour of NAMI-A in Whole Human Serum

EPR measurements of protein-bound fractions from NAMI-A incubated at 37 °C in whole human serum reveal strong spectra at all time points up to 24 hours (**Figure 3-5**). Prior to incubation at this temperature signals from *NAMI-A-H₂O-A*, *NAMI-A-H₂O-E*, and the hsA-bound complex *NAMI-A-hsA-3* are observed. This indicates that these interactions, non-coordinate for *NAMI-A-H₂O-A/E*, and coordinate for *NAMI-A-hsA-3*, form very rapidly with hsA, as described above for similar experiments with the protein in buffer. After 20 minutes of incubation the predominant EPR signals correspond to the coordinately hsA-bound Ru(III) complexes *NAMI-A-hsA-1* and *NAMI-A-hsA-2*, demonstrating that albumin-bound mono-nuclear Ru(III) species formed by coordinate interactions with protein side chains are predominant in serum. After the initial formation of coordinately-bound hsA complexes, the EPR signal intensity remains essentially unchanged, even after 24 hours of incubation at 37 °C, evidence that this process prevents the oligomerization observed in buffer solutions of the complex at pH 7.4. The strong EPR signal intensity shows that mononuclear Ru(III) centres predominate under these conditions and the relatively rapid binding that occurs during early stages of incubation ensures the stability of these species at longer time intervals.

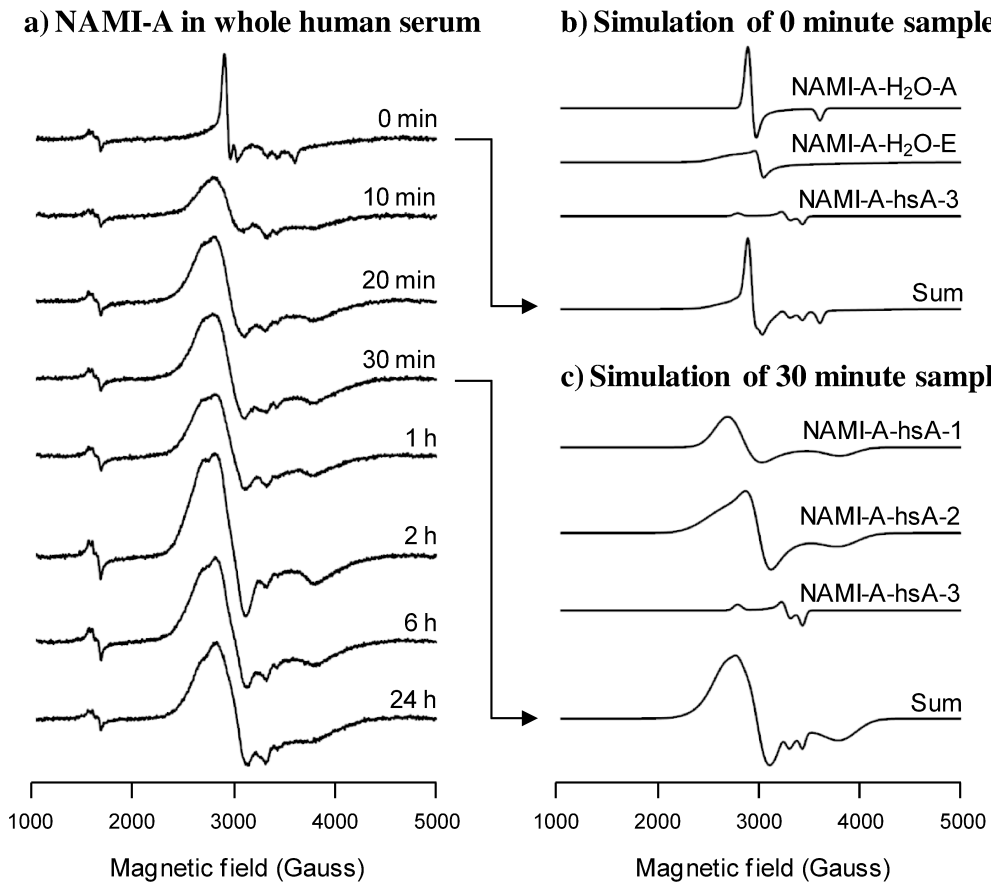


Figure 3-5 EPR spectra from frozen solutions of NAMI-A after incubation in whole human serum at 37 °C. a) EPR spectra following incubation times of 0 – 24 hours. b) Deconvolution of 0 minute spectrum by simulation, c) Deconvolution of 30 minute spectrum by simulation. For simulation parameters (g values and linewidths) see main text.

3.3.4. Reduction of NAMI-A by Ascorbic Acid

NAMI-A has a relatively high reduction potential (235 mV vs. NHE)¹¹⁶ and consequently can be reduced by a variety of agents present *in vivo*, including ascorbic acid, uric acid, and glutathione.^{178,201,205} Previous studies have shown that the Ru(III) centre of NAMI-A is readily reduced to Ru(II) in the presence of ascorbic acid.^{178,201} This process can be followed by EPR through loss of signal intensity due to the production of diamagnetic Ru(II) species. As shown in **Figure 3-6a**, when NAMI-A (670 µM) is dissolved in a physiological buffer solution containing 85 µM ascorbic acid at 37 °C, reduction of almost all Ru(III) centres occurs within 10 minutes. To gain insight into the

concentration and temperature dependence of the reduction rate, a series of experiments with different concentrations of ascorbic acid (6–670 µM) were performed at both 25 and 37 °C. From measurements after 0 minutes and 10 minutes of incubation with these various conditions (Appendix A – **Figure A-5**), it is clear that this modest increase in temperature significantly accelerates the reduction process. Furthermore, relatively low concentrations of the reducing agent in the buffer solution can reduce NAMI-A and its aquation products within 10 minutes at 37 °C. When EPR measurements were made on samples where reduction was incomplete, two uniaxial spectra were observed with g values corresponding to NAMI-A and *NAMI-A-H₂O-A* (**Figure 3-6a**). In these spectra, *NAMI-A-H₂O-A* has a higher intensity relative to NAMI-A after comparable incubation times in buffer only, indicating that ligand exchange slows the rate of reduction under these conditions.

3.3.5. Effect of hsA Interactions on Reduction of NAMI-A

As outlined in the introductory chapter, the oxidation state of the ruthenium centre likely plays an important role in the biological activity of NAMI-A since it influences the propensity for ligand exchange. Although there is growing evidence that intracellular processes are not as relevant to the activity of NAMI-A, modulation of the oxidation state of NAMI-A in blood following intravenous infusion will be equally important to interactions with extracellular biomolecules, influencing its observed antimetastatic activity.^{108,125,127,164,165,191}

The influence of protein binding on the reduction of the Ru(III) centres of NAMI-A and its aquation products was determined through two different studies. In the first instance, protein-bound fractions of NAMI-A and its aquation products were prepared as described above, after which ascorbic acid was added and the samples were very briefly mixed at 25 °C before being frozen in liquid nitrogen for EPR measurements. At short incubation times only very weak signals were detected, demonstrating the absence of non-coordinately protein bound Ru(III) species. This indicates that the complexes are still accessible to ascorbic acid in the buffer solution under these conditions, demonstrating that the hydrophobic binding domains of hsA do not provide protection from reducing

agents *in vivo*. This suggests the potential for non-specific interactions of the complexes with hSA, where binding of the complexes occurs outside of the main hydrophobic binding sites. However, with further incubation at 37 °C, followed by addition of ascorbic acid, signals from the coordinately-bound species *NAMI-A-hsA-1*, *NAMI-A-hsA-2*, and *NAMI-A-hsA-3* were observed with signal intensities comparable to the experiments with hSA alone (**Figure 3-6b**). In this case, the complexes are expected to be bound primarily to surface imidazoles (*NAMI-A-hsA-1* and *NAMI-A-hsA-2*) and should be easily accessible to reducing agents.

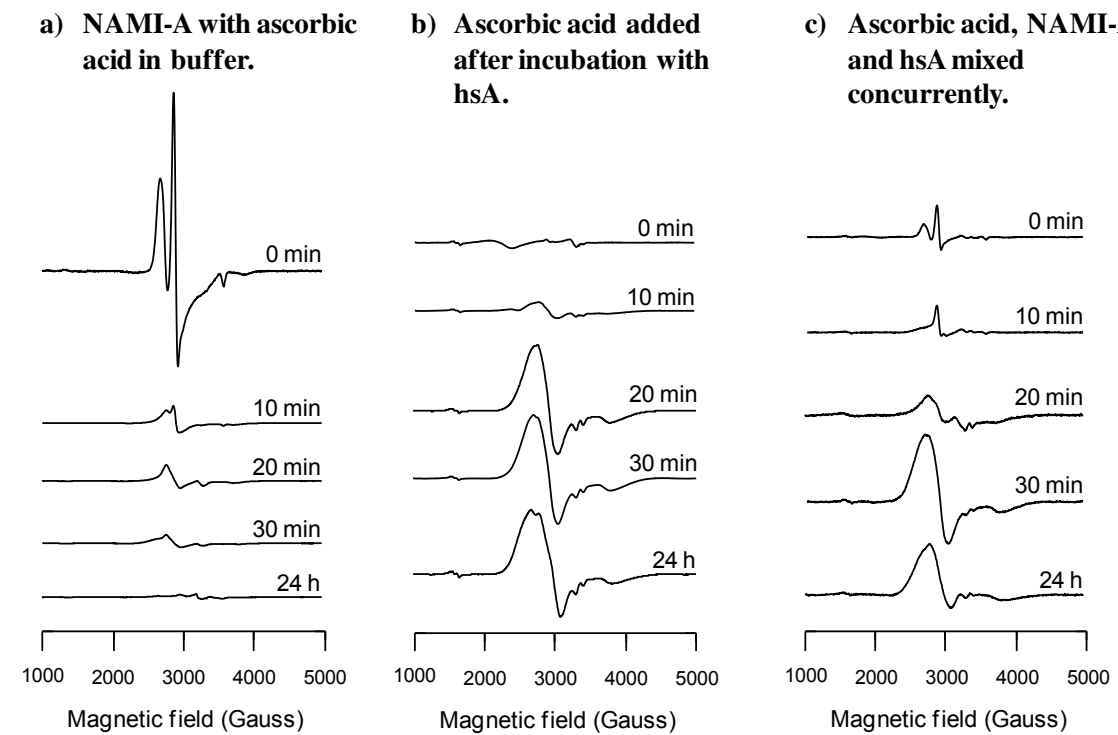


Figure 3-6 EPR spectra from NAMI-A frozen solutions after incubation at 37 °C with: (a) ascorbic acid (85 µM), (b) hSA, followed by addition of ascorbic acid, (c) hSA and ascorbic acid.

Binding of a histidine imidazole to the axial position of NAMI-A or *NAMI-A-H₂O-A*, as anticipated based on the protein binding studies described above, produces a ligand set that is similar to the structurally-related complex KP418, which has two axial imidazole ligands. KP418 has a sufficiently negative reduction potential (-274 mV vs. NHE) so that the 3+ oxidation state is stable towards reducing agents found in serum.⁵³ A

lowering of the reduction potential with coordinate protein binding thus accounts for the reductive stability of the Ru(III) centres of *NAMIA-hsA-1* and *NAMI-A-hsA-2* observed.

In the case of *NAMI-A-hsA-3*, replacement of sulfur-bound DMSO from NAMI-A with a cysteine thiolate seems unlikely to change the reduction potential significantly. The reductive stability of this species, as demonstrated by the EPR experiments, may arise from coordination to cysteine-34 of hsA. This residue is located within a hydrophobic cavity on the surface of the protein which could limit the access of ascorbic acid to the Ru(III) centre.²³⁷

In a scenario more consistent with a treatment procedure, a second set of experiments was performed where NAMI-A, ascorbic acid, and hsA in buffer solutions were mixed simultaneously, then incubated at 37 °C. After selected incubation times, protein-bound fractions were separated using ultrafiltration. Within the first 10 minutes of incubation, small EPR signals from non-coordinately bound NAMI-A, *NAMI-A-H₂O-A*, and *NAMIA-H₂O-E* are observed (**Figure 3-6c**), indicating interactions of these complexes with hsA prior to reduction in solution. Following 30 minutes of incubation, these signals were replaced by relatively intense signals from both *NAMI-A-hsA-1* and *NAMI-A-hsA-2*. Coordinate binding of Ru(III) complexes may be involved in the observation of these species, as described above. However, a more compelling explanation is that the complexes are initially reduced to Ru(II) species in solution, prior to hsA binding. Ru(II) complexes coordinated to hsA may then be oxidised back to Ru(III) via electron transfer to internal disulfides of hsA, generating thiolates.^{250,251} These protein bound species are very stable at 37 °C as shown by strong EPR signals after 24 hours of incubation (**Figure 3-6c**).

Similar experiments performed in human serum show that binding to hsA also gives the Ru(III) species *NAMI-A-hsA-1* and *NAMI-A-hsA-2* in the presence of naturally occurring biological reducing agents. These experiments are directly relevant to intravenous treatment with freshly prepared solutions of NAMI-A, and indicate that protein-bound Ru(III) complexes are the dominant species *in vivo* under such conditions.

3.4. Conclusions

For NAMI-A and other Ru(III)-based anticancer compounds to advance further in clinical development, a greater understanding of the origin of their activity is required. The intrinsic complexity arising from the many ligand-exchange and redox processes relevant to metal complexes under physiological conditions make this particularly challenging, as compared to studies of the behaviour of more conventional organic compounds. This is highlighted in the case of NAMI-A, which exhibits quite distinct activity compared to other structurally-similar Ru(III) compounds. Using EPR spectroscopy important new insights into the origin of this unique behaviour has been attained by analyzing ligand exchange processes and their influence on the oxidation state of the ruthenium centre. Treatment with NAMI-A via intravenous infusion first requires dissolution in buffer, a process which this study demonstrates produces an array of aquated species but is rapidly dominated by the production of oligomers. However, if the addition of the complex to serum is sufficiently rapid, oligomerization is prevented through rapid binding to serum albumin. Furthermore, coordinate protein interactions produce Ru(III) centres, even in the presence of biological agents such as ascorbic acid. Thus, treatment with fresh solutions of NAMI-A will produce mononuclear albumin-bound Ru(III) complexes as the dominant species *in vivo*.

4. Pyridine-based Analogues of the Antimetastatic Ru(III) Complex NAMI-A: Targeting Non-Coordinate Interactions with Albumin^c

4.1. Introduction

In the previous chapters, EPR was used to identify the transformations that KP418, KP1019, and NAMI-A undergo under physiological conditions. A particularly important finding of these studies was that KP1019 forms non-coordinate interactions with hsA more readily than KP418.²⁴⁶ This has been correlated with the greater ability of the indazole ligands of KP1019 to form interactions with the hydrophobic domains of hsA, as compared to the imidazole ligands of KP418. These observations form the basis of the hypothesis that non-coordinate interactions with hsA can be tuned to control the speciation and transport of the complexes *in vivo*. To explore this further, a series of pyridine-based analogues of NAMI-A have been synthesized and structurally characterized (**Figure 4-1**). This is a novel drug design strategy which has the potential to accelerate the formation of initial protein interactions while limiting coordinate binding. The latter consideration is particularly important since it impacts the bioavailability of the compounds.^{175,191}

The ligands chosen, **1**, pyridine (Pyr); **2**, 4-methylpyridine (MePyr); **3**, 4-phenylpyridine (PhPyr); **4**, diphenyl-4-pyridyl-methane (DiPhenPyr); **5**, 4-(4-nitrobenzyl)pyridine (NBenzPyr), were chosen to probe the importance of steric, hydrophobic, and electrostatic interactions with protein amino acid side chains. In addition to the NAMI-A analogues, which have a protonated heterocyclic ligand serving

[c] This chapter is based on a published paper and reproduces material with permission from: Webb, M.I.; Chard, R.A.; Al-Jobory, Y.M.; Jones, M.R.; Wong, E.W.Y.; Walsby, C.J. "Pyridinium Analogs of the Antimetastatic Ru(III) Complex NAMI-A Targeting Non-Covalent Interactions with Albumin" Inorganic Chemistry 2012, 51 (2), 954-966. Copyright 2012, American Chemical Society.

as the counterion (series **a**), the corresponding sodium compensated complexes (series **b**), which are analogues of NAMI¹⁵¹ (**Figure 4-1**) were also synthesized. This has enabled analysis of the effect of the counterions on protein interactions, while sodium-ion compensation improved the aqueous solubility of the compounds, particularly for the complexes with highly hydrophobic ligands (**3b** - **5b**). The synthesis of complexes with different counterions was also motivated by reports that this has evoked different specificities for the biomolecule interactions and anticancer activity of several Ru(III) complexes.^{113,143}

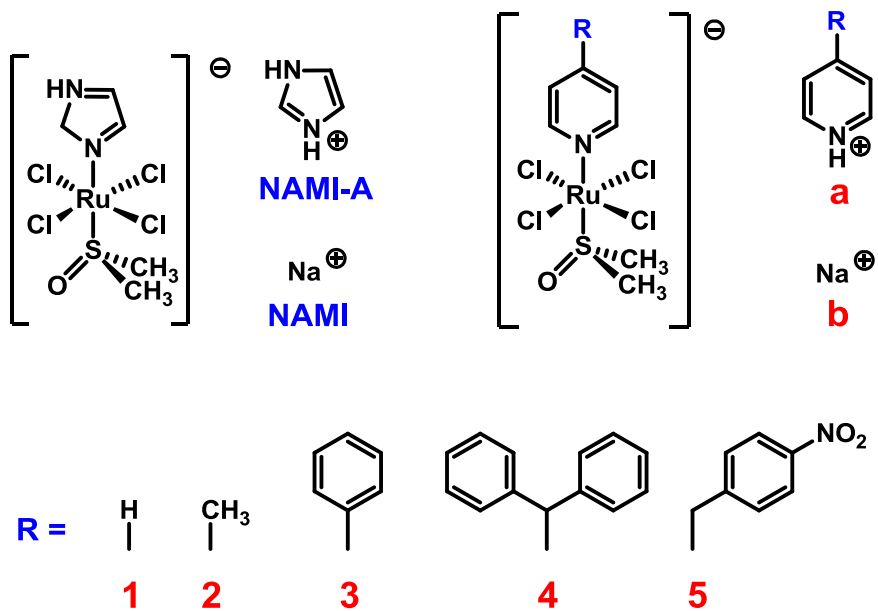


Figure 4-1 The promising antimetastatic agents, NAMI and NAMI-A, and the pyridine-based analogues whose synthesis is described in this chapter.

EPR was used to characterize the ligand-exchange processes of these compounds and their interactions with hsA. These studies demonstrate that the aqueous solution behaviour of the complexes is similar to NAMI-A, with exchange of Cl^- and DMSO ligands. However, the pyridine ligands have significant and distinct effects on the interactions with hsA. A trend in the stability of non-coordinate binding was observed, which correlated with the increasing ability of ligands **1** – **5** to promote interactions with the hydrophobic binding domains of hsA. These interactions forestall the formation of coordinate interactions and influence the final concentration of hsA-coordinated Ru(III)

species. The reduction potentials of **1a,b – 5a,b** are found to be higher than NAMI-A, and non-coordinate interactions with hsA do not prevent the reduction of the complexes in the presence of ascorbic acid, indicating that non-coordinately protein bound Ru(II) species may be generated. By contrast, protein coordinated Ru(III) complexes are found to be resistant to reduction, demonstrating the potential of hsA interactions to tune the behaviour of these compounds *in vivo*.

4.2. Experimental

4.2.1. Synthesis

PyrH[*trans*-RuCl₄(1*H*-Pyr)(DMSO-S)] (**1a**). [(DMSO)₂H][*trans*-Ru(DMSO-S)₂Cl₄] (212 mg, 0.38 mmol) was dissolved in methanol (15 mL) at room temperature. Pyridine (123 μ L, 1.52 mmol) was added directly to the reaction mixture. The resulting solution was stirred at room temperature for 24 hours, after which a light orange-yellow precipitate was observed. The solution was filtered and washed with methanol and diethyl ether. Yield: 74% C₁₂H₁₇N₂SOCl₄Ru Calc. C 30.01, H 3.57, N 5.83. Found C 30.05, H 3.48, N 5.74. Melting point 179–181 °C (decomp.) ¹H NMR (D₂O): δ = 8.73, 8.54, 8.00, 4.29, 2.65, −2.92, −14.51. Crystals suitable for X-ray diffraction were isolated from the reaction filtrate after cooling to −20 °C for several days.

Na[*trans*-RuCl₄(1*H*-Pyr)(DMSO-S)] (**1b**). Na[*trans*-Ru(DMSO-S)₂Cl₄] (105 mg, 0.25 mmol) was dissolved in acetone (8 mL) at room temperature. Pyridine (60 μ L, 1 mmol) was added directly to the reaction mixture. The resulting solution was mixed for 20 minutes at room temperature, after which a clear orange-yellow solution was observed. The clear solution was stirred at room temperature for an additional 2.5 hours, after which diethyl ether was added until precipitation was observed. The resulting red precipitate was isolated by suction filtration and washed with dichloromethane and diethyl ether. Yield: 77% C₇H₁₁NSOCl₄RuNa Calc. C 19.87, H 2.62, N 3.31. Found C 19.82, H 2.87, N 3.37. Melting point 206–208 °C (decomp.) ¹H NMR (D₂O): δ = 4.30, −2.89, −14.51. Crystals suitable for X-ray diffraction were isolated from the reaction filtrate.

$\text{MePyrH}[\text{trans-RuCl}_4(1\text{H-MePyr})(\text{DMSO-S})]$ (**2a**). $[(\text{DMSO})_2\text{H}][\text{trans-Ru}(\text{DMSO-S})_2\text{Cl}_4]$ (177 mg, 0.32 mmol) was mixed with acetone (12 mL) at room temperature. 4-methylpyridine (123 μL , 1.26 mmol) was added directly to the reaction mixture, which immediately produced an orange precipitate. The resulting solution was stirred at room temperature for 3 hours, then subsequently filtered and washed with acetone. Yield: 86% $\text{C}_{14}\text{H}_{21}\text{N}_2\text{SOCl}_4\text{Ru}$ Calc. C 33.08, H 4.16, N 5.51. Found C 33.11, H 4.23, N 5.40. Melting point 182-184 °C (decomp.) ^1H NMR (D_2O): δ = 8.50, 7.78, 2.57, -2.63, -3.03, -14.85. Crystals suitable for X-ray diffraction were isolated from the reaction filtrate after cooling to -20 °C for several days.

$\text{Na}[\text{trans-RuCl}_4(1\text{H-MePyr})(\text{DMSO-S})]$ (**2b**). $\text{Na}[\text{trans-Ru}(\text{DMSO-S})_2\text{Cl}_4]$ (68.5 mg, 0.16 mmol) was dissolved in acetone (5 mL) at room temperature. 4-methylpyridine (47.5 μL , 0.49 mmol) was added directly to the reaction mixture. The resulting solution was stirred at room temperature for 3 hours, yielding a clear golden-yellow solution. Solvent was removed under decreased pressure to a minimal volume, followed by the addition of dichloromethane until a precipitate was observed. The resulting mixture was filtered and washed with diethyl ether. Yield: 81% $\text{C}_8\text{H}_{13}\text{NSOCl}_4\text{RuNa}$ Calc. C 21.98, H 3.00, N 3.20. Found C 21.67, H 3.05, N 3.33. Melting point 199-200 °C (decomp.) ^1H NMR (D_2O): δ = -2.62, -3.01, -14.64. Crystals suitable for X-ray diffraction were isolated from the reaction filtrate after cooling to -20 °C for several days.

$\text{PhPyrH}[\text{trans-RuCl}_4(1\text{H-PhPyr})(\text{DMSO-S})]$ (**3a**). $[(\text{DMSO})_2\text{H}][\text{trans-Ru}(\text{DMSO-S})_2\text{Cl}_4]$ (117 mg, 0.21 mmol) was dissolved in acetone (10 mL) at room temperature. 4-phenylpyridine (136 mg, 0.88 mmol) was dissolved in acetone (5 mL) and added dropwise to the reaction mixture. The resulting clear yellow solution was stirred at room temperature for 2 hours, yielding a cloudy yellow mixture. The solution was filtered and washed with acetone, giving the desired yellow powder product. Yield: 87% $\text{C}_{24}\text{H}_{25}\text{N}_2\text{SOCl}_4\text{Ru}$ Calc. C 45.58, H 3.98, N 4.43. Found C 45.85, H 4.23, N 4.45. Melting point 213-214 °C (decomp.) ^1H NMR (CDCl_3): δ = 9.19, 8.18, 7.85, 7.39, 6.91, 6.31, 5.61, 1.23, -1.86, -12.84. Crystals suitable for X-ray diffraction were isolated from the reaction filtrate after cooling to -20 °C for several days.

Na[*trans*-RuCl₄(1*H*-PhPyr)(DMSO-*S*)] (3b**).** Na[*trans*-Ru(DMSO-*S*)₂Cl₄] (77 mg, 0.18 mmol) was dissolved in acetone (10 mL) at room temperature. 4-phenylpyridine (57 mg, 0.37 mmol) was dissolved in acetone (10 mL) and added dropwise to the reaction mixture. The resulting orange-yellow solution was stirred at room temperature for 4 hours, yielding a clear golden-yellow solution. Solvent was removed under reduced pressure to a minimal volume, after which diethyl ether was added until precipitation was observed. The resulting mixture was filtered and washed with diethyl ether, giving the desired orange powder product. Yield: 77% C₁₃H₁₅NSOCl₄RuNa·H₂O Calc. C 30.19, H 3.31, N 2.71. Found C 30.48, H 3.33, N 2.58. Melting point 188-190 °C (decomp.) ¹H NMR (D₂O): δ = 6.31, 5.61, 1.23, -1.86, -12.84.

DiPhenPyrH[*trans*-RuCl₄(1*H*-DiPhenPyr)(DMSO-*S*)] (4a**).** [(DMSO)₂H][*trans*-Ru(DMSO-*S*)₂Cl₄] (204 mg, 0.37 mmol) was dissolved in methanol (10 mL) at room temperature. Diphenyl-4-pyridyl-methane (537 mg, 2.19 mmol) was dissolved in methanol (10 mL) then added dropwise to the reaction mixture. The resulting clear orange solution was stirred at room temperature for 30 minutes, affording a clear golden-yellow solution. Solvent was removed under reduced pressure until a yellow precipitate was observed. The solution was subsequently filtered and washed with methanol. Yield: 40% C₃₆H₃₇N₂OSOCl₄Ru Calc. C 54.83, H 4.73, N 3.55. Found C 54.92, H 4.79, N 3.59. Melting point 143-145 °C (decomp.) ¹H NMR (CDCl₃): δ = 8.84, 7.64, 7.52, 6.64, 6.46, 6.24, 5.09, 1.52, 1.01, -2.40, -13.37.

Na[*trans*-RuCl₄(1*H*-DiPhenPyr)(DMSO-*S*)] (4b**).** Na[*trans*-Ru(DMSO-*S*)₂Cl₄] (63.8 mg, 0.15 mmol) was dissolved in acetone (5 mL) at room temperature. Diphenyl-4-pyridyl-methane (111 mg, 0.45 mmol) was dissolved in acetone (2 mL) then added dropwise to the reaction mixture. The solution was stirred at room temperature for 3 hours, resulting in a clear golden-yellow solution. Solvent was removed under decreased pressure to a minimal volume, then dichloromethane was added until precipitation was observed. The resulting mixture was filtered, yielding an orange powder which was dried at 75 °C for 3 hours. Yield: 58% C₂₀H₂₁NSOCl₄RuNa Calc. C 40.76, H 3.59, N 2.38. Found C 40.40, H 3.41, N 2.07. Melting point 225-227 °C (decomp.) ¹H NMR (D₂O): δ =

6.59, 6.36, 5.38, 4.87, 0.98, -3.13, -14.81. Crystals suitable for X-ray diffraction were isolated from an ethyl acetate solution upon cooling to -20 °C for several days.

NBenzpyrH[*trans*-RuCl₄(1*H*-NBenzpyr)(DMSO-S)] (5a). [(DMSO)₂H][*trans*-Ru(DMSO-S)₂Cl₄] (91 mg, 0.16 mmol) was dissolved in methanol (6 mL) at room temperature. 4(4-Nitrobenzyl)pyridine (138 mg, 0.65 mmol) was dissolved in methanol (3 mL) and added dropwise to the reaction mixture. The resulting solution was stirred at room temperature for 3 hours, after which a yellow-orange precipitate was observed. The solution was filtered and washed with methanol. Yield: 55% C₂₆H₂₇N₄O₅SCl₄Ru Calc. C 41.61, H 3.63, N 7.47. Found C 41.45, H 3.61, N 7.39. Melting point 165-167 °C (decomp.) ¹H NMR (CDCl₃): δ = 8.92, 8.53, 7.85, 7.37, 5.48, 4.94, 1.55, -0.41, -1.98, -12.68. Crystals suitable for X-ray diffraction were obtained by dissolution in acetone, followed by the addition of an equal amount of dichloromethane with the resulting mixture being left at room temperature for several hours.

Na[*trans*-RuCl₄(1*H*-NBenzpyr)(DMSO-S)] (5b). Na[*trans*-Ru(DMSO-S)₂Cl₄] (104 mg, 0.25 mmol) was dissolved in acetone (6 mL) at room temperature. 4(4-Nitrobenzyl)pyridine (157 mg, 0.74 mmol) was dissolved in acetone (4 mL) then added dropwise to the reaction mixture. The resulting solution was stirred at room temperature for thirty minutes, after which a clear golden-yellow solution was observed. Solvent was removed under decreased pressure to a minimal volume, then dichloromethane and diethyl ether were added until precipitation was observed. The solution was left standing for 10 minutes to complete the precipitation and was subsequently filtered and washed with diethyl ether. Yield: 81% C₁₄H₁₆N₂O₃SCl₄RuNa Calc. C 30.12, H 2.89, N 5.02. Found C 30.07 H 2.80, N 4.98. Melting point 156-158 °C (decomp.) ¹H NMR (D₂O): δ = 6.75, 4.85, -0.30, -3.05, -14.63. Crystals suitable for X-ray diffraction were isolated from product dissolved in ethyl acetate at elevated temperatures followed by gradual cooling to room temperature.

4.2.2. Crystallographic Structure Determination

Single crystal X-ray crystallographic analysis was performed on a Bruker SMART diffractometer equipped with an APEX II CCD area detector fixed at a distance of 6.0 cm from the crystal and a Mo K α fine focus sealed tube ($\lambda = 0.71073$ nm) operating at 1.5 kW (50 kV, 30 mA) and filtered with a graphite monochromator. The temperature was regulated using an Oxford Cryosystems Cryostream. Structures were solved using direct methods (SIR92) and refined by least-squares procedures in CRYSTALS.²⁵² Diagrams of **1a,b**, **2a,b**, **3a**, **4b**, and **5a,b** were generated by ORTEP-3 for Windows (v. 2.00).²⁵³ Crystal data, data collection parameters, and details of structure refinement for compounds **1a,b**, **2a,b**, **3a**, **4b**, and **5a,b** are listed in **Table 4-1**.

4.2.3. Electrochemical Measurements

Cyclic voltammograms were recorded on a Princeton Applied Research potentiostat/galvanostat Model 263A, equipped with an Ag/AgCl (3 M KCl) reference electrode, a platinum disk working electrode and a platinum disk counter electrode. All spectra were collected in an aqueous buffer consisting of 50 mM Na₂HPO₄, 150 mM NaCl, and 20 mM NaHCO₃, pH 7.4, henceforth “physiological buffer”. K₄[Fe(CN)₆] was used as a calibration. Measurements were performed using 5 mM concentrations of each complex in 5 mL of solvent using a 100 mV/s scan rate. All scans were conducted under these conditions unless otherwise noted.

4.2.4. Optical Measurements

UV-Vis spectra were measured using a Cary 1E UV-Visible Spectrophotometer, connected to a Haake F3 waterbath which maintained an internal spectrophotometer temperature of 37 °C. All spectra were collected using physiological buffer. Solution measurements were performed using a 200 μ M concentration of each complex in 1 mL sample volumes. Protein binding measurements were performed using 200 μ M concentrations of each complex mixed with 100 μ M hSA in 1 mL solutions. All buffer solutions were measured at 37 °C for a total of 2 hours. Scans were taken at 10 minute

intervals, beginning at 0 minutes of incubation, at a scan rate of 10 nm/sec. Samples of complexes incubated with hsA were also measured for 2 hours under identical conditions.

4.2.5. Preparation of EPR Samples

Complexes in Buffer. Compounds were dissolved in physiological buffer to give a concentration of 3 mM, and incubated at 37 °C. Aliquots of 210 µL were withdrawn at the following time points: 0, 10, 20, 30, 60, and 120 minutes. Each sample was promptly mixed with 90 µL of glycerol and frozen in liquid nitrogen.

Complexes with hsA. To 600 µL of a 0.75 mM solution of hsA in physiological buffer, 600 µL of a 1.5 mM solution of each complex was added also in physiological buffer. The combined solution was then diluted to 4 mL with physiological buffer and incubated at 37 °C for one of the following time periods: 0, 10, 20, 30, 60, and 120 minutes. Each 4 mL solution was concentrated down to a volume of less than 200 µL using an Amicon centrifugal filter unit (molecular-weight cut-off 30 kDa) by centrifuging at 8 °C and 4500 rpm for 30 minutes, or until a volume of less than 200 µL was attained. The resulting filtered product was then mixed with 90 µL of glycerol and diluted to a final volume of 300 µL with physiological buffer, and finally transferred to an EPR tube and immediately frozen in liquid nitrogen.

Complexes with Ascorbic Acid in Buffer. A 1 mM solution of each complex was prepared in physiological buffer at 25 °C. Ascorbic acid was subsequently added to give a concentration of 1 mM. The resulting solutions were then incubated at 37 °C for either 0 or 120 minutes. Aliquots of 210 µL were mixed with 90 µL of glycerol and transferred to an EPR tube and immediately frozen in liquid nitrogen.

Complexes with hsA and Ascorbic Acid. A 1 mM solution of each complex was mixed with a 0.5 mM solution of hsA and incubated at 37 °C for either 0 or 120 minutes. After incubation and isolation of the protein bound fractions, ascorbic acid was added to the mixture, giving a final acid concentration of 1 mM. Protein-bound fractions were separated by ultrafiltration as described above for the complexes incubated with hsA in buffer.

4.2.6. EPR Measurements and Simulation

See section 2.2.4.

4.2.7. EPR Experimental Conditions

See section 2.2.5.

4.3. Results and Discussion

4.3.1. Synthesis

Compounds **1a – 5a** and **1b – 5b** were synthesized using procedures based on those reported for NAMI-A and NAMI, respectively.^{147,150,245} Initial synthesis of the bis-DMSO complexes, $[(\text{DMSO})_2\text{H}][\text{trans-Ru}(\text{DMSO}-\text{S})_2\text{Cl}_4]$ and $\text{Na}[\text{trans-Ru}(\text{DMSO}-\text{S})_2\text{Cl}_4]$, was followed by addition of the ligands **1 – 5**, to give **1a – 5a** and **1b – 5b** respectively, in good yield. The identity and purity of these compounds was confirmed by elemental analysis, NMR, EPR, and X-ray crystallography. Although the original patents describing NAMI-A and related complexes encompass compounds with a variety of heterocyclic nitrogen ligands,²⁴⁵ synthesis and, particularly, characterization of NAMI and NAMI-A derivatives has been somewhat limited. In the case of NAMI-A analogues with different heterocyclic nitrogen donor ligands, a number of imidazole-based derivatives have been reported,^{254,255} along with a modest number of compounds with other types of nitrogen heterocycles, including thiazoles,^{256,257} triazoles,^{45,116,130} pyridines,^{121,149,247,258-262} and various other azole ligands.^{116,121,148,263} Of the compounds described here, syntheses of **1a,b** and **2a,b** have been previously reported.^{149,247,259,260} However, aside from NMR and UV-Vis studies of **2a**,²⁶⁰ only **1a** has been fully structurally characterized.²⁵⁹ No NAMI-A derivatives similar to **3a,b**, **4a,b**, and **5a,b** have been reported prior to this work. As described here, all ten compounds **1a,b – 5a,b** were characterized prior to studying their aqueous solution behaviour, protein interactions, and electrochemistry.

4.3.2. Crystal Structures

The structures of compounds **1a,b**, **2a,b**, **3a**, **4b**, and **5a,b** were determined by X-ray crystallography and are shown in **Figure 4-2**. The significant differences in the solvent preferences of the azole ligands and counterions required different approaches to obtain crystals suitable for X-ray diffraction studies. Crystals of complexes **1a**, **1b**, **2a**, **2b**, and **3a** were all isolated directly from the reaction filtrate after standing for several days at low temperature. For **5a**, dissolution in acetone followed by the addition of dichloromethane (1:1) resulted in X-ray quality crystals within minutes, while single crystals of **5b** were obtained by dissolution in ethyl acetate at elevated temperatures followed by a very gradual cooling period. Despite numerous attempts using a wide array of conditions and solvent systems, no crystals suitable for X-ray diffraction studies of compounds **3b** and **4a** were attained. However, crystals of **4b** were obtained from a solution of ethyl acetate after several days at low temperature. The crystal structure of **1a** has been reported previously,²⁵⁹ and the metrical parameters found here agree with this earlier study within experimental error.

For all of the structures solved, similar octahedral geometry around the ruthenium(III) metal centre is observed. In all cases the DMSO ligand is coordinated via the sulfur atom while the pyridine ligand is coordinated through the heterocyclic nitrogen. An equatorial plane of four chlorides completes the coordination sphere. This type of coordination environment around the ruthenium metal centre has been well documented, and is typical of analogous complexes.^{115,116,129,150,247,254,257,261}

The bond lengths for all of the complexes are listed in Appendix C, **Table C-3**. The metal-ligand bond lengths of all the synthesized complexes are similar to NAMI-A²⁵⁷ and its sodium-compensated analogue NAMI.¹⁵⁰ For the crystallographically characterized complexes (**1a,b**, **2a,b**, **3a**, **4b**, **5a,b**), the average Ru–N bond distance (2.126 Å) is similar to the reported value for NAMI (2.081 Å) and NAMI-A (2.099 Å). The corresponding average Ru–S bond distances (2.291 Å) are also very similar to the values for both NAMI (2.296 Å) and NAMI-A (2.293 Å). Ru–Cl bond distances were evaluated individually across all the complexes, with the resulting average Ru–Cl bond distance of 2.350 Å close to those of NAMI-A (2.353 Å) and NAMI (2.342 Å).

In the case of the sodium salts, all of the structures (**1b** – **5b**) were solved as dimers, since the sodium cations exhibit a distorted octahedral geometry between chloride ligands on neighboring ruthenium centres and co-crystallize with solvent molecules. Low temperature collection of diffraction data was required to prevent desolvation of crystals of **1b**, **2b**, and **5b**, which otherwise reduced the crystals to powder. Similar behaviour has been reported for crystals of NAMI.¹⁵⁰ The bridging oxygen atoms in **1b** and **2b** and the free oxygen atom in **2b** were modeled as water molecules. Determination of the identity of these water molecules was complicated by the disorder present in both **1b** and **2b**, which is evident in the pyridine rings and the anisotropic temperature factors of the equatorial chlorides. Lastly, for **4b** and **5b**, co-crystallizing ethyl acetate molecules were modeled; with relative ease in the case of **5b** and with significant disorder for **4b**, which required two solvent molecules being modeled with partial occupancy.

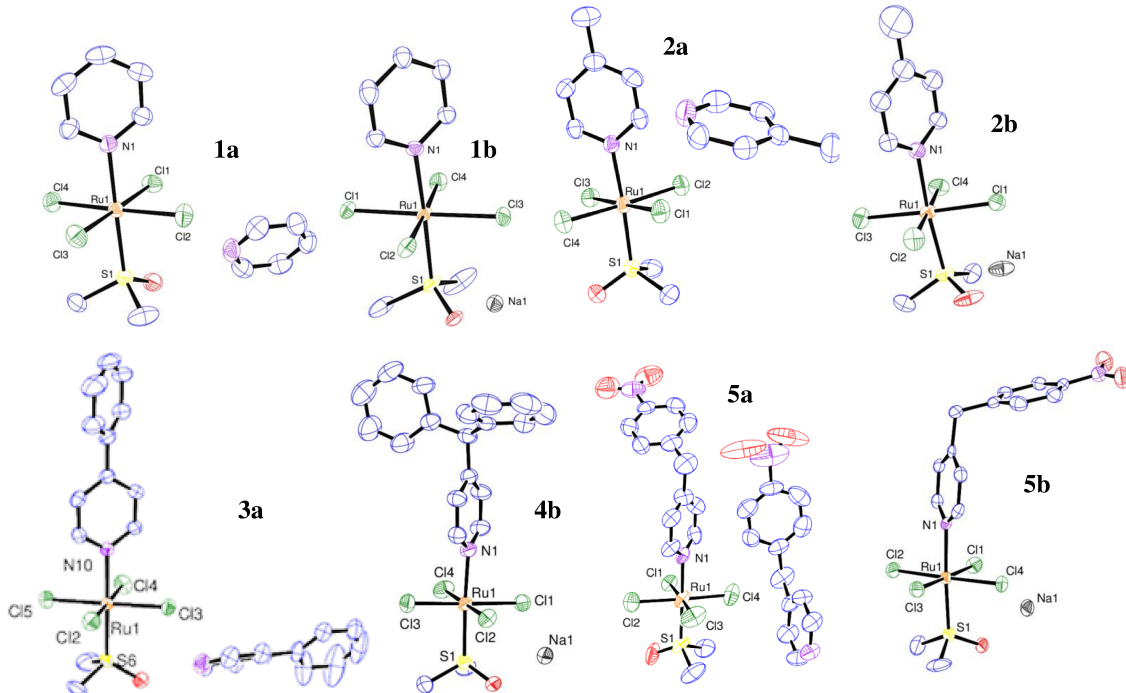


Figure 4-2 Crystal structures of compounds **1a,b**, **2a,b**, **3a**, **4b**, and **5a,b**.

Complex	1a	1b	2a	2b	3a	4b	5a	5b
Empirical formula	C _{13.5} H ₂₀ N ₂ S O _{1.5} Cl ₄ Ru	C _{5.25} H ₉ NS _{0.75} O _{1.12} Cl ₃ Ru _{0.75} Na _{0.75}	C ₁₄ H ₂₁ N ₂ SO Cl ₄ Ru	C ₈ H ₁₇ NS O _{2.5} Cl ₄ RuNa	C ₂₄ H ₂₅ Cl ₄ N ₂ OSRu	C ₂₈ H ₃₇ NSO ₅ Cl ₄ RuNa	C ₂₆ H ₂₇ N ₄ SO ₅ SCl ₄ Ru	C ₁₈ H ₂₄ N ₂ SO ₅ Cl ₄ RuNa
M (g mol ⁻¹)	509.27	324.09	508.28	465.16	632.42	765.54	750.47	646.34
Space group	Triclinic P1	Trigonal P3121	Triclinic P1	Orthorhombic Fdd2	Monoclinic P121	Triclinic P1	Orthorhombic Pca21	Triclinic P1
a (Å)	7.351	13.143	9.273	23.882	7.226	11.468	27.495	8.922
b (Å)	8.532	13.143	15.340	26.026	11.764	12.632	7.945	9.724
c (Å)	15.098	19.609	15.871	11.443	15.724	14.731	14.515	14.839
α (deg)	88.243	90	99.532	90	90	93.075	90	99.805
β (deg)	79.191	90	105.574	90	94.753	109.88	90	90.656
γ (deg)	88.959	120	107.318	90	90	116.24	90	96.222
V (Å ³)	978.22	2933.6	2000.8	7112.9	1332.16	1746.81	3171.0	1260.5
Z	2	8	4	16	2	2	4	2
ρ _{cal} (g cm ⁻³)	1.729	1.467	1.687	1.737	1.577	1.455	1.572	1.703
μ (g mm ⁻¹)	1.460	1.464	1.425	1.620	1.090	0.862	0.939	1.178
λ (Å)	0.71073	0.71073	0.71073	0.71073	0.71073	0.71073	0.71073	0.71073
T (K)	298	150	298	150	298	298	298	150
goodness of fit	1.46	1.04	1.42	1.88	1.13	1.02	1.31	1.05
R ₁	0.0319	0.0637	0.0292	0.0395	0.0373	0.0497	0.0532	0.0348
wR ₂	0.0376	0.0663	0.0311	0.0559	0.0285	0.0637	0.0442	0.0284

Table 4-1 Crystal data and details of data collection and refinement for compounds **1a,b**, **2a,b**, **3a**, **4b**, and **5a,b**.

4.3.3. Aqueous Solution Behaviour - EPR

Before studying the protein interactions of compounds **1a,b – 5a,b**, it was first necessary to characterize their ligand-exchange processes in physiological buffer. Principally, it was important to determine whether their fundamental solution behaviour was similar, and whether it would play a significant role in the rate of formation of interactions with hsA. As outlined in the previous chapters, EPR is well suited for studies of Ru(III) complexes as they undergo complex ligand-exchange processes under physiological conditions. Analysis of g values and signal intensities from frozen solutions of Ru(III) compounds enables identification of species produced by ligand exchange and determination of the rates of these processes. Under the physiologically relevant experimental conditions used in these studies (pH 7.4, 37 °C), Ru(III) complexes generally exhibit relatively slow ligand exchange.⁴¹

To compare the solution behaviour of **1a,b – 5a,b**, the compounds were incubated in physiological buffer (pH 7.4) at 37 °C for time periods of 0, 10, 20, 30, 60, and 120 minutes before freezing in liquid nitrogen and measurement by EPR. The resulting EPR spectra are shown in **Figure 4-3** for **1a** and **4b**, and in Appendix C – **Figures C-1** and **C-2** for the remaining complexes. For each complex a well-resolved uniaxial spectrum was observed prior to incubation at 37 °C, as expected for mononuclear low-spin Ru(III) complexes with tetragonal symmetry, indicating detection of the parent compound in each case. The g values of the parent compounds, determined by simulation (**Figure 4-3**, right-hand panels and Appendix C – **Table C-1**), are similar with $g_{\perp} = 2.43 – 2.44$ and $g_{\parallel} = 1.75 – 1.80$, as expected since the substituents on the pyridine ligands do not affect the ligand field of the Ru(III) ion significantly. In the case of compounds **3a – 5a**, the spectra obtained before incubation in buffer at 37 °C are not strictly uniaxial. Relatively poor water solubility results in some aggregation of the complexes in solution. This produces a weak, broad EPR signal which distorts the axial peak from the dissolved complexes. By contrast, their sodium analogues, **3b – 5b**, are readily soluble in aqueous media and thus do not display this signal.

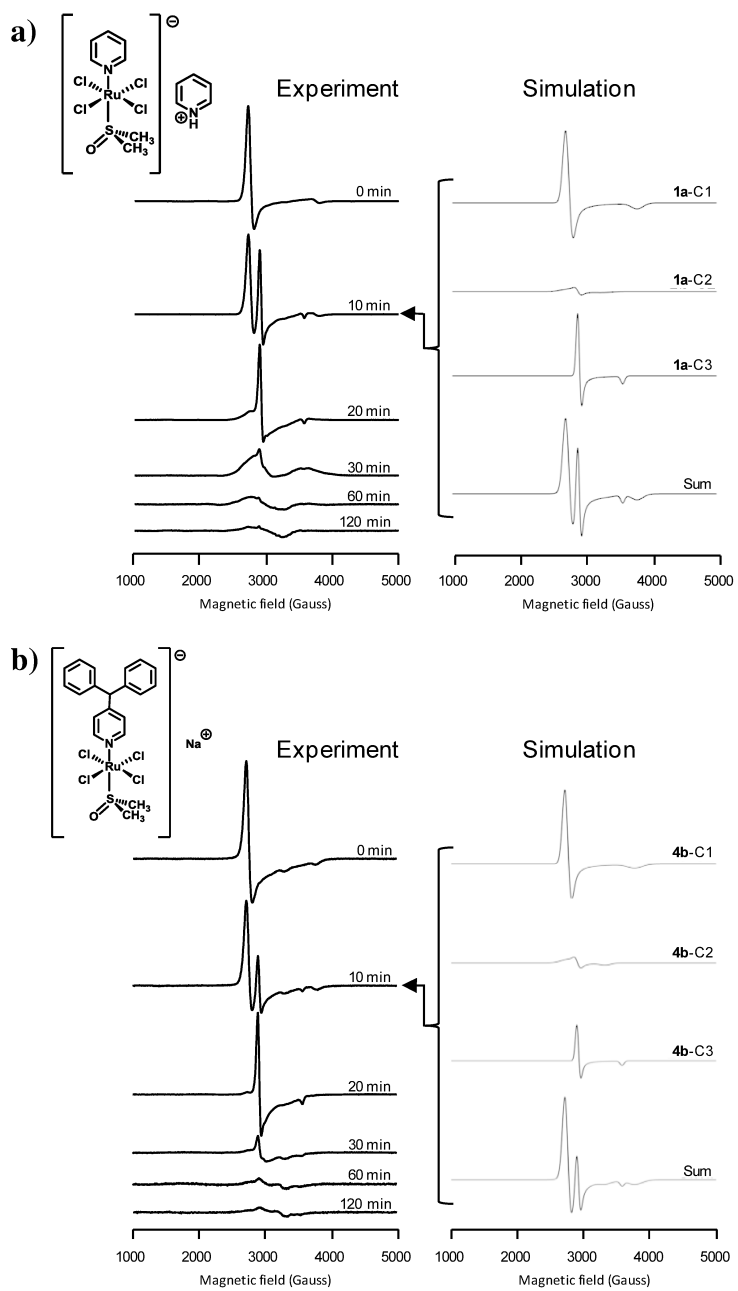


Figure 4-3 EPR measurements of a) **1a** and b) **4b** incubated in physiological buffer at 37 °C, and deconvolution of spectra collected after 10 minutes of incubation. For EPR experimental conditions see 2.2.5. For parameters used in each simulation see Appendix C – **Table C-1**.

With incubation at 37 °C, a new uniaxial EPR signal was observed in measurements of each complex with $g_{\perp} = 2.30 - 2.31$ and $g_{\parallel} = 1.87 - 1.88$ (EPR spectra

labelled as **1a**-C3 and **4b**-C3 in **Figure 4-3**, and correspondingly for other complexes in Appendix C – **Figures C-5 – C-12**), which steadily replaced the signals from the parent compounds, indicating the loss of one of the axial ligands. Nitrogen donor ligands are generally considered to be kinetically inert under physiological conditions (pH 7.4),¹⁷⁶ implying that the axial DMSO ligand of the complexes exchanges with water in each case. However, to confirm this, NMR measurements of the sodium compensated complexes **1b** – **5b**, were performed following incubation in buffer for 0, 2, and 24 hours (Appendix C – **Figures C-36 –C-40**). Only trace amounts of free pyridine ligands were detected even after 24 hours, confirming $[trans\text{-}RuCl_4(1H\text{-}L)(H_2O)]^-$ as the dominant product in solution after 10 minutes of incubation.

Simulations of the spectra obtained after 10 and 20 minutes of incubation for each complex at 37 °C reveal a smaller contribution from a third species, which exhibits a rhombic EPR spectrum $g = [2.41 - 2.46, 2.25 - 2.31, 2.01 - 2.07]$ (**Figure 4-3**, right-hand panels, Appendix C – **Figures C-5 – C-12**). The lower symmetry species observed are consistent with aqueous exchange of an equatorial chloride ligand, which produces a second mono-aqua species $RuCl_3H_2O(1H\text{-}L)(DMSO-S)$ (**1a**-C2 and **4b**-C2 in **Figure 4-3**). The lower signal intensity from this species in each case indicates that Cl^- exchange occurs concurrently with loss of DMSO, but at a significantly slower rate. The g values for each compound ([**1a,b** – **5a,b**]-C1), and their mono-aqua derivatives ([**1a,b** – **5a,b**]-C2 and [**1a,b** – **5a,b**]-C3) are listed in Appendix C – **Table C-1**.

Further incubation of the compounds in solution leads to a considerable decrease in the overall EPR signal intensity. This behaviour has been previously reported for NAMI-A (Chapter 3), and is accompanied by a distinct change in the color of the solution from yellow to dark brown.^{176,264} A similar phenomenon was also observed for each of the pyridine complexes described here. Additionally, precipitation was observed in the samples for complexes **3a,b** – **5a,b**. This is likely due to the decrease in solubility of the aquated, neutral derivatives, due to their highly hydrophobic axial azole ligands. Despite the precipitation event, EPR signals from the remaining soluble species are still observed at all time points. Although these signals are significantly attenuated after longer incubation periods, it is still possible to observe ongoing changes in the spectra. This

indicates that a small proportion of the complexes remain as mononuclear Ru(III) species and continue exchanging Cl^- ligands to give polyaqua species. However, the very low concentration of these species indicates that they are unlikely to play a significant role in the activity of the compounds.

Overall, the rates of ligand exchange processes do not vary dramatically depending either on the axial ligands or the counter ions. In every case the axial mono-aqua complex dominates after 10 minutes of incubation at 37 °C, and the overall signal intensity is significantly reduced after 30 minutes. The spectroscopic parameters of each complex are also relatively similar, as expected, given the similar ligand-fields provided by the axial ligands in each case. Furthermore, changing the counter ions did not affect the EPR spectra noticeably, thus, the spectra shown for **1a** and **4a** in **Figure 4-3** are similar to those observed for the other compounds (Appendix C – **Figures C-5 – C-12**). The only exception was **4a**, which was relatively insoluble in aqueous media because of its hydrophobic DiBenzPyr axial ligand and DiBenzPyrH counter ion, requiring 20% DMSO for sufficient dissolution. The resulting EPR spectra, although showing contributions from the parent compound and mono-aqua complexes in solution, are dominated by a broad signal, which is relatively unchanged even following longer incubation periods, and likely arises from aggregated complexes. This was confirmed by measurement of a powder sample of **4a**, which gave a broad signal matching that seen in the frozen solution experiment (data not shown). By contrast, the sodium analogue, **4b**, dissolves readily in buffer and shows the typical speciation behaviour.

The aqueous solution behaviour of NAMI-A has been studied extensively by a variety of techniques, demonstrating that aquation products and oligomers predominate after incubation of the complex in aqueous buffer solutions at pH 7.4.^{116,176,201,231,264} From the previously reported EPR characterization of NAMI-A in physiological buffer (Chapter 3), similar speciation and ligand-exchange rates are observed to those of the pyridine complexes described in this work.²⁶⁴ This further demonstrates that although the axial azole ligands influence the electrochemistry and biomolecule interactions of this family of compounds, they do not significantly impact the fundamental aqueous solution behaviour. This is an important observation since solutions of these types of compounds

are frequently prepared in physiological saline, prior to intravenous administration. The time taken between the preparation of these solutions and infusion determines the actual compounds delivered to patients, therefore significantly affects *in vivo* behaviour and activity.

4.3.4. Aqueous solution Behaviour - UV-Vis

To gain further insight into the aqueous solution behaviour of the synthesized complexes, ligand exchange was monitored using UV-Vis spectroscopy. Each sample measured was prepared analogously to the previously described EPR samples to facilitate the comparison between the different spectroscopic techniques. The complexes were dissolved in physiological buffer and incubated at 37 °C within the spectrometer. Spectra were measured at 10 minute intervals over a two hour time period. Stacked plots of the data collected for complexes **1b** and **4b** are shown in **Figure 4-4**, and in Appendix C – **Figures C-53 – C-62** for all remaining complexes. Substitution at the 4' position of the pyridine ring had a minimal effect on the initially observed spectra. However, as the incubation time progressed, complexes **3a,b – 5a,b** were observed to precipitate, which resulted in a broadening of the spectral line shape. Altering the cation from pyridinium (**a**) to sodium (**b**) had no significant effect on the observed spectra.

For all of the complexes measured, absorption bands in both the visible and ultraviolet regions of the spectrum are readily observed. The most intense peak was observed at 239-280 nm for all complexes and was assigned to the auxochrome signal from the pyridine ligand.²⁵⁵ The next most intense peak is observed at 307-341 nm which is consistent with $\pi-\pi^*$ transitions for Ru(III) complexes with pyridine ligands.²⁶⁵ Two remaining peaks are seen around 400-410 nm and 460-471 nm. These peaks lie within the region of the spectrum that is typical for ligand to metal charge transfer (LMCT) transitions for octahedral Ru(III) complexes with bound nitrogen heterocycles.²⁶⁶

With incubation in buffer, the peak at 239-280 nm decreases coincident with an increase in a second peak at 307-341 nm. This led to an isosbestic point around 280 nm, signifying that ligand exchange to give a single major product was occurring, behaviour

that was well established in the EPR studies. This phenomenon was most pronounced in the more soluble complexes of **1a,b**, and **2a,b**. Although similar exchange processes are indicated by the spectra of complexes **3a,b – 5a,b**, due to precipitation following aquation, these processes are obscured by subsequent line broadening.

As with the peak at 239-280, the peak around 400-410 nm decreases significantly with incubation, and is barely observable after only 20 minutes. This is followed by the increase of a peak at 347-352 nm, thereby creating a second isosbestic point around 370 nm, which is easily identified in the spectra of all complexes. Continued incubation leads to the loss of the isosbestic point around 370 nm, which is evidence of further aquation.¹⁷³

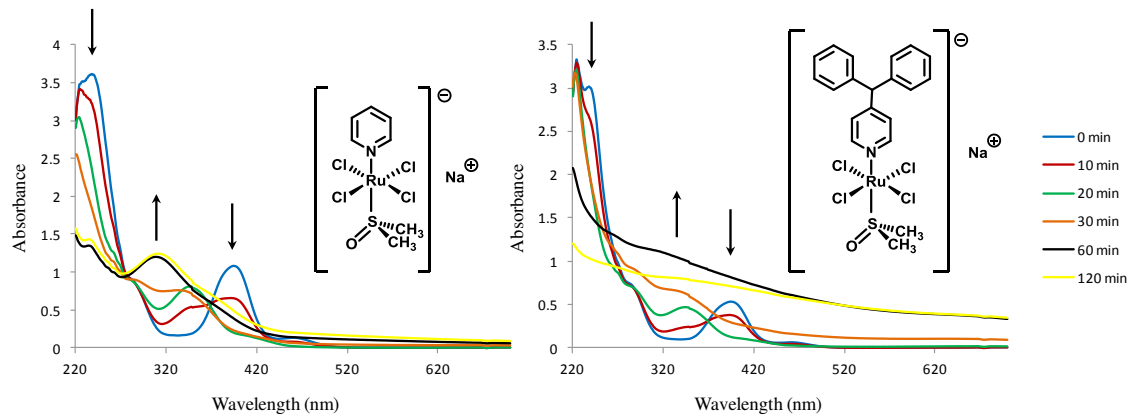


Figure 4-4 UV-Vis spectra for complexes **1a** and **4a** in physiological buffer, with incubation at 37 °C for up to 2 hours.

Similar isosbestic points have been observed previously in UV-Vis studies of NAMI-A in aqueous solution (277, 300, and 365 nm). These were assigned to a single transformation around the Ru(III) metal centre.¹⁷³ Another study assigned the peak which shifted to 346 nm for NAMI-A, to a species which has exchanged a chloride group for a water molecule.²⁰² However, from supporting EPR measurements, it was confirmed that the loss of the axial DMSO ligand upon aquation is the dominant transformation (Chapter 3). Previous UV-Vis studies on the reduced form of NAMI-A did not report isosbestic points, suggesting a stepwise chloride dissociation from the metal centre,¹⁸⁰ producing a variety of aquated Ru(II) complexes. For all complexes, the changes in the observed

spectra are assigned to changes around the Ru(III) metal centre. The two isosbestic points observed demonstrate the complexity of aqueous ligand exchange for these complexes, a trait that is reflected in the EPR data.

4.3.5. Interactions of the Complexes with hsA - EPR

As described previously in Chapter 3, EPR was used to show that NAMI-A, and the mono-aqua complex formed by DMSO exchange, both rapidly form non-coordinate interactions with hsA.²⁶⁴ Although these species are predominant shortly after dissolution in the presence of hsA, or in whole human serum, they are steadily converted to coordinately bound species with further incubation via ligand exchange with amino acid side chains.²⁶⁴ The hsA binding behaviour of each synthesized complex was studied to determine the effect of hydrophobic axial ligands on non-coordinate protein interactions.

The complexes **1a,b – 5a,b** were incubated for 0, 10, 20, 30, 60, and 120 minutes at 37 °C in buffer solutions of hsA. Protein bound fractions were then isolated by ultrafiltration, with a molecular-weight cutoff of 30 kDa, frozen in liquid nitrogen, and studied by EPR. The resulting spectra for each incubation time are shown in **Figure 4-5** for **1a** and **4a**, and in Appendix C – **Figures C-3 – C-4** for the other complexes. This approach allows us to observe exclusively hsA-bound Ru(III) species while excluding contributions from free complexes in solution, and has been used in earlier studies to identify both coordinate and non-coordinate binding interactions of NAMI-A and the “Keppler-type” family of complexes KP1019 and KP418 with hsA, as shown in Chapters 2 and 3 respectively.^{246,264}

For each of the pyridine complexes **1a,b – 5a,b** incubated with hsA, EPR measurements after short incubation periods reveal signals that correspond to the parent compounds (**[1a,b – 5a,b]-C1**) and the mono-aqua complexes (**[1a,b – 5a,b]-C2** and **[1a,b – 5a,b]-C3**) that were observed in the buffer-solution experiment described previously. Since only protein bound fractions are present, these signals are due to complexes bound to hsA without ligand exchange with the protein, that is, non-coordinately bound species. The strong signals observed in each case, even prior to

incubation at 37 °C, demonstrate that these interactions form readily with hsA and initially predominate in solution.

After longer incubation periods the EPR spectra from all of the pyridine complexes are increasingly dominated by two overlapping broader signals, which are not observed in the buffer solution experiments, with g values of $g_{\perp} = 2.33 - 2.40$ and $g_{\parallel} = 1.76$, and $g = [2.56 - 2.59, 2.24 - 2.30, 1.76 - 1.78]$. The distinct g values of these species indicate new Ru(III) ligand environments due to protein interactions. This reflects coordination to amino acid side chains, most probably histidine imidazoles, as suggested in previous studies.^{122,178,202,246,264,267} The hsA protein has upwards of 6 surface histidine residues that are capable of coordinating to exogenous species,^{79,83,268,269} and previous studies have demonstrated that up to 5 equivalents of NAMI-A can bind to the protein.^{178,202} In these experiments the ratio of complex to hsA was 2:1. This increases the possibility of different coordination modes, as compared to a 1:1 ratio, but was not an excessive concentration for non-coordinate interactions. The strong EPR signals observed over the course of the experiment indicate that protein coordination is highly favoured, likely giving more than one Ru(III) complex coordinated per protein molecule. Furthermore, EPR measurements of the filtrate after separation of protein bound fractions did not show detectable concentrations of Ru(III).

As shown by the spectral deconvolution of the EPR spectrum of **1a** after 30 minutes of incubation with hsA, (**Figure 4-5**, right-hand panel, and for the other pyridine complexes in Appendix C – **Figures C-13 – C-20**), one of these species has a uniaxial EPR spectrum (**1a**-hsA-2), indicating coordination at the labile DMSO axial site, while the other has a rhombic spectrum (**1a**-hsA-1) demonstrating coordination to an equatorial position previously occupied by chloride in the parent complex. These observations are similar to those reported for NAMI-A, indicating that the pyridine complexes have the same types of coordinate interactions with hsA.²⁶⁴ However, as shown by the corresponding spectra for **4a** (**Figure 4-5**), the chemical structure of the pyridine ligands strongly affects the rates that the various protein-bound species form, and their relative concentrations.

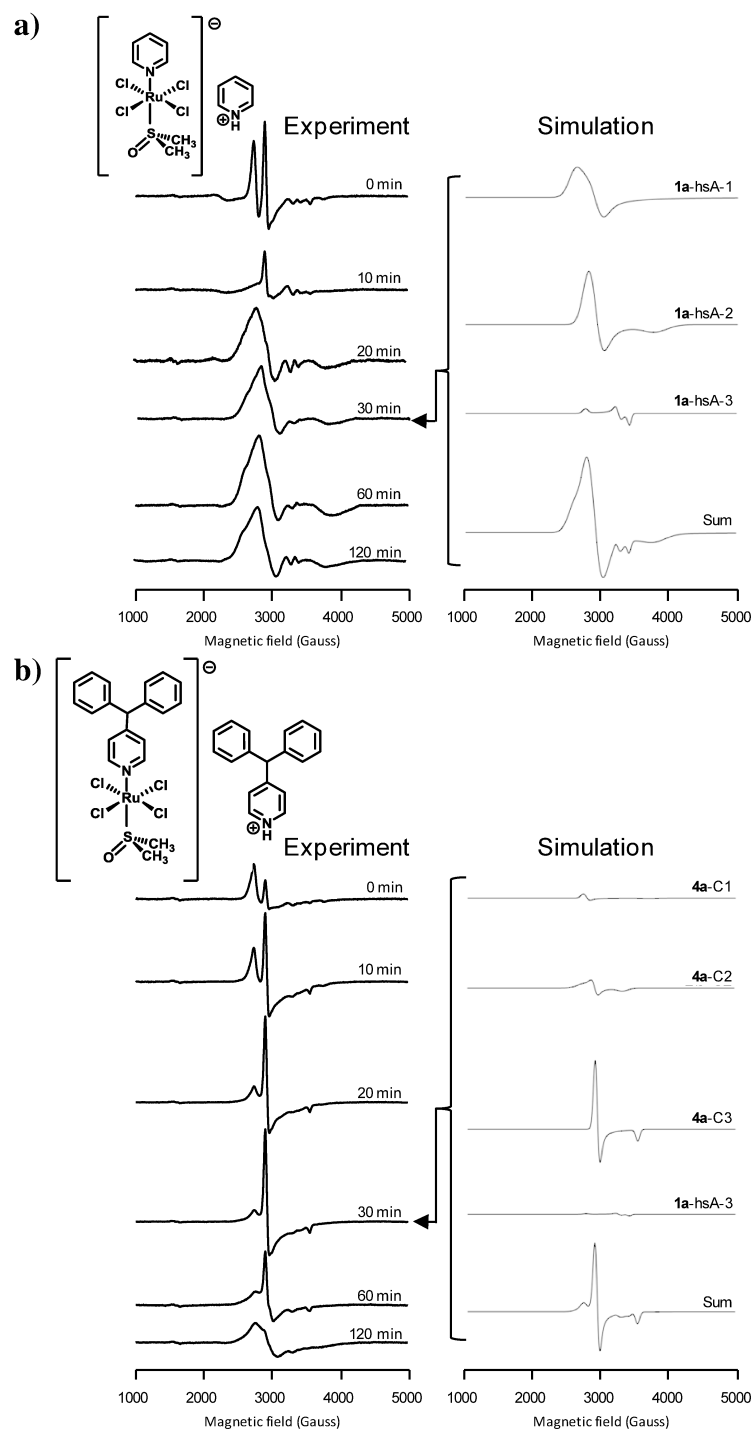


Figure 4-5 EPR spectra of a) **1a** and b) **4a** incubated with hsA in physiological buffer at 37 °C, and spectral deconvolution of spectra collected after 30 minutes of incubation.

A third protein-coordinated species is also evident for each complex (**1a**-hsA-3 and **4a**-hsA-3 in **Figure 4-5**, and corresponding species in Appendix C – **Figures C-13 – C-20**) which is characterized by a sharp, rhombic EPR spectrum with $g = [2.42, 2.06, 1.96]$. Although the EPR signal intensity of this species is much lower than the main protein-bound species described above, it forms more rapidly, essentially reaching its maximum concentration before incubation at 37 °C. The smaller g value dispersion and narrow linewidths of this species demonstrate a different ligand environment from the other protein-coordinated species. A similar species was observed for NAMI-A incubated with hsA, exhibiting a very similar EPR signal (Chapter 3), and was assigned to coordination to the one free cysteine (Cys-34) of the protein²⁶⁴

The incubation time-dependence of the EPR signals from **1a** with hsA closely resembles that of NAMI-A (Chapter 3),²⁶⁴ as might be expected given the similar propensity of the imidazole and pyridine ligands to form hydrophobic interactions with hsA. In both cases, EPR measurements reveal the formation of non-coordinately bound species prior to incubation. After 10 minutes of incubation at 37 °C, these species have mostly disappeared, and by 20 minutes they are completely replaced by coordinately bound complexes whose concentration continues to increase, reaching a maximum after about 1 hour (**Figure 4-5**). Almost identical behaviour is observed for the sodium compensated complex, **1b** (Appendix C – **Figure C-16b**), demonstrating that the counter ions do not significantly influence the protein interactions in this case. These results indicate that by using fresh solutions of each complex for intravenous treatment, coordinately bound species will rapidly predominate *in vivo*. By contrast, the MePyr analogues **2a** and **2b**, show significant concentrations of the mono-aqua complex, *trans*-RuCl₄(1*H*-mePyr)(H₂O), non-coordinately bound to the protein after 10 minutes of incubation (Appendix C – **Figures C-17b** and **C-18b**), demonstrating that these species are significantly stabilized toward non-coordinate interactions with hsA by the presence of the methyl group at the 4' position as compared to **1a** and **1b**. This effect is even more pronounced in the other pyridine derivatives, with the PhPyr complexes **3a** and **3b** displaying minor non-coordinate interactions after 60 minutes of incubation (Appendix C – **Figures C-19e** and **C-20e**). The DiphenPyr complexes, **4a** and **4b**, are found primarily

in non-coordinate interactions after at least 60 and 30 minutes of incubation with hsA at 37 °C respectively (Appendix C – **Figures C-21e** and **C-22d**), and the NBenzPyr complexes **5a** and **5b** show non-coordinate interactions dominating after 20 minutes of incubation (Appendix C – **C-23c** and **C-24c**).

The relative concentrations of coordinately and non-coordinately hsA-bound Ru(III) complexes were determined for **1a,b** – **5a,b** over the first 60 minutes of incubation by first simulating the overlapping spectral signals using weighting factors, as described in the Chapter 1. Using values of the double integrals of the simulated spectra gave the relative concentrations of each of the species present following incubation of **1a,b** – **5a,b** for 0, 10, and 60 minutes at 37 °C. As summarized in **Figure 4-6**, these calculations reveal a trend in the stability of the non-coordinate interactions of **1a,b** – **5a,b** with hsA that correlates with the ability of their axial ligands to facilitate interactions with the hydrophobic binding domains of hsA. The relative proportions of coordinately and non-coordinately bound Ru(III) species demonstrate that the axial ligands increase the persistence of non-coordinately bound species according to DiPhenPyr > PhPyr > NBenzPyr > MePyr > Pyr. **Figure 4-6** highlights the dramatic difference between the protein interactions of **1a** and **4a**. The Pyr complex (**1a**) is observed solely as coordinately bound species after 60 minutes of incubation with hsA, whereas the DiPhenPyr complex (**4a**) still shows a contribution from non-coordinately bound species after 120 minutes. Spectral deconvolution for all protein-bound species at all incubation time points, in addition to those in **Figure 4-5**, are shown in Appendix C – **Figures C15 – C-24**.

The sodium compensated analogues of the complexes described here are desirable in consideration of their pharmaceutical potential because of the possible toxicity of the pyridine counterions in **1a** – **5a**.²⁷⁰ Furthermore, as described above, the sodium salts also have significantly improved solubility in aqueous solution, which is particularly important when highly hydrophobic ligands such as DiPhenPyr are used. However, the counterion choice does not seem to significantly impact the interactions with hsA. The notable exception to this is in the behaviour of the DiPhenPyr compounds, where the sodium compensated complex (**4b**) very rapidly forms non-coordinate interactions with

the protein, while the DiPhenPyrH salt (**4a**) initially exhibits relatively low levels of hsA-bound species. This is consistent with the relative insolubility of **4a** in aqueous solution, which leads to the formation of aggregated species, as described above. With further incubation, the signals from non-coordinately bound **4a** increase significantly, demonstrating that the protein interactions effectively solubilize the complex.

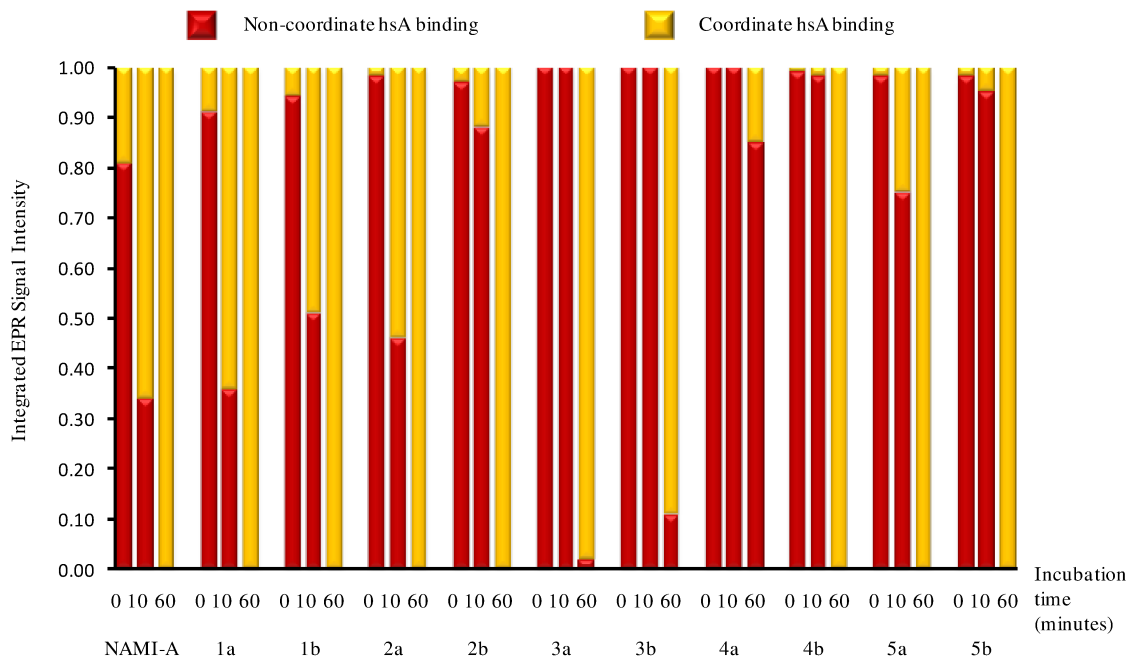


Figure 4-6 Relative fractions of coordinate (gold) and non-coordinate (red) hsA bound Ru(III) complexes following 0, 10, and 60 minutes of incubation at 37 °C, as determined from integrated EPR signal intensity.

While it is clear that increased derivatization of the pyridine ligands forestalls the formation of coordinate interactions with hsA, by stabilizing non-coordinate binding, it also influences the final concentrations of coordinated Ru(III) species (**Figure 4-5** and **Figure 4-6**, Appendix C – Figures C15 – C-24). The Pyr compounds **1a** and **1b** show strong, and similar intensity, EPR signals from hsA-coordinated complexes after 2 hours of incubation at 37 °C. Comparison with the MePyr complexes **2a** and **2b** shows signal intensities that are 40 and 60% lower, respectively, after the same incubation time. This effect is even more pronounced for the PhPyr, NBenzPyr, and DiPhenPyr analogues with the concentrations of the analogous species reduced by 70-80%. Formation of coordinate interactions is slow, as expected for ligand exchange reactions of Ru(III) complexes

under these conditions,⁴¹ but is thermodynamically favoured and thus dominates at longer time periods. However, these data indicate that stabilizing non-coordinate interactions leads to less total hsA-coordinated Ru(III) species after long incubation times.

4.3.6. Interactions of the Complexes with hsA - UV-Vis

The coordination of NAMI-A to serum proteins has been established to coincide with the emergence of new transitions between 460 and 610 nm in the UV-Vis spectrum.²⁰² Additional studies on interactions of the reduced form of NAMI-A with hsA showed the appearance of a broad peak around 540 nm.¹⁷⁸ In both cases these features were attributed to *d-d* transitions from NAMI-A-hsA adducts, the nature of which is thought to be from coordination to surface histidine residues.^{178,202} To confirm the direct coordination of the synthesized complexes to hsA, UV-Vis samples were prepared analogously to the previously described EPR samples. For all complexes (Appendix C – **Figures C-63 – C-72**), transitions were observed that were similar to their solution behaviour in addition to a broad, low intensity band around 534-598 nm, as shown in the inset of **Figure 4-7** for complex **4b**. As described above, these results are in good agreement with the EPR, confirming that the complexes coordinate directly to hsA. Additionally, no precipitation is observed for any of the complexes throughout the duration of the experiment.

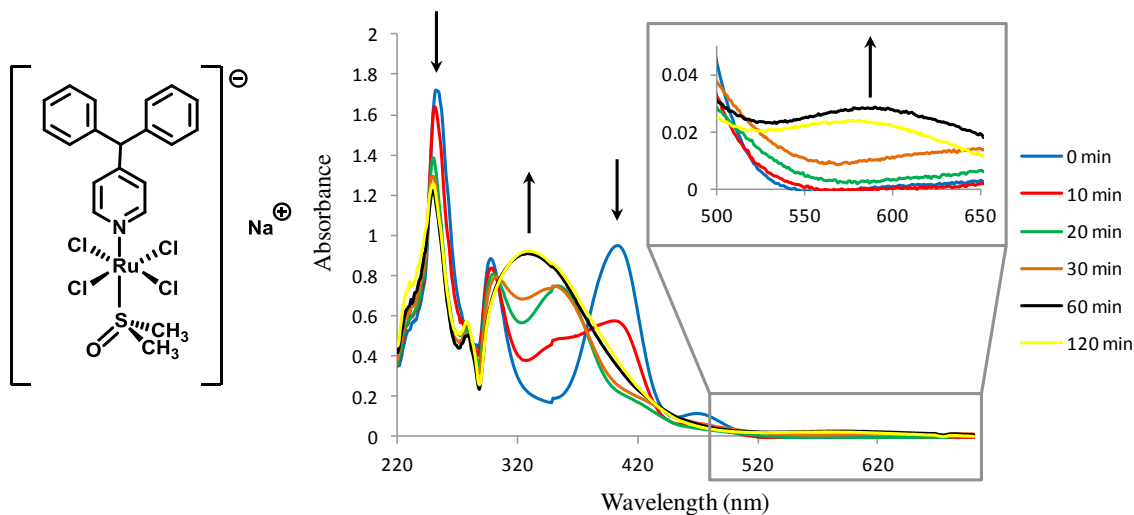


Figure 4-7 UV-Vis spectrum of complex **4b** in physiological buffer with hsA over 2 hours.

4.3.7. Effect of Protein Binding on Reductive Stability

The evolution of the ruthenium oxidation state in blood after intravenous infusion is anticipated to be important to mediate interactions with many extracellular biomolecule targets, and is likely an important component of antimetastatic activity of NAMI-A and its analogues.^{108,125,127,164,165,191} To study the redox behaviour of pyridine-based NAMI-A analogues the cyclic voltammograms of compounds **1a,b**, **2a,b**, and **5a,b** were measured in physiological buffer with a Ag/AgCl working electrode and scan rates of 100 mV/s (Appendix C – **Figures C-41 – C-44**, and **C-49 – C-50**). Due to the lower solubility of compounds **3a**, **3b**, **4a**, and **4b**, they were dissolved in a 1:1 mixture of DMSO and buffer before measurement of their cyclic voltammograms (Appendix C – **Figures C-47** and **C-48**). To determine the effect of DMSO on the reduction potentials, the cyclic voltammograms of NAMI-A were measured in both buffer (Appendix C – **Figure C-51**) and 1:1 DMSO / physiological buffer (Appendix C – **Figure C-52**). These measurements indicate a shift in electrochemical potential to lower values (ca. 160 mV).

For each complex a one-electron Ru(III) → Ru(II) redox couple was observed. As shown in **Table 4-2**, the values of $E_{1/2}$ for **1a,b – 5a,b** are very similar, as expected given the similar donating properties of the pyridine ligands, and fall in the range of 320–340 mV. Addition of the solvent correction for **4a** and **4b** gives 320 and 330 mV, respectively. These values are all slightly higher than previous electrochemical measurements which report $E_{1/2}$ for **1b** in aqueous solution of 300 mV²⁴⁷ and for **2a** in buffered saline (pH 7.40),²⁶⁰ of 310 mV vs. NHE in each case,^d likely reflecting minor differences in the experimental methods used.

As pointed out in previous reports,^{45,46} the reduction potentials of these types of ruthenium complexes can be estimated using the additive description of ligand contributions to $E_{1/2}$ given by Lever's Equation (equation 4.1):²⁷¹

[d] Original measurement of electrochemical potential for **1b** vs SSCE, $E_{1/2}$ vs NHE calculated by adding 236 mV; **2a** vs SCE, $E_{1/2}$ vs NHE calculated by adding 241 mV.

$$E = S_M \sum E_L + I_M \quad (4.1)$$

Table 4-2 Reduction potentials of compounds **1a,b – 5a,b** vs. NHE; peak-to-peak differences in parentheses ($E_{pc} - E_{pal}$).

LH ⁺ counterion	1a	2a	3a	4a	5a
$E_{1/2}$ Ru(III/II) (mV)	330 (80)	320 (70)	262 (114)*	160 (100)*	330 (120)
Na ⁺ counterion	1b	2b	3b	4b	5b
$E_{1/2}$ Ru(III/II) (mV)	330 (70)	320 (70)	248 (118)*	170 (90)*	330 (80)

The electrochemical ligand parameter, E_L , correlates with the net electron donating character of the constituent ligands of redox-active metal complexes. S_M and I_M are parameters derived from the empirical correspondence between ΣE_L , and experimental values of $E_{1/2}$ for a particular redox couple. The reduction potential has been shown to be dependent on solvent environment and the overall charge of the complexes measured.²⁷¹ Reisner *et al.* have reported values of $S_M = 0.88$ and $I_M = 0.46$ for Ru(III)(-1) → Ru(II)(-2) in neutral phosphate buffer solutions.⁴⁶ Ligand parameters of $E_L(\text{Cl}^-) = -0.24$,²⁷¹ $E_L(\text{DMSO, S-coordinated}) = 0.57$,²⁷² $E_L(\text{Pyr}) = 0.25$,²⁷¹ and $E_L(\text{MePyr}) = 0.23$,²⁷¹ and $E_L(\text{PhPyr}) = 0.23$,²⁷¹ give, from equation 4.1, $E_{1/2}(\mathbf{1a,b}) = 330$ mV, $E_{1/2}(\mathbf{2a,b}) = 320$ mV, and $E_{1/2}(\mathbf{3a,b}) = 320$ mV, in good agreement with the experimental values for complexes **1a,b** and **2a,b** (Table 4-2). Values of E_L for NBenzPyr and DiBenzPyr have not been reported previously, but the experimental values of $E_{1/2}$ found here indicate they are very similar to Pyr and MePyr, with $E_L \approx 0.25$.

The values of $E_{1/2}$ for the pyridine analogues described here are significantly more positive than NAMI-A, which has previously been reported as $E_{1/2} = 260$ mV versus NHE in a 0.10 M phosphate buffer system at pH 7.4,²⁰⁵ and is found to be $E_{1/2} = 270$ mV under the aqueous buffer conditions used in this work.^e The higher reduction potentials of **1a,b – 5a,b** reflect the greater net electron donating character of pyridine as compared to imidazole ($E_L(\text{imidazole}) = 0.09$).²²¹ These reduction potentials are readily accessible to

[e] Original measurement of electrochemical potential for NAMI-A vs SCE, $E_{1/2}$ vs NHE calculated by adding 241 mV.

biological reducing agents such as ascorbic acid ($E^\circ = +60$ mV vs. NHE) and glutathione ($E^\circ = -250$ mV vs. NHE).⁴⁶ Several earlier studies have shown that the Ru(III) centre of NAMI-A is reduced readily to Ru(II) in the presence of ascorbic acid.^{178,201,264} EPR measurements can be used to follow this process by tracking the overall loss of signal intensity because of the production of diamagnetic Ru(II) centres from paramagnetic Ru(III) species. To study the reduction behaviour of the pyridine complexes described here, each compound was initially incubated with an equimolar concentration of ascorbic acid in buffer (pH 7.4) at 37 °C. For each complex, **1a,b – 5a,b**, this leads to essentially complete loss of the EPR signal after less than 10 minutes of incubation (data not shown), demonstrating that reduction of almost all Ru(III) centres occurs very rapidly, as expected, given the relatively high reduction potential of these compounds.

To determine the influence of protein interactions on the reduction of the Ru(III) centres of **1a,b – 5a,b** the complexes were first incubated with hsA and the resulting solutions were then mixed with buffered ascorbic acid solutions, to give solutions with 1:1 molar ratios of ruthenium complexes to ascorbic acid. In the first of these experiments, protein-bound fractions of each complex were prepared by briefly mixing each complex with hsA in buffer at 25 °C, followed by ultrafiltration. These solutions were then combined with buffered ascorbic acid and briefly mixed at 25 °C. As described in the previous sections, this initial incubation procedure with hsA produces significant concentrations of non-coordinately bound complexes for **1a,b – 5a,b**, as shown by distinctive EPR signals (**Figure 4-5** and Appendix C – **Figures C-25**). However, as shown by the EPR spectra labelled “0 minutes” in **Figure 4-8**, the addition of ascorbic acid reduces these species to give EPR-silent Ru(II) centres, demonstrating that non-coordinate binding to the hydrophobic binding domains of hsA does not limit interactions with exogenous reducing agents.

Incubation of **1a,b – 5a,b** with hsA for 120 minutes at 37 °C, gives, almost exclusively, complexes that are coordinately protein bound, as described above, with corresponding EPR spectra (**Figure 4-5** and Appendix C – **Figures C15 – C-24**). In contrast to the non-coordinately bound species, addition of ascorbic acid causes no change to the appearance or intensity of the EPR spectra from these species (**Figure 4-8**).

This indicates that coordinate binding to hsA prevents reduction and thus can give mononuclear Ru(III) species *in vivo*. This increase in the reductive stability can be explained by the effect of ligand exchange on $E_{1/2}$. Since the complexes are expected to be bound primarily to surface imidazoles of hsA histidine residues, the effect of coordinate binding on the reduction potential can be estimated from equation 4.1 using the value of the ligand parameter for imidazole. Histidine imidazole (His-Im) coordination at the axial position, initially occupied by DMSO (species **1a**-hsA-2 in **Figure 4-5** and corresponding species in Appendix C – **Figures C15 – C-24** for other complexes) gives $[\text{trans}-\text{RuCl}_4(1H-\text{L})(\text{His-Im})]^-$. Assuming that this Ru(III) species can be described with a -1 charge, and correspondingly $S_M = 0.88$ and $I_M = 0.46$, then equation 4.1 gives $E_{1/2} = -0.90$ mV, which is sufficiently negative to prevent reduction by ascorbic acid. Substitution of a Cl^- ligand for a histidine imidazole gives $\text{RuCl}_3(\text{His-Im})(1H-\text{L})(\text{DMSO-S})$. This neutral complex is then described by equation 4.1 with $S_M = 0.97$ and $I_M = 0.04$,⁴⁶ which gives $E_{1/2} = 220$ mV, and thus this species is predicted to be readily reduced by ascorbic acid. However, if the lower-symmetry hsA-coordinated species (such as **1a**-hsA-1 in **Figure 4-5**) has histidine imidazole coordination at an equatorial position, and undergoes DMSO exchange with water ($E_L(\text{H}_2\text{O}) = 0.04$), to give the neutral species $\text{RuCl}_3(\text{His-Im})(1H-\text{L})(\text{H}_2\text{O})$, then equation 4.1 gives $E_{1/2} = -390$ mV, and so this species is expected to be resistant to reduction by ascorbic acid. This scenario seems reasonable, given the demonstrated proclivity of these complexes to undergo DMSO exchange. Although there is some uncertainty in these calculations for a variety of reasons, they do demonstrate the overall concept that a combination of ligand exchange with H_2O and protein side chains can produce species that are resistant to reduction under physiological conditions.

Similar enhancement in reductive stability with protein binding has also been reported for NAMI-A,²⁶⁴ and this has been suggested as a method for targeted activation of these types of compounds.⁴⁶ Lowering of the reduction potential by protein binding allows for transport *in vivo* in the Ru(III) oxidation state without reduction by physiological reducing agents. However, the reduction potential found in proliferating cells ($E_{1/2} \approx -240$ mV),²⁷³ can be reduced by as much as 100 mV in hypoxic tumour environments.²⁷⁴ This provides the potential for reduction of Ru(III) species that would

otherwise be redox stabilized under physiological conditions.²⁰⁵ The production of more labile Ru(II) species then facilitates coordination to biomolecules and apoptosis.^{46,49}

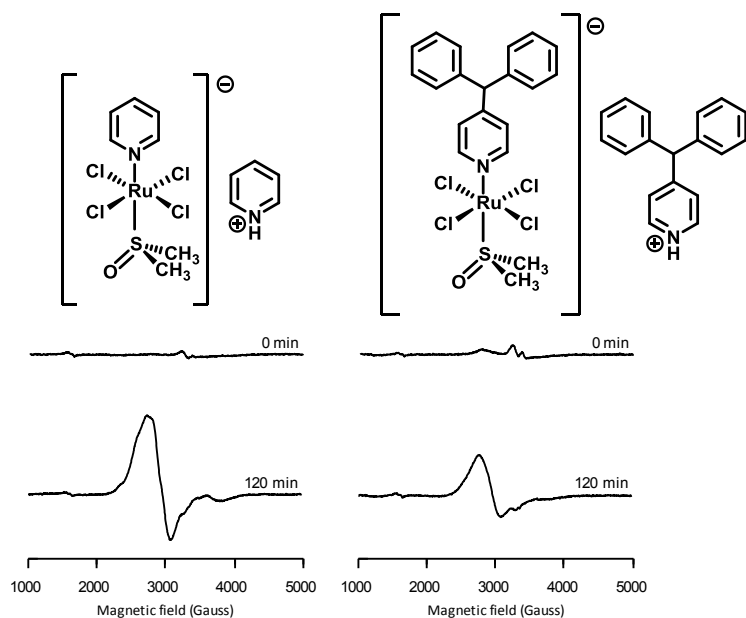


Figure 4-8 EPR measurement of **1a** and **4a** after initial incubation with hsA in physiological buffer at 37 °C for the times shown; followed by the addition of ascorbic acid. For EPR experimental conditions see 2.2.5. For EPR spectra of analogous experiments with the remaining complexes see Appendix C – **Figure C-25**.

4.4. Conclusions

It is now widely accepted that protein interactions are a key component of the pro-drug behaviour of Ru(III) anticancer complexes. Binding to hsA is expected to be predominant *in vivo* and is thus central to the transport and speciation of these compounds. From the EPR and UV-Vis studies of pyridine-based NAMI-A analogues described in this chapter, the properties of the axial azole ligand of “NAMI-A-like” complexes have been shown to play a critical role in modulating interactions with hsA. The EPR studies have demonstrated that the rates of ligand exchange in buffer solution are relatively unaffected by the characteristics of the pyridine ligands. However, these ligands do control the persistence of non-coordinate protein interactions, through distinct

abilities to interact with the hydrophobic binding domains of hSA. This not only controls speciation, as compared to buffer solution, but also affects the concentration of coordinately bound mononuclear Ru(III) species after long incubation periods. As shown here, non-coordinate bound complexes are readily reduced by ascorbic acid, while coordinately bound complexes are not. Consequently, it seems likely that increased stability of non-coordinate interactions reduces the concentration of Ru(III) species found *in vivo*. Overall, these results indicate that tuning non-coordinate interactions of Ru(III) complexes with hSA through the selection of suitable axial azole ligands is an important component of their activity and selectivity, and should be considered as part of future drug design strategies.

5. Pyridine-based Analogues of the Antineoplastic Ru(III) Complex KP1019: Using Non-coordinate Interactions with Albumin to Increase Bioavailability

5.1. Introduction

As shown in Chapter 2, EPR was used to characterize the formation of both the non-coordinate and coordinate hSA interactions of KP1019 and KP418,²⁴⁶ with the axial ligands playing a critical role in the protein binding behaviour of each complex. KP1019 was observed to form rapid, non-coordinate protein interactions which were quickly converted to coordinate protein bonds. In the case of KP418, non-coordinate protein interactions were observed at a slower rate while coordinate interactions were minimal even after prolonged exposure to the protein.²³⁶ The ability of KP1019 to form rapid non-coordinate interactions was attributed to enhanced interactions of its indazole ligands with the hydrophobic binding pockets of hSA,²⁴⁶ as compared to the imidazole ligands of KP418.²³⁶ Based on these observations, it was hypothesized that the bioavailability of these and other “Keppler-type” complexes could be enhanced by promoting hydrophobic interactions with hSA and consequently inhibiting the formation of coordinated species. To explore this concept a series of pyridine-based KP1019/1339 analogues were synthesized. These compounds have a range of substituents at the 4' position of the axial pyridine ligands, generating complexes with different tendencies to interact with the hydrophobic regions of hSA. The ligands chosen for these studies were: **1**, pyridine (Pyr); **2**, 4-methylpyridine (MePyr); **3**, 4-phenylpyridine (PhPyr); **4**, diphenyl-4-pyridylmethane (DiPhenPyr); **5**, 4-(4-nitrobenzyl)pyridine (NBenzPyr) (**Figure 5-1**). Each complex was synthesized with both protonated pyridine ligands (series **a**) and sodium ions (series **b**) as compensating cations (**Figure 5-1**). The latter were required to make the compounds sufficiently soluble for the testing of their anticancer activity.

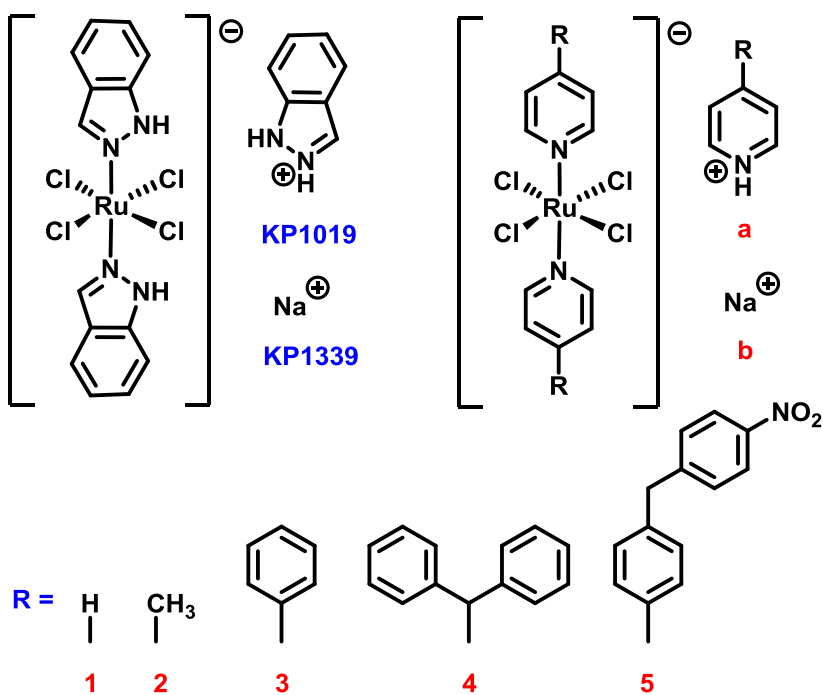


Figure 5-1 The promising Ru(III) “Keppler-type” anticancer compounds KP1019 and KP1339 and their pyridine-based analogues whose synthesis is described in this chapter.

To see how the improved stability of hydrophobic interactions correlates with anticancer activity, the compounds were tested against the SW480 human colon carcinoma cell line. In these experiments, the complexes were screened both after preparation in buffered solution and following initial incubation with hsA. These studies indicate that the enhancement of non-coordinate interactions can enhance the activity of the complexes both through inhibition of protein coordination and by increasing solubility.

5.2. Experimental

5.2.1. Synthesis

PyrH[*trans*-RuCl₄(Pyr)] (1a). RuCl₃•H₂O (0.293 g, 1.4 mmol) was dissolved in ethanol (6 mL) and HCl (1 M, 6 mL). The solution was refluxed for 3 hours resulting in a clear, brown-orange solution. Pyridine (683 μL, 8.5 mmol) was mixed with ethanol (1.5

mL) and HCl (6 M, 1.5 mL). This solution was added dropwise to the ruthenium solution and then refluxed for 3 hours. The mixture was allowed to cool to room temperature and then stored at -20°C . The red-orange precipitate that formed was collected by vacuum filtration using ethanol and diethyl ether as washes. Recrystallization in ethanol gave the product as an orange microcrystalline solid. Yield: 48% $\text{C}_{15}\text{H}_{16}\text{N}_3\text{Cl}_4\text{Ru}$ Calc. 37.44 C, 3.35 H, 8.73 N Found 37.02 C, 3.38 H, 8.68 N. Mel. Temp 230 - 232 $^{\circ}\text{C}$ (decomp.) ^1H NMR (D_2O): 8.72, 8.52, 7.98, -0.23 , -6.54 . Crystals suitable for X-ray diffraction were isolated from the reaction filtrate upon cooling to -20°C for several days.

$\text{Na}[\text{trans-RuCl}_4(\text{Pyr})]$ (**1b**). Complex **1a** (0.037 g, 0.077 mmol) was mixed with dichloromethane (25 mL). Sodium tetraphenylborate (0.059 g, 0.154 mmol) was dissolved in acetone (5 mL) and added dropwise to the solution of **1a**. The resulting mixture was heated to 95°C for 1 hour, resulting in a clear yellow solution. Solvent was removed under reduced pressure, followed by the addition of chloroform which resulted in the precipitation of the desired orange-brown product which was isolated using vacuum filtration. Yield: 65% $\text{C}_{10}\text{H}_{10}\text{N}_2\text{Cl}_4\text{RuNa}\cdot 2\text{H}_2\text{O}$ Calc. 26.10 C, 3.07 H, 6.09 N Found 26.45 C, 2.81 H, 5.97 N. Mel. Temp 192 - 193 $^{\circ}\text{C}$ (decomp.) ^1H NMR (D_2O): -0.29 , -6.65 .

4-MePyrH[*trans*-RuCl₄(4-MePyr)] (**2a**). RuCl₃•H₂O (0.2056 g, 0.786 mmol) was dissolved in ethanol (2 mL) and HCl (1 M, 2 mL). The solution was refluxed for 3 hours resulting in a clear, brown-orange solution. 4-Methylpyridine (667 μL , 6.854 mmol) was mixed with ethanol (1 mL) and HCl (6 M, 1 mL). This solution was added dropwise to the ruthenium solution and then refluxed for 3 hours. The clear, dark brown mixture was allowed to cool to room temperature and then stored at -20°C overnight. An orange-gold microcrystalline solid formed and was collected by vacuum filtration using ethanol as a wash. Yield: 86% $\text{C}_{18}\text{H}_{22}\text{N}_3\text{Cl}_4\text{Ru}$ Calc. 41.32 C, 4.24 H, 8.03 N Found 41.59 C 4.18 H 7.82 N. Mel. Temp: 196 - 198 $^{\circ}\text{C}$ (decomp.) ^1H NMR (D_2O): 8.51, 7.79, 2.58, -3.48 , -6.12 . Crystals suitable for X-ray diffraction were isolated from the reaction filtrate upon cooling to -20°C for several days.

$\text{Na}[\text{trans-RuCl}_4(4\text{-MePyr})]$ (**2b**). Complex **2a** (0.0797 g, 0.176 mmol) was mixed with chloroform. Sodium tetraphenylborate (0.6497 g, 1.899 mmol) was dissolved in

acetone (5 mL) and added dropwise to the solution of **2a**. The resulting mixture was stirred at room temperature for 1.5 hours, producing an orange-brown solution. Filtration yielded the product as a brown powder. Yield: 57% C₁₂H₁₄N₂Cl₄RuNa Calc. 31.88 C, 3.12 H, 6.20 N Found 31.59 C 3.09 H 6.40 N. Mel. Temp: 229 - 231 °C (decomp.) ¹H NMR (D₂O): 2.15, -3.55, -6.24.

4-PhPyrH[trans-RuCl₄(4-PhPyr)] (3a). RuCl₃•H₂O (0.3019 g, 1.44 mmol) was dissolved in ethanol (6 mL) and HCl (1 M, 6 mL). The solution was refluxed for 3 hours resulting in a clear, brown-orange solution. 4-phenylpyridine (1.3178 g, 8.491 mmol) was dissolved in ethanol (1.5 mL) and HCl (6 M, 1.5 mL). This solution was added dropwise to the ruthenium solution and then refluxed for 3 hours. The resulting orange-brown mixture was cooled to room temperature and then stored at -20 °C. An orange microcrystalline precipitate was collected by vacuum filtration using ethanol as a wash. Yield: 58% C₃₃H₂₈N₃Cl₄Ru Calc. 55.87 C, 3.98 H, 5.92 N Found 55.83 C 3.74 H 5.87 N. Mel. Temp: 258 - 260 °C (decomp.) ¹H NMR (*d*⁶-DMSO): 8.77, 7.99, 7.91, 7.57, 6.60, 5.43, 4.40, -5.96.

Na[trans-RuCl₄(4-PhPyr)] (3b). Complex **3a** (0.0652 g, 0.092 mmol) was dissolved in dichloromethane (30 mL). Sodium tetraphenylborate (0.0612 g, 0.179 mmol) was dissolved in acetone (15 mL) and added dropwise to the solution of **3a**. The resulting mixture was stirred at room temperature for two hours and further filtered yielding a light brown powder. Yield: 97% C₂₂H₁₈N₂Cl₄RuNa Calc. 45.85 C, 3.15 H, 4.86 N Found 45.35 C, 2.95 H, 5.01 N. Mel. Temp: 332 - 336 °C (decomp.) ¹H NMR (D₂O): 5.81, 5.27, 3.27, -6.01. Crystals suitable for X-ray diffraction were isolated from a methanol solution upon cooling to -20 °C for several weeks.

DiPhenPyrH[trans-RuCl₄(DiPhenPyr)] (4a). RuCl₃•H₂O (0.2960 g, 1.42 mmol) was dissolved in ethanol (6 mL) and HCl (1 M, 6 mL). The solution was refluxed for 3 hours resulting in a clear, brown-orange solution. Diphenyl-4-pyridyl-methane (2.0885 g, 8.51 mmol) was dissolved in ethanol (1.5 mL) and HCl (6 M, 1.5 mL). This solution was added dropwise to the ruthenium solution and then refluxed for 3 hours. The mixture was allowed to cool to room temperature and then stored at -20 °C. The mustard yellow precipitate that formed was collected by vacuum filtration using cold ethanol and diethyl

ether as washes. Recrystallization in toluene afforded a light yellow powder product. Yield: 82% C₅₄H₄₆N₃Cl₄Ru Calc. 66.19 C, 4.73 H, 4.29 N Found 66.05 C, 4.55 H, 4.59 N. Mel. Temp: 183 - 185 °C (decomp.) ¹H NMR (CDCl₃): 11.19, 9.35, 7.64, 7.28, 6.30, 6.04, 5.65, 3.23, 1.56, -1.76, -6.63. Crystals suitable for X-ray diffraction were isolated from a 12:1 solution of methanol:dichloromethane upon cooling to -20 °C for several months.

Na[*trans*-RuCl₄(DiPhenPyr)] (**4b**). Complex **4a** (0.0874 g, 0.089 mmol) was dissolved in dichloromethane, resulting in a clear golden yellow solution. Sodium tetraphenylborate (0.0692 g, 0.181 mmol) was dissolved in acetone (5 mL) and added dropwise to the solution of **4a**. The resulting mixture was stirred at room temperature for 90 minutes, after which the solution became a light yellow. Column chromatography was used to isolate the desired product with 1:1 acetone:dichloromethane as the eluent. The resulting fractions were combined and solvent was removed under reduced pressure, yielding a yellow powder. Yield: 30% C₃₆H₃₀N₂Cl₄RuNa•H₂O Calc. 55.83 C, 4.16 H, 3.62 N Found 56.23 C 4.13 H 3.63 N. Mel. Temp: 218 - 219 °C (decomp.) ¹H NMR (*d*⁶-DMSO): 6.17, 5.84, 3.63, -1.76, -6.63.

NBenzPyrH[*trans*-RuCl₄(NBenzPyr)] (**5a**). RuCl₃•H₂O (0.2910 g, 1.40 mmol) was dissolved in ethanol (6 mL) and HCl (1 M, 6 mL). The solution was refluxed for 3 hours resulting in a clear, brown-orange solution. 4-(4-Nitrobenzyl)pyridine (1.8264 g, 8.53 mmol) was dissolved in ethanol (1.5 mL) and HCl (6 M, 1.5 mL). This solution was added dropwise to the ruthenium solution and then refluxed for 3 hours. The mixture was allowed to cool to room temperature and then stored at -20 °C. The orange precipitate that formed was collected by vacuum filtration using ethanol and diethyl ether as washes. Yield: 76% C₃₆H₃₁N₆O₆Cl₄Ru Calc. 48.77 C, 3.52 H, 9.48 N Found 48.90 C, 3.50 H, 9.63 N. Mel. Temp: 198 - 199 °C (decomp.) ¹H NMR (*d*⁶-DMSO): 8.73, 8.22, 7.74, 7.62, 6.70, 4.35, 4.21, -3.48, -6.21. Crystals suitable for X-ray diffraction were isolated from a 1:1 solution of dimethylsulfoxide:dichloromethane upon cooling to -20 °C for several days.

$\text{Na}[\text{trans-RuCl}_4(\text{NBenzPyr})]$ (**5b**). Complex **5a** (89 mg, 0.100 mmol) was mixed with dichloromethane (10 mL), resulting in an orange solution. Sodium tetraphenylborate (76 mg, 0.20 mmol) was dissolved in acetone (5 mL) and added dropwise to the solution of **5a**. The resulting mixture was stirred and heated to reflux for 90 minutes, producing a cloudy solution, from which the desired yellow product was isolated using vacuum filtration. Yield: 52% $\text{C}_{24}\text{H}_{20}\text{N}_4\text{O}_4\text{Cl}_4\text{RuNa}\cdot 2\text{H}_2\text{O}\cdot \text{O}(\text{CH}_3)_2$ Calc. 41.68 C, 4.43 H, 6.48 N Found 41.89 C 4.13 H 6.61 N. Mel. Temp: 192 - 193 °C (decomp.) ^1H NMR (d^6 -DMSO): 6.69, 4.19, -3.53, -6.29.

5.2.2. Crystallographic Structure Determination

All crystal structures were determined using the same parameters outlined in section 4.2.2. Crystal data, data collection parameters, and details of structure refinement for compounds **1a**, **2a**, **3b**, **4a**, and **5a** are listed in **Table 5-1**.

5.2.3. Optical Measurements

UV-Vis spectra were measured using a Cary 1E UV-Visible spectrophotometer, connected to a Haake F3 water bath which maintained each sample's temperature of 37 °C. Spectra were collected from samples dissolved in a phosphate buffered saline (PBS) solution containing: 137 mM NaCl, 2.7 mM KCl, 10 mM Na_2HPO_4 , and 2 mM KH_2PO_4 , pH 7.4, with complexes **3a** – **5b** having 10% DMSO added to aid solubility. Measurements were performed using 200 μM solutions of each complex in 1 mL volumes. Protein binding measurements were performed using solutions containing 200 μM of each complex and 100 μM of hSA in 1 mL volumes, with 4% DMSO added to the solutions of complexes **3a** – **5b**. All samples were measured at 37 °C for a total of 2 hours, with scans taken at 10 minute intervals, at a scan rate of 10 nm/sec. Additional protein samples were prepared to monitor for a weak *d-d* transition corresponding to hSA coordination using 600 μM of each complex and 100 μM hSA. These samples were incubated at 37 °C for 24 hours, with scans taken at 1 hour intervals.

5.2.4. Preparation of EPR Samples

Complexes in Buffer. Compounds were dissolved in PBS with complexes **3a – 5b** having 10% DMSO added to aid in solubility, to give a concentration of 3 mM, and incubated at 37 °C for: 0, 30, and 120 minutes. Each sample was promptly mixed with 30% by volume of glycerol, which acted as a glassing agent, and frozen in liquid nitrogen until use.

Complexes with hsA. A 600 µL solution of hsA (0.75 mM) in PBS was mixed with a 600 µL solution of each complex (1.5 mM), also in PBS with complexes **3a – 5b** having 4% DMSO added to aid solubility. The combined solution was then diluted to 4 mL with PBS and incubated at 37 °C for one of the following time periods: 0 min, 30 min, 1, 2, 6, and 24 hours. Each 4 mL solution was concentrated down to a volume of less than 200 µL using an Amicon centrifugal filter unit (molecular weight cut-off 30 kDa) by centrifuging at 8 °C and 4500 rpm for 30 minutes, or until a volume of less than 200 µL was attained. The resulting filtered product was then mixed with 90 µL of glycerol, diluted to a final volume of 300 µL with PBS, transferred to an EPR tube, and immediately frozen in liquid nitrogen.

5.2.5. EPR Measurements and Simulation

See section 2.2.4.

5.2.6. EPR Experimental Conditions

See section 2.2.5.

5.2.7. Anticancer Activity Testing

All the synthesized complexes were tested for anticancer activity using a standard MTS assay (Promega). SW480 human colon carcinoma cells were obtained from the American Type Culture Collection (ATCC). The cells were cultured using Dulbecco's Modified Eagle Medium (DMEM), supplemented with 10% fetal bovine serum (FBS) and L-glutamine. Fresh stock solutions of each free complex were prepared in cell culture

media with 1% DMSO, at the maximum concentration possible for each complex: 1 mM for complexes **1a/b** and **2a/b**, 500 µM for complexes **3b** and **4b**, and 750 µM for complex **5b**. Due to low aqueous solubility, complexes **3a**, **4a**, and **5a** were not tested. KP1019 was also tested at 1mM, and used as a positive control for activity. Cells were incubated with each complex for 24 hours, after which the absorbance reading at 490 nm was measured as an indicator of activity.

Additional samples were prepared where the complexes were loaded onto hsA. Solutions of each complex in PBS (1 mM, 1% DMSO) were mixed with solutions of hsA in PBS (0.5 mM) and incubated for 10 minutes at 37 °C, after which the protein-bound fractions were isolated, as described above, for the preparation of EPR samples. The fractions were then diluted in cell culture medium and subsequently tested for activity using identical conditions as for the free complexes.

5.3. Results and Discussion

5.3.1. Synthesis

Compounds **1a – 5a** and **1b – 5b** were synthesized using procedures derived from the original syntheses of KP1019 and KP1339 respectively.^{132,133} An alternative synthesis and characterization of complex **1a** has been described elsewhere.¹³¹ However, this is the first report of the sodium analogue of this compound (**1b**) and all the other complexes, with either type of counterion. The identity and purity of these compounds was confirmed by elemental analysis, NMR, EPR, and X-ray crystallography.

There have been a number of reports of derivatives of Ru(III) Keppler-type complexes with different heterocyclic nitrogen ligands.^{45,130,256,275} However, this is the first study using systematic functionalization at a single position on coordinated heterocyclic ligands to manipulate the properties of the complexes.

5.3.2. Crystal Structures

The structures of compounds **1a**, **2a**, **3b**, **4a**, and **5a**, were determined by X-ray crystallography and are shown in **Figure 5-2**. For clarity, the counterions for each

complex are omitted, along with any additional co-crystallizing solvent molecules. The diverse properties of the axial ligands required a variety of solvent conditions to produce suitably diffracting crystals. The structures of each cation type were determined, and other spectroscopic and analytical techniques were used to confirm the synthesis of the compounds with the alternative counterions. The crystal structure of complex **1a** has been described previously,¹³¹ but none of the other compounds have been reported or characterized crystallographically.

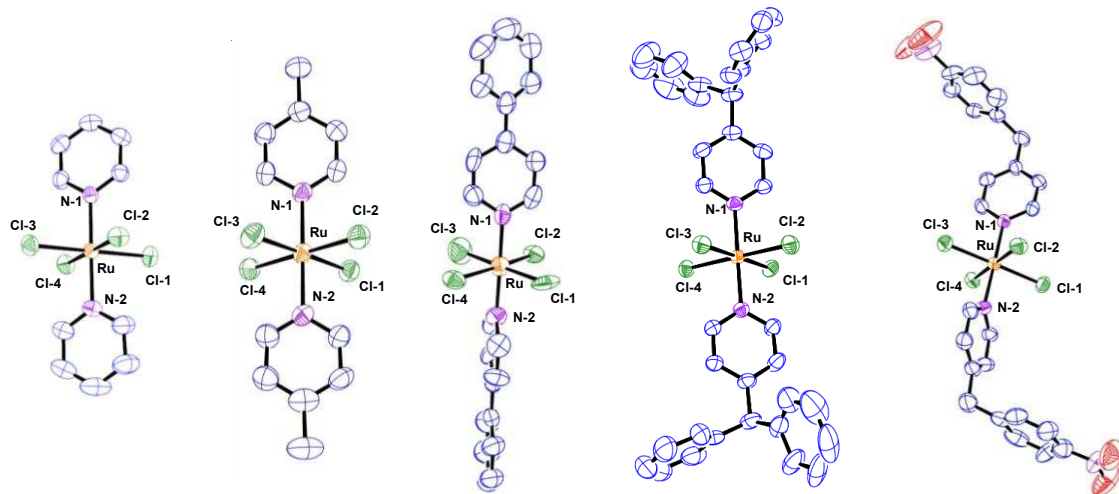


Figure 5-2 Crystal structures of complexes **1a**, **2a**, **3b**, **4a**, and **5a**.

For all of the structures solved, a similar distorted octahedral geometry is observed. The bond lengths around the ruthenium metal centre for all of the complexes are listed in Appendix D – **Table D-3**. In all cases the two pyridine ligands are coordinated *trans* through the heterocyclic nitrogen with an average Ru-N bond distance of 2.097 Å, which is slightly longer than the reported value for both KP418 (2.079 Å)¹²⁹ and KP1019 (2.061 Å).¹³³ An equatorial plane of four chlorides completes the coordination sphere with bond lengths ranging from 2.335 Å to 2.384 Å, which are within experimental error of KP418 (2.342 – 2.356 Å) and KP1019 (2.358 – 2.372 Å). This type of coordination environment is typical of analogous complexes^{130,256,275,276}

Table 5-1 Crystal data and details of data collection and refinement for compounds **1a**, **2a**, **3b**, **4a**, and **5a**.

Complex	1a	2a	3b	4a	5a
empirical formula	C ₁₅ H ₁₆ Cl ₄ N ₃ Ru	C ₁₉ H ₂₂ Cl _{6.93} N ₃ Ru	C ₂₃ H ₁₈ Cl ₄ N ₂ ORu	C ₅₆ H ₄₅ Cl ₆ N ₃ Ru	C ₃₇ H _{32.5} Cl ₆ N ₆ O ₆ Ru
M (g mol ⁻¹)	481.19	639.33	581.29	1073.78	970.99
space group	Monoclinic P121/n1	Monoclinic P121/n1	Monoclinic P121/c1	Orthorhombic Pbca	Triclinic P-1
a (Å)	8.108	9.146	12.500	13.610	8.194
b (Å)	22.504	18.820	14.528	23.010	19.139
c (Å)	10.153	15.806	14.354	33.195	27.153
α (deg)	90	90	90	90	90.067
β (deg)	92.906	105.656	100.364	90	90.146
γ (deg)	90	90	90	90	93.537
V (Å ³)	1850.40	2620.0	2564.1	10396.5	4250.0
Z	4	4	4	8	4
ρ _{calc} (g cm ⁻³)	1.727	1.621	1.506	1.372	1.517
μ(g mm ⁻¹)	1.425	1.318	1.045	1.464	0.797
λ (Å)	0.71073	0.71073	0.71073	0.71073	0.71073
T (K)	293	293	293	293	293
goodness of fit	1.46	1.24	0.83	1.01	1.00
R ₁	0.0319	0.0387	0.0666	0.0391	0.0508
wR ₂	0.0376	0.0726	0.0894	0.0456	0.0516

5.3.3. Aqueous Solution Behaviour – EPR

Due to the clinical success of KP1019, the solution behaviour of this complex has been extensively studied using a variety of techniques.^{170,177,216,226} Aqueous exchange of a chloride ligand occurs within minutes under physiological conditions, resulting in the precipitation of the insoluble mono-aquated derivative.¹⁷² This precipitation event can be inhibited in the presence of other ligands, particularly proteins or other biomolecules.^{172,234} For the compounds **1a,b – 5a,b** reported here, their ligand-exchange processes in PBS were characterized to determine whether their fundamental solution behaviour was similar to KP1019.

Complexes **1a,b** and **2a,b** had sufficient aqueous solubility to be dissolved directly in PBS at a 3 mM concentration and studied by EPR. The other complexes, **3a,b**, **4a,b**, and **5a,b**, required addition of 10% DMSO to give sufficient concentrations. Immediately after dissolution, similar uniaxial EPR spectra were observed for each of the parent Ru(III) complexes, consistent with the tetragonal symmetry of the Ru(III) centres prior to ligand exchange (**1b-C1** and **4a-C1** in **Figure 5-3**). Although the perpendicular

part (g_{\perp}) of the EPR spectrum was well resolved in each case, g_{\parallel} could not be detected. Similar behaviour has been reported in EPR measurements of KP1019 and KP418, and has been assigned to line broadening due to g strain.^{219,246} In the earlier study of KP1019 and KP418 (Chapter 2), adiabatic rapid-passage dispersion-mode measurements determined $g_{\parallel} = 1.20$ for both complexes. Given the structural and bonding similarity of the ruthenium centres with the compounds reported here, the value of g_{\parallel} is likely to be very similar. Thus, a value of $g_{\parallel} = 1.20$ was used for the simulation of **1a – 5a** and **1b – 5b**, with a large linewidth (400 Gauss), but it should be noted that this has essentially no impact on the shape of the spectra in the perpendicular spectral region. Simulation of the perpendicular region gave values in the range $g_{\perp} = 2.64 – 2.66$, and linewidths of $LW_{\perp} = 105-200$ Gauss (Appendix D – **Figures D-1 – D-10** and **Tables D-1** and **D-2**). The different counterions had no effect on the simulations for the spectra of complexes **1a,b** and **2a,b**. A similar phenomenon was observed for complexes **3a,b**, while for complexes **4a,b**, and **5a,b**, the spectra from the pyridinium compensated (**a**) complexes were significantly broader than those with sodium-ion compensation (**b**). This broadening is likely due to the highly hydrophobic nature of the pyridinium cations, leading to some aggregation of the complexes in solution.²⁷⁷

Incubation of 3 mM solutions of each complex in PBS at 37 °C resulted in both precipitation and the formation of some solubilized complexes. EPR was used previously to characterize ligand exchange rates for both KP1019 and KP418 (Chapter 2).²⁴⁶ In this work, rates of aqueous ligand exchange for the new pyridine analogues are observed to be similar to KP1019. As expected, increasing the hydrophobicity of the axial ligands increased the rate of precipitation with incubation under physiological conditions.

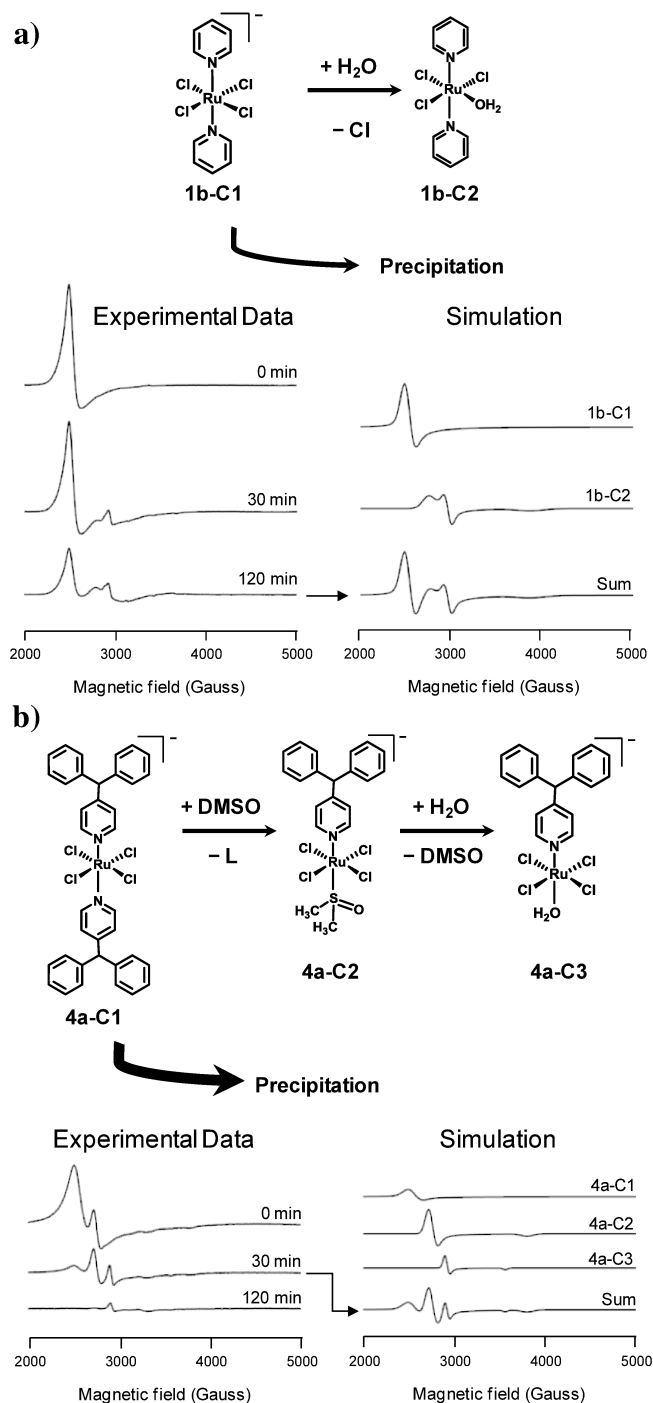


Figure 5-3 EPR measurements of a) **1b** and b) **4a** incubated in PBS buffer at 37 °C, and spectral deconvolution of spectra collected after 120 and 30 minutes respectively. For EPR experimental conditions see 2.2.5. For spectral parameters used in each simulation see Appendix D – **Table D-1**.

EPR measurements report primarily on the complexes in solution, since aggregation of precipitated compounds leads to spectral broadening. As a result, in these studies precipitation is reflected in a decrease in overall EPR signal intensity with increasing incubation. For all the complexes studied here, prolonged incubation was accompanied by a color change from clear yellow to a dark green color. In the case of complexes **3a,b – 5a,b** significant amounts of a green-blue precipitate were also observed after longer incubation times. These observations are consistent with the formation of the mono-aqua derivatives of Kepler-type complexes, as reported for KP1019.^{172,229}

To characterize the behaviour of the complexes remaining in solution, EPR measurements were made after incubation times of 0, 30, and 120 minutes. Spectral components were analyzed by simulation, as described in the experimental section. In the case of complexes **1a,b** a single new species was observed, which was identified by a rhombic EPR spectrum with $g = [2.44, 2.26, 1.72]$ and linewidths = [130, 70, 300] Gauss, labelled **1b-C2** in **Figure 5-3**. This is consistent with the formation of the mono-aqua complex formed by the exchange of an equatorial chloride ligand. Similarly, for complexes **2a,b**, only one new species was detected following dissolution. This was observed after 30 minutes of incubation: labelled **2a,b-C2** in Appendix D – **Figures D-8 and D-9** with $g = [2.47/2.45, 2.27/2.26, 1.78/2.00]$ and linewidths = [125, 100/50, 400] Gauss. The similarity in spectral parameters to **1a,b-C1** indicates that these complexes also form a mono-aqua complex through chloride exchange.

Under physiological conditions nitrogen donor ligands are generally considered to be kinetically inert,¹⁷⁶ leaving only the equatorial chloride ligands available for exchange with water molecules. To confirm this, NMR measurements were made of the sodium compensated complexes **1b** and **2b** in buffered D₂O solutions. These solutions were incubated at 37 °C for 2 hours, and subsequently analyzed using ¹H NMR to monitor for pyridine or 4-methylpyridine ligands respectively (Appendix D – **Figures D-61 and D-62**). In both cases no free pyridine-based ligands were observed, thereby confirming that only chloride ligand exchange occurs.

No soluble ligand-exchanged complexes were observed for the sodium-compensated complexes **3b**, **4b**, and **5b**. The more hydrophobic ligands of these

compounds, as compared to **1a,b** and **2a,b**, likely led to highly insoluble aquated derivatives, which precipitate rapidly and are thus were not observed by EPR.

Although the pyridinium-compensated complexes **3a**, **4a**, and **5a** also precipitate readily, two new uniaxial EPR signals with relatively low intensity are observed. The first species to form ($g_{\perp} = 2.44$, $g_{\parallel} = 1.76$; $LW_{\perp} = 90$ Gauss, $LW_{\parallel} = 125$ Gauss) is labelled **4a-C2** in **Figure 5-3** and correspondingly for complexes **3a** and **5a** in Appendix D – **Figures D-1 – D-10**. With further incubation this was replaced by a second new species ($g_{\perp} = 2.30$, $g_{\parallel} = 1.88$; $LW_{\perp} = 50$ Gauss and $LW_{\parallel} = 50$ Gauss), identified as **4a-C3** in **Figure 5-3** and similarly for the other complexes in Appendix D. Interestingly, the uniaxial EPR spectra for each species indicate tetragonal symmetry, which requires exchange of the pyridine-based ligands. This has not been reported previously for Keppler-type complexes under physiological conditions.

As described above, to achieve sufficient solubility for EPR measurements, 10% DMSO was added to the solutions of, **3a,b**, **4a,b**, and **5a,b**, a procedure that is also common in the preparation of these types of compounds for biological testing. The spectral parameters of the first species formed from **3a**, **4a**, and **5a**, match those previously reported for “NAMI-A-type” pyridine complexes (Chapter 4).²⁷⁷ These complexes have the general formula [*trans*-RuCl₄(1*H*-L)(DMSO-S)], where L is a pyridine-based ligand, DMSO takes up one axial position, and charge compensation is provided by a pyridinium or sodium cation. Therefore, the first species to form, **C2**, is assigned to the exchange of an axial pyridinium ligand for DMSO. The second type of species, **C3**, which form with longer incubation, have spectral parameters that match those of the NAMI-A-type complexes after the DMSO ligand had been exchanged for a water molecule, indicating that the same process is occurring here for complexes **3a**, **4a**, and **5a**.

As further evidence that the initial exchange step involves exchange of a pyridine-based ligand for DMSO, the experiments were repeated with 50% and 100% DMSO. The signal from **3a**-, **4a**-, and **5a-C2**, was observed with increased intensity (Appendix D – **Figure D-26**), consistent with the formation of the DMSO complex. ¹H NMR measurements could not be used in this case to detect exchanged pyridine-based ligands

since their signals were masked by the pyridinium counterions, while the signal intensity was too low for paramagnetic NMR to detect coordinated DMSO.

The replacement of pyridine ligands by DMSO is not unprecedented,²⁷⁸⁻²⁸⁰ but has not been reported for KP1019 under physiological conditions.¹⁰¹ To confirm this, KP1019 was dissolved in PBS with 10% DMSO and measured by EPR (Appendix D – **Figure D-58**). The resulting spectra are identical to those previously reported for the complex in DMSO-free buffer (Chapter 2).^{219170,246} Furthermore, with prolonged incubation at 37 °C the EPR spectrum was unchanged and no precipitation occurred. This demonstrates that DMSO enhances the solubility of KP1019 by inhibiting the formation of the insoluble mono-aqua species, but does not lead to exchange of its indazole ligands.

5.3.4. Aqueous Solution Behaviour – UV-Vis

The ligand-exchange processes of each compound were also characterized by UV-Vis spectroscopy. Samples were prepared in PBS at a concentration of 200 µM. For improved solubility, solutions of complexes **3a,b**, **4a,b**, and **5a,b** included 10% DMSO. The samples were incubated at 37 °C within the spectrophotometer with measurements taken every 10 minutes for two hours.

The UV-Vis spectra from **1a** and **1b** (**Figure 5-4** and Appendix D – **D-27** and **D-28**) are essentially identical with absorption bands in both the ultraviolet and visible ranges. The most intense peak is observed at 257 nm, and is assigned to the auxochrome signal from the pyridine ligand.²⁸¹ The next most intense absorbance peak occurs at 281 nm, which is consistent with pyridine $\pi-\pi^*$ transitions for Ru(III) complexes.²⁶⁵ A third peak at 360 nm is within the typical range of ligand to metal charge transfer (LMCT) transition for octahedral Ru(III) complexes with bound nitrogen heterocycles.²⁶⁶ With incubation, the absorbances at 257 and 360 nm decrease, while the peak at 281 nm shifts slightly longer wavelength. From this, one well defined isosbestic point (347 nm) is observed, which is consistent with only one ligand exchange pathway. This is in agreement with a single aquation step as determined by EPR, while the decrease in the peak at 257 nm is consistent with the observed precipitation in the sample.

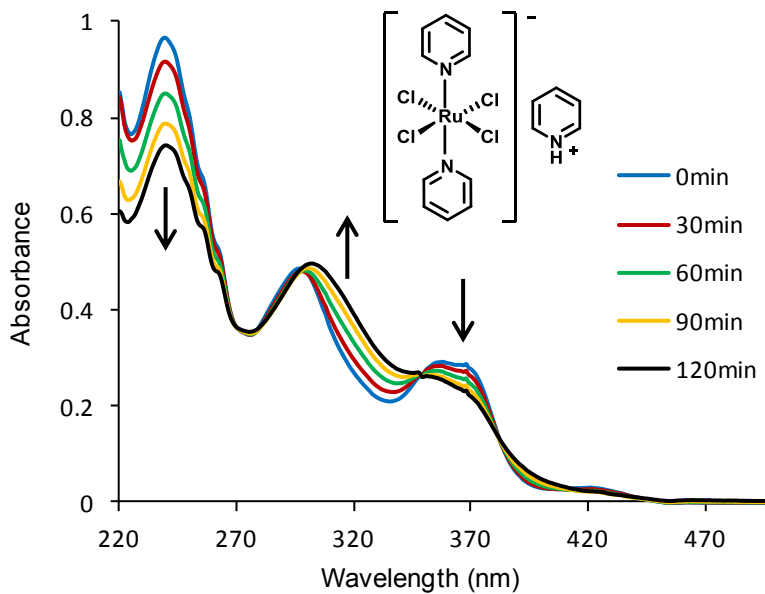


Figure 5-4 UV-Vis spectra for complex **1a** incubated in PBS for 2 hours at 37 °C.

Similar absorbances and spectral changes with incubation were observed for **2a** and **2b** (Appendix D – **Figures D-29** and **D-30**), which is consistent with a single aquation step, also observed by EPR. Complexes **3a,b**, **4a,b**, and **5a,b** had spectra dominated by broad, intense features that did not change significantly with incubation (Appendix D – **Figures D-31 – D-36**). These absorbances are from $\pi-\pi^*$ transitions from the phenyl-based substituents. Subtle changes in signal intensities suggest ligand exchange processes.

Overall, these studies demonstrate that aqueous solubility is a significant issue for all of these compounds, with precipitation occurring readily in aqueous solutions. However, contributions from soluble mono-nuclear Ru(III) species are also notable and there is some diversity in the mechanisms of their formation due to the different axial ligands.

5.3.5. Interactions of Complexes with hsA – EPR

Human serum albumin is the most abundant protein in the circulatory system, and has been identified as a primary target in the transportation of many drugs to their sites of activity.^{75,77,282} Several studies have shown that hsA interactions are the dominant serum-

protein interactions for several Ru(III) complexes under physiological conditions.^{122,123,182,210} The propensity of albumin to form interactions with a variety of pharmaceuticals has been reported and is considered to be an important factor in the delivery to their site of action.^{77,78} Indeed, the use of albumin in drug delivery has developed into a promising area of medicinal chemistry,^{192,283} however, the majority of the uses of albumin rely on coordinate interactions between the pharmaceutical and the protein.²⁸⁴⁻²⁸⁶ Here, the focus is on optimizing non-coordinate hsA interactions, in part to reduce coordination to the protein and thereby increase the bioavailability of the complex.

As shown in Chapter 2, EPR methods were used to show that KP1019 forms rapid non-coordinate interactions with hsA,²⁴⁶ which are gradually converted to coordinate protein interactions after further incubation under physiological conditions. In the case of its toxic imidazole analogue (KP418), both non-coordinate and coordinate protein interactions are also observed. However these form at a much slower rate.^{236,246} The reduced rate of hsA coordination by KP418 has been suggested to leave more of the complex free *in vivo*, and is possibly responsible for the observed toxicity.¹⁴¹ In light of these reports, the ability of complexes **1a,b – 5a,b** to bind to hsA both via hydrophobic interactions and through direct protein coordination were evaluated.

The complexes **1a,b – 5a,b** were incubated for 0 minutes, 30 minutes, 1, 2, 6, and 24 hours at 37 °C in PBS solutions of hsA. Protein-bound fractions were then isolated using centrifugal ultrafiltration and studied by EPR. This approach allows for the exclusive observation of hsA-bound Ru(III) species while removing contributions from free complexes in solution.^{246,264,277} The resulting spectra for select incubation times are shown in **Figure 5-5** for complexes **1a**, **3a**, and **5a**, and in Appendix D – **Figures D-3 – D-5** for the other complexes at all time points.

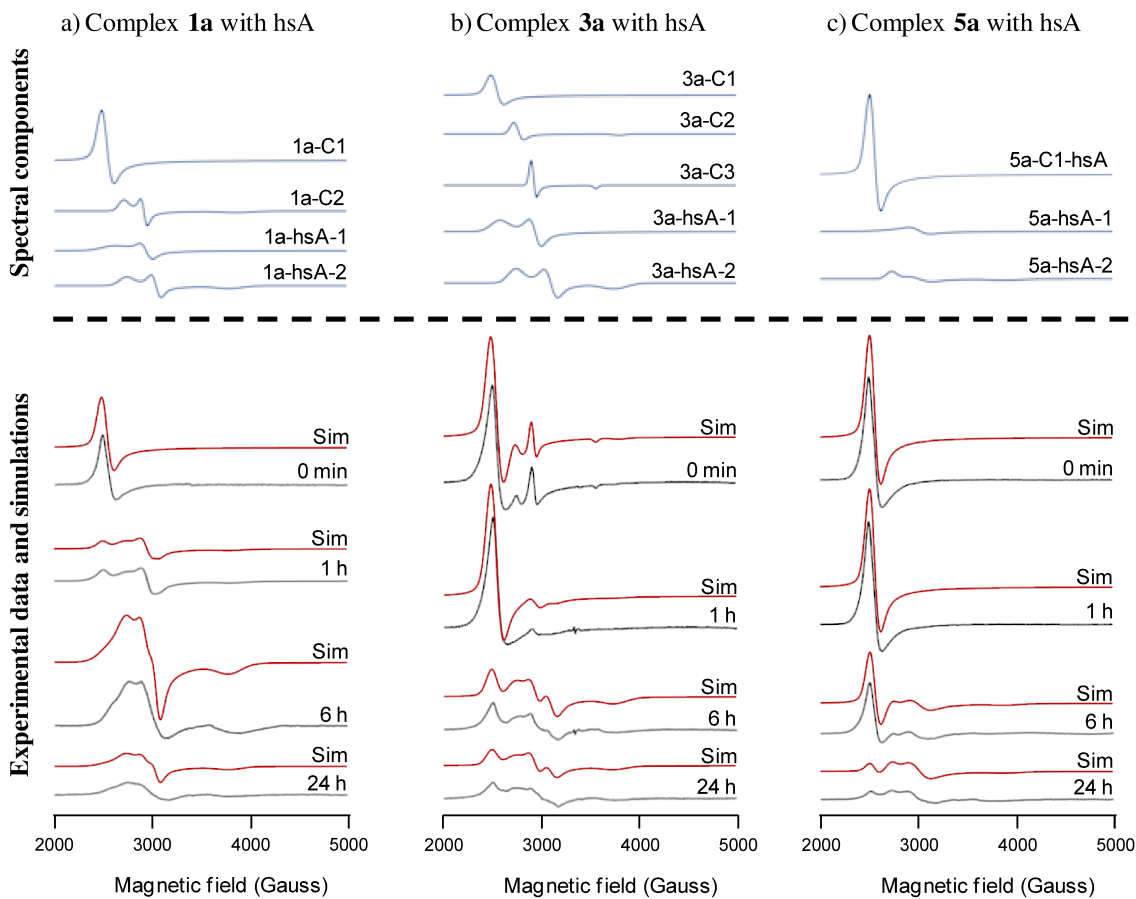


Figure 5-5 EPR measurement of complexes a) **1a**, b) **3a**, and c) **5a** incubated in PBS buffer (1 mM, and 4% DMSO for complexes **3a** and **5a**) with hsA (0.5 mM) at 37 °C, and spectral deconvolution of all spectra collected (shown in red) from individual components (shown in blue). For EPR experimental conditions see 2.2.5. For spectral parameters used in each simulation see Appendix D – **Table D-2**.

After incubation with hsA, spectra from the unsubstituted parent compounds of each complex were observed even at the earliest time point (labelled “0 min” in **Figure 5-5**). This was confirmed by spectral simulation using the parameters determined from the complexes dissolved directly in buffer, and identified previously as species **C1**. Since these measurements are of isolated protein fractions, they demonstrate that each complex readily binds to hsA without exchanging ligands, indicating non-coordinate interactions with the protein. Furthermore, the EPR spectra of the pyridinium-compensated compounds **4a** and **5a**, exhibited narrower linewidths than in buffer alone (labelled **4a**-

C1-hsA and **5a-C1-hsA** in Appendix D – **Figures D-22** and **D-24**), indicating that protein interactions improve the solubility of the complexes.

Aquated derivatives of the complexes **1a,b** and **2a,b** were also observed to form non-coordinate interactions with hsA (Appendix D – **Figures D-16 – D-19**). EPR spectra from these species were detected for the complexes that had previously shown formation of aquated derivatives in buffer solution. Simulation of these spectra gave parameters that agreed, within experimental uncertainty, with the species in buffer alone. For complexes **3a**, and **4a,b** the NAMI-A-type complexes formed by axial ligand exchange were again observed as minor contributors in the experimental spectrum (Appendix D – **Figures D-20, D-22, and D-23**), while only the parent complex for both **5a** and **5b** was visible (Appendix D – **Figures D-24 and D-25**), demonstrating the influence of protein interactions on ligand exchange processes. In previous studies the aquated derivatives of KP418 and NAMI-A were also observed to bind to hsA (Chapters 2 and 3).^{246,264}

Further incubation of each complex with hsA resulted in a gradual decrease in the signals from the parent compounds and their exchanged derivatives, coupled with the appearance of new broad features in their EPR spectra. Spectral simulation revealed two new signals in all cases, with relative intensities and formation rates that varied for each complex. The first new species, labelled **hsA-1** in **Figure 5-5** (Appendix D – **Figures D-16 – D-25** for each complex), has a rhombic spectrum with $g_1 = 2.38 - 2.61$, $g_2 = 2.24 - 2.29$, and $g_3 = 1.20$ and linewidths of: [$LW_1 = 175 - 400$, $LW_2 = 100 - 150$, and $LW_3 = 400$] Gauss. The second species also has a rhombic EPR signal, labelled **hsA-2** in **Figure 5-5**, with $g_1 = 2.38 - 2.45$, $g_2 = 2.16 - 2.22$, and $g_3 = 1.71 - 1.78$ and linewidths of: [$L_1 = 80 - 150$, $L_2 = 80 - 200$, and $L_3 = 250 - 300$] Gauss (See Appendix D – **Tables D-1** and **D-2** for parameters for each complex). In each case, the distinctive *g* values and linewidths of these species are consistent with direct coordination to hsA via ligand exchange. Histidine coordination has previously been implicated in the protein binding of KP1019^{171,287} and other Ru(III) complexes,^{106,264,288} and is expected to be the coordination mode seen here. The rhombic EPR spectra observed are consistent with coordination at equatorial positions, while the presence of two distinct signals indicates concurrent aquation processes. Given that **hsA-1** has greater signal intensity, particularly

at early time points, this is likely the species formed by a single exchange with a histidine imidazole. Subsequent aqueous exchange then produces the second protein-bound species **hsA-2**.

Previous studies of Ru(III) anticancer candidates have reported the coordination of upwards of 5 equivalents of Ru per protein molecule.^{171,235} In this work a 2:1 ratio of each complex to hsA was used to allow for the possibility of different binding modes. Strong signals from **hsA-1** and **hsA-2** were observed for every complex, demonstrating that protein coordination is highly favoured and that the ruthenium centre remains in the 3+ oxidation state. Furthermore, the signal intensity from the coordinated species was maintained even after 24 hours of incubation, demonstrating how effectively these interactions stabilize the compounds in solution. Similar behaviour has been reported previously for KP1019.^{170,172,246}

To determine the effect of the different axial ligands of **1a,b – 5a,b** on interactions with hsA, spectra of each complex were collected at the different incubation time points and analyzed by simulation (Appendix D – **Figures D-16 – D-25**). From this analysis, the relative total signal intensities from non-coordinate and coordinate interactions could be determined from the weighting factors used to scale individual spectral components in each simulation.

Every complex showed significant non-coordinate interactions with hsA after minimal incubation times. However, the rate that these species were replaced by protein coordinated complexes varied dramatically (**Figure 5-6**). In the case of the *bis*-pyridine complex **1a,b**, this process was complete after just 2 hours of incubation, with only the protein bound species **hsA-1** and **hsA-2** observed with subsequent incubation. Similar behaviour was observed for complexes **2a,b**, except that it took up to 6 hours of incubation until non-coordinate species were no longer observed. This demonstrates that the methyl group at the 4' position of the pyridine rings significantly enhances these interactions with the protein. This effect is even more pronounced in the complexes where the pyridine ligands have been functionalized with phenyl-based groups. In the case of complexes **3a** and **3b**, significant contributions from non-coordinated species were observed after 6 hours of incubation, and even after 24 hours for the pyridinium

compensated compound. The protein binding of **4a** and **4b** was very similar to the mono-phenyl derivatives, demonstrating that addition of the second phenyl ring does not significantly enhance non-coordinate interactions. Specific interactions with the hydrophobic binding regions of hsA,^{81,85 81,85 81,85 81,85 81,85 81,85 75,79} Sudlow's sites I and II,^{75,79} have previously been suggested as targets for interactions with Kepler-type complexes.^{36,37} Although increasingly hydrophobic groups would certainly be expected to enhance interactions with these protein sites, observed in the trend in the binding of **1a,b**, **2a,b**, and **3a,b**, steric interactions, such as from the bulky dibenzyl groups of **4a** and **4b**, are likely also to be an important factor.

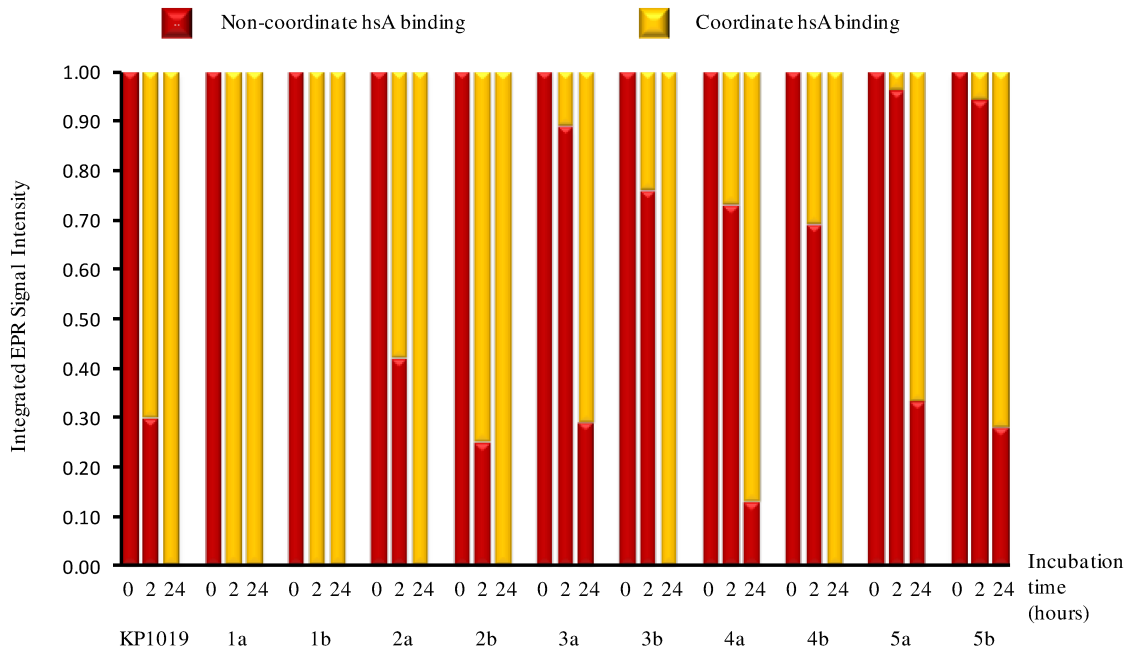


Figure 5-6 Relative fractions of coordinate (yellow) and non-coordinately (red) hsA bound Ru(III) complexes following 0, 2, and 24 hours of incubation at 37 °C, as determined by simulation of the EPR spectra.

Interestingly, the most stabilized non-coordinate interactions are provided by the nitrobenzyl functionalized compounds **5a** and **5b**. Even after 24 hours of incubation, significant signals from non-coordinated species were observed, and the rate of coordination to hsA was lower than any of the other compounds. Spectral simulation determined that the non-coordinate signal for complex **5a** was the largest, accounting for roughly 33% of the observed EPR spectrum (**Figure 5-6**). Comparison with **3a** and **3b** is

particularly relevant since it demonstrates the importance of the nitro groups. Increased stabilization of hydrophobic binding due to electrostatic interactions imparted by this functionality is in agreement with the observation that hsA has a high affinity for anionic species.²⁸⁹ Overall, non-coordinate binding to hsA was more prolonged for the pyridinium compensated (**a**) complexes, as compared to the sodium compensated complexes (**b**), likely reflecting their aqueous insolubility, thereby promoting interactions with the hydrophobic regions of hsA, and inhibiting ligand exchange.

5.3.6. Optical Measurement of hsA Binding

UV-Vis measurements were also used to characterize the interactions of the complexes with hsA. Each compound (200 µM) was incubated with the protein (100 µM) at 37 °C in PBS and monitored for up to 2 hours; 4% DMSO was added to solutions of **3a,b**, **4a,b**, and **5a,b** to aid solubility. The time dependent UV-Vis measurements are shown in Appendix D – **Figures D-37 – D-46** for all of the compounds. During the first 2 hours of incubation, the spectra do not differ significantly from those observed in the absence of the protein, indicating similar species in solution. This is consistent with the EPR observations of the parent compounds of **1a,b – 5a,b** and their aquated derivatives, interacting with hsA via non-coordinate interactions, and may also reflect a fraction of complexes that remain free in solution.

Additional samples were prepared of each complex (600 µM) with hsA (100 µM) to monitor for a weak *d-d* transition at high wavelengths associated with coordinate hsA interactions.^{178,202} Since the EPR experiments demonstrated that such interactions only dominate after prolonged incubation, the samples were measured for up to 24 hours at 37 °C. For each complex, broadening of the spectra and the appearance of a low intensity band at 625 – 657 nm was observed (**Figure 5-7** for **1a**, 24-hour spectra for all complexes shown in Appendix D – **Figures D-47 – D-56**). A similar feature at 575 nm has been reported following incubation of KP1019 with hsA²³⁵ and is also observed for KP1019 under the conditions used in these experiments (Appendix D – **Figure D-60**). This absorbance has been proposed to arise from a *d-d* transition that is specific for hsA coordination to a surface histidine.¹⁷¹ The assignment of this transition for **1a,b – 5a,b**

and the rate that its intensity increases with incubation are in agreement with the EPR results indicating formation of coordinate interactions of the complexes with hsA.

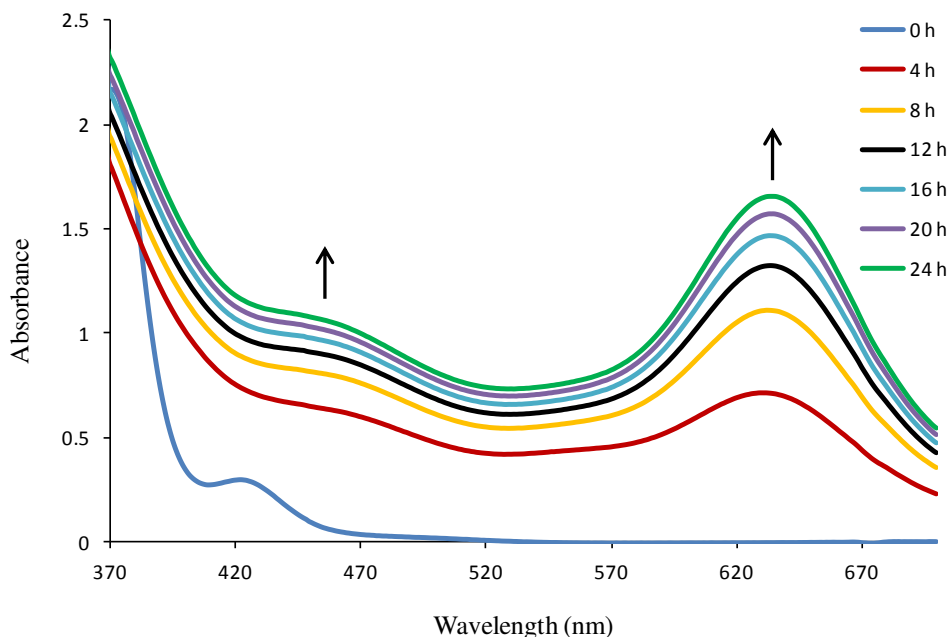


Figure 5-7 UV-Vis spectra for complex **1a** incubated with hsA in PBS buffer for 24 hours at 37 °C.

The observation of ligand-dependent stabilization of non-coordinate interactions with hsA has important implications for drug design. The coordination of KP1019 to hsA has been suggested to potentially impact its observed anticancer activity.¹¹³ As demonstrated here, enhancement of non-coordinate interactions with hydrophobic ligands, possibly with the addition of polarized groups, can inhibit the formation of coordinated species. This design strategy has the potential to increase the concentration of the active species *in vivo*.

As shown in this chapter, non-coordinate interactions with hsA also enhance the solubility of these complexes. This suggests that preparation of the compounds with hsA prior to intravenous administration could help stabilize them in solution while also increasing the concentrations of the active species. In essence, such an approach can be considered as the application of non-coordinate protein conjugates. To test the viability of this approach, the anticancer activity of the new compounds described here was evaluated with and without prior incubation with hsA.

5.3.7. Biological Activity

Anticancer activity screening was performed against the SW480 human colorectal cancer cell line. This cell line was chosen to allow for comparison with previous studies of KP1019 and KP1339.^{136,137,143} Due to limited aqueous solubility, the pyridinium compensated complexes **3a**, **4a**, and **5a** were not tested. However, all the remaining compounds, **1a/b**, **2a/b**, **3b**, **4b**, and **5b** were screened along with KP1019, which was used as a positive control. The maximum concentrations used in testing of the free complexes varied due to differences in solubility.

To study the effect of hsA interactions on the activity of the compounds, two sets of experiments were performed: (i) the compounds were dissolved in cell culture medium with 1% DMSO and then incubated with the SW480 cells for 24 hours, and (ii) the compounds were dissolved in PBS with 1% DMSO and incubated with hsA for 10 minutes, after which the protein-bound fractions were isolated and further prepared as discussed in the experimental section.

A significant consequence of incubating the complexes with hsA was improved solubility. This is an important observation since even clinically successful Kepler-type complexes do not show particularly low IC₅₀ values in comparison to many conventional chemotherapeutics. For example, in our experiments KP1019 was determined to have an IC₅₀ of 150 μM (**Figure 5-8**) and has been reported to be as low as ~35 μM in studies with the SW480 cell line.^{136,137} The *in vivo* activity^{136,137,211} and clinical success¹⁸¹ of this compound and its sodium-compensated analogue, KP1339, are due in part to the very low levels of side effects they exhibit.¹⁰⁷ This allows high concentrations of the compounds to be used during treatments.¹¹⁰ In the studies reported here, the compounds were dissolved in culture media and then added to an equal volume of cells and media, which reduced the testing concentration by a factor of two. Thus, for the highest concentration solutions used in testing, 500 μM, an initial solution with a concentration of 1 mM was required. At this concentration, precipitation was significant for **3b**, **4b**, and **5b** which could only be prepared in concentrations of half this value or less. However, if the complexes were first incubated with hsA then they could all be prepared at the maximum concentration without precipitation. This immediately suggests an advantage

in preparing these types of compounds with hsA for clinical studies by preventing precipitation and allowing for higher concentration treatment solutions.

Screening of the free complexes revealed low activity: **1a,b** had an $IC_{50} \geq 500 \mu M$ with **2a,b** being slightly more active with an $IC_{50} \sim 400 \mu M$, while complexes, **3b**, **4b**, and **5b**, were less active (**Figure 5-8**). However, this is not particularly surprising given that even the clinically successful compounds do not show high cytotoxicity during *in vitro* studies. Furthermore, the design of these compounds targets protein interactions for comparative studies, rather than activity specifically. No significant differences in activity were observed upon changing the cation from pyridinium to sodium for complexes **1** and **2**.

Pre-incubation of the compounds with hsA had differing effects on their activity (**Figure 5-8**). For complexes **1a** and **1b**, no significant change in anticancer activity was observed. By contrast, complexes **2a** and **2b** showed a substantial decrease in activity following incubation with hsA. This observation is consistent with coordination of the complexes to the protein, which reduces their bioavailability. Similarly, when KP1019 was pre-incubated with hsA the activity was low, and no IC_{50} value could be determined. Complex **3b** shows similar activity to the free complex, which can be explained by more stabilized non-coordinate interactions possibly preventing deactivation by coordination. Due to increased solubility in the presence of the protein, a concentration sufficient to reach the IC_{50} ($\sim 500 \mu M$) could be determined. Similarly, for complex **5b**, no significant change in anticancer activity was observed following incubation with hsA, however, with the increased solubility due to protein interactions, the IC_{50} of the complex is almost attainable.

The most significant testing results following pre-incubation with hsA were from complex **4b**. Not only could higher concentrations of the compound be prepared than for the free complex, but a significant increase in anticancer activity was observed. In fact, this preparation provided the most activity of any of the tests with an IC_{50} value of $\sim 150 \mu M$, which is similar to free KP1019 under these conditions. This is particularly impressive given the relative inactivity of the free complex. It seems likely that stabilized

hydrophobic interactions observed for this compound may play a role in its activation, likely through the inhibition of coordination.

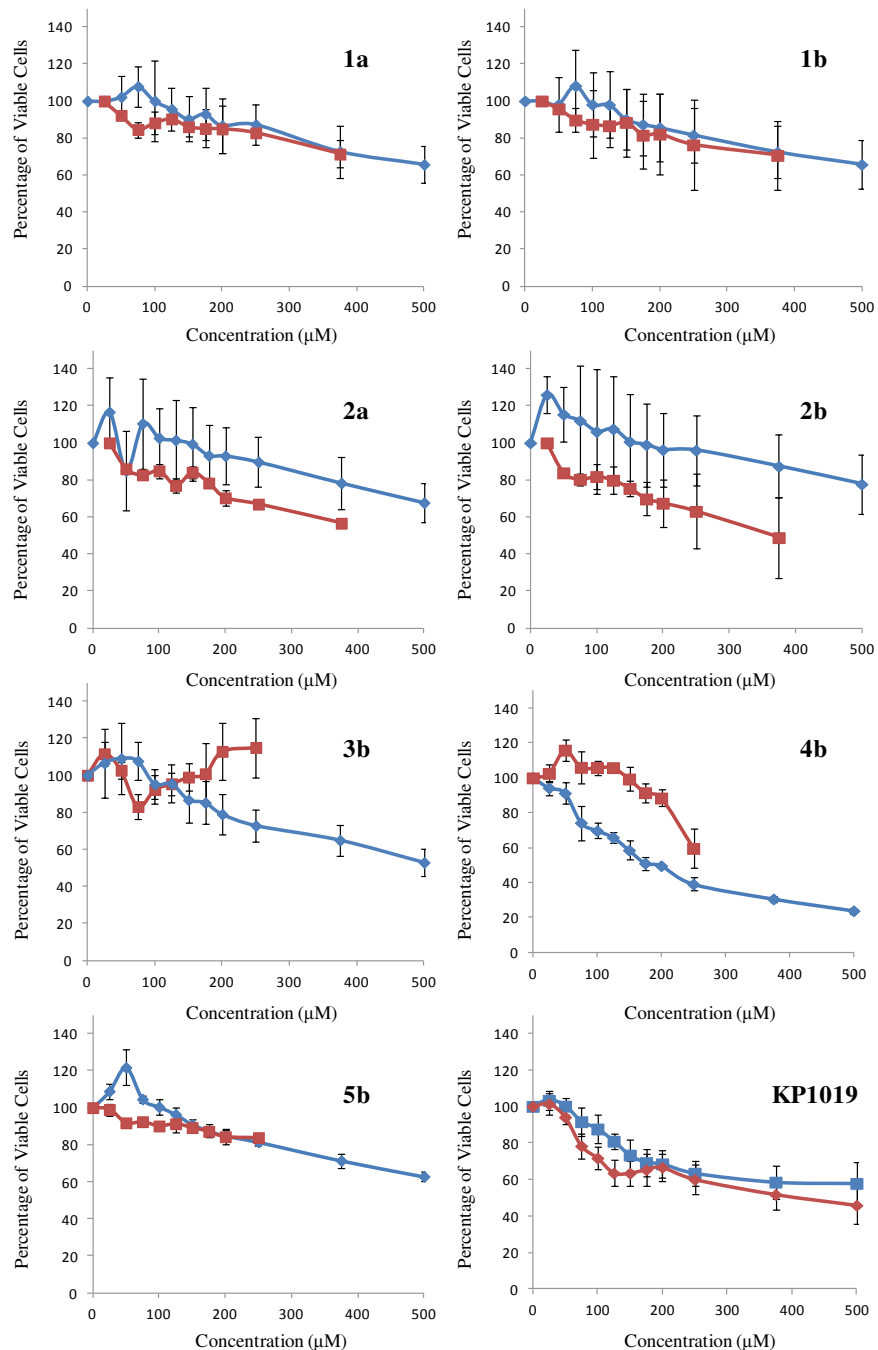


Figure 5-8 MTS assay results for all sodium compensated complexes following incubation with the cells for 24 hours, where: ■ = free complex in solution and ♦ = complex pre-incubated with hsA.

Overall, it is clear that interactions with hsA can significantly influence the anticancer activity of the compounds. While improved solubility is observed for all of the compounds, the effect on activity is quite varied. Greater protein coordination of compounds **2a,b** appears to be correlated with lower overall activity, and the greater stability of non-coordinate binding of **4b** correlates with its higher anticancer activity. However, lack of enhancement of the activity of **5b**, suggests that there may be some other factors involved in activity differences.

5.4. Conclusions

For Kepler-type Ru(III) anticancer complexes, two key aspects of their prodrug behaviour are aqueous ligand exchange, and serum-protein interactions. This can lead to a variety of species in solution which may inhibit or promote their activity. As shown here, hydrophobic interactions with albumin can potentially enhance the concentration of active species *in vitro*. At the most fundamental level, this is from increased solubilization of the complexes in aqueous solution through inhibition of precipitation. This suggests that preparation of these complexes for intravenous therapy with hsA could be advantageous for stabilizing the active species prior to treatment. While DMSO has traditionally been used for this purpose, as shown here, this can potentially influence ligand-exchange processes by coordination of DMSO through replacement of azole ligands. Such processes are expected to reduce the cytotoxicity of the compounds by producing species analogous to NAMI-A-type complexes.

Since the origin of the anticancer activity of Kepler-type complexes remains unknown, the effect of modifications to their axial azole ligands continues to be hard to rationalize. In this chapter it was shown how these ligands can influence interactions with hsA, and how this correlates with the hydrophobic properties of their substituents. While the predicted stabilization of non-coordinate protein interactions generally correlates with the hydrophobic properties of the ligands, closer analysis indicates other factors are also important. The observation that the dibenzyl complex does not provide the anticipated increase in non-coordinate interactions over the benzyl substituted compound suggests that steric factors should also be considered. Furthermore, the remarkable stability of

non-coordinate interactions with the nitrobenzyl compounds suggests that polarizable substituents could increase interactions with the binding sites, possibly through hydrogen bonding.

While the addition of hsA certainly increases the solubility of the compound for the *in vitro* studies, in some cases it also has a distinct effect on the activity of the compounds. Comparison of complexes **2a,b** and **4b** is particularly interesting since the former shows a decrease in activity in the presence of the protein, while the later shows an increase. This indicates that different types of protein interactions, most likely coordinate and non-coordinate respectively, are dominant and can directly influence activity. In the case of **4b** this is particularly notable since it is relatively inactive as the free complex, but, after pre-treatment with hsA, exhibits activity close to that of the clinically successful compounds KP1019 and KP1339. Overall, these results suggest that targeting of non-coordinate interactions with hsA could be an important aspect of the on-going development of Kepler-type Ru(III) anticancer complexes.

6. Using *in vitro* EPR to Probe the Mechanism of Action of Ruthenium(III) Anticancer Agents.

6.1. Introduction

Whole-cell EPR has been used in a number of studies to characterize endogenous metal ions and radical species.^{290,291} However, applications of this technique to the cellular uptake and intracellular speciation of exogenous metal species are comparatively rare. Previous reports have demonstrated that Cu(II)²⁹²⁻²⁹⁶, Mn(II)^{297,298}, V(IV)²⁹⁹, Fe(III)³⁰⁰, and Cr(III)³⁰¹ are amenable to such studies. However, the studies reported herein are the first EPR measurements of intracellular Ru(III). The main barrier to the application of EPR to intracellular metal-ion speciation is the fundamental detection limit of the technique.³⁰² This is particularly challenging in the case of paramagnetic metal ions, as compared to radicals, because the broad spectra observed disperse the total signal intensity across wide field ranges. As described below, the lower limit of detectability for Ru(III) in the EPR experiments described here was found to be ~75 µM for KP1019 and ~50 µM for NAMI-A. This meant that it was possible to get acceptable signal-to-noise from cells incubated with Ru(III) complexes at concentrations of 1 mM. It should be noted that the experiments reported in this chapter were conducted using standard X-band EPR equipment, and thus this approach has potential further application in the field of Ru(III)-based drug candidates.

Previous studies using other analytical techniques have reported on the cell-uptake and *in-cellulo* speciation of NAMI-A and KP1019. Inductively coupled plasma mass spectrometry (ICP-MS) has proven particularly valuable for determining the overall uptake of both compounds in human cancer cells^{143,179,186,303} and the eukaryotic yeast model *Saccharomyces cerevisiae*.³⁰⁴ When coupled with size-exclusion chromatography (SEC) this technique has also provided insight into sub-cellular localization in the cytosol, particulate, and nuclear fractions.^{143,303} Atomic absorption spectroscopy (AAS)

has also been used to quantify cellular uptake and accumulation of ruthenium from NAMI-A and KP1019 in human cancer cells.^{74,175,176,305} Despite these and other studies,⁷⁴ the mechanisms of Ru(III) anticancer complexes remain poorly understood, providing motivation for new analytical approaches to understand the origin of their activity. The whole-cell EPR approach described here provides information that is complementary to other analytical techniques. While AAS and ICP-MS provide accurate measurements of total concentration,³⁰⁶ and with coupling to separation techniques such as SEC can probe the interactions of ruthenium with specific cellular fractions, they cannot provide the details of the speciation of the complexes. Although EPR does not have the sensitivity of these techniques, it can specifically detect the Ru(III) oxidation state and characterize the ligand environment. As shown in this chapter, these abilities enabled specific types of interactions with cell components to be characterized, providing insight into the different *in vivo* behaviour of the Ru(III) anticancer complexes.

6.2. Experimental

6.2.1. Cell Growth and Isolation of Cell Fractions

Saccharomyces cerevisiae cells were grown using YED (Yeast extract dextrose, pH 5.0) liquid medium for 16 hours at 30 °C (220 rpm). Cell density was determined using optical density measurements ($OD_{600} = 0.1$, 1×10^7 cells/mL). The isolation of individual cellular components was performed according to published procedures,³⁰⁷ as outlined briefly below.

Cell Wall, Cytoplasmic Fraction, and Nuclear Fraction Isolation. Published procedures for cell lysis were applied, as follows.³⁰⁷ Liquid cell cultures were pelleted and re-suspended in acetate buffer (50 mM, pH 5.0) with “complete protease inhibitor” (Sigma) (25 µL/mL). Cells were lysed by addition of acid-washed glass beads (Sigma) to the cell suspension (1:2), followed by agitation using a bench-top vortex mixer for brief intervals (30 sec), with intermediate cooling on ice (1 minute). This agitation process was repeated 6 times. The supernatant broken-cell suspension was isolated from the beads then centrifuged (3000 g, 10 min, 4 °C) to give the cell wall fraction as a pellet; the

supernatant was saved, and further centrifuged (14000 g, 5 min) to give the nuclear fraction as a pellet, while the supernatant contained the cytoplasmic fraction. This procedure for the isolation of the cytoplasmic and nuclear fractions is in line with a previous report.¹⁴³ Further purification of the cell wall was achieved through multiple washing steps using ethanol, a 1:1 chloroform/methanol solution, a 1:1 ethanol/ether solution and one final rinse with distilled water. Final rinsing was performed using Tris-HCl buffer (10 mM, pH 8). The desired cell wall product was stored at -20 °C until use.

Isolation of the Mitochondria.. Following published procedures,³⁰⁷ liquid cell cultures were pelleted and re-suspended in lysis buffer (0.6 M sorbitol, 1 mM EDTA, 10 mM Tris-HCl, pH 7.4) with “complete protease inhibitor” (25 µL/mL) and lysed as described above. The resulting cell lysate was centrifuged (2500 g, 10 min, 5 °C), to give a pellet which was discarded. Subsequently the supernatant was centrifuged (15000 g, 10 min, 5 °C) to pellet the mitochondria.

6.2.2. Preparation of EPR Samples

EPR with Individual Cellular Components. Each complex was dissolved (1 mM) in a phosphate buffered saline (PBS) solution containing: 137 mM NaCl, 2.7 mM KCl, 10 mM Na₂HPO₄, and 2 mM KH₂PO₄, pH 7.4. Individual cellular components were added and the resulting solutions were incubated at 30 °C with 4 mL aliquots taken after the following incubation time points: 0 minutes, 30 minutes, 2 hours, and 24 hours. Isolation of ruthenium species bound to cell components was achieved using centrifugal ultrafiltration (10 kDa cut-off columns for the cytoplasmic component and 100 kDa cut-off columns for the remaining components) until a volume below 200 µL was attained (3000 g, 8 °C, 20 min). The filtered product was mixed with 30% glycerol and diluted to a final volume of 300 µL with PBS, then transferred to an EPR tube and immediately frozen in liquid nitrogen.

Whole-cell EPR. Each complex was dissolved (1 mM) in PBS, pH 7.4. Yeast cells were added from a liquid culture, affording a final cell concentration of 10⁶ cells/mL. The resulting solution was incubated at 30 °C with 4 mL aliquots taken after the following incubation time points: 0 minutes, 30 minutes, 1, 2, 4, 6, 8, 12, and 24

hours. Isolation of cell-bound species was achieved using centrifugal ultrafiltration (100 kDa cut-off columns) until a volume below 200 μ L was attained (3000 g, 8 °C, 20 min). The filtered product was diluted to a final volume of 300 μ L with PBS and mixed with 30% glycerol, then transferred to an EPR tube and immediately frozen in liquid nitrogen.

6.2.3. EPR Measurements and Simulation

See section 2.2.4.

6.2.4. EPR Experimental Conditions

The cellular component, whole cell, and calibration curve spectra were collected using the same experimental parameters to facilitate comparison between data sets. The conditions used were: frequency = 9.378 GHz, microwave power = 2.0 mW, time constant = 40.96 ms, modulation amplitude = 6 Gauss, average of fifteen 2-minute scans, measurement temperature = 20 K. All hsA spectra were collected using the same experimental conditions, with only five scans performed.

6.3. Results and Discussion

6.3.1. EPR of Interactions with Isolated Cellular Components

To gain insight into the cellular targets of NAMI-A, KP1019, and the ruthenium species involved, the complexes were incubated with isolated components of *S. cerevisiae* cells and studied by EPR. The chosen cellular components were: (i) cell walls, (ii) mitochondria, (iii) the cytoplasmic protein fraction, and (iv) the nuclear fraction. In each case, the samples were incubated at 30 °C with the complexes for 0 minutes, 30 minutes, 2 hours and 24 hours.

NAMI-A. After incubation with each cellular fraction for 30 minutes, EPR measurements of NAMI-A revealed strong signals from two distinct species. The more intense of these signals is predominant at the shortest incubation times and has a uniaxial g tensor with $g_{\perp} = 2.47$ and $g_{\parallel} = 1.72$ and linewidths of $LW_{\perp} = 105$ and $LW_{\parallel} = 180$ Gauss (**Figure 6-1**). These spectral parameters correspond to the reported values (see Chapter 3)

for the parent complex (*NAMI-A*).²⁶⁴ The second species also exhibits a uniaxial spectrum ($g_{\perp} = 2.32$, $g_{\parallel} = 1.87$, $LW_{\perp} = 75$, $LW_{\parallel} = 60$ Gauss) (**Figure 6-1**), which has been identified previously as the mono-aquated derivative (*NAMI-A-H₂O*) formed by the exchange of the axial DMSO ligand of NAMI-A for water.²⁶⁴ Since large molecular-weight components of each cellular fraction sample were isolated by ultrafiltration, as described in the experimental section, the possibility of free complexes is excluded. Instead, the presence of both of these signals demonstrates that each complex binds to components of the yeast cells without undergoing ligand exchange. Such non-coordinate interactions have been determined previously in Chapter 3, where EPR was used to monitor NAMI-A following incubation with human serum albumin.²⁶⁴ In this earlier report the protein binding was attributed to interactions of the axial imidazole ligand of the complex with hydrophobic regions of hsA. Related EPR studies of a series of NAMI-A analogues having pyridine based axial ligands with varying hydrophobicity support this conclusion (Chapter 4).²⁷⁷ In this case, increased stability of non-coordinate interaction with hsA was correlated with the hydrophobicity of the ligand, demonstrating that this is an important interaction for NAMI-A *in vivo*. It is important to note that these EPR studies did not provide specific insight into the exact sites of hydrophobic interactions with hsA. Although hsA has specific hydrophobic binding domains,^{81,85,308} non-specific interactions are commonly observed for this protein.⁷⁷ Consequently, the observation of non-coordinate interactions with the yeast cell components is not unexpected.

After longer incubation times the signal intensity from each cellular component is significantly reduced and the EPR spectra of the non-coordinated species are replaced by new signals (**Figure 6-1**, and Appendix E – **Figures E-5, E-7, E-9, and E-11**). Similar behaviour has been reported for the interactions of NAMI-A with serum proteins.²⁶⁴ Taking first the isolated cell wall fragments, two new signals become increasingly dominant with longer incubation: *NAMI-A-Cell-Wall-1*, with $g = [2.45, 2.21, 1.10]$ and linewidths = [300, 80, 200] Gauss and *NAMI-A-Cell-Wall-2*, with $g = [2.40, 2.18, 1.80]$ and linewidths = [350, 250, 300] Gauss (**Figure 6-1(i)**). The distinctive g values and linewidths of these species are characteristic of coordinate interactions with the isolated cell wall fragments. *NAMI-A-Cell-Wall-1* forms more rapidly and dominates the EPR

spectrum after two hours of incubation (Appendix E – **Figure E-5**). The second signal from cell-wall coordination, *NAMI-A-Cell-Wall-2*, becomes increasingly dominant at longer incubation times, and after 24 hours is the only signal present in the EPR spectrum. It should be noted that in the simulation of *NAMI-A-Cell-Wall-1* the g_3 value was not observed experimentally. This was either due to line broadening from g strain effects and/or poor signal-to-noise. In this instance, g_3 was simulated outside the range of the spectrum. This phenomenon was further observed in the simulation of other cell-bound Ru(III) species.

Comparison of the spectra from the cell wall fragments with those from the other fractions after longer incubation times reveals spectra with features that are broadly similar but are readily revealed to be distinct by spectral simulation. In each case, longer incubation leads to a reduction in signal intensity and the observation of new species with broad spectral features. For example, exposure of NAMI-A to the mitochondrial fraction for 120 minutes at 30 °C results in EPR signals from a species, *NAMI-A-Mitochondria-1*, with $g = [2.40, 2.21, 1.10]$ and linewidths = [400, 70, 200] Gauss, while 24 hours of incubation produces a broad rhombic signal, *NAMI-A-Mitochondria-2*, with $g = [2.40, 2.22, 1.75]$ and linewidths = [200, 175, 350] Gauss (**Figure 6-1(ii)**). Similar species with comparable rates of formation are also observed for the isolated fractions, *NAMI-A-Nuclear-Fraction-1*, $g = [2.40, 2.22, 1.10]$, linewidths = [400, 100, 200] Gauss, and *NAMI-A-Nuclear-Fraction-2*, with $g = [2.48, 2.30, 1.88]$ and linewidths = [250, 150, 350] Gauss (**Figure 6-1(iv)**), while only one species is observed for the isolated cytosolic protein fraction, *NAMI-A-Cyto.-Proteins*, $g = [2.42, 2.25, 1.84]$, linewidths = [200, 175, 350] Gauss (**Figure 6-1(iii)**).

The broad signals observed in each fraction are reminiscent, though distinct from, EPR signals previously reported from studies of NAMI-A coordinated to hsA (Chapter 3).²⁶⁴ In this earlier study longer incubation times with hsA produced spectra from two species: *NAMI-A-hsA-1*, $g_{\perp} = 2.43$, $g_{\parallel} = 1.76$, $LW_{\perp} = 300$, $LW_{\parallel} = 300$ G, and *NAMI-A-hsA-2*, with $g = [2.54, 2.26, 1.76]$ and linewidths = [450, 175, 350] Gauss. These signals were assigned to NAMI-A coordinated to the protein via histidine imidazoles, consistent with previous reports that have also suggested binding of the complex via coordinate

interactions.^{57,122,175} Although the complete ligand set of these species could not be identified from the EPR spectra, the differences in g-tensor symmetry and linewidth parameters were attributed to histidine imidazole coordination at either the axial or equatorial positions of NAMI-A following DMSO or Cl⁻ exchange respectively.²⁶⁴

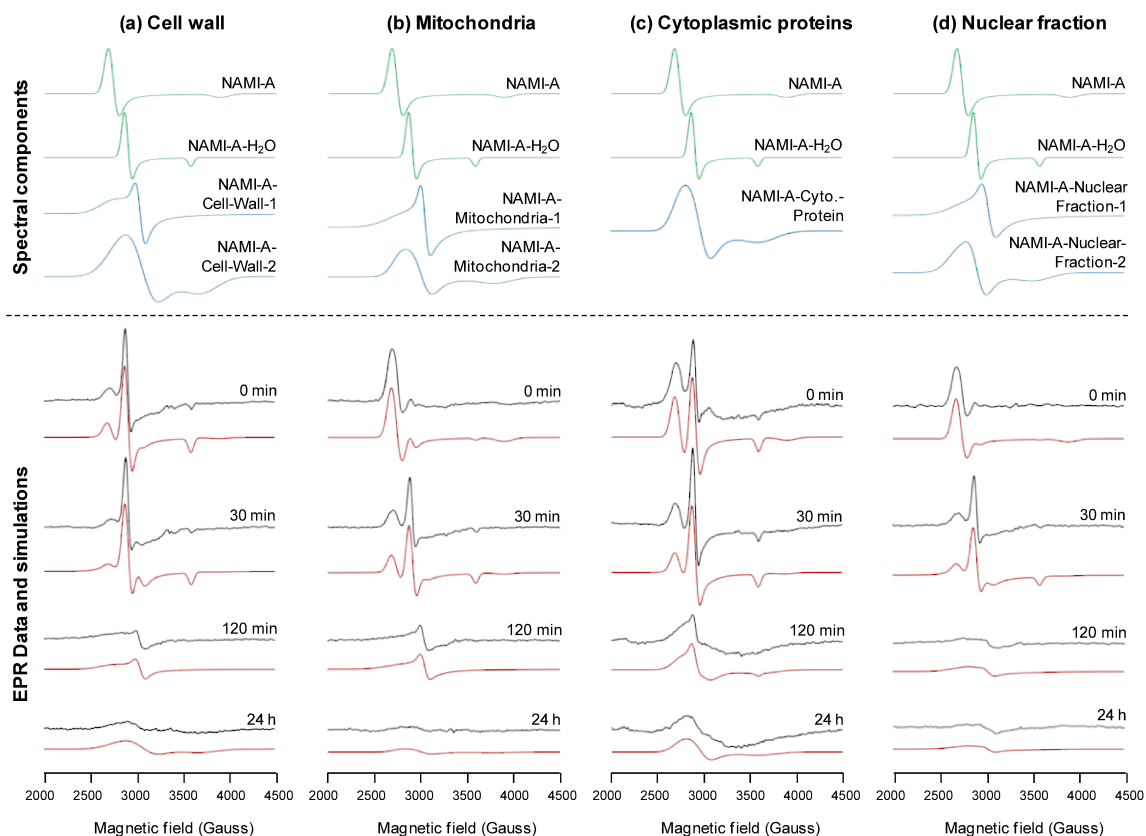


Figure 6-1 Experimental EPR and spectral simulations for NAMI-A incubated with isolated *S. Cerevisiae* cell components: (a) cell walls, (b) mitochondria, (c) cytoplasmic protein fraction, and (d) nuclear fraction. Upper panels: individual simulated spectral components; g values and linewidths in main text and Appendix E – **Table E-1**. Lower panels: experimental EPR spectra and simulations constructed from weighted sums of spectral components. For EPR experimental conditions see 6.2.4.

Although a casual examination of the experimental spectra from the coordinated species might suggest that they are all quite similar, there are distinct differences in the g values and linewidths that allow discrimination by spectral simulation. As shown in the upper panels of **Figure 6-1**, deconvolution of the spectra at longer incubation times

indicates spectral components for coordinated species that are distinct between the different cellular fractions. In particular, comparison of g values indicates that the cell wall component may have somewhat different coordinate interactions with NAMI-A versus the other components. Differences in the linewidths of the other species are indicative of different secondary coordination spheres leading to differences in g-strain effects.²¹⁹ Such linewidth differences are potentially useful indicators of different cellular environments when the first coordination sphere is unchanged or very similar.

KP1019. At incubation times up to 30 minutes, EPR spectra of KP1019 show evidence for the formation of non-coordinate interactions with each of the cellular components. These species can be identified by a characteristic signal from the unexchanged complex which is comprised of overlapping axial (*KP1019-Uniaxial*, $g_{\perp} = 2.64$, $g_{\parallel} = 1.20$, $LW_{\perp} = 120$, $LW_{\parallel} = 500$ Gauss) and rhombic (*KP1019-Rhombic*, $g = [2.94, 2.31, 0.95]$, linewidths = [100, 200, 600] Gauss) signals as previously reported in Chapter 2.²⁴⁶ In these studies of KP1019, it was reported that the complex rapidly forms non-coordinate interactions with human serum albumin, but does not form similar interactions with human serum transferrin.²⁴⁶ These observations indicate that KP1019 interacts specifically with the hydrophobic binding domains of hsA. This has been corroborated by recent fluorescence studies of KP1019 that show the complex binds within the hydrophobic binding subdomains of hsA,^{189,235} Sudlow's sites I and II.^{81,85} The EPR signals from KP1019 due to non-coordinate interactions with each cell component are significantly weaker than those from comparable NAMI-A species. This is consistent with a lower proclivity of KP1019 to form non-specific hydrophobic interactions and indicates a fundamental difference in the cellular interactions of each complex.

KP1019 shows the formation of coordinate interactions with the cell fractions even at short incubation times (**Figure 6-2**, and Appendix E – **Figures E-6, E-8, E-10, and E-12**). This indicates that protein binding via ligand exchange occurs more rapidly for KP1019 than for NAMI-A, possibly due to reduced competition from non-coordinate interactions. Similar to NAMI-A, in the case of KP1019 two coordinated species are observed. For the cell wall fraction (**Figure 6-2(i)**), the first species (*KP1019-Cell-Wall-1*, $g = [2.50, 2.30, 1.80]$, linewidths = [300, 200, 250] Gauss) dominates after 30 minutes

of incubation, and is gradually replaced by the second coordinated species (*KP1019-Cell-Wall-2*, $g = [2.40, 2.20, 1.88]$, linewidths = [250, 100, 350] Gauss) which persists as the only species observed after 24 hours.

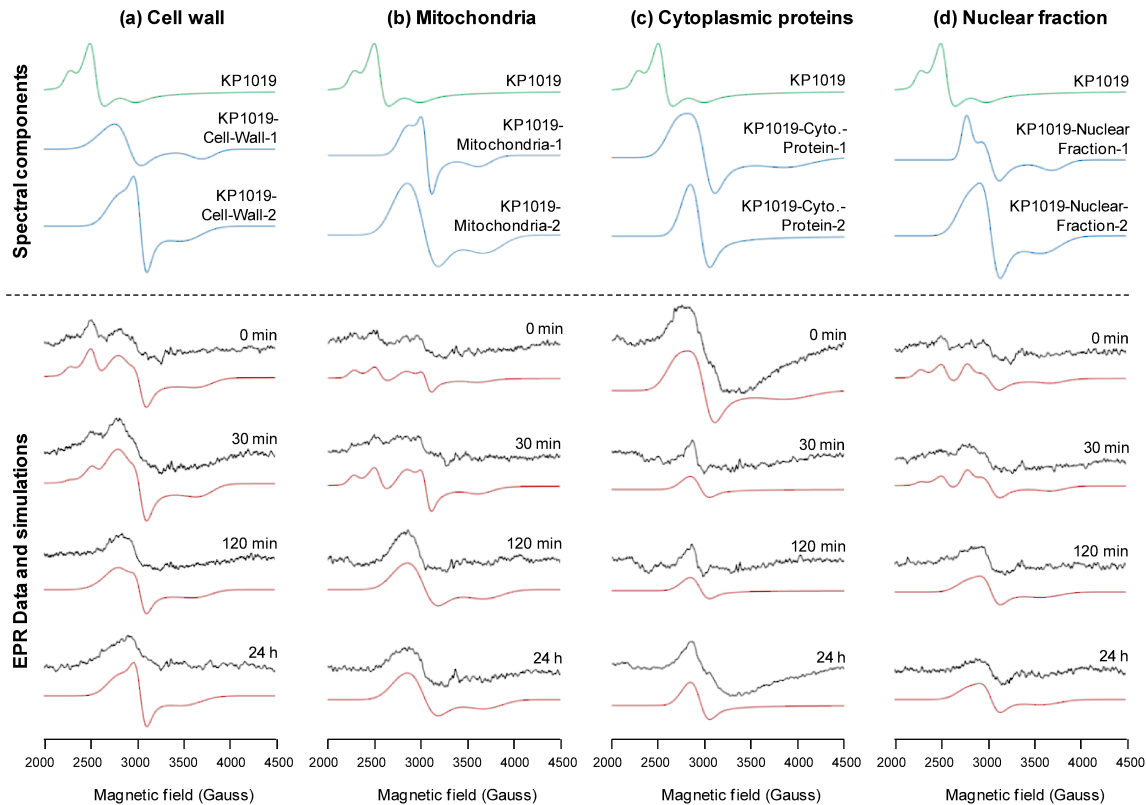


Figure 6-2 Experimental EPR and spectral simulations for KP1019 incubated with isolated *S. Cerevisiae* cell components: (a) cell walls, (b) mitochondria, (c) cytoplasmic protein fraction, and (d) nuclear fraction. Upper panels: individual simulated spectral components; g values and linewidths in main text and Appendix E – **Table E-1**. Lower panels: experimental EPR spectra and simulations constructed from weighted sums of spectral components. For EPR experimental conditions see 6.2.4.

Similar phenomena are observed for the mitochondria (**Figure 6-2(ii)**) where the first coordinated species, (*KP1019-Mitochondria-1*, $g = [2.36, 2.19, 1.84]$, linewidths = [175, 85, 250] Gauss), is replaced by a second coordinated species (*KP1019-Mitochondria-2*, $g = [2.40, 2.20, 1.80]$, linewidths = [275, 225, 350]), and also with the isolated cytoplasmic proteins (**Figure 6-2(iii)**) (*KP1019-Cyto.-Proteins-1*, $g = [2.47, 2.23, 1.80]$, linewidths = [250, 175, 500] Gauss and *KP1019-Cyto.-Proteins-2*, $g = [2.38, 2.27,$

1.10], linewidths = [200, 150, 250] Gauss, and the nuclear fraction (**Figure 6-2(iv)**) (*KP1019-Nuclear-Fraction-1*, $g = [2.41, 2.20, 1.80]$, linewidths = [100, 150, 250] Gauss and *KP1019-Nuclear-Fraction-2*, $g = [2.40, 2.20, 1.84]$, linewidths = [250, 150, 350] Gauss). In each case the rate of formation of these two coordinate species is relatively similar.

In the earlier EPR study of KP1019 (Chapter 2), coordination of the complex to both albumin and transferrin were reported.²⁴⁶ The spectra of the coordinated species were simulated with uniaxial symmetry using the same g values: *KP1019-hsA/hsTf*, $g_{\perp} = 2.32$, $g_{\parallel} = 1.84$, $LW_{\perp} = 90$, $LW_{\parallel} = 80$ Gauss, and assigned to histidine coordination. Comparison with the spectral parameters of the coordinate species reported here reveals that $(g_1 + g_2) / 2 \approx g_{\perp}$ and $g_3 \approx g_{\parallel}$, indicating coordination environments similar to that observed with the proteins. In contrast to NAMI-A, for KP1019, no aquated derivatives were observed to coordinate to any of the cellular fractions, an observation that is in line with the previous EPR studies of protein interactions in Chapter 2.²⁴⁶

Although for both NAMI-A and KP1019 the signals observed following incubation with the individual cellular components are assigned to a single species, this is not likely the case. The signals observed are likely from a heterogeneous mixture of species, all with similar ligand environments which in turn result in similar spectral parameters. The summation of these individual species is what gives rise to the observed EPR transitions, where differences observed between different fractions likely reflect the changes in the concentration or amount of the species present.

6.3.2. EPR of Whole Cell Interactions

The cellular speciation of NAMI-A and KP1019 was probed with whole cells of *S. cerevisiae*. Each complex was incubated with a liquid culture of yeast cells, and samples for EPR analysis were taken after selected incubation periods. Additional measurements were also performed on the cells without exposure to the Ru(III) complexes (Appendix E – **Figure E-19**). No signals were observed, therefore no interference with any observed Ru(III) EPR signals is expected.

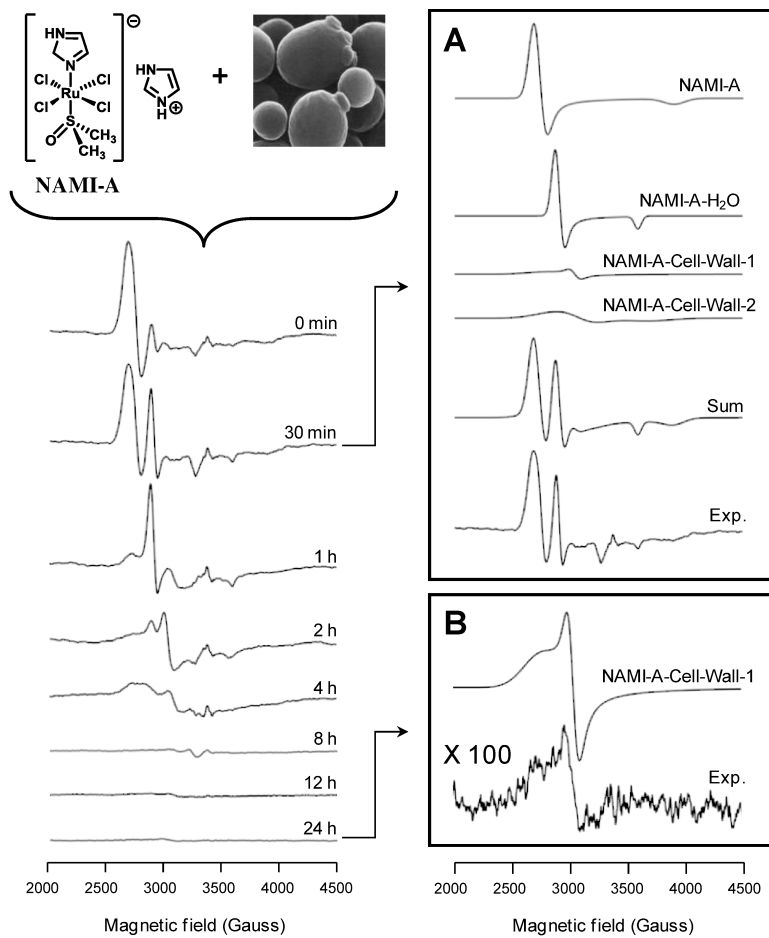


Figure 6-3 EPR spectra and simulations of NAMI-A incubated with whole cells of *S. Cerevisiae*. Left panel: Spectra after different incubation time periods. **A:** Simulation of the EPR spectrum after 2 hours of incubation. **B:** Simulation of the EPR spectrum after 24 hours of incubation. For EPR experimental conditions see 6.2.4.

NAMI-A. In the case of NAMI-A, minimal exposure time to whole yeast cells (“0 min” in **Figure 6-3**) produced uniaxial EPR signals with g values and linewidths for both the parent complex (*NAMI-A*) and its mono-aquated derivative (*NAMI-A-H₂O*) (**Figure 6-3**).²⁶⁴ Similar observations of NAMI-A incubated with the individual cellular components, described above, demonstrate that these species are from non-coordinate interactions with the yeast cells. Additionally, further incubation led to a reduction in the overall signal intensity becoming particularly apparent after 2 hours. At this time point, the spectra are also increasingly dominated by contributions from broader spectral

components, consistent with the formation of coordinate interactions with *S. cerevisiae* cells (**Figure 6-3**).

To gain detailed insight into the origin of the broad signals, the spectra were compared to those from each of the individual cellular components. As shown in panels **A** and **B** of **Figure 6-3** and Appendix E – **Figures E-1** and **E-2**, all the EPR spectra at incubation time points up to 24 hours can be simulated accurately using the parameters determined for Ru(III) species coordinated to cell walls, *NAMI-A-Cell-Wall-1* and *NAMI-A-Cell-Wall-2*. After 24 hours the only remaining signal was from *NAMI-A-Cell-Wall-1*, suggesting differences in the stability of the two cell-wall bound species. These results are consistent with a previous report using X-ray fluorescence which identified NAMI-A as binding predominantly with cellular membranes.¹¹² Recent studies of NAMI-A incubated with whole-cells of *S. cerevisiae* using ICP-MS also report cellular accumulation of Ru.³⁰⁴

KP1019. EPR measurements of the interactions of KP1019 with *S. cerevisiae* cells show some distinct differences from NAMI-A. Particularly noticeable are lower overall signal intensities, particularly at short incubation times (**Figure 6-4**). At time points of 4 hours or less, significant signals are observed from the parent complex (**Figure 6-4**, Panel **A**). As described previously, this signal is comprised of distinct uniaxial and rhombic components.²⁴⁶ As with NAMI-A, detection of the parent complex demonstrates that KP1019 initially interacts with cell components without undergoing ligand exchange. Consequently, observation of these signals demonstrates non-coordinate interactions with components of the yeast cells; however, the lower signal intensity suggests that these interactions are less prevalent for KP1019 than for NAMI-A. As described earlier, the indazole ligands of KP1019 promote rapid formation of hydrophobic interactions with hSA and thus likely form interactions with hydrophobic environments of the *S. cerevisiae* cells.^{189,235}

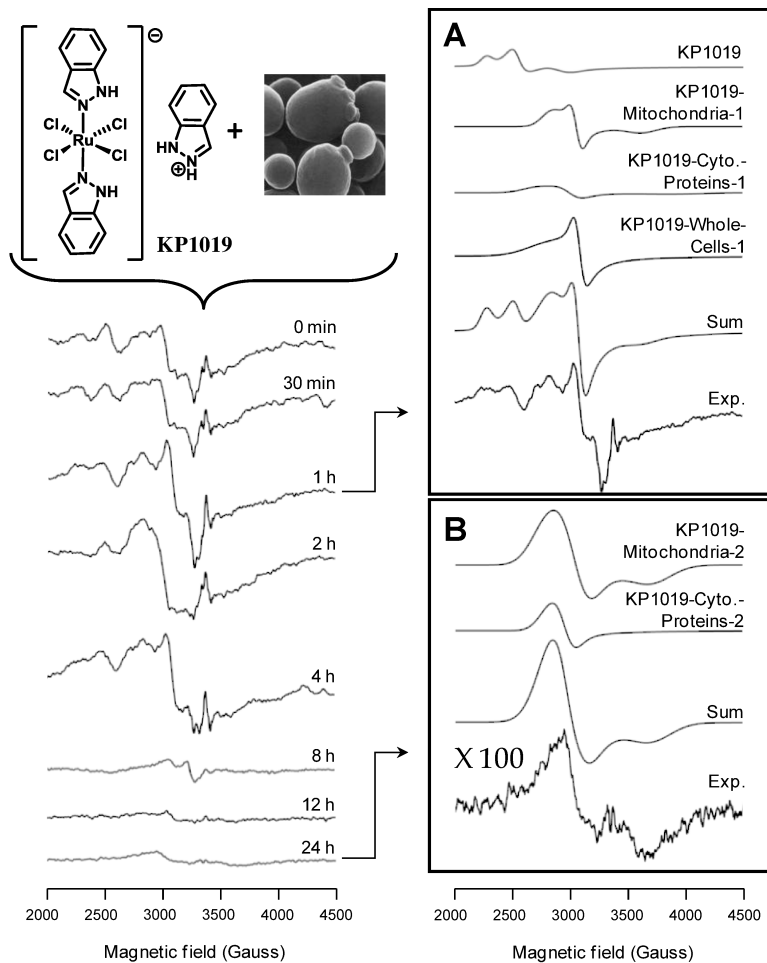


Figure 6-4 EPR spectra and simulations of KP1019 incubated with whole cells of *S. Cerevisiae*. Left panel: Spectra after different incubation time periods. **A:** Simulation of the EPR spectrum after 30 minutes of incubation. **B:** Simulation of the EPR spectrum after 24 hours of incubation. For EPR experimental conditions see 6.2.4.

In addition to signals from the non-coordinate species, broader spectral components are visible at each incubation time (**Figure 6-4**). As for NAMI-A, simulation of these signals was attempted using the spectral parameters for Ru(III) species coordinated to isolated cellular components. This procedure suggests contributions from mitochondrial and cytoplasmic protein interactions are dominant. Key features in the EPR spectra were simulated using the parameters determined previously for *KP1019-Mitochondria-1* and *KP1019-Cyt.-Proteins-1* (**Figure 6-4**, Panel A, and Appendix E – **Figures E-3** and **E-4**) at shorter incubation times, and *KP1019-Mitochondria-2* and

KP1019-Cyt.-Proteins-2 at later time points (**Figure 6-4, Panel B**). In addition to these signals, a third species was identified that was not seen in the individual cell component studies, *KP1019-Whole-Cells-1*, $g = [2.40, 2.18, 1.10]$, linewidths = [400, 80, 500] Gauss. This additional species has g values and linewidths that are most similar to *KP1019-Cyt.-Proteins-1*, suggesting it results from a similar ligand exchange process. Since the new species is only observed in the presence of whole yeast cells, it is likely that the signal arises from a non-isolated cellular component.

After 24 hours the only signals remaining are from *KP1019-Mitochondria-2* and *KP1019-Cyt.-Proteins-2*, suggesting that coordinate interactions with the cytosol proteins and mitochondria are the ultimate fates of a significant proportion of the complexes. These observations are in line with previous reports using ESI-MS,⁷⁴ ICP-MS,³⁰³ and X-ray absorption and fluorescence,^{112,188,195} which identify both cellular components as potential targets for KP1019.

6.3.3. Temperature Dependence

To determine the impact of temperature on the interaction of the complexes with the yeast cells, whole-cell EPR experiments were also performed with incubation of the samples at 4 °C, rather than 30 °C. The lower temperature is expected to allow molecules only to gain entry to cells of *S. cerevisiae* via passive diffusion, while any cell-mediated means of transportation would be greatly reduced.^{305,309} For KP1019, the EPR spectra from incubation at 4 °C, although similar in appearance to those observed following incubation at 30 °C, have significantly reduced intensity (Appendix E – **Figure E-18**). This demonstrates that lower temperatures reduce the rate of transportation of KP1019 into the yeast cells, suggesting both passive diffusion and an active intracellular transportation pathway, which is consistent with previous studies.^{188,195}

The spectra from NAMI-A incubated with whole yeast cells at 4 °C were quite different from those observed at higher temperature. Even after 24 hours of incubation, only signals from non-coordinated species were observed (Appendix E – **Figure E-17**), with no evidence for the formation of any coordinated species. This suggests that the ligand exchange reactions for NAMI-A are affected by the decrease in temperature.

Previous studies have shown that the use of low temperatures dramatically reduces the uptake of NAMI-A by tumour cells, reducing the observed antimetastatic activity.^{125,305}

6.3.4. Concentrations of Detected Ru(III) Species

The detection limit of EPR can be in the nanomolar regime under ideal conditions for measurements of radicals in liquid solution.^{310,311} Sensitivity, however, is significantly less for paramagnetic metal centres in frozen solutions or powders due to the effects of broad lines and g dispersion.³¹¹⁻³¹³ To determine the detection limits for NAMI-A and KP1019, and to estimate their concentrations in the whole-cell experiments, measurements were performed on standardized samples with a concentration range of 10 to 500 µM. A calibration curve was constructed for each complex using the integrated intensities determined from spectral simulation; these data and the original EPR signals at each concentration are shown in Appendix E – **Figures E-11 and E-12** for NAMI-A, and **Figures E-13 and E-14** for KP1019. From these measurements, it was determined that the detection limit for Ru(III) using the experimental parameters defined in section 6.2.4 was approximately 50 µM for NAMI-A and 75 µM for KP1019.

The calibration curves were also used to determine the approximate concentrations of the Ru(III) complexes associated with cells of *S. cerevisiae*, after incubation in 1 mM solutions of each complex. For NAMI-A, the maximum concentration was observed at the earliest incubation time point. Here, the total concentration of the non-coordinated cell-bound complex was found to be ~400 µM. As discussed previously, these signals are gradually converted with increasing incubation to coordinate interactions with the yeast cell walls. The total concentration for the coordinated species is estimated to reach a maximum of ~100 µM after 2 hours, although this calculation was difficult due to the different line shapes of these species. For KP1019, the concentration of the parent complex was found to be ~300 µM at the earliest time point. These signals were replaced over time by coordinate interactions with cellular components, with an estimated maximum concentration of ~200 µM after 4 hours of incubation.

Overall, these results demonstrate that a significant proportion of each complex associates with the yeast cells. Furthermore, the EPR data show that the Ru(III) oxidation state is prevalent, particularly at early incubation times, and persistent, as shown by measurable signals after several hours.

6.4. Conclusions

These studies sought to evaluate EPR as a technique for probing the intracellular interactions of Ru(III) anticancer compounds, and potentially other paramagnetic metal-based therapeutics. Most importantly, it was demonstrated that concentrations sufficient for detection are achievable. In these studies the yeast cells were incubated in 1 mM solutions of each complex, concentrations that are low enough to be relevant to treatment conditions. The limit of detectability for Ru(III) using a relatively standard EPR experimental set-up suggests this approach could be applicable to cancer cells and tumour tissues. It is worth noting that the broad lines and wide g value dispersion of many of the Ru(III) complexes significantly increase the lower level of detection, as compared to Cu(II) complexes, for example. However, as shown here, this has not prevented the measurement of signals from Ru(III) interacting directly with cells of *S. cerevisiae*.

Clearly, although the sensitivity of the EPR method is sufficient for these types of experiments, it is significantly lower than techniques such as ICP-MS and AAS for the detection of free and biomolecule-bound complexes. As demonstrated here, however, EPR studies can potentially provide complementary information. As shown above, in each case signals from Ru(III) species were observed. This demonstrates that a significant portion of both NAMI-A and KP1019 remain unaffected by endogenous reducing agents. Furthermore, EPR measurements provide insight into the coordination environment of the complexes. Importantly, this demonstrates the difference between complexes interacting with biomolecules through non-coordinate interactions and via direct coordination to biological ligands.

The EPR approach to probing intracellular speciation of Ru(III) species does involve some challenges. The presence of overlapping signals from several species, particularly in the whole-cell samples, can make data interpretation difficult.

Furthermore, spectral differences between similar species can be hard to determine by the untrained eye. Each of these issues can only be addressed through simulation of experimental signals, which can be a time-consuming process. However, as demonstrated here, the reward for this effort can be valuable information on the behaviour of Ru(III) complexes in cellular environments, providing insight into their speciation and activity.

7. Probing the Mechanism of Action of Ru(III) Anticancer Agents Using ENDOR Spectroscopy

7.1. Introduction

As shown in Chapters 2, 3, 4, 5, and 6, EPR can be used to monitor the aqueous speciation and protein binding behaviour of Ru(III) anticancer complexes. However, due to the broad linewidths typically observed in Ru(III) EPR signals, and the spectral overlap in the “powder-pattern” spectra from the frozen solutions used in these studies, hyperfine couplings between the Ru(III) centre and neighbouring nuclei cannot be detected. These hyperfine interactions can potentially provide atomic-level details of the coordination environment around the paramagnetic metal centre. This information can be recovered using electron nuclear double resonance (ENDOR) spectroscopy, which can resolve single-crystal-like hyperfine structures from randomly oriented paramagnetic systems.

ENDOR spectroscopy has been described as “EPR detected NMR”, and typically uses high microwave power to saturate EPR transitions at a selected magnetic field, while simultaneously irradiating nuclear spin transitions with radiofrequency (RF) radiation.³¹⁴ Under these conditions reduction in the EPR signal due to relaxation is detected as the observed ENDOR transition. This technique has been applied to successfully characterize the coordination sphere of a variety of systems, including metal complexes, defect centres in solids, and metalloenzymes.³¹⁵⁻³¹⁷ Currently, there are only a few examples of ENDOR studies of ruthenium complexes,³¹⁸⁻³²⁰ the majority of which study Ru(II) ligand radicals, while only one has ruthenium as a paramagnetic centre.³²¹ This chapter describes the first study of the solution behaviour and protein binding of the Ru(III) anticancer complexes KP1019 and NAMI-A using ENDOR spectroscopy. With this technique, further insight into the structure of ligand-exchanged and protein-bound Ru(III) complexes was obtained through proton and nitrogen hyperfine interactions.³²² To facilitate the assignment of the

¹H and ¹⁴N signals in the ENDOR spectra, the synthesis of several isotopically labelled NAMI-A derivatives (**Figure 7-1**) was performed. Furthermore, analysis of the NAMI-A starting compound, the *bis*-dimethylsulfoxide Ru(III) complex $[(\text{DMSO})_2\text{H}][\text{trans-RuCl}_4(\text{DMSO}-\text{S})_2]$ (*bis*-DMSO) (**Figure 7-1**), was also carried out to identify the coordinated DMSO ¹H peaks in the ENDOR spectrum. This is the first reported study where isotope labelling was utilized to examine the mechanism of action of Ru(III) anticancer compounds. Isotopic labelling of KP1019 was not performed since such indazole derivatives were not commercially available or easily synthesized.

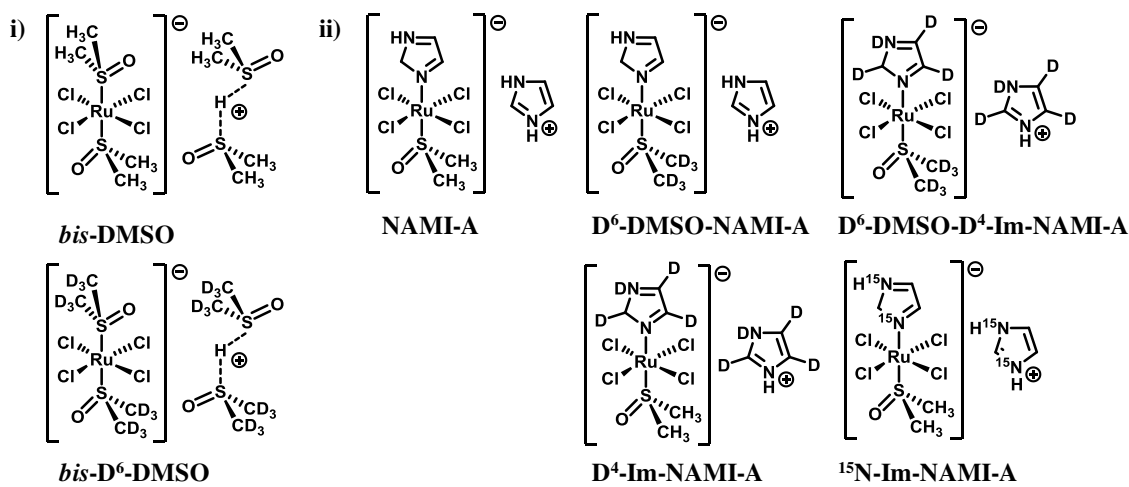


Figure 7-1 Isotopically labelled i) *bis*-DMSO and ii) NAMI-A complexes synthesized and studied using ENDOR. (D = ²H in each deuterium labelled compound and Im = imidazole).

Further analysis of KP1019, NAMI-A, and the *bis*-DMSO Ru(III) complex with hsA and individual amino acids was performed in an attempt to identify the residues responsible for coordinate hsA interactions.

7.2. Principles of ENDOR Spectroscopy

7.2.1. Introduction to ENDOR

ENDOR spectroscopy can be used to study any paramagnetic species which has a coordinated spin-bearing nucleus ($I \neq 0$). One analogy is the interaction between a spokesperson (the electron) and an audience (the nuclei), as depicted in **Figure 7-2**. The

goal of the spokesperson is to obtain information (the hyperfine splittings) from the individuals in the audience (individual nuclei). In an EPR experiment, the electron is asked for the nuclear information, but the electron cannot supply this information easily. The electron cannot hear the message because the large crowd of nuclei are shouting the information to the electron all at the same time. In an ENDOR experiment, each individual nucleus in the crowd is asked to stand up one at a time and pass the information on to the electron. Now the electron can make sense out of the message, which can be measured in the ENDOR spectrum.³²³

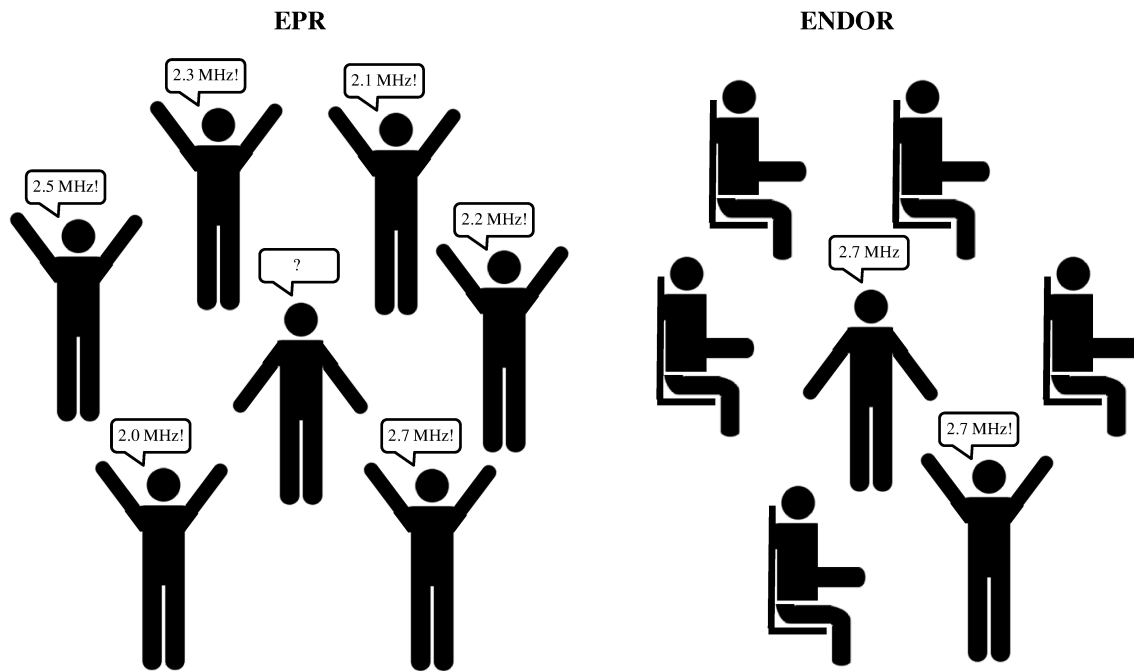


Figure 7-2 A pictorial comparison between EPR and ENDOR spectroscopy (figure adapted from reference 298).³²³

The first step in acquiring ENDOR data is to measure the EPR spectrum and determine the magnetic field values at which the signals appear. The magnetic field can then be set to specific values within the EPR envelope during the ENDOR experiment. Next, the microwave power is increased until a maximum EPR signal, or saturation, is obtained. Once this is achieved, an RF amplifier and a coil within the EPR resonator are used to sweep through radiofrequencies while monitoring the EPR signal. When the RF

drives an NMR transition, a decrease in the EPR signal occurs, and is observed as the resultant ENDOR transition.²¹⁹

7.2.2. ENDOR Theory

The underlying concepts of ENDOR can be understood using the spin Hamiltonian (equation 7.1). The largest interaction in typical $S = \frac{1}{2}$ EPR experiments is the electronic Zeeman effect, represented by the first term in equation 7.1, which includes the Bohr magneton (μ_B), the applied magnetic field (B), the g factor (g), and the electronic spin operator (\hat{S}). This term determines at which magnetic field the EPR transitions will occur. The second term is the nuclear Zeeman term, from the interaction of $I > 0$ nuclei with the applied magnetic field. Here, μ_N is the nuclear magneton, g_N is the nuclear g value, and \hat{I} is the nuclear spin operator. Since the value of g_N is specific to different nuclei, ENDOR is able to identify the types of nuclei interacting with the unpaired electron.

$$\hat{H} = \mu_B B \mathbf{g} \hat{S} + \mu_N B g_N \hat{I} + \hat{S} \mathbf{A} \hat{I} + \hat{I} \mathbf{P} \hat{I} \quad (7.1)$$

As mentioned in Chapter 1, the unpaired electron is highly sensitive to its surrounding environment. The interaction between the electron and the nuclei with $I > 0$ is the hyperfine interaction, and is given by the third term in the spin Hamiltonian, where \mathbf{A} is the hyperfine matrix. The observed hyperfine splitting gives a wealth of information, including: (i) the identity of the atoms surrounding the paramagnetic centre, (ii) their distances from the unpaired electron, and (iii) the electron spin densities at the nuclei. Lastly, the fourth term in the spin Hamiltonian represents the nuclear electric quadrupolar interactions of the nucleus, which are only observed for nuclei with $I \geq 1$, and arises from interactions of the nuclear charge ellipsoid with local electric field gradients.

As mentioned in the introductory chapter, there are two types of hyperfine interactions: anisotropic and isotropic. The anisotropic hyperfine interaction arises from through-space interactions between the magnetic dipole of the unpaired electron with the magnetic dipole of a nearby nucleus. This type of hyperfine interaction is orientation dependent with respect to the magnetic field direction and is observed in paramagnetic

samples of crystals, powders, and frozen solutions. Conversely, the isotropic hyperfine interaction does not depend on orientation with respect to the magnetic field. This interaction occurs through bonds within the paramagnetic system, relying on the direct Fermi-contact interaction of the electron spin with the nuclear spin and can be observed in liquid solutions and solid samples. In the simplest case, with $S = \frac{1}{2}$, $I = \frac{1}{2}$, the energy levels can be determined using the first three terms in the spin Hamiltonian shown in equation 7.1. The different electron spin manifolds are then given by:

$$E(M_s = +\frac{1}{2}, M_I) = +\frac{1}{2} g\mu_e B + \frac{1}{2} AM_I - g_N\mu_N B M_I \quad (7.2)$$

$$E(M_s = -\frac{1}{2}, M_I) = -\frac{1}{2} g\mu_e B - \frac{1}{2} AM_I + g_N\mu_N B M_I \quad (7.3)$$

The energy levels for this kind of system are shown in **Figure 7-3i**. The selection rules for EPR are $\Delta M_S = \pm 1$ and $\Delta M_I = 0$, resulting in resonant frequencies of:

$$\nu_{\text{EPR}} = \nu_e \pm a / 2 \quad (7.4)$$

The EPR signal for this system is therefore split into two transitions, separated by the value of a . For NMR transitions, outlined in **Figure 7-3ii**, the selection rules are opposite to those of EPR, in that $\Delta M_S = 0$ and $\Delta M_I = \pm 1$. This results in two ENDOR transitions of:

$$\nu_{\text{ENDOR}} = |\nu_N \pm a / 2| \quad (7.5)$$

Here, we are unable to distinguish between positive and negative frequencies, meaning that the centre of the observed ENDOR transition is dependent on the magnitude of hyperfine splitting (a) and the Larmor frequency (ν_N) of the measured nucleus, which is given by:

$$\nu_N = g_N\mu_N B_0 \quad (7.6)$$

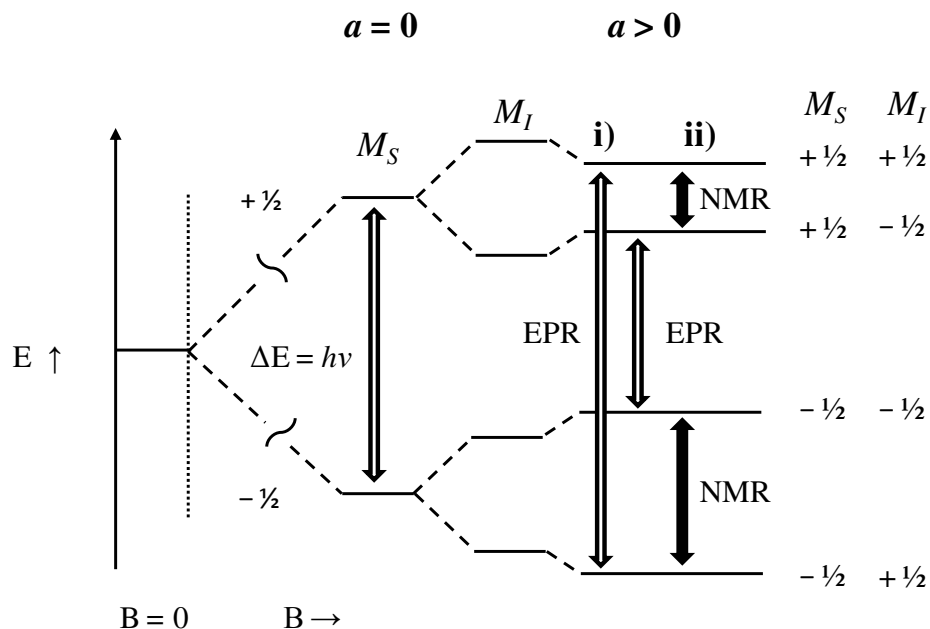


Figure 7-3 Energy level diagram for an $S = \frac{1}{2}$, $I = \frac{1}{2}$ system, (i) EPR with hyperfine interactions, and (ii) ENDOR transitions.

Depending on the magnitude of a and ν_N , the measured ENDOR signal can be either “Larmor centred” or “hyperfine centred” due to the absolute value in equation 7.5, as shown in **Figure 7-4**.

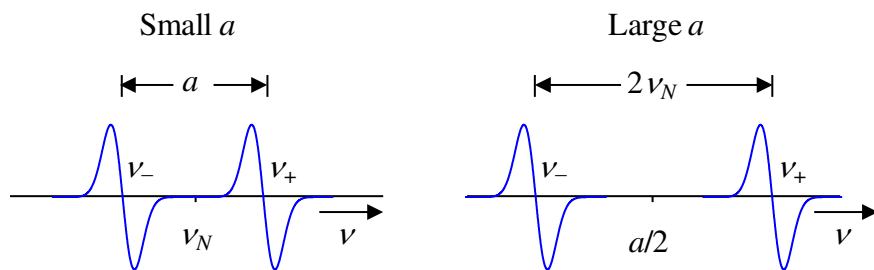


Figure 7-4 Two possible ENDOR line splitting patterns for systems where $S = \frac{1}{2}$, $I = \frac{1}{2}$.

7.3. Experimental

7.3.1. Synthesis

NAMI-A and KP1019 were synthesized according to literature procedures.^{132,150,245} Isotopically labelled analogues of NAMI-A were also synthesized following the same literature procedures for NAMI-A, with the incorporation of D₆-DMSO (99.9%, Cambridge isotope laboratories), D₄-imidazole (98%, Cambridge isotope laboratories) and ¹⁵N-Imidazole (98%, Sigma Aldrich). Synthesis of ¹⁵N-labelled imidazole was attempted using ¹⁵N-ammonium chloride (98%, Sigma Aldrich) following a previously published synthesis for unlabelled imidazole.³²⁴ This proved unsuccessful as impurities in the resulting material made this route unsuitable for the synthesis of NAMI-A, leading to the purchase of ¹⁵N-imidazole from Sigma. Each complex was checked for elemental purity using CHN analysis with the results listed below.

KP1019 EA: Calc. C 42.14 H 3.20 N 14.05, Found C 41.75 H 3.18 N 13.68. *bis*-DMSO EA: Calc. C 17.27 H 4.53, Found C 17.41 H 4.52. *bis*-D₆-DMSO EA: Calc. C 16.52, Found C 16.51. NAMI-A EA: Calc. C 20.97 H 3.30 N 12.23, Found C 21.16 H 3.29 N 12.08. D₆-DMSO-NAMI-A EA: Calc. C 20.70 N 12.07, Found C 20.67 N 11.69. D₄-Im-NAMI-A EA: Calc. C 20.79 N 12.13, Found C 20.46, N 11.74. D₆-DMSO-D₄-Im-NAMI-A EA: Calc. C 20.30 N 11.84, Found C 20.39, N 11.37. ¹⁵N-Im-NAMI-A•2H₂O EA: Calc. C 19.30 H 3.85, Found C 19.17 H 3.94.

7.3.2. Preparation of ENDOR Samples

KP1019 in DMSO. A 20 mM sample of KP1019 was prepared by dissolving the complex in 150 µL of DMSO, followed by the addition of 150 µL of glycerol (50%). The sample was mixed and immediately frozen in liquid nitrogen until use. For all ENDOR samples measured a high concentration of glycerol was necessary since this acted as a glassing agent, which is particularly important in ENDOR studies. The glassing agent prevents the formation of crystalline domains and thus reduces long range ordering. This

limits spin-spin communication between paramagnetic centres in the frozen solutions that contribute to faster relaxation times and resultant broadening of ENDOR signals.³²⁵ By increasing this relaxation time, better resolution and signal-to-noise in the resulting ENDOR spectra can be obtained.

NAMI-A and the *bis*-DMSO complex in buffer. For NAMI-A and its *bis*-DMSO starting material complex, 20 mM ENDOR samples were prepared by dissolving each complex in 150 µL of a phosphate buffered saline (PBS) solution (pH 7.4) containing 137 mM NaCl, 2.7 mM KCl, 10 mM Na₂HPO₄ and, 2 mM KH₂PO₄ followed by the addition 150 µL of glycerol. The samples were mixed, and immediately frozen in liquid nitrogen until use.

***bis*-DMSO complex solution behaviour samples.** To study the solution behaviour of the *bis*-DMSO complex, samples were prepared by dissolving the complex in PBS (3 mM, 1050 µL) followed by incubation at 37 °C. After 0, 10, 20, 30, and 60 minutes of incubation 210 µL aliquots were isolated and mixed with 90 µL of glycerol and immediately frozen in liquid nitrogen until use.

Ru(III) complexes with hsA. Each Ru(III) complex was dissolved in PBS (20 mM, 600 µL), and immediately mixed with a solution of hsA (2.5 mM, 600 µL) and diluted to a final volume of 4 mL using PBS. For KP1019, 4% DMSO was used to fully dissolve the complex prior to mixing with the protein solution. The resulting solutions were incubated at 37 °C for 30 minutes, after which protein-bound fractions were isolated using Amicon centrifugal filter units (30 kDa molecular weight cut-off) by centrifuging at 8 °C and 4500 rpm for 30 minutes, or until a volume of less than 200 µL was attained. The filtered product was promptly diluted to 210 µL using PBS and mixed with 90 µL of glycerol before being transferred to an EPR tube and frozen in liquid nitrogen until use.

Ru(III) complexes with amino acids. Each Ru(III) complex was dissolved in PBS (10 mM, 1050 µL). The individual amino acids (alanine, cysteine, and histidine) were added (10 mM) to each Ru(III) solution, resulting in a 1:1 ratio of Ru to each amino acid. Each solution was then incubated for 0, 10, 20, 30, and 60 minutes at 37 °C, after

which 210 µL fractions were taken and mixed with 90 µL of glycerol and immediately frozen in liquid nitrogen until use.

7.3.3. EPR Measurements and Simulation

See section 2.2.4.

7.3.4. EPR Experimental Conditions

See section 2.2.5.

7.3.5. ENDOR Experimental Conditions

All samples were measured at 20 K. ENDOR experimental conditions: modulation frequency = 25 kHz, modulation amplitude = 0 Gauss, microwave power = 31.7 mW, frequency = 9.47 GHz, time constant = 1.28 ms, RF modulation depth = 250 kHz, RF attenuation = 6 db, average of 100 five-second scans.

7.4. Results and Discussion

Previous studies of Ru(III) anticancer agents have demonstrated a propensity for aqueous ligand exchange as well as interactions with proteins such as hsA under physiological conditions. In this work, the nature of the aquated species was studied using ^1H ENDOR of coordinated water molecules and DMSO. Samples of hsA-bound complexes have also been characterized by analyzing changes in the ^{14}N and ^1H regions of the ENDOR spectrum. Further analysis using individual amino acids has provided further insight into the nature of the protein-bound Ru(III) species.

7.4.1. Aqueous Solution Behaviour

The aqueous solution behaviour of both KP1019 and NAMI-A has been described previously in Chapters 2 and 3 respectively. To describe details of ligand exchange processes, these studies were expanded using ENDOR. The nuclei of interest for the ENDOR studies are shown in **Table 7-1** for $B = 3330$ Gauss ($g \approx 2$ at X-band).

Table 7-1 ENDOR-active nuclei studied in this work.

Isotope	Spin (I)	g_N	Larmor Freq. (ν_N) (MHz at $B = 3330$ G)
1H	$\frac{1}{2}$	5.58569	14.9
2H	1	0.85744	2.3
^{14}N	1	0.40376	1.1
^{15}N	$\frac{1}{2}$	-0.56638	1.5

KP1019. Due to the rapid precipitation of KP1019 following aquation, only the parent compound was studied using ENDOR spectroscopy. This was achieved by dissolution of the complex in a DMSO and PBS buffer mixture (1:1), facilitating the preparation of highly concentrated samples that were necessary for ENDOR measurements. As mentioned above, the first step in ENDOR spectroscopy is to measure the EPR spectrum for each sample. In this case, although a high concentration of DMSO was used, the observed EPR spectrum was indistinguishable from a previously measured sample of KP1019 in HEPES buffer (Chapter 2), and could be simulated using identical parameters (Appendix F – **Figure F-1**). The EPR spectrum of KP1019 exhibits two overlapping species, a uniaxial species, *KP1019-Uniaxial*, and a rhombic species, *KP1019-Rhombic*. Therefore, the ENDOR field was set at the visible principle g values for each species, that being g_{\perp} (2.64) of *KP1019-Uniaxial*, and g_1 (2.94) and g_2 (2.31) of *KP1019-Rhombic*. The remaining g values for these two complexes are at higher field values and are only observable under adiabatic rapid-passage conditions (Chaper 2).

ENDOR measurements show signals in regions typical for both 1H and ^{14}N nuclei (**Figure 7-5** and Appendix F – **Figure F-2**). This was expected, since the coordinating indazole ligands have both nitrogen and hydrogen atoms. In the 1H region of the ENDOR spectrum, for all three fields, a broad signal is observed with a coupling of < 1 MHz around $\nu(^1H)$. This is consistent with contributions from couplings to distant solvent protons,³²⁶⁻³²⁸ and has been observed in previous reports on the ENDOR of molecules

which have been studied in frozen aqueous media.³²⁸ This signal was observed in the subsequent ^1H ENDOR spectra for all samples measured in PBS buffer, and will therefore not be mentioned in the following discussions. In addition to this feature, two sets of signals are observed in the ENDOR spectra measured at g_{\perp} and g_2 . For g_{\perp} the signals have couplings of 1.9 and 4.0 MHz around $\nu(^1\text{H})$, while at g_2 the couplings are 1.6 and 3.6 MHz around $\nu(^1\text{H})$. These ^1H ENDOR signals are from protons on the coordinating indazole ligand (**Figure 7-5**), however, the assignment of the peaks to specific protons is complicated due to the overlapping nature of the EPR signals from the uniaxial and rhombic EPR spectra.

Since ^{14}N has an integer spin ($I = 1$) it usually exhibits nuclear electric quadrupole interactions, which are observed as a 2-line splitting in the ENDOR spectrum,³²⁹ complicating the analysis of the ^{14}N peaks. In the ^{14}N region, for all three fields, sharp peaks are observed near $\nu(^{14}\text{N})$, which track with the changes in the static field. This indicates that these peaks are from ligands bound to the Ru(III) metal centre, and therefore are assigned to the ^{14}N nuclei of the indazole ligands.

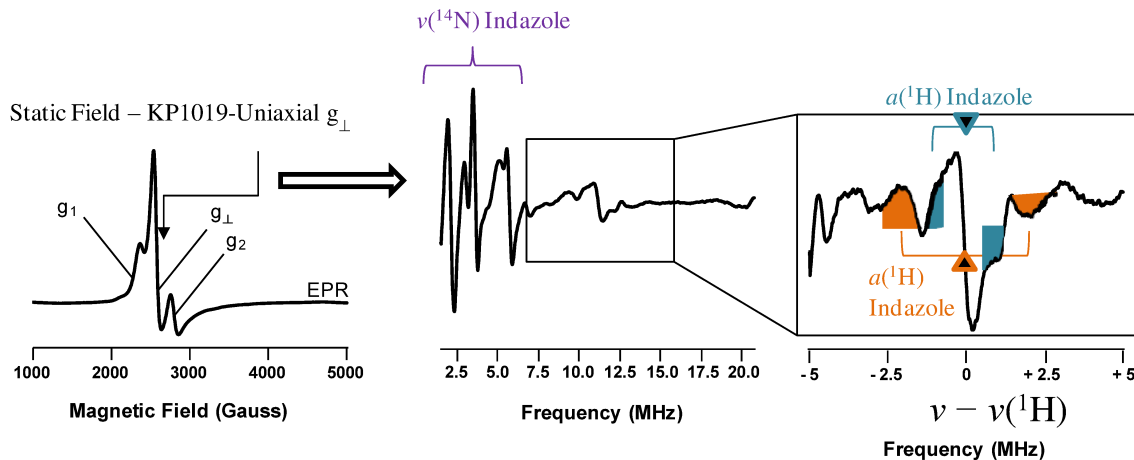


Figure 7-5 Solution EPR and ENDOR spectrum of KP1019 in 1:1 DMSO:glycerol, with the static field set at g_{\perp} for KP1019-Uniaxial.

Bis-DMSO. Before any ENDOR spectra were measured, the solution behaviour of the *bis*-DMSO complex was studied using EPR. Other ruthenium-sulfoxide complexes have been observed to readily undergo ligand-exchange in aqueous solution,^{330,331} and the

bis-DMSO complex has previously been shown to rapidly release one of its *trans* *S*-bonded DMSO ligands upon dissolution in water.¹⁴⁷ To monitor the extent and relative rate of aquation, samples were prepared analogously to the previously described studies of NAMI-A in buffer using EPR (Chapter 3). The solution behaviour for the unlabelled *bis*-DMSO complex was monitored here by EPR.

At the first time point, “0 min” in **Figure 7-6**, a single uniaxial signal is observed. This signal was simulated with $g_{\perp} = 2.43$ and $g_{||} = 1.77$ and linewidths of $LW_{\perp} = 100$ and $LW_{||} = 150$ Gauss, which are similar to those of NAMI-A (Appendix F – **Table F-1**), suggesting that a similar ligand field exists around the Ru(III) metal centre. There are three possible species which have tetragonal geometry that could have been responsible for this signal. They are: i) the unsubstituted parent complex, ii) the mono-aqua complex where one axial DMSO ligand is exchanged for a water molecule, and iii) the di-aqua complex where both axial DMSO ligands are exchanged for water molecules. However, it is hard to discriminate between these species by EPR. As shown below, ENDOR spectroscopy was used to determine the identity of this species, which was the mono-aqua complex (*bis*-DMSO- H_2O).

Further incubation led to several changes (**Figure 7-6**), most significantly with the appearance of the solution. Following dissolution of *bis*-DMSO in PBS, a clear bright yellow-orange coloured solution was initially obtained. After 20 minutes the solution turned a darker yellow colour, while after 60 minutes a clear dark brown solution remained. This has been observed previously for the solution behaviour of NAMI-A,^{176,247} and was assigned to the formation of antiferromagnetically coupled dimers, which one expects to have $S = 0$ and therefore be “EPR silent”, and whose formation leads to a decrease in overall EPR signal intensity.²⁶⁴ A similar phenomenon was observed here, since increased incubation led to a decrease in the EPR signal intensity; however the change was not as rapid as the previously reported study of NAMI-A (Chapter 3). This is likely due to the different buffer solutions, since the PBS buffer used here has a higher concentration of chloride ions, which have been shown to affect the rate of aquation for NAMI-A.^{176,332}

Changes are also evident in the EPR spectra of *bis*-DMSO with increasing incubation. After 20 minutes small contributions from two new signals are observed, which upon spectral simulation were found to be a uniaxial and a rhombic signal (**Figure 7-6**). The uniaxial signal was simulated with the *g* values: $g_{\perp} = 2.35$ and $g_{||} = 1.80$ and linewidths: [LW_⊥ = 110 and LW_{||} = 200] Gauss, and is assigned to the di-aqua compound (*bis*-DMSO-(H₂O)₂-ax) formed by aqueous exchange of the second DMSO ligand from *bis*-DMSO-H₂O.

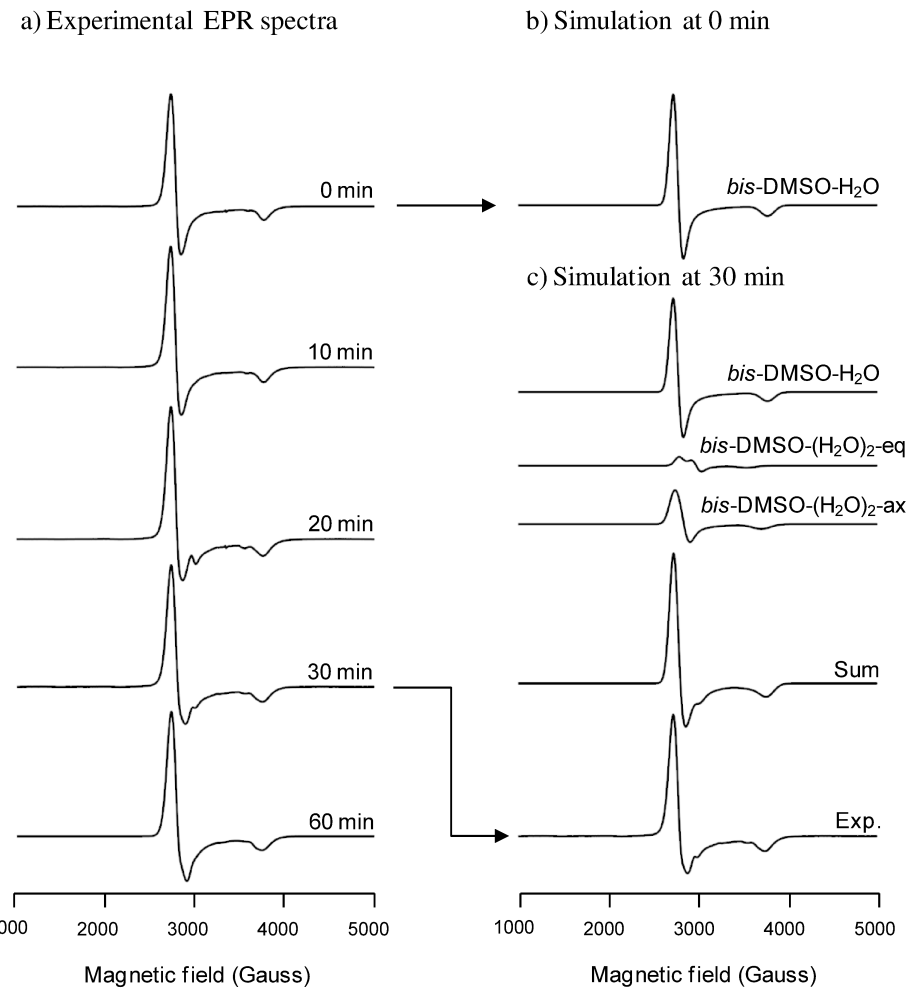


Figure 7-6 Frozen solution behaviour of the *bis*-DMSO complex: a) EPR spectra measured over 60 minutes of incubation at 37 °C, b) simulation of the EPR spectrum after 0 minutes of incubation, c) deconvolution of the EPR spectrum following 30 minutes of incubation.

The second, rhombic species was simulated with the g values: $g_1 = 2.40$, $g_2 = 2.24$, and $g_3 = 1.88$ and linewidths: [$LW_1 = 90$, $LW_2 = 90$, and $LW_3 = 200$] Gauss. Due to the observed decrease in symmetry, this signal is assigned to the species formed after the mono-aqua complex has undergone aqueous exchange of an equatorial chloride ligand, leading to the lower symmetry species (*bis*-DMSO-(H_2O)₂-*eq*). Further incubation to 30 minutes led to a maximum intensity of the signal from *bis*-DMSO-(H_2O)₂-*eq*, while after 60 minutes only the two uniaxial signals were observed, the signal from *bis*-DMSO-(H_2O)₂-*ax* being the dominant species present. As mentioned above, ENDOR measurements made at $g_{\perp} = 2.43$ and $g_{||} = 1.77$ were used to identify the original species observed in solution, which aid in the assignment of all the EPR signals observed during the solution behaviour study.

ENDOR measurements of the unlabelled *bis*-DMSO revealed well-defined features in the 1H region of the spectra. At g_{\perp} , two distinct sets of signals were observed with couplings of 2.2 and 3.9 MHz around $\nu(^1H)$ (**Figure 7-7** and Appendix F – **Figure F-5**). When the field was set to $g_{||}$ (**Figure 7-7** and Appendix F – **Figure F-5**), again two distinct sets of signals were observed in 1H region of the spectrum, with couplings of 3.2 and 4.9 MHz around $\nu(^1H)$. To determine the origin of these peaks, 1H ENDOR spectra were obtained from *bis*-D₆-DMSO.

The EPR spectrum of the deuterated *bis*-DMSO complex was found to be uniaxial and indistinguishable from its undeuterated analogue (Appendix F – **Figure AF-4a**). However, upon setting the field to g_{\perp} , changes were observed in the resulting ENDOR spectrum (**Figure 7-7** and Appendix F – **Figure F-6**). A sharp signal is observed at 2.1 MHz, which is close to the 2H Larmor frequency of 1.8 MHz (Appendix F – **Figure F-6**). This signal was absent in the spectrum of the unlabelled complex and was therefore assigned to the 2H ENDOR signal from the coordinated D₆-DMSO ligands. In the 1H region of the spectrum, only one set of signals was observed with a coupling of 3.9 MHz around $\nu(^1H)$. No signals from 1H -DMSO are expected, due to the 2H isotopic labelling, therefore the 1H signals observed here are assigned to protons from a coordinated water molecule. This demonstrates that the original species measured in solution is not the

parent compound, but the mono-aqua complex (*bis*-DMSO- H_2O), where one of the axial DMSO ligands is exchanged for a water molecule, thereby retaining its tetragonal symmetry. Furthermore, these measurements demonstrate that the signals with a coupling of $a(^1H) = 2.2$ MHz in the unlabelled complex are from the coordinated 1H -DMSO ligand. Similar couplings for both DMSO and water have been previously observed when coordinated to an Fe(III) centre.^{333,334}

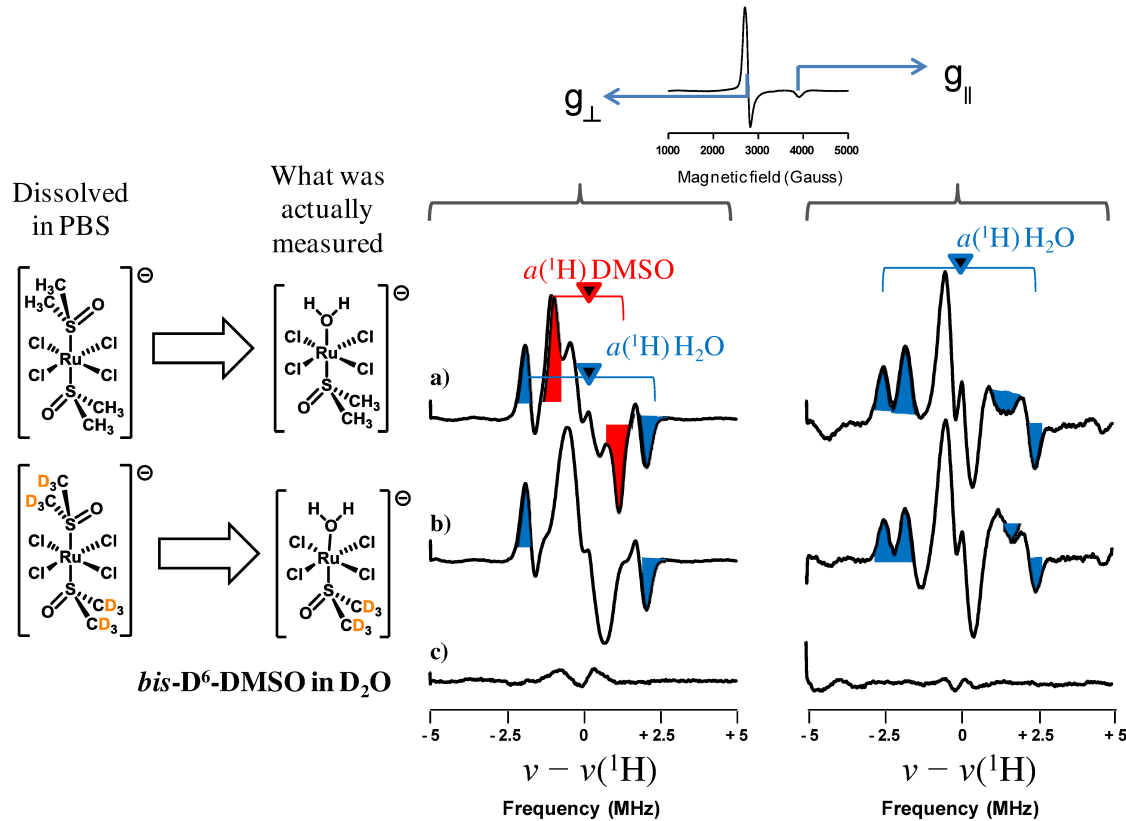


Figure 7-7 1H ENDOR spectra of a) the unlabelled Ru(III) *bis*-DMSO complex, and its D_6 -DMSO-labelled derivatives in b) PBS, and c) D_2O , centred at the 1H Larmor frequency.

At $g_{||}$, a sharp peak is observed in the 2H region of the spectrum at 2.7 MHz (Appendix F – **Figure F-5**). This signal tracks with changes in the static field around the Larmor frequency of deuterium ($\nu(^2H) = 2.5$ MHz), confirming that this signal arises from deuterium labelled DMSO coordinated to the Ru(III) metal centre. In the 1H region of the ENDOR spectrum at $g_{||}$, two sets of peaks appeared with couplings of 3.4 and 5.1

MHz around $\nu(^1\text{H})$. Since both these peaks are observed in the presence of ^1H - and ^2H -DMSO, they must be from water molecules coordinated to the Ru(III) metal centre, which is consistent with the observations in the ENDOR spectra measured at g_{\perp} . The peaks from the coordinated DMSO are not visible at this field, possibly due to small couplings.

To further confirm the presence of coordinated water, the *bis*-d⁶-DMSO complex was dissolved in buffered D₂O. The observed EPR spectrum was essentially identical to the unlabelled complex in H₂O (Appendix F – **Figure F-4c**). In the ENDOR spectra at both g_{\perp} and $g_{||}$ (Appendix F – **Figure F-7**), a large sharp peak was observed in the ^2H region of the spectrum at 2.1 ($\nu(^2\text{H}) = 1.8$ MHz) and 2.7 MHz ($\nu(^2\text{H}) = 2.4$ MHz), which is close to the Larmor frequency of deuterium at each field, consistent with the deuterium labelled DMSO ligand and coordinated D₂O. In the ^1H region of the spectrum, a very weak signal was observed around $\nu(^1\text{H})$ with a small hyperfine coupling. This feature is similar to the signal previously assigned to distant proton couplings from surrounding solvent molecules, although with much lower intensity. This arises from protons in the buffering agents, Na₂HPO₄ and KH₂PO₄, and possibly small amounts of atmospheric H₂O mixing with the D₂O over time.³³⁵ No additional splittings or signals were observed, demonstrating that the assignment of the strongly coupled peaks ($a_{\perp}(^1\text{H}) = 3.9$ MHz, $a_{||}(^1\text{H}) = 3.4$ and 5.1 MHz) in the previous ENDOR spectra of the *bis*-DMSO complex in buffer to water molecules is correct.

NAMI-A. NAMI-A and its isotopically labelled derivatives were also analyzed using ENDOR. The aqueous speciation of NAMI-A under physiological conditions has been well documented using a variety of analytical techniques,^{176,214,215} including EPR (Chapter 3).²⁶⁴ Isotopic labelling of NAMI-A had no significant effect on the EPR spectra, since only small changes in the g values and linewidths compared to the unlabelled compound were observed (Appendix F – **Figure F-4d**). The ENDOR spectra of the unlabelled and labelled complexes were measured at both g_{\perp} and $g_{||}$, with a particular emphasis on the ^1H region of the spectrum and the effects of deuterium-labelling on the coordinated DMSO and imidazole ligands.

ENDOR measurements of unlabelled NAMI-A revealed well-defined features in both the ^{14}N and ^1H regions of the spectra when the field was set at either \mathbf{g}_{\perp} (2.47) or $\mathbf{g}_{||}$ (1.72) (**Figure 7-8** and **Figure 7-9**). In the ^1H region at \mathbf{g}_{\perp} (**Figure 7-8**), two sets of signals were identified with couplings of 2.0 MHz and 3.4 MHz around $\nu(^1\text{H})$. Signals similar to the more weakly coupled protons were seen previously in the ENDOR spectrum of *bis*-DMSO- H_2O and were assigned to coordinated DMSO. The two new peaks with $a = 3.4$ MHz in the ^1H region have smaller couplings than those assigned to water ligands coordinated to the Ru(III) metal centre of *bis*-DMSO- H_2O , and therefore must arise from the protons of the coordinated imidazole ligand. Both the DMSO and imidazole ^1H couplings are similar to previously reported values for each ligand coordinated to a Fe(III) centre.^{323,333} At $\mathbf{g}_{||}$, in the ^1H region, one set of peaks with a coupling of 3.4 MHz were observed. As shown later in the isotope labelling studies, the protons responsible for these peaks were determined to be from the coordinated imidazole ligand overlapping the ^1H DMSO signals.

At both \mathbf{g}_{\perp} and $\mathbf{g}_{||}$ in the ^{14}N region of the spectrum, there are several sharp signals observed around $\nu(^{14}\text{N})$. Similar to above for KP1019, the interpretation of the peaks is complicated due to the spin ($I = 1$) of the ^{14}N nucleus. The position of the peaks around $\nu(^{14}\text{N})$, however, suggests that these are from the imidazole ligand coordinated to Ru(III). Previous ENDOR studies of metalloproteins containing histidine imidazoles coordinated to Fe(III) and Cu(II) centres show broader signals with larger couplings.^{329,336-338} Further simulation of the ^{14}N region of the ENDOR spectrum is required to fully interpret the peaks observed. This remains an ongoing project, outside the scope of this chapter.

Selective deuteration of NAMI-A gave distinct changes in the ^1H and ^2H ENDOR spectral regions (**Figure 7-8** and Appendix F - **Figures F-8 – F-10**). In the ^2H region of the spectrum, deuterium labelling produced a sharp peak that was observed at low field for all samples. When the field was set to \mathbf{g}_{\perp} , this peak was observed at 2.3 MHz, around the Larmor frequency ($\nu(^2\text{H}) = 1.8$ MHz), similar to the D_6 -DMSO labelling of the *bis*-DMSO complex. When the field was set at $\mathbf{g}_{||}$, this peak was observed at 3.0 MHz,

tracking with the Larmor frequency ($\nu(^2\text{H}) = 2.6$ MHz). As the amount of ^2H incorporation into the coordinating ligands increased, the corresponding ^2H signal intensity also increased relative to the ^{14}N signals.

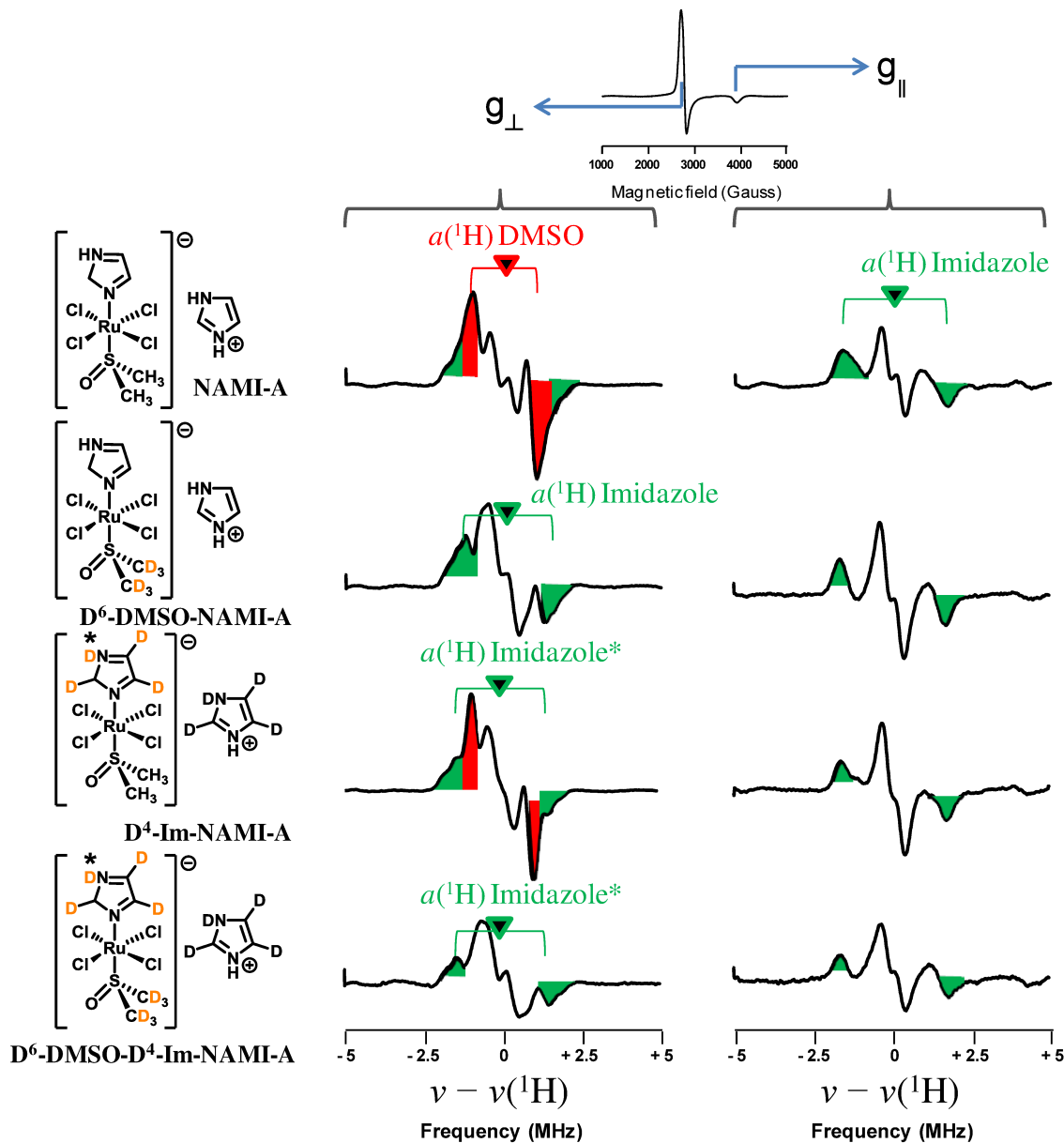


Figure 7-8 ^1H ENDOR of NAMI-A and its deuterated derivatives, centred at the proton Larmor frequency, where * = exchangeable.

For all deuterated complexes of NAMI-A, the ENDOR spectra measured at g_{\perp} had ^1H signals that were weaker than those of unlabelled NAMI-A (Figure 7-8). For D_4 -

Im-NAMI-A, peaks corresponding to the coordinated ^1H -DMSO are readily observed ($a(^1\text{H}) = 2.0$ MHz), while small peaks from the imidazole ligand remain. These more strongly coupled peaks ($a(^1\text{H}) = 3.4$ MHz) are from exchange of the deuterium on the distal nitrogen for a solvent proton. When the ^1H ENDOR of the D₆-DMSO-NAMI-A and D₆-DMSO-D₄-Im-NAMI-A (**Figure 7-8** and Appendix F – **Figure F-8** and **F-10**) were measured at g_{\perp} , very similar spectral features were observed. In each case, the only peaks detected were from coordinated imidazole. These signals were significantly weaker than the ^1H ENDOR spectra for the other deuterated derivatives, since contributions from the DMSO ligand were now excluded.

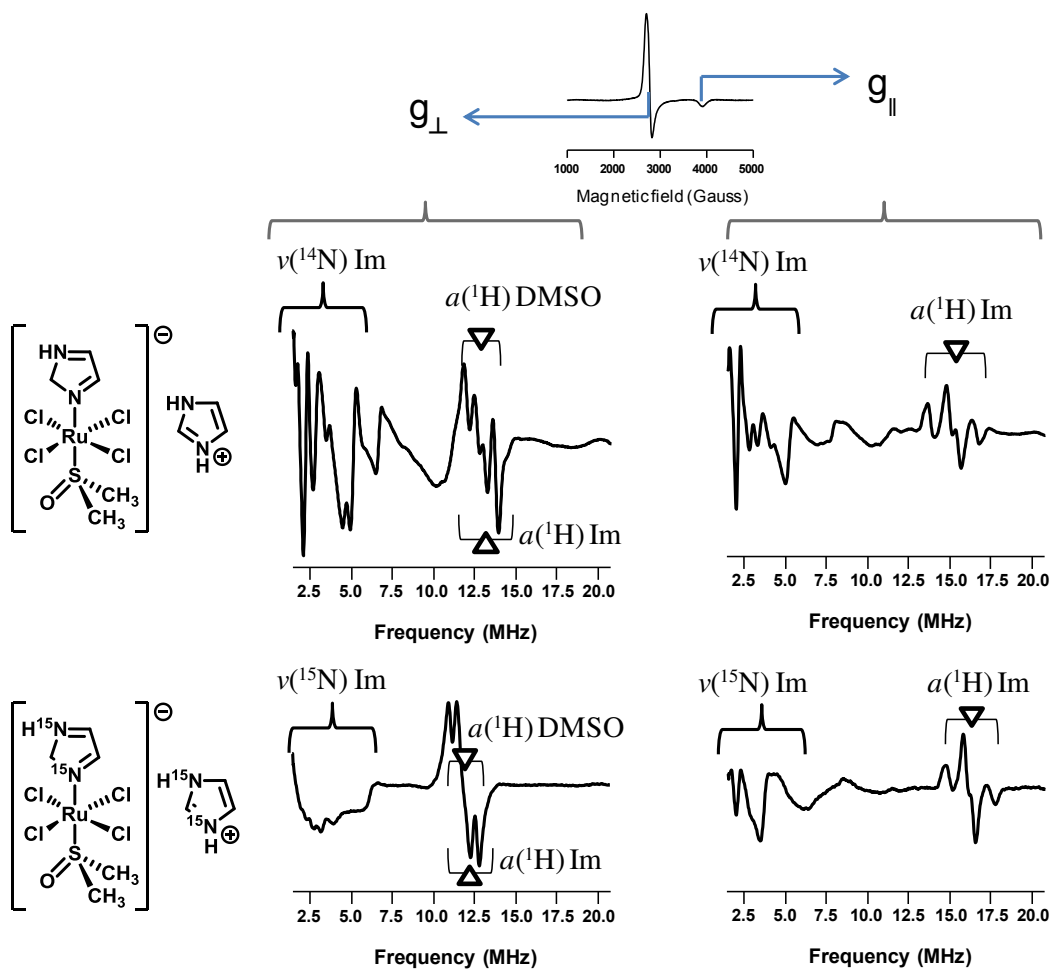


Figure 7-9 ENDOR of NAMI-A and its ^{15}N -imidazole derivative.

When the magnetic field was set to $g_{||}$, similar ENDOR spectral features were observed for all deuterium labelled compounds, with only one set of peaks observed

(Figure 7-8). These peaks $a(^1\text{H} = 3.5 \text{ MHz})$ around $\nu(^1\text{H})$ are comparable to the peaks previously observed for the unlabelled NAMI-A. The intensity of these peaks is decreased with imidazole labelling, but seemingly unchanged when labelled DMSO is used. This suggests that these peaks are from the coordinated imidazole ligand, while the peaks from the DMSO are unresolved, possibly due to being weakly coupled.

The final isotopically labelled NAMI-A derivative was synthesized using ^{15}N -imidazole (Figure 7-9). The use of ^{15}N ($I = 1/2$) was expected to simplify the resulting nitrogen ENDOR signals, since the splittings would be easier to interpret compared to the ^{14}N labelled compound, due to the absence of quadrupole interactions. As with the other isotopically labelled compounds, the EPR spectrum for this complex in buffer also has only one uniaxial signal corresponding to the unexchanged parent compound. ENDOR was measured at g_{\perp} (2.45) and $g_{||}$ (1.74), with measurements taken in both the ^{15}N and ^1H Larmor frequency regions. In the ^1H region of the spectrum at g_{\perp} and $g_{||}$, similar features are observed to that of the unlabelled parent compound. For the ENDOR spectrum in the ^{15}N frequency region (< 10 MHz), significant differences are observed when compared to the previous samples. At g_{\perp} , the previously observed sharp ^{14}N peaks from unlabelled NAMI-A were replaced by a distinct absence of any significant peaks in the ^{15}N region of the spectrum. However, when the field was set to $g_{||}$, a new peak was observed in the ^{15}N region of the spectrum at 2.6 MHz, suggesting that at g_{\perp} the peaks are possibly below the minimum frequency for continuous wave X-band ENDOR (~2 MHz). Unfortunately no coupling was obtained from these measurements. However, the absence of the strong signals at lower frequency observed for the unlabelled complex upon ^{15}N -labelling confirms the assignment of the ^{14}N imidazole ENDOR signals for the unlabelled NAMI-A complex.

7.4.2. Ligand Exchange Studies.

Additional samples of each complex were prepared where NAMI-A and its isotopically labelled analogues were incubated for 20 minutes at 37 °C in an attempt to determine the primary species formed following aquation. From the EPR studies of the solution behaviour of NAMI-A (Chapter 3), a new uniaxial species is expected to be

observed. However, overlapping EPR signals from the parent and ligand-exchanged species complicated the resulting ENDOR spectra, since the signals observed are a combination of all species present in solution. For all ^2H -NAMI-A analogues, incubation led to significant changes in both the ^1H and ^2H regions of the spectrum when the magnetic field was set to \mathbf{g}_{\perp} . In the ^2H region, the sharp signal around 2.3 MHz ($\nu(^2\text{H}) = 2.6$ MHz) from coordinated deuterium ligands is significantly reduced following incubation (**Figure 7-10** and Appendix F – **Figure F-11**). This is indicative of ligand exchange, where the axial ^2H -DMSO-ligand is exchanged for a water molecule. The intensity of the peak at 2.3 MHz was compared to neighbouring ^{14}N peaks, using unlabelled NAMI-A as a reference.

For unlabelled NAMI-A in the ^1H region, when the magnetic field was set to \mathbf{g}_{\perp} , peaks from the coordinated DMSO were found to decrease, while peaks from the coordinated imidazole were unaffected. From the previous EPR study (Chapter 3), DMSO dissociation followed by water coordination is anticipated; however, no additional peaks were resolved at \mathbf{g}_{\perp} . By contrast, when the field was set to $\mathbf{g}_{||}$, new, low intensity signals were observed with strong couplings of 4.9 MHz around $\nu(^1\text{H})$ (**Figure 7-10**). Peaks with similar couplings were observed in the ENDOR spectra of the *bis*-DMSO complex after dissolution in buffer and were assigned to a coordinated water molecule. These signals are more easily observed in the more deuterated NAMI-A analogues, that being $\text{D}_6\text{-DMSO-NAMI-A}$ and $\text{D}_6\text{-DMSO-D}_4\text{-Im-NAMI-A}$.

In the ^{14}N region at both \mathbf{g}_{\perp} and $\mathbf{g}_{||}$, sharp features are observed for all complexes, confirming that the imidazole ligand does not dissociate following aquation. Taken together, these results are consistent with the previous EPR study of the speciation of NAMI-A in buffer (Chapter 3), in that the DMSO ligand is lost via ligand exchange with water.

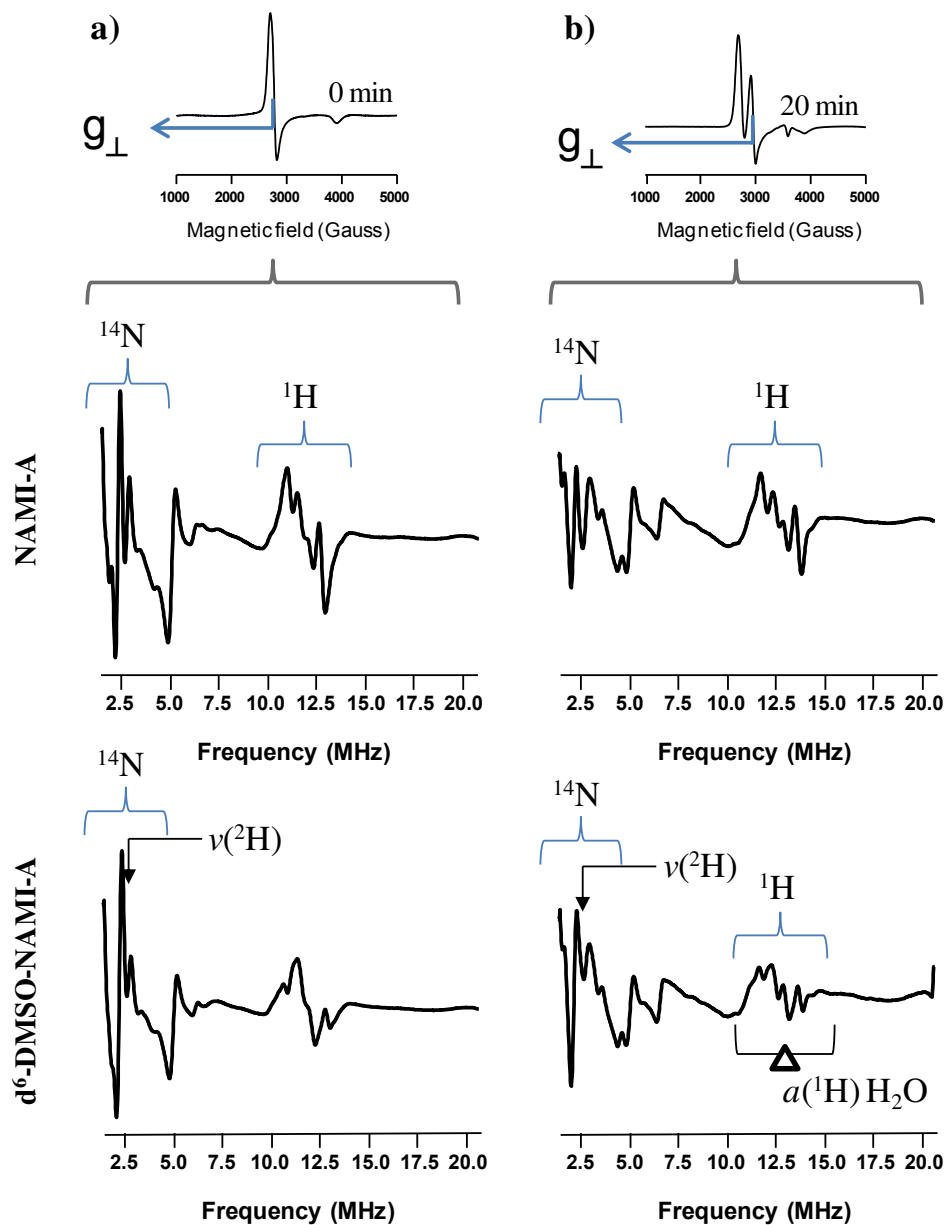


Figure 7-10 ENDOR spectra of a) NAMI-A and b) D₆-DMSO-NAMI-A after 0 and 20 minutes of incubation at 37 °C, pH 7.4 measured with the field set at g_⊥.

7.4.3. Interactions with hsA.

KP1019. EPR has been used previously to identify the interactions between KP1019 and hsA (Chapter 2). It was observed that within 30 minutes of incubation under physiological conditions (37 °C, pH 7.4) coordinate interactions began to dominate the EPR spectrum.²⁴⁶ In an effort to further characterize these coordinate interactions,

KP1019 was incubated with hsA for 30 minutes, after which protein-bound species was isolated and studied using ENDOR. From the simulation of the EPR signal (Appendix F – **Figure F-12**), a total of five species are present. The first two signals are from the unexchanged parent compound (*KP1019-Uniaxial/Rhombic*), while the remaining three are from protein-bound species (*KP1019-hsA-1/2/3*), as described in Chapter 2. Given the broad nature of the protein-bound signals, ENDOR measurements were taken at the g values of *KP1019-hsA-1* ($g_{\perp} = 2.32$ and $g_{||} = 1.84$), since this was the dominant protein-bound signal observed, accounting for ~60% of the total EPR intensity.

In the ^1H region (Appendix F – **Figure F-13**), two peaks were observed with couplings of 2.6 MHz around $\nu(^1\text{H})$ when the field was set at g_{\perp} . Such signals and couplings were not seen for KP1019 in buffer alone, supporting the conclusions from the EPR data that a new coordination environment is observed. For NAMI-A and its labelled derivatives, imidazole couplings were observed to be larger ($a_{\perp}(^1\text{H}) = 3.4$ MHz), suggesting that the new peaks observed for KP1019 may not be from histidine imidazoles of the protein. When the field was set at $g_{||}$, two peaks were also observed with couplings of 4.3 MHz around $\nu(^1\text{H})$, which are reminiscent of the previously observed H_2O couplings for the mono-aqua *bis*-DMSO complex ($a_{||}(^1\text{H}) = 3.4$ and 5.1 MHz). The absence of precipitation during this experiment provides further evidence that protein coordination is highly favoured, as described earlier in Chapter 2.

In the ^{14}N region of the ENDOR spectrum (Appendix F – **Figure F-13**), significant changes are observed when compared with the parent complex in buffer alone (**Figure 7-5**). When the field was set to g_{\perp} , two signals are observed at 2.3 and 4.1 MHz, while at $g_{||}$, only one signal is observed at 2.3 MHz. The signals observed in this region are likely from the coordinated indazole ligands of KP1019, while the incorporation of further nitrogen-based ligands cannot be excluded, based on the changes observed from the spectrum of KP1019 in buffer. Taken together, the changes in both the ^1H and ^{14}N regions of the ENDOR spectrum suggest that a new nitrogen-based ligand, likely a histidine imidazole, has coordinated to the Ru(III) metal centre.

Bis-DMSO. As with KP1019, the importance of hsA coordination to the NAMI-A family of Ru(III) antimetastatic agents has been reported in the literature, with histidine coordination thought to be the dominant interaction.²⁰² Proton ENDOR studies of the *bis*-DMSO complex were used to clarify the assignment of the ¹H couplings observed for NAMI-A with hsA. Additionally, the observation ¹⁴N ENDOR spectra would provide direct evidence for coordination of a nitrogen ligand. The nitrogen-based ligands available for protein-coordination are amino acids, and consideration of pKa values of the nitrogen containing side-chains at pH 7.4 indicates that histidine is favoured. For these studies the *bis*-DMSO complex and its deuterated derivative were incubated with hsA for 30 minutes to identify the nature of coordinate protein interactions. Similar bipyridine Ru(III) complexes with a coordinated DMSO ligand have demonstrated an affinity for bovine serum albumin,³³⁹ however, is the first report of both EPR and ENDOR studies of such interactions for the *bis*-DMSO complex. In the EPR study, a broad signal was observed after incubation with hsA for 30 minutes at 37 °C for both the labelled and unlabelled complexes (Appendix F – **Figure F-14a** and **b**). Spectral deconvolution determined that the signal observed for each complex was comprised of three new overlapping EPR signals. The simulation parameters (g values and linewidths) for these signals were similar to those of NAMI-A and its hsA coordinated derivatives, which is indicative of protein coordination. Further insight into the nature of this interaction was gained by measuring the ENDOR spectrum at the average g_⊥ (2.35) and g_{||} (1.71) of the two protein-bound signals.

For both the unlabelled and labelled compound, the ¹⁴N and ¹H regions of the ENDOR spectrum following incubation with hsA were very similar (**Figure 7-11** and Appendix F – **Figures F-15** and **16**). Furthermore, the absence of ²H signals from the labelled complex suggests that both D₆-DMSO ligands are replaced during protein binding. In the ¹H region, signals from coordinated water are identified with a coupling of 4.3 MHz around ν(¹H) at g_⊥. In addition to these signals, another set of peaks with a coupling of 2.6 MHz around ν(¹H) are seen. Peaks such as these have been identified previously for NAMI-A as imidazole protons. This suggests that histidine imidazoles are binding to the ruthenium metal centre and are primarily responsible for the observed

coordinate hsA interactions. Additionally, no peaks that were previously identified to be from coordinated DMSO were observed for the unlabelled *bis*-DMSO complex, further suggesting that complete dissociation of DMSO is achieved during hsA coordination. When the magnetic field was set to $g_{||}$, peaks from coordinated ligands could not be resolved for either the labelled or unlabelled complexes.

For the labelled and unlabelled *bis*-DMSO complexes in the ^{14}N region, with the magnetic field set at either g_{\perp} or $g_{||}$, distinct ENDOR signals were detected. The observation of ^{14}N signals is unequivocal proof of coordination to nitrogen containing ligands of the protein. These signals are similar to those of NAMI-A in solution, suggesting that histidine imidazoles are now coordinated to the ruthenium metal centre.

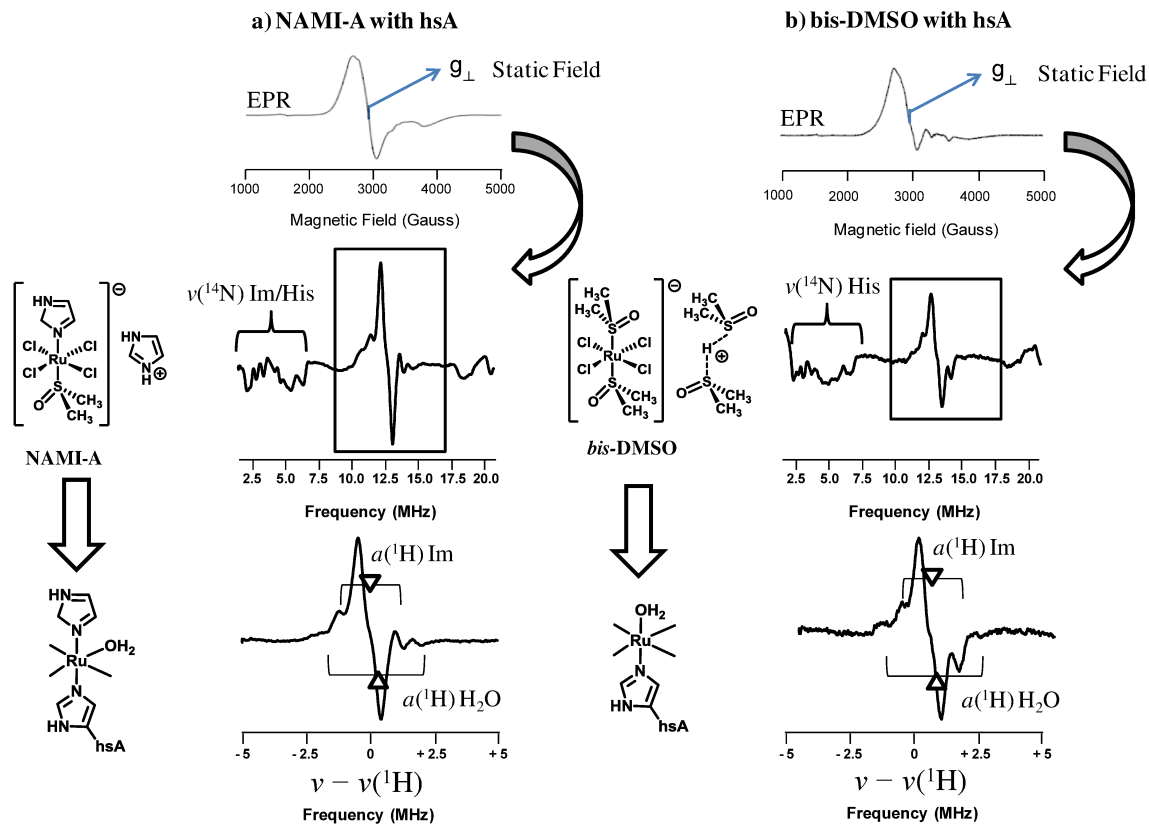


Figure 7-11 ENDOR of a) NAMI-A and the b) *bis*-DMSO complex following incubation with hsA for 30 minutes at 37 °C, pH 7.4.

NAMI-A. Lastly, NAMI-A was incubated with hsA under physiological conditions for 30 minutes (Appendix F – **Figure F-14c**) with the resulting protein-bound species analyzed by measuring the ENDOR spectrum at the average g values ($g_{\perp} = 2.36$ and $g_{||} = 1.76$) of the two dominant protein-bound species (*NAMI-A-hsA-1/2*). In the ^1H region when the field was set to g_{\perp} (**Figure 7-11c**), a similar ENDOR signal to that of the *bis*-DMSO complexes after incubation with hsA was observed. As observed with the *bis*-DMSO complexes, couplings from coordinated imidazole (2.6 MHz) and water (3.9 MHz) are also observed around $\nu(^1\text{H})$. As observed with the *bis*-DMSO complex following incubation with hsA, when the field was set to g_{\perp} , no resolved signals from coordinated ligands were observed in the ^1H region. In the ^{14}N region of the spectrum at both g_{\perp} and $g_{||}$, (Appendix F – **Figure F-17**), peaks were observed that were not detected in the ENDOR spectrum of the complex in buffer (**Figures 7-8 and 7-9**). Overall, the observation of ^1H ENDOR consistent with the imidazole ligand and the emergence of new ^{14}N peaks suggest that the original imidazole ligand is maintained and that histidine coordination likely has occurred. To aid in determining the exact nature of the coordinating nitrogen ligand, NAMI-A was incubated with histidine in solution.

7.4.4. Interactions with Individual Amino Acids

As shown above and in Chapters 2 and 3, both KP1019 and NAMI-A bind to serum proteins, with hsA likely the dominant target *in vivo*. It has been widely hypothesized that coordination occurs via surface histidine residues;^{57,202,287} however this has not been validated experimentally. In an effort to identify the amino acid residues responsible for the observed hsA coordination, each complex was incubated with alanine, cysteine, and histidine. The samples were then monitored using EPR and ENDOR for any interactions between the Ru(III) complexes and the individual amino acids. Additional analysis of the *bis*-DMSO complex with each amino acid was also performed to assist with the interpretation of the ENDOR spectra for NAMI-A.

KP1019. Solutions of KP1019 incubated with alanine, cysteine, and histidine at pH 7.4, 37 °C were each studied by EPR (Appendix F – **Figure F-18**). Initially, for each

amino acid, the EPR spectra were all identical, since unsubstituted KP1019 was observed. Following further incubation, minor amounts of precipitation was observed in all cases, which corresponded to a decrease in the observed signal intensity. Throughout the course of the experiment, however, no changes were observed in the EPR spectra of KP1019 with any of the amino acids. In each case, the parent compound persisted as the only observed signal (Appendix F – **Figures F-19 – F-21**). A representative sample of the complex after incubation with histidine for 30 minutes was further analyzed by ENDOR (Appendix F – **Figure F-22**), since this correlates with the hypothesized protein coordination mode. ENDOR was measured at g_{\perp} (2.64) of *KP1019-Axial*, since this was the most intense part of the EPR signal, and the resulting spectrum was indistinguishable from the free complex in buffer (**Figure 7-5**). These results indicate that KP1019 does not coordinate to any of the amino acids evaluated in this study, and that another amino acid, not evaluated here, is responsible for the observed protein-binding of KP1019 to hsA.

Bis-DMSO. As described in the previous section, the *bis*-DMSO complex was found to coordinate to hsA under physiological conditions. To aid in determining the amino acid residues responsible for this interaction, the three amino acids were incubated with the *bis*-DMSO complex, following the same procedure as above for KP1019. When the *bis*-DMSO complex was incubated with alanine and cysteine (Appendix F – **Figures F-23a and b**), the EPR spectra are similar to that of the free complex in solution. This was confirmed by spectral simulation (Appendix F – **Figures F-24 and F-25**), and demonstrates that the solution behaviour of the complex was unaffected by the presence of the amino acids. Furthermore, the solution darkened from a bright yellow to dark brown, as observed for the complex in buffer alone. These results demonstrate that neither alanine nor cysteine influence the solution behaviour of the *bis*-DMSO complex.

Upon incubation of the *bis*-DMSO complex with histidine, the spectra for up to 20 minutes of incubation are similar to the complex in buffer alone (Appendix F – **Figure F-23c**). After 30 minutes of incubation, however, a significant change is observed, as a new uniaxial signal is seen in the EPR spectrum. Simulation of this signal (Appendix F – **Figure F-26**) gave spectral parameters ($g_{\perp} = 2.37$ and $g_{||} = 1.81$) for this new species that

are remarkably similar to those of *NAMI-A-H₂O* ($g_{\perp} = 2.30$ and $g_{||} = 1.88$) in buffer. This is in line with the expectation of histidine coordination to the Ru(III) metal centre via its imidazole side chain, where replacement of the axial DMSO ligand of *bis-DMSO-H₂O* gives the observed uniaxial signal. Further incubation up to 60 minutes leads to an increase in this signal, coinciding with a loss in the signal from the parent compound.

NAMI-A. As for the other complexes, NAMI-A was incubated with individual amino acids in an effort to identify the residue responsible for hSA coordination. The EPR spectra of the alanine and cysteine samples (Appendix F – **Figures F-27a and b**) are indistinguishable from NAMI-A following incubation in PBS, since only one uniaxial signal is observed at the early time points, followed by the incorporation of a second uniaxial signal due to aqueous ligand exchange of the axial DMSO ligand. This was confirmed by spectral simulation for both solutions which showed that only two species were observed for the duration of the experiment (Appendix F – **Figures F-28 and F-30**). The simulation parameters used were identical to those of the parent complex (*NAMI-A* with $g_{\perp} = 2.47$ and $g_{||} = 1.72$) and its mono-aquated derivative (*NAMI-A-H₂O* with $g_{\perp} = 2.30$ and $g_{||} = 1.88$), previously identified in Chapter 3. This indicates that neither alanine nor cysteine coordinate with NAMI-A in solution, as observed for the *bis*-DMSO complex. Further confirmation was obtained from the ENDOR spectra of NAMI-A following 30 minutes of incubation with alanine and cysteine, since the peaks observed were similar to that of the parent compound in buffer (Appendix F – **Figures F-29 and F-31**).

The EPR spectrum following incubation with histidine is similar at early time points to the complex in buffer. After 30 minutes of incubation, a new broad signal that is very similar to NAMI-A following incubation with serum proteins (Chapter 3) is observed (**Figure 7-12a**). This was further confirmed by spectral simulation (Appendix F – **Figure F-32**), since similar parameters were used to that of *NAMI-A-hsA-2* ($g = 2.54$, 2.26 , 1.76 and $LW = 450, 175, 350$ Gauss) with: $g = [2.52, 2.29, 1.78]$ and $LW = [175, 175, 400]$ Gauss, labelled *NAMI-A-His* in Appendix F – **Figure F-32**. The resulting ENDOR spectra was measured with the field set at $g_{(1+2)/2}$ (2.41) and g_3 (1.78), since these

represented the regions of maximum signal intensity in the EPR spectrum. The ENDOR spectrum of NAMI-A after incubation with histidine is similar to that of the complex with hsA in both the ^{14}N and ^1H regions of the spectrum (**Figure 7-12b** and Appendix F – **Figure F-33**). In the ^1H region, when the field was set to g_{\perp} , couplings from coordinated imidazole (2.3 MHz) and water (4.1 MHz) are observed around $\nu(^1\text{H})$. As observed for the hsA-bound sample, when the field is set at g_{\parallel} , signals from coordinated ligands are not resolved. In the ^{14}N region, at both g_{\perp} and g_{\parallel} , several low intensity peaks are observed. Taken together, these results suggest that imidazole ligands are coordinated to the Ru(III) metal centre.

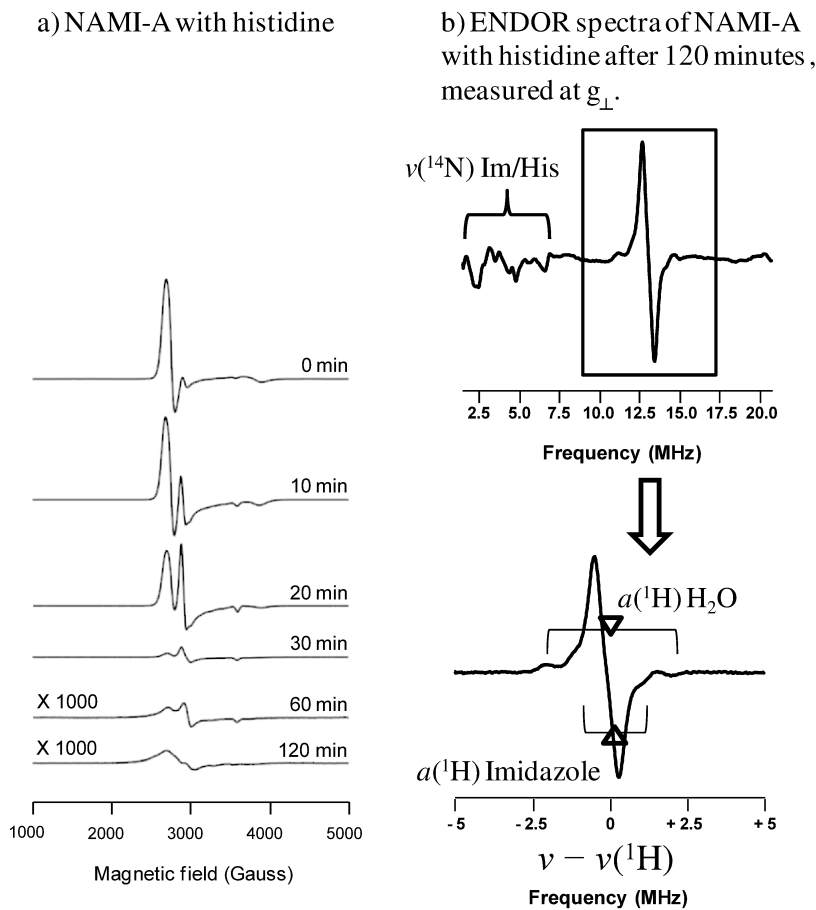


Figure 7-12 ENDOR spectra of a) NAMI-A following incubation with histidine and b) the resulting ENDOR spectrum of the 120 minute sample showing the full spectrum and centred at the proton Larmor frequency.

Since NAMI-A has an imidazole ligand it is difficult to resolve differences in the ENDOR spectra that might arise from coordination of histidine. However, based on the similarity in the EPR data from the complex incubated with hsA and histidine interactions, histidine coordination occurs is inferred in the case of the protein.

7.5. Conclusion

The use of isotopically labelled derivatives of NAMI-A and the related *bis*-DMSO complex facilitated ENDOR studies of the solution behaviour, hsA binding, and amino acid interactions of NAMI-A. This provided a greater understanding of the speciation of the complexes under physiological conditions. In particular, rapid exchange of the *bis*-DMSO complex was observed, such that the parent compound was not detected following dissolution in buffer. ENDOR studies of NAMI-A and the *bis*-DMSO complex with hsA suggest a similar coordination environment around each ruthenium metal centre, since the ^1H and ^{14}N regions for both complexes following incubation with hsA were very similar. This was confirmed by incubating each complex with individual amino acids, with only histidine reproducing signals that were observed in the hsA spectra. This is the first direct detection of histidine coordination, confirming the widely cited hypothesis in the literature. Interestingly, despite the similarities in the EPR for hsA coordination between the complexes, no binding interactions were observed for KP1019 with any of the amino acids used. This suggests that hsA coordination of KP1019 may occur with a different amino acid, which should be determined in further studies.

8. Future Directions

As shown in this thesis, ruthenium(III) anticancer agents are ideal candidates to be analyzed using EPR. Since it can selectively probe the ligand environment and greatly facilitates the studies of such compounds under biological conditions, this technique only observes the environment around the paramagnetic metal centre. This approach to study the physiological speciation of Ru(III) anticancer compounds has developed from a novel idea into a promising area of research. These studies have suggested additional potential projects, which are each outlined briefly below.

8.1. EPR of Ruthenium(III) Anticancer Agents in Biological Media

The next step in the study of Ru(III) anticancer compounds would be to monitor their behaviour in a variety of biological situations. One example would be whole human blood. This would represent the most accurate depiction of the complexes following intravenous administration. From the studies on the interactions of KP1019 and NAMI-A in human serum, Chapters 2 and 3 respectively, it is anticipated that hsA will be the dominant protein interaction. These previous studies will greatly facilitate interpretation, and simulation, of the acquired EPR spectra. Preliminary results indicate that the Ru(III) oxidation state is maintained, while broad features are observed in the spectrum, suggesting biomolecule interactions. Additionally, with the recent success of the *in vitro* analysis of NAMI-A and KP1019 in *Saccharomyces cerevisiae* cells (Chapter 6), further studies of these complexes in human cancer cells and tumour tissue would aid in determining their respective biological targets, and if their Ru(III) oxidation state is maintained in hypoxic tumour environments.

8.2. Relating the Binding Constants of Ru(III) Complexes to Antimetastatic Activity

As outlined in Chapter 4, the synthesis of complexes that exhibit enhancement of non-coordinate interactions with hsA was achieved using pyridine analogues of NAMI/NAMI-A. The next step in the characterization of these complexes is to determine their relative antimetastatic activity, and the effect non-coordinate protein interactions have on their observed activity. To determine the potential impact of hsA acting as a Ru(III) drug transporter the binding constants for each complex to the protein should be determined. This has been done previously for both KP1019 and KP1339 using fluorescence.¹⁸⁹ Using similar experimental methods, the binding constants to hsA of all synthesized pyridine-based NAMI-A analogues, along with NAMI-A, could be determined.

Appropriate fluorescent probes in these experiments would be warfarin for site I^{81,340} and dansylglycine for site II.³⁴¹ Each probe (10 µM) should be incubated individually with hsA (20 µM) for 30 minutes prior to treatment with Ru(III) complexes. The resulting solution should be incubated at 37 °C within the fluorimeter, with measurements taken at short time intervals. The excitation wavelength is 310 nm for warfarin and 335 nm for dansylglycine, with the resulting emission spectrum collection beginning at 330 and 420 nm respectively. The concentration of each Ru(III) complex should be varied, to ensure the displacement of the fluorescent probe. The binding constant of each Ru(III) complex to hsA can be determined by comparing the initial fluorescence from the probe in the absence of the complex with the decrease in fluorescence observed upon incubation with each Ru(III) complex.¹⁸⁹ Relating the binding constants of each compound to their observed antimetastatic activity would be of importance in future drug design considerations.

8.3. Determining the Binding Constants of Ru(III) Anticancer Agents to hsTf

As described above, the binding constants of Ru(III) anticancer complexes to the other highly important iron-transporting serum protein, hsTf, could also be determined. It

is known that hsTf can bind many metals other than iron.⁵⁸ Previous studies have probed not only metal-protein binding parameters,^{342,343} but also the binding constant of Fe(III) to hsTf.³⁴⁴ Additionally, competitive binding to hsTf has been probed using different metals such as Cr(III),³⁴⁵ Ni(II),³⁴⁵ and Ti(IV),^{346,347} with Ti(IV) binding better to hsTf than Fe(III). The diversity of metal ion binding by hsTf, along with the upregulation of hsTf receptors on rapidly dividing tumour cells, has made this serum protein a desirable targeting agent in the transportation and delivery of several anticancer agents.⁵⁸ The binding constant for NAMI-A to hsTf has been previously determined,¹⁸⁴ however it remains unknown for other Ru(III) anticancer agents, particularly KP1019 and KP1339. Unlike hsA, there are no known fluorescent probes for hsTf which have an affinity for either binding site. The protein itself, however, does contain 8 tryptophan residues, which display fluorescence that is sensitive to changes in their surrounding environment.^{348,349} Using a similar experimental protocol to above,¹⁷⁰ KP1019 and KP1339 could be incubated with apo-hsTf, at a range of molar ratios. The resulting solutions should be incubated at 37 °C within the fluorometer, with measurements taken at short time intervals. Here, the excitation wavelength would be 295 nm, with emission detected between 305 and 500 nm. The quenching of the observed fluorescence would be used to determine the binding constant of each complex to hsTf, which is an important consideration for the proposed mechanism of action of these complexes.

8.4. Synthesis of Further Hydrophobic Ru(III) Complexes

As shown in both Chapters 4 and 5, by incorporating hydrophobic axial ligands in the design of Ru(III) anticancer agents, non-coordinate protein interactions can be significantly stabilized. In some cases, this has allowed complexes with poor aqueous solubility to be dissolved and made available for interactions with cancer cells (Section 5.3.8). This idea can be extended using hydrophobic imidazole ligands, in an attempt to further understand the importance of the axial ligands with regards to observed anticancer activity.

Previous studies have synthesized NAMI-A analogues using various azole ligands^{149,150} in addition to imidazole derivatives using benzimidazole,³⁵⁰ and

histamine.²⁵⁴ As outlined in **Figure 8-1**, there are several imidazole ligands that are commercially available that could be used to synthesize a small library of compounds, gradually increasing the hydrophobic nature of the axial ligand. Additionally, by incorporating fluorine into the ligand backbone, further spectroscopic information can be obtained using ¹⁹F NMR. There is precedence for such complexes in the literature, since the Ru(III) complex with 1-methylimidazole^{150,351} has been previously reported,^{140,315} however all other complexes are novel. The synthesis of these compounds could follow the synthetic route for the pyridine-based analogues of NAMI-A that was established in Chapter 4.²⁷⁷

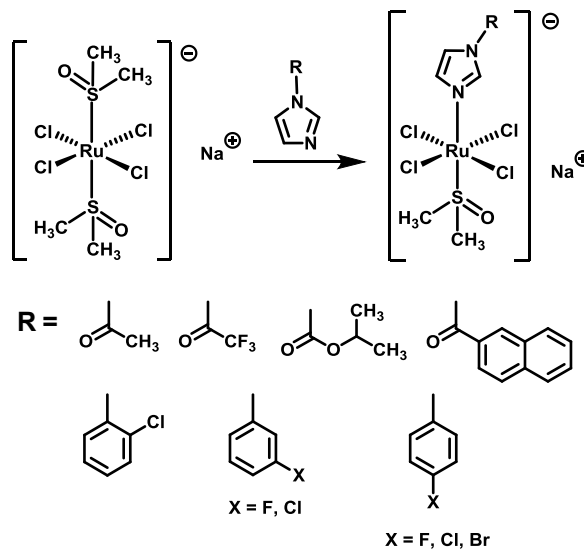


Figure 8-1 Scheme to synthesize further Ru(III) compounds for potential anticancer activity.

8.5. EPR of Other Paramagnetic Anticancer Metal Complexes

Due to the successful analysis of Ru(III) anticancer agents using EPR, it is only logical to study other paramagnetic drugs using this technique. Currently, several Cu(II) complexes have shown promising anticancer activities against a human cervical epidermoid carcinoma cell line (ME180).³⁵²⁻³⁵⁵ This has led to the development of further derivatives with differing biological activities.^{333,338} Using EPR, the solution behaviour and protein interactions of Cu(II) complexes could be probed in an effort to better

understand their mechanism of action, and similar to above, contribute to their design and development.

8.6. Concluding Statements

This thesis has demonstrated the value of EPR and ENDOR spectroscopy to probe the solution behaviour, protein interactions, and cellular speciation of Ru(III) anticancer agents. Initial studies were on the clinically successful compounds KP1019 and NAMI-A. Following dissolution in physiological buffer, complex solution behaviour was observed, with ligand-exchange resulting in several aquated derivatives for NAMI-A and precipitation for KP1019. Upon exposure to serum proteins, aqueous ligand-exchange is diminished, while interactions with hsA and hsTf were observed for both complexes. Both complexes formed non-coordinate interactions with each protein, which were subsequently converted to direct protein coordination. In the case of KP418, the cytotoxic imidazole analogue of KP1019, these interactions occurred at a significantly slower rate, which led to the observation that the axial ligands mediate non-coordinate protein binding. This motivated the design and synthesis of new compounds targeting hydrophobic interactions with hsA. It was found that by increasing the hydrophobicity of the axial heterocyclic nitrogen ligand non-coordinate hsA interactions could be significantly stabilized. This can potentially enhance the transport of the Ru(III) complexes, thereby increasing their bioavailability. This was a significant discovery, and can be of importance in the design of future therapeutic agents.

Further insight into the nature of the coordinative hsA interactions was gained using ENDOR spectroscopy. Using a *bis*-DMSO complex to facilitate the interpretation of the resulting ENDOR spectra of NAMI-A, it was found that coordination via histidine imidazoles is favoured for both complexes. Additionally, the hsA-coordinated species are aquated, confirming the results from the EPR studies where both the parent compound and its aquated derivatives were observed to form coordinate interactions with hsA. For KP1019, no histidine coordination was observed, suggesting that another amino acid is responsible for hsA binding.

In addition to the synthesis of new compounds, further analysis into the biological targets of KP1019 and NAMI-A was achieved by performing *in vitro* EPR. For both complexes, non-coordinate and coordinate interactions with cellular components influenced the behaviour of the complexes. From these studies, KP1019 was found to interact predominantly with cytoplasmic proteins and the mitochondria, while NAMI-A was observed to bind with the cell wall. These differences in cellular speciation are reflected in their observed anticancer activity, and aid in understanding the mechanism of action of both complexes.

In conclusion, the application of detailed spectroscopic studies, complemented with ligand design and the synthesis of new compounds, has provided new insight into the *in vivo* behaviour of the clinically successful Ru(III) anticancer compounds. The importance of aqueous ligand-exchange and protein binding has provided inspiration for the development of new Ru(III) anticancer drugs, targeting non-coordinate protein interactions to increase the stability and bioavailability of the complex.

References

- (1) Rosenberg, B.; Vancamp, L.; Krigas, T. *Nature* **1965**, *205*, 698.
- (2) Rosenberg, B.; Vancamp, L.; Trosko, J. E.; Mansour, V. H. *Nature* **1969**, *222*, 385.
- (3) Jakupcic, M. A.; Galanski, M.; Arion, V. B.; Hartinger, C. G.; Keppler, B. K. *Dalton Trans.* **2008**, 183.
- (4) Dyson, P. J.; Sava, G. *Dalton Trans.* **2006**, 1929.
- (5) Giaccone, G. *Drugs* **2000**, *59*, 9.
- (6) Wang, D.; Lippard, S. J. *Nat. Rev. Drug Discovery* **2005**, *4*, 307.
- (7) Reedijk, J. *Proc. Natl. Acad. Sci. U. S. A.* **2003**, *100*, 3611.
- (8) Reedijk, J. *Pure Appl. Chem.* **1987**, *59*, 181.
- (9) Zhen, W. P.; Link, C. J.; Oconnor, P. M.; Reed, E.; Parker, R.; Howell, S. B.; Bohr, V. A. *Mol. Cell. Biol.* **1992**, *12*, 3689.
- (10) Mamenta, E. L.; Poma, E. E.; Kaufmann, W. K.; Delmastro, D. A.; Grady, H. L.; Chaney, S. G. *Cancer Res.* **1994**, *54*, 3500.
- (11) Kool, M.; deHaas, M.; Scheffer, G. L.; Scheper, R. J.; vanEijk, M. J. T.; Juijn, J. A.; Baas, F.; Borst, P. *Cancer Res.* **1997**, *57*, 3537.
- (12) Hambley, T. W. *Coord. Chem. Rev.* **1997**, *166*, 181.
- (13) Kelland, L. R.; Abel, G.; McKeage, M. J.; Jones, M.; Goddard, P. M.; Valenti, M.; Murrer, B. A.; Harrap, K. R. *Cancer Res.* **1993**, *53*, 2581.
- (14) Bitha, P.; Carvajal, S. G.; Citarella, R. V.; Child, R. G.; Delossantos, E. F.; Dunne, T. S.; Durr, F. E.; Hlavka, J. J.; Lang, S. A.; Lindsay, H. L.; Morton, G. O.; Thomas, J. P.; Wallace, R. E.; Lin, Y. I.; Haltiwanger, R. C.; Pierpont, C. G. *J. Med. Chem.* **1989**, *32*, 2015.
- (15) Tashiro, T.; Kawada, Y.; Sakurai, Y.; Kidani, Y. *Biomed. Pharmacother.* **1989**, *43*, 251.
- (16) Khokhar, A. R.; Albaker, S.; Krakoff, I. H.; Perezsoler, R. *Cancer Chemother. Pharmacol.* **1989**, *23*, 219.
- (17) Rixe, O.; Ortuzar, W.; Alvarez, M.; Parker, R.; Reed, E.; Paull, K.; Fojo, T. *Biochem. Pharmacol.* **1996**, *52*, 1855.
- (18) Kelland, L. R. *Drugs* **2000**, *59*, 1.

- (19) Gibson, D. *Dalton Trans.* **2009**, 10681.
- (20) Wong, E.; Giandomenico, C. M. *Chem. Rev.* **1999**, 99, 2451.
- (21) Natile, G.; Coluccia, M. *Coord. Chem. Rev.* **2001**, 216, 383.
- (22) Lovejoy, K. S.; Lippard, S. J. *Dalton Trans.* **2009**, 10651.
- (23) Ronconi, L.; Fregona, D. *Dalton Trans.* **2009**, 10670.
- (24) Komeda, S.; Casini, A. *Curr. Top. Med. Chem.* **2012**, 12, 219.
- (25) Alessio, E. *Bioinorganic Medicinal Chemistry*; Wiley-VCH: Weinheim, 2011.
- (26) Durig, J. R.; Danneman, J.; Behnke, W. D.; Mercer, E. E. *Chem. Biol. Interact.* **1976**, 13, 287.
- (27) Clarke, M. J. *Met. Ions Biol. Syst.* **1980**, 11, 231.
- (28) Clarke, M. J.; Zhu, F. C.; Frasca, D. R. *Chem. Rev.* **1999**, 99, 2511.
- (29) Alessio, E.; Mestroni, G.; Bergamo, A.; Sava, G. *Metal Ions in Biological Systems, Vol 42: Metal Complexes in Tumor Diagnosis and as Anticancer Agents* **2004**, 42, 323.
- (30) Antonarakis, E. S.; Emadi, A. *Cancer Chemother. Pharmacol.* **2010**, 66, 1.
- (31) Bergamo, A.; Sava, G. *Dalton Transactions* **2011**, 40, 7817.
- (32) Meggers, E. *Curr. Opin. Chem. Biol.* **2007**, 11, 287.
- (33) Reedijk, J. *Platinum Met. Rev.* **2008**, 52, 2.
- (34) Allardyce, C. S.; Dyson, P. J. *Platinum Met. Rev.* **2001**, 45, 62.
- (35) Kostova, I. *Curr. Med. Chem.* **2006**, 13, 1085.
- (36) Sherman, S. E.; Lippard, S. J. *Chem. Rev.* **1987**, 87, 1153.
- (37) Meggers, E.; Atilla-Gokcumen, G. E.; Bregman, H.; Maksimoska, J.; Mulcahy, S. P.; Pagano, N.; Williams, D. S. *Synlett* **2007**, 1177.
- (38) Meggers, E.; Atilla-Gokcumen, G. E.; Gruendler, K.; Frias, C.; Prokop, A. *Dalton Trans.* **2009**, 10882.
- (39) Debreczeni, J. E.; Bullock, A. N.; Atilla, G. E.; Williams, D. S.; Bregman, H.; Knapp, S.; Meggers, E. *Angew. Chem. Int. Ed.* **2006**, 45, 1580.
- (40) Williams, D. S.; Atilla, G. E.; Bregman, H.; Arzoumanian, A.; Klein, P. S.; Meggers, E. *Angew. Chem. Int. Ed.* **2005**, 44, 1984.
- (41) Seddon, E. A.; Seddon, K. R. *The Chemistry of Ruthenium*; Elsevier: Amsterdam; New York, 1984.
- (42) Reedijk, J. *Macromol. Symp.* **2008**, 270, 193.
- (43) Taube, H. *Chem. Rev.* **1951**, 50, 69.
- (44) Page, S. *Educ. Chem.* **2012**, 49, 26.

- (45) Reisner, E.; Arion, V. B.; Fatima, M.; da Silva, C. G.; Lichtenecker, R.; Eichinger, A.; Keppler, B. K.; Kukushkin, V. Y.; Pombeiro, A. J. L. *Inorg. Chem.* **2004**, *43*, 7083.
- (46) Reisner, E.; Arion, V. B.; Keppler, B. K.; Pombeiro, A. J. L. *Inorg. Chim. Acta* **2008**, *361*, 1569.
- (47) Gailer, J. *ISRN Chromatography* **2013**, *1*.
- (48) Dabrowiak, J. C. *Metals in Medicine*; Wiley: Hoboken, N.J., 2009.
- (49) Clarke, M. J. *Coord. Chem. Rev.* **2002**, *232*, 69.
- (50) Palmer, B. D.; Wilson, W. R.; Pullen, S. M.; Denny, W. A. *J. Med. Chem.* **1990**, *33*, 112.
- (51) Biskupiak, J. E.; Krohn, K. A. *J. Nucl. Med.* **1993**, *34*, 411.
- (52) Wike-Hooley, J. L.; Haveman, J.; Reinhold, H. S. *Radiother. Oncol.* **1984**, *2*, 343.
- (53) Schluga, P.; Hartinger, C. G.; Egger, A.; Reisner, E.; Galanski, M.; Jakupc, M. A.; Keppler, B. K. *Dalton Trans.* **2006**, 1796.
- (54) Bergamo, A.; Gaiddon, C.; Schellens, J. H. M.; Beijnen, J. H.; Sava, G. *J. Inorg. Biochem.* **2012**, *106*, 90.
- (55) Graf, N.; Lippard, S. J. *Adv. Drug Del. Rev.* **2012**, *64*, 993.
- (56) Mangiapia, G.; D'Errico, G.; Simeone, L.; Irace, C.; Radulescu, A.; Di Pascale, A.; Colonna, A.; Montesarchio, D.; Paduano, L. *Biomaterials* **2012**, *33*, 3770.
- (57) Timerbaev, A. R.; Hartinger, C. G.; Aleksenko, S. S.; Keppler, B. K. *Chem. Rev.* **2006**, *106*, 2224.
- (58) Sun, H. Z.; Li, H. Y.; Sadler, P. J. *Chem. Rev.* **1999**, *99*, 2817.
- (59) Sava, G.; Bergamo, A. *Int. J. Oncol.* **2000**, *17*, 353.
- (60) Allardyce, C. S.; Dorcier, A.; Scolaro, C.; Dyson, P. J. *Appl. Organomet. Chem.* **2005**, *19*, 1.
- (61) Galanski, M.; Arion, V. B.; Jakupc, M. A.; Keppler, B. K. *Curr. Pharm. Des.* **2003**, *9*, 2078.
- (62) Kratz, F.; Messori, L. *J. Inorg. Biochem.* **1993**, *49*, 79.
- (63) Dejong, G.; Vandijk, J. P.; Vaneijk, H. G. *Clin. Chim. Acta* **1990**, *190*, 1.
- (64) Macgillivray, R. T. A.; Mendez, E.; Shewale, J. G.; Sinha, S. K.; Linebackzins, J.; Brew, K. *J. Biol. Chem.* **1983**, *258*, 3543.
- (65) Macgillivray, R. T. A.; Mendez, E.; Sinha, S. K.; Sutton, M. R.; Linebackzins, J.; Brew, K. *Proc. Natl. Acad. Sci. U. S. A.* **1982**, *79*, 2504.
- (66) Ponka, P.; Lok, C. N. *Int. J. Biochem. Cell Biol.* **1999**, *31*, 1111.
- (67) Bali, P. K.; Zak, O.; Aisen, P. *Biochemistry* **1991**, *30*, 324.

- (68) Costa Pessoa, J.; Tomaz, I. *Curr. Med. Chem.* **2010**, *17*, 3701.
- (69) Harris, W. R. *Structure and Bonding*; Springer Verlag: Berlin, 1998; Vol. 92.
- (70) Harris, W. R.; Wang, Z. P.; Brook, C.; Yang, B. S.; Islam, A. *Inorg. Chem.* **2003**, *42*, 5880.
- (71) Beyer, U.; Roth, T.; Schumacher, P.; Maier, G.; Unold, A.; Frahm, A. W.; Fiebig, H. H.; Unger, C.; Kratz, F. *J. Med. Chem.* **1998**, *41*, 2701.
- (72) Wang, J.; Tian, S.; Petros, R. A.; Napier, M. E.; DeSimone, J. M. *J. Am. Chem. Soc.* **2010**, *132*, 11306.
- (73) Kratz, F.; Beyer, U.; Roth, T.; Tarasova, N.; Collery, P.; Lechenault, F.; Cazabat, A.; Schumacher, P.; Unger, C.; Falken, U. *J. Pharm. Sci.* **1998**, *87*, 338.
- (74) Pongratz, M.; Schluga, P.; Jakupc, M. A.; Arion, V. B.; Hartinger, C. G.; Allmaier, G.; Keppler, B. K. *J. Anal. At. Spectrom.* **2004**, *19*, 46.
- (75) Quinlan, G. J.; Martin, G. S.; Evans, T. W. *Hepatology* **2005**, *41*, 1211.
- (76) Varshney, A.; Sen, P.; Ahmad, E.; Rehan, M.; Subbarao, N.; Khan, R. H. *Chirality* **2010**, *22*, 77.
- (77) Colmenarejo, G. *Med. Res. Rev.* **2003**, *23*, 275.
- (78) Kragh-Hansen, U.; Chuang, V. T. G.; Otagiri, M. *Biol. Pharm. Bull.* **2002**, *25*, 695.
- (79) Ivanov, A. I.; Christodoulou, J.; Parkinson, J. A.; Barnham, K. J.; Tucker, A.; Woodrow, J.; Sadler, P. J. *J. Biol. Chem.* **1998**, *273*, 14721.
- (80) Petitpas, I.; Bhattacharya, A. A.; Twine, S.; East, M.; Curry, S. *J. Biol. Chem.* **2001**, *276*, 22804.
- (81) Sudlow, G.; Birkett, D. J.; Wade, D. N. *Mol. Pharmacol.* **1975**, *11*, 824.
- (82) Curry, S.; Mandelkow, H.; Brick, P.; Franks, N. *Nat. Struct. Biol.* **1998**, *5*, 827.
- (83) Sugio, S.; Kashima, A.; Mochizuki, S.; Noda, M.; Kobayashi, K. *Protein Eng.* **1999**, *12*, 439.
- (84) Petitpas, I.; Grune, T.; Bhattacharya, A. A.; Curry, S. *J. Mol. Biol.* **2001**, *314*, 955.
- (85) Sudlow, G.; Birkett, D. J.; Wade, D. N. *Mol. Pharmacol.* **1976**, *12*, 1052.
- (86) Ascoli, G. A.; Domenici, E.; Bertucci, C. *Chirality* **2006**, *18*, 667.
- (87) Rozga, M.; Sokolowska, M.; Protas, A. M.; Bal, W. *J. Biol. Inorg. Chem.* **2007**, *12*, 913.
- (88) Bennett, M. A. *Coord. Chem. Rev.* **1997**, *166*, 225.
- (89) Dyson, P. J. *Chimia* **2007**, *61*, 698.
- (90) Dougan, S. J.; Sadler, P. J. *Chimia* **2007**, *61*, 704.

- (91) Ang, W. H.; Dyson, P. J. *Eur. J. Inorg. Chem.* **2006**, 4003.
- (92) Gasser, G.; Ott, I.; Metzler-Nolte, N. *J. Med. Chem.* **2011**, 54, 3.
- (93) Scolaro, C.; Chaplin, A. B.; Hartinger, C. G.; Bergamo, A.; Cocchietto, M.; Keppler, B. K.; Sava, G.; Dyson, P. J. *Dalton Trans.* **2007**, 5065.
- (94) Scolaro, C.; Geldbach, T. J.; Rochat, S.; Dorcier, A.; Gossens, C.; Bergamo, A.; Cocchietto, M.; Tavernelli, I.; Sava, G.; Rothlisberger, U.; Dyson, P. J. *Organometallics* **2006**, 25, 756.
- (95) Allardyce, C. S.; Dyson, P. J.; Ellis, D. J.; Salter, P. A.; Scopelliti, R. *J. Organomet. Chem.* **2003**, 668, 35.
- (96) Yan, Y. K.; Melchart, M.; Habtemariam, A.; Sadler, P. J. *Chem. Commun.* **2005**, 4764.
- (97) Suess-Fink, G. *Dalton Trans.* **2009**, 39, 1673.
- (98) Morris, R. E.; Aird, R. E.; Murdoch, P. D.; Chen, H. M.; Cummings, J.; Hughes, N. D.; Parsons, S.; Parkin, A.; Boyd, G.; Jodrell, D. I.; Sadler, P. J. *J. Med. Chem.* **2001**, 44, 3616.
- (99) Chen, H. M.; Parkinson, J. A.; Parsons, S.; Coxall, R. A.; Gould, R. O.; Sadler, P. J. *J. Am. Chem. Soc.* **2002**, 124, 3064.
- (100) Chen, H. M.; Parkinson, J. A.; Morris, R. E.; Sadler, P. J. *J. Am. Chem. Soc.* **2003**, 125, 173.
- (101) Aird, R. E.; Cummings, J.; Ritchie, A. A.; Muir, M.; Morris, R. E.; Chen, H.; Sadler, P. J.; Jodrell, D. I. *Br. J. Cancer* **2002**, 86, 1652.
- (102) Scolaro, C.; Bergamo, A.; Brescacin, L.; Delfino, R.; Cocchietto, M.; Laurenczy, G.; Geldbach, T. J.; Sava, G.; Dyson, P. J. *J. Med. Chem.* **2005**, 48, 4161.
- (103) Vock, C. A.; Scolaro, C.; Phillips, A. D.; Scopelliti, R.; Sava, G.; Dyson, P. J. *J. Med. Chem.* **2006**, 49, 5552.
- (104) Allardyce, C. S.; Dyson, P. J.; Ellis, D. J.; Heath, S. L. *Chem. Commun.* **2001**, 1396.
- (105) Chatterjee, S.; Kundu, S.; Bhattacharyya, A.; Hartinger, C. G.; Dyson, P. J. *J. Biol. Inorg. Chem.* **2008**, 13, 1149.
- (106) Bergamo, A.; Masi, A.; Dyson, P. J.; Sava, G. *Int. J. Oncol.* **2008**, 33, 1281.
- (107) Hartinger, C. G.; Zorbas-Seifried, S.; Jakupc, M. A.; Kynast, B.; Zorbas, H.; Keppler, B. K. *Journal of Inorganic Biochemistry* **2006**, 100, 891.
- (108) Levina, A.; Mitra, A.; Lay, P. A. *Metallomics* **2009**, 1, 458.
- (109) Hartinger, C. G.; Jakupc, M. A.; Zorbas-Seifried, S.; Groessl, M.; Egger, A.; Berger, W.; Zorbas, H.; Dyson, P. J.; Keppler, B. K. *Chem. Biodivers.* **2008**, 5, 2140.

- (110) Lentz, F.; Drescher, A.; Lindauer, A.; Henke, M.; Hilger, R. A.; Hartinger, C. G.; Scheulen, M. E.; Dittrich, C.; Keppler, B. K.; Jaehde, U. *Anti-Cancer Drugs* **2009**, *20*, 97.
- (111) Rademaker-Lakhai, J. M.; van den Bongard, D.; Pluim, D.; Beijnen, J. H.; Schellens, J. H. M. *Clin. Cancer Res.* **2004**, *10*, 3717.
- (112) Aitken, J. B.; Antony, S.; Weekley, C. M.; Lai, B.; Spiccia, L.; Harris, H. H. *Metalomics* **2012**, *4*, 1051.
- (113) Polec-Pawlak, K.; Abramski, J. K.; Ferenc, J.; Foteva, L. S.; Timerbaev, A. R.; Keppler, B. K.; Jarosz, M. *J. Chromatogr. A* **2008**, *1192*, 323.
- (114) Zhao, G.; Lin, H. *Curr. Med. Chem. - Anti-Cancer Agents* **2005**, *5*, 137.
- (115) Delferro, M.; Marchio, L.; Tegoni, M.; Tardito, S.; Franchi-Gazzola, R.; Lanfranchi, M. *Dalton Trans.* **2009**, 3766.
- (116) Groessl, M.; Reisner, E.; Hartinger, C. G.; Eichinger, R.; Semenova, O.; Timerbaev, A. R.; Jakupec, M. A.; Arion, V. B.; Keppler, B. K. *J. Med. Chem.* **2007**, *50*, 2185.
- (117) Wisniewski, M. Z.; Wietrzyk, J.; Opolski, A. *Arch. Immunol. Ther. Exp. (Warsz.)* **2000**, *48*, 51.
- (118) Anderson, C. M.; Taylor, I. R.; Tibbetts, M. F.; Philpott, J.; Hu, Y.; Tanski, J. M. *Inorg. Chem.* **2012**, *51*, 12917.
- (119) Higgins, S. L. H.; White, T. A.; Winkel, B. S. J.; Brewer, K. J. *Inorg. Chem.* **2011**, *50*, 463.
- (120) Herman, A.; Tanski, J. M.; Tibbetts, M. F.; Anderson, C. M. *Inorg. Chem.* **2008**, *47*, 274.
- (121) Ravera, M.; Gabano, E.; Baracco, S.; Sardi, M.; Osella, D. *Inorg. Chim. Acta* **2008**, *361*, 2879.
- (122) Groessl, M.; Hartinger, C. G.; Egger, A.; Keppler, B. K. *Metal Ions in Biology and Medicine* **2006**, *9*, 111.
- (123) Polec-Pawlak, K.; Abramski, J. K.; Semenova, O.; Hartinger, C. G.; Timerbaev, A. R.; Keppler, B. K.; Jarosz, M. *Electrophoresis* **2006**, *27*, 1128.
- (124) Bicek, A.; Turel, I.; Kanduser, M.; Miklavcic, D. *Bioelectrochemistry* **2007**, *71*, 113.
- (125) Sava, G.; Frausin, F.; Cocchietto, M.; Vita, F.; Podda, E.; Spessotto, P.; Furlani, A.; Scarcia, V.; Zabucchi, G. *Eur. J. Cancer* **2004**, *40*, 1383.
- (126) Alessio, E.; Mestroni, G.; Bergamo, A.; Sava, G. *Curr. Top. Med. Chem.* **2004**, *4*, 1525.
- (127) Sava, G.; Zorzet, S.; Turrin, C.; Vita, F.; Soranzo, M.; Zabucchi, G.; Cocchietto, M.; Bergamo, A.; DiGiovine, S.; Pezzoni, G.; Sartor, L.; Garbisa, S. *Clin. Cancer Res.* **2003**, *9*, 1898.

- (128) Bergamo, A.; Gagliardi, R.; Scarcia, V.; Furlani, A.; Alessio, E.; Mestroni, G.; Sava, G. *J. Pharmacol. Exp. Ther.* **1999**, 289, 559.
- (129) Keppler, B. K.; Rupp, W.; Juhl, U. M.; Endres, H.; Niebl, R.; Balzer, W. *Inorg. Chem.* **1987**, 26, 4366.
- (130) Reisner, E.; Arion, V. B.; Eichinger, A.; Kandler, N.; Giester, G.; Pombeiro, A. J. L.; Keppler, B. K. *Inorg. Chem.* **2005**, 44, 6704.
- (131) Batista, A. A.; Onofre, S. A.; Queiroz, S. L.; Oliva, G.; Fontes, M. R. M.; Nascimento, O. R. *J. Braz. Chem. Soc.* **1997**, 8, 641.
- (132) Lipponer, K.-G.; Vogel, E.; Keppler, B. K. *Met.-Based Drugs* **1996**, 3, 243.
- (133) Peti, W.; Pieper, T.; Sommer, M.; Keppler, B. K.; Giester, G. *Eur. J. Inorg. Chem.* **1999**, 1551.
- (134) Galeano, A.; Berger, M. R.; Keppler, B. K. *Arzneim.-Forsch.* **1992**, 42-1, 821.
- (135) Depenbrock, H.; Schmelcher, S.; Peter, R.; Keppler, B. K.; Weirich, G.; Block, T.; Rastetter, J.; Hanuske, A. R. *Eur. J. Cancer* **1997**, 33, 2404.
- (136) Kapitza, S.; Jakupc, M. A.; Uhl, M.; Keppler, B. K.; Marian, B. *Cancer Lett.* **2005**, 226, 115.
- (137) Kapitza, S.; Pongratz, M.; Jakupc, M. A.; Heffeter, P.; Berger, W.; Lackinger, L.; Keppler, B. K.; Marian, B. *J. Cancer Res. Clin. Oncol.* **2005**, 131, 101.
- (138) Kreuser, E. D.; Keppler, B. K.; Berdel, W. E.; Piest, A.; Thiel, E. *Semin. Oncol.* **1992**, 19, 73.
- (139) Heffeter, P.; Pongratz, M.; Steiner, E.; Chiba, P.; Jakupc, M. A.; Elbling, L.; Marian, B.; Korner, W.; Sevelda, F.; Micksche, M.; Keppler, B. K.; Berger, W. *J. Pharmacol. Exp. Ther.* **2005**, 312, 281.
- (140) Kratz, F.; Keppler, B. K.; Messori, L.; Smith, C.; Baker, E. N. *Met.-Based Drugs* **1994**, 1, 169.
- (141) Kersten, L.; Braunlich, H.; Keppler, B. K.; Gliesing, C.; Wendelin, M.; Westphal, J. *J. Appl. Toxicol.* **1998**, 18, 93.
- (142) Hudej, R.; Turel, I.; Kanduser, M.; Scancar, J.; Kranjc, S.; Sersa, G.; Miklavcic, D.; Jakupc, M. A.; Keppler, B. K.; Cemazar, M. *Anticancer Res.* **2010**, 30, 2055.
- (143) Heffeter, P.; Bock, K.; Atil, B.; Hoda, M. A. R.; Korner, W.; Bartel, C.; Jungwirth, U.; Keppler, B. K.; Micksche, M.; Berger, W.; Koellensperger, G. *J. Biol. Inorg. Chem.* **2010**, 15, 737.
- (144) Sava, G.; Pacor, S.; Zorzet, S.; Alessio, E.; Mestroni, G. *Pharmacol. Res.* **1989**, 21, 617.
- (145) Alessio, E. *Chem. Rev.* **2004**, 104, 4203.
- (146) Elford, B. C. *J. Phys. (Lond.)* **1970**, 209, 187.

- (147) Alessio, E.; Balducci, G.; Calligaris, M.; Costa, G.; Attia, W. M.; Mestroni, G. *Inorg. Chem.* **1991**, *30*, 609.
- (148) Anderson, C. M.; Herman, A.; Rochon, F. D. *Polyhedron* **2007**, *26*, 3661.
- (149) Sava, G.; Pacor, S.; Bergamo, A.; Cocchietto, M.; Mestroni, G.; Alessio, E. *Chem. Biol. Interact.* **1995**, *95*, 109.
- (150) Alessio, E.; Balducci, G.; Lutman, A.; Mestroni, G.; Calligaris, M.; Attia, W. M. *Inorg. Chim. Acta* **1993**, *203*, 205.
- (151) Sava, G.; Pacor, S.; Mestroni, G.; Alessio, E. *Clin. Exp. Metastasis* **1992**, *10*, 273.
- (152) Gagliardi, R.; Sava, G.; Pacor, S.; Mestroni, G.; Alessio, E. *Clin. Exp. Metastasis* **1994**, *12*, 93.
- (153) Sava, G.; Capozzi, I.; Clerici, K.; Gagliardi, G.; Alessio, E.; Mestroni, G. *Clin. Exp. Metastasis* **1998**, *16*, 371.
- (154) Sava, G.; Alessio, E.; Bergamo, A.; Mestroni, G. *Sulfoxide Ruthenium Complexes: Non-Toxic Tools for the Selective Treatment of Solid Tumour Metastases*, 1999; Vol. 1.
- (155) Sava, G.; Clerici, K.; Capozzi, I.; Cocchietto, M.; Gagliardi, R.; Alessio, E.; Mestroni, G.; Perbellini, A. *Anti-Cancer Drugs* **1999**, *10*, 129.
- (156) Zorzet, S.; Sorc, A.; Casarsa, C.; Cocchietto, M.; Sava, G. *Met.-Based Drugs* **2001**, *8*, 1.
- (157) Pintus, G.; Tadolini, B.; Posadino, A. M.; Sanna, B.; Debidda, M.; Bennardini, F.; Sava, G.; Ventura, C. *Eur. J. Biochem.* **2002**, *269*, 5861.
- (158) Zorzet, S.; Bergamo, A.; Cocchietto, M.; Sorc, A.; Gava, B.; Alessio, E.; Iengo, E.; Sava, G. *J. Pharmacol. Exp. Ther.* **2000**, *295*, 927.
- (159) Bergamo, A.; Zorzet, S.; Gava, B.; Sorc, A.; Alessio, E.; Iengo, E.; Sava, G. *Anti-Cancer Drugs* **2000**, *11*, 665.
- (160) Cocchietto, M.; Zorzet, S.; Sorc, A.; Sava, G. *Invest. New Drugs* **2003**, *21*, 55.
- (161) Pacor, S.; Zorzet, S.; Cocchietto, M.; Bacac, M.; Vadori, M.; Turrin, C.; Gava, B.; Castellarin, A.; Sava, G. *J. Pharmacol. Exp. Ther.* **2004**, *310*, 737.
- (162) Bacac, M.; Vadori, M.; Sava, G.; Pacor, S. *Cancer Immunol. Immunother.* **2004**, *53*, 1101.
- (163) Frausin, F.; Scarcia, V.; Cocchietto, M.; Furlani, A.; Serli, B.; Alessio, E.; Sava, G. *J. Pharmacol. Exp. Ther.* **2005**, *313*, 227.
- (164) Gava, B.; Zorzet, S.; Spessotto, P.; Cocchietto, M.; Sava, G. *J. Pharmacol. Exp. Ther.* **2006**, *317*, 284.
- (165) Bergamo, A.; Sava, G. *Dalton Trans.* **2007**, 1267.
- (166) Aragon-Ching, J. B.; Zujewski, J. A. *Clin. Cancer Res.* **2007**, *13*, 1644.

- (167) Reya, T.; Morrison, S. J.; Clarke, M. F.; Weissman, I. L. *Nature* **2001**, *414*, 105.
- (168) Coghlin, C. M., Graeme I *J. Pathol.* **2010**, *222*, 1.
- (169) Vadori, M.; Pacor, S.; Vita, F.; Zorzet, S.; Cocchietto, M.; Sava, G. *J. Inorg. Biochem.* **2013**, *118*, 21.
- (170) Kung, A.; Pieper, T.; Wissiack, R.; Rosenberg, E.; Keppler, B. K. *J. Biol. Inorg. Chem.* **2001**, *6*, 292.
- (171) Piccioli, F.; Sabatini, S.; Messori, L.; Orioli, P.; Hartinger, C. G.; Keppler, B. K. *J. Inorg. Biochem.* **2004**, *98*, 1135.
- (172) Kratz, F.; Hartmann, M.; Keppler, B.; Messori, L. *J. Biol. Chem.* **1994**, *269*, 2581.
- (173) Bouma, M.; Nuijen, B.; Jansen, M. T.; Sava, G.; Bult, A.; Beijnen, J. H. *J. Pharm. Biomed. Anal.* **2002**, *30*, 1287.
- (174) Bouma, M.; Nuijen, B.; Jansen, M. T.; Sava, G.; Flaibani, A.; Bult, A.; Beijnen, J. H. *Int. J. Pharm.* **2002**, *248*, 239.
- (175) Bergamo, A.; Messori, L.; Piccioli, F.; Cocchietto, M.; Sava, G. *Invest. New Drugs* **2003**, *21*, 401.
- (176) Bacac, M.; Hotze, A. C. G.; van der Schilden, K.; Haasnoot, J. G.; Pacor, S.; Alessio, E.; Sava, G.; Reedijk, J. *J. Inorg. Biochem.* **2004**, *98*, 402.
- (177) Pieper, T.; Peti, W.; Keppler, B. K. *Met.-Based Drugs* **2000**, *7*, 225.
- (178) Brindell, M.; Stawoska, I.; Supel, J.; Skoczowski, A.; Stochel, G.; van Eldik, R. *J. Biol. Inorg. Chem.* **2008**, *13*, 909.
- (179) Bartel, C.; Egger, A. E.; Jakupc, M. A.; Heffeter, P.; Galanski, M.; Berger, W.; Keppler, B. K. *J. Biol. Inorg. Chem.* **2011**, *16*, 1205.
- (180) Brindell, M.; Piotrowska, D.; Shoukry, A. A.; Stochel, G.; van Eldik, R. *J. Biol. Inorg. Chem.* **2007**, *12*, 809.
- (181) Henke, M. M.; Richly, H.; Drescher, A.; Grubert, M.; Alex, D.; Thyssen, D.; Jaehde, U.; Scheulen, M. E.; Hilger, R. A. *Int. J. Clin. Pharmacol. Ther.* **2009**, *47*, 58.
- (182) Hartinger, C. G.; Hann, S.; Koellensperger, G.; Sulyok, M.; Groessl, M.; Timerbaev, A. R.; Rudnev, A. V.; Stingededer, G.; Keppler, B. K. *Int. J. Clin. Pharmacol. Ther.* **2005**, *43*, 583.
- (183) Khalaila, I.; Bergamo, A.; Bussy, F.; Sava, G.; Dyson, P. J. *Int. J. Oncol.* **2006**, *29*, 261.
- (184) Mazuryk, O.; Kurpiewska, K.; Lewinski, K.; Stochel, G.; Brindell, M. *J. Inorg. Biochem.* **2012**, *116*, 11.
- (185) Reisner, E. *Insights into the Mode of Action of Bioreductive Ruthenium Cytotoxins*; Nova Science Publishers, Inc., 2009.

- (186) Egger, A. E.; Rappel, C.; Jakupc, M. A.; Hartinger, C. G.; Heffeter, P.; Keppler, B. K. *J. Anal. At. Spectrom.* **2009**, *24*, 51.
- (187) Sava, G.; Pacor, S.; Bregant, F.; Ceschia, V.; Mestroni, G. *Anti-Cancer Drugs* **1990**, *1*, 99.
- (188) Levina, A.; Aitken, J. B.; Gwee, Y. Y.; Lim, Z. J.; Liu, M.; Singharay, A. M.; Wong, P. F.; Lay, P. A. *Chem. Eur. J.* **2013**, *19*, 3609.
- (189) Dömötör, O.; Hartinger, C. G.; Bytzek, A. K.; Kiss, T.; Keppler, B. K.; Enyedy, E. A. *J. Biol. Inorg. Chem.* **2013**, *18*, 9.
- (190) Ang, W. H.; Daldini, E.; Juillerat-Jeanneret, L.; Dyson, P. J. *Inorg. Chem.* **2007**, *46*, 9048.
- (191) Liu, M. M.; Lim, Z. J.; Gwee, Y. Y.; Levina, A.; Lay, P. A. *Angew. Chem. Int. Ed.* **2010**, *49*, 1661.
- (192) Kratz, F.; Elsadek, B. *J. Controlled Release* **2012**, *161*, 429.
- (193) Frühauf, S.; Zeller, W. *J. Cancer Res.* **1991**, *51*, 2943.
- (194) Malina, J.; Novakova, O.; Keppler, B. K.; Alessio, E.; Brabec, V. *J. Biol. Inorg. Chem.* **2001**, *6*, 435.
- (195) Hummer, A. A.; Heffeter, P.; Berger, W.; Filipits, M.; Batchelor, D.; Buchel, G. E.; Jakupc, M. A.; Keppler, B. K.; Rompel, A. *J. Med. Chem.* **2013**, *56*, 1182.
- (196) Bergamo, A.; Delfino, R.; Casarsa, C.; Sava, G. *Anti-Cancer Agents in Medicinal Chemistry* **2012**, *12*, 949.
- (197) Vacca, A.; Bruno, M.; Boccarelli, A.; Coluccia, M.; Ribatti, D.; Bergamo, A.; Garbisa, S.; Sartor, L.; Sava, G. *Br. J. Cancer* **2002**, *86*, 993.
- (198) Morbidelli, L.; Donnini, S.; Filippi, S.; Messori, L.; Piccioli, F.; Orioli, P.; Sava, G.; Ziche, M. *Br. J. Cancer* **2003**, *88*, 1484.
- (199) Debidda, M.; Sanna, B.; Cossu, A.; Posadino, A. M.; Tadolini, B.; Ventura, C.; Pintus, G. *Int. J. Oncol.* **2003**, *23*, 477.
- (200) Messori, L.; Kratz, F.; Alessio, E. *Met.-Based Drugs* **1996**, *3*, 1.
- (201) Sava, G.; Bergamo, A.; Zorzet, S.; Gava, B.; Casarsa, C.; Cocchietto, M.; Furlani, A.; Scarcia, V.; Serli, B.; Iengo, E.; Alessio, E.; Mestroni, G. *Eur. J. Cancer* **2002**, *38*, 427.
- (202) Messori, L.; Orioli, P.; Vullo, D.; Alessio, E.; Iengo, E. *Eur. J. Biochem.* **2000**, *267*, 1206.
- (203) Casini, A.; Mastrobuoni, G.; Terenghi, M.; Gabbianni, C.; Monzani, E.; Moneti, G.; Casella, L.; Messori, L. *J. Biol. Inorg. Chem.* **2007**, *12*, 1107.
- (204) Ravera, M.; Baracco, S.; Cassino, C.; Colangelo, D.; Bagni, G.; Sava, G.; Osella, D. *J. Inorg. Biochem.* **2004**, *98*, 984.

- (205) Ravera, M.; Baracco, S.; Cassino, C.; Zanello, P.; Osella, D. *Dalton Trans.* **2004**, 2347.
- (206) Sulyok, M.; Hann, S.; Hartinger, C. G.; Keppler, B. K.; Stingeder, G.; Koellensperger, G. *J. Anal. At. Spectrom.* **2005**, 20, 856.
- (207) Ascone, I.; Messori, L.; Casini, A.; Gabiani, C.; Balerna, A.; Dell'Unto, F.; Castellano, A. C. *Inorg. Chem.* **2008**, 47, 8629.
- (208) Harris, T. V.; Szilagyi, R. K.; Holman, K. L. M. *J. Biol. Inorg. Chem.* **2009**, 14, 891.
- (209) Hummer, A. A.; Rompel, A. *Metalomics* **2013**, 5, 597.
- (210) Szpunar, J.; Makarov, A.; Pieper, T.; Keppler, B. K.; Lobinski, R. *Anal. Chim. Acta* **1999**, 387, 135.
- (211) Bytzek, A. K.; Boeck, K.; Hermann, G.; Hann, S.; Keppler, B. K.; Hartinger, C. G.; Koellensperger, G. *Metalomics* **2011**, 3, 1049.
- (212) Timerbaev, A. R.; Rudnev, A. V.; Semenova, O.; Hartinger, C. G.; Keppler, B. K. *Anal. Biochem.* **2005**, 341, 326.
- (213) Chen, J. C.; Chen, L. M.; Liao, S. Y.; Zheng, K. C.; Ji, L. N. *J. Phys. Chem. B* **2007**, 111, 7862.
- (214) Vargiu, A. V.; Robertazzi, A.; Magistrato, A.; Ruggerone, P.; Carloni, P. *J. Phys. Chem. B* **2008**, 112, 4401.
- (215) Besker, N.; Coletti, C.; Marrone, A.; Re, N. *J. Phys. Chem. B* **2008**, 112, 3871.
- (216) Chen, J. C.; Chen, L. M.; Liao, S. Y.; Zheng, K.; Ji, L. N. *Dalton Trans.* **2007**, 3507.
- (217) Reedijk, J. *Macromol. Symp.* **1994**, 80, 95.
- (218) Abragam, A.; Bleaney, B. *Electron paramagnetic resonance of transition ions*; Oxford University Press: Oxford, 1970.
- (219) Weil, J. A.; Bolton, J. R. *Electron paramagnetic resonance: elementary theory and practical applications*; 2nd ed.; Wiley-Interscience: Hoboken, N.J., 2007.
- (220) Eichinger, R.; Sulyok, M.; Paschkunova-Martic, I.; Hann, S.; Kollensperger, G.; Jakupc, M. A.; Keppler, B. K. *Clin. Cancer Res.* **2005**, 11, 9151S.
- (221) Clarke, M. J.; Bailey, V. M.; Doan, P. E.; Hiller, C. D.; LaChanceGalang, K. J.; Daghlian, H.; Mandal, S.; Bastos, C. M. *Inorg. Chem.* **1996**, 35, 4896.
- (222) Mason, A. B.; Halbrooks, P. J.; James, N. G.; Connolly, S. A.; Larouche, J. R.; Smith, V. C.; MacGillivray, R. T. A.; Chasteen, N. D. *Biochemistry* **2005**, 44, 8013.
- (223) Gadsby, P. M. A.; Peterson, J.; Foote, N.; Greenwood, C.; Thomson, A. J. *Biochem. J.* **1987**, 246, 43.
- (224) Telser, J.; Pardi, L. A.; Krzystek, J.; Brunel, L. C. *Inorg. Chem.* **1998**, 37, 5769.

- (225) Ross, R. T. *J. Chem. Phys.* **1965**, *42*, 3919.
- (226) Dhubhghaill, O. M. N.; Hagen, W. R.; Keppler, B. K.; Lipponer, K. G.; Sadler, P. J. *Dalton Trans.* **1994**, 3305.
- (227) Mailer, C.; Taylor, C. P. S. *Biochim. Biophys. Acta* **1973**, *322*, 195.
- (228) McGarvey, B. R. *Coord. Chem. Rev.* **1998**, *170*, 75.
- (229) Cebrian-Losantos, B.; Reisner, E.; Kowol, C. R.; Roller, A.; Shova, S.; Arion, V. B.; Keppler, B. K. *Inorg. Chem.* **2008**, *47*, 6513.
- (230) Telser, J.; Reisner, E.; Tierney, D. L.; Keppler, B. K., Private Communication.
- (231) Anderson, C.; Beauchamp, A. L. *Can. J. Chem.* **1995**, *73*, 471.
- (232) Chatlas, J.; Vaneldik, R.; Keppler, B. K. *Inorg. Chim. Acta* **1995**, *233*, 59.
- (233) Groessl, M.; Hartinger, C. G.; Polec-Pawlak, K.; Jarosz, M.; Keppler, B. K. *Electrophoresis* **2008**, *29*, 2224.
- (234) Groessl, M.; Hartinger, C. G.; Dyson, P. J.; Keppler, B. K. *J. Inorg. Biochem.* **2008**, *102*, 1060.
- (235) Trynda-Lemiesz, L.; Karaczyn, A.; Keppler, B. K.; Kozlowski, H. *J. Inorg. Biochem.* **2000**, *78*, 341.
- (236) Trynda-Lemiesz, L.; Keppler, B. K.; Kozlowski, H. *J. Inorg. Biochem.* **1999**, *73*, 123.
- (237) Kratz, F.; Warnecke, A.; Scheuermann, K.; Stockmar, C.; Schwab, J.; Lazar, P.; Druckes, P.; Esser, N.; Drevs, J.; Rognan, D.; Bissantz, C.; Hinderling, C.; Folkers, G.; Fichtner, I.; Unger, C. *J. Med. Chem.* **2002**, *45*, 5523.
- (238) Pedersen, A. O.; Jacobsen, J. *Eur. J. Biochem.* **1980**, *106*, 291.
- (239) Narazaki, R.; Hamada, M.; Harada, K.; Otagiri, M. *Pharm. Res.* **1996**, *13*, 1317.
- (240) Summa, D.; Spiga, O.; Bernini, A.; Venditti, V.; Priora, R.; Frosali, S.; Margaritis, A.; Di Giuseppe, D.; Niccolai, N.; Di Simplicio, P. *Proteins: Struct. Funct. Bioinform.* **2007**, *69*, 369.
- (241) McGarvey, B. R. *Quim. Nova* **1998**, *21*, 206.
- (242) Sava, G.; Bergamo, A. *Anticancer Res.* **1999**, *19*, 1117.
- (243) Sava, G.; Gagliardi, R.; Bergamo, A.; Alessio, E.; Mestroni, G. *Anticancer Res.* **1999**, *19*, 969.
- (244) Cocchietto, M.; Salerno, G.; Alessio, E.; Mestroni, G.; Sava, G. *Anticancer Res.* **2000**, *20*, 197.
- (245) Mestroni, G.; Alessio, E.; Sava, G. United States Patent 6,221,905, 2001.
- (246) Cetinbas, N.; Webb, M. I.; Dubland, J. A.; Walsby, C. J. *J. Biol. Inorg. Chem.* **2010**, *15*, 131.

- (247) Mestroni, G.; Alessio, E.; Sava, G.; Pacor, S.; Coluccia, M.; Boccarelli, A. *Met.-Based Drugs* **1993**, *1*, 41.
- (248) Cocchietto, M.; Sava, G. *Pharmacol. Toxicol.* **2000**, *87*, 193.
- (249) Gonias, S. L.; Pizzo, S. V. *J. Biol. Chem.* **1983**, *258*, 5764.
- (250) Katchalski, E.; Benjamin, G. S.; Gross, V. *J. Am. Chem. Soc.* **1957**, *79*, 4096.
- (251) Drincovich, M. F.; Andreo, C. S. *Biochim. Biophys. Acta, Protein Struct. Mol. Enzymol.* **1994**, *1206*, 10.
- (252) Betteridge, P. W.; Carruthers, J. R.; Cooper, R. I.; Prout, K.; Watkin, D. J. *J. Appl. Crystallogr.* **2003**, *36*, 1487.
- (253) Farrugia, L. J. *J. Appl. Crystallogr.* **1997**, *30*, 565.
- (254) Kljun, J.; Petricek, S.; Zigon, D.; Hudej, R.; Miklavcic, D.; Turel, I. *Bioinorg. Chem. App.* **2010**.
- (255) Liang, Y. H.; Bi, W.; Yang, B.; Zhao, L. A.; Liang, G. G. *Chem. J. Chinese U.* **2011**, *32*, 210.
- (256) Mura, P.; Camalli, M.; Messori, L.; Piccioli, F.; Zanello, P.; Corsini, M. *Inorg. Chem.* **2004**, *43*, 3863.
- (257) Velders, A. H.; Bergamo, A.; Alessio, E.; Zangrando, E.; Haasnoot, J. G.; Casarsa, C.; Cocchietto, M.; Zorzet, S.; Sava, G. *J. Med. Chem.* **2004**, *47*, 1110.
- (258) Griffith, D.; Cecco, S.; Zangrando, E.; Bergamo, A.; Sava, G.; Marmion, C. J. *J. Biol. Inorg. Chem.* **2008**, *13*, 511.
- (259) de Paula, Q. A.; Batista, A. A.; Nascimento, O. R.; da Costa, A. J.; Schultz, M. S.; Bonfadini, M. R.; Oliva, G. *J. Braz. Chem. Soc.* **2000**, *11*, 530.
- (260) Liang, Y. H.; Bi, W.; Liang, G. G. *Chin. J. Inorg. Chem.* **2011**, *27*, 595.
- (261) Geremia, S.; Alessio, E.; Todone, F. *Inorg. Chim. Acta* **1996**, *253*, 87.
- (262) Alberti, F. M.; Fiol, J. J.; Garcia-Raso, A.; Torres, M.; Terron, A.; Barcelo-Oliver, M.; Prieto, M. J.; Moreno, V.; Molins, E. *Polyhedron* **2010**, *29*, 34.
- (263) Travnicek, Z.; Matikova-Malarova, M.; Novotna, R.; Vanco, J.; Stepankova, K.; Suchy, P. *J. Inorg. Biochem.* **2011**, *105*, 937.
- (264) Webb, M. I.; Walsby, C. J. *Dalton Trans.* **2011**, *40*, 1322.
- (265) Manohara, P. T.; Mehrotra, P. K.; Taquikha, M. M.; Andal, R. K. *Inorg. Chem.* **1973**, *12*, 2753.
- (266) Kroghjespersen, K.; Schugar, H. J. *Inorg. Chem.* **1984**, *23*, 4390.
- (267) Messori, L.; Gonzales Vilchez, F.; Vilaplana, R.; Piccioli, F.; Alessio, E.; Keppler, B. *Met.-Based Drugs* **2000**, *7*, 335.
- (268) Hnizda, A.; Santrucek, J.; Sanda, M.; Strohalm, M.; Kodicek, M. *J. Biochem. Bioph. Methods* **2008**, *70*, 1091.

- (269) Hu, W.; Luo, Q.; Ma, X.; Wu, K.; Liu, J.; Chen, Y.; Xiong, S.; Wang, J.; Sadler, P. J.; Wang, F. *Chem. Eur. J.* **2009**, *15*, 6586.
- (270) Seward, J. R.; Cronin, M. T. D.; Schultz, T. W. *SAR QSAR Environ. Res.* **2002**, *13*, 325.
- (271) Lever, A. B. P. *Inorg. Chem.* **1990**, *29*, 1271.
- (272) da Silva, M.; Pombeiro, A. J. L.; Geremia, S.; Zangrandi, E.; Calligaris, M.; Zinchenko, A. V.; Kukushkin, V. Y. *Dalton Trans.* **2000**, 1363.
- (273) Schafer, F. Q.; Buettner, G. R. *Free Radical Biol. Med.* **2001**, *30*, 1191.
- (274) Miklavcic, D.; Sersa, G.; Novakovic, S.; Rebersek, S. *J. Bioelectricity* **1990**, *9*, 133.
- (275) Jakupc, M. A.; Reisner, E.; Eichinger, A.; Pongratz, M.; Arion, V. B.; Galanski, M.; Hartinger, C. G.; Keppler, B. K. *J. Med. Chem.* **2005**, *48*, 2831.
- (276) David, S.; Perkins, R. S.; Fronczek, F. R.; Kasiri, S.; Mandal, S. S.; Srivastava, R. S. *J. Inorg. Biochem.* **2012**, *111*, 33.
- (277) Webb, M. I.; Chard, R. A.; Al-Jobory, Y. M.; Jones, M. R.; Wong, E. W. Y.; Walsby, C. J. *Inorg. Chem.* **2012**, *51*, 954.
- (278) Santos, J. M.; Cipriano, C.; Faria, R. B.; FigueroaVillar, J. D. *Can. J. Chem.* **1997**, *75*, 890.
- (279) Santos, J. M.; Formiga, A. L. B.; Figueroa-Villar, J. D. *J. Mol. Struct.* **2002**, *608*, 143.
- (280) Santos, J. M.; da Silva, R. R.; Formiga, A. L. B.; Tinoco, L. W.; Figueroa-Villar, J. D. *Chem. Phys.* **2004**, *306*, 143.
- (281) Siek, T. J.; Osiewicz, R. J. *J. Forensic Sci.* **1975**, *20*, 18.
- (282) Wanwimolruk, S.; Birkett, D. J.; Brooks, P. M. *Mol. Pharmacol.* **1983**, *24*, 458.
- (283) Elsadek, B.; Kratz, F. *J. Controlled Release* **2012**, *157*, 4.
- (284) Kratz, F. *J. Controlled Release* **2008**, *132*, 171.
- (285) Wunder, A.; Muller-Ladner, U.; Stelzer, E. H. K.; Funk, J.; Neumann, E.; Stehle, G.; Pap, T.; Sinn, H.; Gay, S.; Fiehn, C. *J. Immunol.* **2003**, *170*, 4793.
- (286) Murphy, E. A.; Majeti, B. K.; Mukthavaram, R.; Acevedo, L. M.; Barnes, L. A.; Cheresh, D. A. *Mol. Cancer Ther.* **2011**, *10*, 972.
- (287) Smith, C. A.; Sutherland-Smith, A. J.; Keppler, B. K.; Kratz, F.; Baker, E. N. *J. Biol. Inorg. Chem.* **1996**, *1*, 424.
- (288) Winkler, J. R.; Gray, H. B. *Chem. Rev.* **1992**, *92*, 369.
- (289) Song, Y.; Gunner, M. R. *J. Mol. Biol.* **2009**, *387*, 840.

- (290) Sajfutdinov, R. G.; Larina, L. I.; Vakul'skaya, T. I. i.; Voronkov, M. G. e. *Electron paramagnetic resonance in biochemistry and medicine*; Kluwer Academic/Plenum Publishers: New York, 2001.
- (291) Brustolon, M.; Giamello, E. *Electron paramagnetic resonance: a practitioner's toolkit*; Wiley: Hoboken, N.J., 2009.
- (292) Golab, Z.; Breitenbach, M.; Jezierski, A. *Water Air Soil Pollut.* **1995**, *82*, 713.
- (293) Kihn, J. C.; Mestdagh, M. M.; Rouxhet, P. G. *Can. J. Microbiol.* **1987**, *33*, 777.
- (294) Byrnes, R. W.; Antholine, W. E.; Petering, D. H. *Free Radical Biol. Med.* **1992**, *12*, 457.
- (295) Antholine, W. E.; Petering, D. H.; Pickart, L. *J. Inorg. Biochem.* **1989**, *35*, 215.
- (296) Pezeshk, A.; Antholine, W. E.; Petering, D. H. *J. Inorg. Biochem.* **1987**, *31*, 283.
- (297) Chang, E. C.; Kosman, D. J. *J. Biol. Chem.* **1989**, *264*, 12172.
- (298) Kihn, J. C.; Dassargues, C. M.; Mestdagh, M. M. *Can. J. Microbiol.* **1988**, *34*, 1230.
- (299) Zoroddu, M. A.; Fruianu, M.; Dallocchio, R.; Masia, A. *Biometals* **1996**, *9*, 91.
- (300) Mielczarek, E. V.; Andrews, S. C.; Bauminger, R. *Biometals* **1992**, *5*, 87.
- (301) Nair, S.; Krishnamurthi, V. S. *Indian J. Exp. Biol.* **1993**, *31*, 516.
- (302) Hagen, W. R. *Metalomics* **2009**, *1*, 384.
- (303) Groessl, M.; Zava, O.; Dyson, P. J. *Metalomics* **2011**, *3*, 591.
- (304) Hostetter, A. A.; Miranda, M. L.; DeRose, V. J.; Holman, K. L. M. *J. Biol. Inorg. Chem.* **2011**, *16*, 1177.
- (305) Frausin, F.; Cocchietto, M.; Bergamo, A.; Searcia, V.; Furlani, A.; Sava, G. *Cancer Chemother. Pharmacol.* **2002**, *50*, 405.
- (306) Boutry, S.; Forge, D.; Burtea, C.; Mahieu, I.; Murariu, O.; Laurent, S.; Elst, L. V.; Muller, R. N. *Contrast Media Mol. Imaging* **2009**, *4*, 299.
- (307) Campbell, I.; Duffus, J. H. *Yeast: a practical approach*; IRL Press: Washington, D.C., 1988.
- (308) Ghuman, J.; Zunszain, P. A.; Petitpas, I.; Bhattacharya, A. A.; Otagiri, M.; Curry, S. *J. Mol. Biol.* **2005**, *353*, 38.
- (309) Redon, M.; Borrull, A.; Lopez, M.; Salvado, Z.; Cordero, R.; Mas, A.; Manuel Guillamon, J.; Rozes, N. *Yeast* **2012**, *29*, 443.
- (310) Bunce, N. J. *J. Chem. Educ.* **1987**, *64*, 907.
- (311) Burns, D. T.; Flockhart, B. D. *Philos. Trans. Roy. Soc. A* **1990**, *333*, 37.
- (312) Mordvintcev, P.; Mulsch, A.; Busse, R.; Vanin, A. *Anal. Biochem.* **1991**, *199*, 142.

- (313) Hagen, W. R. *Dalton Trans.* **2006**, 4415.
- (314) Feher, G. *Physical Review* **1959**, *114*, 1219.
- (315) Hoffman, B. M. *Acc. Chem. Res.* **1991**, *24*, 164.
- (316) Hoffman, B. M. *Acc. Chem. Res.* **2003**, *36*, 522.
- (317) Thomann, H.; Bernardo, M. *Metallobiochemistry, Pt D* **1993**, *227*, 118.
- (318) Fees, J.; Kaim, W.; Moschersch, M.; Matheis, W.; Klima, J.; Krejcik, M.; Zalis, S. *Inorg. Chem.* **1993**, *32*, 166.
- (319) Bullock, J. E.; Vagnini, M. T.; Ramanan, C.; Co, D. T.; Wilson, T. M.; Dicke, J. W.; Marks, T. J.; Wasielewski, M. R. *J. Phys. Chem. B* **2010**, *114*, 1794.
- (320) Bell, S. E.; Field, J. S.; Haines, R. J.; Moschersch, M.; Matheis, W.; Kaim, W. *Inorg. Chem.* **1992**, *31*, 3269.
- (321) Stull, J. A.; Stich, T. A.; Hurst, J. K.; Britt, R. D. *Inorg. Chem.* **2013**, *52*, 4578.
- (322) Hoffman, B. M. *Proc. Natl. Acad. Sci. U. S. A.* **2003**, *100*, 3575.
- (323) Scholes, C. P.; Falkowski, K. M.; Chen, S.; Bank, J. *J. Am. Chem. Soc.* **1986**, *108*, 1660.
- (324) Gridnev, A. A.; Mihaltseva, I. M. *Synth. Commun.* **1994**, *24*, 1547.
- (325) Scott, R. A.; Lukehart, C. M. *Applications of Physical Methods to Inorganic and Bioinorganic Chemistry*; Wiley: Hoboken, NJ, 2007.
- (326) Epel, B.; Niklas, J.; Sinnecker, S.; Zimmermann, H.; Lubitz, W. *J. Phys. Chem. B* **2006**, *110*, 11549.
- (327) Sivaraja, M.; Stouch, T. R.; Dismukes, G. C. *J. Am. Chem. Soc.* **1992**, *114*, 9600.
- (328) Tan, X. L.; Bernardo, M.; Thomann, H.; Scholes, C. P. *J. Chem. Phys.* **1993**, *98*, 5147.
- (329) Gurbiel, R. J.; Batie, C. J.; Sivaraja, M.; True, A. E.; Fee, J. A.; Hoffman, B. M.; Ballou, D. P. *Biochemistry* **1989**, *28*, 4861.
- (330) Alessio, E.; Milani, B.; Mestroni, G.; Calligaris, M.; Faleschini, P.; Attia, W. M. *Inorg. Chim. Acta* **1990**, *177*, 255.
- (331) Costa, G.; Balducci, G.; Alessio, E.; Tavagnacco, C.; Mestroni, G. *J. Electroanal. Chem.* **1990**, *296*, 57.
- (332) Mu, C. Ph.D. Thesis, Simon Fraser University, 2013.
- (333) DeRose, V. J.; Liu, K. E.; Lippard, S. J.; Hoffman, B. M. *J. Am. Chem. Soc.* **1996**, *118*, 121.
- (334) Mulks, C. F.; Scholes, C. P.; Dickinson, L. C.; Lapidot, A. *J. Am. Chem. Soc.* **1979**, *101*, 1645.
- (335) Ellis, J. W.; Sorge, B. W. *J. Chem. Phys.* **1934**, *2*.

- (336) Cline, J. F.; Hoffman, B. M.; Mims, W. B.; Lahaie, E.; Ballou, D. P.; Fee, J. A. *J. Biol. Chem.* **1985**, *260*, 3251.
- (337) Smoukov, S. K.; Davydov, R. M.; Doan, P. E.; Sturgeon, B.; Kung, I. Y.; Hoffman, B. M.; Kurtz, D. M. *Biochemistry* **2003**, *42*, 6201.
- (338) Van Camp, H. L.; Sands, R. H.; Fee, J. A. *J. Chem. Phys.* **1981**, *75*, 2098.
- (339) Tan, C. P.; Liu, J.; Chen, L. M.; Shi, S.; Ji, L. N. *J. Inorg. Biochem.* **2008**, *102*, 1644.
- (340) Chignell, C. F. *Mol. Pharmacol.* **1970**, *6*, 1.
- (341) Chignell, C. F. *Mol. Pharmacol.* **1969**, *5*, 244.
- (342) Zhang, Y.; Akilesh, S.; Wilcox, D. E. *Inorg. Chem.* **2000**, *39*, 3057.
- (343) Zhang, Y.; Wilcox, D. E. *J. Biol. Inorg. Chem.* **2002**, *7*, 327.
- (344) Lin, L. N.; Mason, A. B.; Woodworth, R. C.; Brandts, J. F. *Biochemistry* **1994**, *33*, 1881.
- (345) Quarles, C. D., Jr.; Marcus, R. K.; Brumaghim, J. L. *J. Biol. Inorg. Chem.* **2011**, *16*, 913.
- (346) Tinoco, A. D.; Incarvito, C. D.; Valentine, A. M. *J. Am. Chem. Soc.* **2007**, *129*, 3444.
- (347) Tinoco, A. D.; Valentine, A. M. *J. Am. Chem. Soc.* **2005**, *127*, 11218.
- (348) Montavon, G.; Apostolidis, C.; Bruchertseifer, F.; Repinc, U.; Morgenstern, A. *J. Inorg. Biochem.* **2009**, *103*, 1609.
- (349) Michon, J.; Frelon, S.; Garnier, C.; Coppin, F. *J. Fluoresc.* **2010**, *20*, 581.
- (350) Nikolova, A.; Ivanov, D.; Buyukliev, R.; Konstantinov, S.; Karaivanova, M. *Arzneim.-Forsch.* **2001**, *51*, 758.
- (351) Liang, Y.-H.; Liang, G.-G. *Chin. J. Inorg. Chem.* **2008**, *24*, 1983.
- (352) Rajendiran, V.; Karthik, R.; Palaniandavar, M.; Stoeckli-Evans, H.; Periasamy, V. S.; Akbarsha, M. A.; Srinag, B. S.; Krishnamurthy, H. *Inorg. Chem.* **2007**, *46*, 8208.
- (353) Barnes, K. R.; Lippard, S. J. *Metal Ions in Biological Systems, Vol 42: Metal Complexes in Tumor Diagnosis and as Anticancer Agents* **2004**, *42*, 143.
- (354) Devereux, M.; Shea, D. O.; Kellett, A.; McCann, M.; Walsh, M.; Egan, D.; Deegan, C.; Kgdziora, K.; Rosair, G.; Muelller-Bunz, H. *J. Inorg. Biochem.* **2007**, *101*, 881.
- (355) Ramakrishnan, S.; Rajendiran, V.; Palaniandavar, M.; Periasamy, V. S.; Srinag, B. S.; Krishnamurthy, H.; Akbarshat, M. A. *Inorg. Chem.* **2009**, *48*, 1309.

Appendices

Appendix A. Supplementary Information for Chapter 2.

Table A-1 EPR simulation parameters, g values and linewidths (Gauss), used in the simulation of all EPR spectra.

Species	g ₁	g ₂	g ₃	LW ₁	LW ₂	LW ₃
KP418-Uniaxial	2.58	2.58	1.20	230	230	600
KP418-Rhombic	3.08	2.30	0.95	100	800	800
KP418-H ₂ O	2.47	2.26	1.79	80	70	100
KP418-(H ₂ O) ₂ - <i>trans</i>	2.59	2.34	1.72	80	120	350
KP418-(H ₂ O) ₂ - <i>cis</i>	2.51	2.20	1.73	80	70	250
KP418-hsA-1	2.42	2.06	1.96	80	70	55
KP418-hsTf	2.38	2.38	1.66	200	200	250
KP418-unlabelled	2.40	2.15	1.87	30	30	30
KP1019-Uniaxial	2.64	2.64	1.20	120	120	500
KP1019-Rhombic	2.94	2.31	0.95	100	200	600
KP1019-hsA-1	2.44	2.24	1.79	120	90	200
KP1019-hsA-2	2.32	2.32	1.84	90	80	80
KP1019-hsA-3	2.42	2.06	1.96	80	70	55

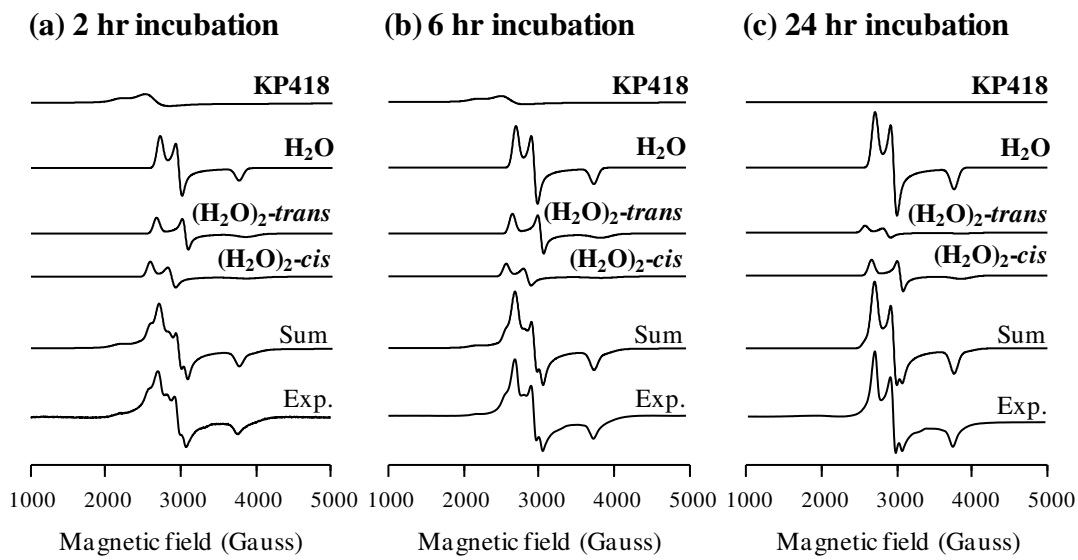


Figure A-1 Deconvolution of X-band EPR spectra from KP418 in HEPES buffer after various periods of incubation at 37 °C. **Experimental conditions:** see section 2.2.5. **Simulation parameters:** For g values and linewidths, see **Table A-1**.

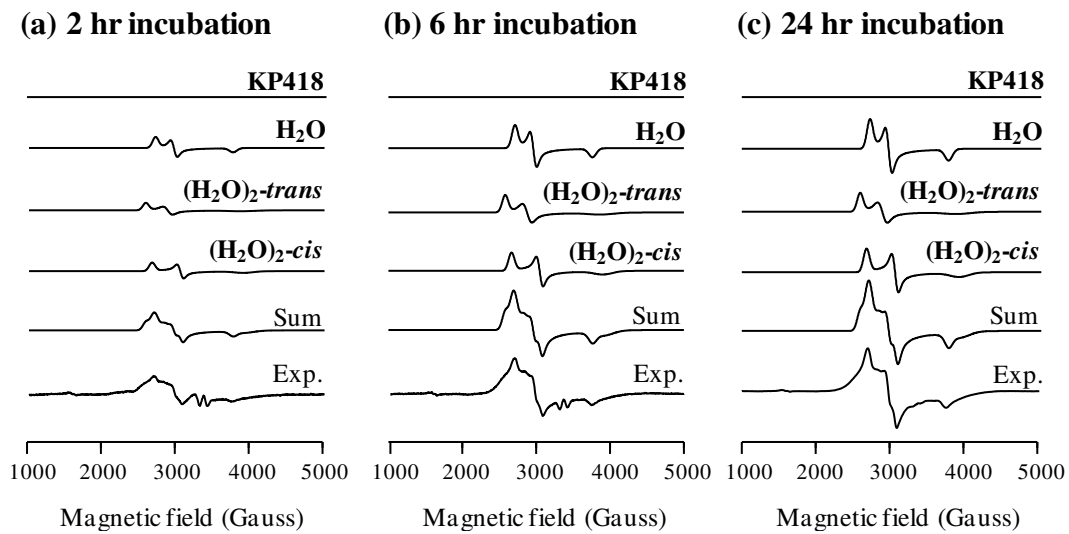


Figure A-2 Deconvolution of X-band EPR spectra from KP418 bound to hsA in HEPES buffer after various periods of incubation at 37 °C. **Experimental conditions:** see section 2.2.5. **Simulation parameters:** For g values and linewidths, see **Table A-1**.

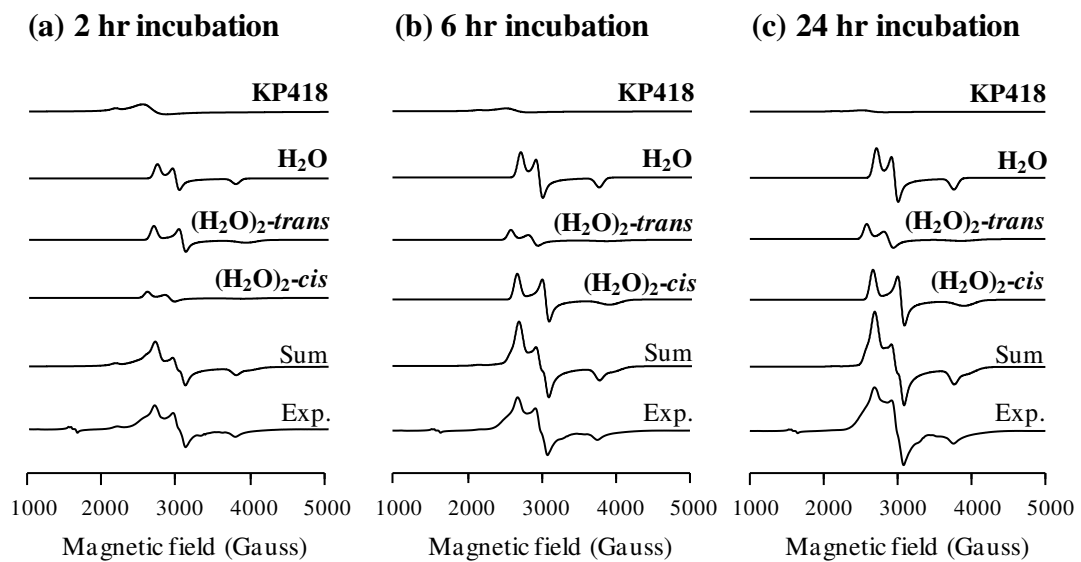


Figure A-3 Deconvolution of EPR spectra from KP418 incubated with human serum in HEPES buffer at 37 °C. **Experimental conditions:** see section 2.2.5. **Simulation parameters:** For g values and linewidths, see **Table A-1**.

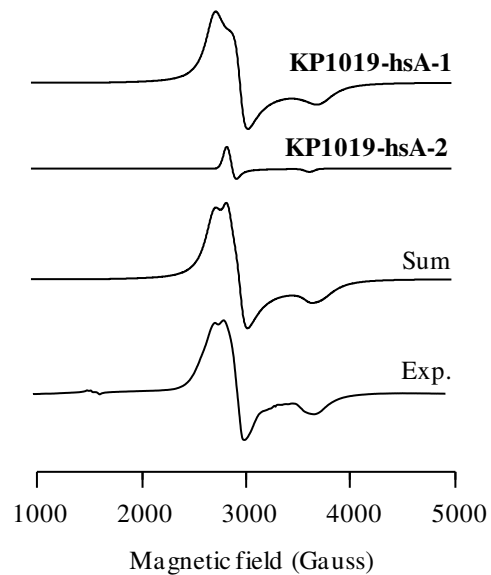


Figure A-4 Experimental and simulated EPR spectra from KP1019 bound to hsA in HEPES buffer after 24 hours of incubation at 37 °C. **Experimental conditions:** see section 2.2.5. **Simulation parameters:** For g values and linewidths, see **Table A-1**.

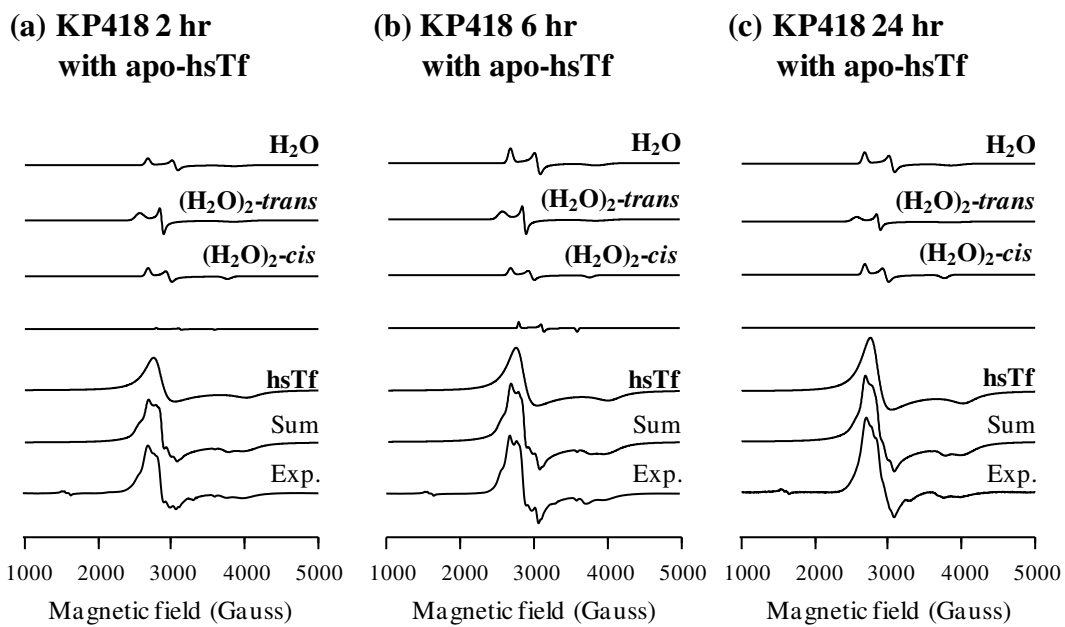
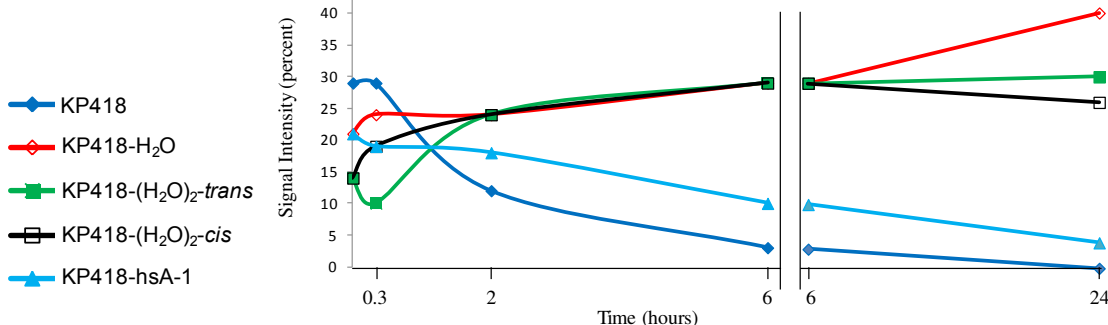


Figure A-5 Deconvolution of EPR spectra from KP418 incubated with hsTf in HEPES buffer at 37 °C. **Experimental conditions:** see section 2.2.5. **Simulation parameters:** For g values and linewidths, see **Table A-1**.

(a) KP418with hsA



(b) KP418 with serum

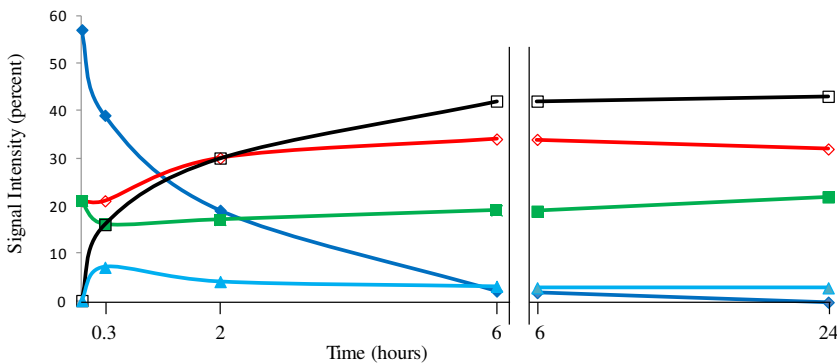


Figure A-6 Time dependence of signal intensities for KP418 incubated with (a) hsA and (b) whole human serum, determined by simulation as described in the text.

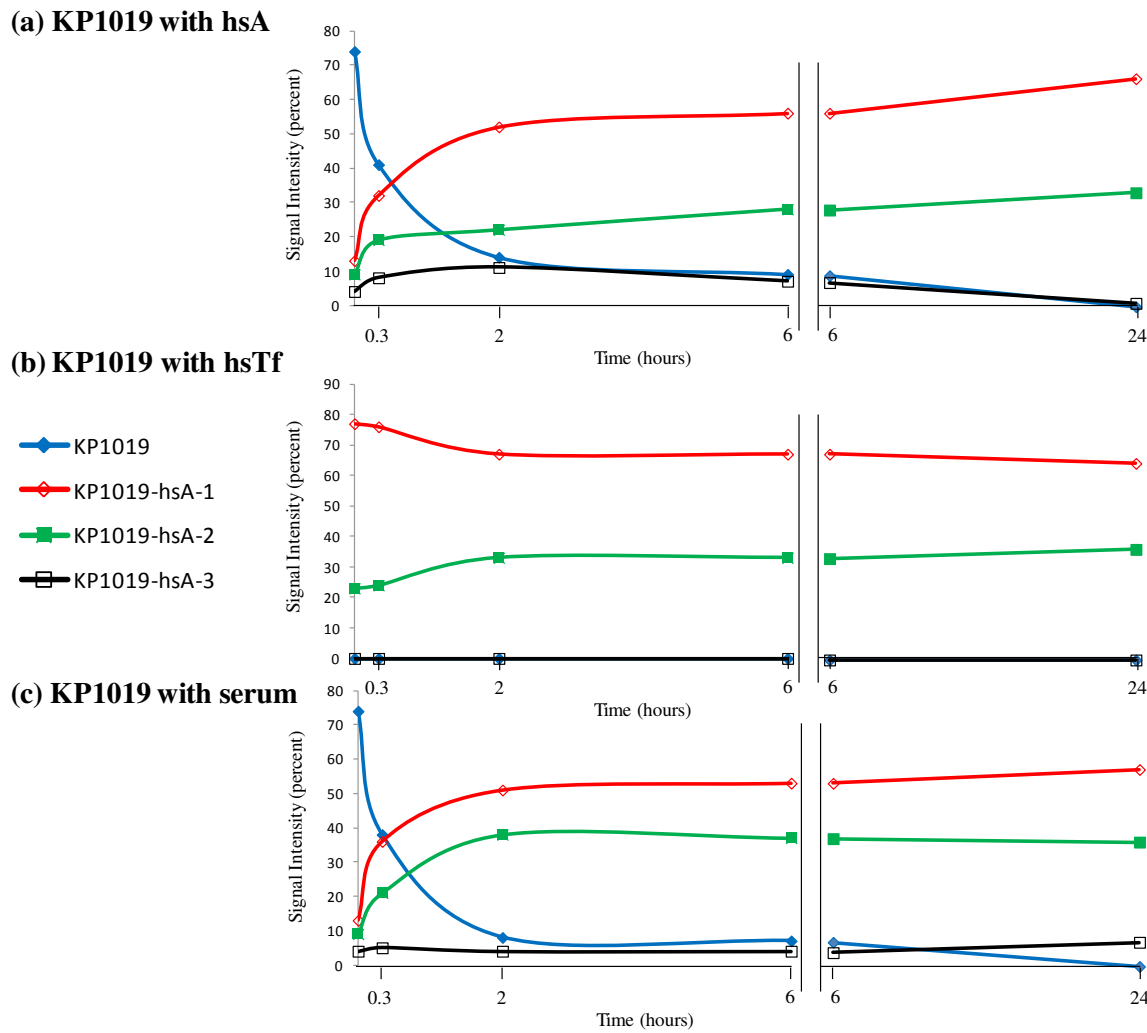


Figure A-7 Time dependence of signal intensities for KP1019 incubated with (a) hsA, (b) hsTf, and (c) whole human serum, determined by simulation as described in the text.

Ligand-field analysis of low-spin d^5 ligand-field parameters from experimental g values.

Distorted octahedral Ru(III) complexes are typically strong-field d^5 systems, with characteristic low-spin $S = \frac{1}{2}$ EPR spectra, such as those reported here. The cubic component of the ligand field splits the d orbitals into the familiar higher energy e_g doublet and lower level t_{2g} triplet. In a tetragonal system, the t_{2g} triplet may be further split by tetragonal and rhombic distortion components, with energies given by the parameters Δ and V respectively (**Figure A-8a**) divided by the single electron spin-orbit constant (ξ). The original theoretical analysis of the relationship between the observed g values and ligand-field parameters for such systems was reported by Bleaney and O'Brian.^{A1} Subsequently, a variety of theoretical treatments have been used for such analyses, which differ in their choice of: (i) basis set for the t_2 orbitals ($d_{\pm 1}$ and d_{xy} versus d_{xz} , d_{yz} , and d_{xy}); (ii) electron or hole formalisms; (iii) definition of axis systems. This has led to confusion and inconsistency within the literature. Fortunately, two reviews by McGarvey^{A2, A3} describe the relationship between the different treatments and provide an elegant approach for determining the ligand-field parameters from the experimental g values. In this chapter the formalism recommended in these reports was followed, due to the efficiency and clarity of this approach. Briefly, this method uses the d_{xy} , $d_{\pm 1}$ basis set and defines the molecular z direction as the major axis of distortion by requiring that $|V| \leq 2|\Delta|/3$ (**Figure A-8b**). The molecular x and y axes are defined by also requiring that Δ and V have the same sign. The ground-state Kramer's doublet is written in terms of the basis functions $|M_L, M_S\rangle$ as shown below.

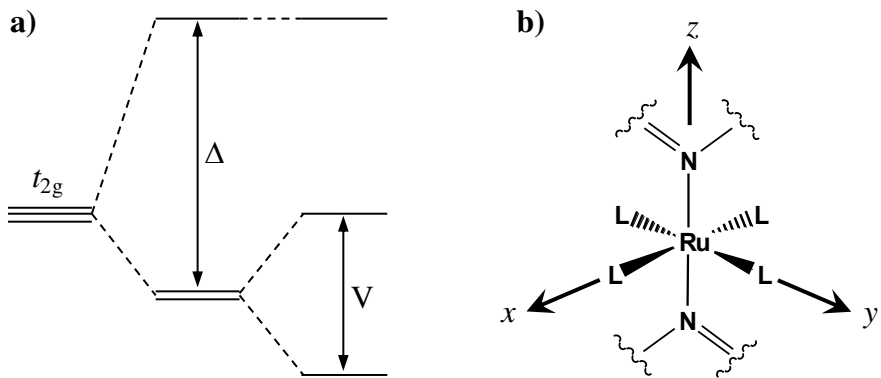


Figure A-8 **a)** Ligand-field energy level splittings for a t_{2g}^5 system. The diagram as shown represents the tetragonally elongated case ($\Delta > 0$); **b)** definition of molecular axis system for KP418, KP1019, and hydrolysed or protein-bound species.

$$|\alpha\rangle = a|+1,-\frac{1}{2}\rangle + b|0,+\frac{1}{2}\rangle + c|-1,-\frac{1}{2}\rangle$$

$$|\beta\rangle = a|-1,+\frac{1}{2}\rangle + b|0,-\frac{1}{2}\rangle + c|+1,+\frac{1}{2}\rangle$$

A-1

These are used to determine the $S = \frac{1}{2}$ effective spin Hamiltonian that gives the Zeeman energy of this doublet when the degeneracy of the states is lifted by an applied magnetic field. In these energy calculations there is potential for confusion in determining the absolute signs of the coefficients (a , b , and c) of the basis eigenfunctions. The sign convention in equations A-2, shown below, was used for the calculation of g-matrix principle values, which is appropriate to systems with small distortions from octahedral symmetry ($|\Delta/\xi| < 5$).^{A3}

$$g_x = -2[-2ac + b^2 + k\sqrt{2}b(a - c)]$$

$$g_y = -2[2ac + b^2 + k\sqrt{2}b(a + c)]$$

$$g_z = -2[a^2 + b^2 - c^2 + k(a^2 - c^2)]$$

A-2

Parameter k is the orbital reduction factor, which accounts for spin density lost from the metal centre via covalent bonding with ligand atoms.^{A4, A5} A value of $k = 1$ implies a completely ionic complex, while values less than 1 indicate covalency in the metal-ligand interactions. With powder-pattern EPR spectra, such as reported in Chapter 2, the assignment of the three principle g values to the molecular axis system can be intractable, and these are typically numbered simply in terms of increasing magnetic field position: g_1 = lowest field, g_2 = intermediate field, g_3 = highest field. However, for the distorted octahedral d^5 systems described here, consideration of appropriate boundary conditions determines the following rules for assignment of the g values: (i) $g_2 = g_y$; (ii) $g_1 = g_z$ and $g_3 = g_x$ if $\Delta > 0$, or $g_1 = g_x$ and $g_3 = g_z$ if $\Delta < 0$, (iii) g_1 and $g_2 < 0$, while g_3 can have either sign.^{A3} This then leaves four possible assignments of the principle g values, two of which can be excluded on the grounds that they violate the requirement that $|V| \leq 2|\Delta|/3$. By applying equations (2), and the normalization requirement, $a + b + c = 1$, all four parameters a , b , c , and k can then be obtained from the experimental g values. Procedures for obtaining these values are rarely described, with the exception of McGarvey,^{A2} who reformulates equations A-2 to provide useful expressions, which allow systematic refinement of each parameter, and describes a cyclic calculation method for their refinement. From these expressions the following equations can be derived, which are forms useful for refinement of parameters a , b , c and k from the experimental principle g values.

$$a = \sqrt{\frac{(2-gz)}{2(2+k)} - \frac{(2-k)c^2}{(2+k)}} \quad \text{A-3}$$

$$b = \sqrt{1 - a^2 - c^2} \quad \text{A-4}$$

$$c = \frac{(gx-gy)}{4(2a+\sqrt{2}kb)} \quad \text{A-5}$$

$$k = -\frac{[2b^2 + \gamma_2(gx+gy)]}{2\sqrt{2}ab} \quad \text{A-6}$$

Similar expressions were first shown by McGarvey,^{A2} but with sign errors in A-3, A-5 and A-6. These are clearly typographical errors that occurred during the publication process, since calculations in this, and another very helpful paper on the interpretation of g values for d^5 systems by the same author,^{A3} are all consistent with the equations as shown here. The parameters a , b , c , and k can be refined directly from equations A-2 and the normalisation condition (A-4), in a straightforward manner, using commercially available optimization tools, and initial conditions of $a = b = c = 0$ and $k = 1$.^{A6} The ligand-field parameters can then be calculated from the following equations:^{A2}

$$\frac{\Delta}{\xi} = \frac{[b(1-b^2) + \sqrt{2a(1-2a^2)}]}{2b(a^2-c^2)} \quad \text{A1-7}$$

$$\frac{V}{\xi} = \frac{c(2a+\sqrt{2b})}{(c^2-a^2)} \quad \text{A1-8}$$

For every complex described in Chapter 2, one of the two acceptable solutions can be discarded due to a calculated orbital reduction factor significantly greater than 1, and a predicted tetragonal distortion energy (Δ) significantly lower than anticipated for an octahedral Ru(III) system. **Table A-2** contains the g values for all major species characterized in this chapter and the corresponding acceptable ligand-field parameters. A complete table containing all pairs of mathematically allowed solutions is not presented here.

The ligand-field analysis demonstrates that in all the major complexes characterized in this study, unpaired electron density is found predominantly in the $4d_{xy}$ orbital of the Ru(III) ion. The calculated orbital reduction factors, in some cases

significantly less than 1.0, demonstrate delocalization of spin density onto the azole ligands in the unexchanged complexes and show covalent interactions with new ligands after exchange. In general, ligand exchange leads to increased delocalization, which is consistent with the greater covalent character of bonding to water and protein side-chain ligands, as compared to the original chloride ligands.

Table A-2 g values and corresponding ligand-field parameters for KP418, KP1019, and their derivatives.

Species	g_x	g_y	g_z	a	b	c	Δ/ξ	V/ξ	k
KP418									
Uniaxial	-2.58	-2.58	1.20	0.373	0.928	0.000	1.975	0.000	0.877
Rhombic	-3.08	-2.30	0.95	0.416	0.905	-0.093	1.849	1.196	0.990
H ₂ O	-2.47	-2.26	1.79	0.191	0.981	-0.034	4.139	1.709	0.830
(H ₂ O) ₂ - <i>trans</i>	-2.59	-2.34	1.72	0.217	0.975	-0.036	3.637	1.430	0.938
(H ₂ O) ₂ - <i>cis</i>	-2.51	-2.20	1.73	0.218	0.974	-0.052	3.748	2.112	0.757
hsTf	-2.38	-2.38	1.66	0.249	0.968	0.000	3.067	0.000	0.739
KP1019									
Uniaxial	-2.64	-2.64	1.20	0.369	0.930	0.000	2.002	0.000	0.941
Rhombic	-2.94	-2.31	0.95	0.421	0.904	-0.078	1.776	0.965	0.921
hsA-1	-2.44	-2.24	1.79	0.193	0.981	-0.034	4.100	1.675	0.778
hsA-2	-2.32	-2.32	1.84	0.169	0.986	0.000	4.502	0.000	0.800

References:

- [A1] Bleaney, B.; O'Brien, M.C.M. Proceedings of the Physical Society, London **1956**, 69B, 1216-1230.
- [A2] McGarvey, B.R. *Quim. Nova* **1998**, 21, 206-213.
- [A3] McGarvey, B.R. *Coord. Chem. Rev.* **1998**, 170, 75-92.
- [A4] Stevens, K.W.H. Proceedings of the Royal Society of London Series a-Mathematical and Physical Sciences **1953**, 219, 542-555.
- [A5] Gerloch, M.; Miller, J.R.; *Prog. Inorg. Chem.* **1968**, 10, 1-47.
- [A6] The “solver” function in Microsoft Excel optimizes the parameters a , b , c , and k almost instantaneously from these equations.

Appendix B. Supplementary Information for Chapter 3.

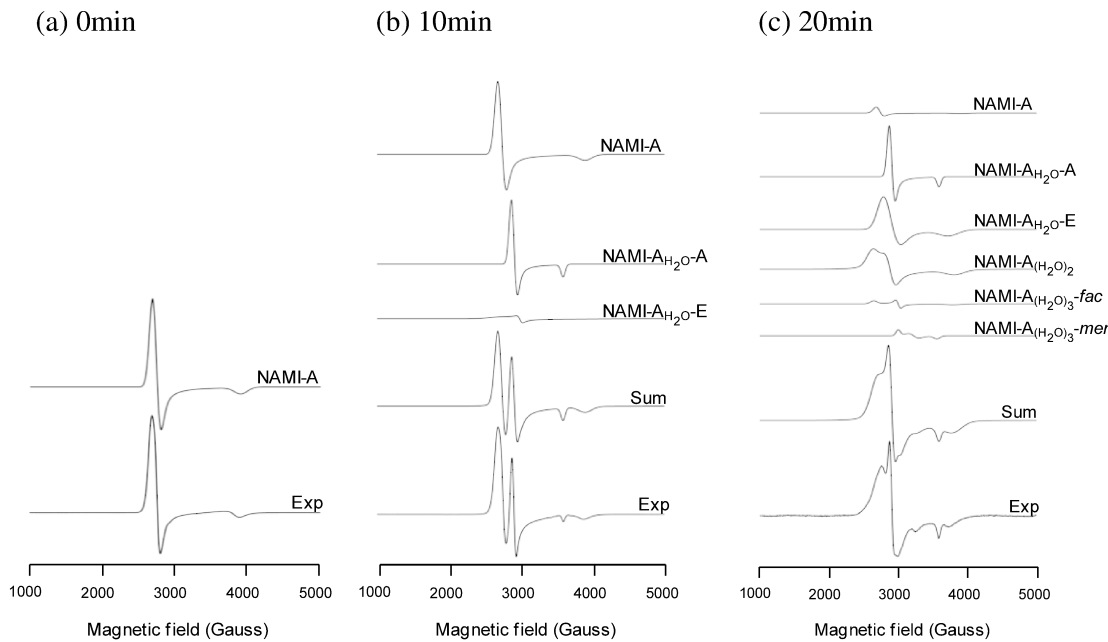
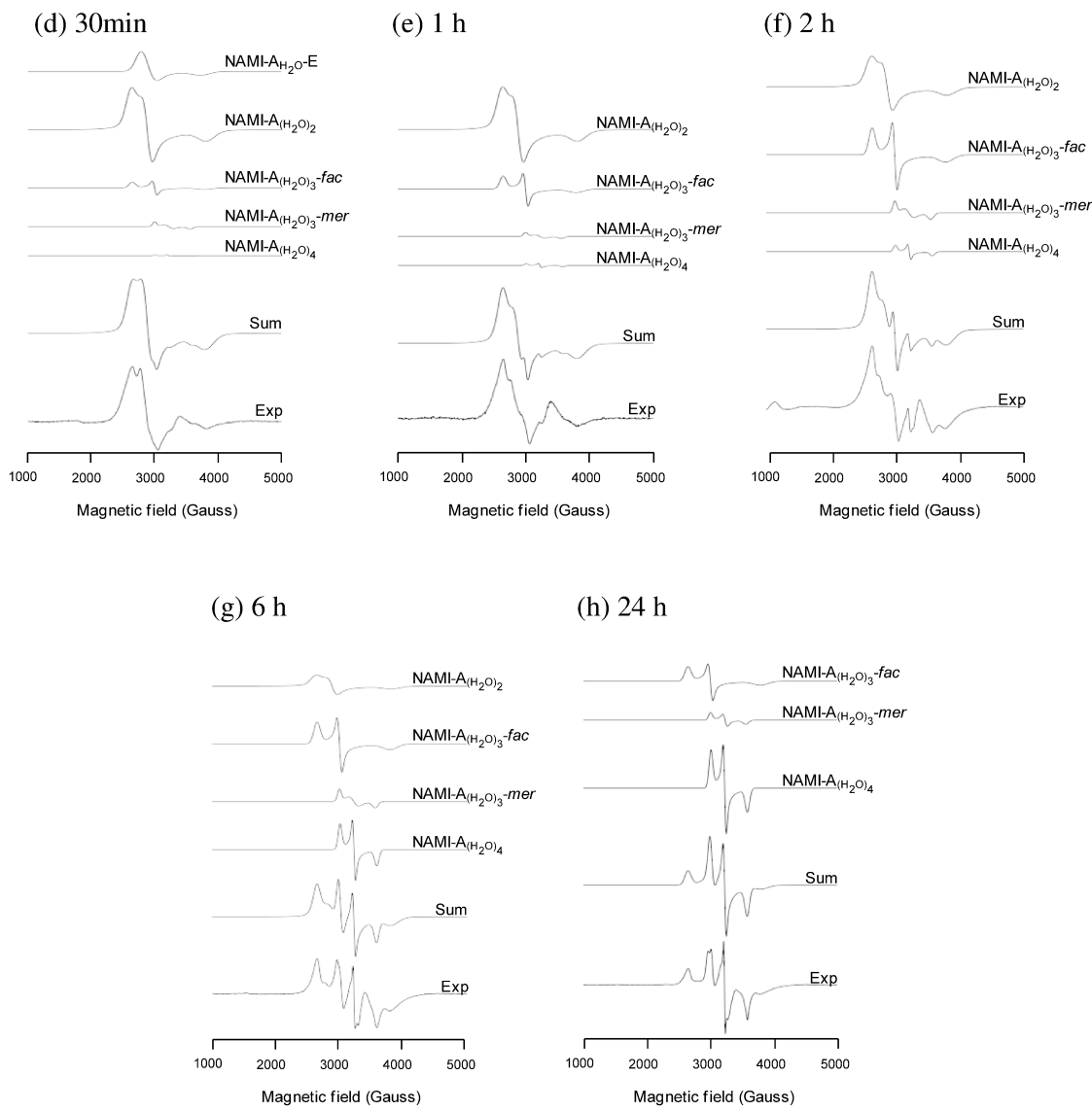
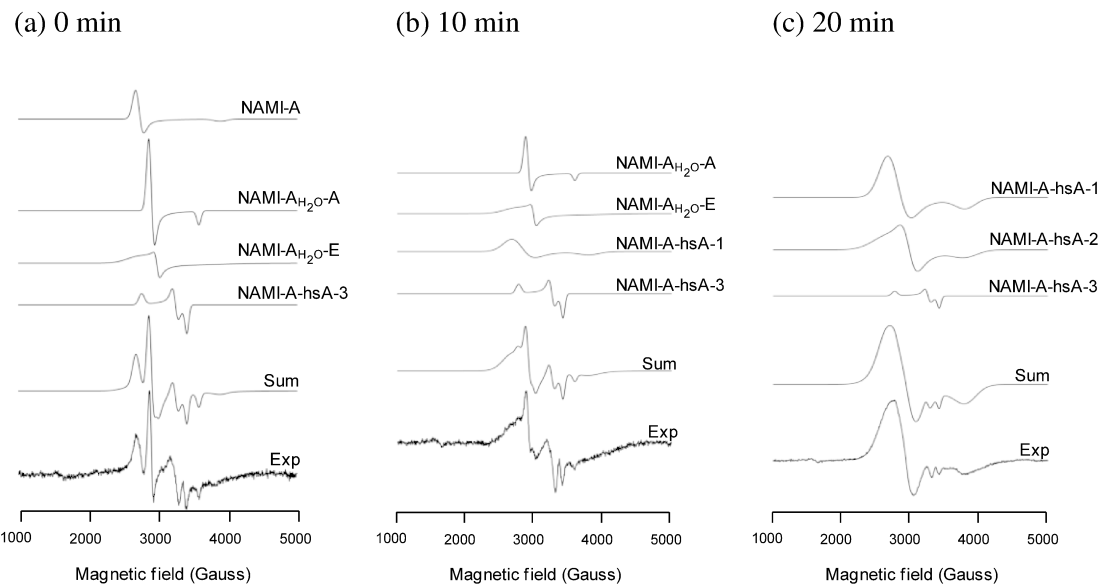


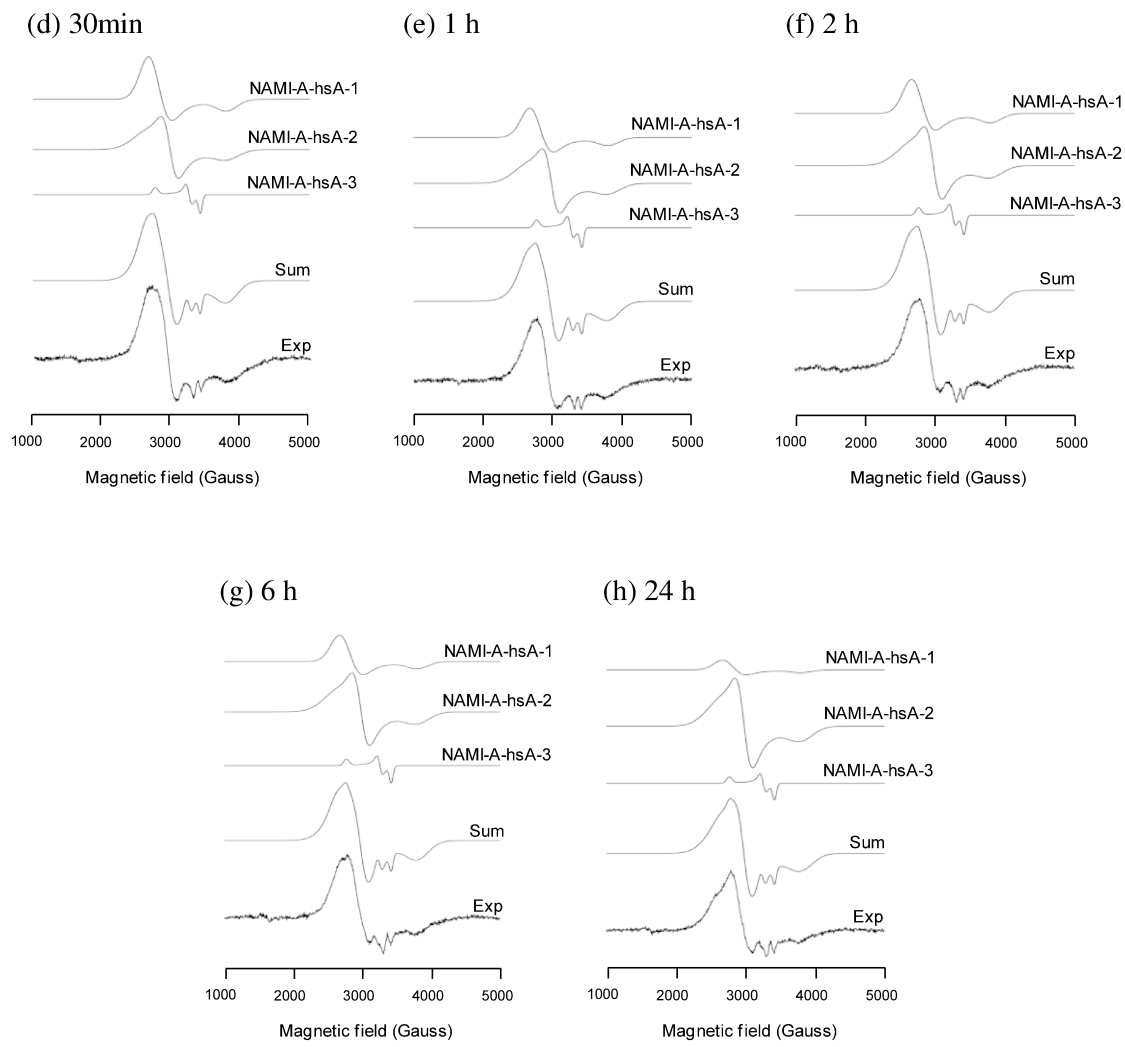
Figure B-1 (a-c) Deconvolution of EPR spectra from NAMI-A in buffer after incubation for 0, 10 and 20 minutes at 37 °C. **Experimental conditions:** see section 2.2.5. **Simulation parameters:** For g values and linewidths, see main text. Relative intensities used in simulations, NAMI-A : NAMI-A_{H₂O}-A : NAMI-A_{H₂O}-E : NAMI-A_{(H₂O)₂} : NAMI-A_{(H₂O)₃}-fac : NAMI-A_{(H₂O)₃}-mer : NAMI-A_{(H₂O)₄}, (a) 0 mins, 1.0 : 0 : 0 : 0 : 0 : 0, (b) 10 mins, 0.63 : 0.28 : 0.09 : 0 : 0 : 0, (c) 20 mins, 0.03 : 0.12 : 0.39 : 0.04 : 0.03 : 0.



Figures B-1 (d-h) Deconvolution of EPR spectra from NAMI-A in buffer after incubation for: 30 minutes and; 1, 2, 6 and 24 hours, at 37 °C. Experimental conditions as above. **Simulation parameters:** For g values and linewidths, see main text. Relative intensities used in simulations, NAMI-A : NAMI-A_{H₂O}-A : NAMI-A_{H₂O}-E : NAMI-A_{(H₂O)₂} : NAMI-A_{(H₂O)₃-fac} : NAMI-A_{(H₂O)₃-mer} : NAMI-A_{(H₂O)₄}, (d) 30 mins, 0 : 0 : 0.209 : 0.699 : 0.067 : 0.022 : 0.002, (e) 1 h, 0 : 0 : 0 : 0.796 : 0.174 : 0.022 : 0.008, (f) 2 h, 0 : 0 : 0 : 0.56 : 0.35 : 0.06 : 0.03, (g) 6 h, 0 : 0 : 0 : 0.30 : 0.42 : 0.09 : 0.18, (h) 24 h, 0 : 0 : 0 : 0 : 0.47 : 0.09 : 0.44.



Figures B-2 (a-c) Deconvolution of EPR spectra from NAMI-A in buffer with hsA after incubation for 0, 10 and 20 minutes at 37 °C. **Experimental conditions:** see section 2.2.5. **Simulation parameters:** For g values and linewidths, see main text. Relative intensities used in simulations, NAMI-A : NAMI-A_{H₂O}-A : NAMI-A_{H₂O}-E : NAMI-A-hsA-1 : NAMI-A-hsA-2 : NAMI-A-hsA-3 (a) 0 mins, 0.20 : 0.50 : 0.10 : 0 : 0 : 0.20, (b) 10 mins, 0 : 0.43 : 0.14 : 0.14 : 0 : 0.29, (c) 20 mins, 0 : 0 : 0 : 0.51 : 0.31 : 0.18.

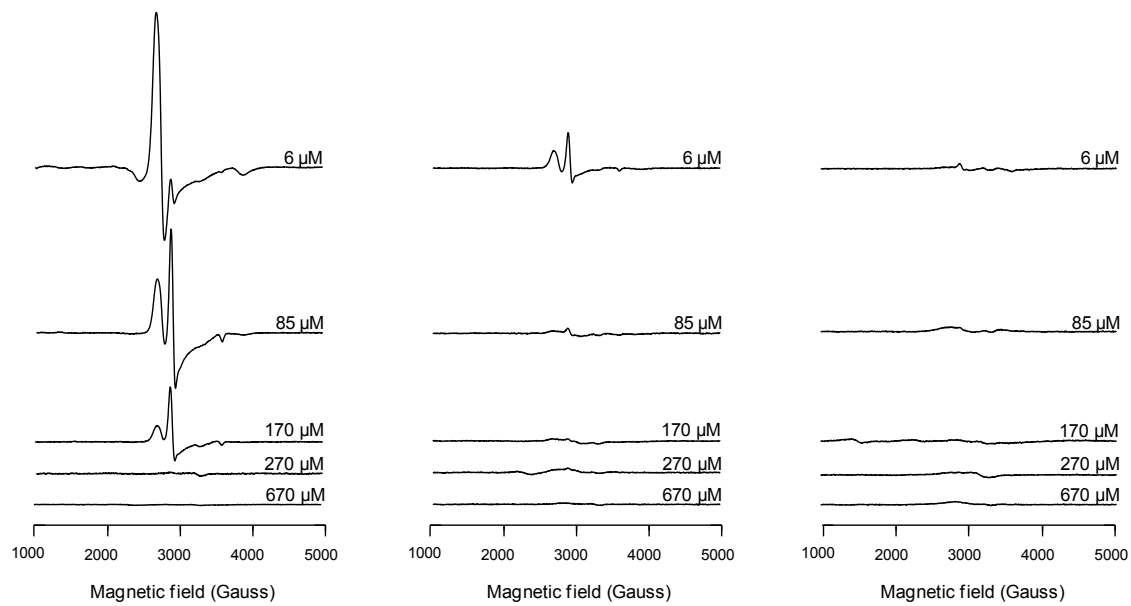


Figures B-2 **(d-h)** Deconvolution of EPR spectra from NAMI-A in buffer with hsA for: 30 minutes and; 1, 2, 6 and 24 hours, at 37 °C. Experimental conditions as above. **Simulation parameters:** Relative intensities used in simulations, NAMI-A : NAMI-A_{H₂O}-A : NAMI-A_{H₂O}-E : NAMI-A-hsA-1 : NAMI-A-hsA-2 : NAMI-A-hsA-3 **(d)** 30 mins, 0 : 0 : 0 : 0.45 : 0.35 : 0.20, **(e)** 1 h, 0 : 0 : 0 : 0.35 : 0.41 : 0.24, **(f)** 2 h, 0 : 0 : 0 : 0.37 : 0.42 : 0.21, **(g)** 6 h, 0 : 0 : 0 : 0.32 : 0.47 : 0.21, **(h)** 24 h, 0 : 0 : 0 : 0.13 : 0.64 : 0.23.

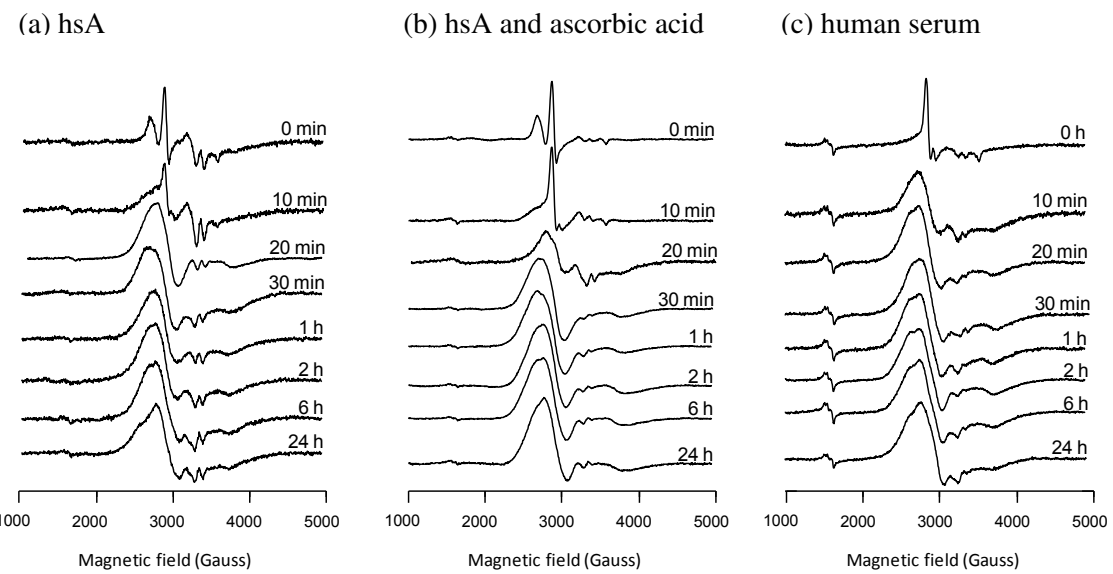
(a) Immediately frozen.

(b) Incubated for 10min at room temperature.

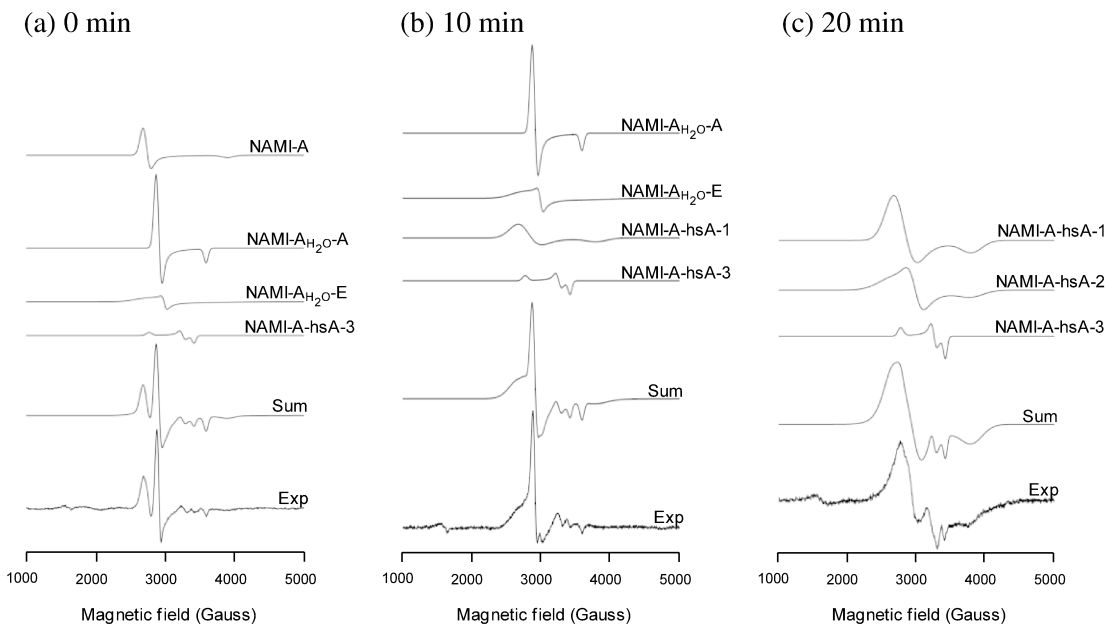
(c) Incubated for 10min at 37 °C.



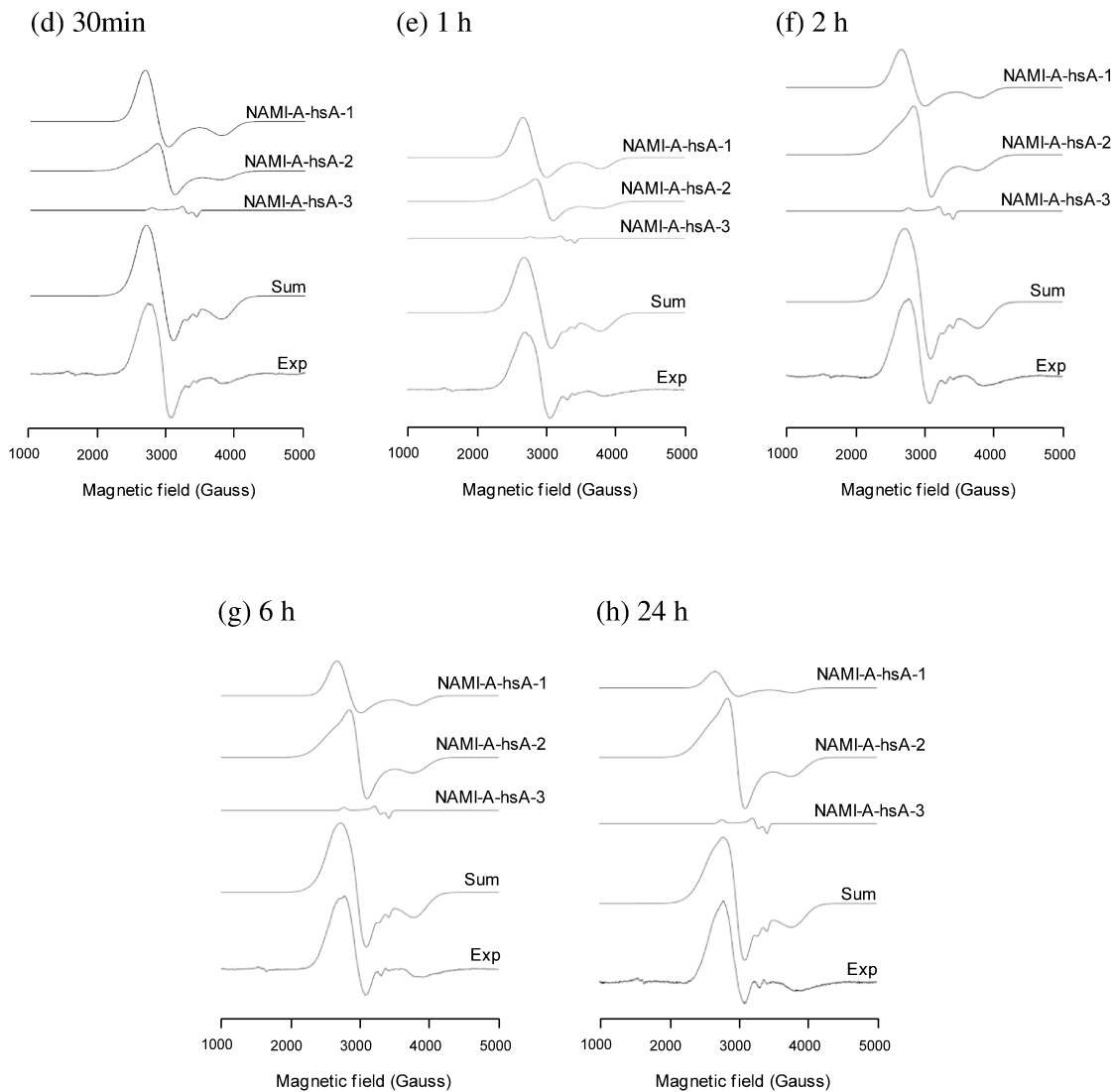
Figures B-3 (a-c) Effect of ascorbic acid concentration and incubation time on reduction of NAMI-A and aquated complexes as determined by EPR.



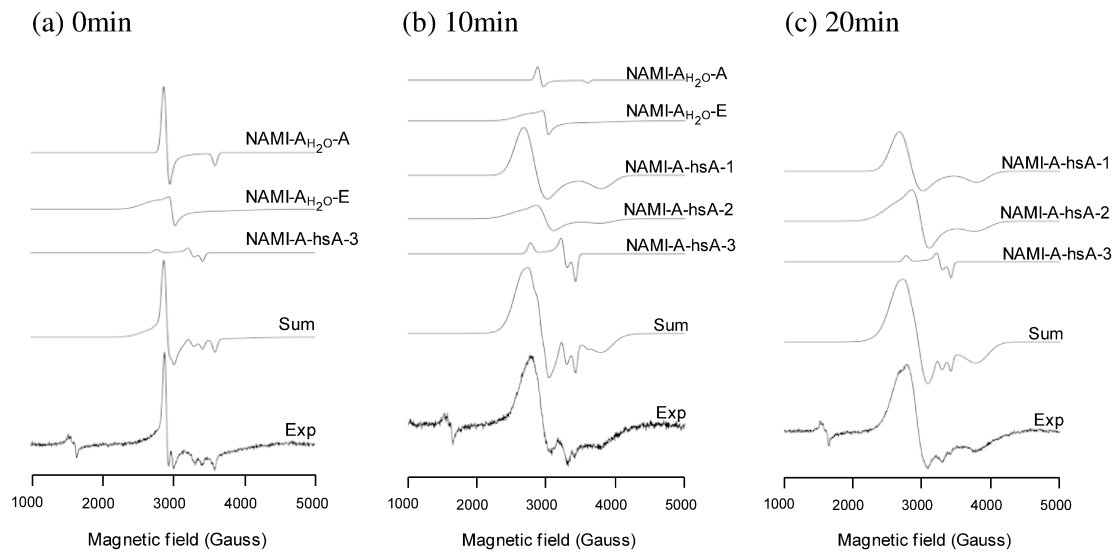
Figures B-4 (a-c) Comparison of EPR spectra from NAMI-A incubated with: (a) hsA, (b) hsA and ascorbic acid, (c) human serum.



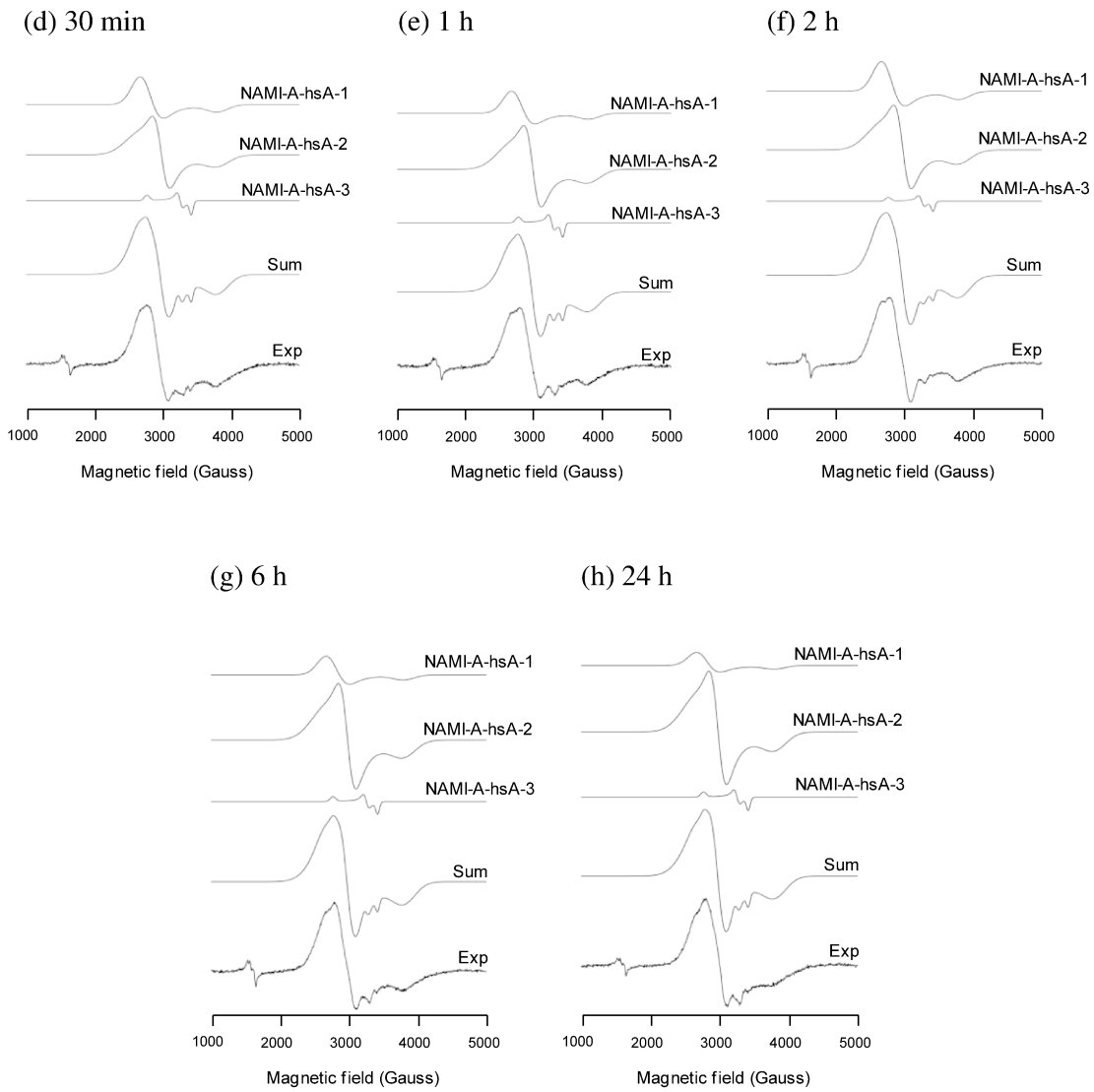
Figures B-5 (a-c) Deconvolution of EPR spectra from NAMI-A in buffer with hsA and ascorbic acid after incubation for 0, 10 and 20 minutes at 37 °C.
Experimental conditions: see section 2.2.5. **Simulation parameters:** For g values and linewidths, see main text. Relative intensities used in simulations, NAMI-A : NAMI-A_{H₂O}-A : NAMI-A_{H₂O}-E : NAMI-A-hsA-1 : NAMI-A-hsA-2 : NAMI-A-hsA-3 (a) 0 mins, 0.23 : 0.63 : 0.07 : 0 : 0 : 0.07, (b) 10 mins, 0 : 0.67 : 0.11 : 0.11 : 0 : 0.11, (c) 20 mins, 0 : 0 : 0 : 0.50 : 0.25 : 0.25.



Figures B-5 **(d-h)** Deconvolution of EPR spectra from NAMI-A in buffer with hsA and ascorbic acid after incubation for: 30 minutes and; 1, 2, 6 and 24 hours, at 37 °C. Experimental conditions as above. **Simulation parameters:** Relative intensities used in simulations, NAMI-A : NAMI-A_{H₂O}-A : NAMI-A_{H₂O}-E : NAMI-A-hsA-1 : NAMI-A-hsA-2 : NAMI-A-hsA-3 **(d)** 30 mins, 0 : 0 : 0 : 0.60 : 0.32 : 0.08, **(e)** 1 h, 0 : 0 : 0 : 0.60 : 0.33 : 0.07, **(f)** 2 h, 0 : 0 : 0 : 0.40 : 0.51 : 0.09, **(g)** 6 h, 0 : 0 : 0 : 0.39 : 0.53 : 0.08, **(h)** 24 h, 0 : 0 : 0 : 0.19 : 0.69 : 0.12.



Figures B-6 (a-c) Deconvolution of EPR spectra from NAMI-A in human serum after incubation for 0, 10 and 20 minutes at 37 °C. **Experimental conditions:** see section 2.2.5. **Simulation parameters:** For g values and linewidths, see main text. Relative intensities used in simulations, NAMI-A : NAMI-A_{H₂O}-A : NAMI-A_{H₂O}-E : NAMI-A-hsA-1 : NAMI-A-hsA-2 : NAMI-A-hsA-3 (a) 0 mins, 0 : 0.73 : 0.18 : 0 : 0 : 0.09, (b) 10 mins, 0 : 0.12 : 0.12 : 0.41 : 0.12 : 0.23, (c) 20 mins, 0 : 0 : 0 : 0.46 : 0.36 : 0.18.



Figures B-6 (d-h) Deconvolution of EPR spectra from NAMI-A in human serum after incubation after incubation for: 30 minutes and; 1, 2, 6 and 24 hours, at 37 °C. **Experimental conditions:** as above. **Simulation parameters:** Relative intensities used in simulations, NAMI-A : NAMI-A_{H₂O}-A : NAMI-A_{H₂O}-E : NAMI-A-hsA-1 : NAMI-A-hsA-2 : NAMI-A-hsA-3 (d) 30 mins, 0 : 0 : 0 : 0.35 : 0.48 : 0.17, (e) 1 h, 0 : 0 : 0 : 0.27 : 0.55 : 0.18, (f) 2 h, 0 : 0 : 0 : 0.35 : 0.53 : 0.12, (g) 6 h, 0 : 0 : 0 : 0.22 : 0.64 : 0.14, (h) 24 h, 0 : 0 : 0 : 0.15 : 0.70 : 0.15

Appendix C. Supplementary Information for Chapter 4.

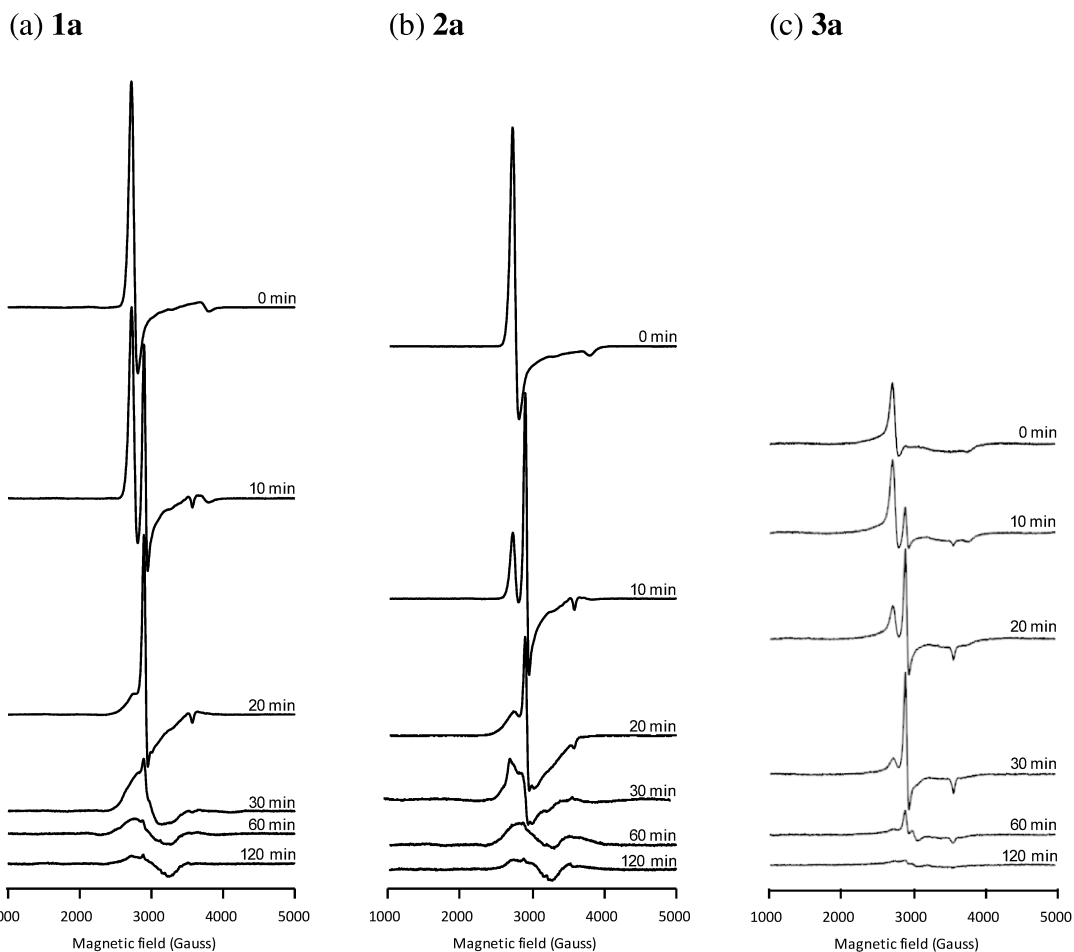


Figure C-1 (a-c) EPR spectra for the solution behaviour of complexes **1a** (a), **2a** (b), and **3a** (c) in buffer (3 mM) after incubation at 37 °C. **Experimental conditions:** see section 2.2.5.

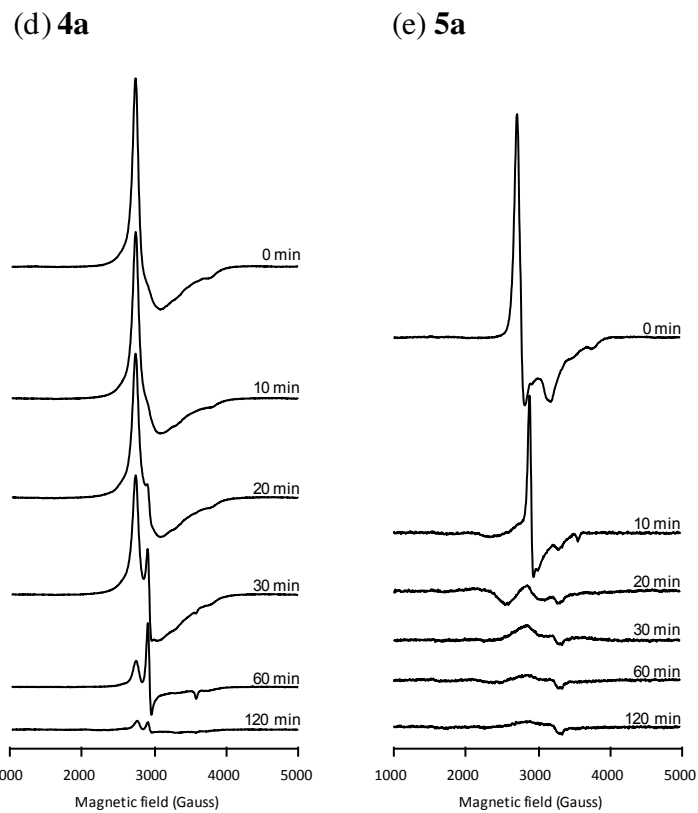


Figure C-1 (d-e) EPR spectra for the solution behaviour of complexes **4a** (d) and **5a** (e) in buffer* (3 mM) after incubation at 37 °C. **Experimental conditions:** see section 2.2.5. (*Complex **4a** dissolved in a 20% DMSO solution.)

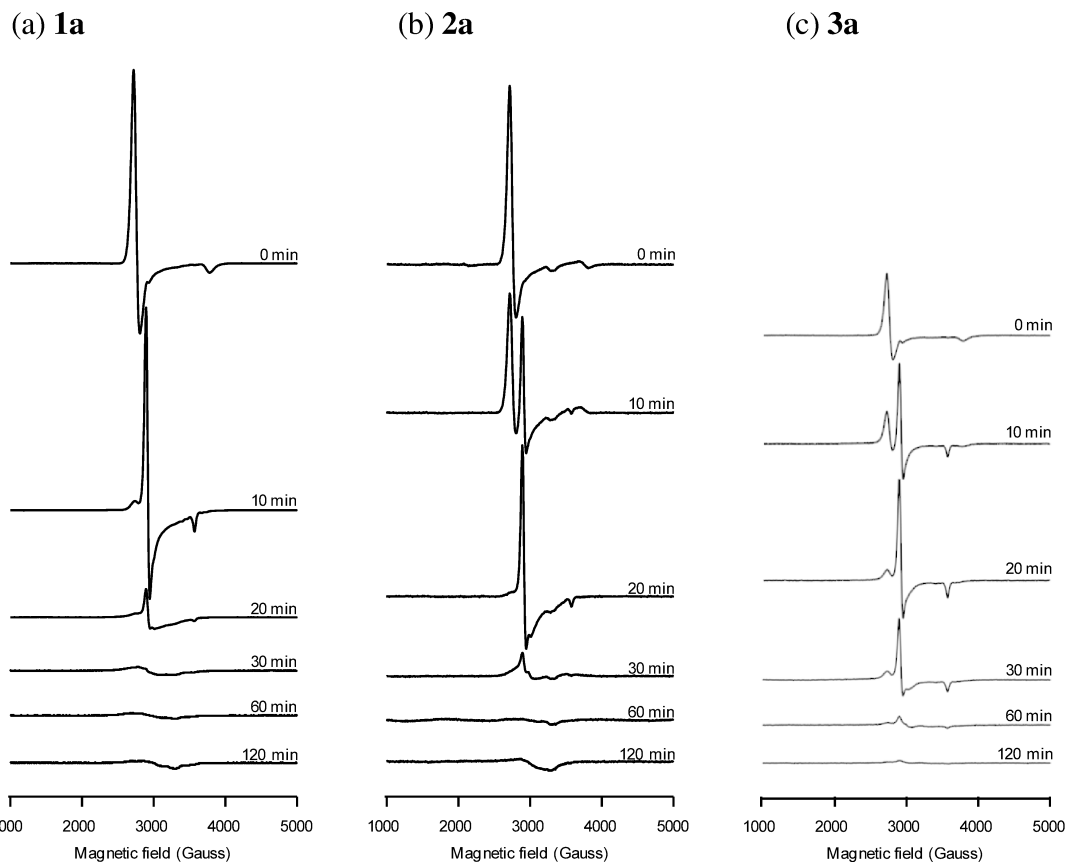


Figure C-2 (a-c) EPR spectra for the solution behaviour of complexes **1b** (a), **2b** (b), and **3b** (c) in buffer (3 mM) after incubation at 37 °C. **Experimental conditions:** see section 2.2.5.

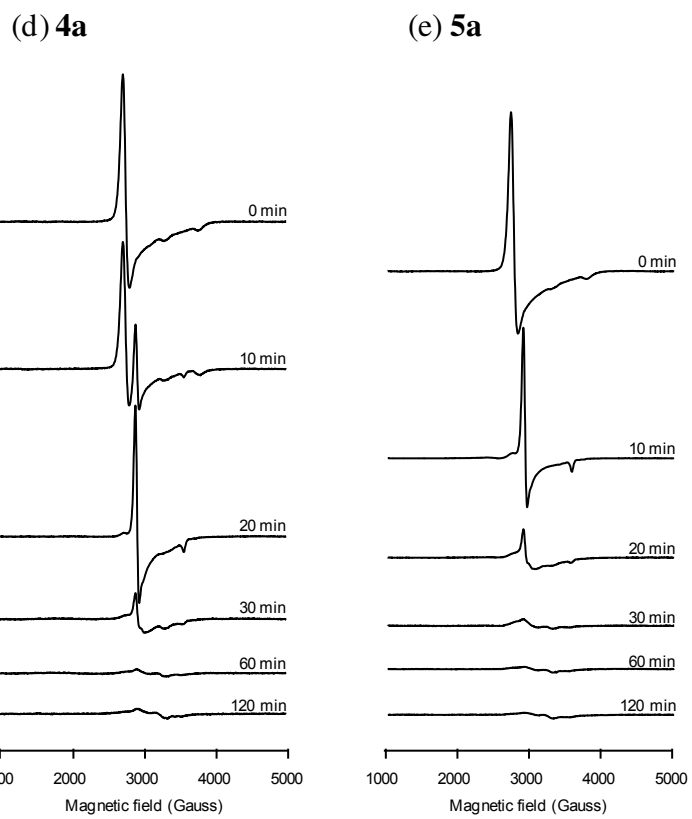


Figure C-2 (d-e) EPR spectra for the solution behaviour of complexes **4b** (d) and **5b** (e) in buffer (3 mM) after incubation at 37 °C. **Experimental conditions:** see section 2.2.5.

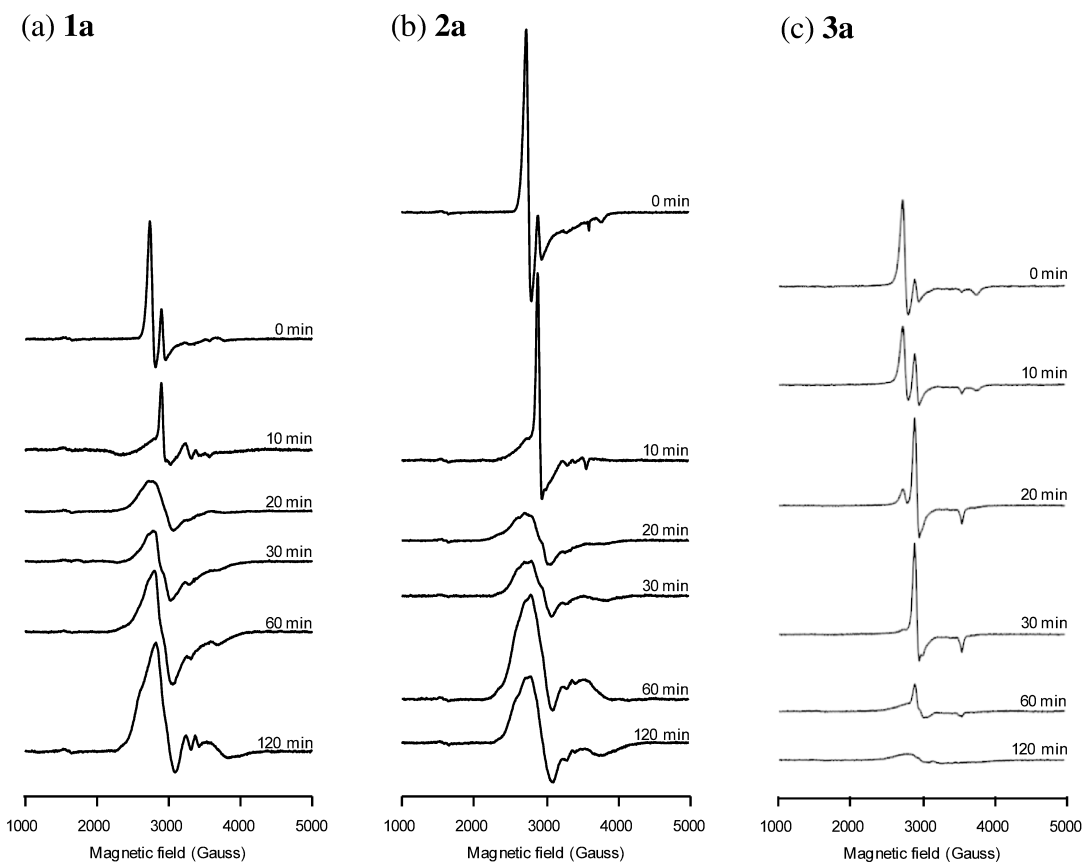


Figure C-3 (a-c) EPR spectra for the protein binding behaviour of complexes **1a** (a), **2a** (b), and **3a** (c) in buffer (1 mM) with hsA (0.5 mM) after incubation at 37 °C. **Experimental conditions:** see section 2.2.5.

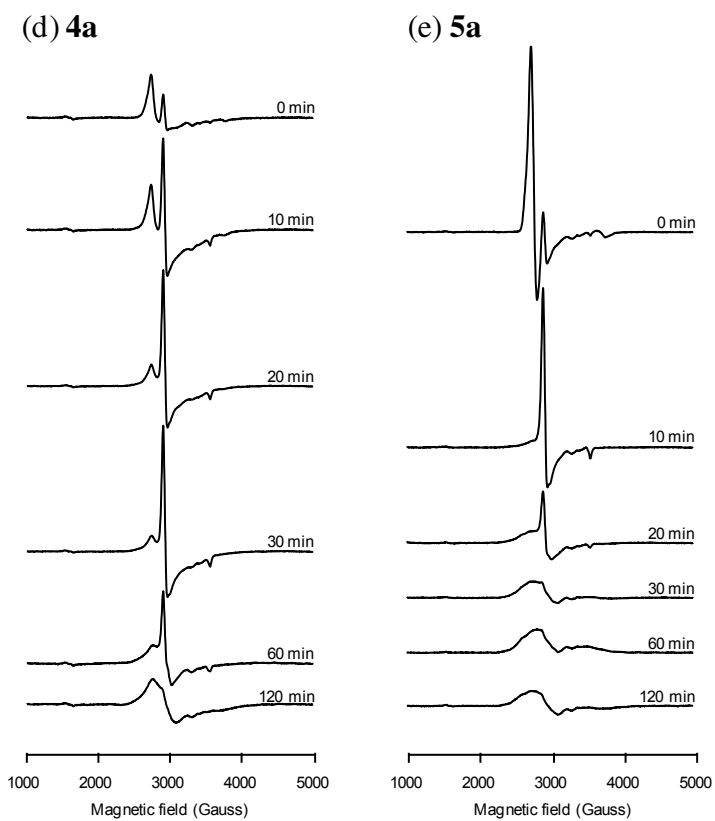


Figure C-3 (d-e) EPR spectra for the protein binding behaviour of complexes **4a** (d), and **5a** (e) in buffer (1 mM) with hsA (0.5 mM) after incubation at 37 °C.
Experimental conditions: see section 2.2.5.

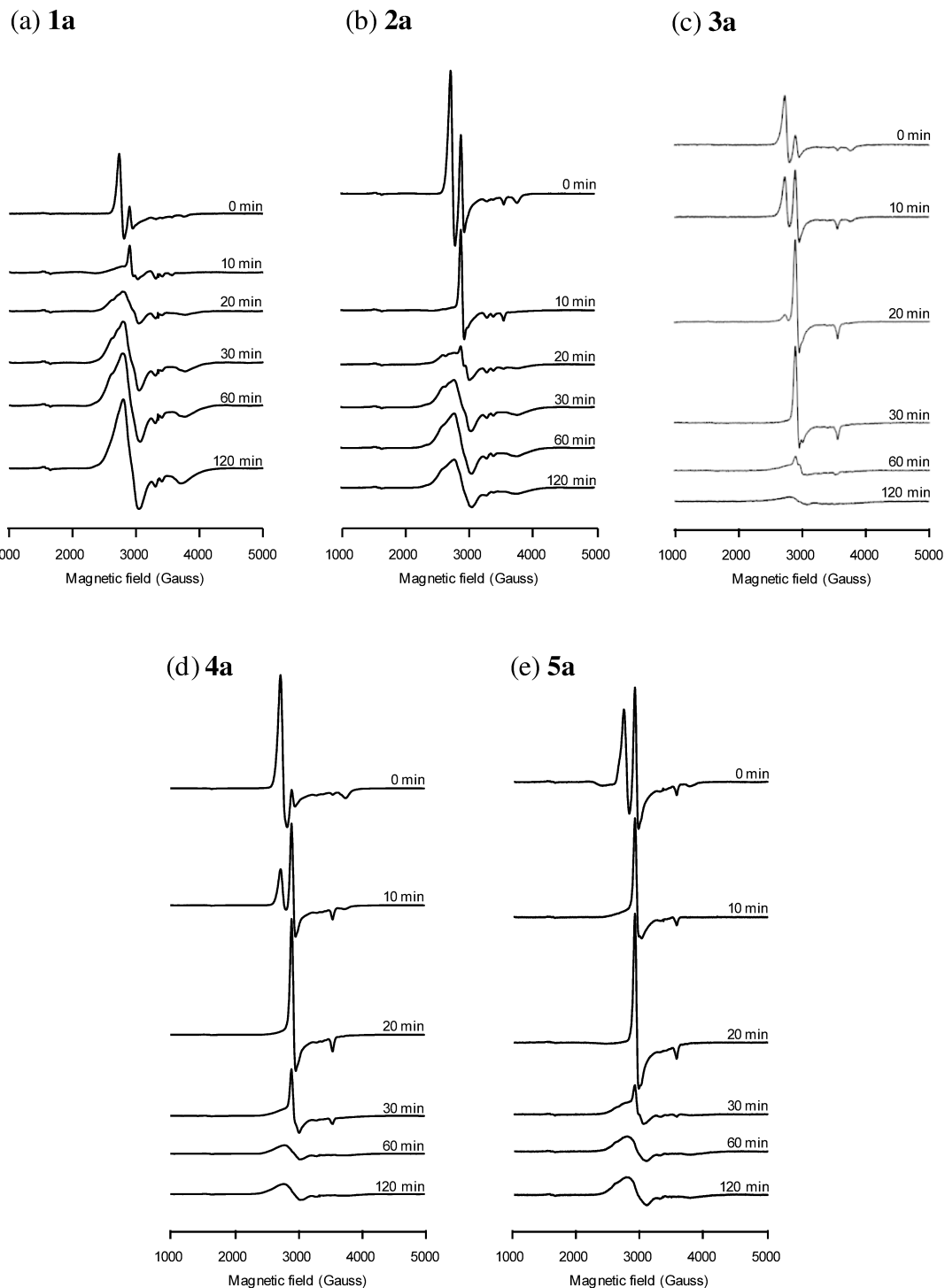


Figure C-4 (a-e) EPR spectra for the protein binding behaviour of complexes **1b** (a), **2b** (b), **3b** (c), **4b** (d), and **5b** (e) in buffer (1 mM) with hSA (0.5 mM) after incubation at 37 °C. **Experimental conditions:** see section 2.2.5.

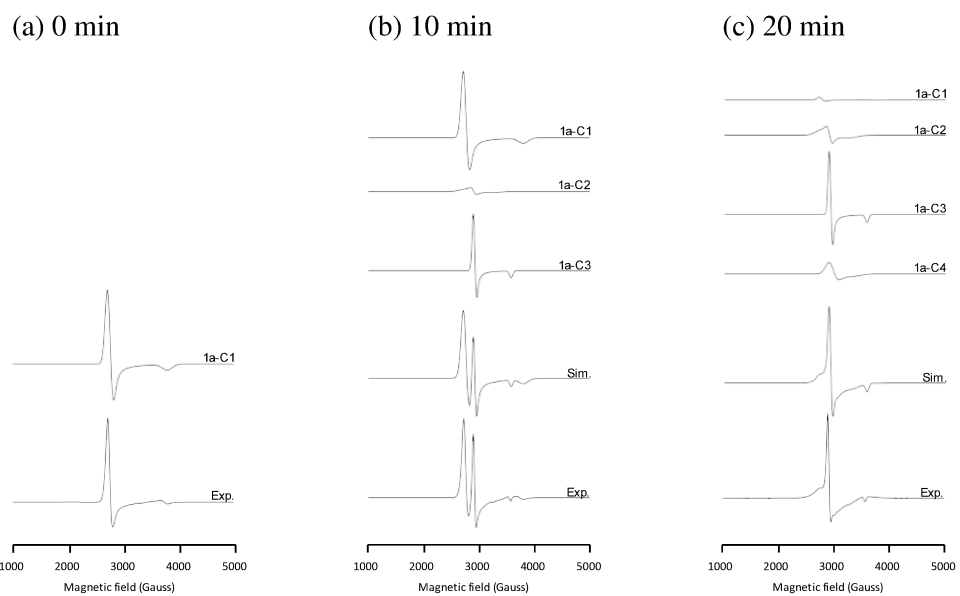


Figure C-5 (a-c) Deconvolution of EPR spectra from **1a** in buffer after incubation for 0, 10, and 20 minutes at 37 °C. **Experimental conditions:** see section 2.2.5. **Simulation parameters:** For g values and linewidths, see **Table C-1**. Relative intensities used in simulations, 1a-C1 : 1a-C2 : 1a-C3 : 1a-C4 (a) 0 mins, 1 : 0 : 0 : 0, (b) 10 mins, 0.52 : 0.03 : 0.45 : 0, (c) 20 mins, 0.03 : 0.10 : 0.73 : 0.13.

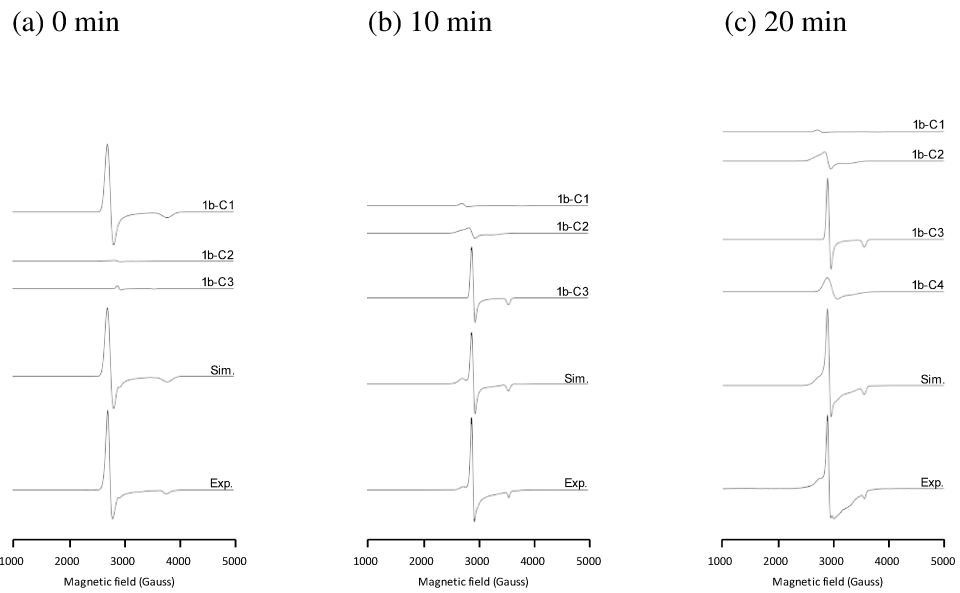


Figure C-6 (a-c) Deconvolution of EPR spectra from **1b** in buffer after incubation for 0, 10, and 20 minutes at 37 °C. **Experimental conditions:** see section 2.2.5. **Simulation parameters:** For g values and linewidths, see **Table C-1**. Relative intensities used in simulations, 1b-C1 : 1b-C2 : 1b-C3 : 1b-C4 (a) 0 mins, 0.95 : 0.01 : 0.04 : 0, (b) 10 mins, 0.04 : 0.10 : 0.87 : 0, (c) 20 mins, 0.02 : 0.11 : 0.71 : 0.16.

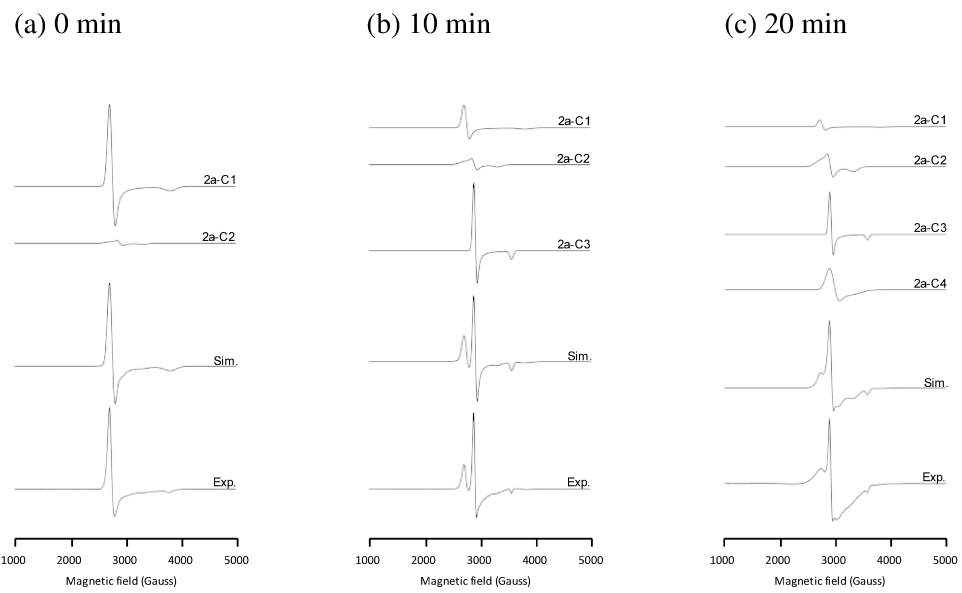


Figure C-7 (a-c) Deconvolution of EPR spectra from **2a** in buffer after incubation for 0, 10, and 20 minutes at 37 °C. **Experimental conditions:** see section 2.2.5. **Simulation parameters:** For g values and linewidths, see **Table C-1**. Relative intensities used in simulations, 2a-C1 : 2a-C2 : 2a-C3 : 2a-C4 (a) 0 mins, 0.94 : 0.06 : 0 : 0, (b) 10 mins, 0.23 : 0.06 : 0.70 : 0, (c) 20 mins, 0.08 : 0.15 : 0.51 : 0.26.

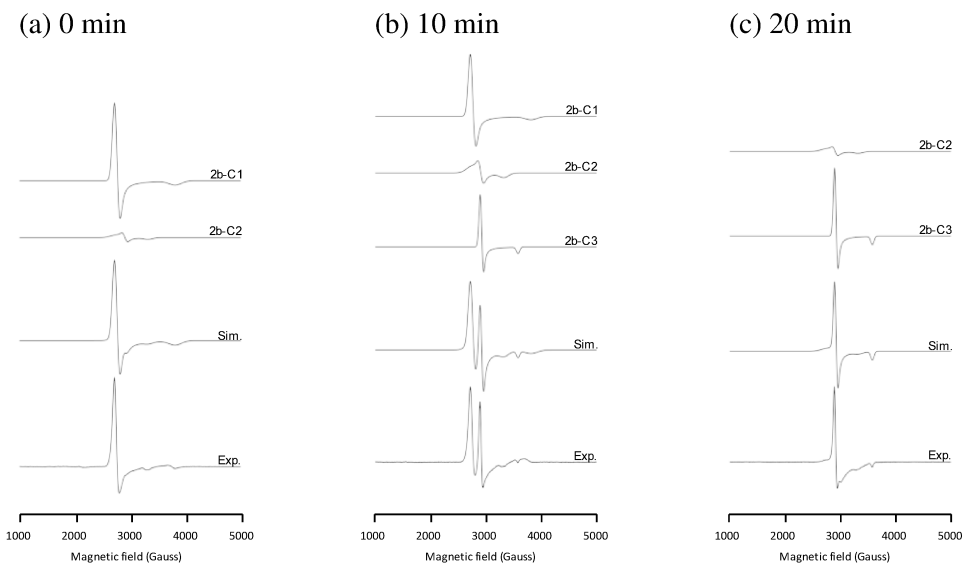


Figure C-8 (a-c) Deconvolution of EPR spectra from **2b** in buffer after incubation for 0, 10, and 20 minutes at 37 °C. **Experimental conditions:** see section 2.2.5. **Simulation parameters:** For g values and linewidths, see Table C-1. Relative intensities used in simulations, 2b-C1 : 2b-C2 : 2b-C3 (a) 0 mins, 0.94 : 0.06 : 0, (b) 10 mins, 0.49 : 0.10 : 0.41, (c) 20 mins, 0 : 0.07 : 0.93.

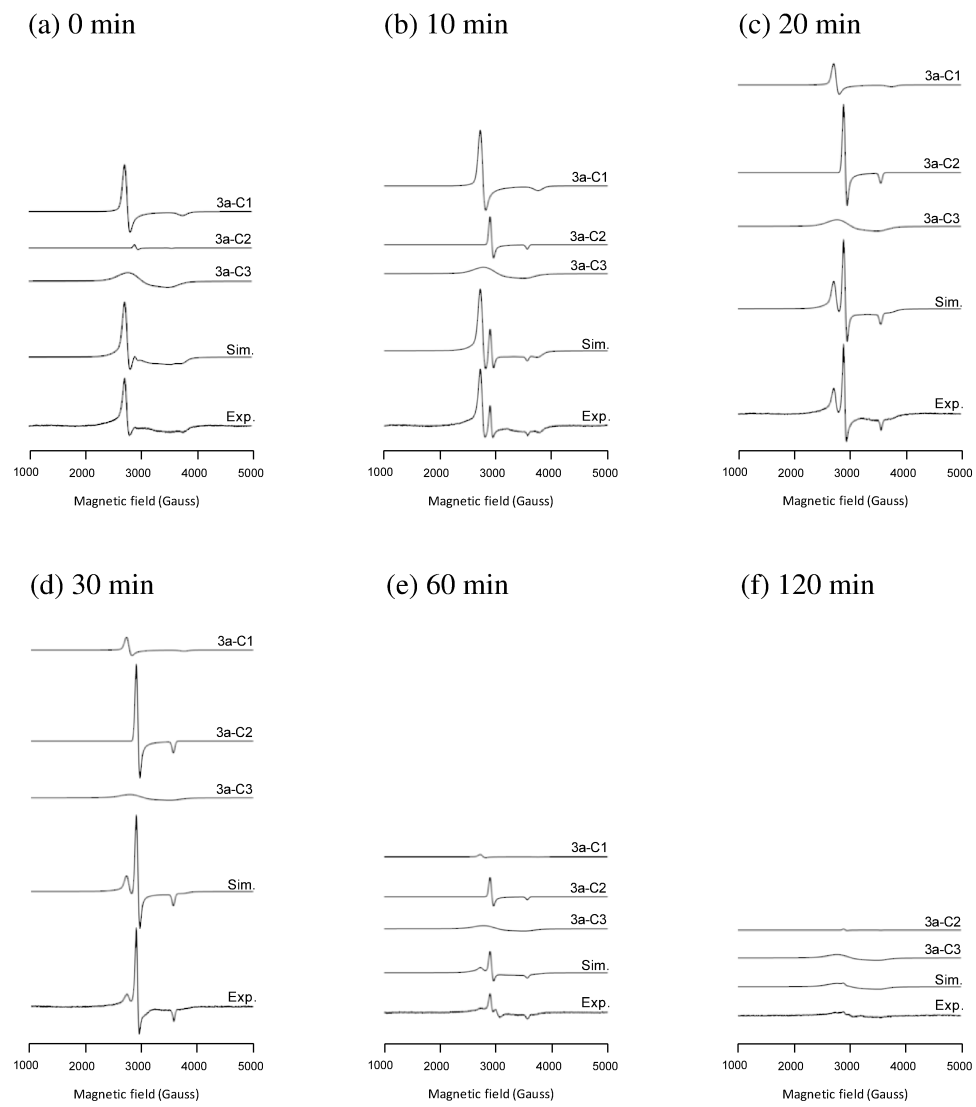


Figure C-9 (a-f) Deconvolution of EPR spectra from **3a** in buffer after incubation for 0, 10, 20, 30, 60, and 120 minutes at 37 °C. **Experimental conditions:** see section 2.2.5. **Simulation parameters:** For g values and linewidths, see **Table C-1**. Relative intensities used in simulations, 3a-C1 : 3a-C2 : 3a-C3 (a) 0 mins, 0.80 : 0.05 : 0.15, (b) 10 mins, 0.62 : 0.31 : 0.07, (c) 20 mins, 0.22 : 0.71 : 0.07, (d) 30 mins, 0.14 : 0.83 : 0.03, (e) 60 mins, 0.09 : 0.78 : 0.13, (f) 120 mins, 0 : 0.25 : 0.75.

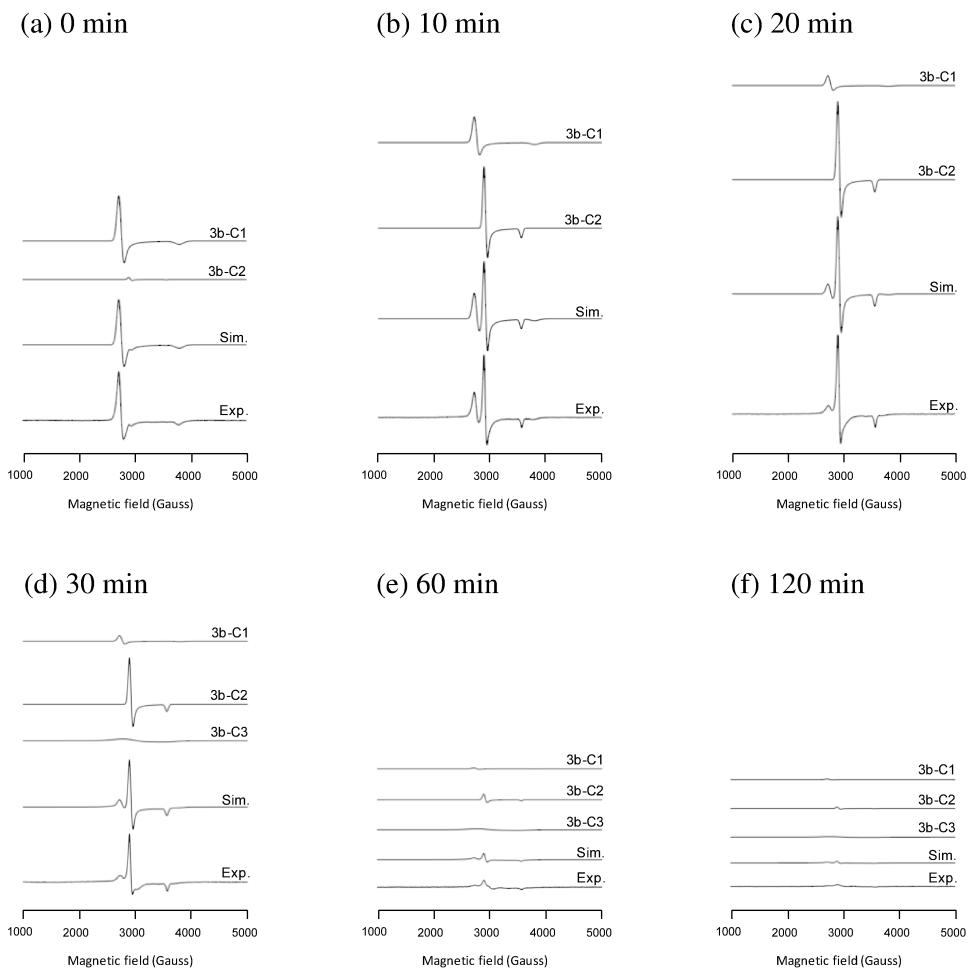


Figure C-10 (a-f) Deconvolution of EPR spectra from **3b** in buffer after incubation for 0, 10, 20, 30, 60, and 120 minutes at 37 °C. **Experimental conditions:** see section 2.2.5. **Simulation parameters:** For g values and linewidths, see **Table C-1**. Relative intensities used in simulations, 3b-C1 : 3b-C2 : 3b-C3 (a) 0 mins, 0.96 : 0.04 : 0, (b) 10 mins, 0.29 : 0.71 : 0, (c) 20 mins, 0.11 : 0.89 : 0, (d) 30 mins, 0.10 : 0.87 : 0.03, (e) 60 mins, 0.13 : 0.74 : 0.13, (f) 120 mins, 0.2 : 0.6 : 0.2.

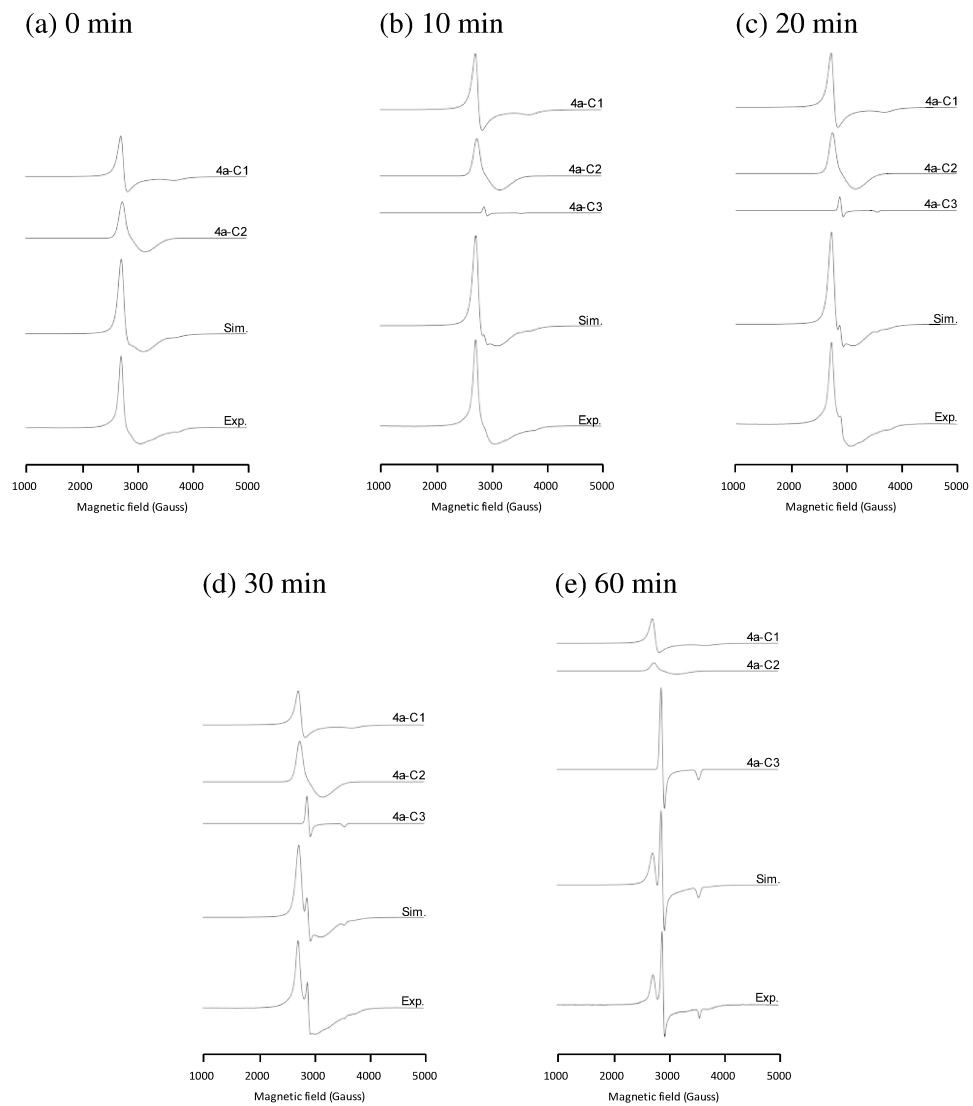


Figure C-11 (a-e) Deconvolution of EPR spectra from **4a** in 20% DMSO and buffer after incubation for 0, 10, 20, 30 and 60 minutes at 37 °C. **Experimental conditions:** see section 2.2.5. **Simulation parameters:** For g values and linewidths, see **Table C-1**. Relative intensities used in simulations, 4a-C1 : 4a-C2 : 4a-C3 (a) 0 mins, 0.53 : 0.47 : 0, (b) 10 mins, 0.56 : 0.38 : 0.06, (c) 20 mins, 0.50 : 0.38 : 0.13. (d) 30 mins, 0.33 : 0.40 : 0.27, (e) 60 mins, 0.21 : 0.07 : 0.71.

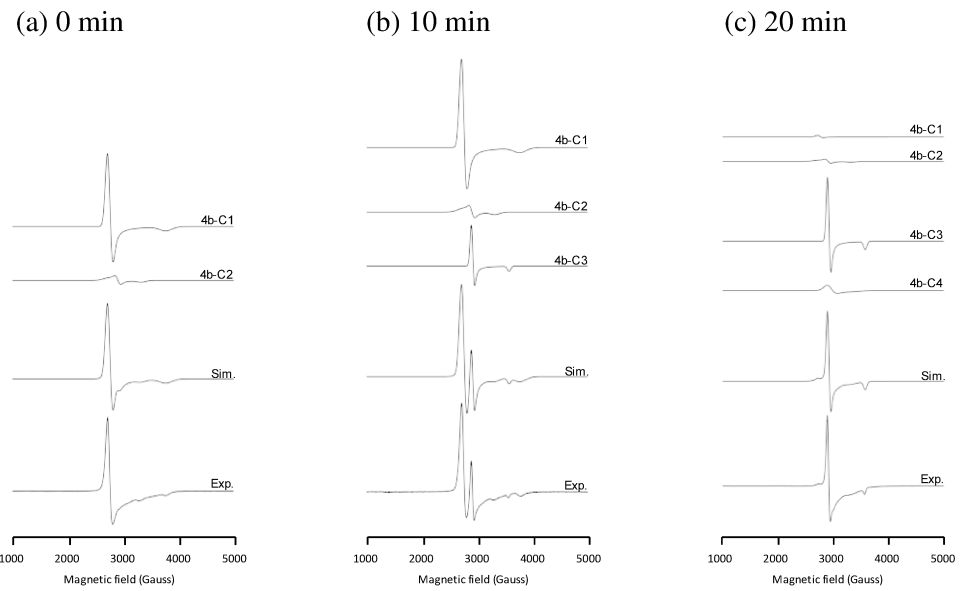


Figure C-12 (a-c) Deconvolution of EPR spectra from **4b** in buffer after incubation for 0, 10, and 20 minutes at 37 °C. **Experimental conditions:** see section 2.2.5. **Simulation parameters:** For g values and linewidths, see **Table C-1**. Relative intensities used in simulations, 4b-C1 : 4b-C2 : 4b-C3 : 4b-C4 **(a)** 0 mins, 0.94 : 0.06 : 0 : 0, **(b)** 10 mins, 0.65 : 0.05 : 0.30 : 0, **(c)** 20 mins, 0.02 : 0.03 : 0.88 : 0.07.

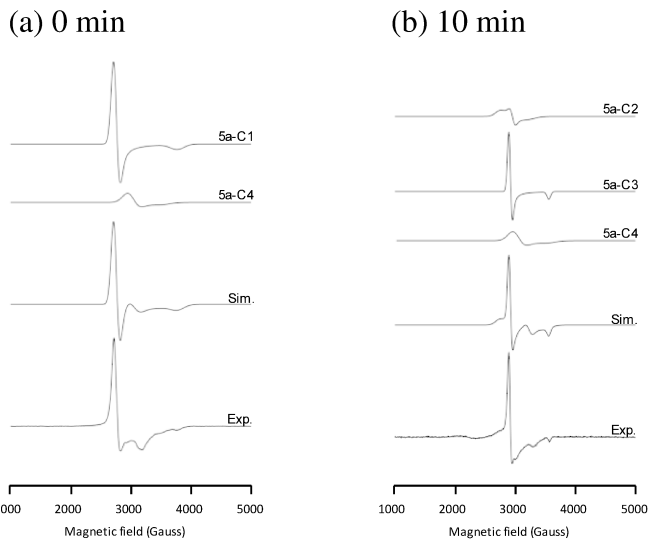


Figure C-13 (a-b) Deconvolution of EPR spectra from **5a** in buffer after incubation for 0 and 10 minutes at 37 °C. **Experimental conditions:** see section 2.2.5. **Simulation parameters:** For g values and linewidths, see **Table C-1**. Relative intensities used in simulations, 5a-C1 : 5a-C2 : 5a-C3 : 5a-C4 (a) 0 mins, 0.90 : 0 : 0 : 0.10, (b) 10 mins, 0 : 0.12 : 0.80 : 0.08.

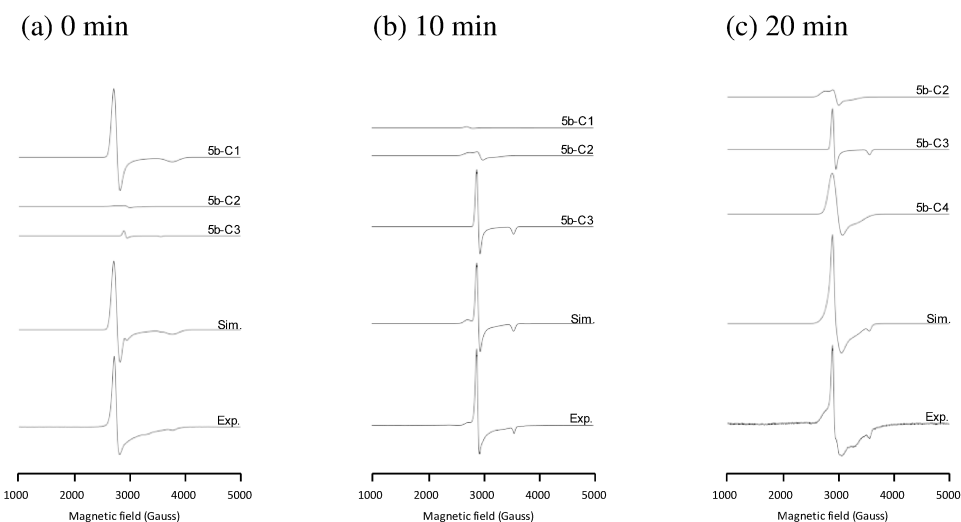


Figure C-14 (a-c) Deconvolution of EPR spectra from **5b** in buffer after incubation for 0, 10, and 20 minutes at 37 °C. **Experimental conditions:** see section 2.2.5. **Simulation parameters:** For g values and linewidths, see **Table C-1**. Relative intensities used in simulations, 5b-C1 : 5b-C2 : 5b-C3 : 5b-C4 (a) 0 mins, 0.92: 0.013 : 0.066 : 0, (b) 10 mins, 0.02 : 0.07 : 0.91 : 0, (c) 20 mins, 0 : 0.09 : 0.45 : 0.45.

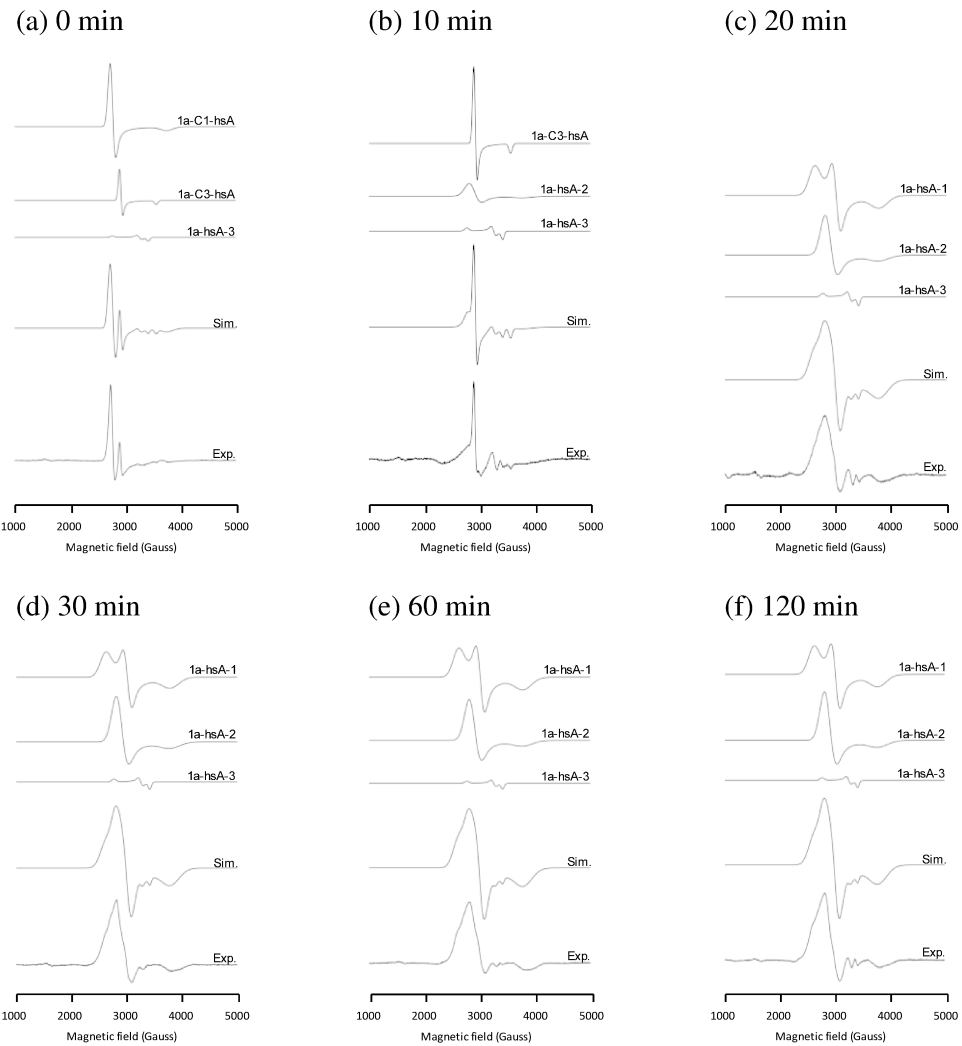


Figure C-15 (a-f) Deconvolution of EPR spectra from **1a** in buffer with hsA after incubation for 0 to 120 minutes at 37 °C. **Experimental conditions:** see section 2.2.5. **Simulation parameters:** For g values and linewidths, see **Table C-2**. Relative intensities used in simulations, 1a-C1-hsA : 1a-C3-hsA : NAMI-A-hsA-3 : 1a-hsA-1 : 1a-hsA-2 (a) 0 mins, 0.64 : 0.32 : 0.04 : 0 : 0, (b) 10 mins, 0 : 0.78 : 0.09 : 0.13 : 0, (c) 20 mins, 0 : 0 : 0.11 : 0.42 : 0.47, (d) 30 mins, 0 : 0 : 0.09 : 0.36 : 0.55, (e) 60 mins, 0 : 0 : 0.07 : 0.43 : 0.50, (f) 120 mins, 0 : 0 : 0.08 : 0.38 : 0.54.

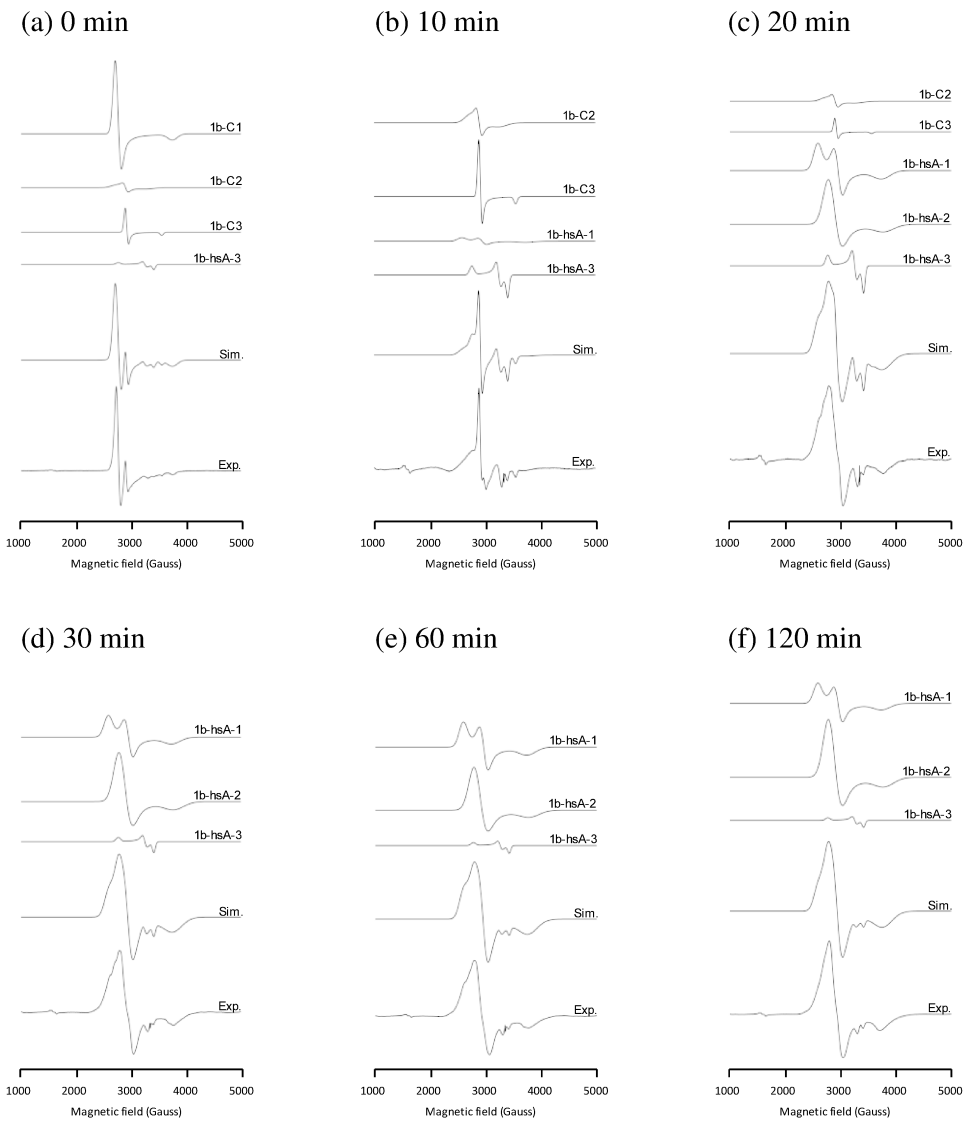


Figure C-16 (a-f) Deconvolution of EPR spectra from **1b** in buffer with hsA after incubation for 0 to 120 minutes at 37 °C. **Experimental conditions:** see section 2.2.5. **Simulation parameters:** For g values and linewidths, see **Table C-2**. Relative intensities used in simulations, 1b-C1 : 1b-C2 : 1b-C3 : NAMI-A-hsA-3 : 1b-hsA-1 : 1b-hsA-2 (a) 0 mins, 0.68 : 0.05 : 0.23 : 0.05 : 0 : 0, (b) 10 mins, 0 : 0.15 : 0.58 : 0.23 : 0.03 : 0, (c) 20 mins, 0 : 0.06 : 0.11 : 0.23 : 0.23 : 0.38, (d) 30 mins, 0 : 0 : 0 : 0.13 : 0.27 : 0.60, (e) 60 mins, 0 : 0 : 0 : 0.10 : 0.33 : 0.56, (f) 120 mins, 0 : 0 : 0 : 0.08 : 0.24 : 0.68.

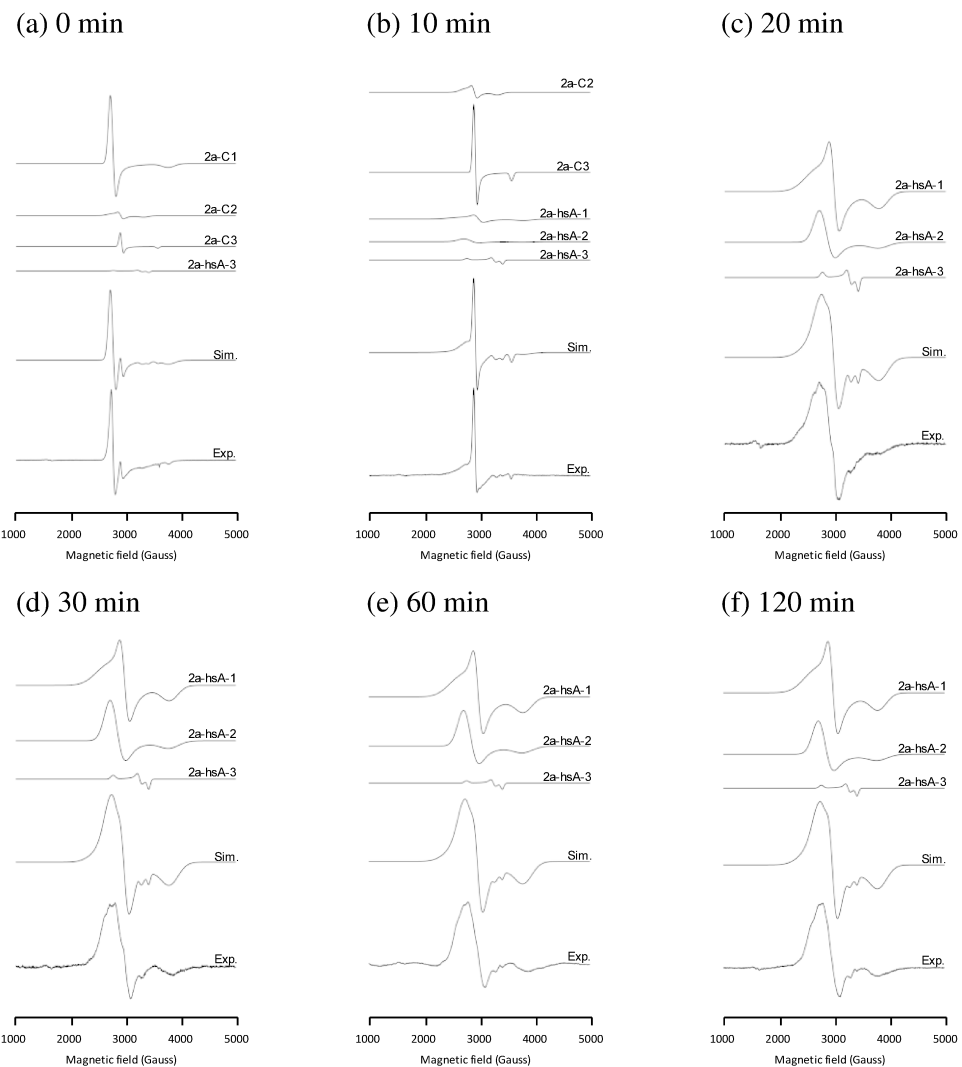


Figure C-17 (a-f) Deconvolution of EPR spectra from **2a** in buffer with hsA after incubation for 0 to 120 minutes at 37 °C. **Experimental conditions:** see section 2.2.5. **Simulation parameters:** For g values and linewidths, see **Table C-2**. Relative intensities used in simulations, 2a-C1 : 2a-C2 : 2a-C3 : NAMI-A-hsA-3 : 2a-hsA-1 : 2a-hsA-2 (**a**) 0 mins, 0.78 : 0.04 : 0.16 : 0.02 : 0 : 0, (**b**) 10 mins, 0 : 0.08 : 0.79 : 0.05 : 0.05 : 0.03, (**c**) 20 mins, 0 : 0 : 0 : 0.14 : 0.52 : 0.33, (**d**) 30 mins, 0 : 0 : 0 : 0.11 : 0.47 : 0.42, (**e**) 60 mins, 0 : 0 : 0 : 0.07 : 0.52 : 0.40, (**f**) 120 mins, 0 : 0 : 0 : 0.08 : 0.56 : 0.36.

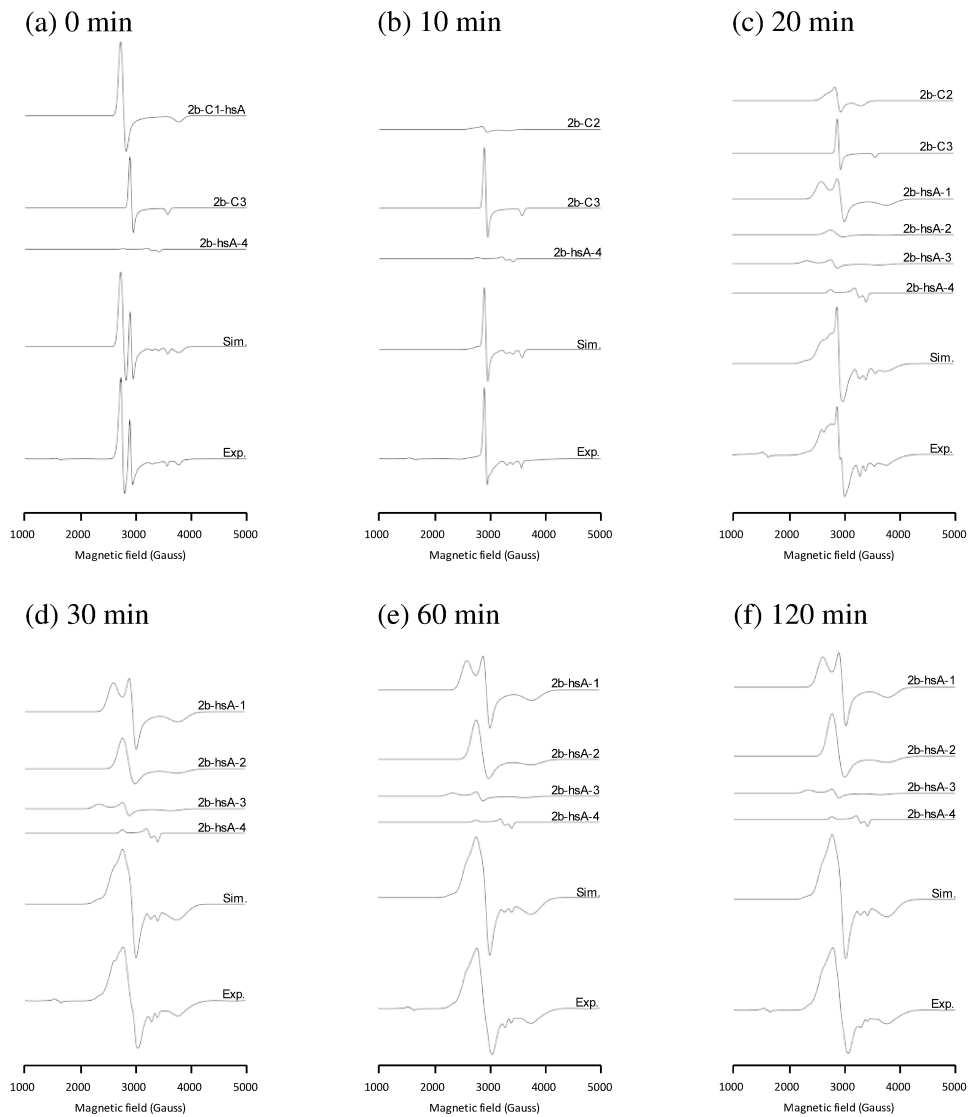


Figure C-18 (a-f) Deconvolution of EPR spectra from **2b** in buffer with hsA after incubation for 0 to 120 minutes at 37 °C. **Experimental conditions:** see section 2.2.5. **Simulation parameters:** For g values and linewidths, see **Table C-2**. Relative intensities used in simulations, 2b-C1-hsA : 2b-C2 : 2b-C3 : NAMI-A-hsA-3 : 2b-hsA-1 : 2b-hsA-2 : 2b-hsA-3 (a) 0 mins, 0.58 : 0 : 0.40 : 0.02 : 0 : 0 : 0, (b) 10 mins, 0 : 0.05 : 0.91 : 0.05 : 0 : 0 : 0, (c) 20 mins, 0 : 0.15 : 0.38 : 0.10 : 0.26 : 0.05, 0.05 (d) 30 mins, 0 : 0 : 0 : 0.10 : 0.45 : 0.37 : 0.08, (e) 60 mins, 0 : 0 : 0 : 0.07 : 0.43 : 0.45 : 0.05, (f) 120 mins, 0 : 0 : 0 : 0.08 : 0.42 : 0.46 : 0.05.

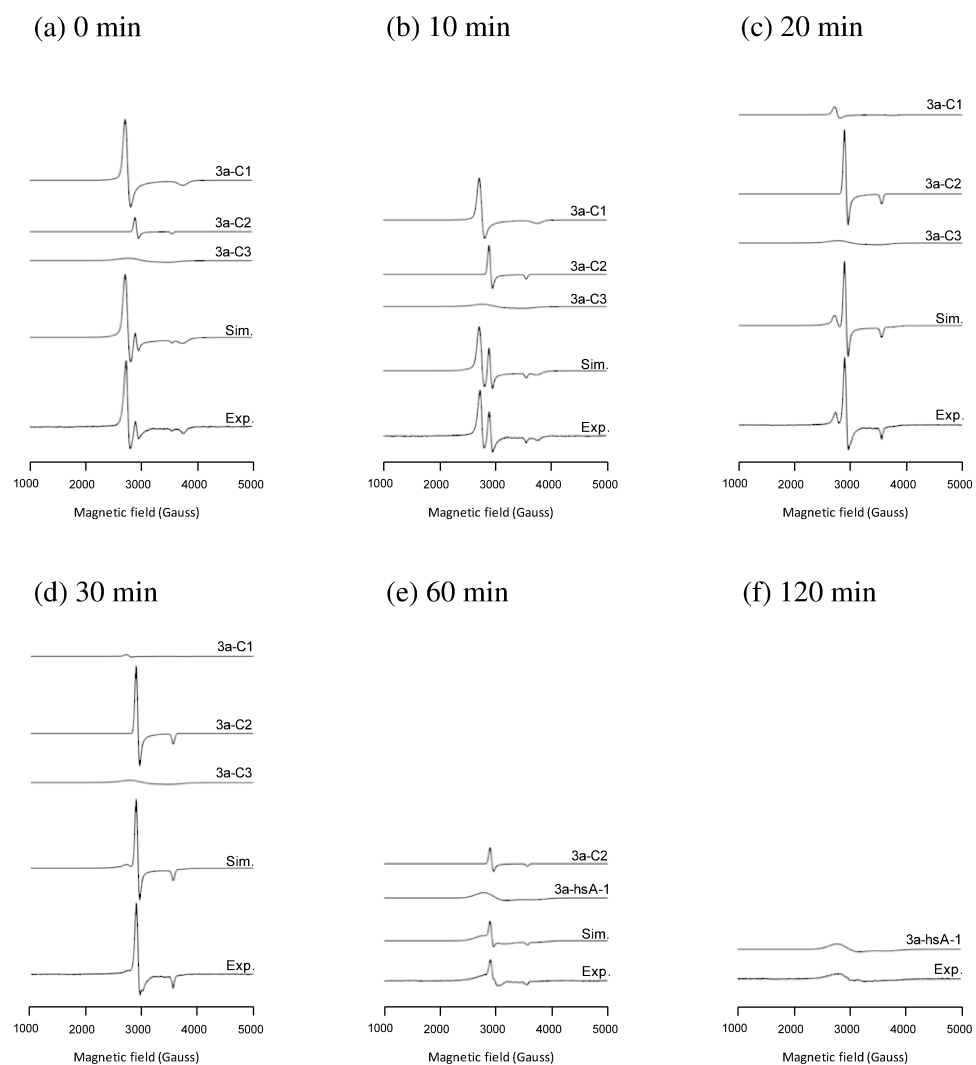


Figure C-19 (a-f) Deconvolution of EPR spectra from **3a** in buffer with hsA after incubation for 0 to 120 minutes at 37 °C. **Experimental conditions:** see section 2.2.5. **Simulation parameters:** For g values and linewidths, see **Table C-2**. Relative intensities used in simulations, 3a-C1-hsA : 3a-C2 : 3a-C3 : 3a-hsA-1 (a) 0 mins, 0.58 : 0 : 0.40 : 0.02, (b) 10 mins, 0 : 0.05 : 0.91 : 0.05, (c) 20 mins, 0 : 0.15 : 0.38 : 0.10, (d) 30 mins, 0 : 0 : 0 : 0.10, (e) 60 mins, 0 : 0 : 0 : 0.07, (f) 120 mins, 0 : 0 : 0 : 0.08.

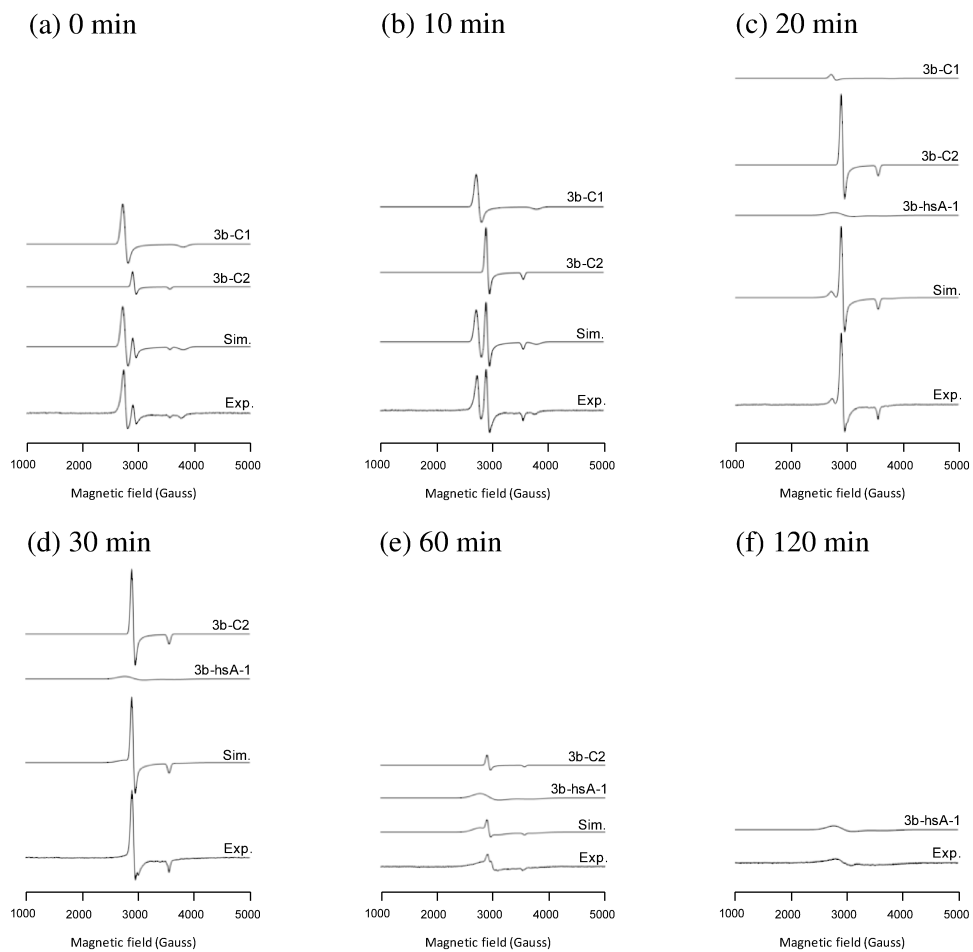


Figure C-20 (a-f) Deconvolution of EPR spectra from **3b** in buffer with hsA after incubation for 0 to 120 minutes at 37 °C. **Experimental conditions:** see section 2.2.5. **Simulation parameters:** For g values and linewidths, see **Table C-2**. Relative intensities used in simulations, 3b-C1 : 3b-C2 : 3b-hsA-1 **(a)** 0 mins, 0.72 : 0.28 : 0, **(b)** 10 mins, 0.42 : 0.58 : 0, **(c)** 20 mins, 0.07 : 0.90 : 0.03, **(d)** 30 mins, 0 : 0.96 : 0.04, **(e)** 60 mins, 0 : 0.7 : 0.3, **(f)** 120 mins, 0 : 0 : 1.0.

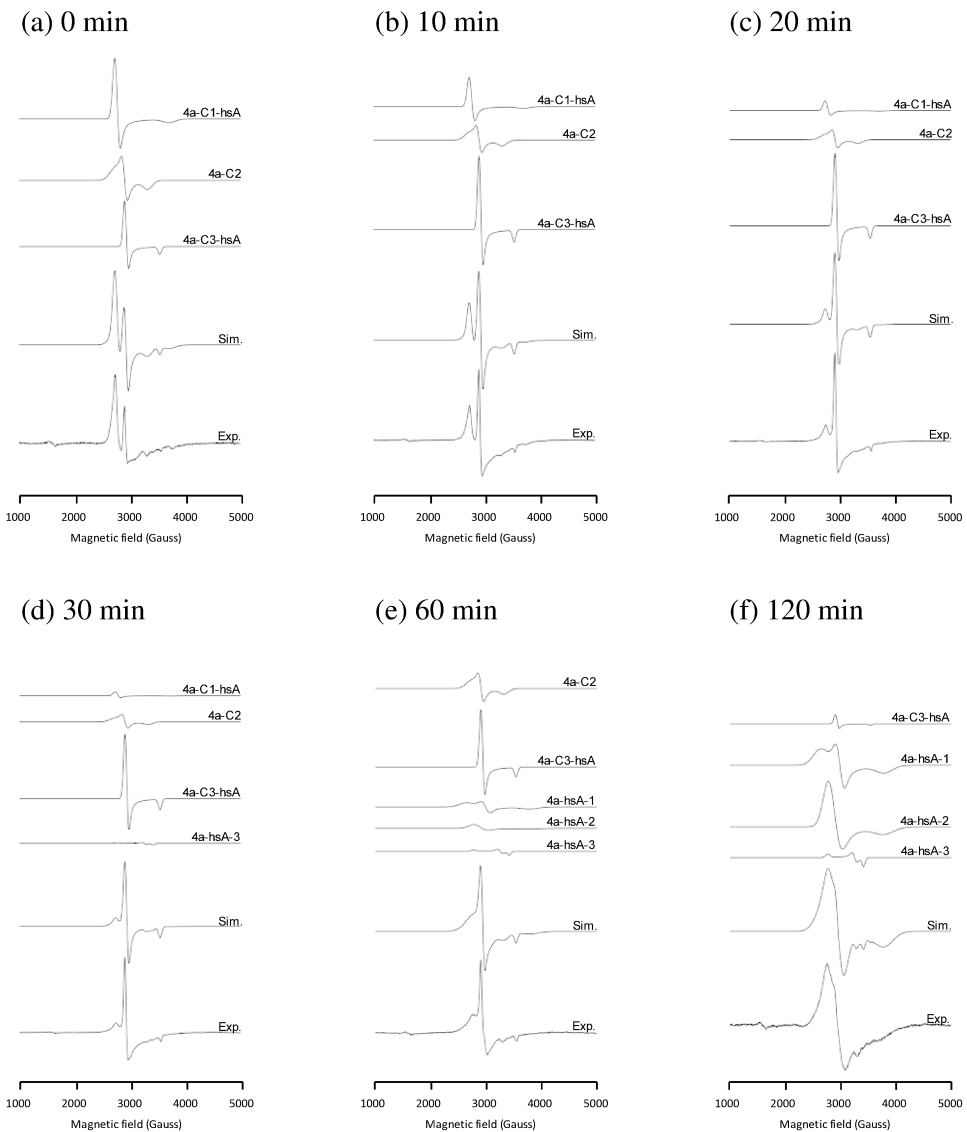


Figure C-21 (a-f) Deconvolution of EPR spectra from **4a** in buffer with hsA after incubation for 0 to 120 minutes at 37 °C. **Experimental conditions:** see section 2.2.5. **Simulation parameters:** For g values and linewidths, see **Table C-2**. Relative intensities used in simulations, 4a-C1-hsA : 4a-C2 : 4a-C3-hsA : NAMI-A-hsA-3 : 4a-hsA-1 : 4a-hsA-2 (a) 0 mins, 0.47 : 0.19 : 0.35 : 0 : 0 : 0, (b) 10 mins, 0.25 : 0.13 : 0.63 : 0 : 0 : 0, (c) 20 mins, 0.11 : 0.11 : 0.79 : 0 : 0 : 0, (d) 30 mins, 0.05 : 0.10 : 0.83 : 0.02 : 0 : 0, (e) 60 mins, 0 : 0.18 : 0.67 : 0.04 : 0.07 : 0.04, (f) 120 mins, 0 : 0 : 0.11 : 0.11 : 0.26 : 0.53.

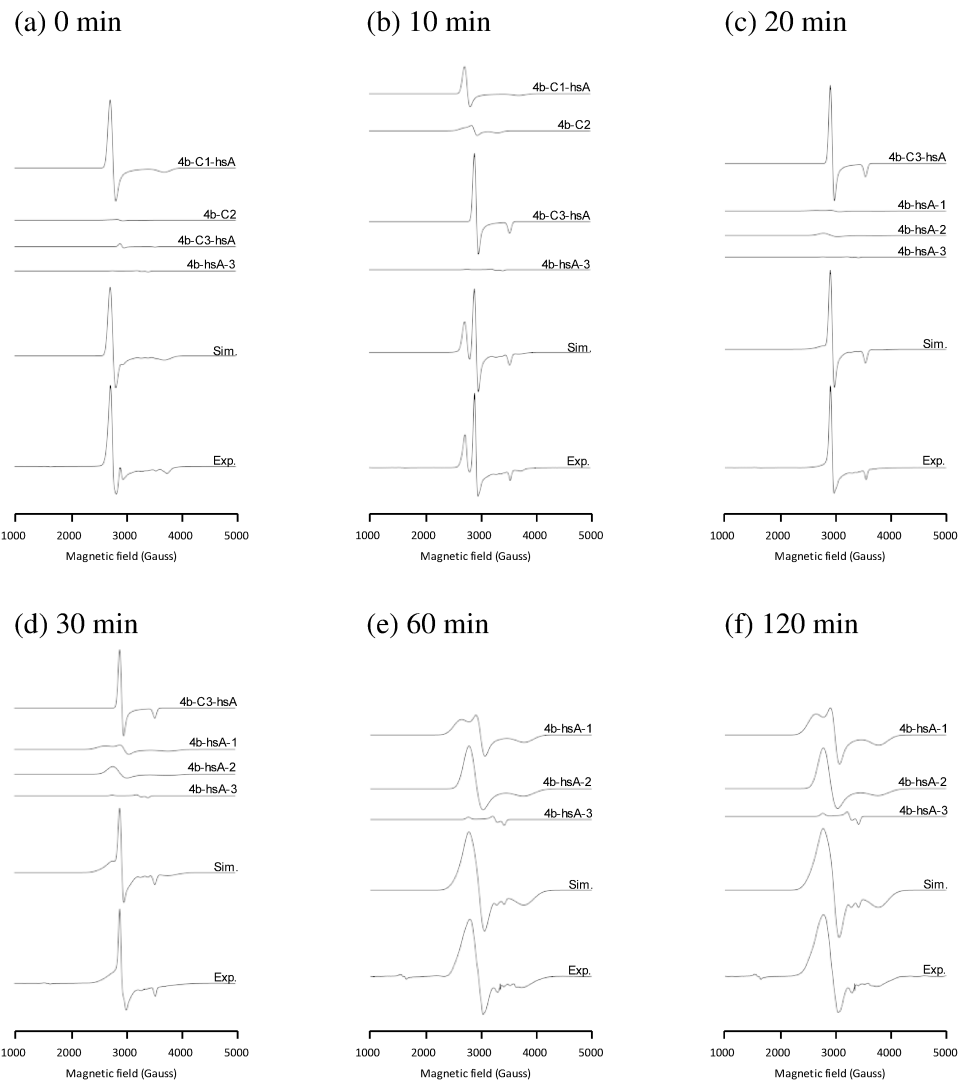


Figure C-22 (a-f) Deconvolution of EPR spectra from **4b** in buffer with hsA after incubation for 0 to 120 minutes at 37 °C. **Experimental conditions:** see section 2.2.5. **Simulation parameters:** For g values and linewidths, see **Table C-2**. Relative intensities used in simulations, 4b-C1-hsA : 4b-C2 : 4b-C3-hsA : NAMI-A-hsA-3 : 4b-hsA-1 : 4b-hsA-2 (a) 0 mins, 0.94 : 0.01 : 0.04 : 0.01 : 0 : 0, (b) 10 mins, 0.27 : 0.05 : 0.67 : 0.01 : 0 : 0, (c) 20 mins, 0 : 0 : 0.95 : 0.01 : 0.03, (d) 30 mins, 0 : 0 : 0.80 : 0.03 : 0.07 : 0.11, (e) 60 mins, 0 : 0 : 0 : 0.08 : 0.31 : 0.61, (f) 120 mins, 0 : 0 : 0 : 0.10 : 0.38 : 0.53.

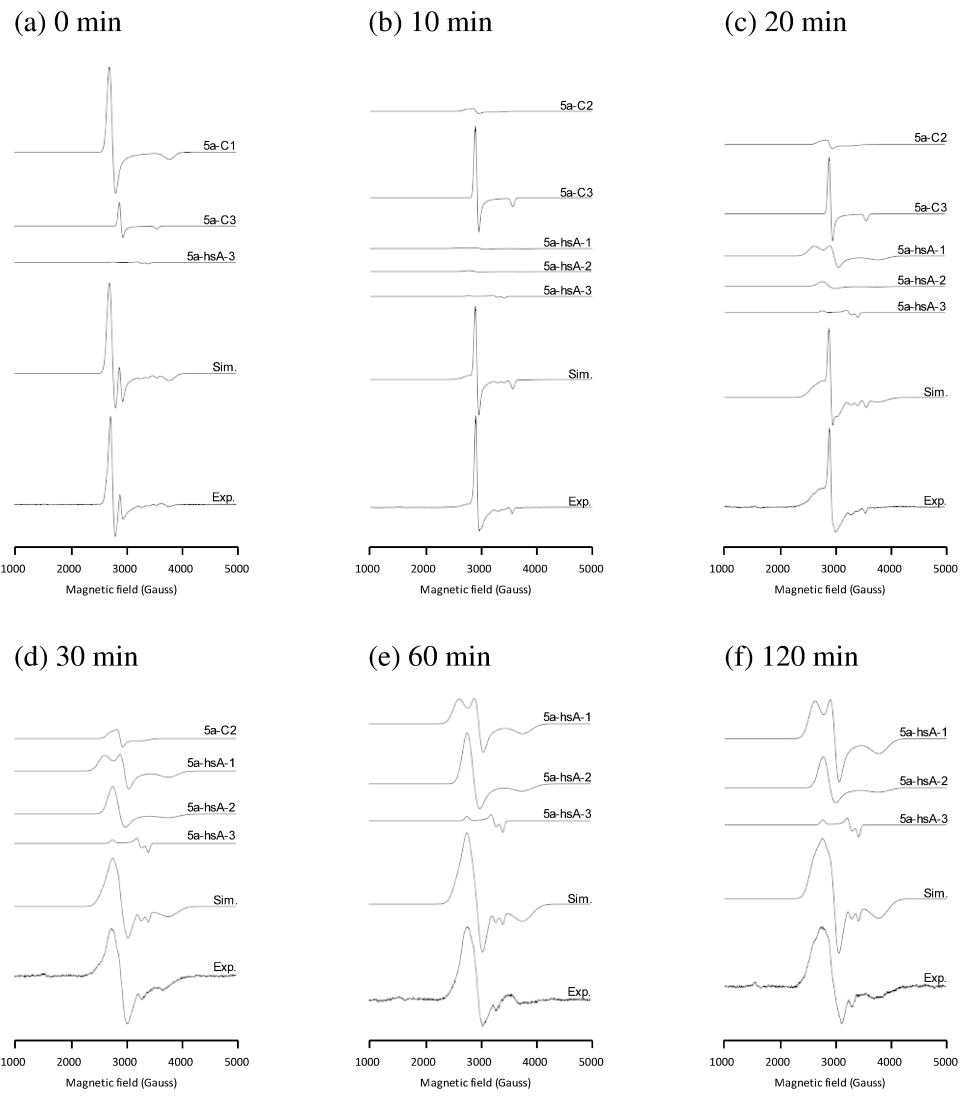


Figure C-23 (a-f) Deconvolution of EPR spectra from **5a** in buffer with hsA after incubation for 0 to 120 minutes at 37 °C. **Experimental conditions:** see section 2.2.5. **Simulation parameters:** For g values and linewidths, see **Table C-2**. Relative intensities used in simulations, 5a-C1 : 5a-C2 : 5a-C3 : NAMI-A-hsA-3 : 5a-hsA-1 : 5a-hsA-2 (a) 0 mins, 0.73 : 0 : 0.20 : 0.01 : 0 : 0, (b) 10 mins, 0 : 0.03 : 0.92 : 0.02 : 0.01 : 0.01, (c) 20 mins, 0 : 0.06 : 0.69 : 0.06 : 0.14 : 0.06, (d) 30 mins, 0 : 0.13 : 0 : 0.13 : 0.27 : 0.47, (e) 60 mins, 0 : 0 : 0 : 0.13 : 0.31 : 0.56, (f) 120 mins, 0 : 0 : 0 : 0.14 : 0.50 : 0.36.

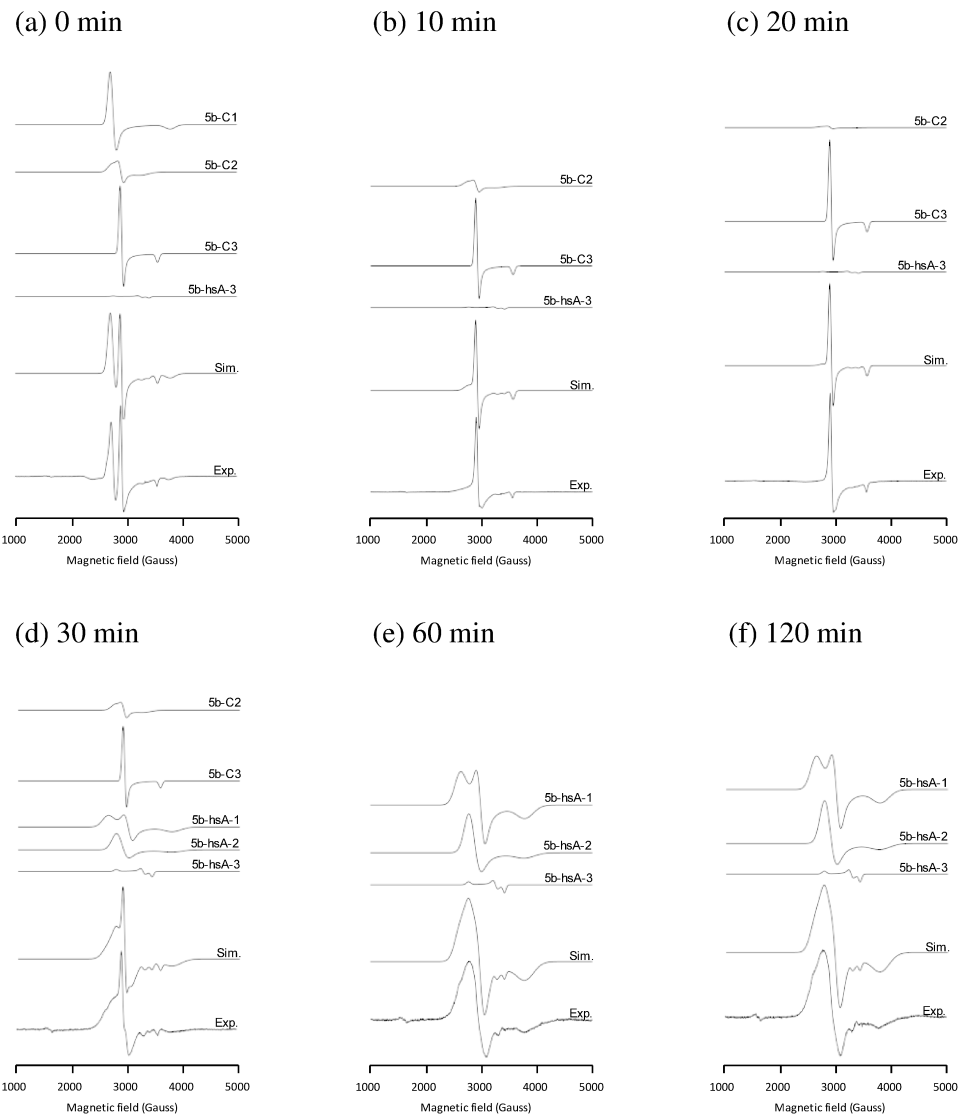


Figure C-24 (a-f) Deconvolution of EPR spectra from **5b** in buffer with hsA after incubation for 0 to 120 minutes at 37 °C. **Experimental conditions:** see section 2.2.5. **Simulation parameters:** For g values and linewidths, see **Table C-2**. Relative intensities used in simulations, 5b-C1 : 5b-C2 : 5b-C3 : NAMI-A-hsA-3 : 5b-hsA-1 : 5b-hsA-2 (a) 0 mins, 0.40 : 0.08 : 0.51 : 0.01 : 0 : 0, (b) 10 mins, 0 : 0.08 : 0.90 : 0.02 : 0 : 0, (c) 20 mins, 0 : 0.02 : 0.97 : 0.02 : 0 : 0, (d) 30 mins, 0 : 0.08 : 0.56 : 0.06 : 0.14 : 0.17, (e) 60 mins, 0 : 0 : 0 : 0.09 : 0.45 : 0.45, (f) 120 mins, 0 : 0 : 0 : 0.19 : 0.43 : 0.48.

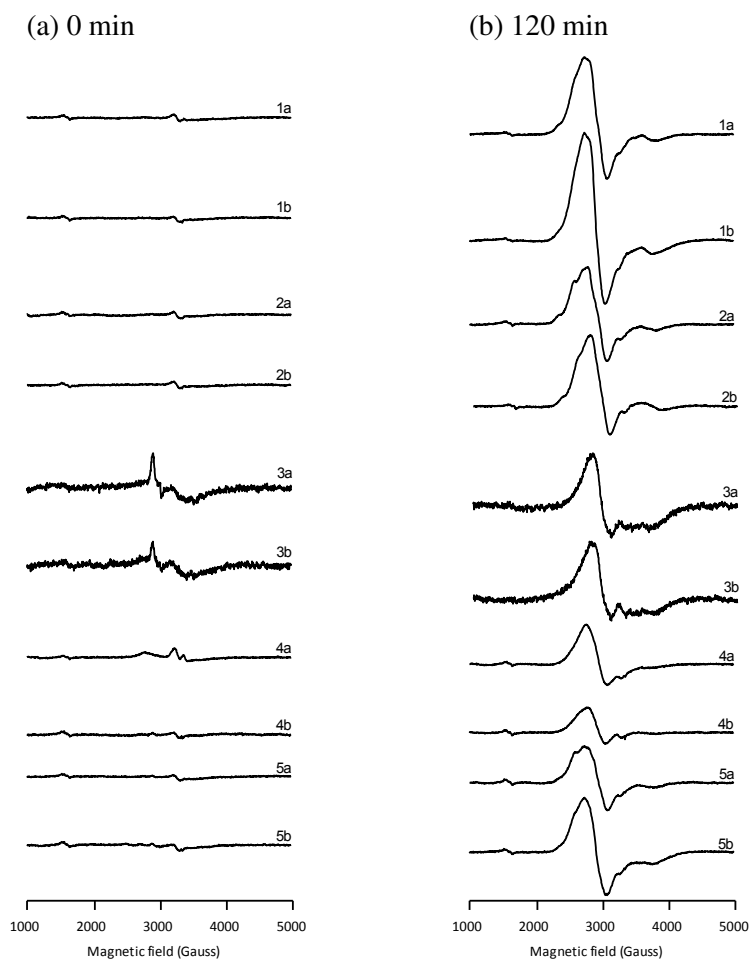


Figure C-25 (a,b) Monitoring the effect of ascorbic acid (1 mM) on the reduction of non-coordinate and coordinate protein-bound complexes with hsA.
Experimental conditions: see section 2.2.5.

Table C-1 Simulation parameters, g values and linewidths (Gauss), which were used for all of the EPR spectra attained for all of the complexes in buffered solution.

Complex	g values			Linewidths		
	g ₁	g ₂	g ₃	LW ₁	LW ₂	LW ₃
1a-C1	2.44	2.44	1.76	100	100	175
1a-C2	2.46	2.31	2.03	200	75	260
1a-C3	2.30	2.30	1.87	55	55	60
1a-C4	2.30	2.25	2.00	150	150	300
1b-C1	2.44	2.44	1.76	100	100	175
1b-C2	2.46	2.31	2.03	200	75	260
1b-C3	2.30	2.30	1.88	55	55	60
1b-C4	2.30	2.25	2.00	150	150	300
2a-C1	2.44	2.44	1.75	90	90	220
2a-C2	2.46	2.31	2.01	200	75	160
2a-C3	2.30	2.30	1.87	55	55	60
2a-C4	2.30	2.25	2.00	150	150	300
2b-C1	2.44	2.44	1.75	90	90	220
2b-C2	2.46	2.31	2.01	200	75	160
2b-C3	2.30	2.30	1.87	55	55	60
3a-C1	2.44	2.44	1.78	85	85	150
3a-C2	2.30	2.30	1.88	55	55	50
3a-C3	2.32	2.32	1.90	400	400	300
3b-C1	2.44	2.44	1.76	85	85	150
3b-C2	2.30	2.30	1.88	55	55	50
3b-C3	2.32	2.32	1.90	400	400	300
4a-C1	2.43	2.43	1.80	90	90	220
4a-C2	2.41	2.25	2.05	90	300	350
4a-C3	2.31	2.31	1.88	55	55	60
4b-C1	2.44	2.44	1.77	90	90	220
4b-C2	2.46	2.31	2.01	200	75	160
4b-C3	2.30	2.30	1.87	55	55	60
4b-C4	2.30	2.25	2.00	150	150	300
5a-C1	2.44	2.44	1.75	100	100	225
5a-C2	2.44	2.26	2.07	150	75	260
5a-C3	2.30	2.30	1.88	55	55	60
5a-C4	2.25	2.20	1.90	200	200	300
5b-C1	2.44	2.44	1.77	100	100	225
5b-C2	2.44	2.26	2.07	150	75	260
5b-C3	2.30	2.30	1.88	55	55	60
5b-C4	2.30	2.25	2.00	150	150	300

Table C-2 Simulation parameters, g values and linewidths (Gauss), which were used for all of the EPR spectra attained for all of the complexes in buffered solution with hsA.

Complex	g values			Linewidths		
	g ₁	g ₂	g ₃	LW ₁	LW ₂	LW ₃
1a-C1-hsA	2.43	2.43	1.78	90	90	220
1a-C3-hsA	2.30	2.30	1.88	55	55	60
1a-hsA-1	2.56	2.22	1.76	200	125	300
1a-hsA-2	2.33	2.33	1.76	200	200	350
1a-hsA-3	2.42	2.06	1.96	80	70	55
1b-hsA-1	2.59	2.26	1.78	150	125	300
1b-hsA-2	2.35	2.35	1.76	225	225	350
1b-hsA-3	2.42	2.06	1.96	80	70	55
2a-hsA-1	2.56	2.26	1.76	450	125	300
2a-hsA-2	2.40	2.40	1.76	250	250	350
2a-hsA-3	2.42	2.06	1.96	80	70	55
2b-C1-hsA	2.43	2.43	1.77	90	90	150
2b-hsA-1	2.58	2.26	1.76	175	125	300
2b-hsA-2	2.36	2.36	1.76	250	250	350
2b-hsA-3	2.86	2.36	1.82	175	100	300
2b-hsA-4	2.42	2.06	1.96	80	70	55
3a-hsA-1	2.32	2.32	1.80	350	350	400
3b-hsA-1	2.34	2.34	1.80	300	300	400
4a-C1-hsA	2.43	2.43	1.80	90	90	220
4a-C3-hsA	2.29	2.29	1.89	65	65	60
4a-hsA-1	2.56	2.24	1.76	250	125	300
4a-hsA-2	2.35	2.35	1.76	225	225	350
4a-hsA-3	2.42	2.06	1.96	80	70	55
4b-C1-hsA	2.43	2.43	1.80	90	90	220
4b-C3-hsA	2.29	2.29	1.89	65	65	60
4b-hsA-1	2.56	2.24	1.76	250	125	300
4b-hsA-2	2.35	2.35	1.76	225	225	350
4b-hsA-3	2.42	2.06	1.96	80	70	55
5a-hsA-1	2.56	2.24	1.76	200	125	300
5a-hsA-2	2.36	2.36	1.76	200	200	350
5a-hsA-3	2.42	2.06	1.96	80	70	55
5b-hsA-1	2.56	2.24	1.76	200	125	300
5b-hsA-2	2.36	2.36	1.76	200	200	350
5b-hsA-3	2.42	2.06	1.96	80	70	55

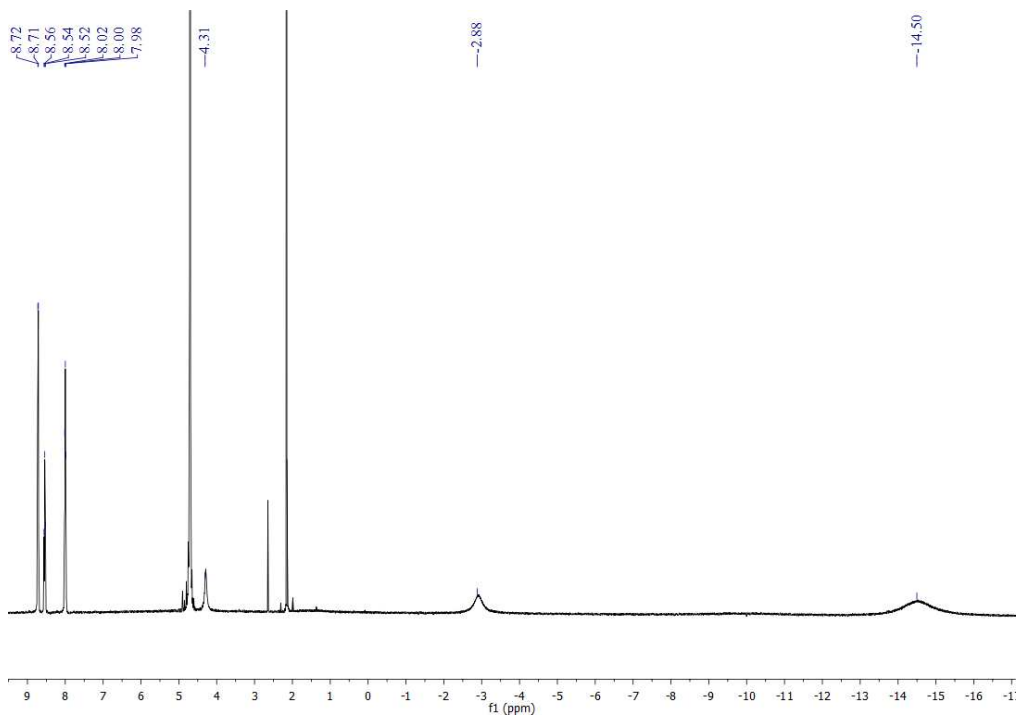


Figure C-26 ^1H NMR Spectrum for **1a** in D_2O .

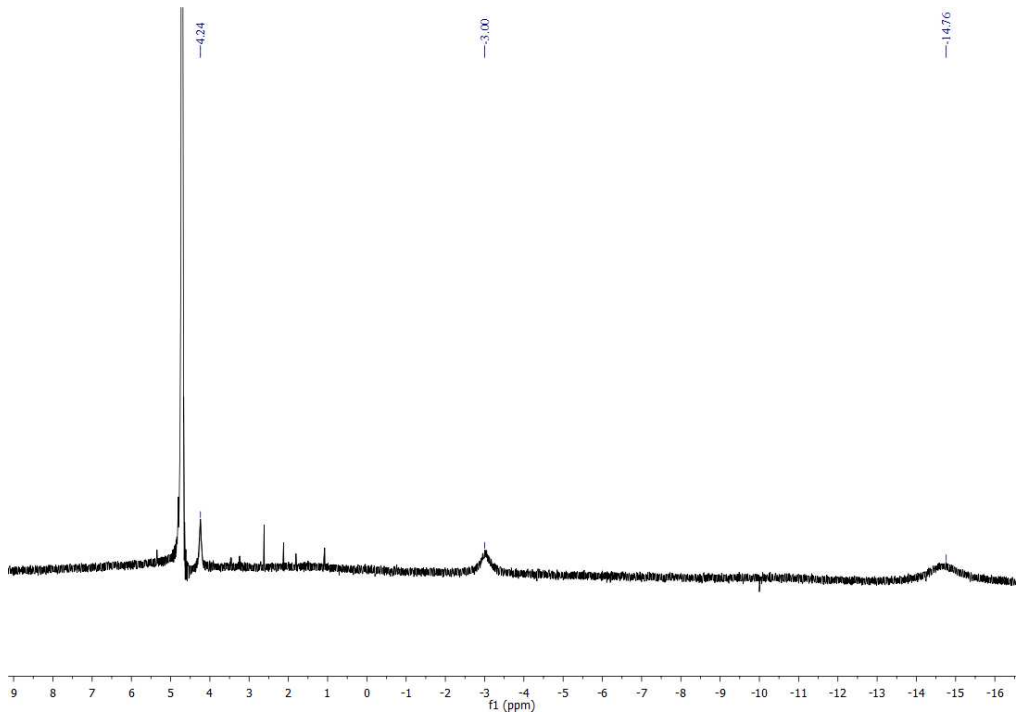


Figure C-27 ^1H NMR Spectrum for **1b** in D_2O .

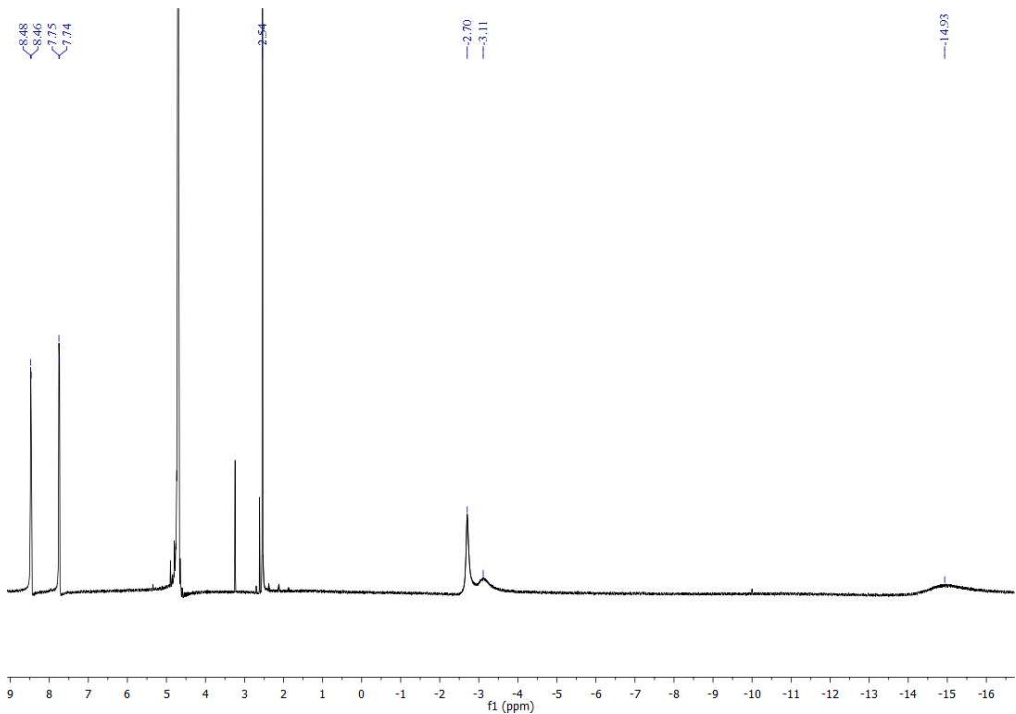


Figure C-28 ¹H NMR Spectrum for 2a in D₂O.

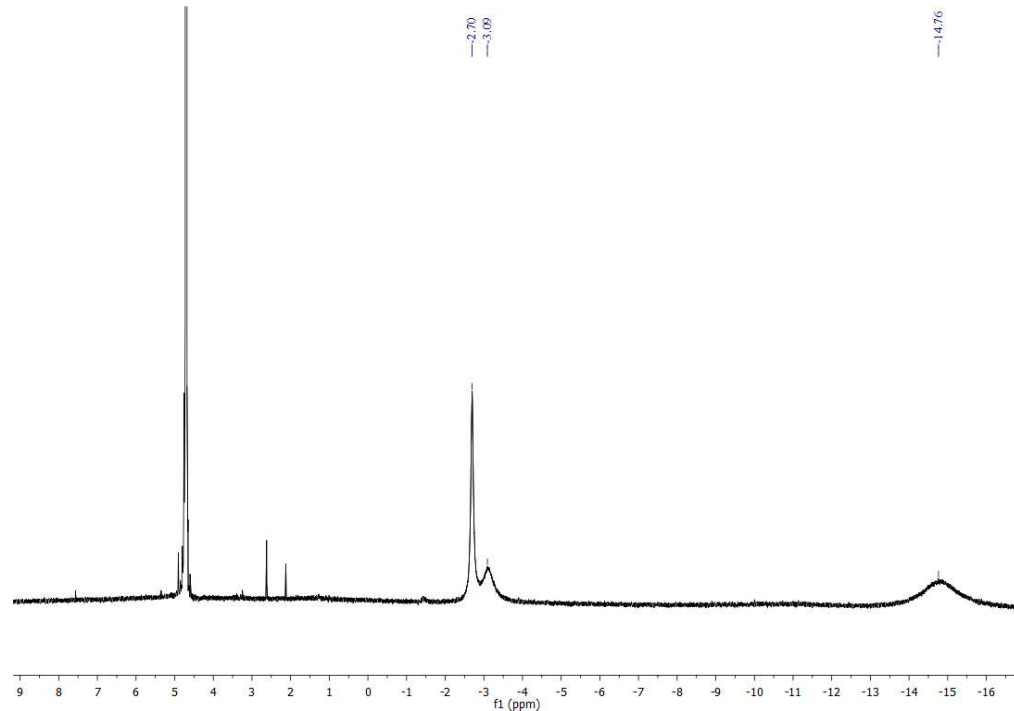


Figure C-29 ¹H NMR Spectrum for 2b in D₂O.

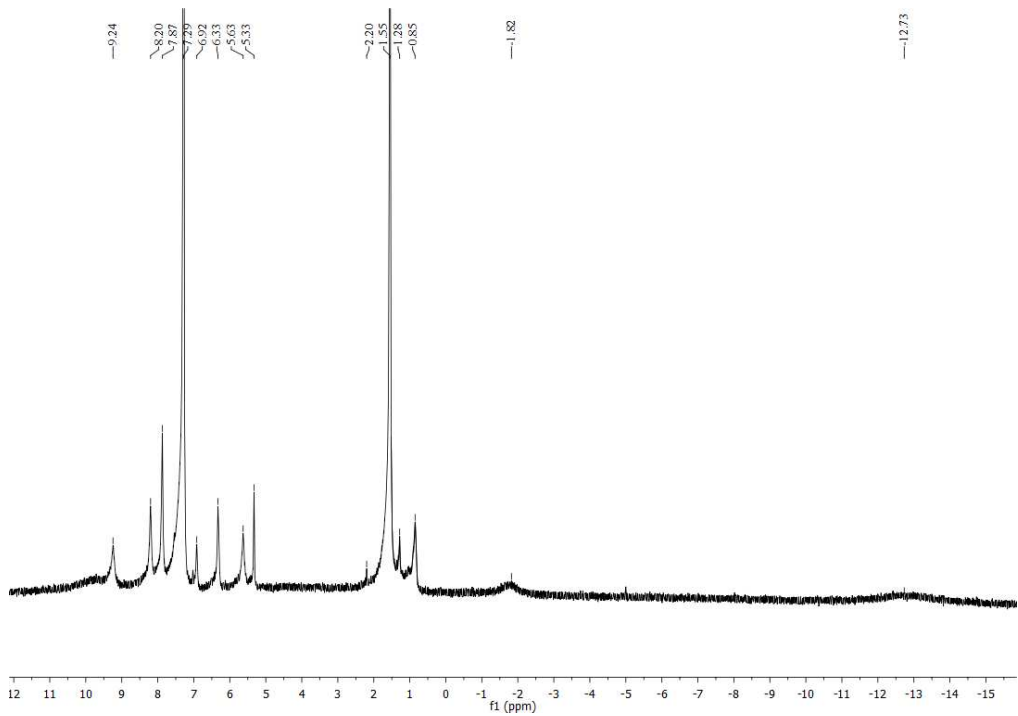


Figure C-30 ^1H NMR Spectrum for **3a** in CDCl_3 .

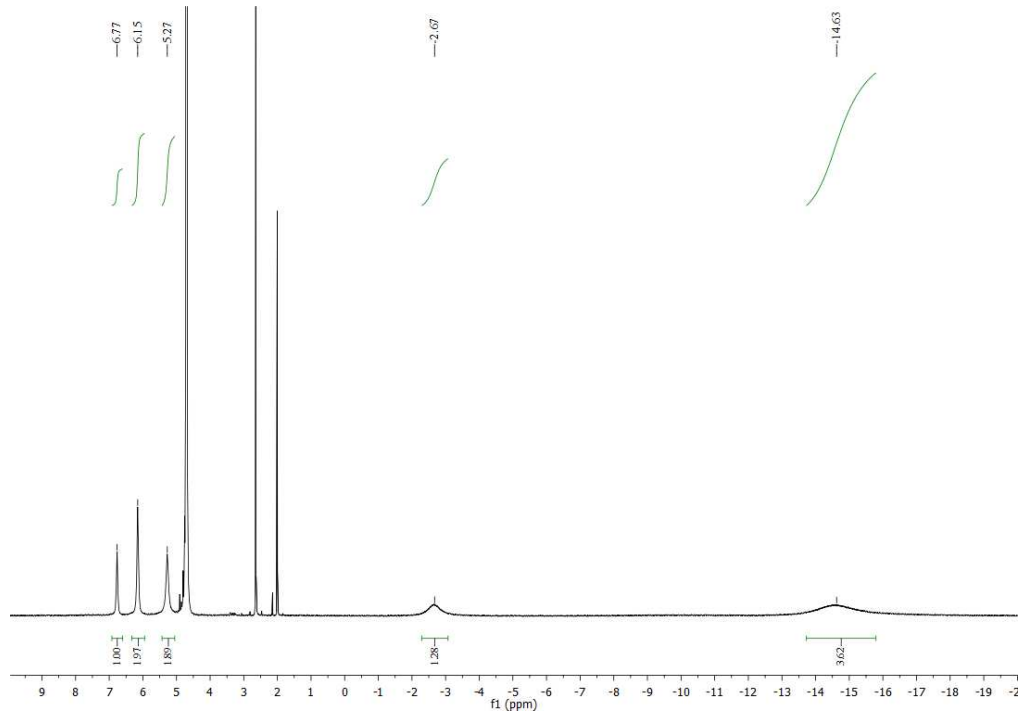


Figure C-31 ^1H NMR Spectrum for **3b** in D_2O .

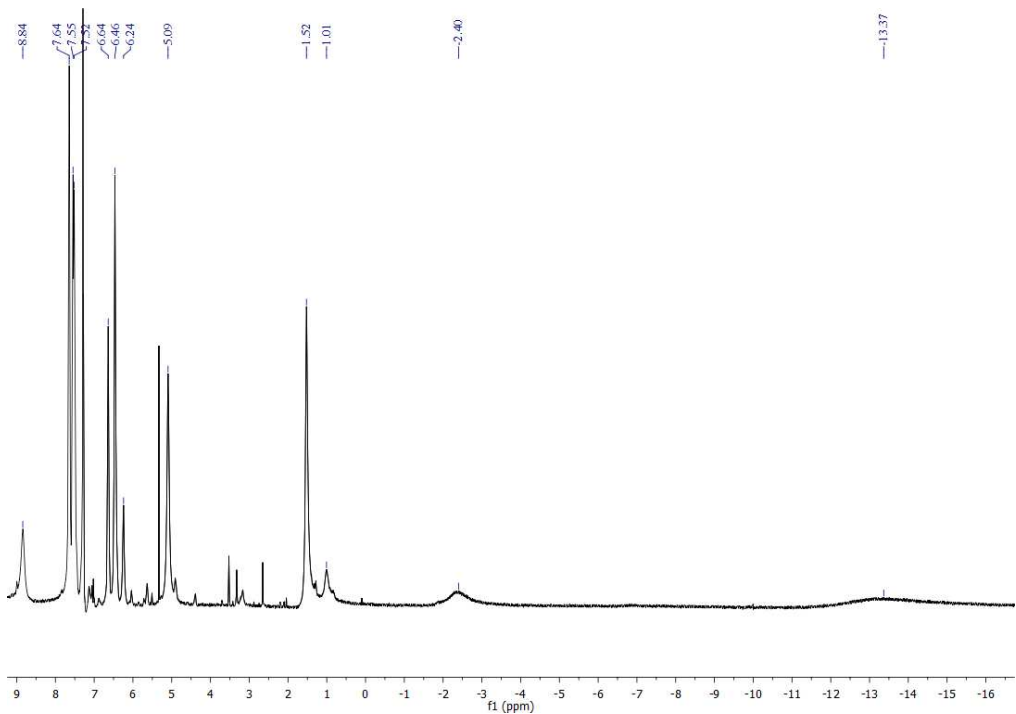


Figure C-32 ¹H NMR Spectrum for **4a** in CDCl_3 .

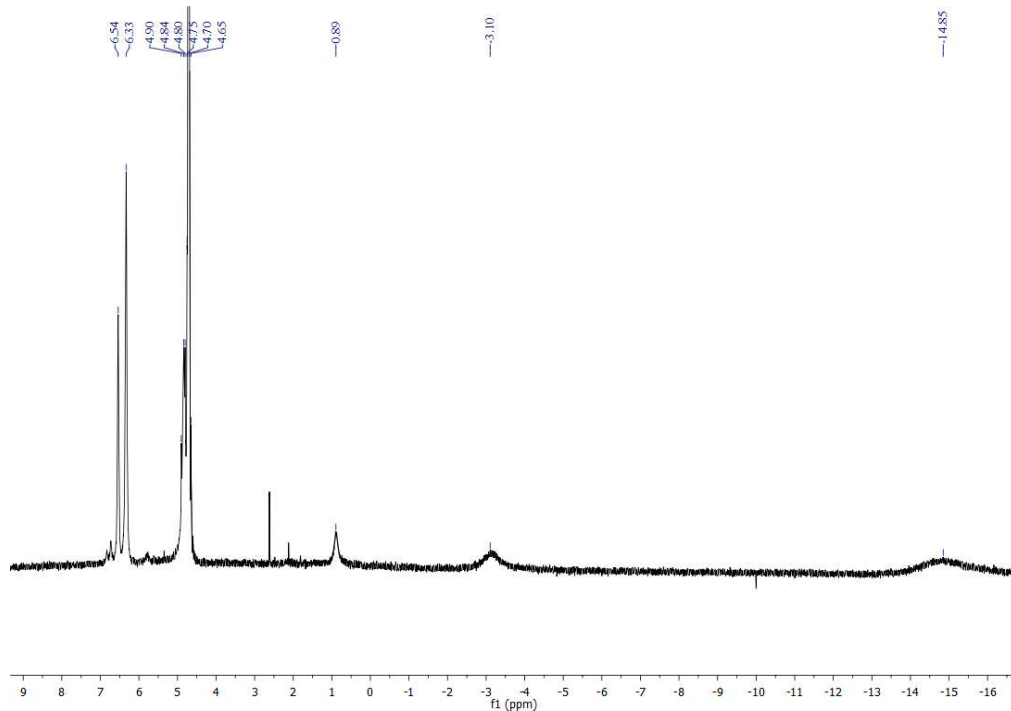


Figure C-33 ¹H NMR Spectrum for **4b** in D_2O .

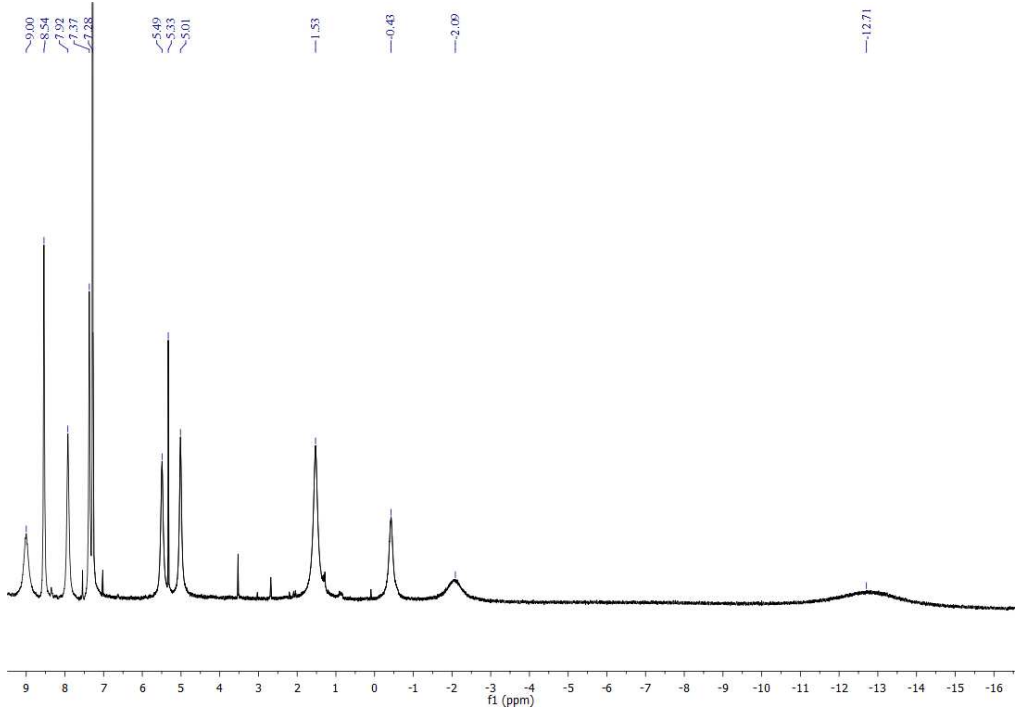


Figure C-34 ^1H NMR Spectrum for **5a** in CDCl_3 .

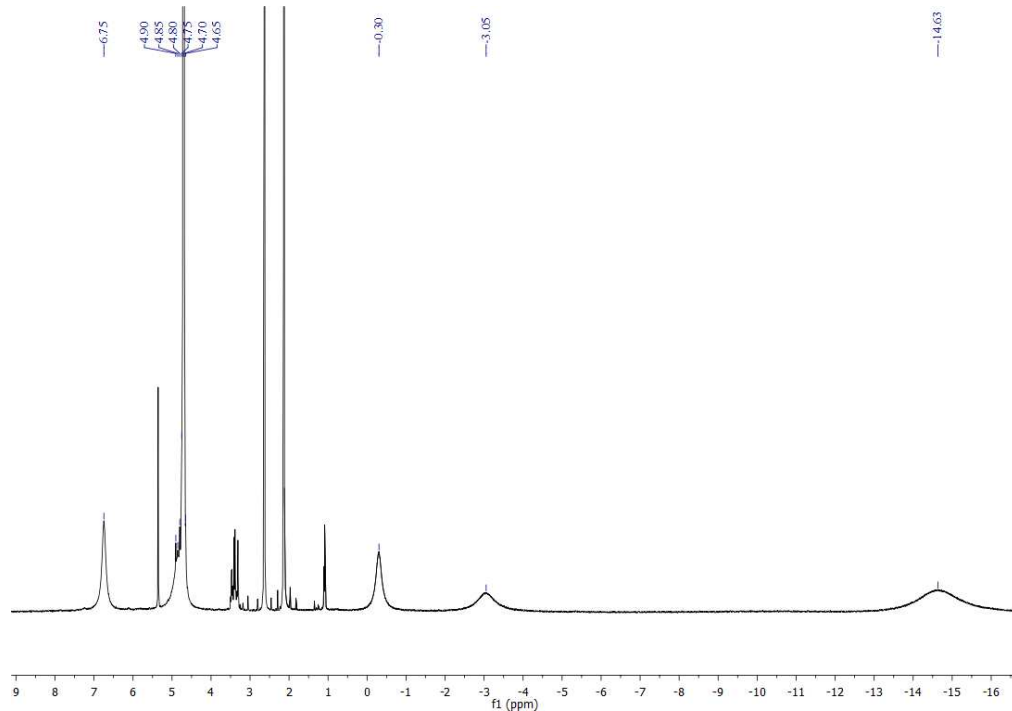


Figure C-35 ^1H NMR Spectrum for **5b** in D_2O .

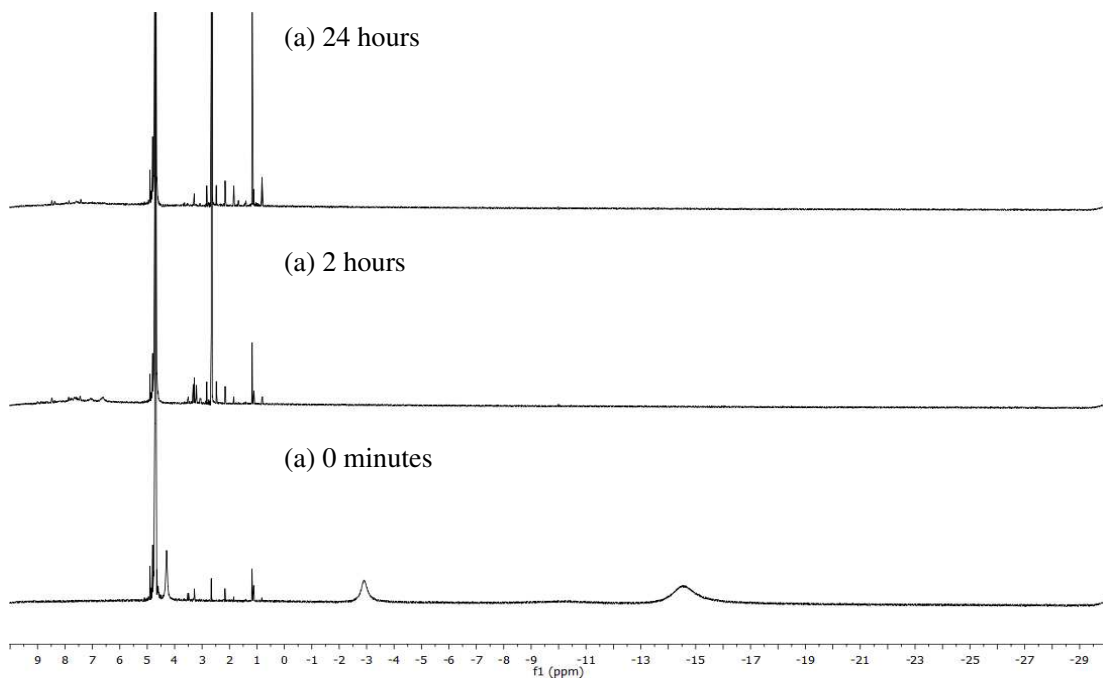


Figure C-36 ¹H NMR Spectrum for **1b** in buffered D₂O after 24 hours.

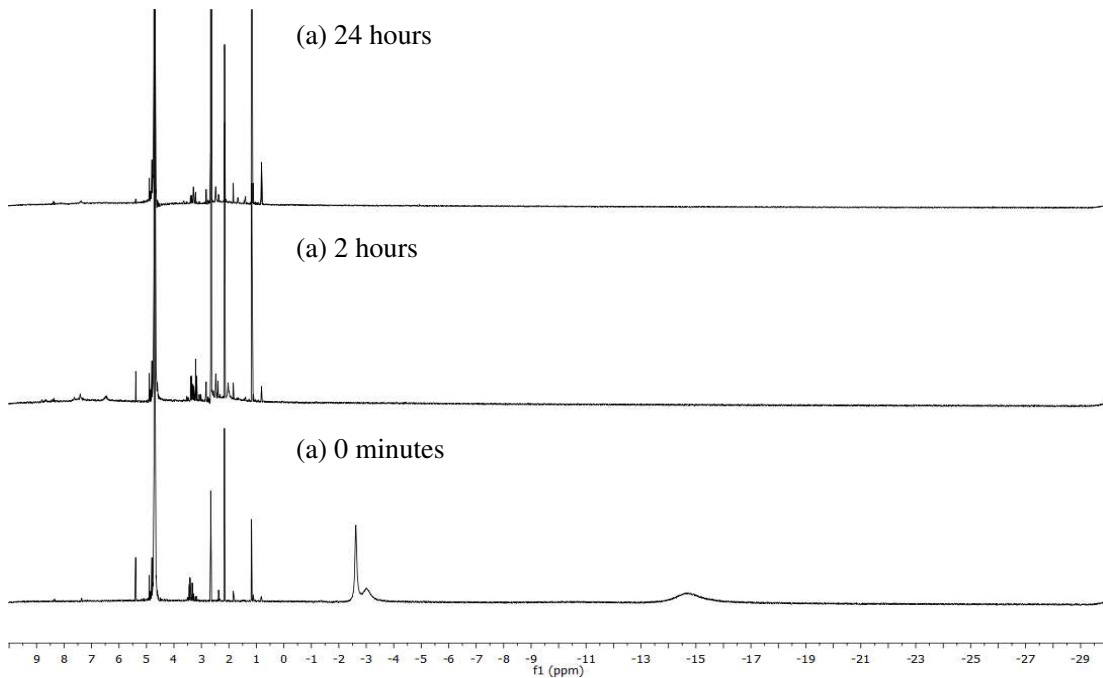


Figure C-37 ¹H NMR Spectrum for **2b** in buffered D₂O after 24 hours.

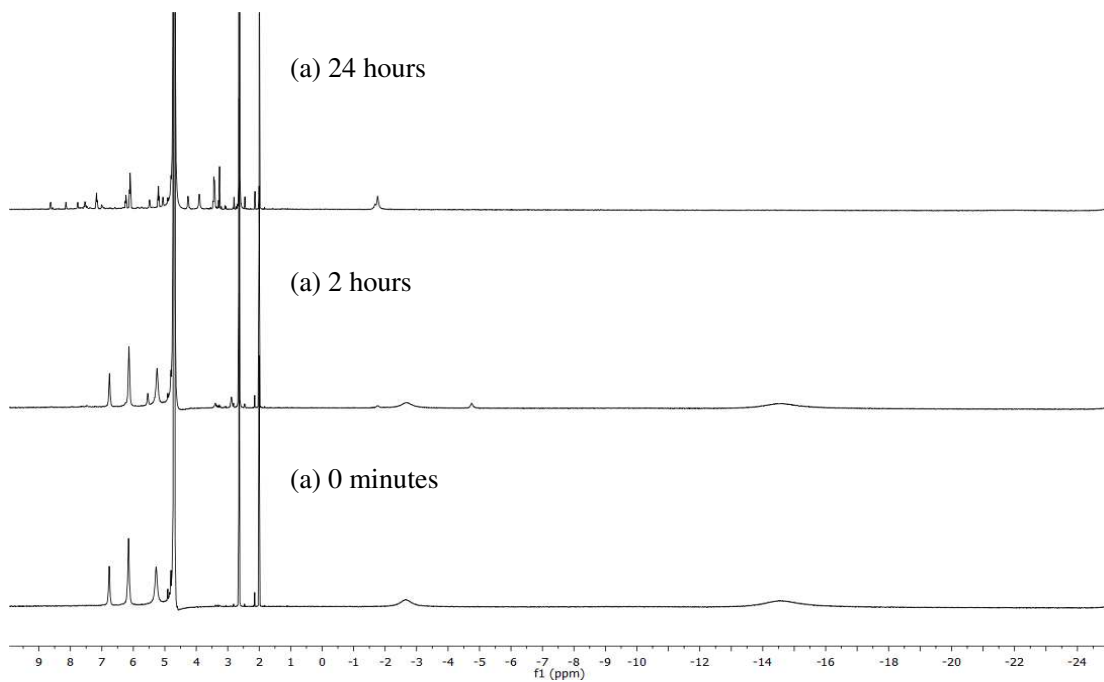


Figure C-38 ¹H NMR Spectrum for **3b** in buffered D₂O after 24 hours.

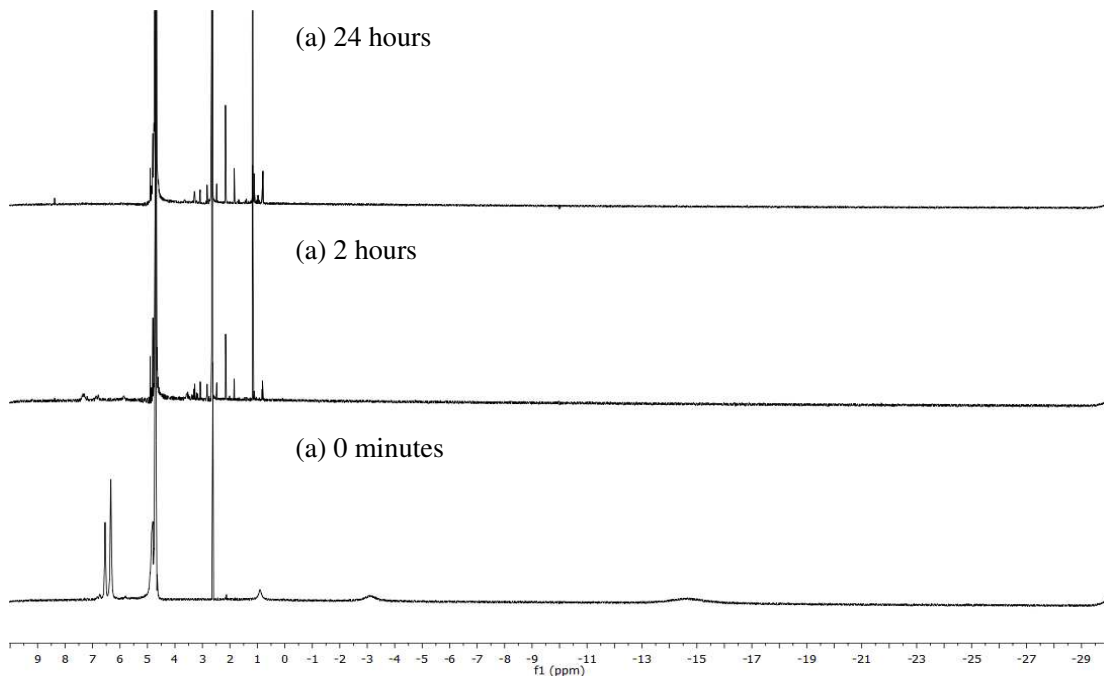


Figure C-39 ¹H NMR Spectrum for **4b** in buffered D₂O after 24 hours.

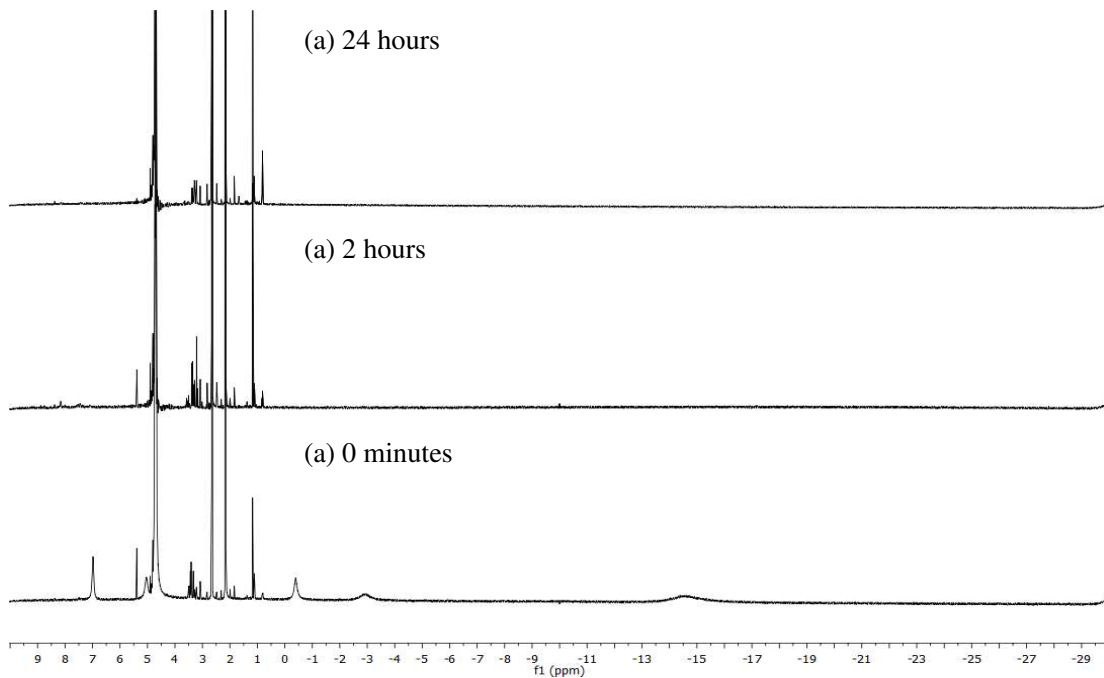


Figure C-40 ¹H NMR Spectrum for **5b** in buffered D₂O after 24 hours.

Table C-3 Metal-ligand bond distances (Å) of the pyridine-based NAMI-A derivatives. * - Bond distances previously reported within the literature. (Reference 232)

Complex	Ru-N	Ru-S	Ru-Cl1	Ru-Cl2	Ru-Cl3	Ru-Cl4
1a	2.117	2.295	2.359	2.360	2.346	2.350
1a*	2.116	2.295	2.349	2.356	2.350	2.360
1b	2.15	2.292	2.353	2.350	2.352	2.347
2a	2.119	2.287	2.344	2.363	2.346	2.353
2b	2.15	2.288	2.35	2.339	2.35	2.358
3a	2.118	2.288	2.315	2.355	2.344	2.354
4b	2.110	2.297	2.369	2.368	2.341	2.341
5a	2.122	2.297	2.370	2.353	2.344	2.337
5b	2.122	2.287	2.353	2.334	2.340	2.365

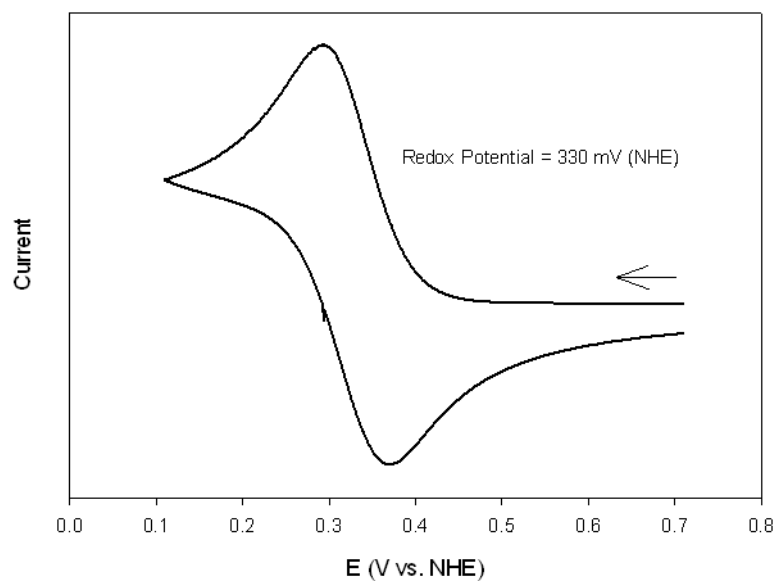


Figure C-41 Cyclic voltammogram of **1a** in physiological buffer.

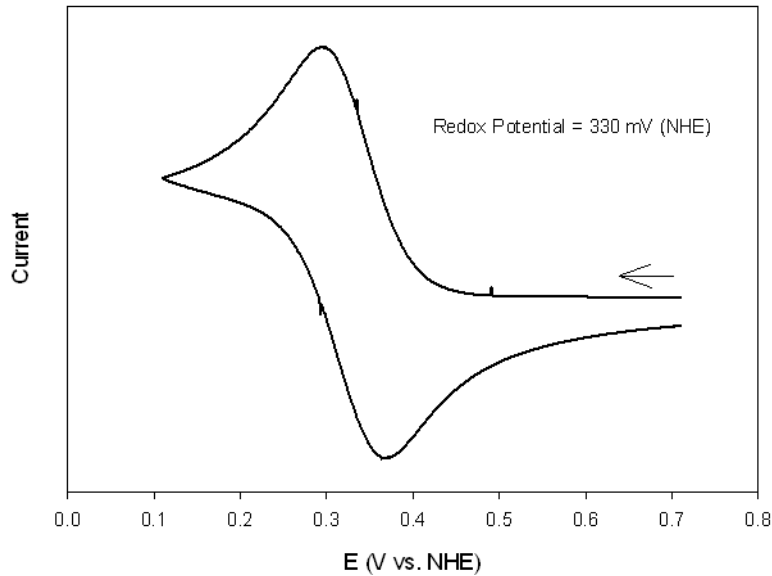


Figure C-42 Cyclic voltammogram of **1b** in physiological buffer.

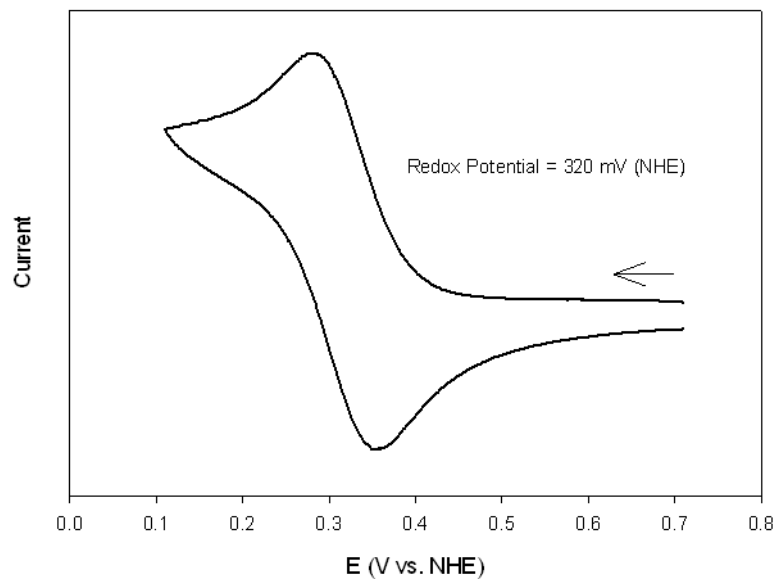


Figure C-43 Cyclic voltammogram of **2a** in physiological buffer.

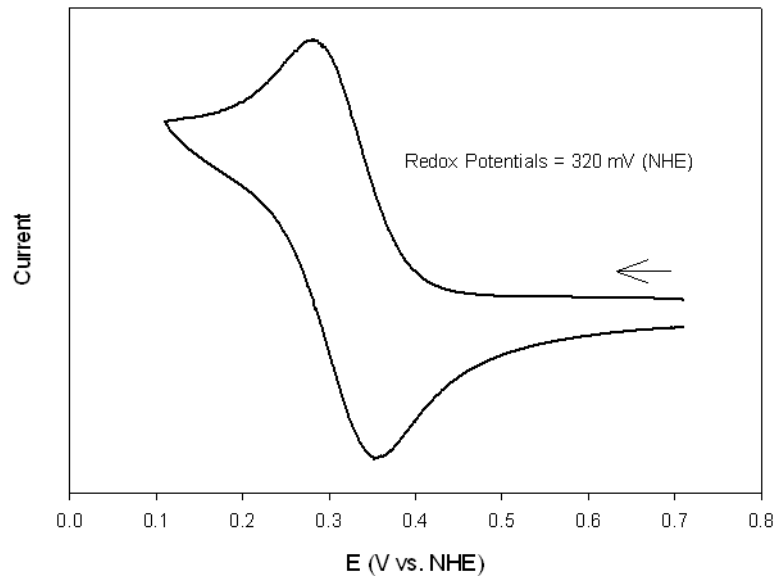


Figure C-44 Cyclic voltammogram of **2b** in physiological buffer.

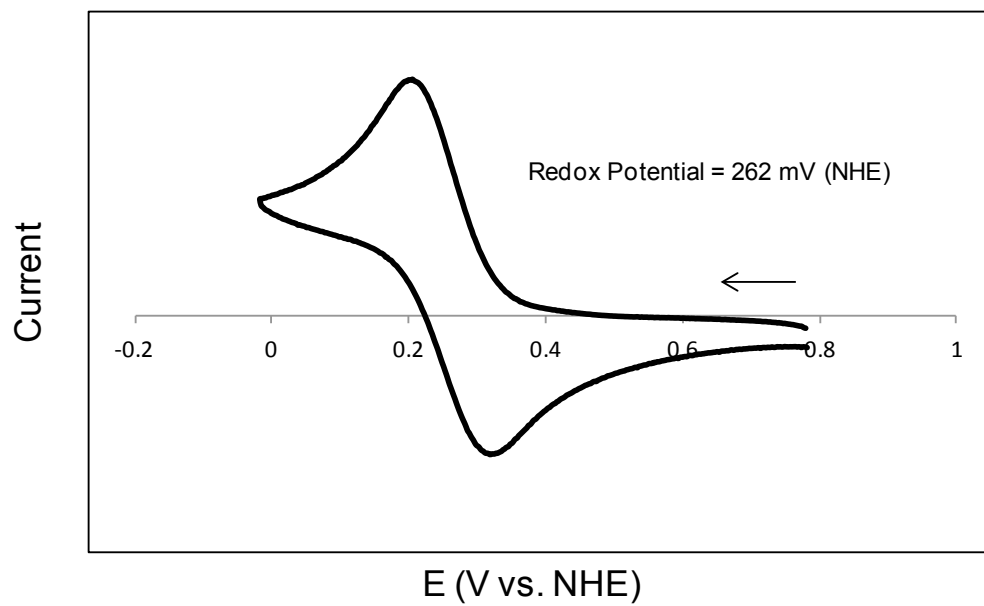


Figure C-45 Cyclic voltammogram of **3a** in a 1:1 mixture of physiological buffer and DMSO.

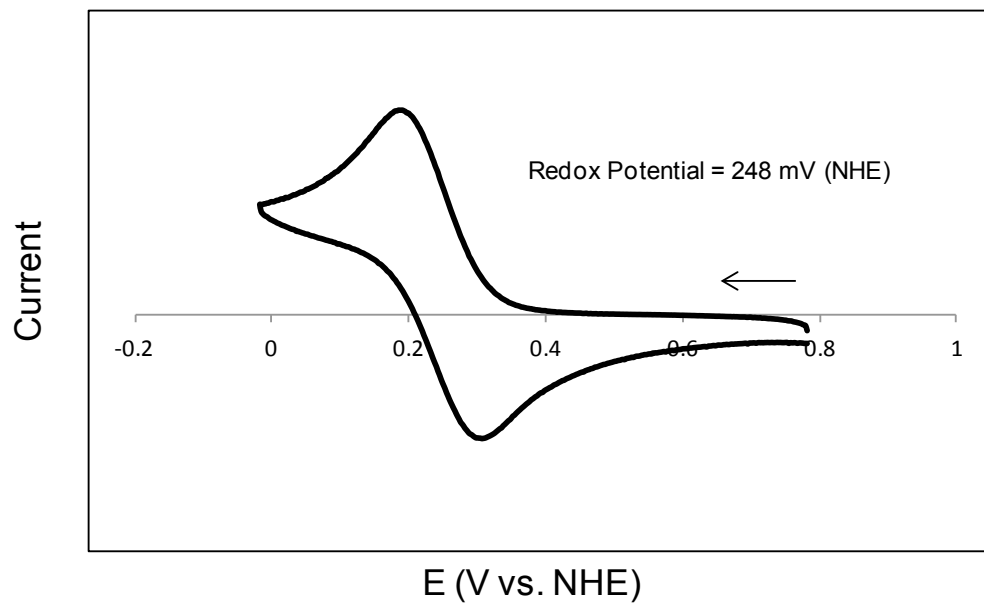


Figure C-46 Cyclic voltammogram of **3b** in a 1:1 mixture of physiological buffer and DMSO.

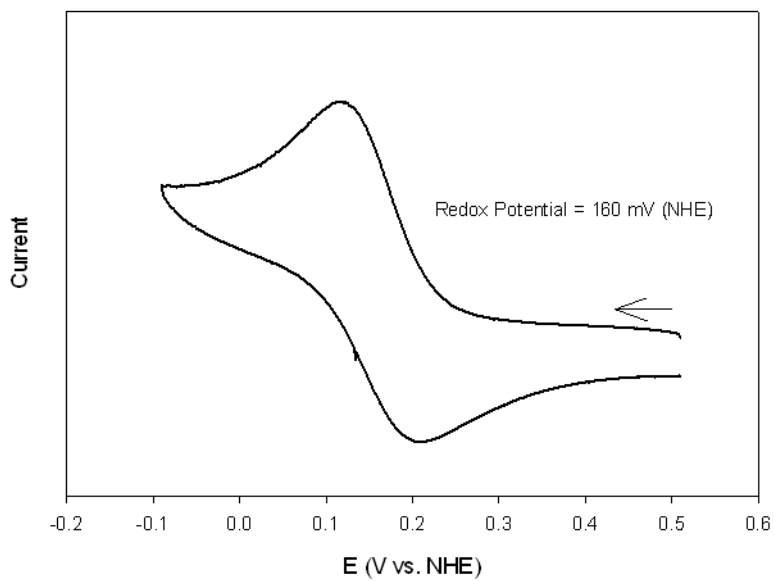


Figure C-47 Cyclic voltammogram of **4a** in a 1:1 mixture of physiological buffer and DMSO.

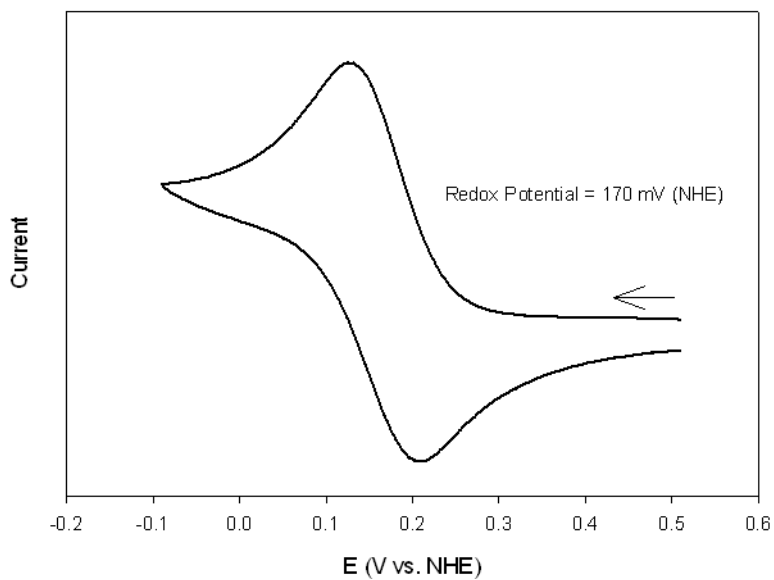


Figure C-48 Cyclic voltammogram of **4b** in a 1:1 mixture of physiological buffer and DMSO.

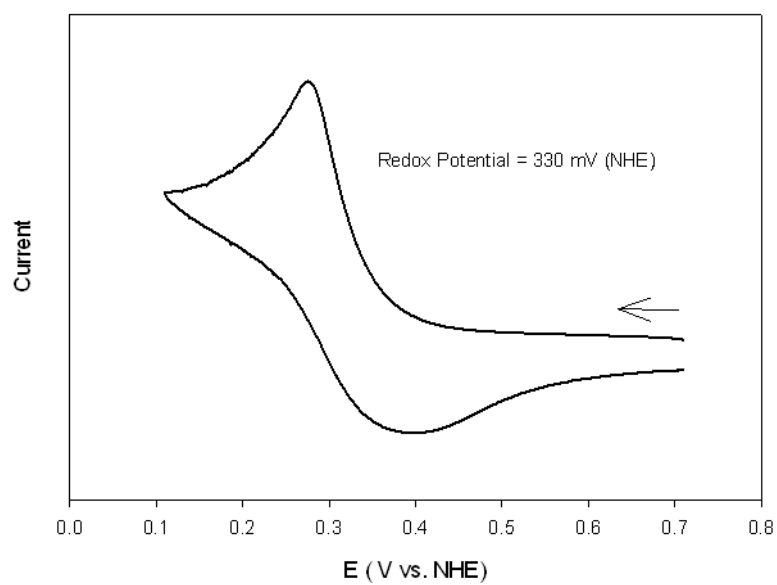


Figure C-49 Cyclic voltammogram of **5a** in physiological buffer.

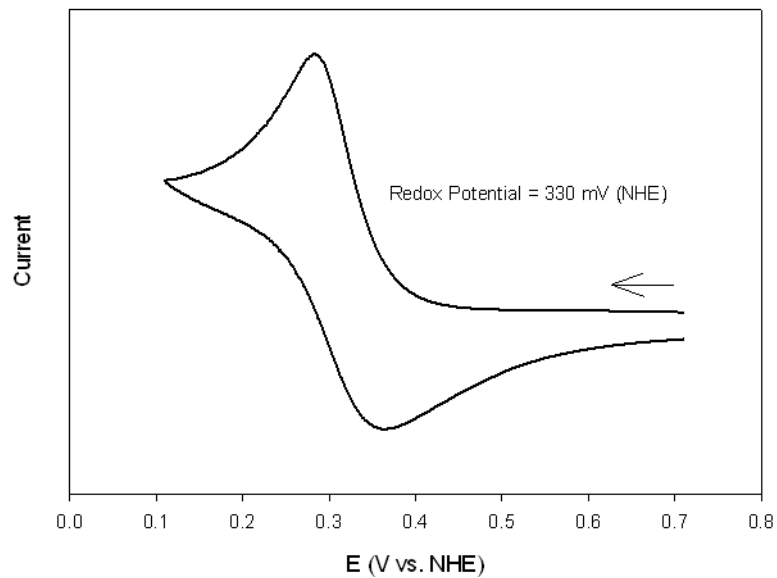


Figure C-50 Cyclic voltammogram of **5b** in physiological buffer.

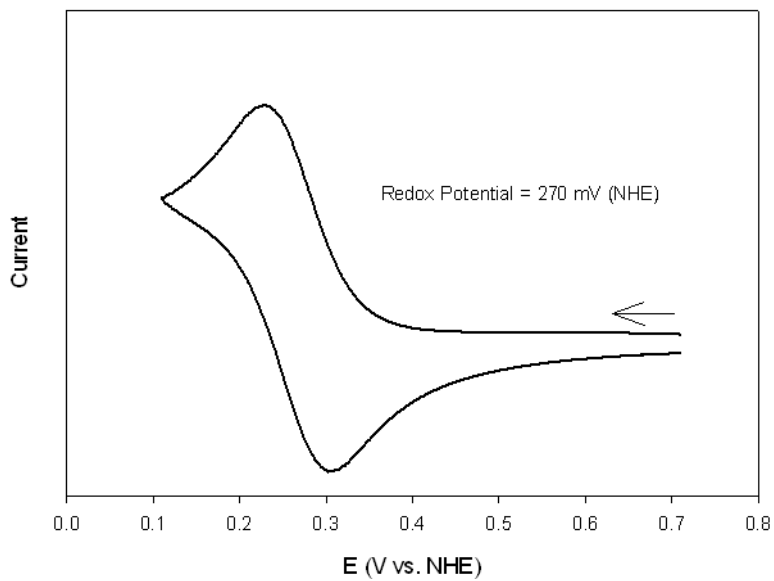


Figure C-51 Cyclic voltammogram of **NAMI-A** in physiological buffer.

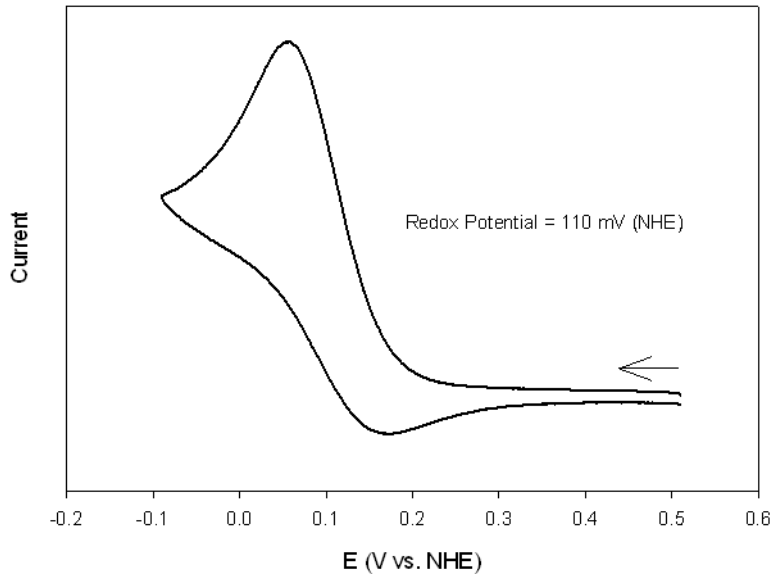


Figure C-52 Cyclic voltammogram of **NAMI-A** in a 1:1 mixture of physiological buffer and DMSO.

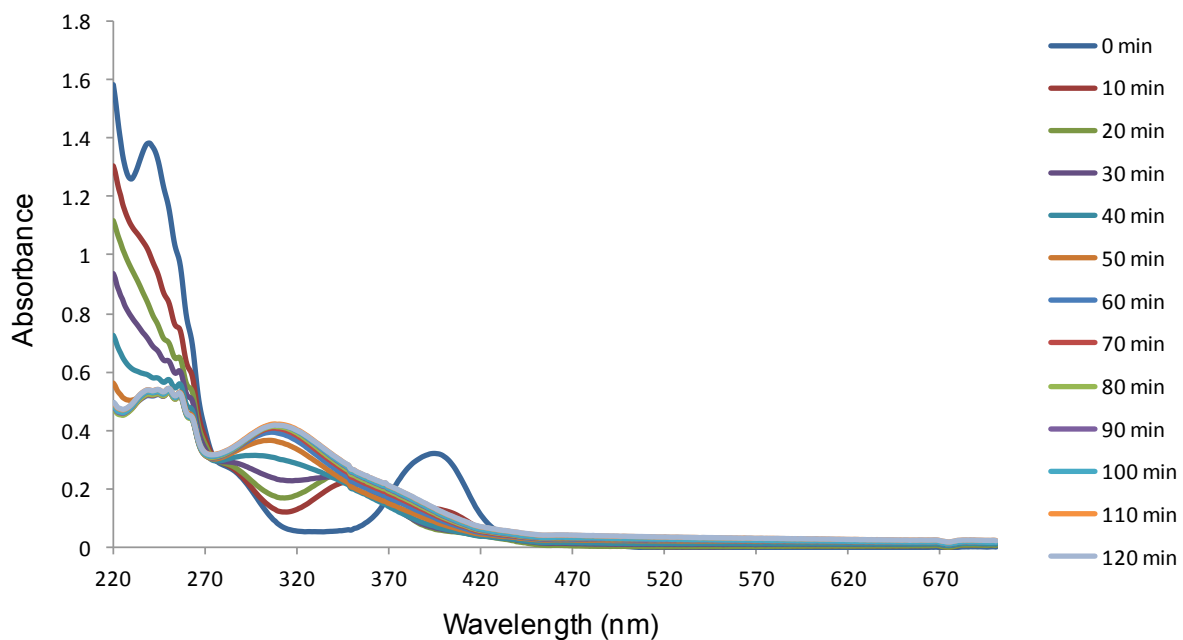


Figure C-53 UV-Vis spectrum of **1a** (200 μM) in physiological buffer at 37°C for two hours.

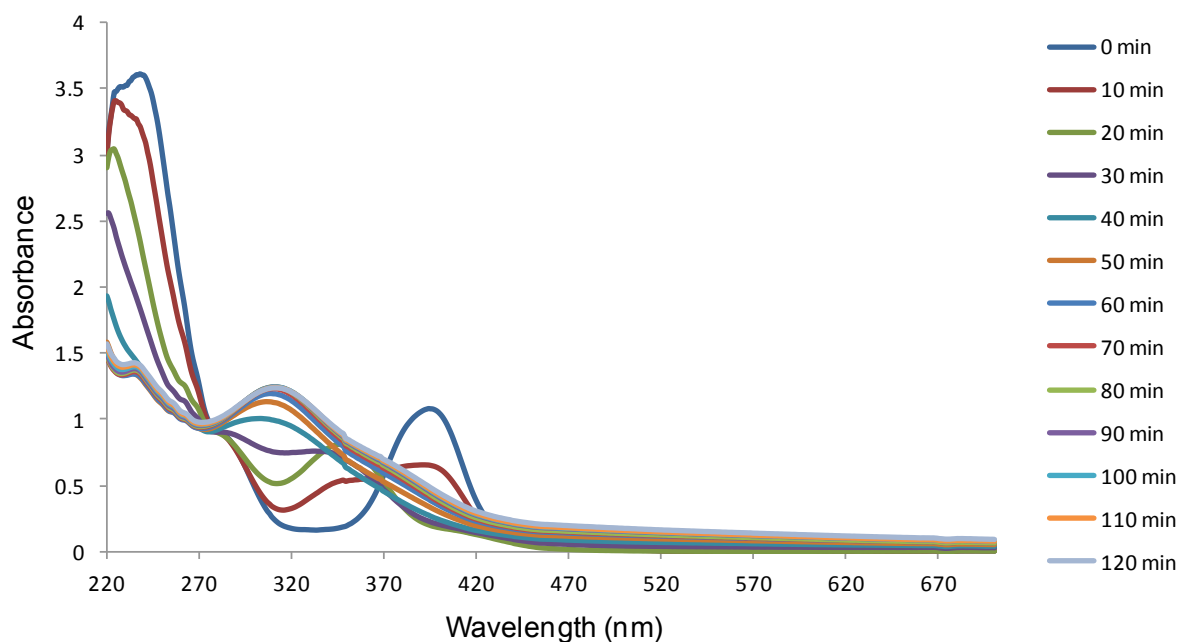


Figure C-54 UV-Vis spectrum of **1b** (200 μM) in physiological buffer at 37°C for two hours.

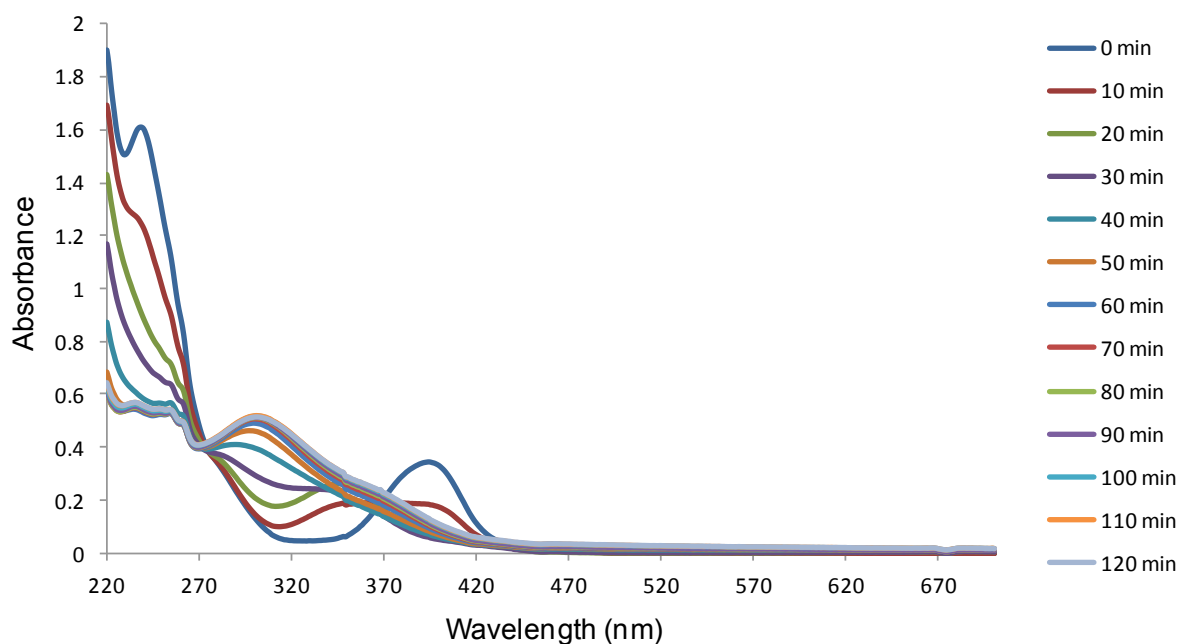


Figure C-55 UV-Vis spectrum of **2a** (200 μM) in physiological buffer at 37°C for two hours.

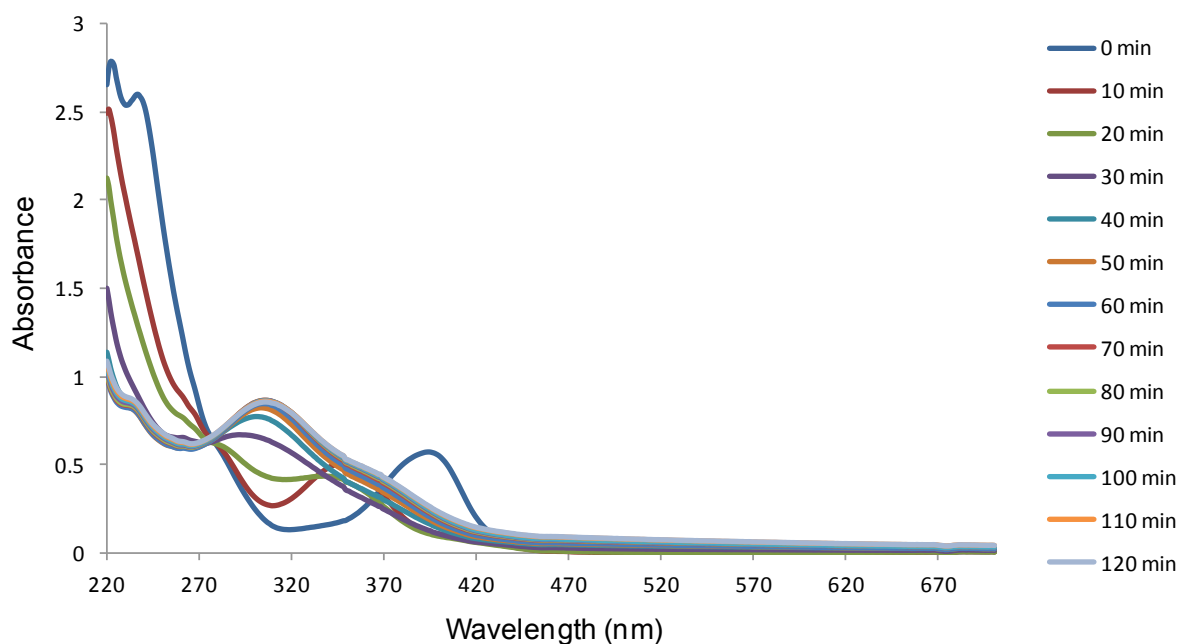


Figure C-56 UV-Vis spectrum of **2b** (200 μM) in physiological buffer at 37°C for two hours.

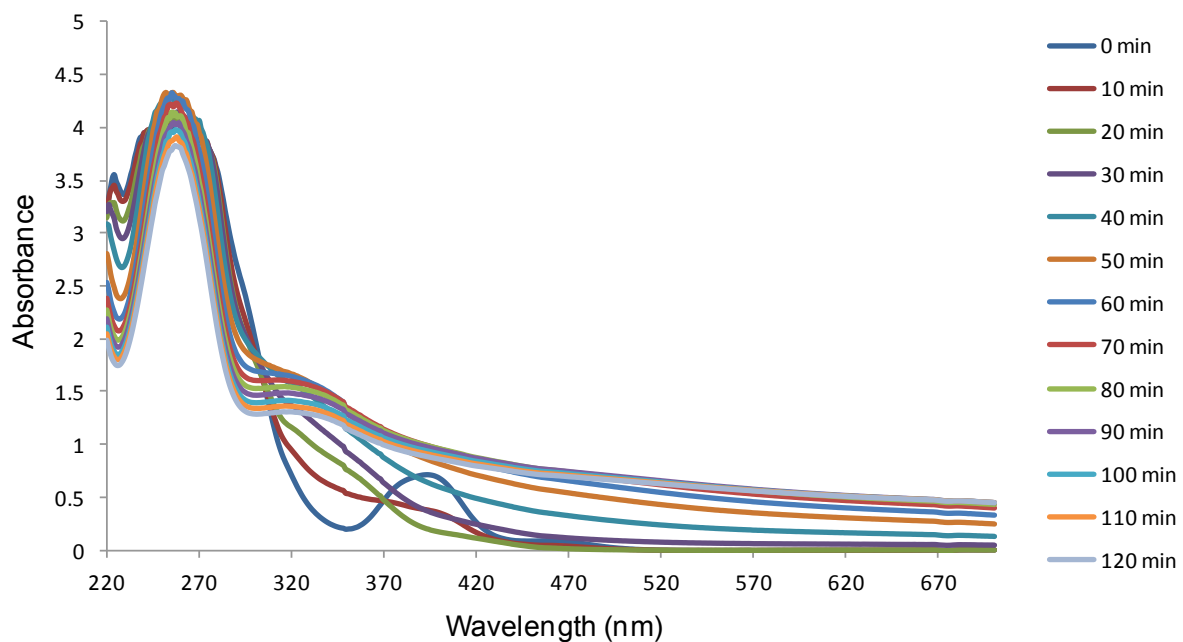


Figure C-57 UV-Vis spectrum of **3a** (200 μM) in physiological buffer at 37°C for two hours.

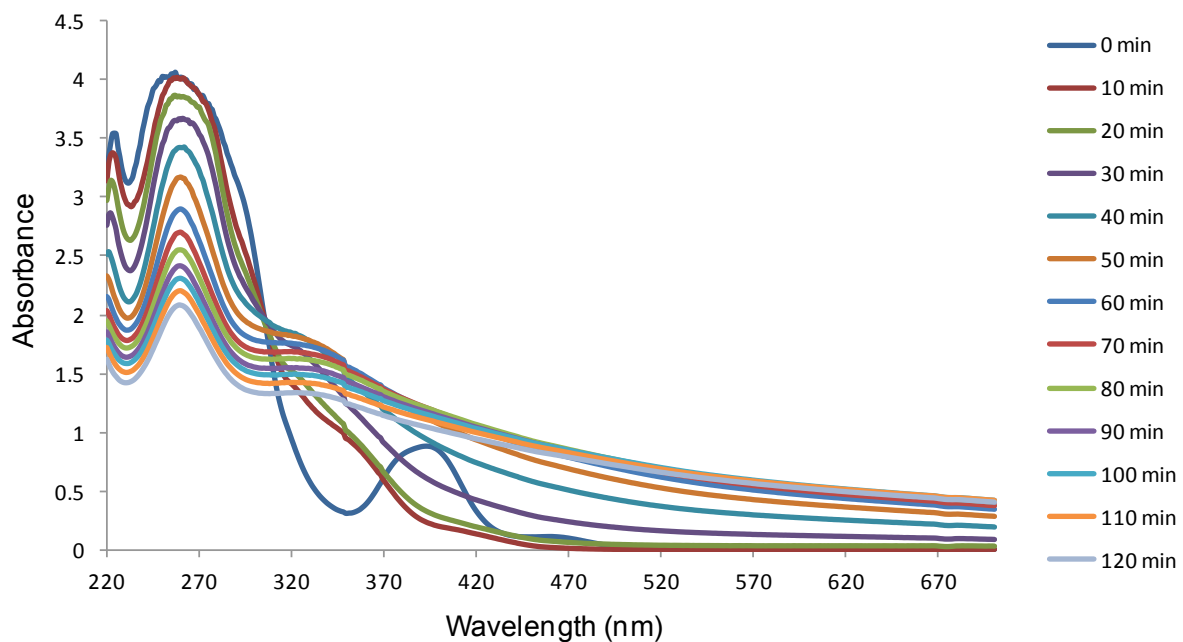


Figure C-58 UV-Vis spectrum of **3b** (200 μM) in physiological buffer at 37°C for two hours.

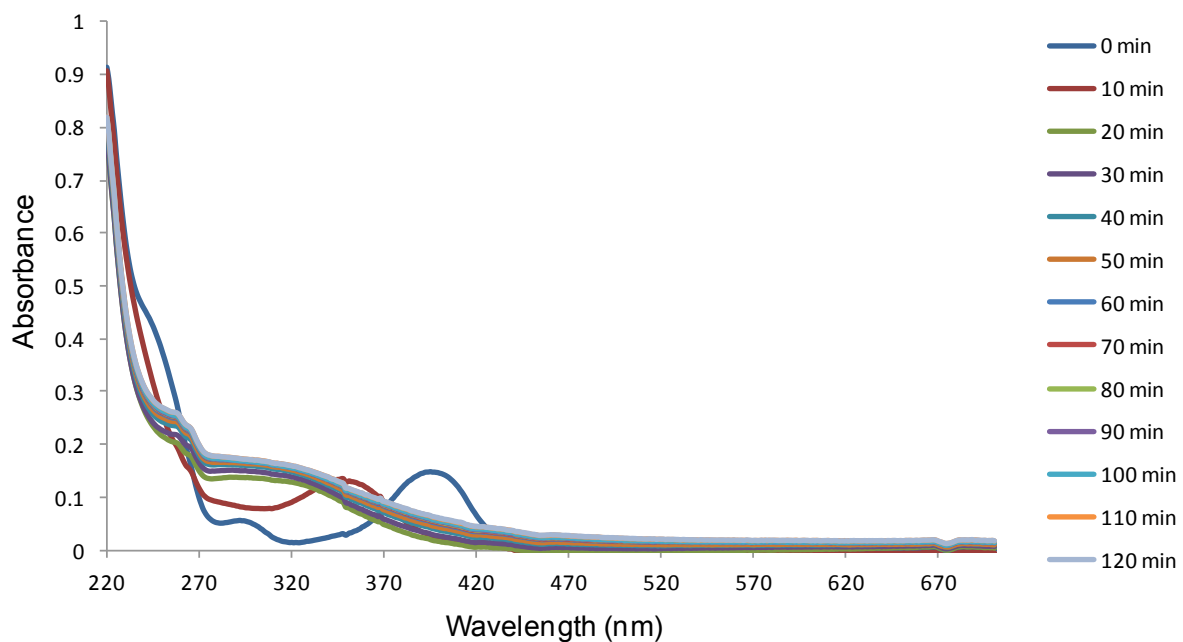


Figure C-59 UV-Vis spectrum of **4a** (200 μM) in physiological buffer at 37°C for two hours.

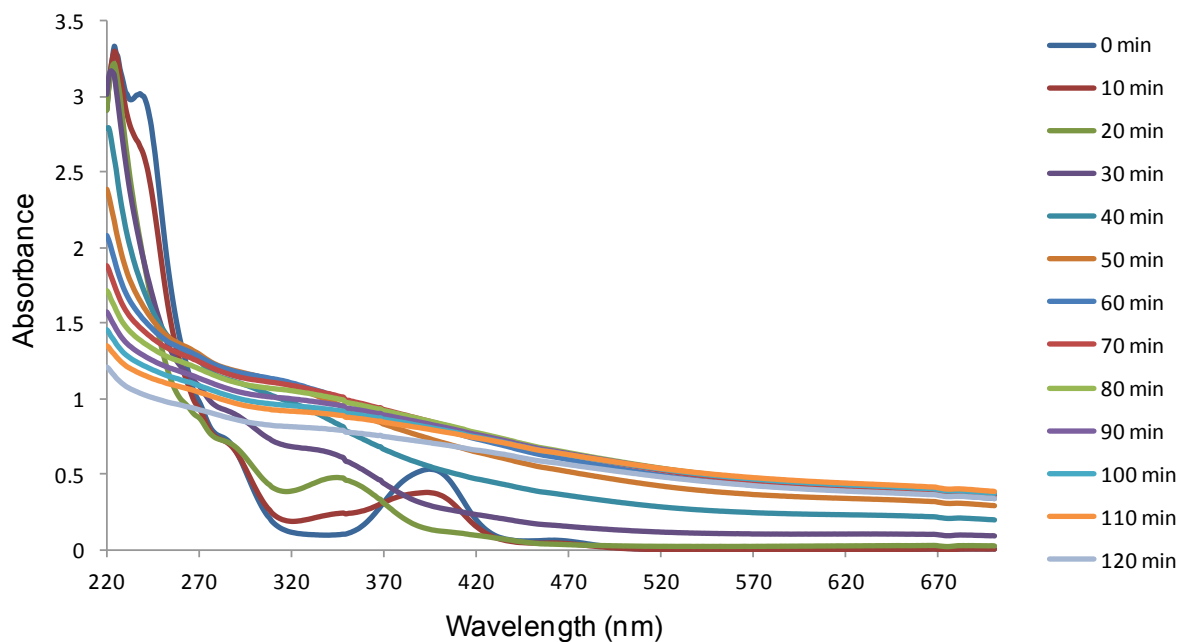


Figure C-60 UV-Vis spectrum of **4b** (200 μM) in physiological buffer at 37°C for two hours.

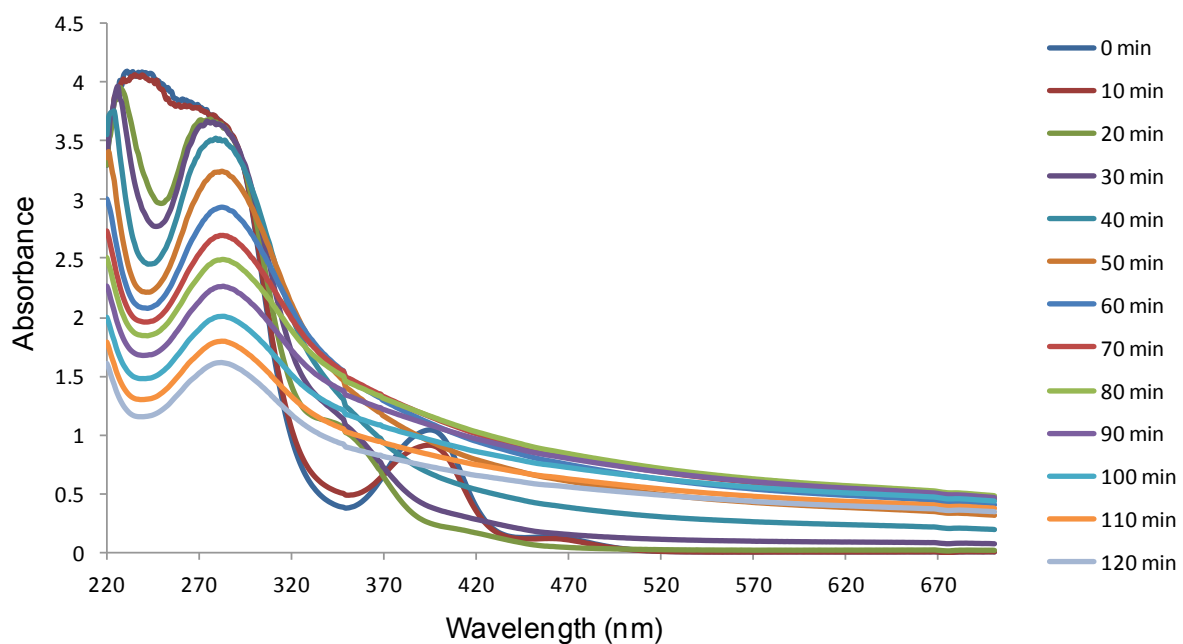


Figure C-61 UV-Vis spectrum of **5a** (200 μM) in physiological buffer at 37°C for two hours.

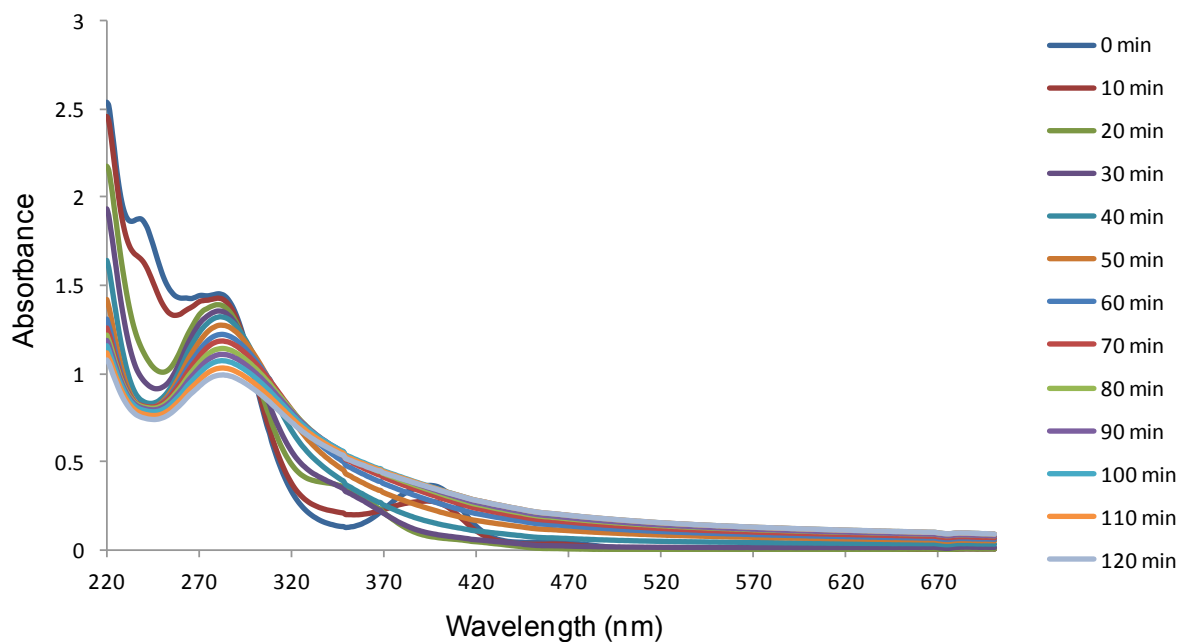


Figure C-62 UV-Vis spectrum of **5b** (200 μM) in physiological buffer at 37°C for two hours.

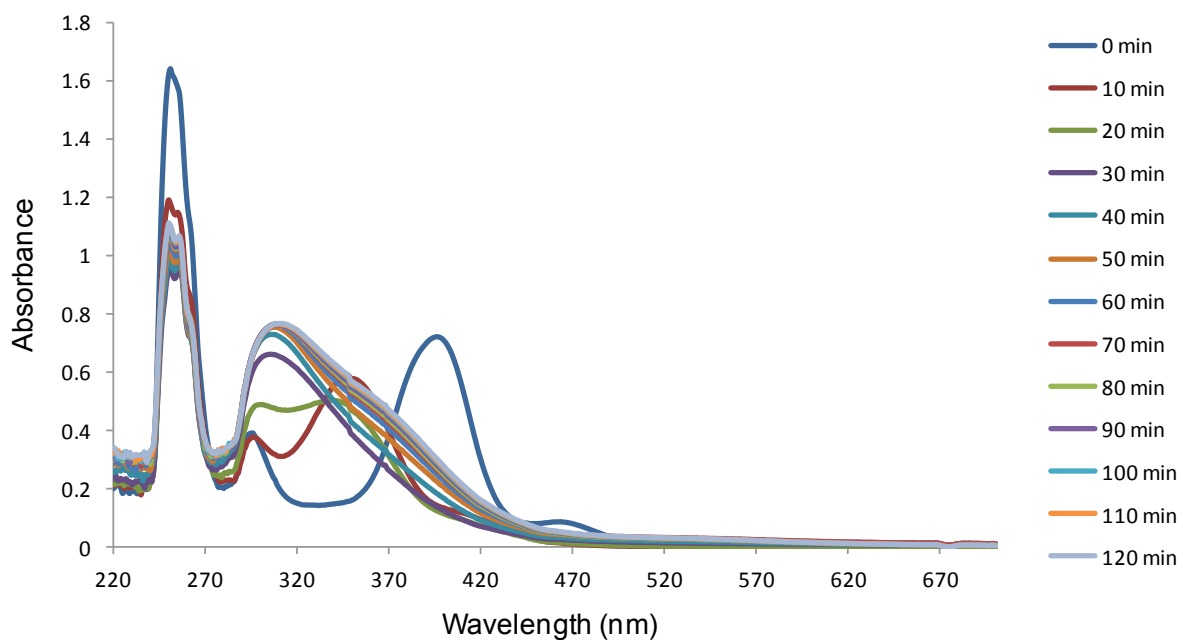


Figure C-63 UV-Vis spectrum of **1a** (200 μM) in physiological buffer with hsA (100 μM) at 37°C for two hours.

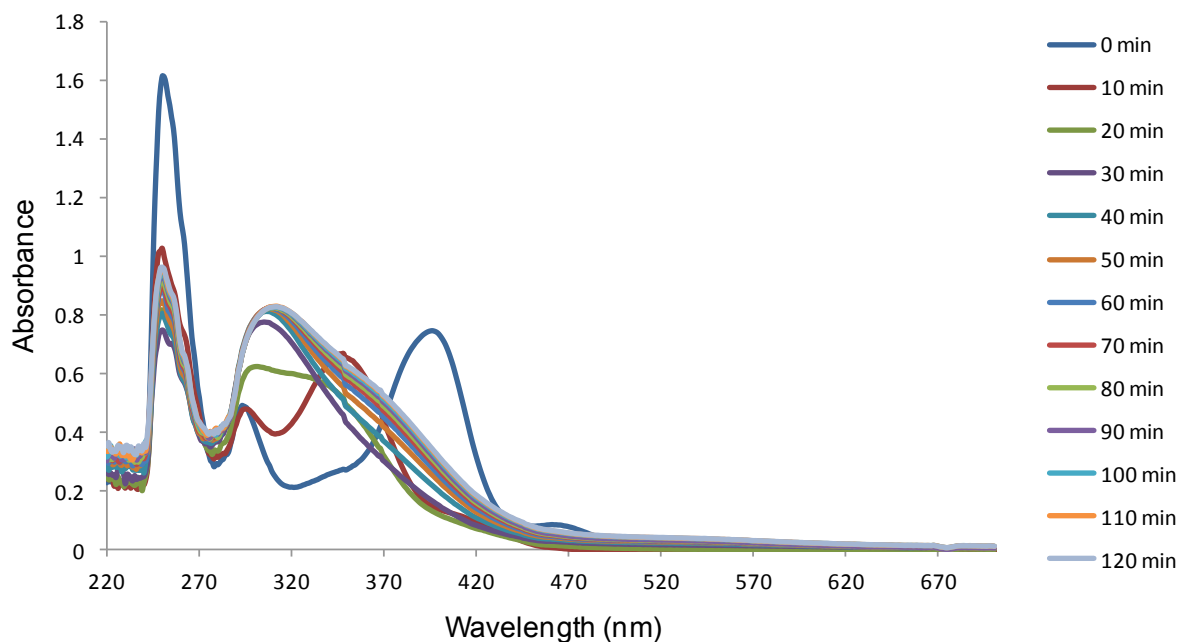


Figure C-64 UV-Vis spectrum of **1b** (200 μM) in physiological buffer with hsA (100 μM) at 37°C for two hours.

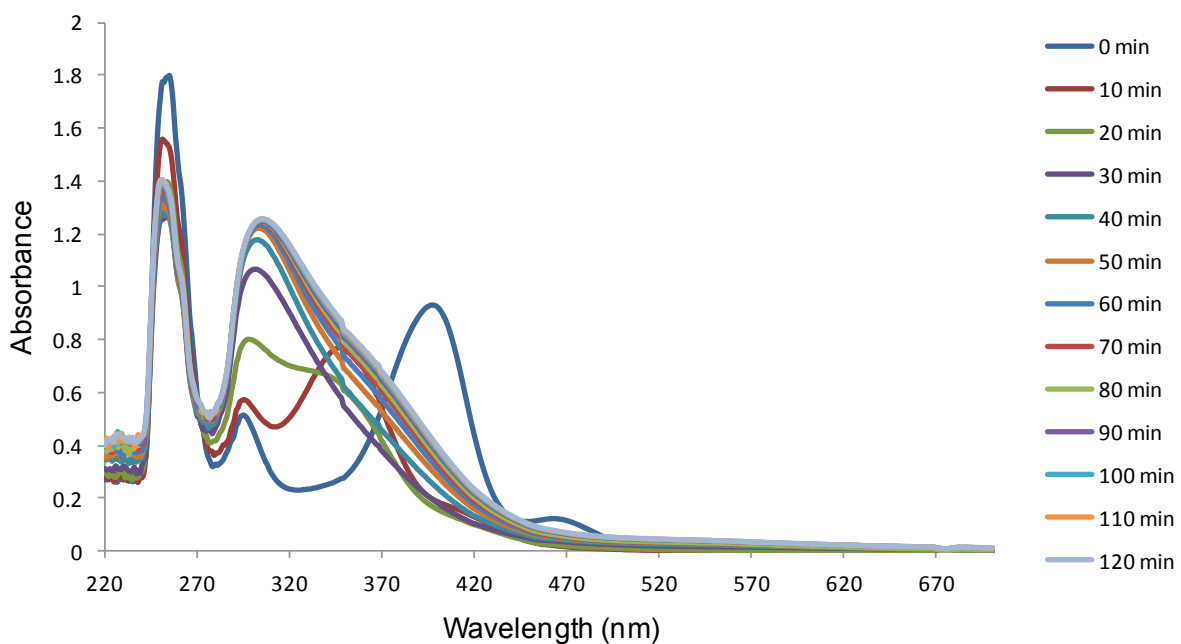


Figure C-65 UV-Vis spectrum of **2a** (200 μM) in physiological buffer with hsA (100 μM) at 37°C for two hours.

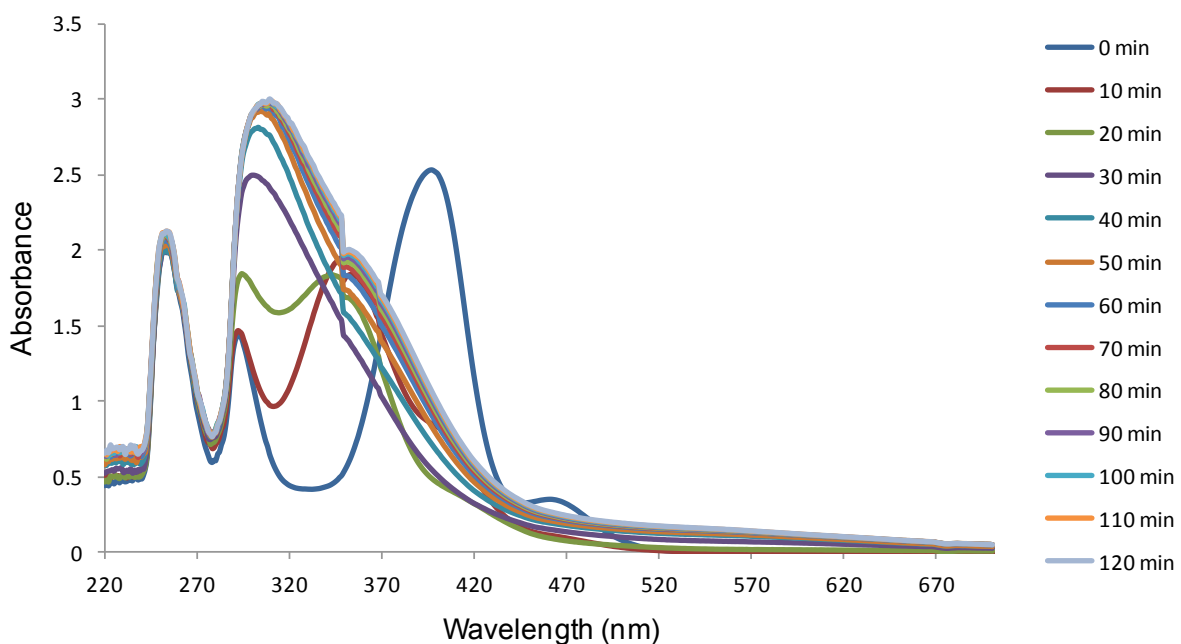


Figure C-66 UV-Vis spectrum of **2b** (200 μM) in physiological buffer with hsA (100 μM) at 37°C for two hours.

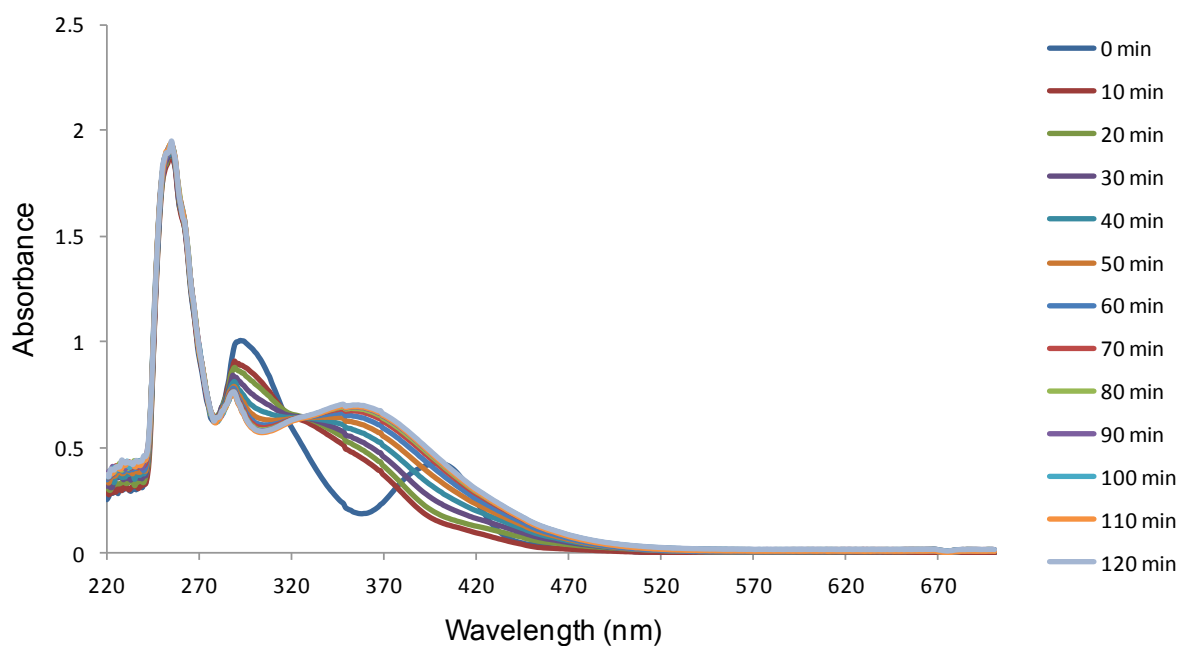


Figure C-67 UV-Vis spectrum of **3a** (200 μ M) in physiological buffer with hsA (100 μ M) at 37°C for two hours.

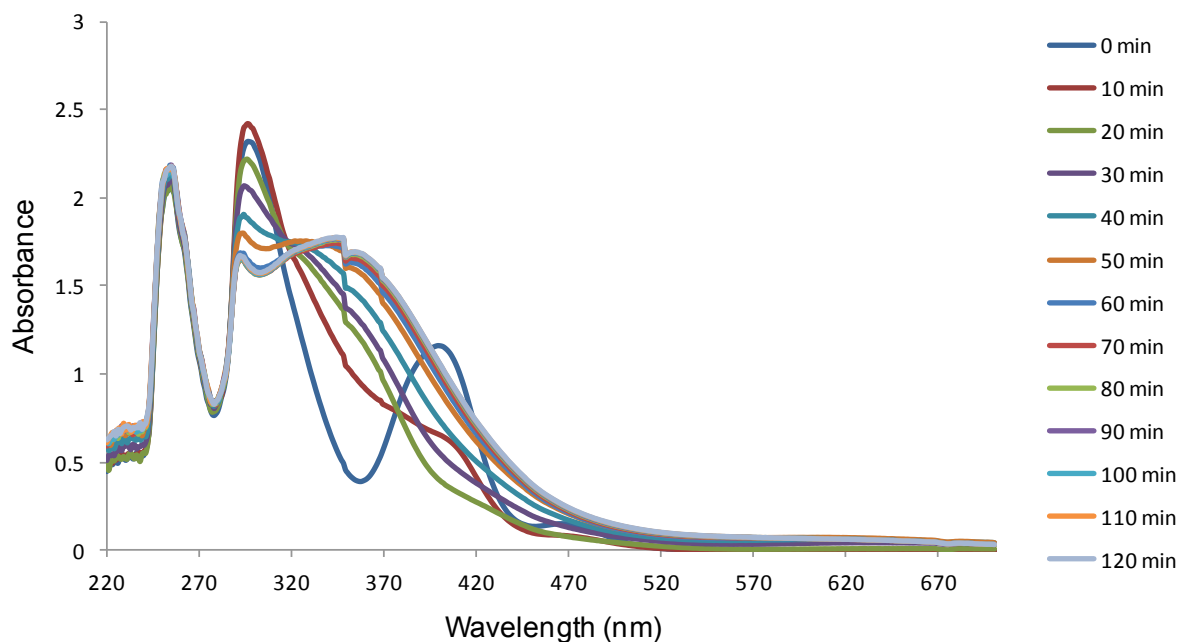


Figure C-68 UV-Vis spectrum of **3b** (200 μ M) in physiological buffer with hsA (100 μ M) at 37°C for two hours.

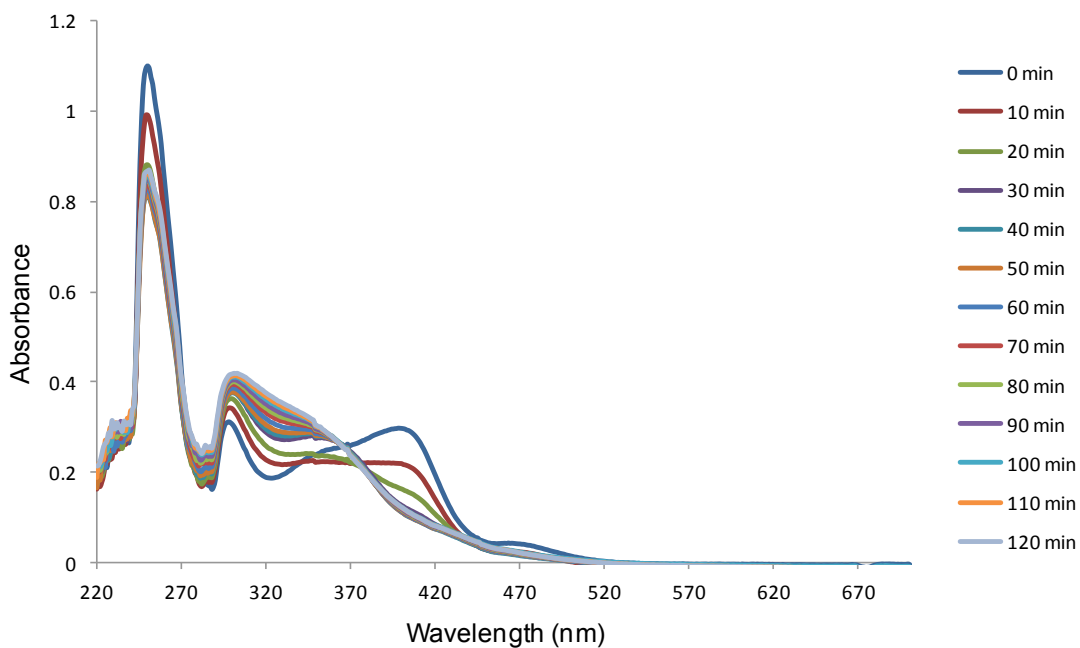


Figure C-69 UV-Vis spectrum of **4a** (200 μ M) in physiological buffer with hsA (100 μ M) at 37°C for two hours.

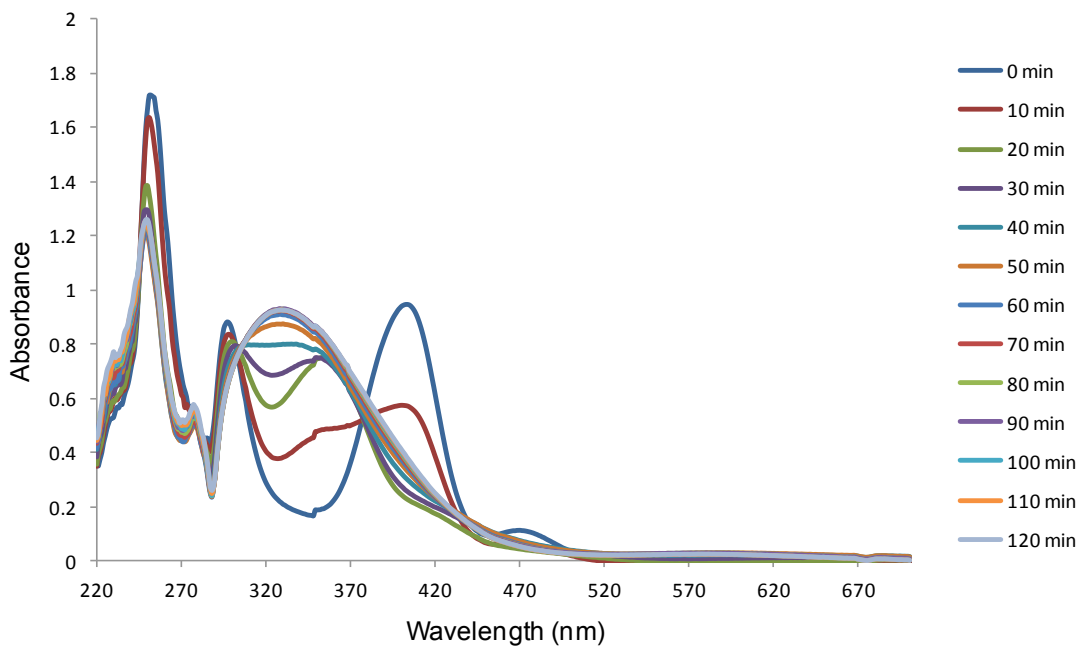


Figure C-70 UV-Vis spectrum of **4b** (200 μ M) in physiological buffer with hsA (100 μ M) at 37°C for two hours.

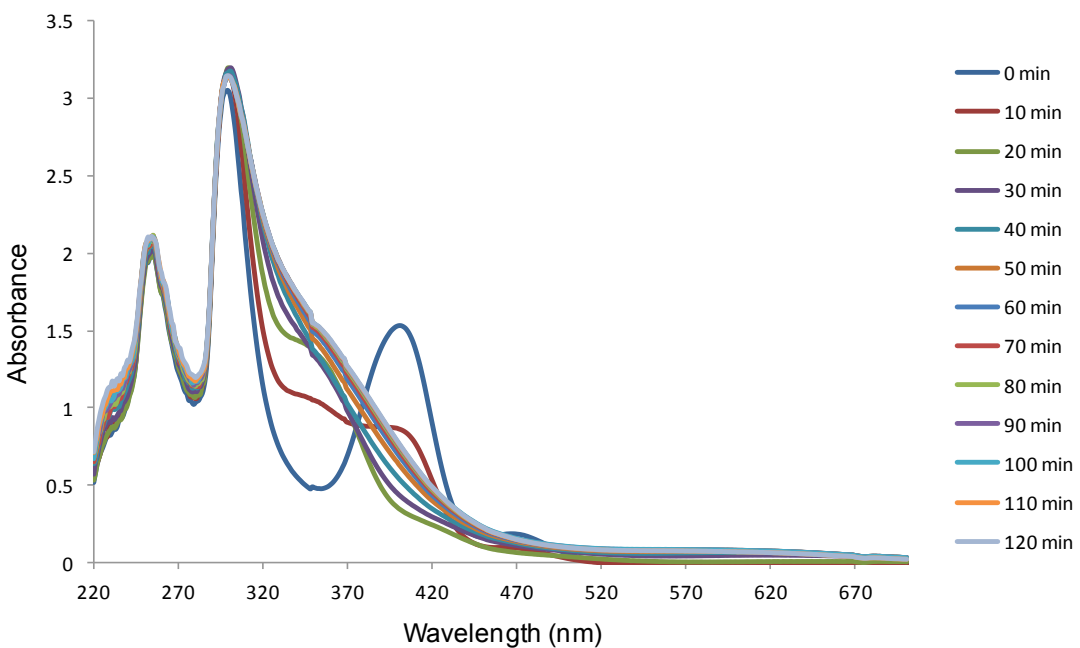


Figure C-71 UV-Vis spectrum of **5a** (200 μ M) in physiological buffer with hsA (100 μ M) at 37°C for two hours.

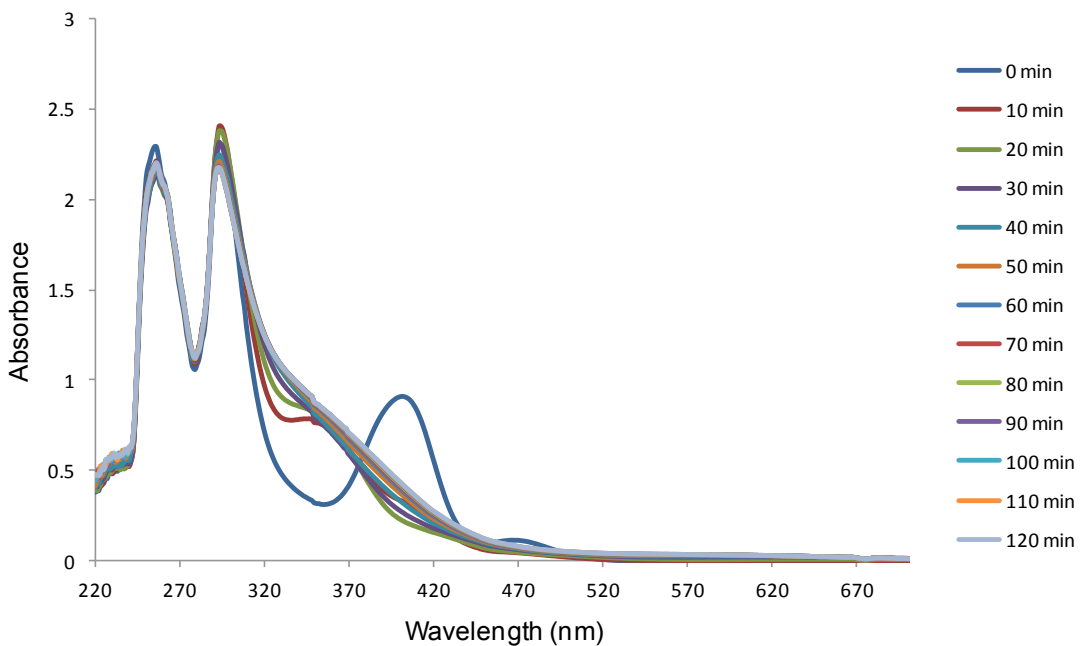


Figure C-72 UV-Vis spectrum of **5b** (200 μ M) in physiological buffer with hsA (100 μ M) at 37°C for two hours.

Appendix D. Supplementary Information for Chapter 5.

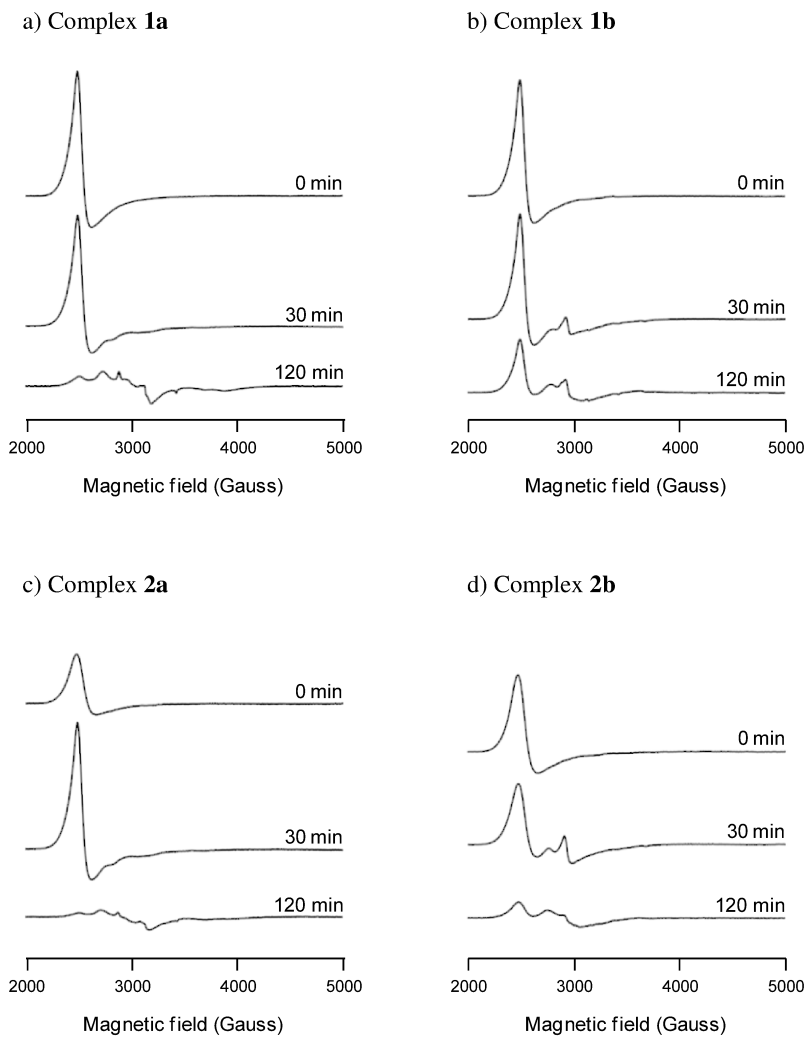


Figure D-1 (a-d) EPR spectra of complexes **1a** - **2b** (3 mM) in PBS after incubation for 0, 30, and 120 minutes at 37 °C. **Experimental conditions:** see section 2.2.5.

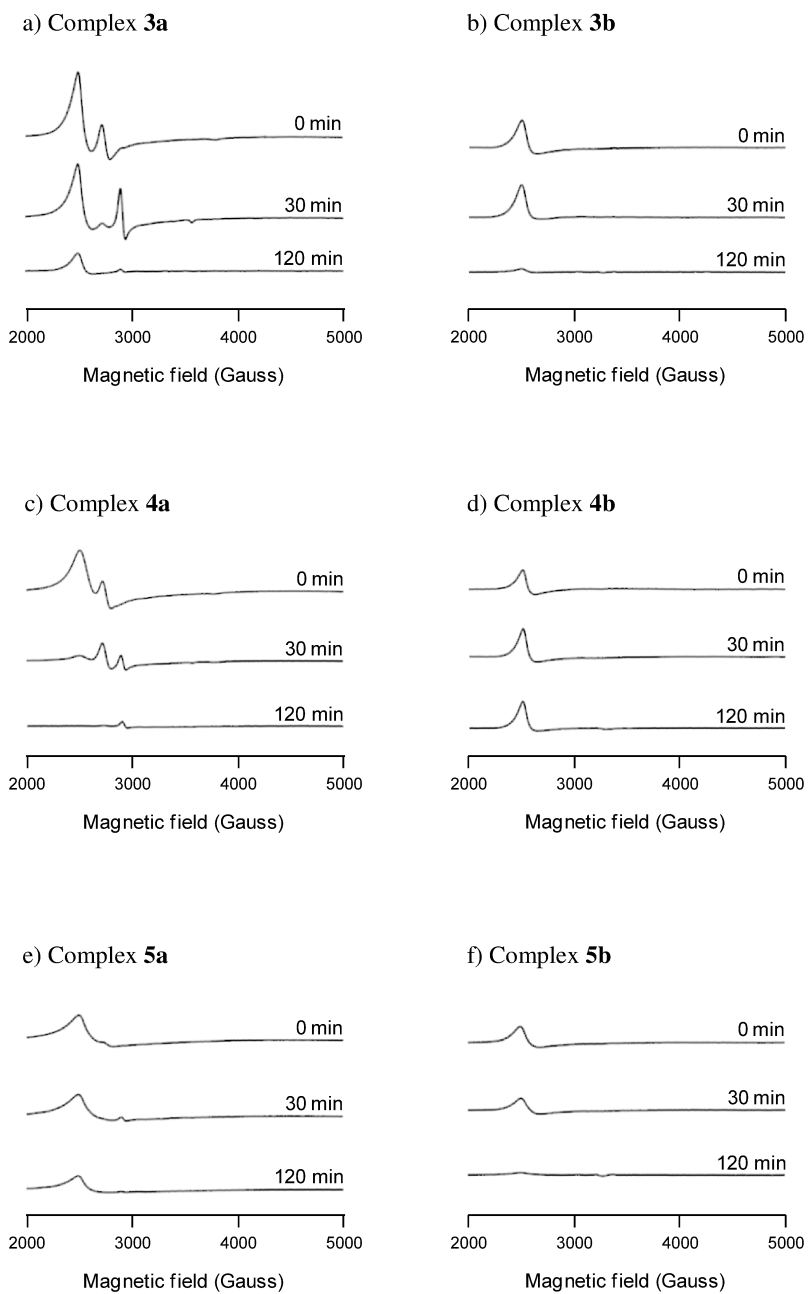


Figure D-2 (a-f) EPR spectra of complexes **3a** - **5b** (3 mM) in PBS with 10 % DMSO after incubation for 0, 30, and 120 minutes at 37 °C. **Experimental conditions:** see section 2.2.5.

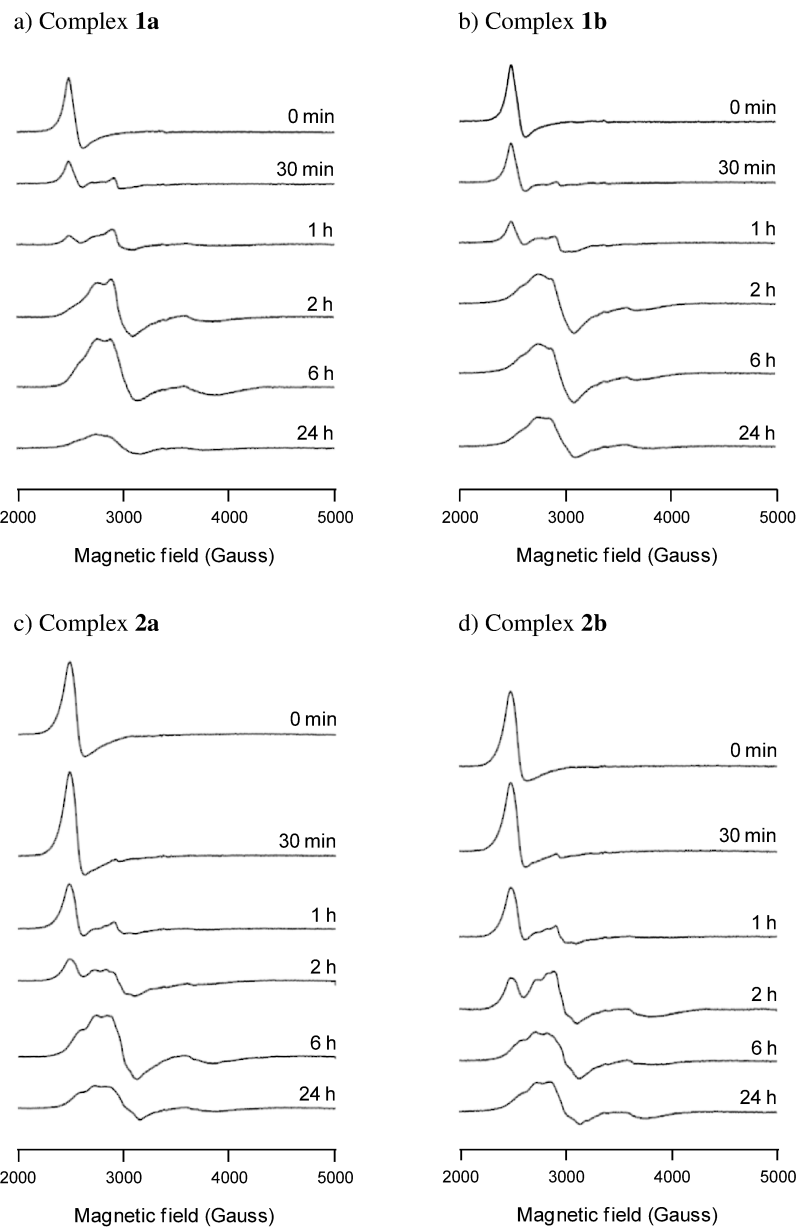


Figure D-3 (a-d) EPR spectra of complex **1a** – **2b** (1 mM) with hsA (0.5 mM) in PBS after incubation for 0 minutes to 24 hours at 37 °C. **Experimental conditions:** see section 2.2.5.

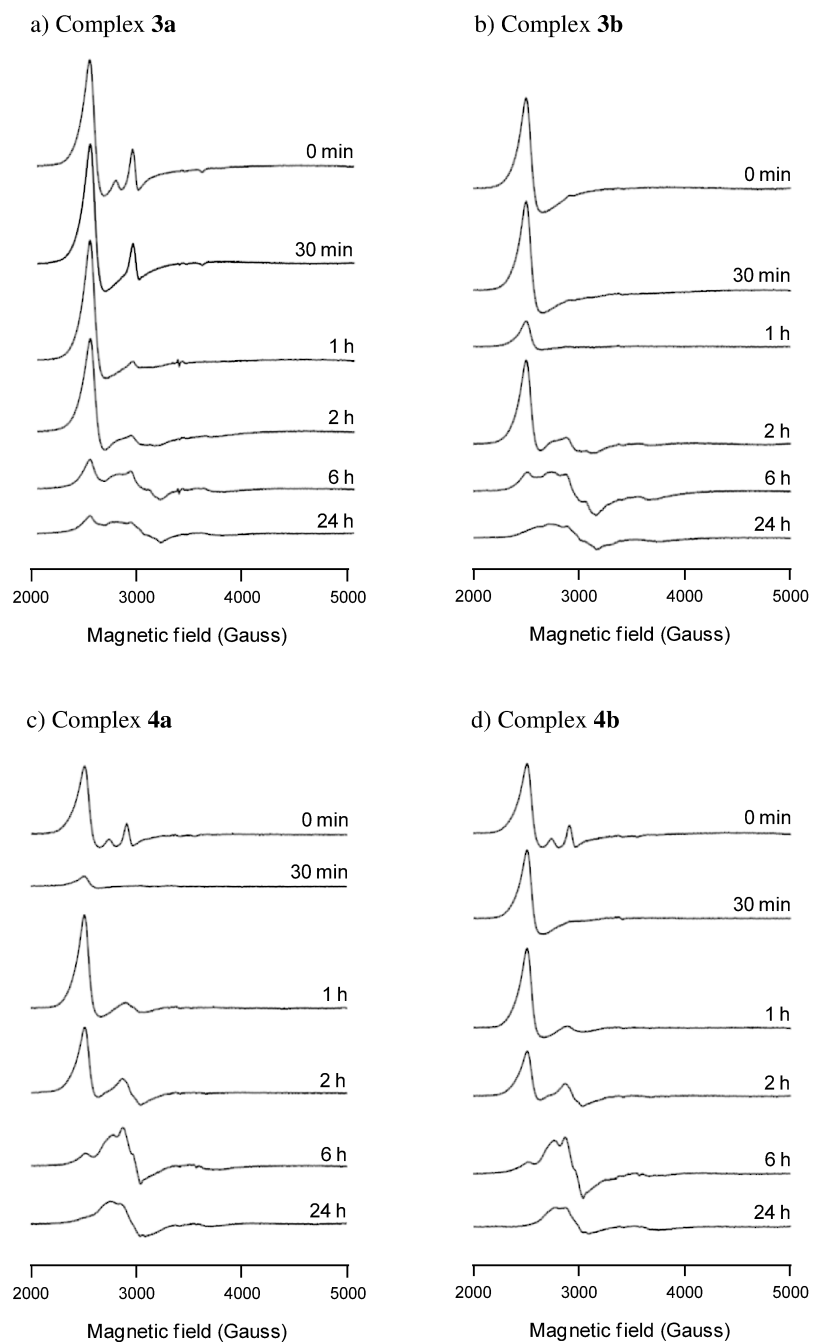
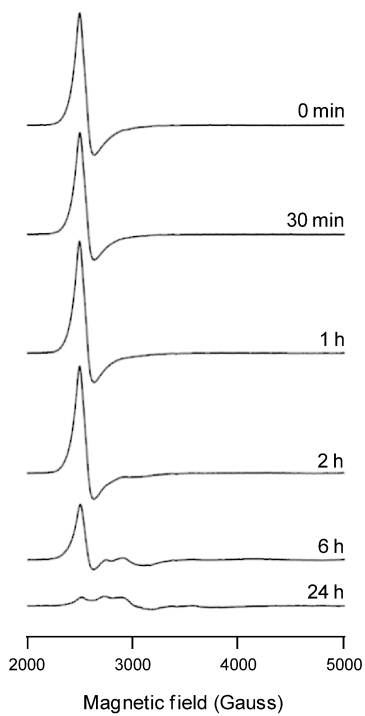


Figure D-4 (a-d) EPR spectra of complex **3a** – **4b** (1 mM) with hsA (0.5 mM) in PBS with 4% DMSO after incubation for 0 minutes to 24 hours at 37 °C.
Experimental conditions: see section 2.2.5.

a) Complex **5a**



b) Complex **5b**

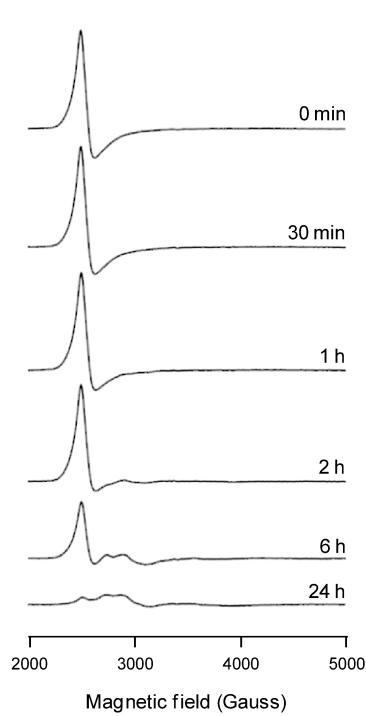


Figure D-5 (a-b) EPR spectra of complex **5a** and **5b** (1 mM) with hsA (0.5 mM) in PBS with 4% DMSO after incubation for 0 minutes to 24 hours at 37 °C.
Experimental conditions: see section 2.2.5.

Table D-1 Simulation parameters, g values and linewidths, used in the simulation of all EPR spectra attained for complexes **1a – 3b**.

Complex	g values			Linewidths		
	g ₁	g ₂	g ₃	LW ₁	LW ₂	LW ₃
1a-C1	2.66	2.66	1.20	110	110	400
1a-C2	2.44	2.26	1.72	130	70	300
1a-hsA-1	2.58	2.28	1.20	250	100	400
1a-hsA-2	2.45	2.20	1.76	150	80	250
1b-C1	2.66	2.66	1.20	110	110	400
1b-C2	2.44	2.26	1.72	130	70	300
1b-hsA-1	2.58	2.28	1.20	250	100	400
1b-hsA-2	2.45	2.20	1.76	150	80	250
2a-C1	2.65	2.65	1.20	140	140	400
2a-C2	2.47	2.27	1.78	125	100	400
2a-hsA-1	2.58	2.27	1.20	250	125	400
2a-hsA-2	2.45	2.18	1.74	150	80	250
2b-C1	2.65	2.65	1.20	140	140	400
2b-C2	2.45	2.26	2.00	125	50	400
2b-hsA-1	2.58	2.27	1.20	250	125	400
2b-hsA-2	2.45	2.18	1.74	150	80	250
3a-C1	2.66	2.66	1.20	115	115	400
3a-C2	2.44	2.44	1.76	90	90	125
3a-C3	2.30	2.30	1.88	50	50	50
3a-hsA-1	2.61	2.28	1.20	175	100	400
3a-hsA-2	2.45	2.16	1.78	150	110	250
3b-C1	2.66	2.66	1.20	115	115	400
3b-C2	2.44	2.44	1.76	90	90	125
3b-C3	2.30	2.30	1.88	50	50	50
3b-hsA-1	2.61	2.28	1.20	175	100	400
3b-hsA-2	2.45	2.16	1.78	150	110	250

Table D-2 Simulation parameters, g values and linewidths, used in the simulation of all EPR spectra attained for complexes **4a – 5b** and KP1019.

Complex	g values			Linewidths		
	g ₁	g ₂	g ₃	LW ₁	LW ₂	LW ₃
4a-C1	2.64	2.64	1.20	145	145	400
4a-C2	2.44	2.44	1.76	90	90	125
4a-C3	2.30	2.30	1.88	50	50	50
4a-C1-hsA	2.64	2.64	1.20	115	115	400
4a-hsA-1	2.38	2.29	1.20	400	100	400
4a-hsA-2	2.44	2.22	1.78	80	150	250
4b-C1	2.64	2.64	1.20	105	105	400
4b-C2	2.44	2.44	1.76	90	90	125
4b-C3	2.30	2.30	1.88	50	50	50
4b-hsA-1	2.38	2.29	1.20	400	100	400
4b-hsA-2	2.44	2.22	1.78	80	150	250
5a-C1	2.64	2.64	1.20	200	200	400
5a-C2	2.44	2.44	1.76	90	90	125
5a-C3	2.30	2.30	1.88	50	50	50
5a-C1-hsA	2.64	2.64	1.20	100	100	400
5a-hsA-1	2.38	2.24	1.20	400	150	400
5a-hsA-2	2.45	2.21	1.71	100	200	300
5b-C1	2.64	2.64	1.20	150	150	400
5b-hsA-1	2.38	2.24	1.20	400	150	400
5b-hsA-2	2.45	2.21	1.71	100	200	300
KP1019-Uniaxial	2.64	2.64	1.20	120	120	500
KP1019-Rhombic	2.94	2.31	0.95	100	200	600
KP1019-hsA-1	2.44	2.24	1.79	120	90	200
KP1019-hsA-2	2.32	2.32	1.84	90	90	80

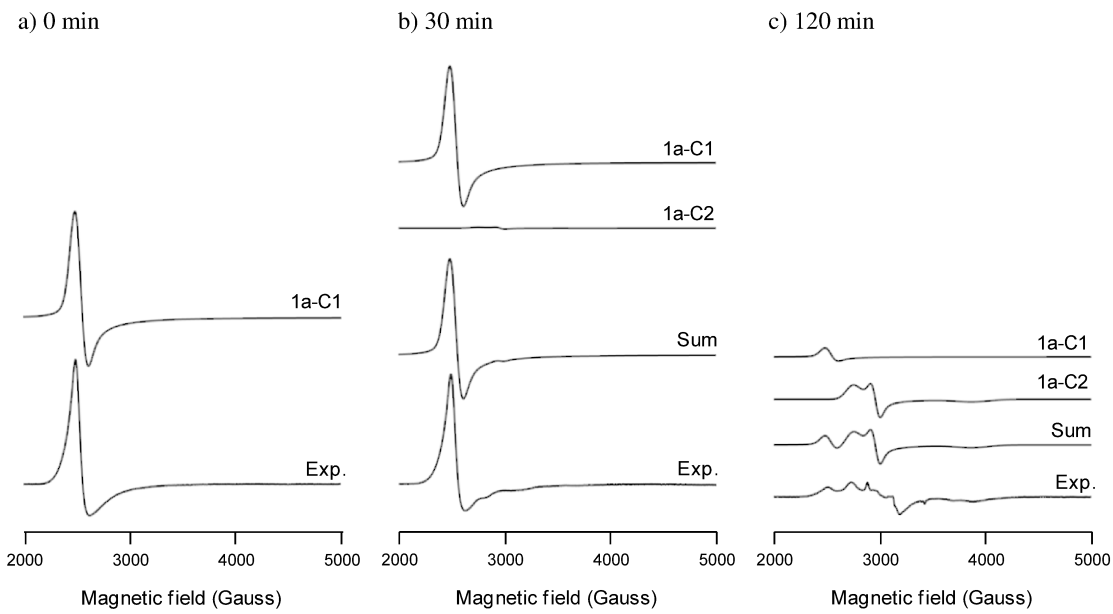


Figure D-6 (a-c) Simulation of EPR spectra of complex **1a** (3 mM) in PBS after incubation for 0, 30, and 120 minutes at 37 °C. **Simulation parameters:** see **Table D-1**.

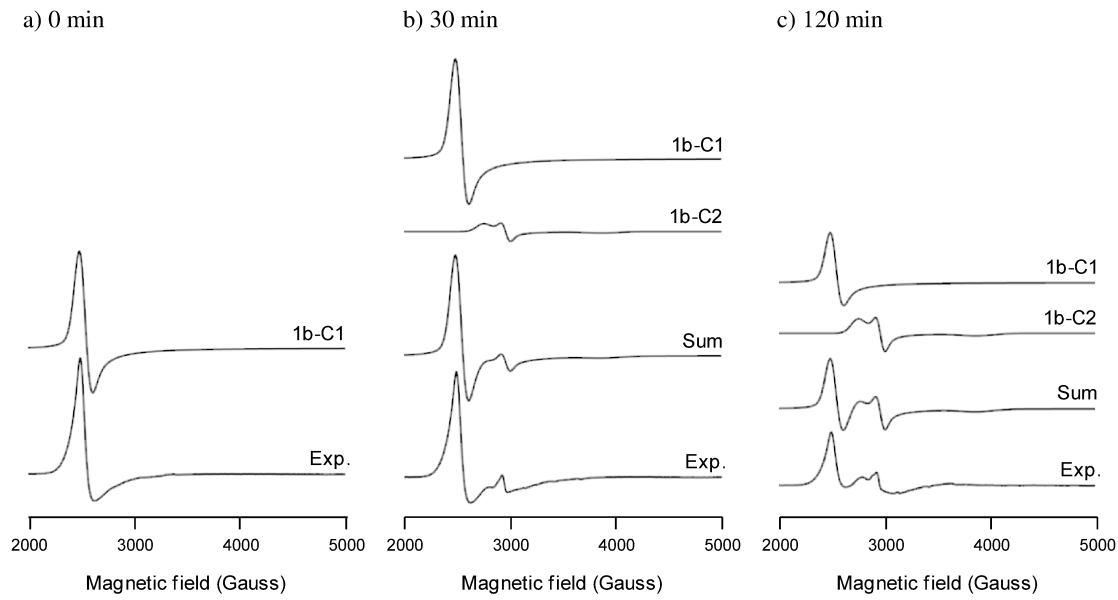


Figure D-7 (a-c) Simulation of EPR spectra of complex **1b** (3 mM) in PBS after incubation for 0, 30, and 120 minutes at 37 °C. **Simulation parameters:** see **Table D-1**.

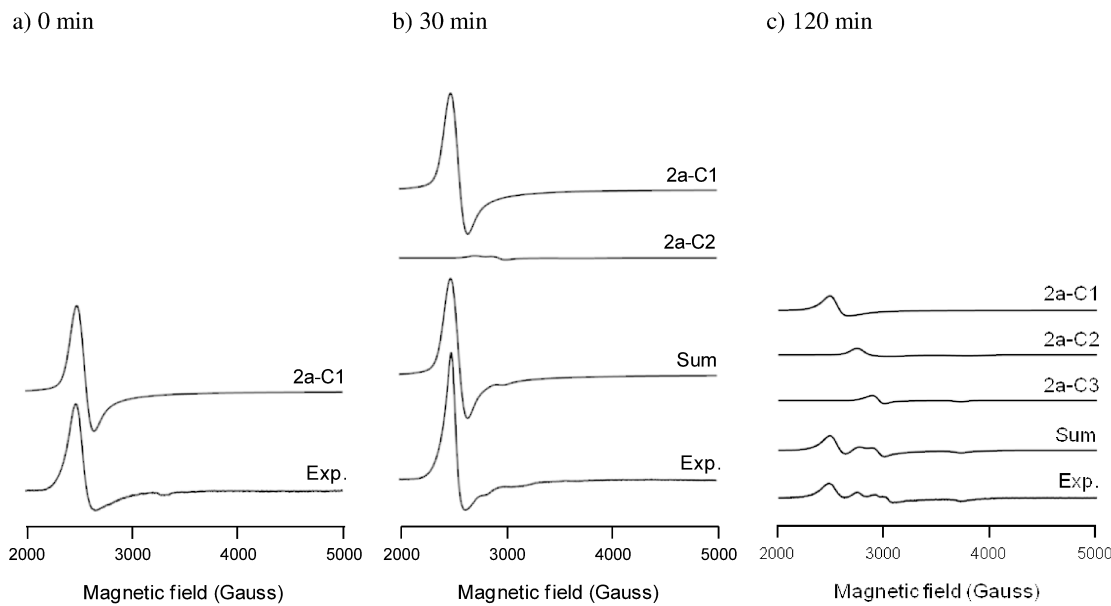


Figure D-8 (a-c) Simulation of EPR spectra of complex **2a** (3 mM) in PBS after incubation for 0, 30, and 120 minutes at 37 °C. **Simulation parameters:** see **Table D-1.**

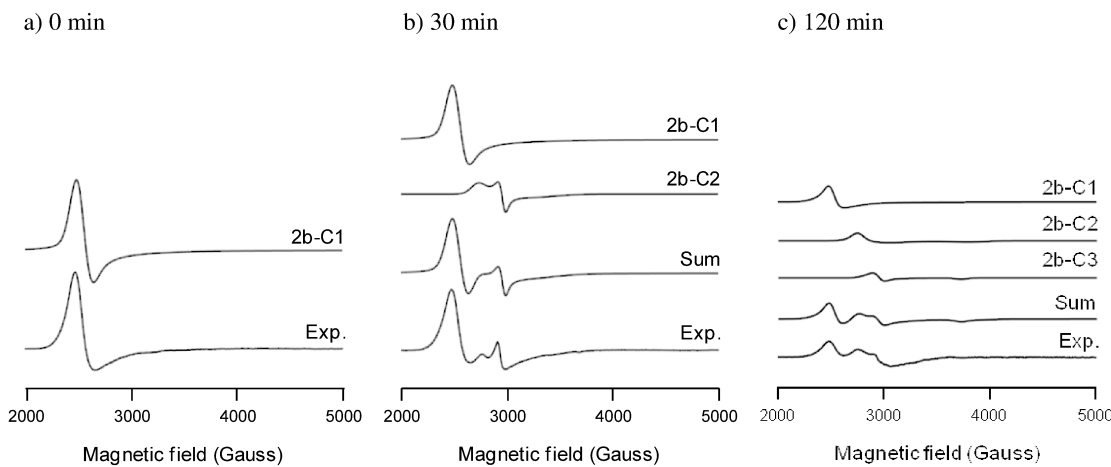


Figure D-9 (a-c) Simulation of EPR spectra of complex **2b** (3 mM) in PBS after incubation for 0, 30, and 120 minutes at 37 °C. **Simulation parameters:** see **Table D-1.**

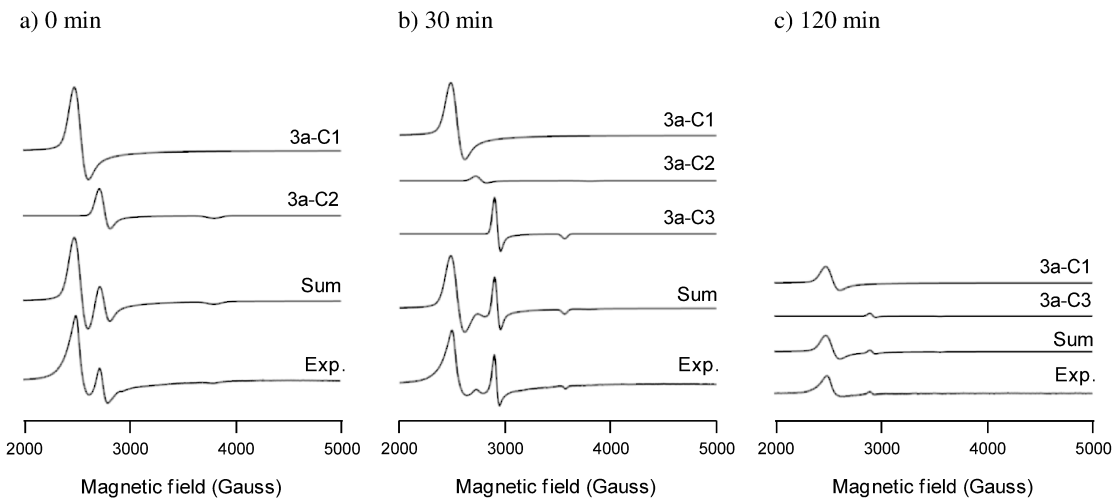


Figure D-10 (a-c) Simulation of EPR spectra of complex **3a** (3 mM) in PBS with 10% DMSO after incubation for 0, 30, and 120 minutes at 37 °C. **Simulation parameters:** see Table D-1.

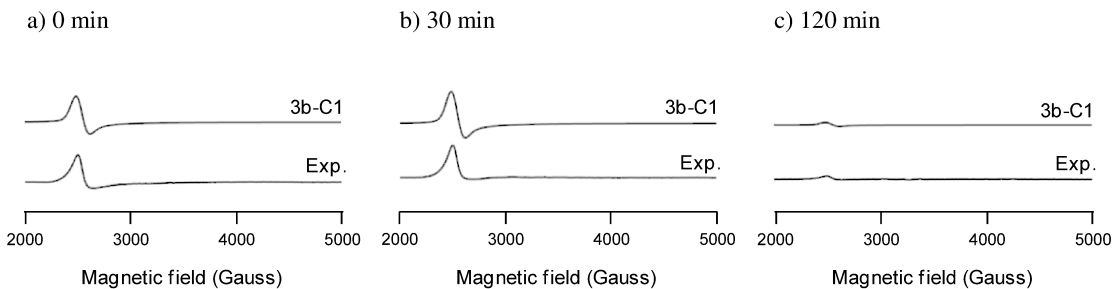


Figure D-11 (a-c) Simulation of EPR spectra of complex **3b** (3 mM) in PBS with 10% DMSO after incubation for 0, 30, and 120 minutes at 37 °C. **Simulation parameters:** see Table D-1.

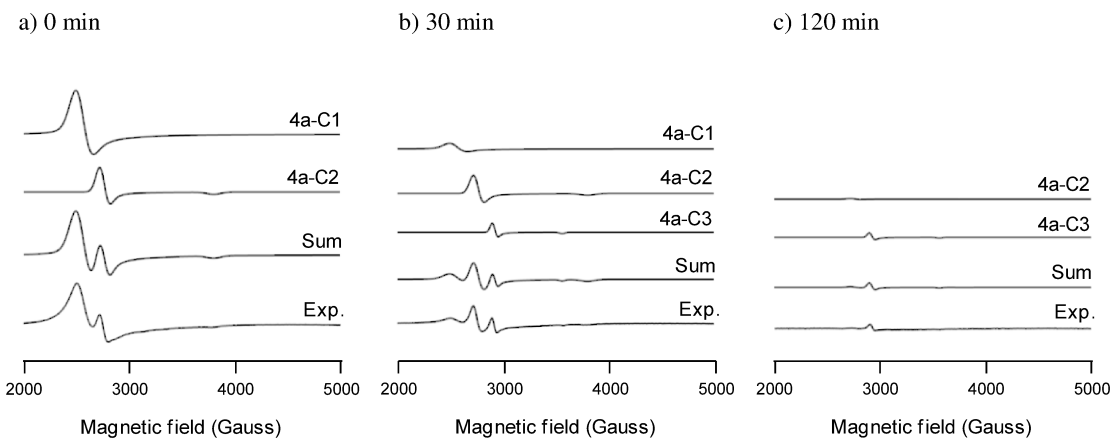


Figure D-12 (a-c) Simulation of EPR spectra of complex **4a** (3 mM) in PBS with 10% DMSO after incubation for 0, 30, and 120 minutes at 37 °C. **Simulation parameters:** see Table D-2.

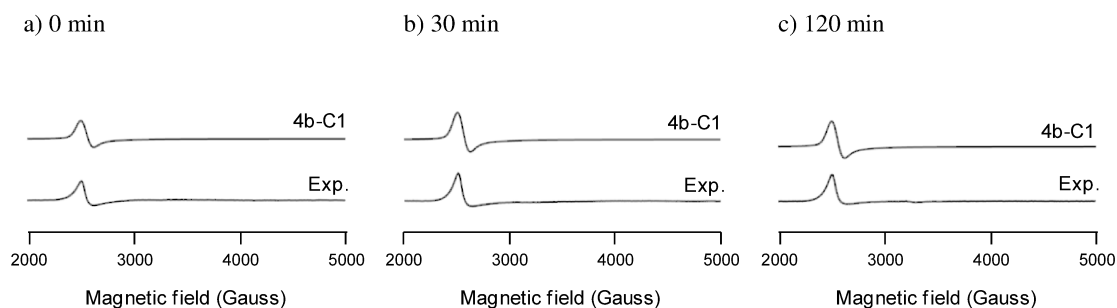


Figure D-13 (a-c) Simulation of EPR spectra of complex **4b** (3 mM) in PBS with 10% DMSO after incubation for 0, 30, and 120 minutes at 37 °C. **Simulation parameters:** see Table D-2.

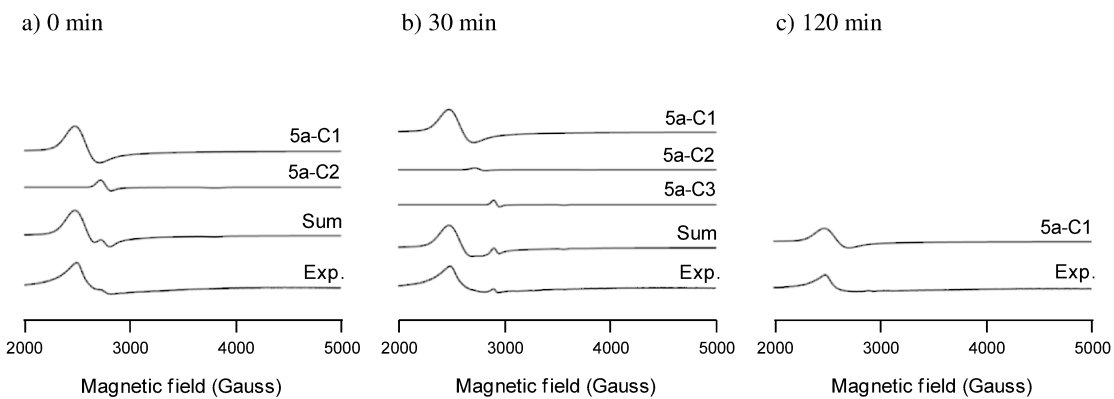


Figure D-14 (a-c) Simulation of EPR spectra of complex **5a** (3 mM) in PBS with 10% DMSO after incubation for 0, 30, and 120 minutes at 37 °C. **Simulation parameters:** see Table D-2.

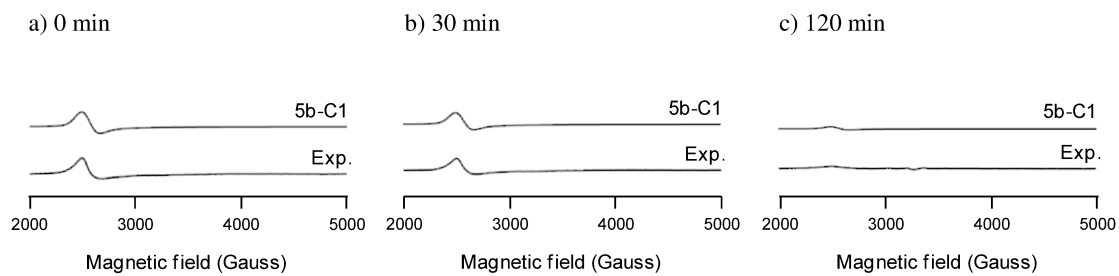


Figure S15 (a-c) Simulation of EPR spectra of complex **5b** (3 mM) in PBS with 10% DMSO after incubation for 0, 30, and 120 minutes at 37 °C. **Simulation parameters:** see Table D-2.

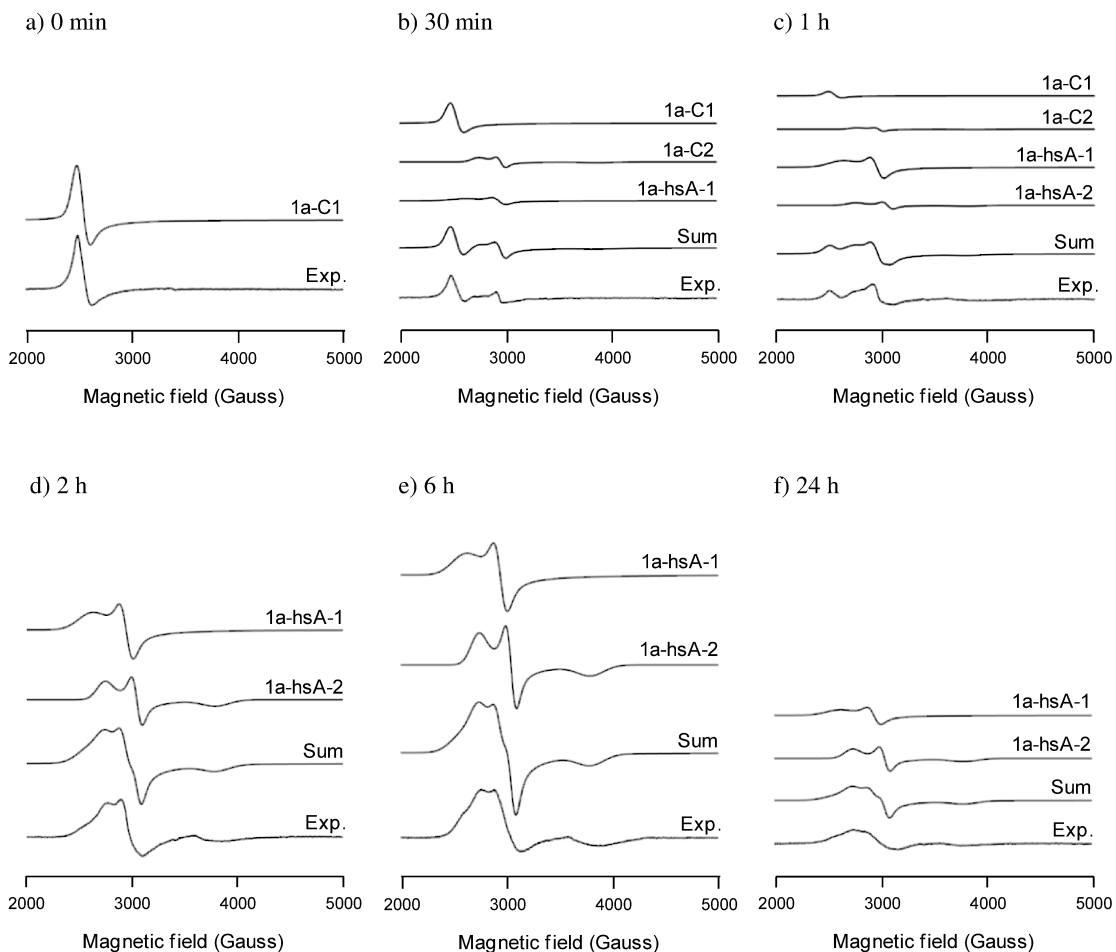


Figure D-16 (a-f) Simulation of EPR spectra of complex **1a** (1 mM) with hsA (0.5 mM) in PBS after incubation for 0 minutes to 24 hours at 37 °C.
Simulation parameters: see Table D-1.

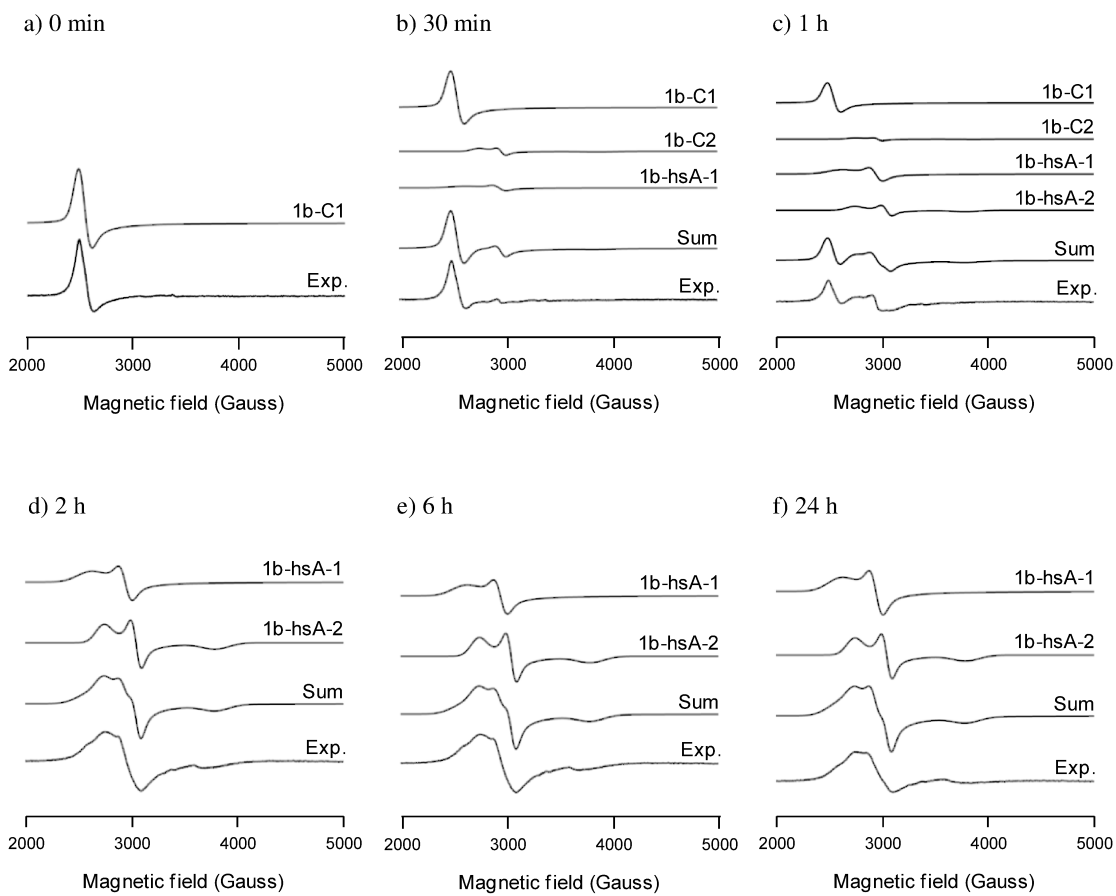


Figure D-17 (a-f) Simulation of EPR spectra of complex **1b** (1 mM) with hsA (0.5 mM) in PBS after incubation for 0 minutes to 24 hours at 37 °C.
Simulation parameters: see **Table D-1.**

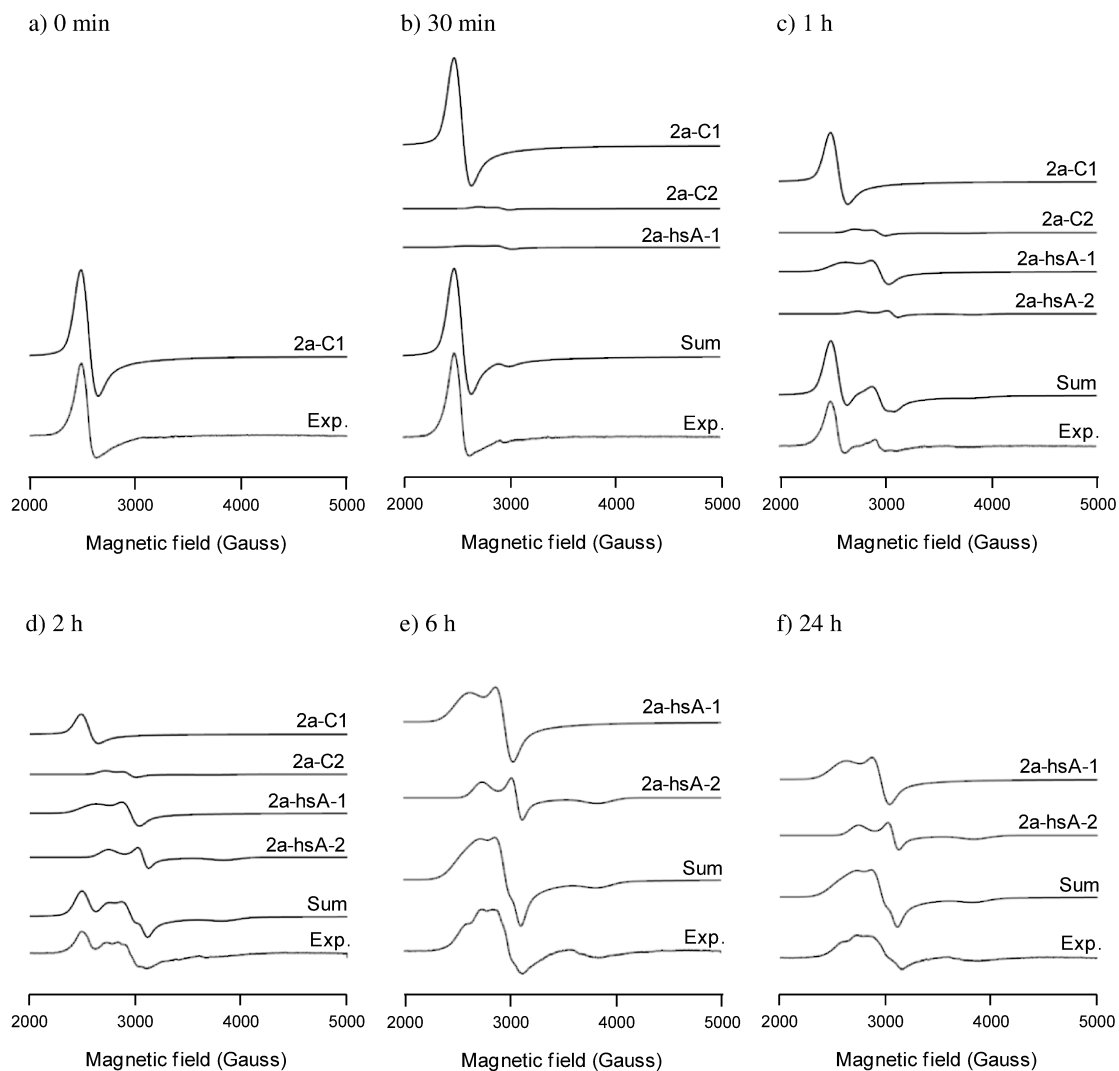


Figure D-18 (a-f) Simulation of EPR spectra of complex **2a** (1 mM) with hsA (0.5 mM) in PBS after incubation for 0 minutes to 24 hours at 37 °C.
Simulation parameters: see Table D-1.

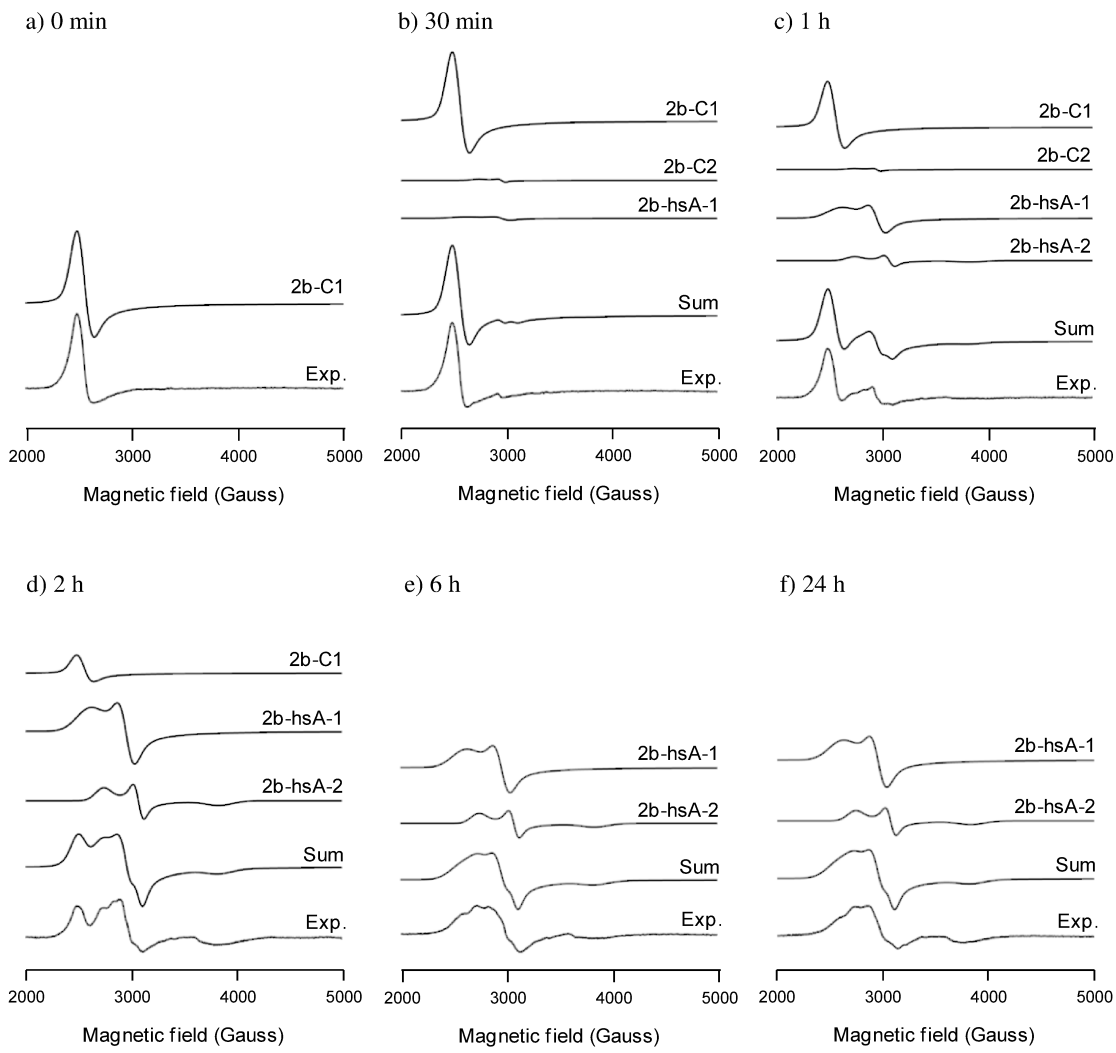


Figure D-19 (a-f) Simulation of EPR spectra of complex **2b** (1 mM) with hsA (0.5 mM) in PBS after incubation for 0 minutes to 24 hours at 37 °C.
Simulation parameters: see **Table D-1.**

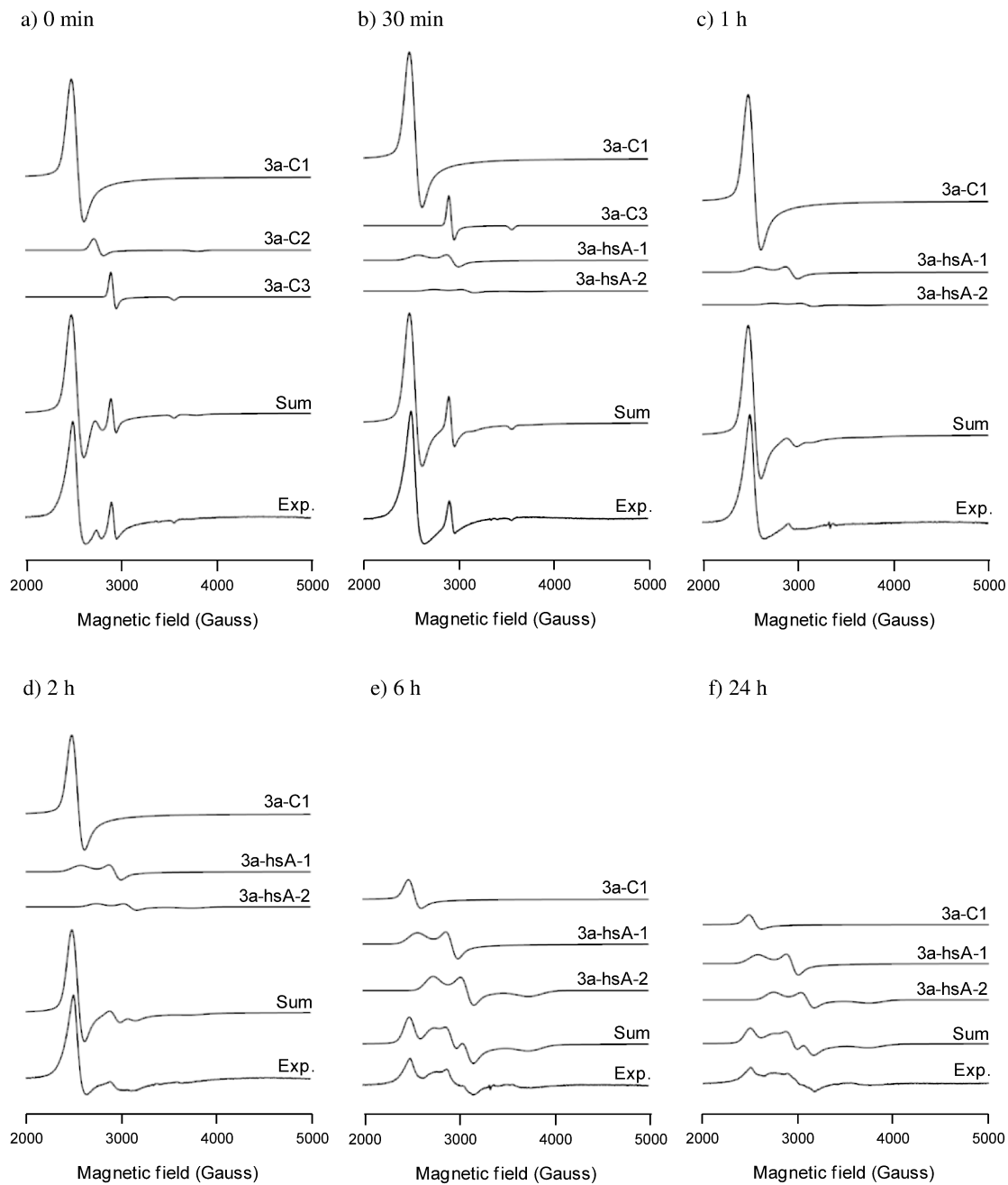


Figure D-20 (a-f) Simulation of EPR spectra of complex **3a** (1 mM) with hsA (0.5 mM) in PBS with 4% DMSO after incubation for 0 minutes to 24 hours at 37 °C. **Simulation parameters:** see **Table D-1**.

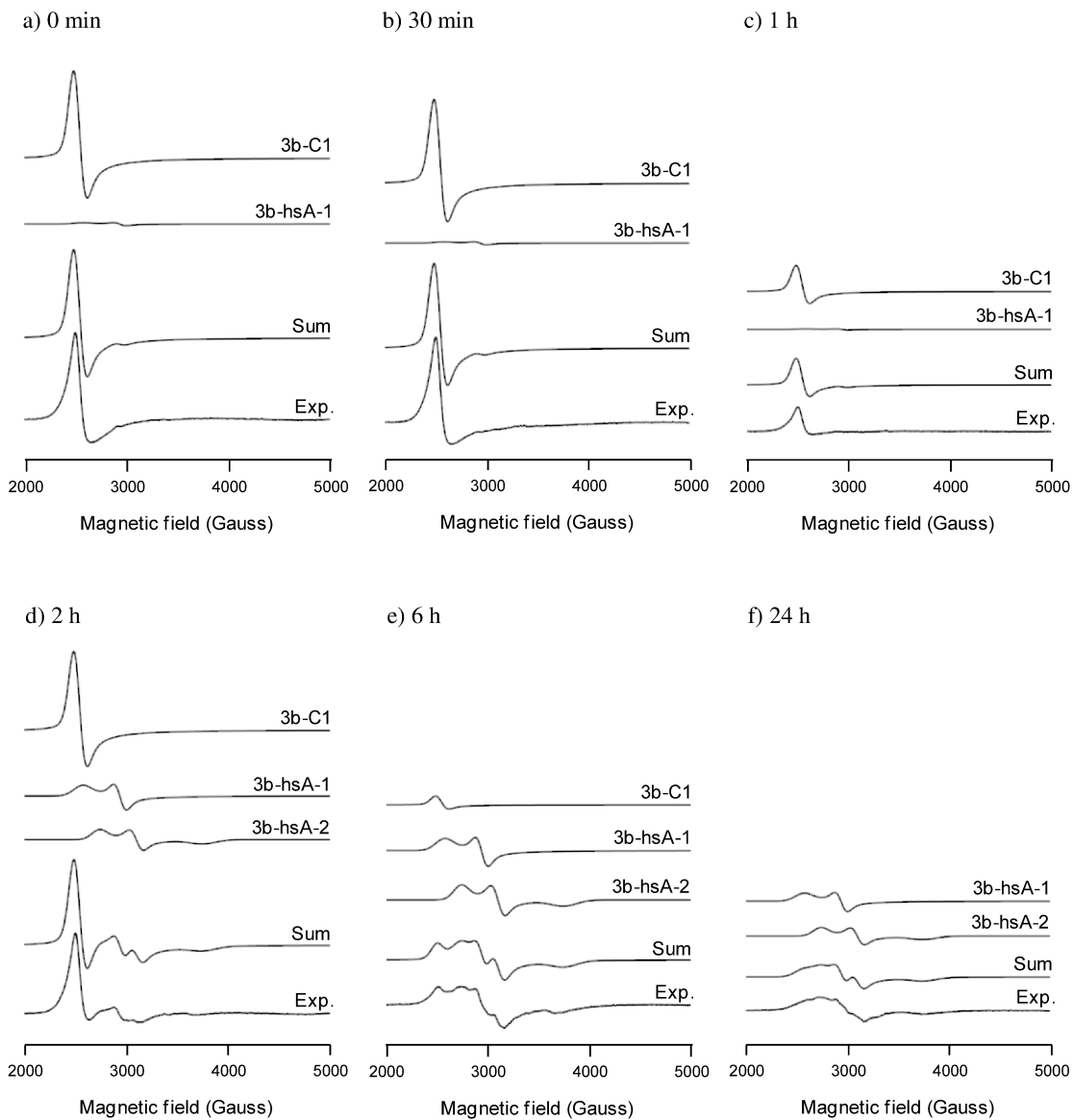


Figure D-21 (a-f) Simulation of EPR spectra of complex **3b** (1 mM) with hsA (0.5 mM) in PBS with 4% DMSO after incubation for 0 minutes to 24 hours at 37 °C. **Simulation parameters:** see Table D-1.

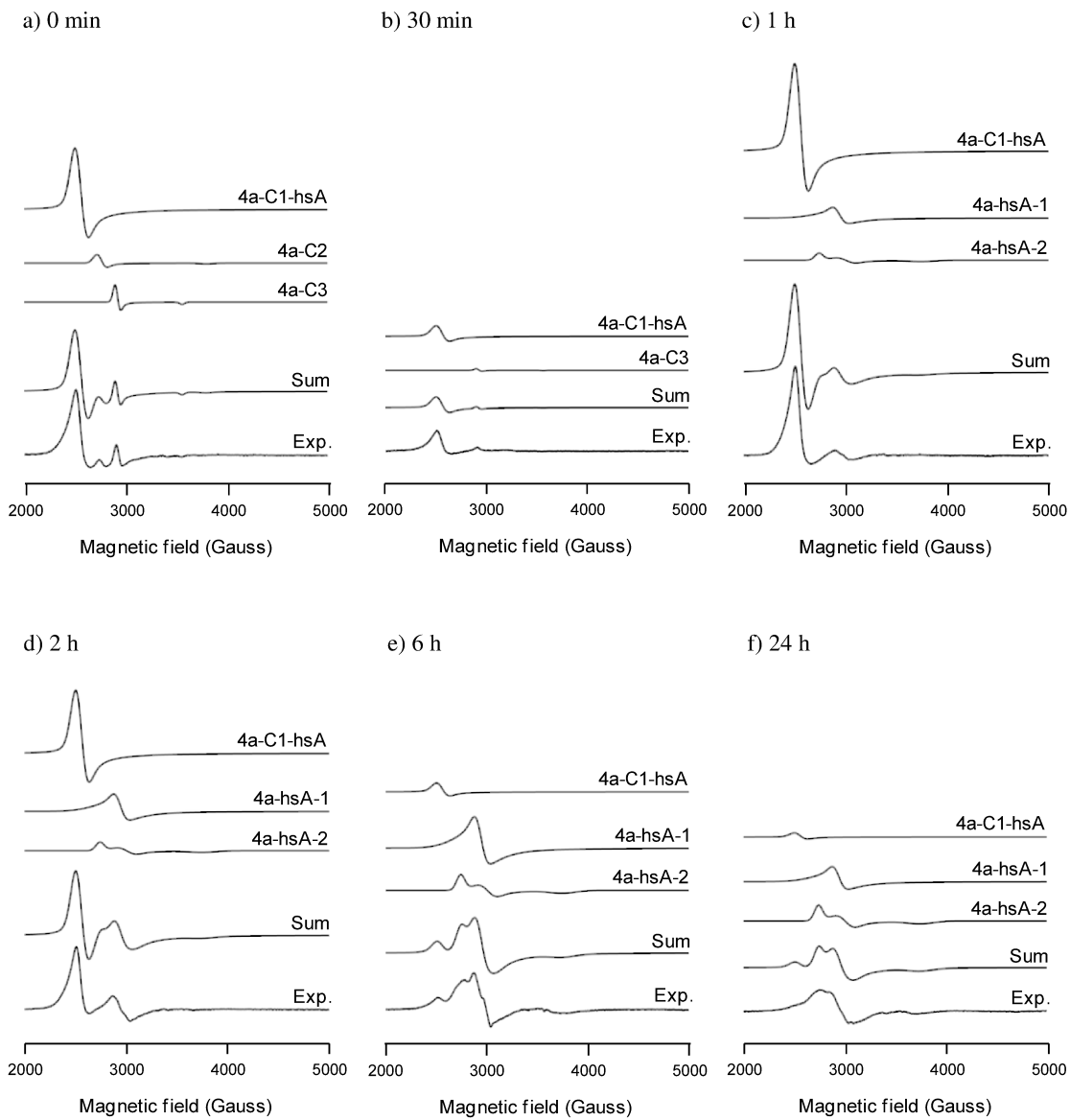


Figure D-22 (a-f) Simulation of EPR spectra of complex **4a** (1 mM) with hsA (0.5 mM) in PBS with 4% DMSO after incubation for 0 minutes to 24 hours at 37 °C. **Simulation parameters:** see Table D-2.

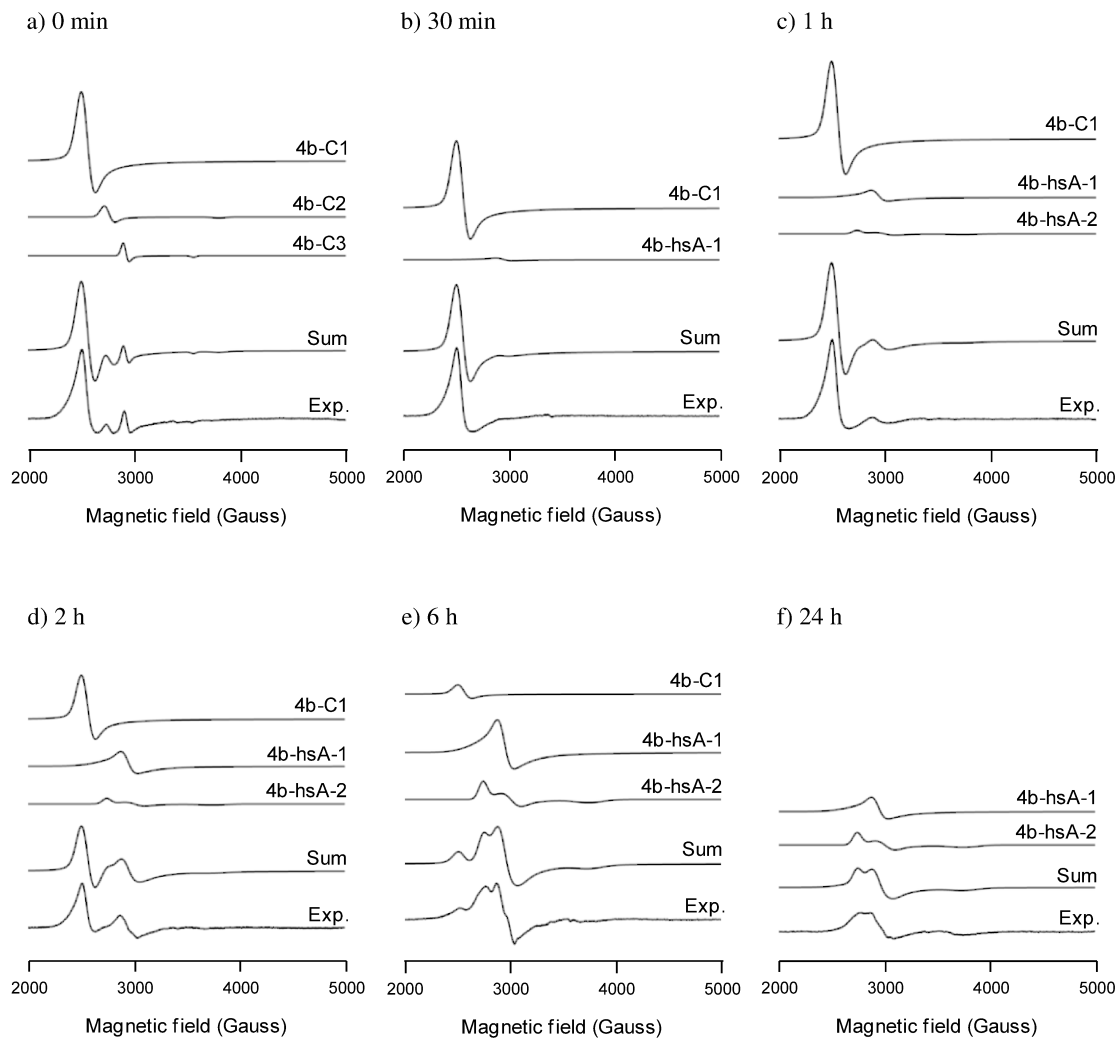


Figure D-23 (a-f) Simulation of EPR spectra of complex **4b** (1 mM) with hsA (0.5 mM) in PBS with 4% DMSO after incubation for 0 minutes to 24 hours at 37 °C. **Simulation parameters:** see Table D-2.

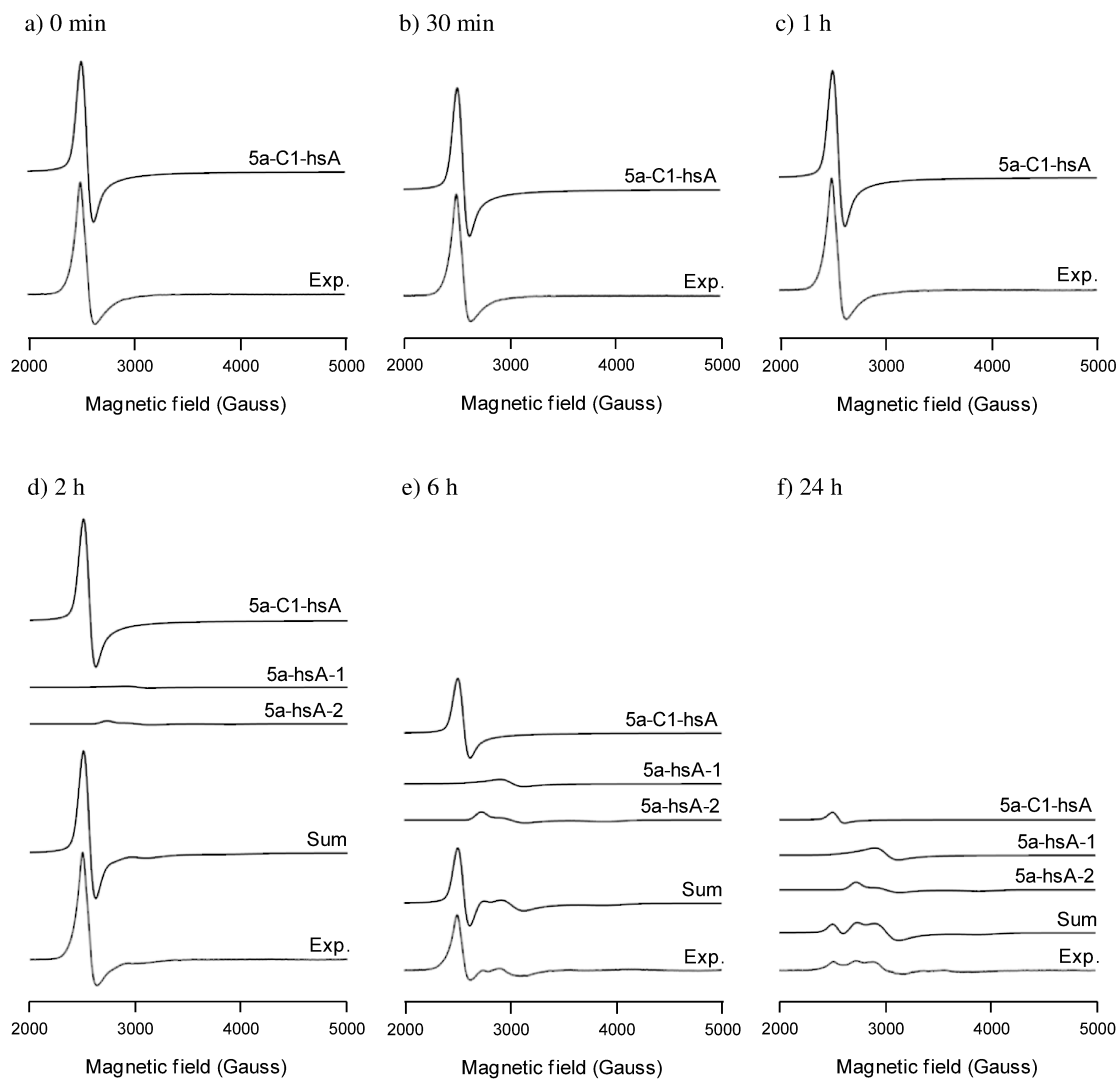


Figure D-24 (a-f) Simulation of EPR spectra of complex **5a** (1 mM) with hsA (0.5 mM) in PBS with 4% DMSO after incubation for 0 minutes to 24 hours at 37 °C. **Simulation parameters:** see Table D-2.

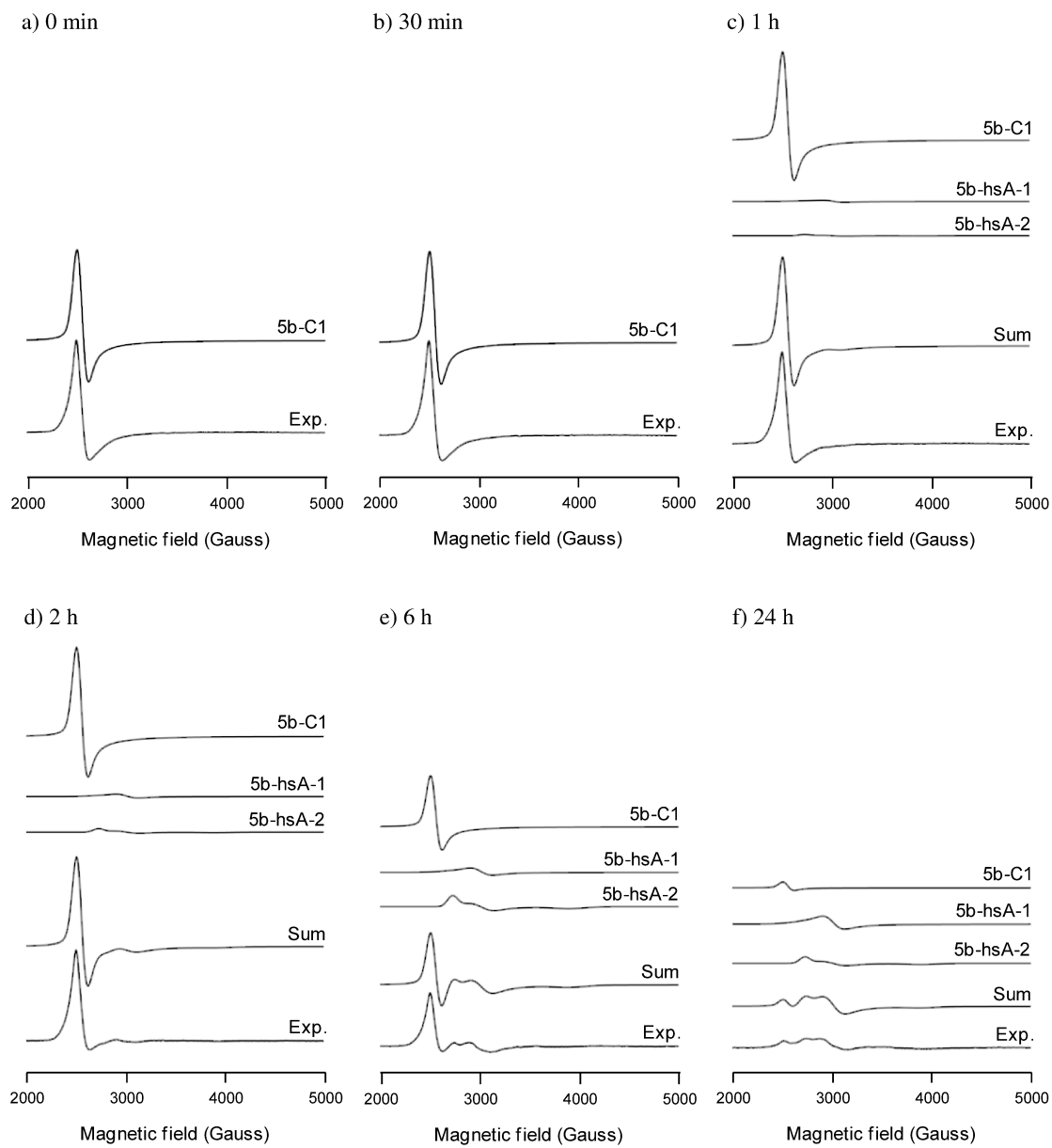


Figure D-25 (a-f) Simulation of EPR spectra of complex **5b** (1 mM) with hsA (0.5 mM) in PBS with 4% DMSO after incubation for 0 minutes to 24 hours at 37 °C. **Simulation parameters:** see Table D-2.

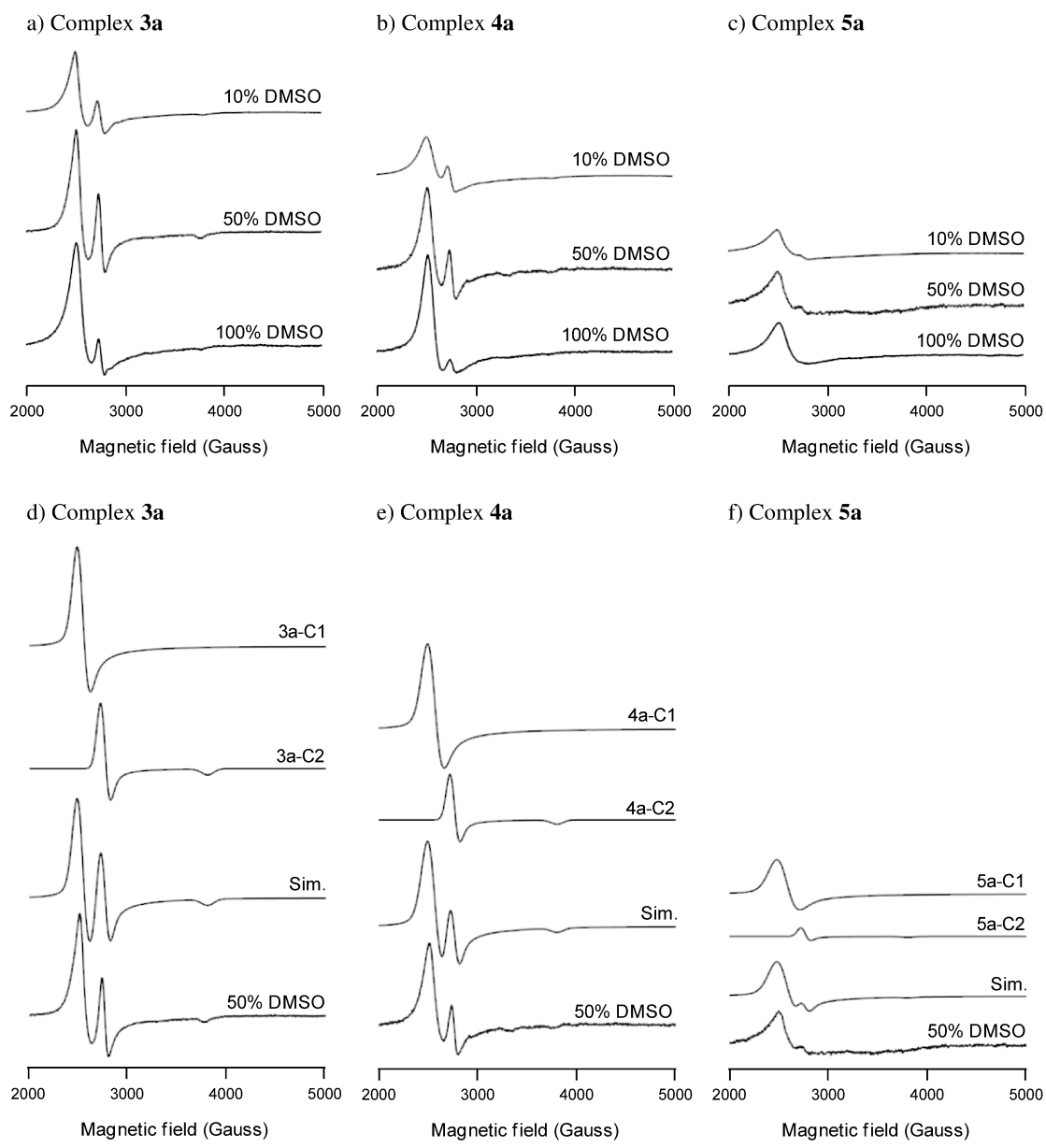


Figure D-26 (a-f) EPR spectra of complexes: a) **3a**, b) **4a**, and c) **5a** (1 mM) in PBS with increasing amounts of DMSO after incubation for 120 minutes at 37 °C, (d-e) – Simulation of the EPR spectrum for each complex with 50% DMSO after incubation for 120 minutes at 37 °C. **Simulation parameters:** see **Table D-2**.

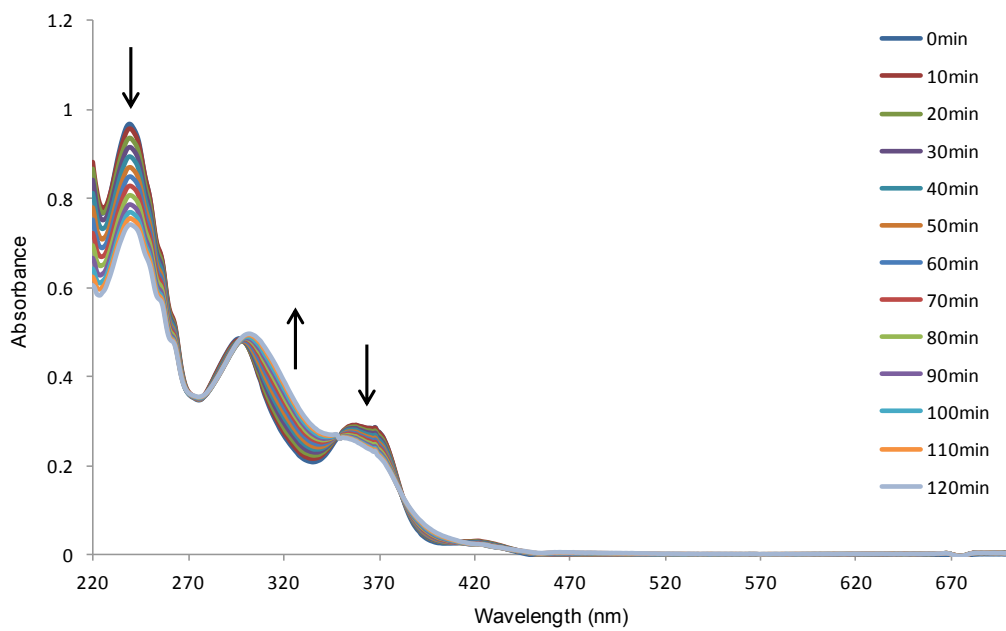


Figure D-27 UV-Vis spectrum of complex **1a** (200 μ M) in PBS pH 7.4 solution at 37 °C for two hours.

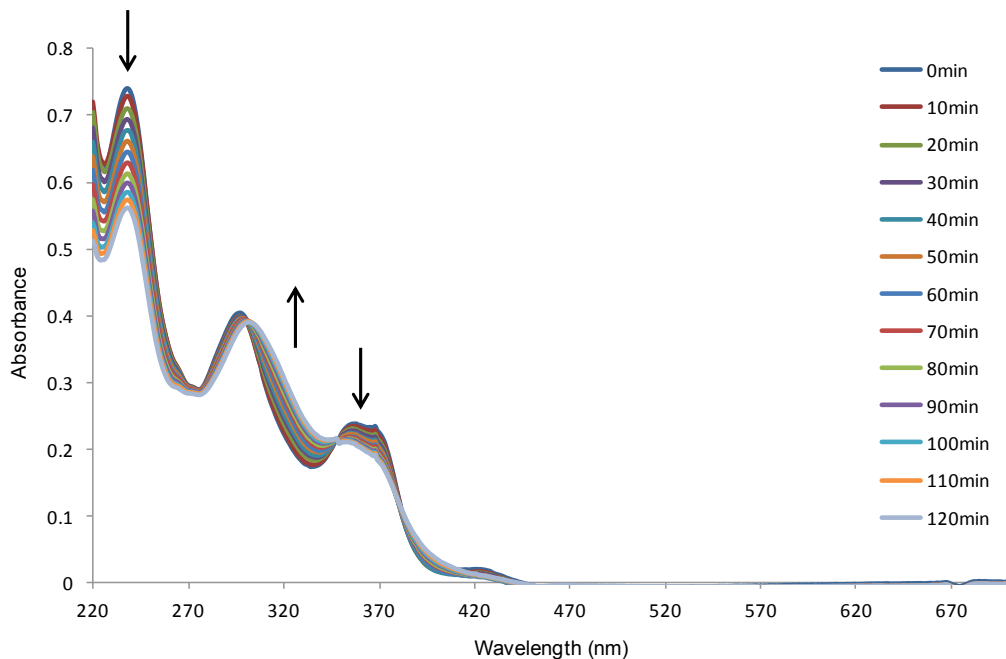


Figure D-28 UV-Vis spectrum of complex **1b** (200 μ M) in PBS pH 7.4 solution at 37 °C for two hours.

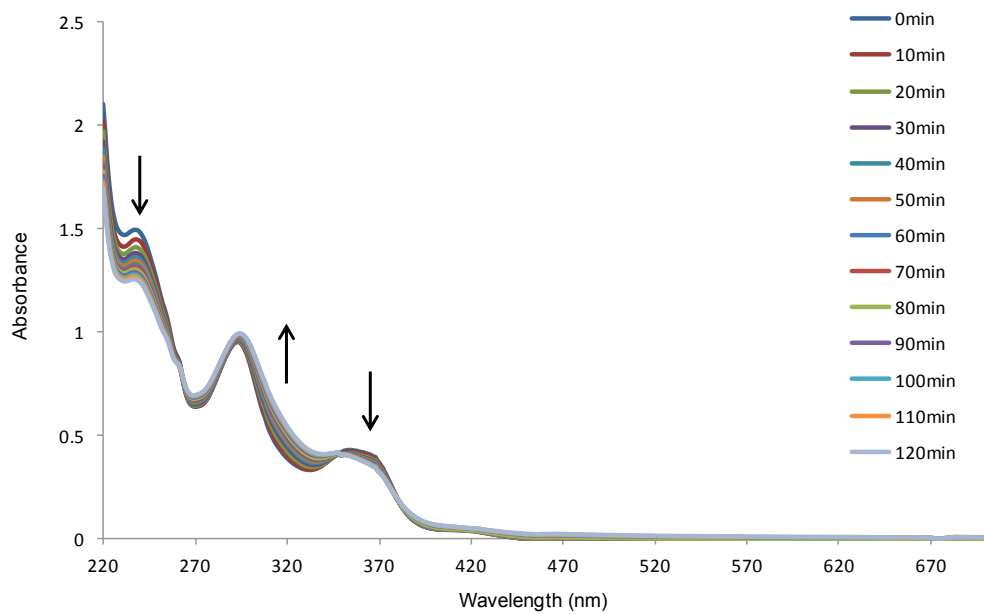


Figure D-29 UV-Vis spectrum of complex **2a** (200 μ M) in PBS pH 7.4 solution at 37 °C for two hours.

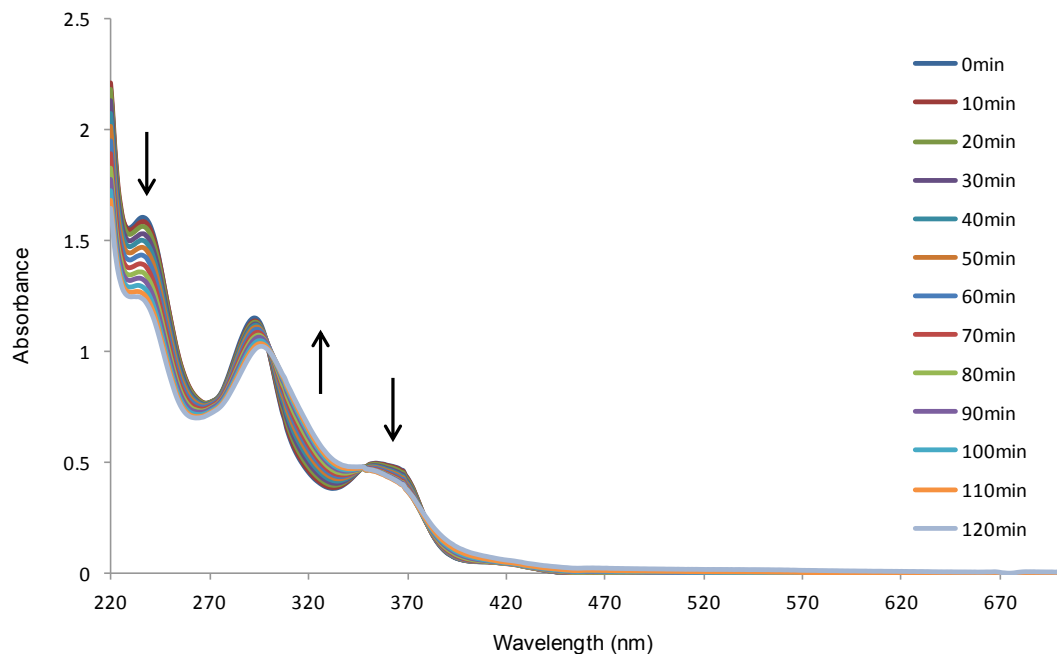


Figure D-30 UV-Vis spectrum of complex **2b** (200 μ M) in PBS pH 7.4 solution at 37 °C for two hours.

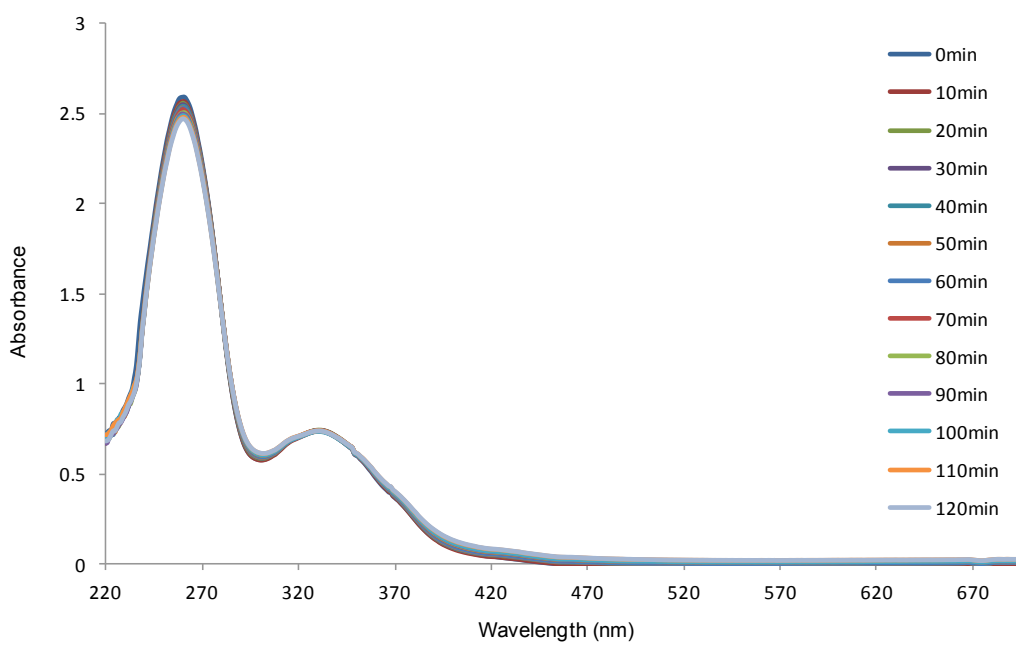


Figure D-31 UV-Vis spectrum of complex **3a** (200 μ M) in PBS pH 7.4 solution, 10% DMSO at 37 °C for two hours.

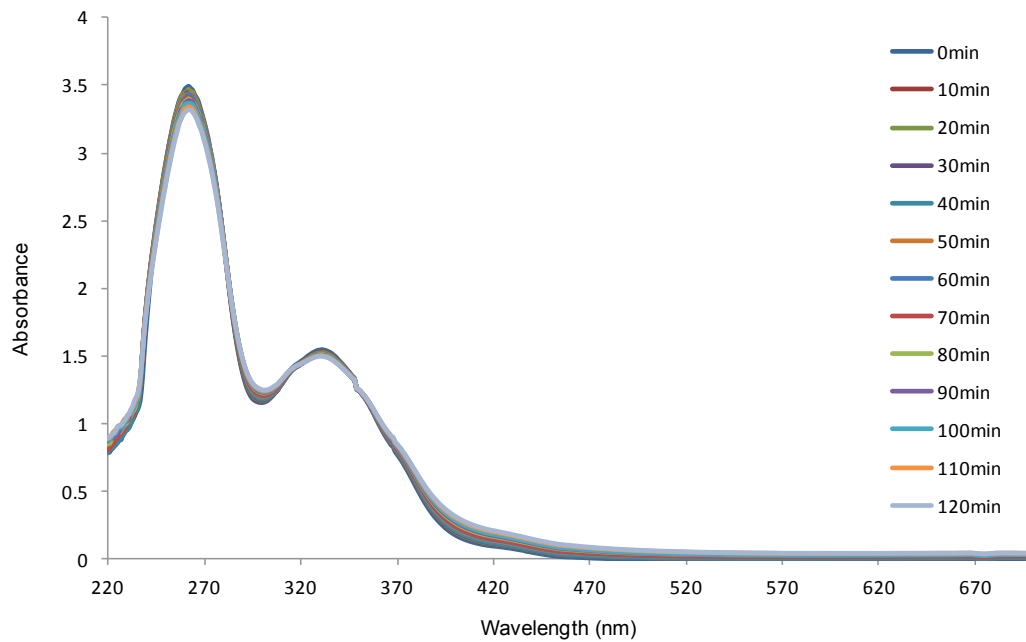


Figure D-32 UV-Vis spectrum of complex **3b** (200 μ M) in PBS pH 7.4 solution, 10% DMSO at 37 °C for two hours.

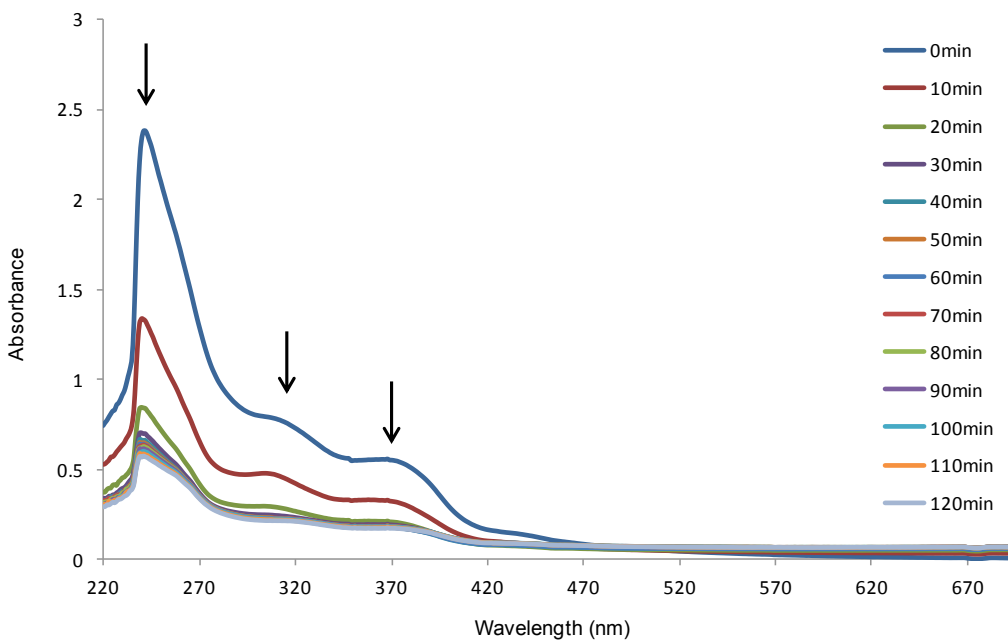


Figure D-33 UV-Vis spectrum of complex **4a** (200 μ M) in PBS pH 7.4 solution, 10% DMSO at 37 °C for two hours.

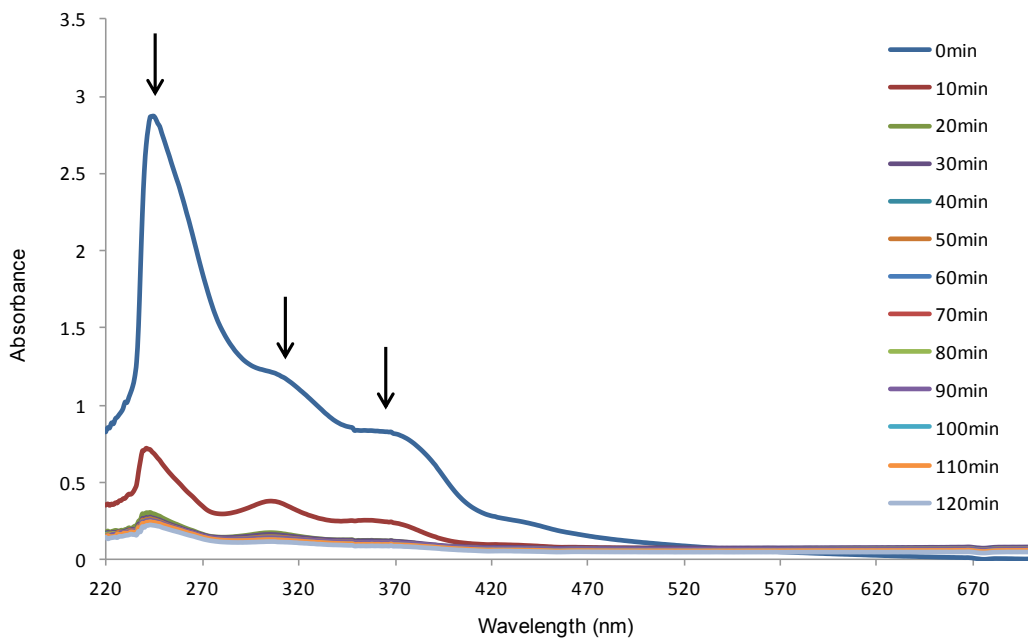


Figure D-34 UV-Vis spectrum of complex **4b** (200 μ M) in PBS pH 7.4 solution, 10% DMSO at 37 °C for two hours.

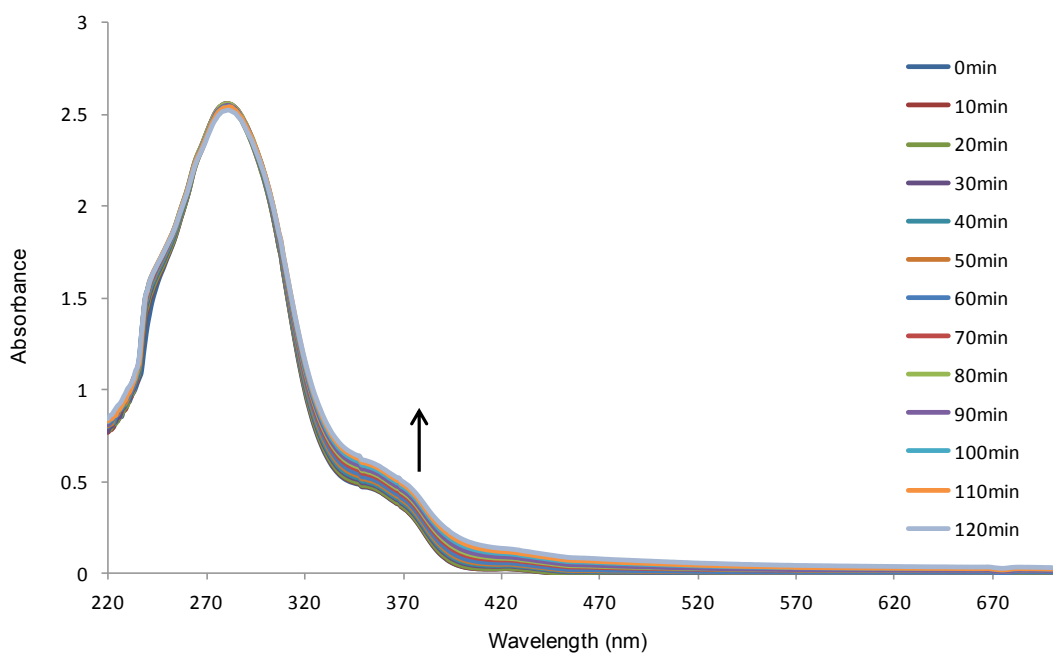


Figure D-35 UV-Vis spectrum of complex **5a** (200 μ M) in PBS pH 7.4 solution, 10% DMSO at 37 °C for two hours.

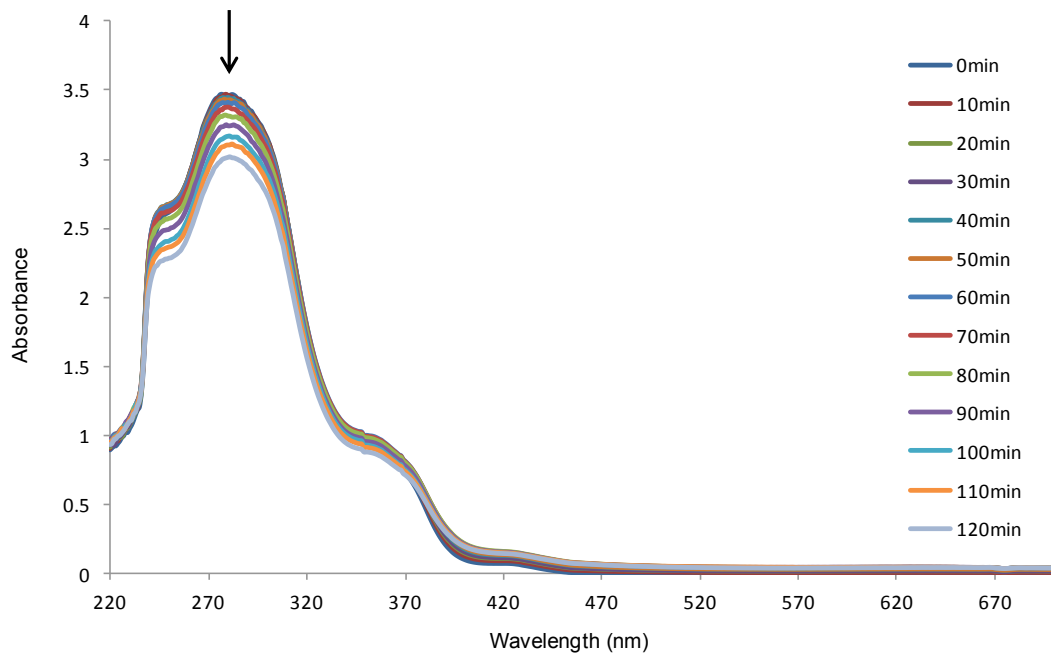


Figure D-36 UV-Vis spectrum of complex **5b** (200 μ M) in PBS pH 7.4 solution, 10% DMSO at 37 °C for two hours.

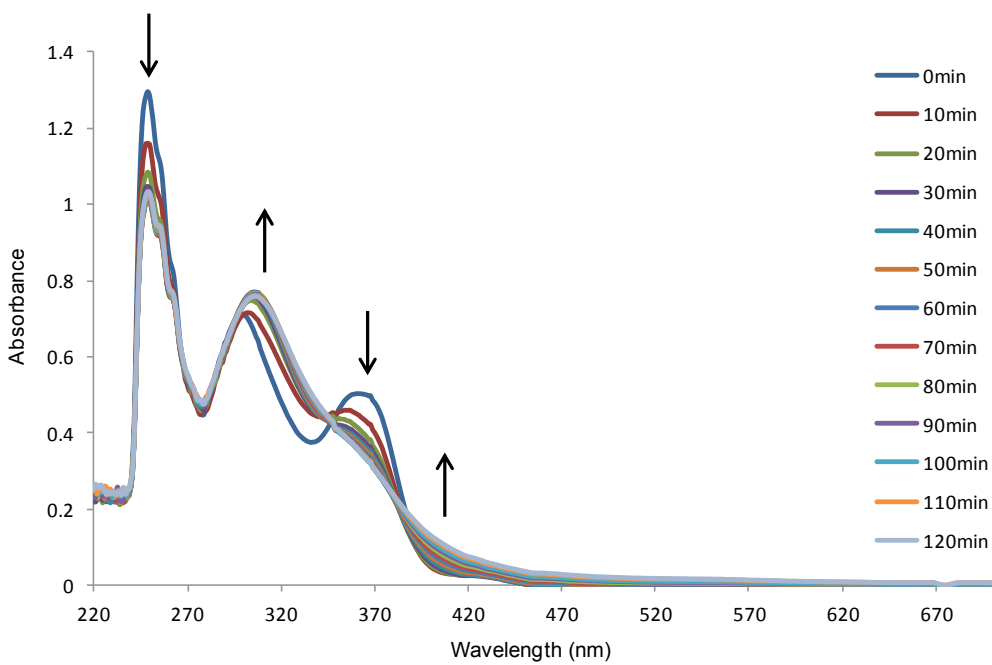


Figure D-37 UV-Vis spectrum of complex **1a** (200 μ M) with human serum albumin (100 μ M) in PBS pH 7.4 solution at 37 °C for two hours.

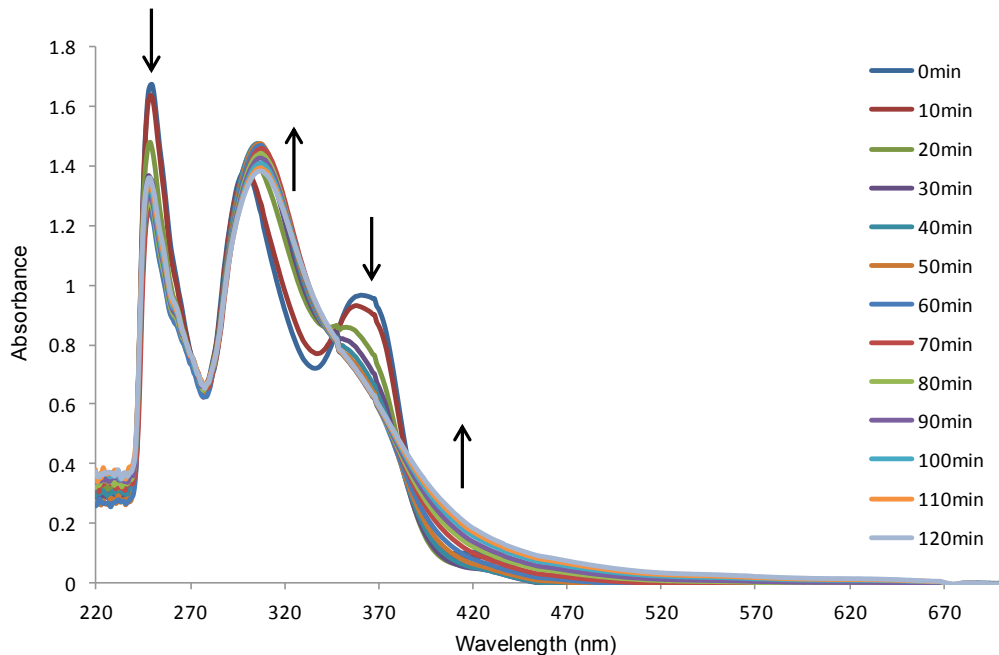


Figure D-38 UV-Vis spectrum of complex **1b** (200 μ M) with human serum albumin (100 μ M) in PBS pH 7.4 solution at 37 °C for two hours.

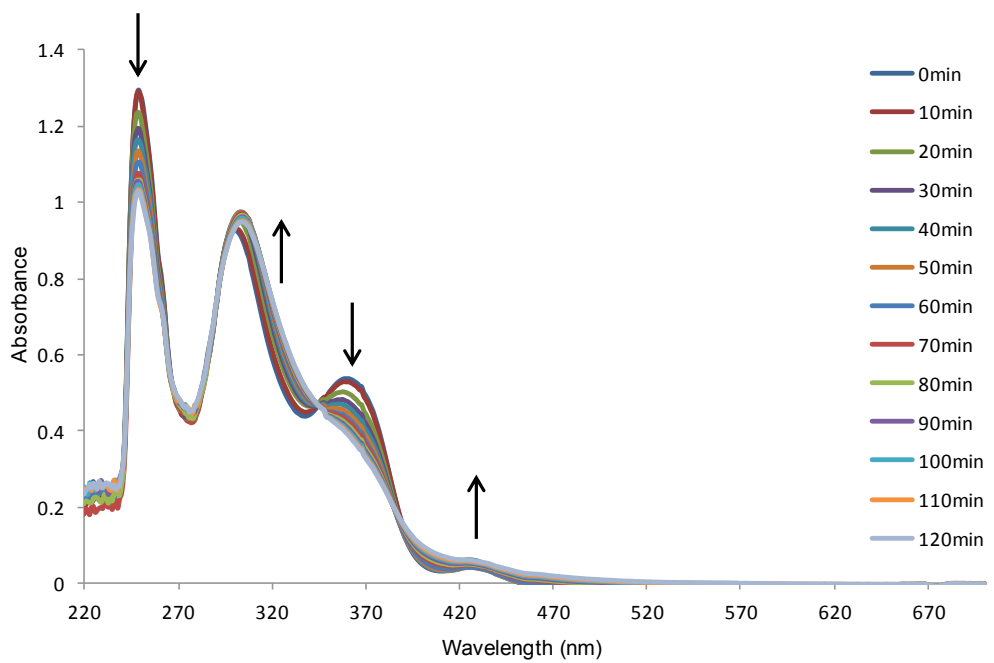


Figure D-39 UV-Vis spectrum of complex **2a** (200 μ M) with human serum albumin (100 μ M) in PBS pH 7.4 solution at 37 °C for two hours.

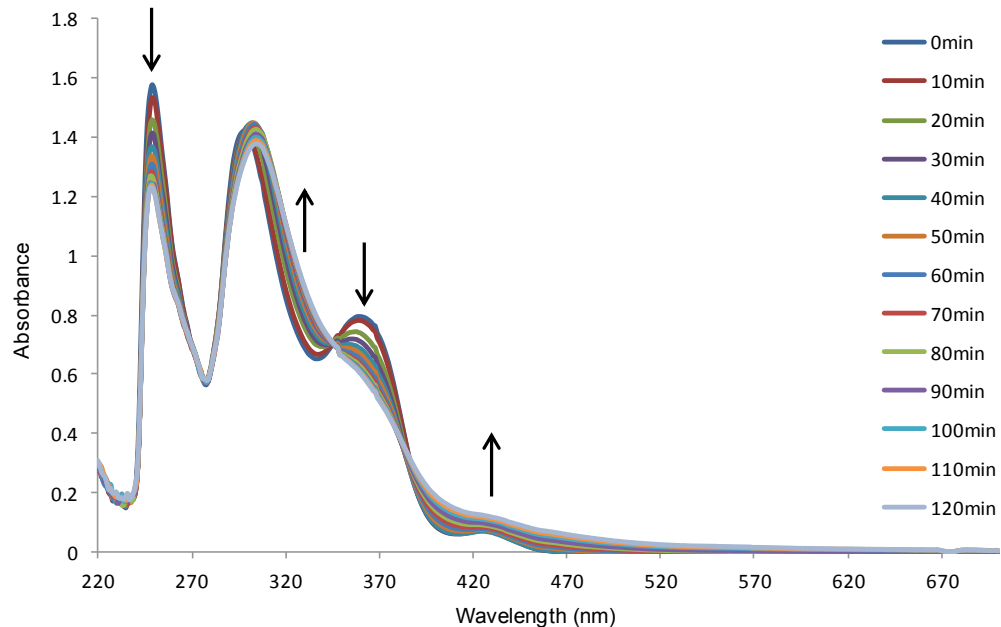


Figure D-40 UV-Vis spectrum of complex **2b** (200 μ M) with human serum albumin (100 μ M) in PBS pH 7.4 solution at 37 °C for two hours.

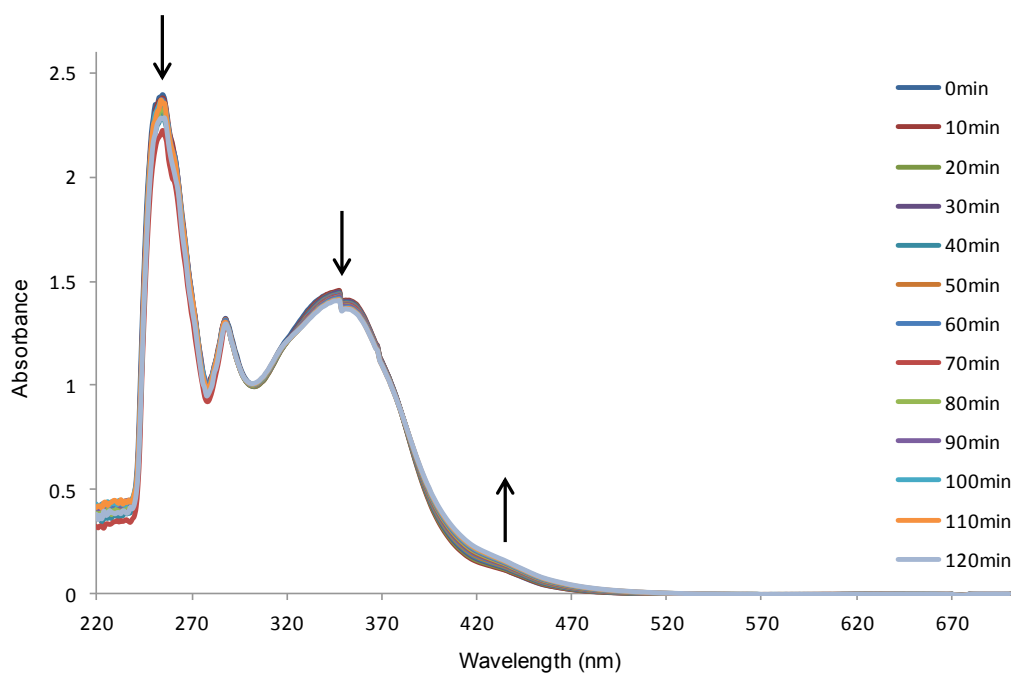


Figure D-41 UV-Vis spectrum of complex **3a** (200 μ M) with human serum albumin (100 μ M) in PBS pH 7.4 solution, 4% DMSO at 37 °C for two hours.

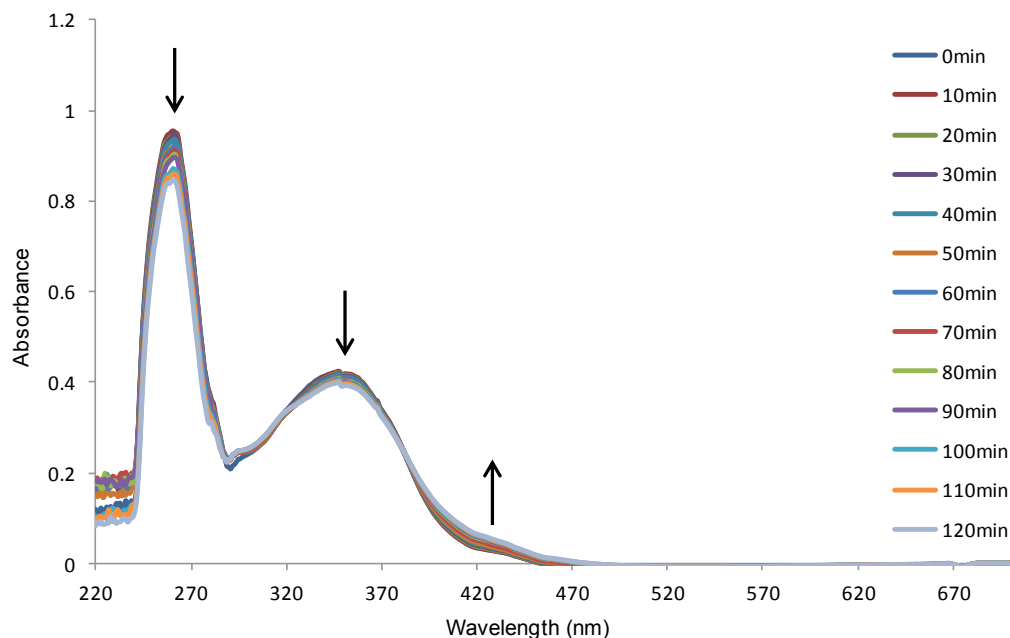


Figure D-42 UV-Vis spectrum of complex **3b** (200 μ M) with human serum albumin (100 μ M) in PBS pH 7.4 solution, 4% DMSO at 37 °C for two hours.

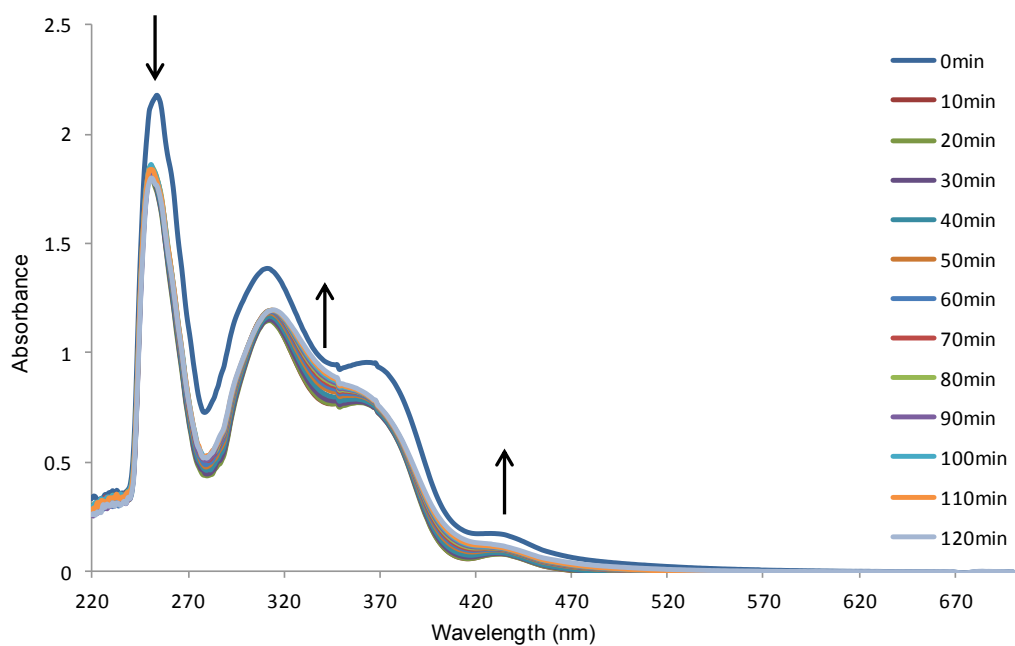


Figure D-43 UV-Vis spectrum of complex **4a** (200 μ M) with human serum albumin (100 μ M) in PBS pH 7.4 solution, 4% DMSO at 37 °C for two hours.

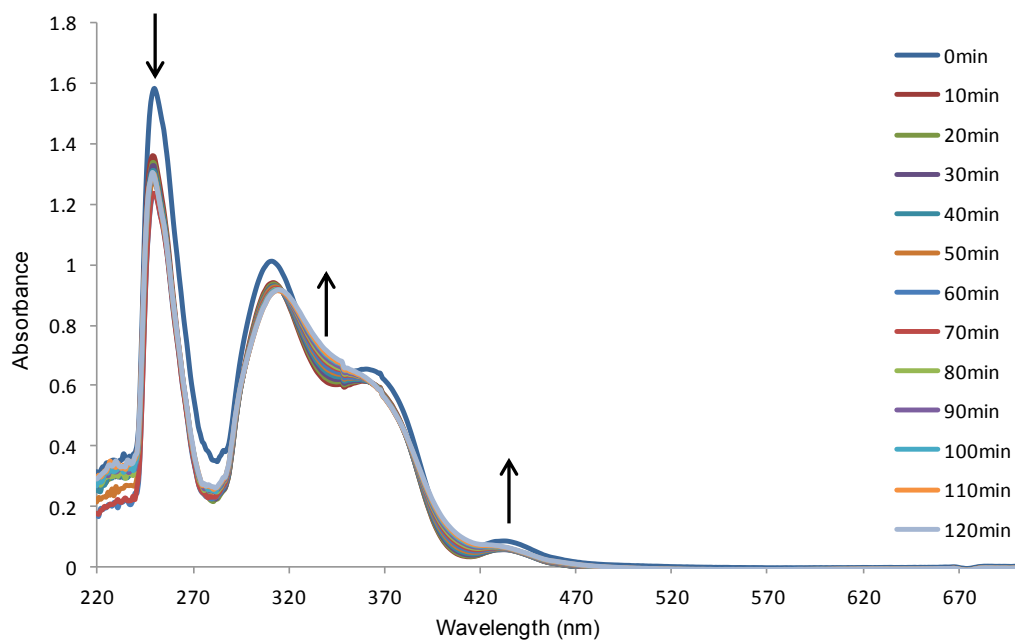


Figure D-44 UV-Vis spectrum of complex **4b** (200 μ M) with human serum albumin (100 μ M) in PBS pH 7.4 solution, 4% DMSO at 37 °C for two hours.

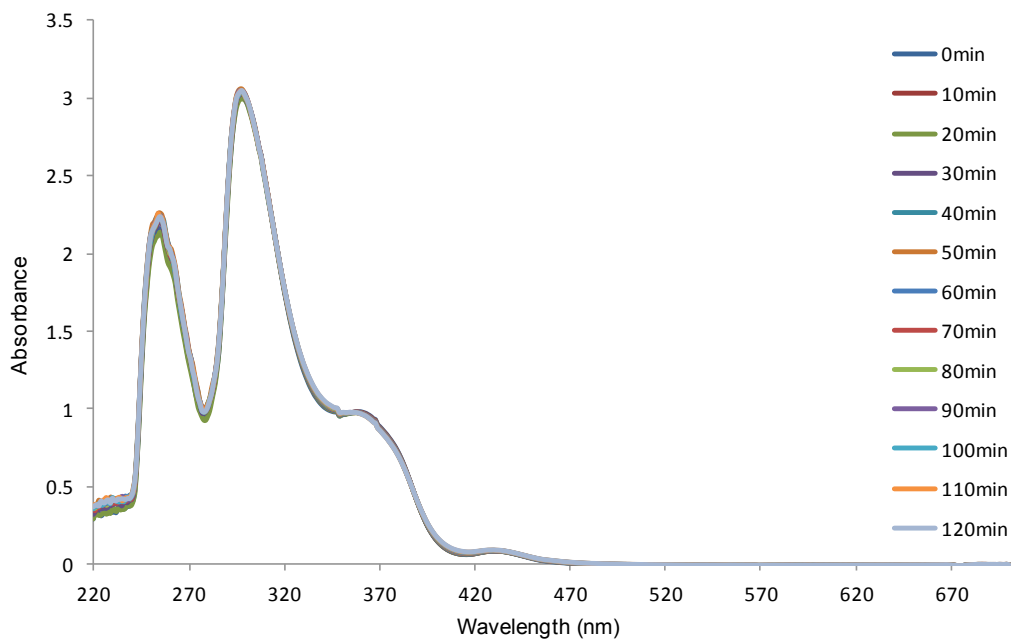


Figure D-45 UV-Vis spectrum of complex **5a** (200 μ M) with human serum albumin (100 μ M) in PBS pH 7.4 solution, 4% DMSO at 37 °C for two hours.

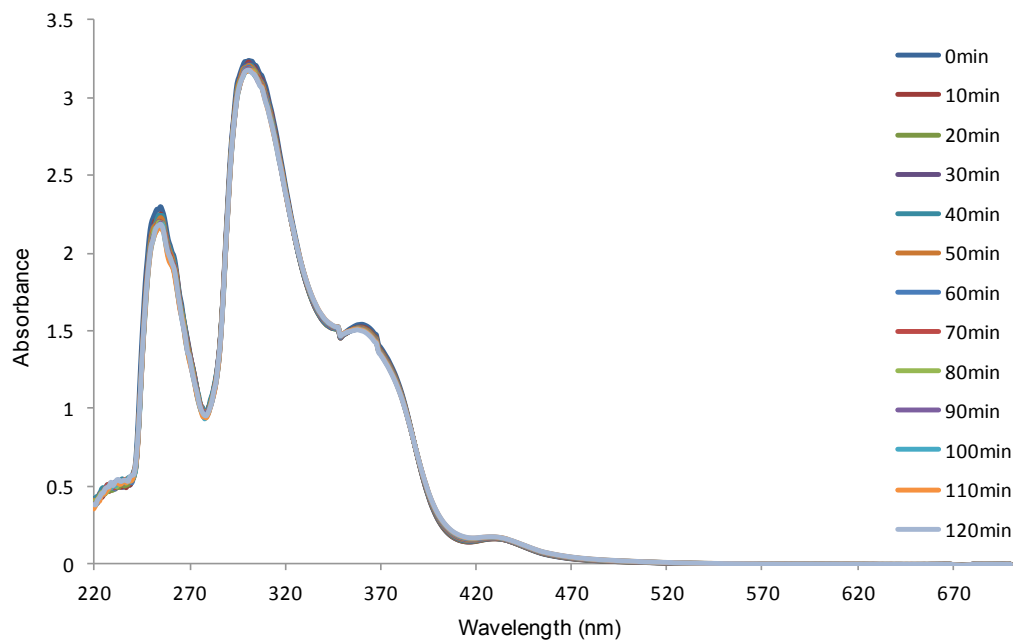


Figure D-46 UV-Vis spectrum of complex **5b** (200 μ M) with human serum albumin (100 μ M) in PBS pH 7.4 solution, 4% DMSO at 37 °C for two hours.

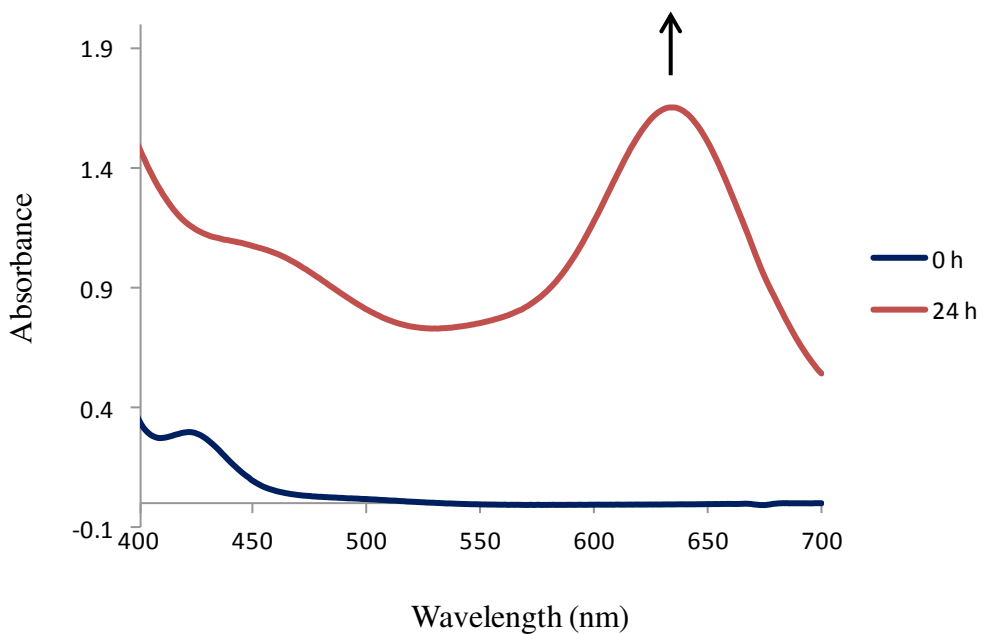


Figure D-47 UV-Vis spectrum of complex **1a** ($200 \mu\text{M}$) with human serum albumin ($100 \mu\text{M}$) in PBS pH 7.4 solution at 37°C for twenty-four hours.

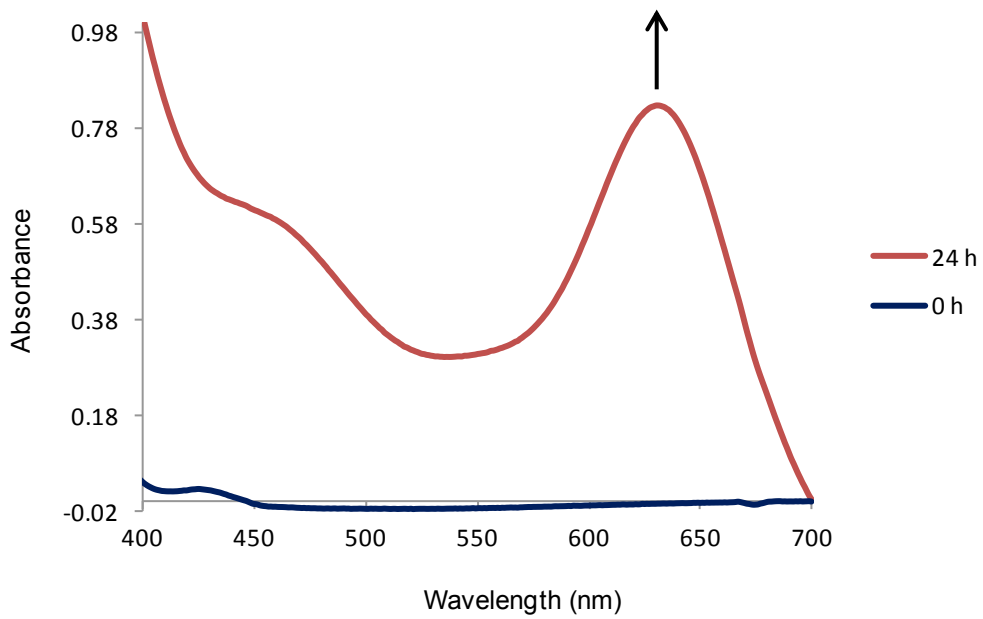


Figure D-48 UV-Vis spectrum of complex **1b** ($400 \mu\text{M}$) with human serum albumin ($100 \mu\text{M}$) in PBS pH 7.4 solution at 37°C for twenty-four hours.

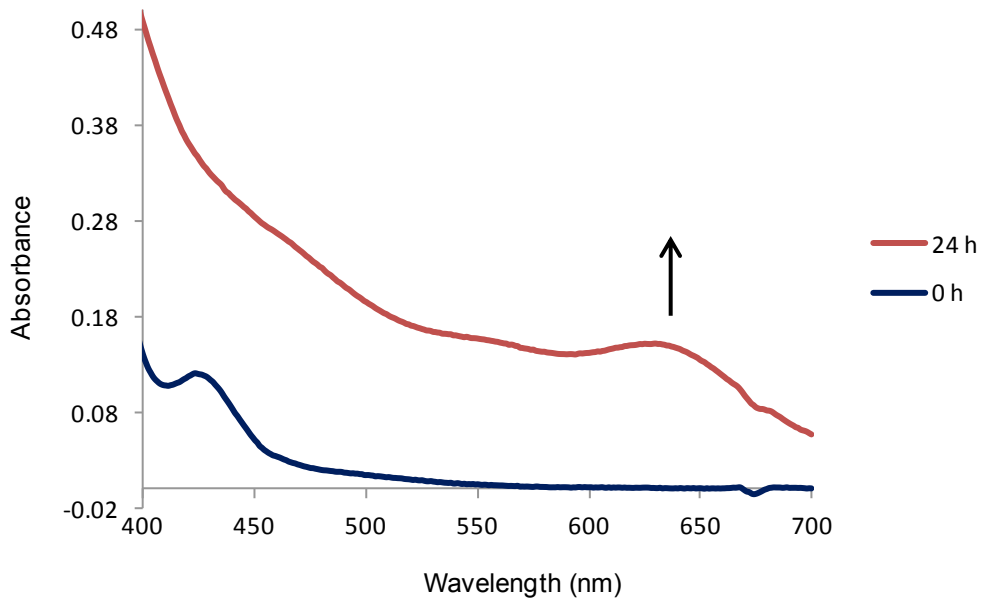


Figure D-49 UV-Vis spectrum of complex **2a** ($200 \mu\text{M}$) with human serum albumin ($100 \mu\text{M}$) in PBS pH 7.4 solution at 37°C for twenty-four hours.

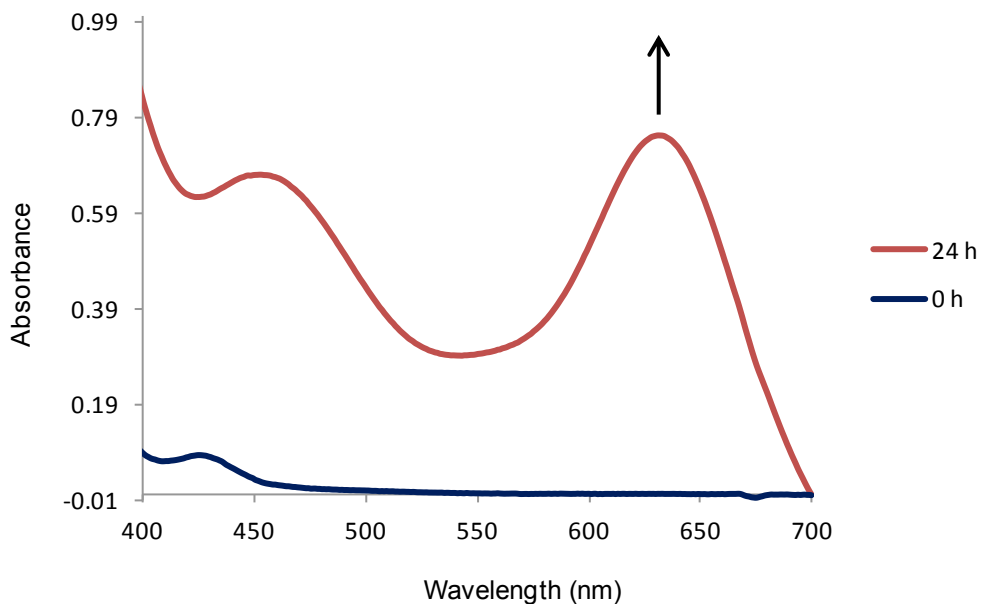


Figure D-50 UV-Vis spectrum of complex **2b** ($400 \mu\text{M}$) with human serum albumin ($100 \mu\text{M}$) in PBS pH 7.4 solution at 37°C for twenty-four hours.

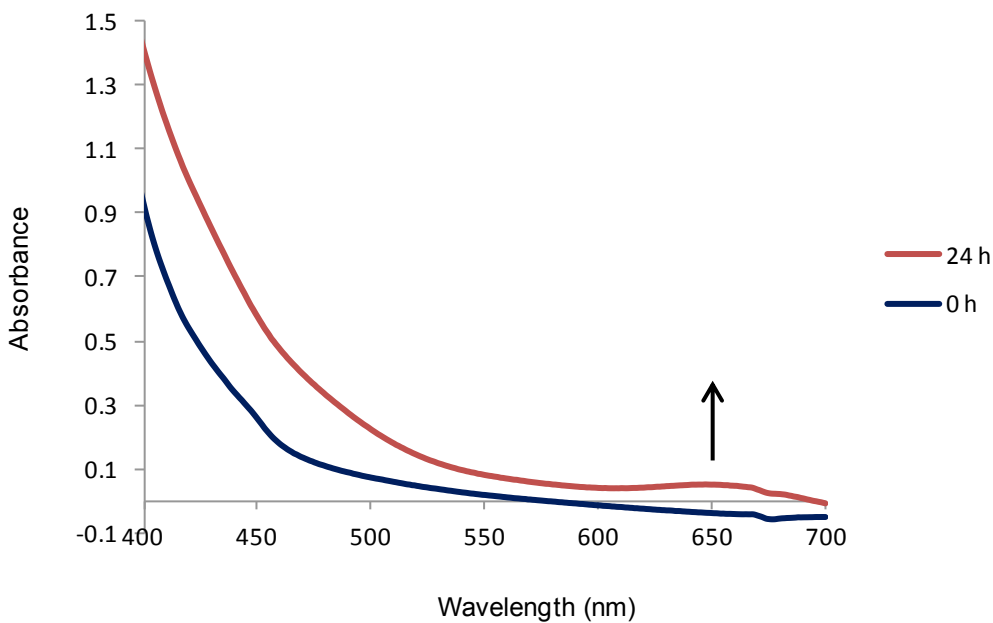


Figure D-51 UV-Vis spectrum of complex **3a** (400 μM) with human serum albumin (100 μM) in PBS pH 7.4 solution, 4% DMSO at 37 °C for twenty-four hours.

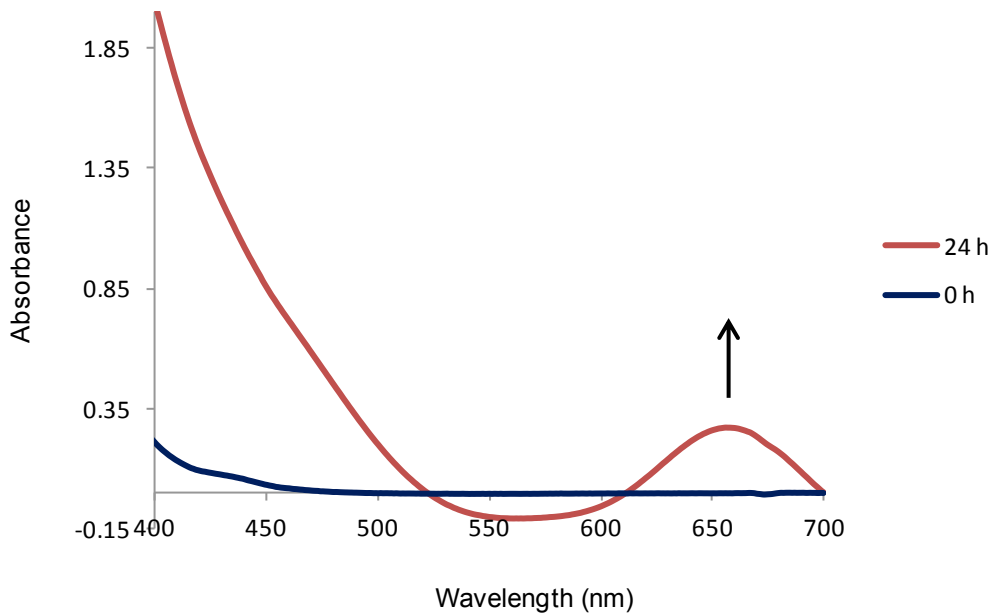


Figure D-52 UV-Vis spectrum of complex **3b** (400 μM) with human serum albumin (100 μM) in PBS pH 7.4 solution, 4% DMSO at 37 °C for twenty-four hours.

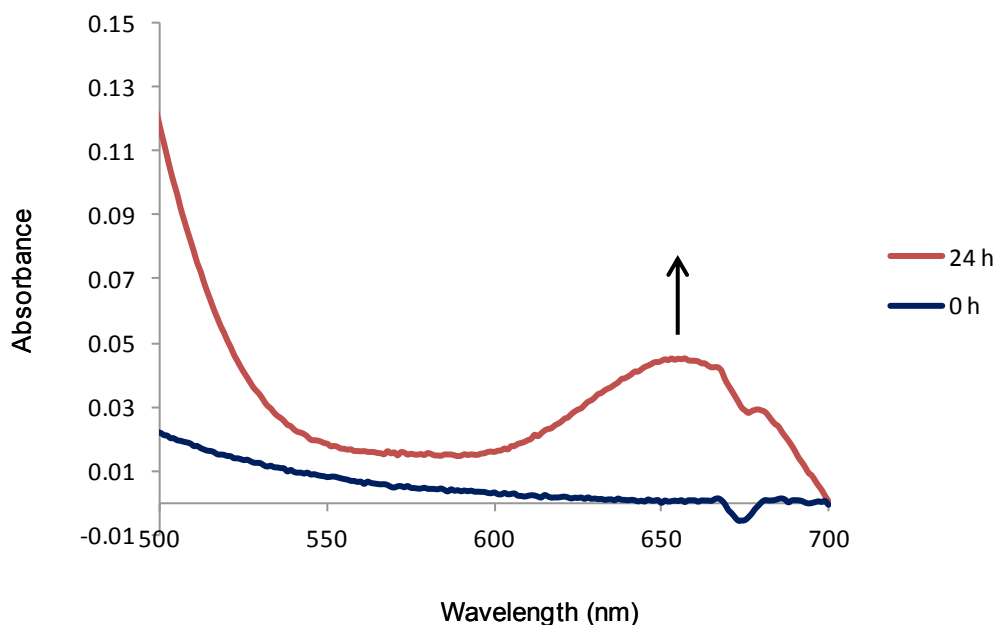


Figure D-53 UV-Vis spectrum of complex **4a** ($400 \mu\text{M}$) with human serum albumin ($100 \mu\text{M}$) in PBS pH 7.4 solution, 4% DMSO at 37°C for twenty-four hours.

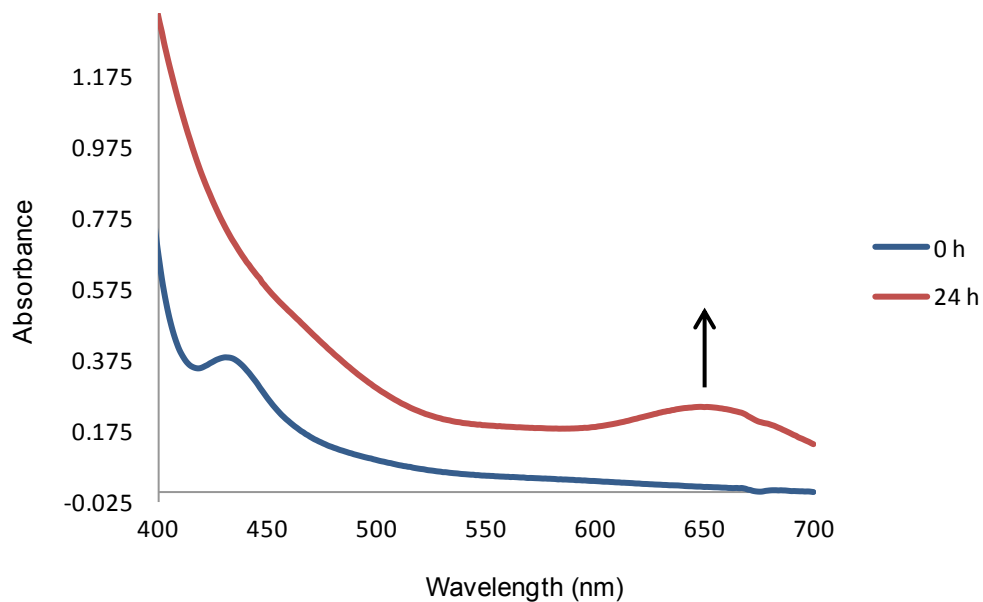


Figure D-54 UV-Vis spectrum of complex **4b** ($400 \mu\text{M}$) with human serum albumin ($100 \mu\text{M}$) in PBS pH 7.4 solution, 4% DMSO at 37°C for twenty-four hours.

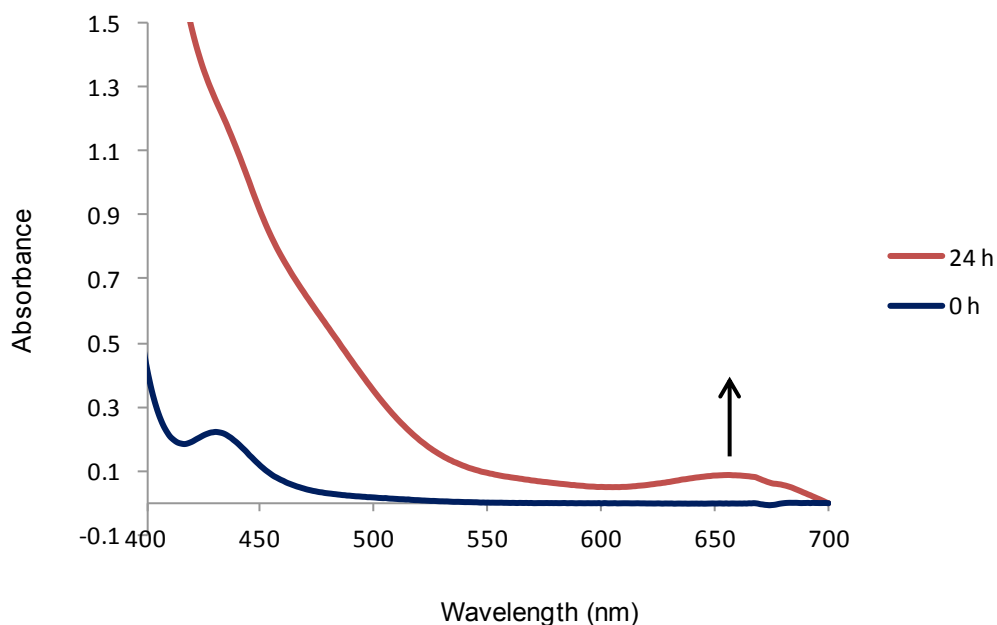


Figure D-55 UV-Vis spectrum of complex **5a** ($400 \mu\text{M}$) with human serum albumin ($100 \mu\text{M}$) in PBS pH 7.4 solution, 4% DMSO at 37°C for twenty-four hours.

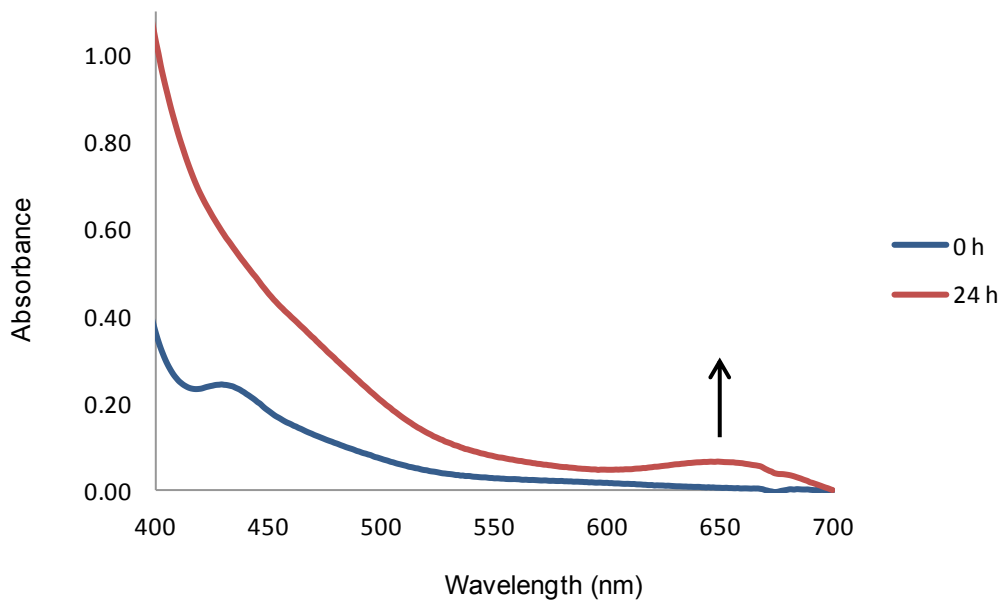


Figure D-56 UV-Vis spectrum of complex **5b** ($400 \mu\text{M}$) with human serum albumin ($100 \mu\text{M}$) in PBS pH 7.4 solution, 4% DMSO at 37°C for twenty-four hours.

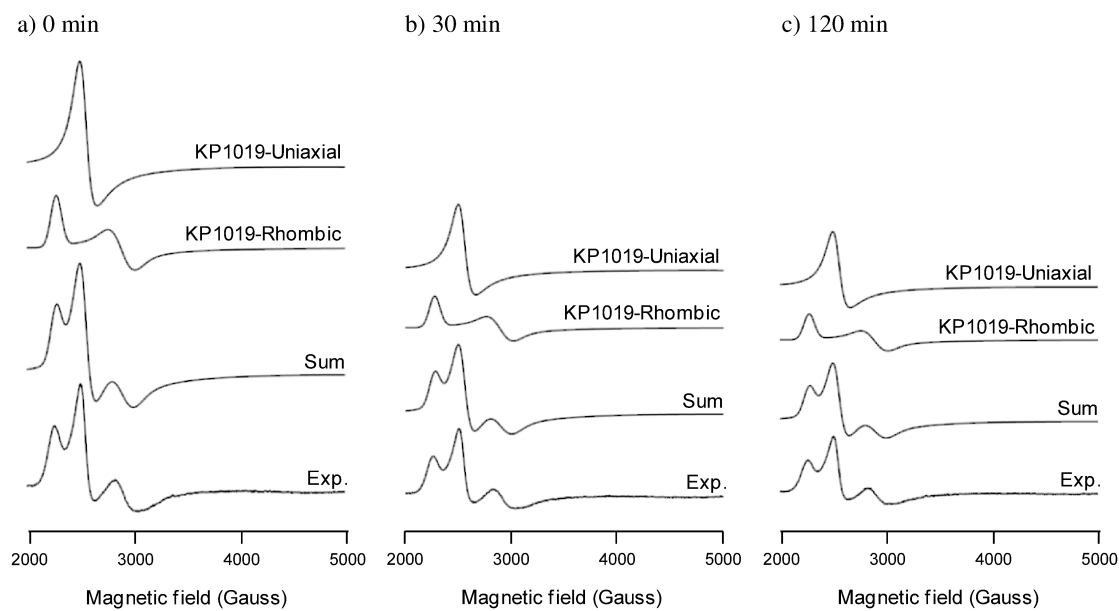


Figure D-57 (a-c) Simulation of EPR spectra of **KP1019** (3 mM) in PBS with 10% DMSO after incubation for 0, 30, and 120 minutes at 37 °C. **Experimental conditions:** see section 2.2.5. **Simulation parameters:** see Table D-2.

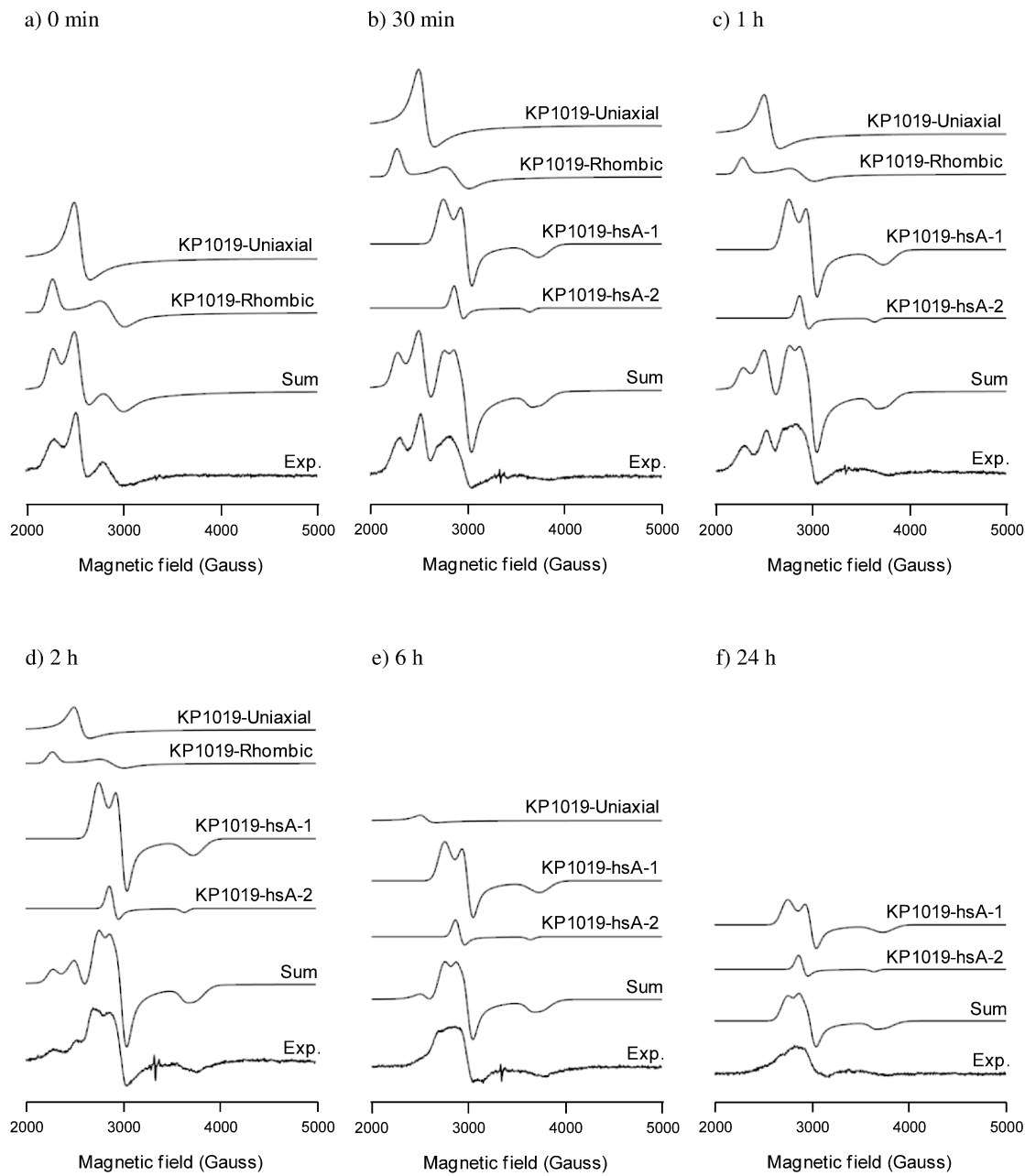


Figure D-58 (a-f) Simulation of EPR spectra of **KP1019** (1 mM) with hsA (0.5 mM) in PBS with 4% DMSO after incubation for 0 minutes to 24 hours at 37 °C. **Experimental conditions:** see section 2.2.5. **Simulation parameters:** see Table D-2.

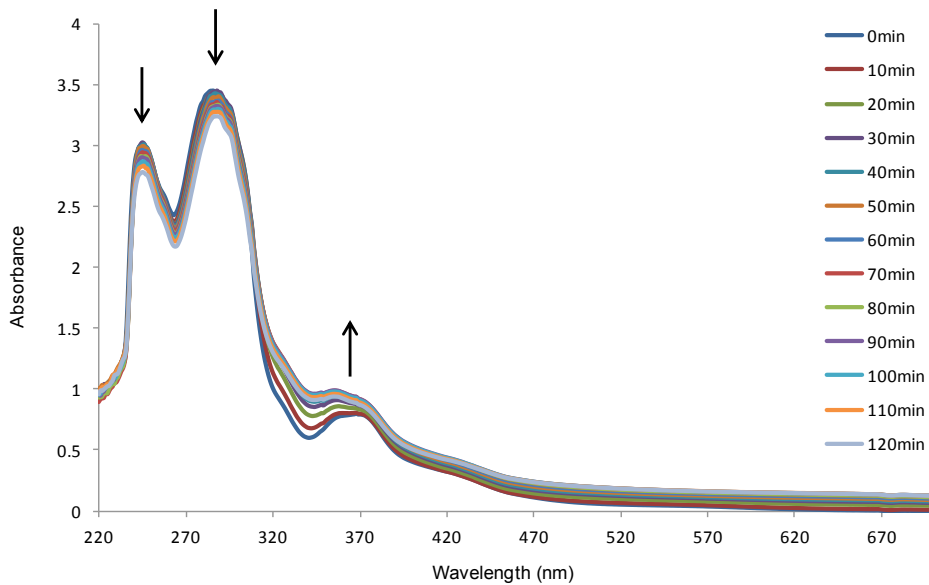


Figure D-59 UV-Vis spectrum of **KP1019** (200 μ M) in PBS pH 7.4 solution, 10% DMSO at 37 °C for two hours.

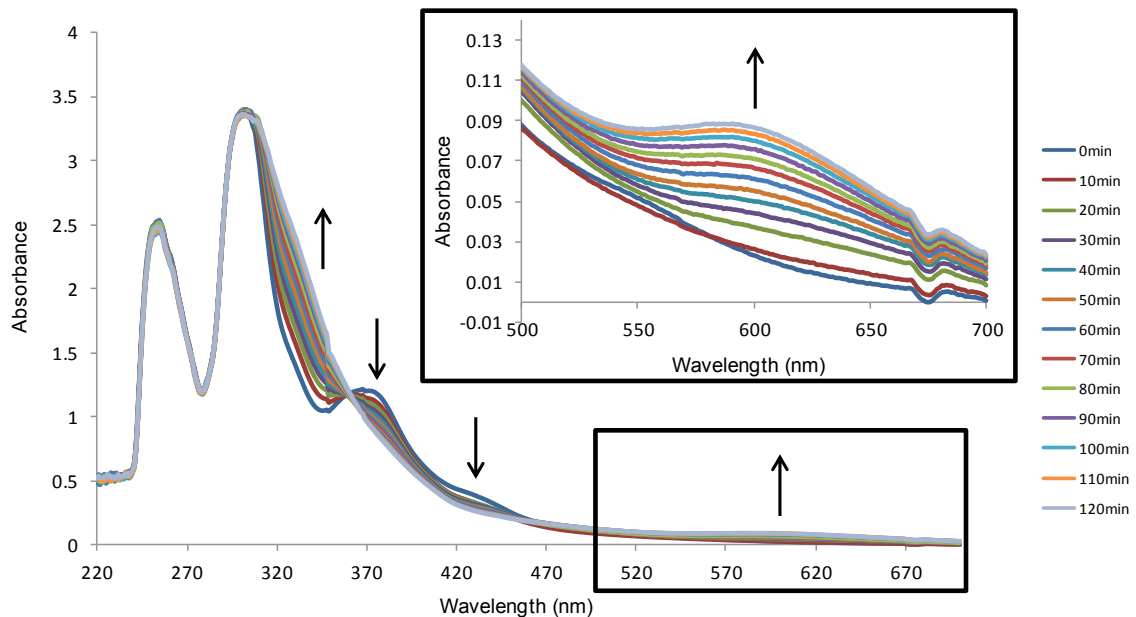


Figure D-60 UV-Vis spectrum of complex **KP1019** (200 μ M) with human serum albumin (100 μ M) in PBS pH 7.4 solution, 4% DMSO at 37 °C for two hours.

Table D-3 Bond lengths (\AA) around the central ruthenium atom as determined by X-ray crystallography.

Complex	Ru-N-1	Ru-N-2	Ru-Cl-1	Ru-Cl-2	Ru-Cl-3	Ru-Cl-4
1a	2.089(2)	2.085(2)	2.3642(6)	2.3665(7)	2.3569(6)	2.3574(7)
2a	2.097(2)	2.096(2)	2.3714(8)	2.345(1)	2.3556(8)	2.378(1)
3b	2.087(9)	2.098(9)	2.29(2)	2.27(2)	2.40(2)	2.095(7)
4a	2.095(3)	2.085(3)	2.335(1)	2.366(1)	2.377(1)	2.341(1)
5a	2.119(5)	2.104(5)	2.397(2)	2.393(2)	2.375(2)	2.384(2)

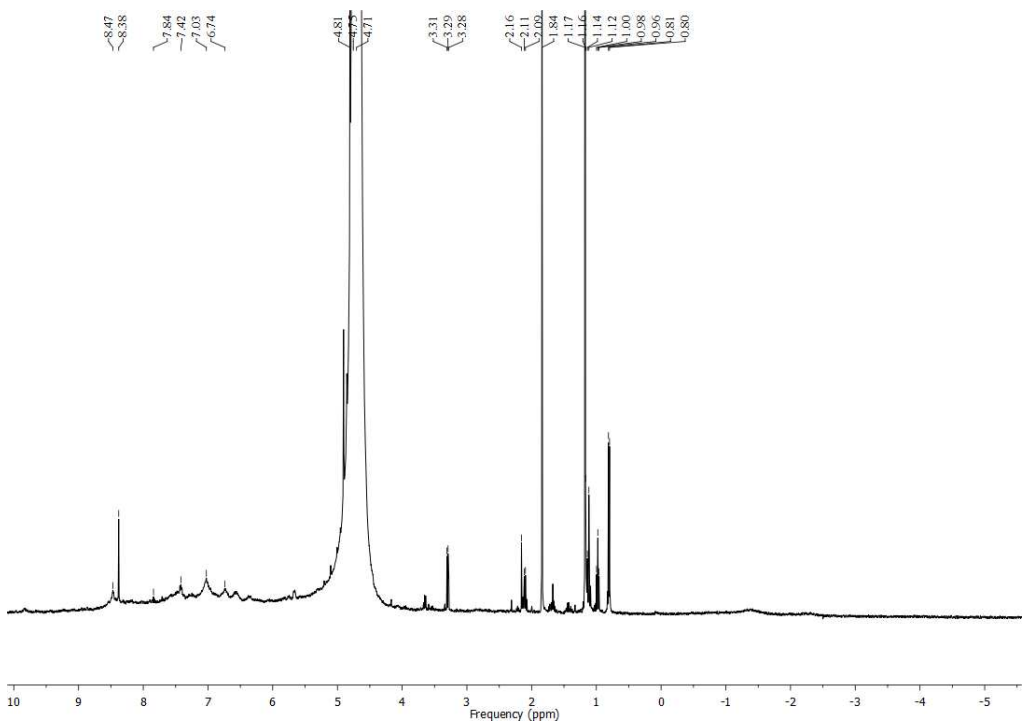


Figure D-61 ^1H NMR of complex **1b** in D_2O after 2 hours at 37°C .

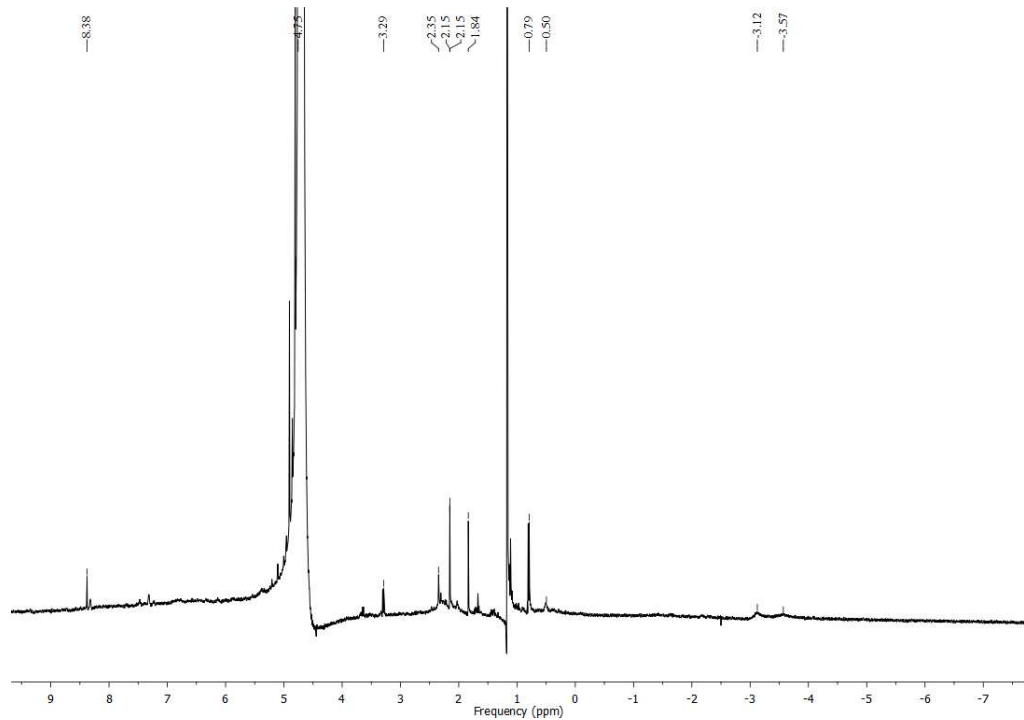


Figure D-62 ^1H NMR of complex **2b** in D_2O after 2 hours at 37°C .

Appendix E. Supplementary Information for Chapter 6.

Table E-1 Simulation parameters, g values and linewidths, used in EPR simulations of Ru(III) species interaction with *Saccharomyces cerevisiae* whole cells and cell components.

Species	g_1	g_2	g_3	L_1	L_2	L_3
NAMI-A						
NAMI-A	2.47	2.47	1.72	105	105	180
NAMI-A-H ₂ O	2.32	2.32	1.87	75	75	60
NAMI-A-Cell-Wall-1	2.45	2.21	1.10	300	80	200
NAMI-A-Cell-Wall-2	2.38	2.18	1.80	325	250	350
NAMI-A-Mitochondria-1	2.40	2.21	1.10	400	70	200
NAMI-A-Mitochondria-2	2.40	2.22	1.75	200	175	350
NAMI-A-Cyto.-Proteins	2.42	2.25	1.84	200	175	350
NAMI-A-Nuclear-Fraction-1	2.40	2.22	1.10	400	100	200
NAMI-A-Nuclear-Fraction-2	2.48	2.30	1.88	250	150	350
KP1019						
KP1019-Uniaxial	2.64	2.64	1.20	120	120	500
KP1019-Rhombic	2.94	2.31	0.95	100	200	600
KP1019-Whole-Cells-1	2.40	2.18	1.10	400	80	500
KP1019-Cell-Wall-1	2.50	2.30	1.80	300	200	250
KP1019-Cell-Wall-2	2.40	2.20	1.88	250	100	350
KP1019-Mitochondria-1	2.36	2.19	1.84	175	85	250
KP1019-Mitochondria-2	2.40	2.20	1.80	275	225	350
KP1019-Cyto.-Proteins-1	2.47	2.23	1.70	250	175	500
KP1019-Cyto.-Proteins-2	2.38	2.27	1.10	200	150	250
KP1019-Nuclear-Fraction-1	2.41	2.20	1.80	100	150	250
KP1019-Nuclear-Fraction-2	2.40	2.20	1.84	250	150	350

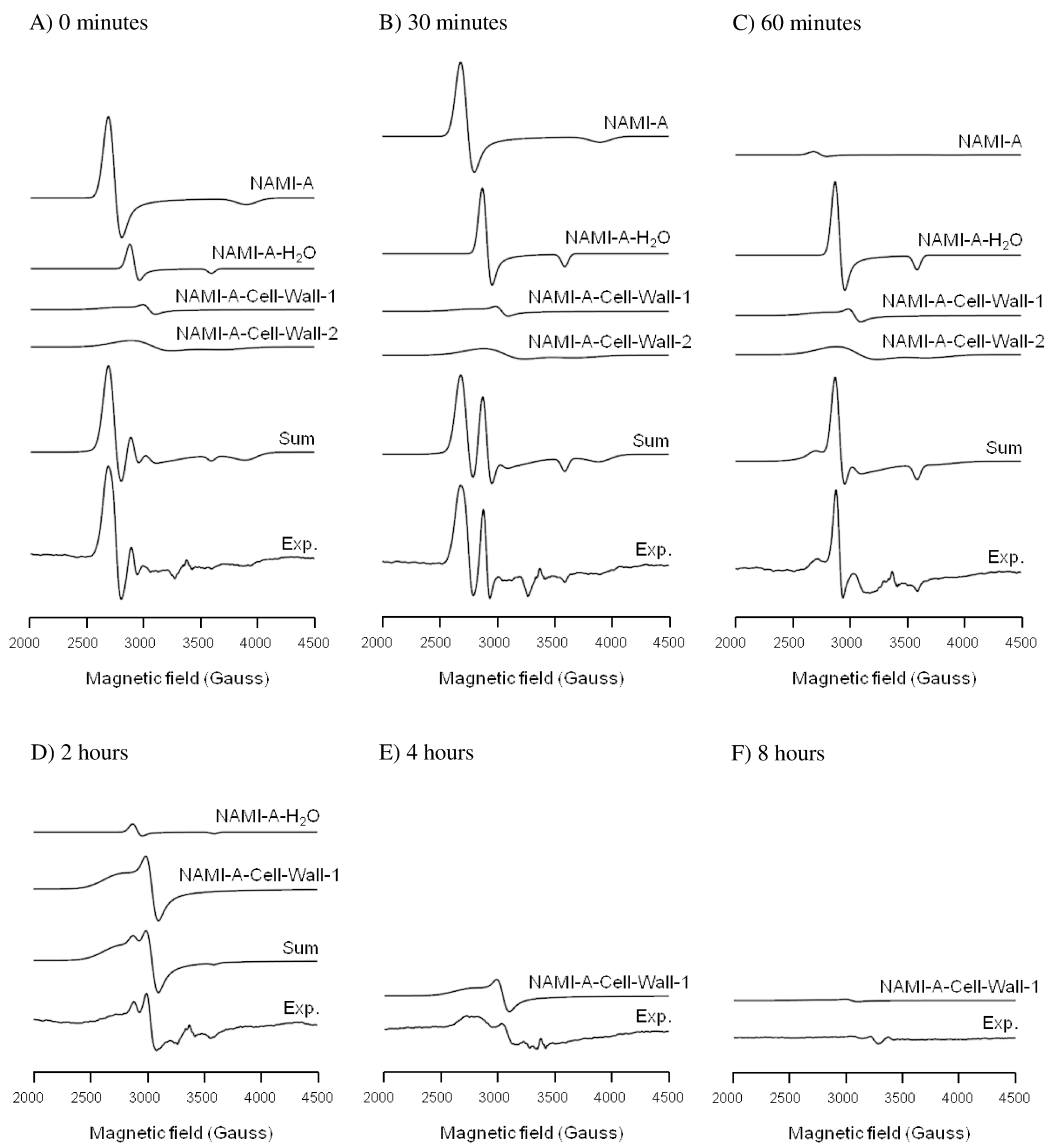


Figure E-1 (A-F) Deconvolution of EPR spectra from NAMI-A in buffer after incubation with yeast cells for 0 minutes, 30 minutes, 1, 2, 4, and 8 hours at 30 °C.

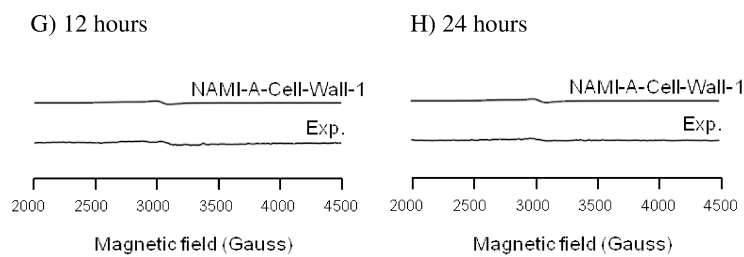


Figure E-2 (G-H) Deconvolution of EPR spectra from NAMI-A in buffer after incubation with yeast cells for 12 and 24 hours at 30 °C.

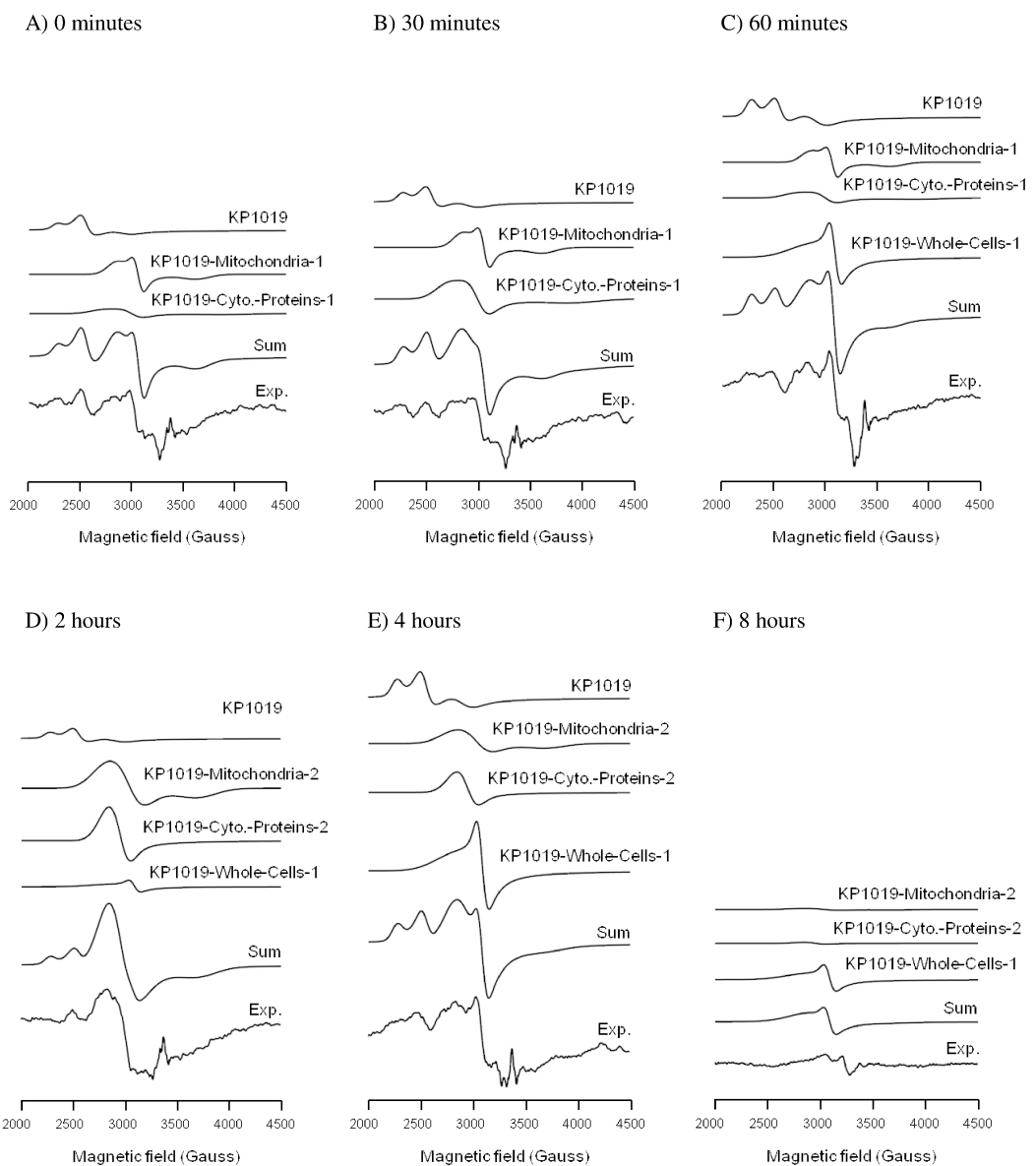
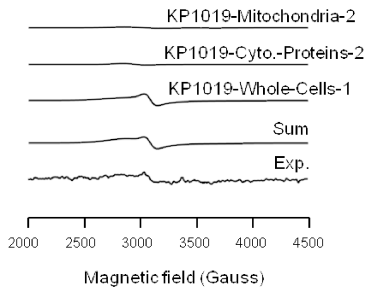


Figure E-3 (A-F) Deconvolution of EPR spectra from KP1019 in PBS after incubation with yeast cells for 0 minutes, 30 minutes, 1, 2, 4, and 8 hours at 30 °C.

F) 12 hours



G) 24 hours

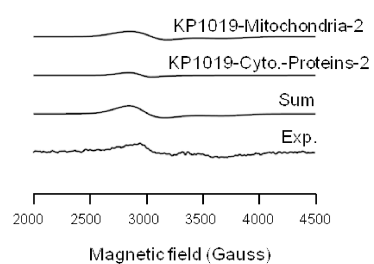


Figure E-4 (F-G) Deconvolution of EPR spectra from KP1019 in PBS after incubation with yeast cells for 12 and 24 hours at 30 °C.

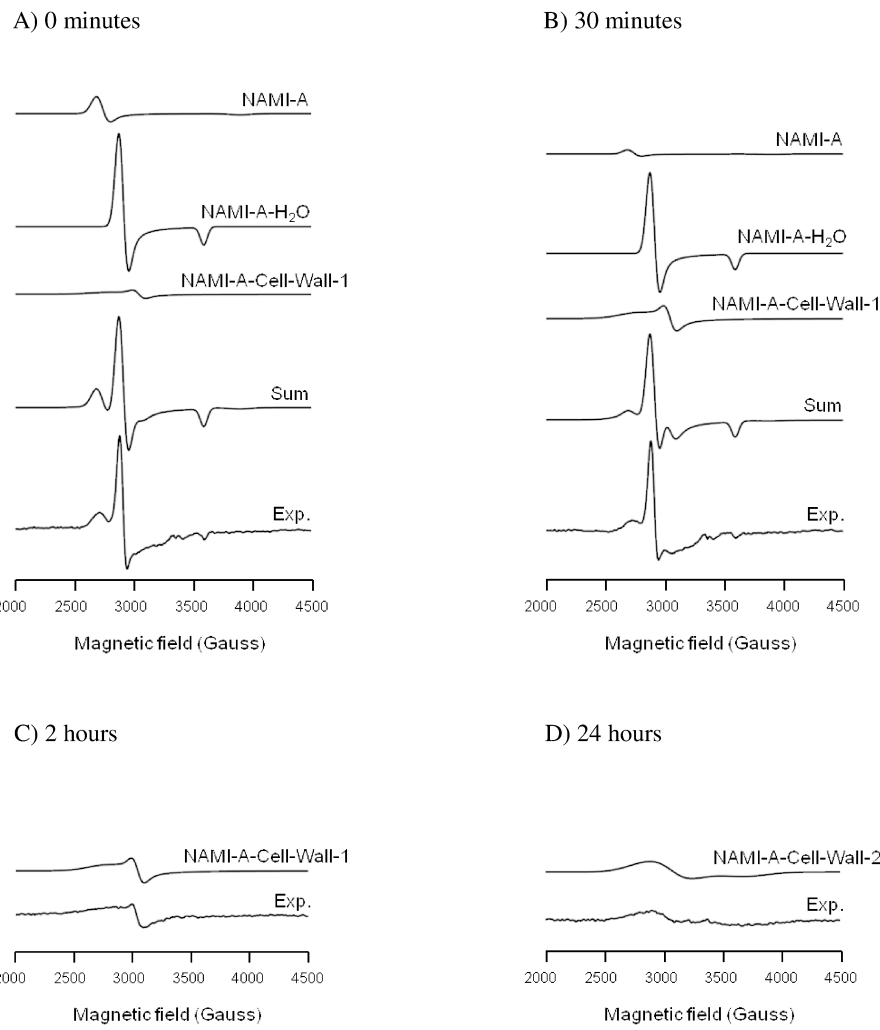


Figure E-5 (A-D) Deconvolution of EPR spectra from NAMI-A in PBS after incubation with yeast cell walls for 0 minutes, 30 minutes, 2, and 24 hours at 30 °C.

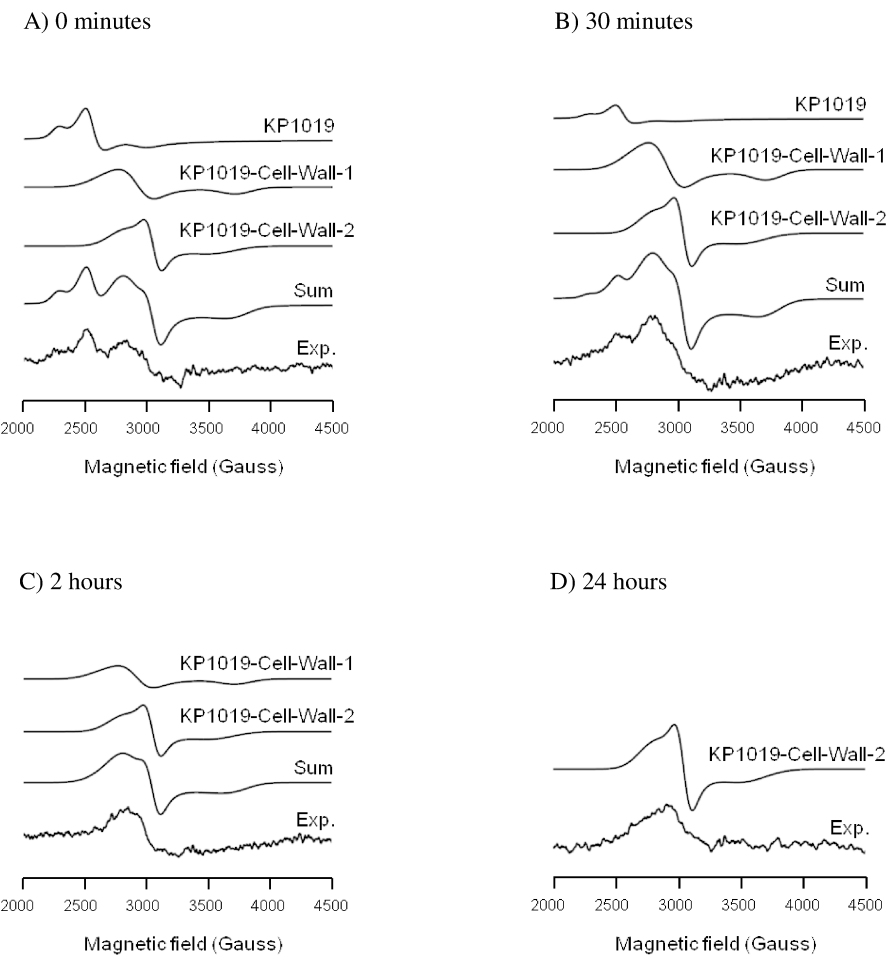


Figure E-6 (A-D) Deconvolution of EPR spectra from KP1019 in PBS after incubation with yeast cell walls for 0 minutes, 30 minutes, 2, and 24 hours at 30 °C.

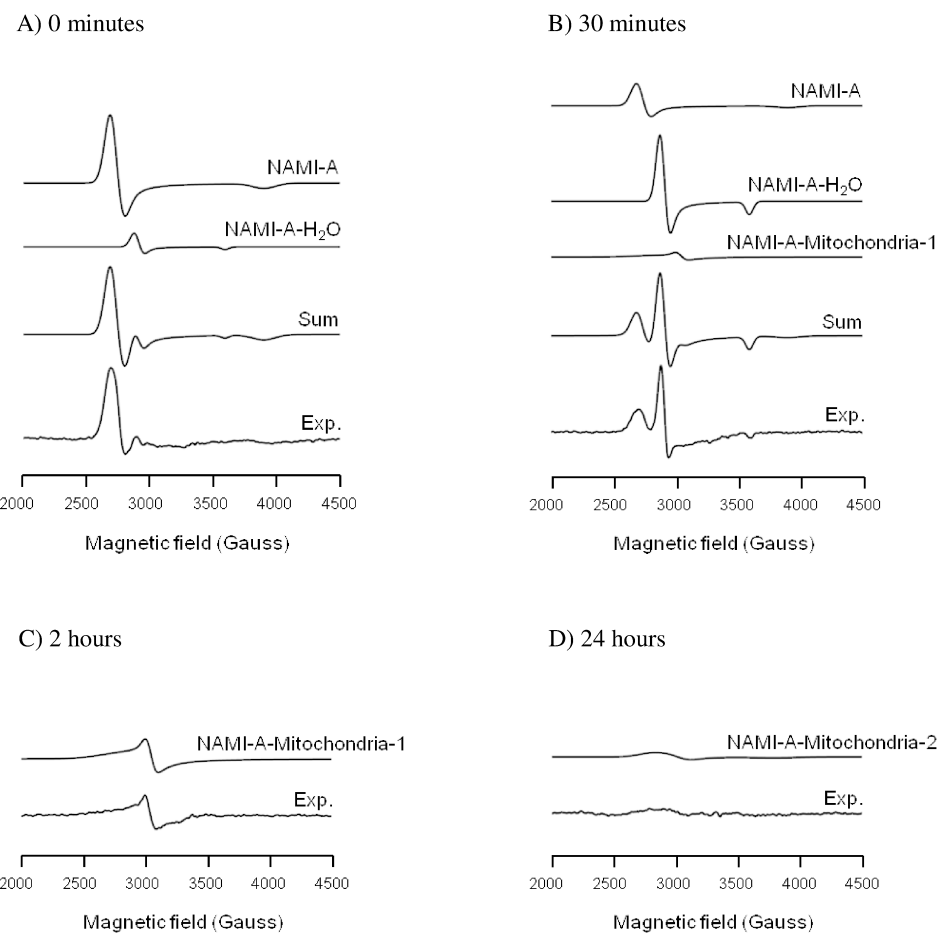


Figure E-7 (A-D) Deconvolution of EPR spectra from NAMI-A in PBS after incubation with yeast cell mitochondria for 0 minutes, 30 minutes, 2, and 24 hours at 30 °C.

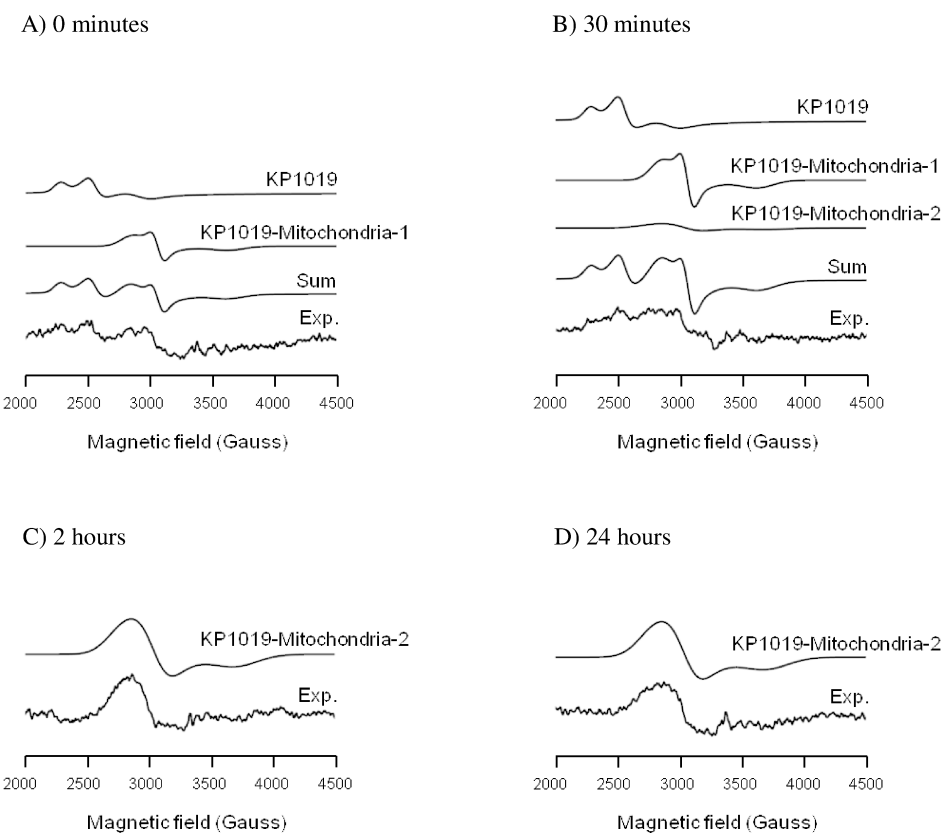


Figure E-8 (A-D) Deconvolution of EPR spectra from KP1019 in PBS after incubation with yeast cell mitochondria for 0 minutes, 30 minutes, 2, and 24 hours at 30 °C.

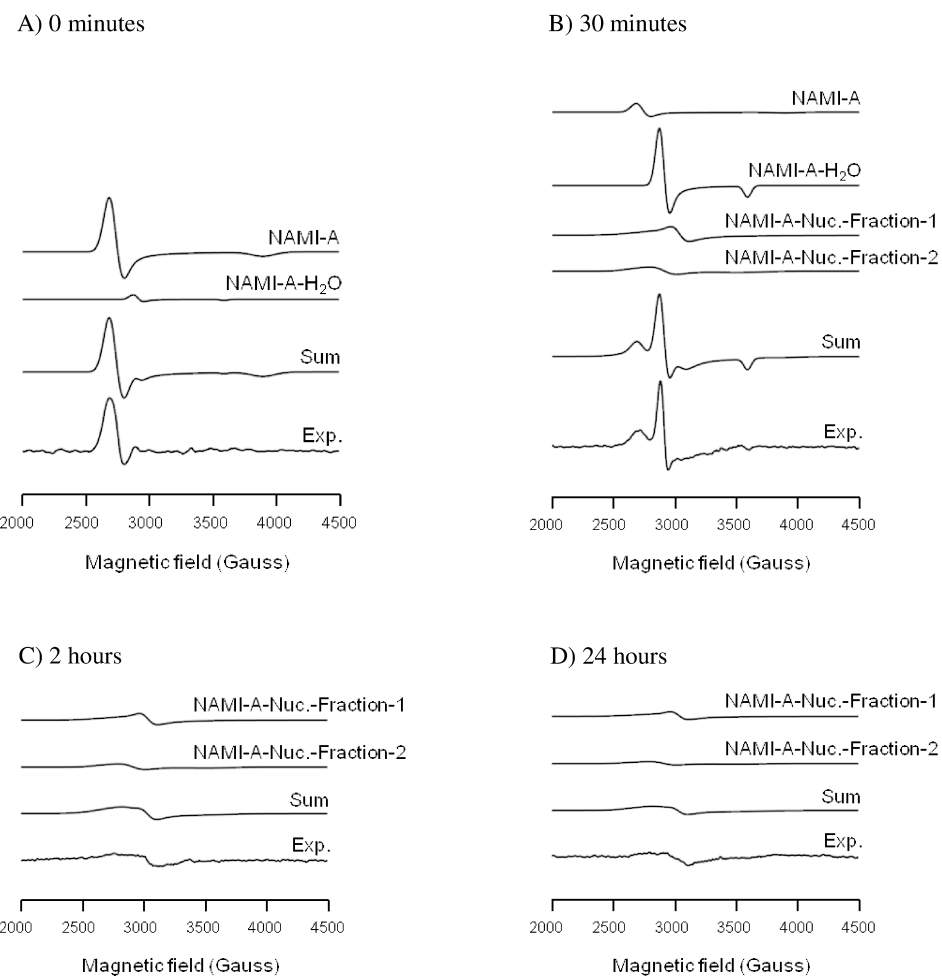


Figure E-9 (A-D) Deconvolution of EPR spectra from NAMI-A in PBS after incubation with yeast cell nuclear fraction for 0 minutes, 30 minutes, 2, and 24 hours at 30 °C.

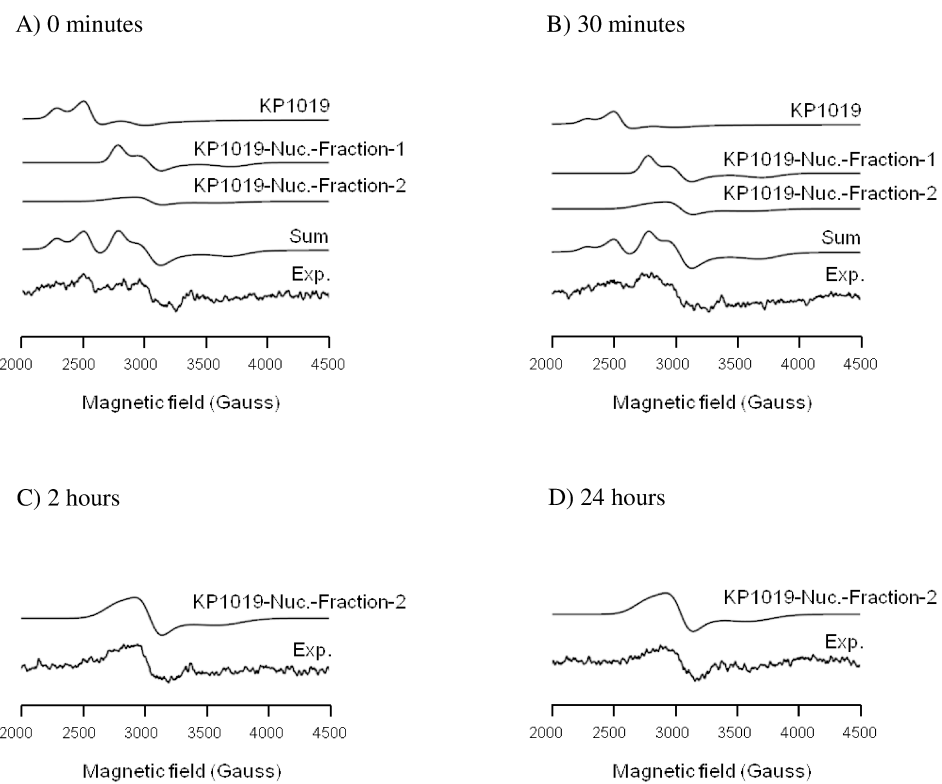


Figure E-10 (A-D) Deconvolution of EPR spectra from KP1019 in PBS after incubation with yeast cell nuclear fraction for 0 minutes, 30 minutes, 2, and 24 hours at 30 °C.

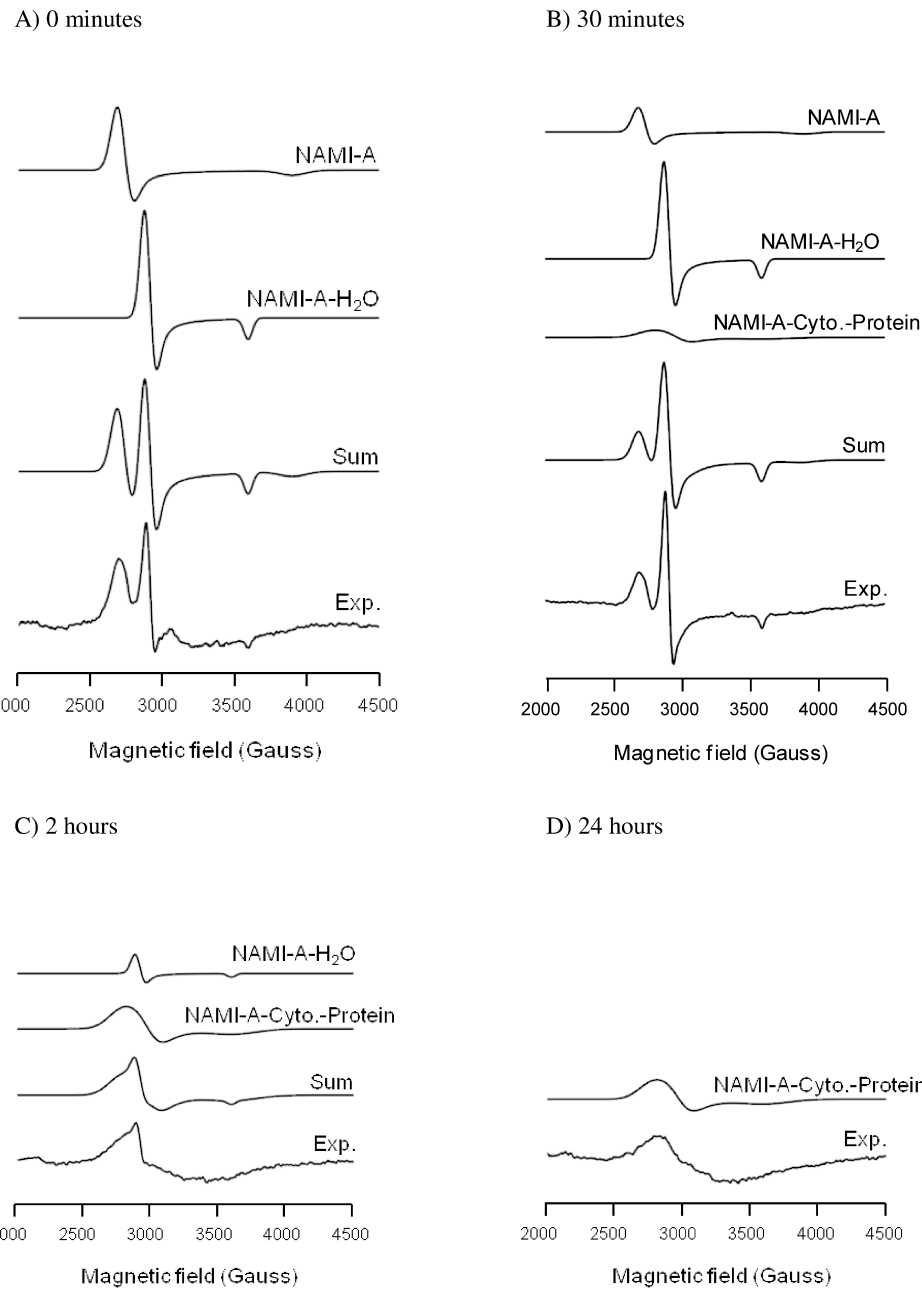


Figure E-11 (A-D) Deconvolution of EPR spectra from NAMI-A in PBS after incubation with yeast cell cytoplasmic protein fraction for 0 minutes, 30 minutes, 2, and 24 hours at 30 °C.

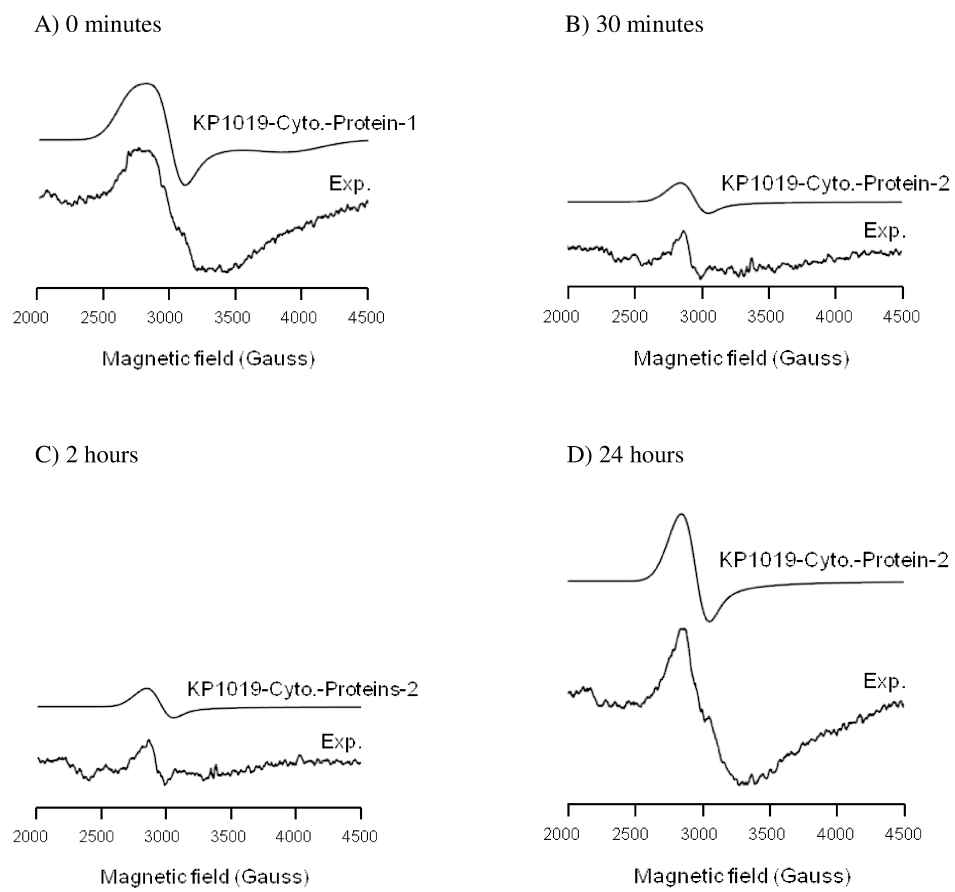


Figure E-12 (A-D) Deconvolution of EPR spectra from KP1019 in PBS after incubation with yeast cell cytoplasmic protein fraction for 0 minutes, 30 minutes, 2, and 24 hours at 30 °C.

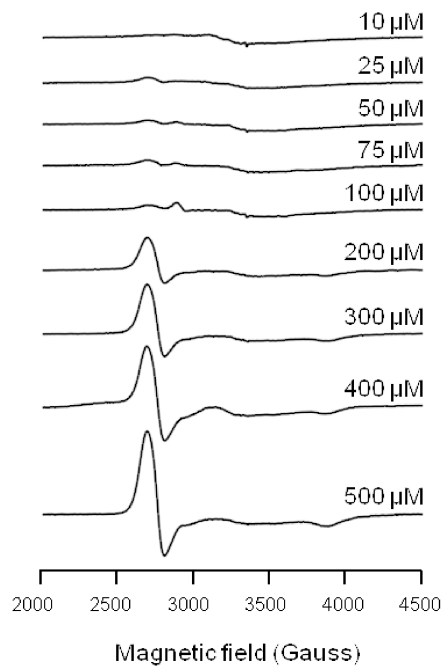


Figure E-13 Serial dilution of NAMI-A in PBS to determine the calibration curve.

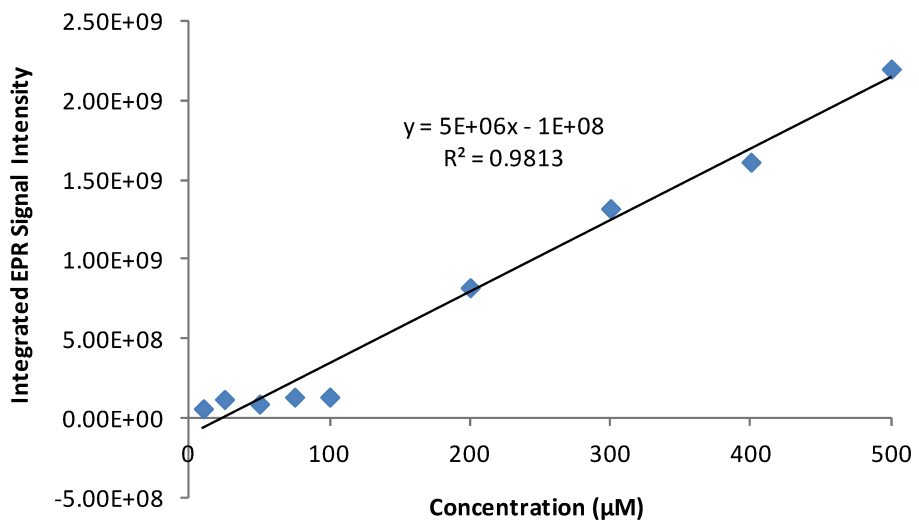


Figure E-14 Plot of the integrated signal intensities determined by the titration of NAMI-A in PBS to determine the detection limit of the EPR spectrometer.

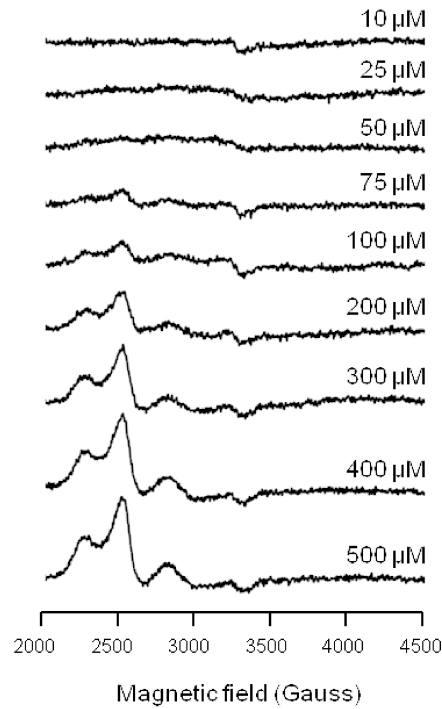


Figure E-15 Serial dilution of KP1019 in PBS to determine the detection calibration curve.

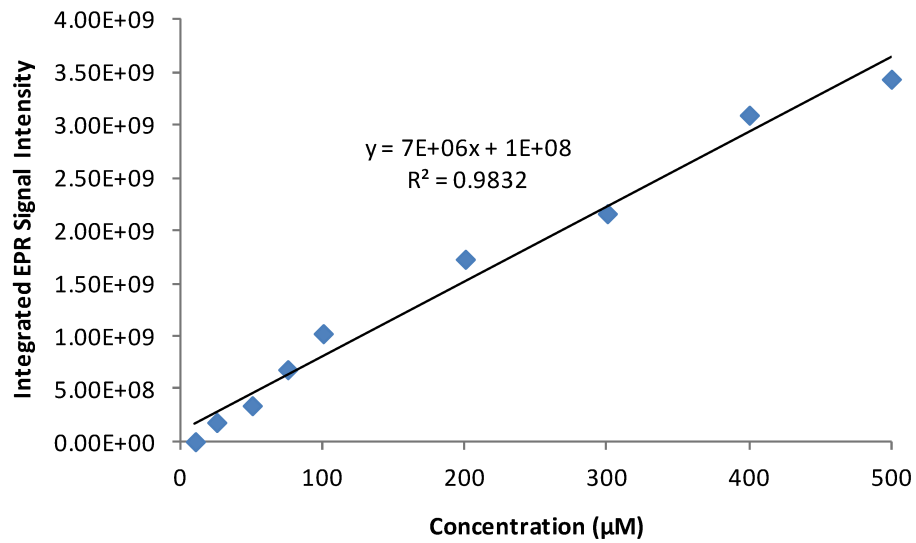


Figure E-16 Plot of the integrated signal intensities determined by the titration of KP1019 in PBS to determine the detection limit of the EPR spectrometer.

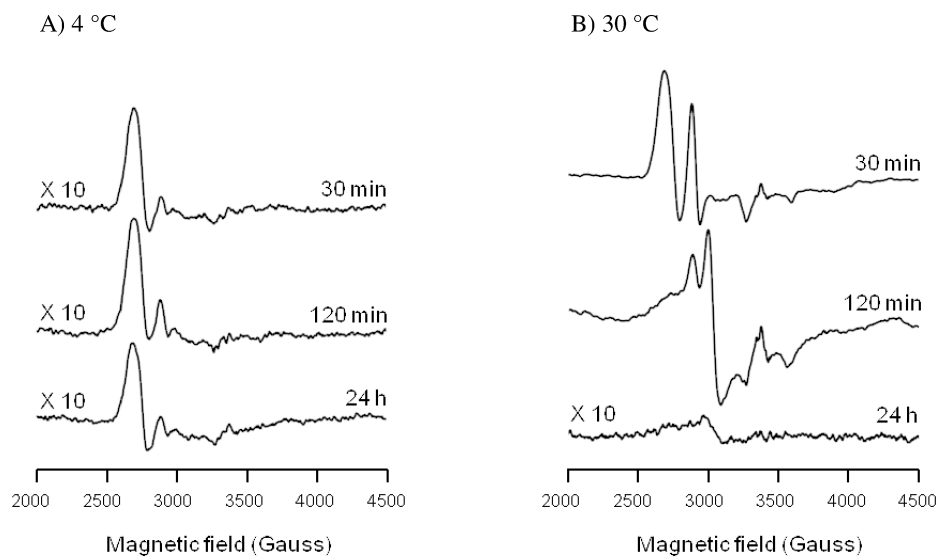


Figure E-17 EPR spectra of NAMI-A in PBS after incubation with whole yeast cells for 30 minutes, 2, and 24 hours at 4 and 30 °C.

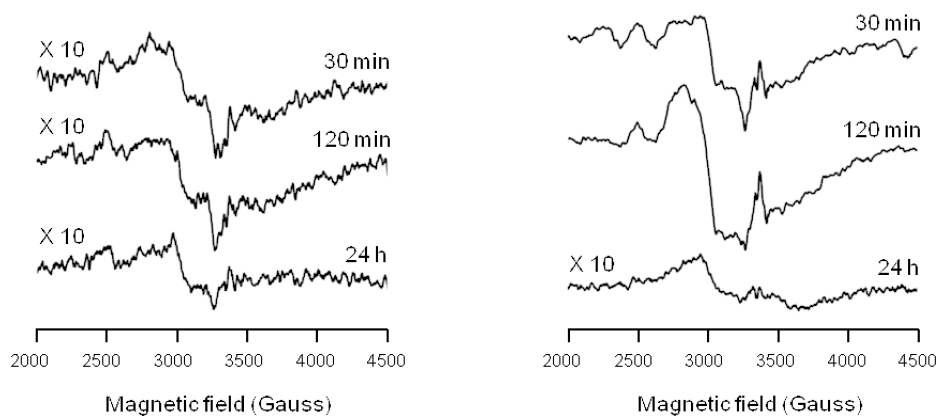


Figure E-18 EPR spectra of KP1019 in PBS after incubation with whole yeast cells for 30 minutes, 2, and 24 hours at 4 and 30 °C.

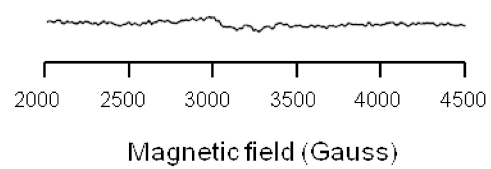


Figure E-19 EPR spectra of whole cells of *Saccharomyces cerevisiae* in PBS.

Appendix F. Supplementary Information for Chapter 7.

Table F-1 EPR simulation parameters, g values and linewidths, used in the simulation of all EPR spectra.

Compound	g values			Linewidths		
	g ₁	g ₂	g ₃	LW ₁	LW ₂	LW ₃
bis-DMSO-H ₂ O	2.43	2.43	1.77	100	100	150
bis-DMSO-(H ₂ O) ₂ -eq	2.40	2.24	1.88	90	90	200
bis-DMSO-(H ₂ O) ₂ -ax	2.35	2.35	1.80	110	110	200
bis-DMSO-hsA-1	2.40	2.40	1.72	250	250	300
bis-DMSO-hsA-2	2.50	2.25	1.70	400	150	350
bis-DMSO-hsA-3	2.42	2.05	1.88	80	70	55
bis-DMSO-His	2.37	2.37	1.81	75	75	90
NAMI-A	2.47	2.47	1.72	105	105	180
NAMI-A-H ₂ O	2.30	2.30	1.88	75	75	90
D-NAMI-A	2.47	2.47	1.72	100	100	170
¹⁵ N-NAMI-A	2.45	2.45	1.74	110	110	200
NAMI-A-hsA-1	2.43	2.43	1.76	300	300	300
NAMI-A-hsA-2	2.54	2.26	1.76	450	175	350
NAMI-A-hsA-3	2.42	2.06	1.96	80	70	55
NAMI-A-His	2.52	2.29	1.78	175	175	400
KP1019-Uniaxial	2.64	2.64	1.20	120	120	500
KP1019-Rhombic	2.94	2.31	0.95	100	200	600
KP1019-hsA-1	2.44	2.24	1.79	120	90	200
KP1019-hsA-2	2.32	2.32	1.84	90	90	80
KP1019-hsA-3	2.42	2.06	1.96	80	70	55

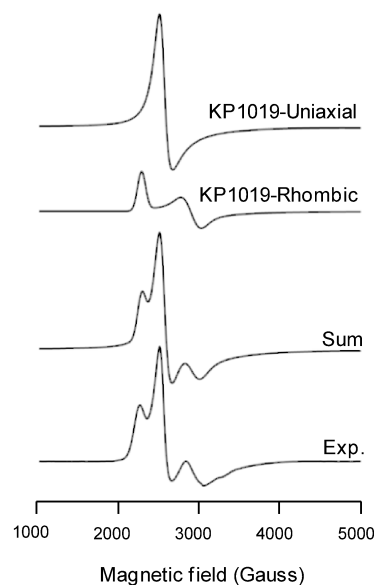


Figure F-1 Deconvolution of EPR spectra from KP1019 in 1:1 DMSO to PBS.
Simulation parameters: For g values and linewidths, see **Table F-1**.

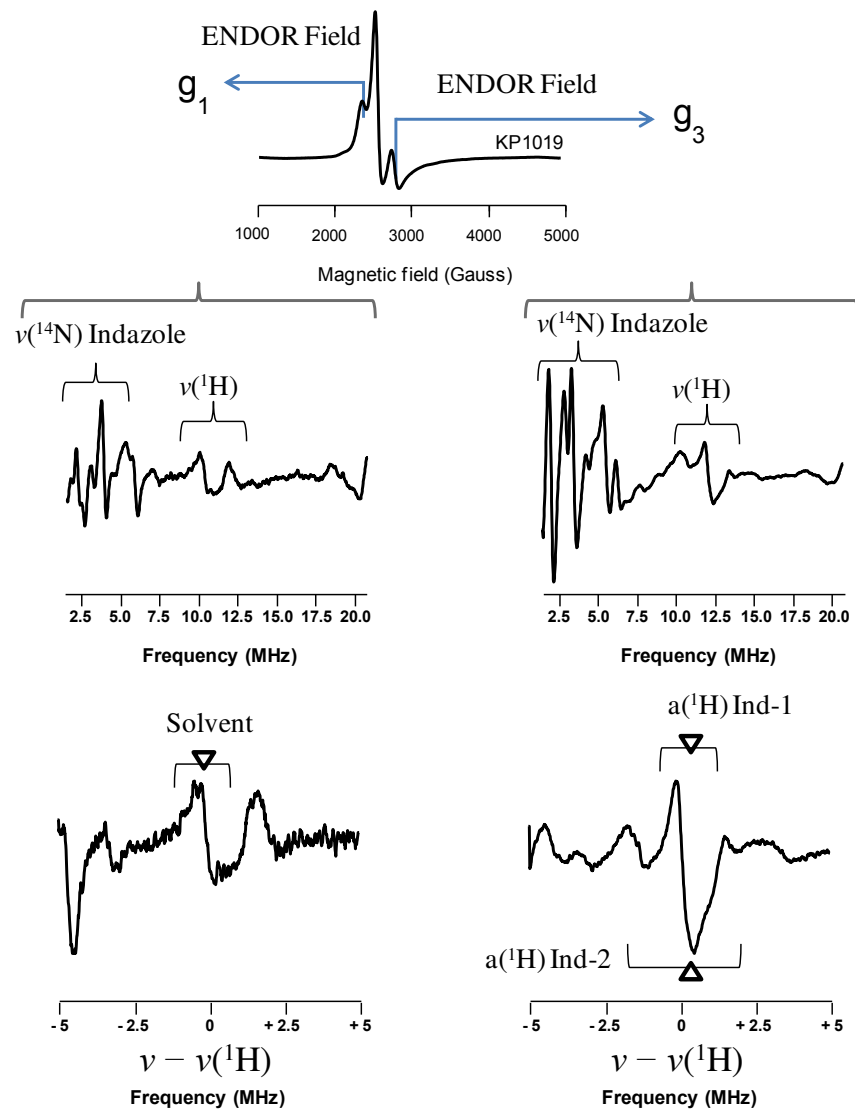


Figure F-2 EPR spectrum of KP1019 in a solution of 1:1 DMSO to PBS and the resulting ENDOR spectra measured at g_1 and g_3 , then expanded around the proton Larmor frequency.

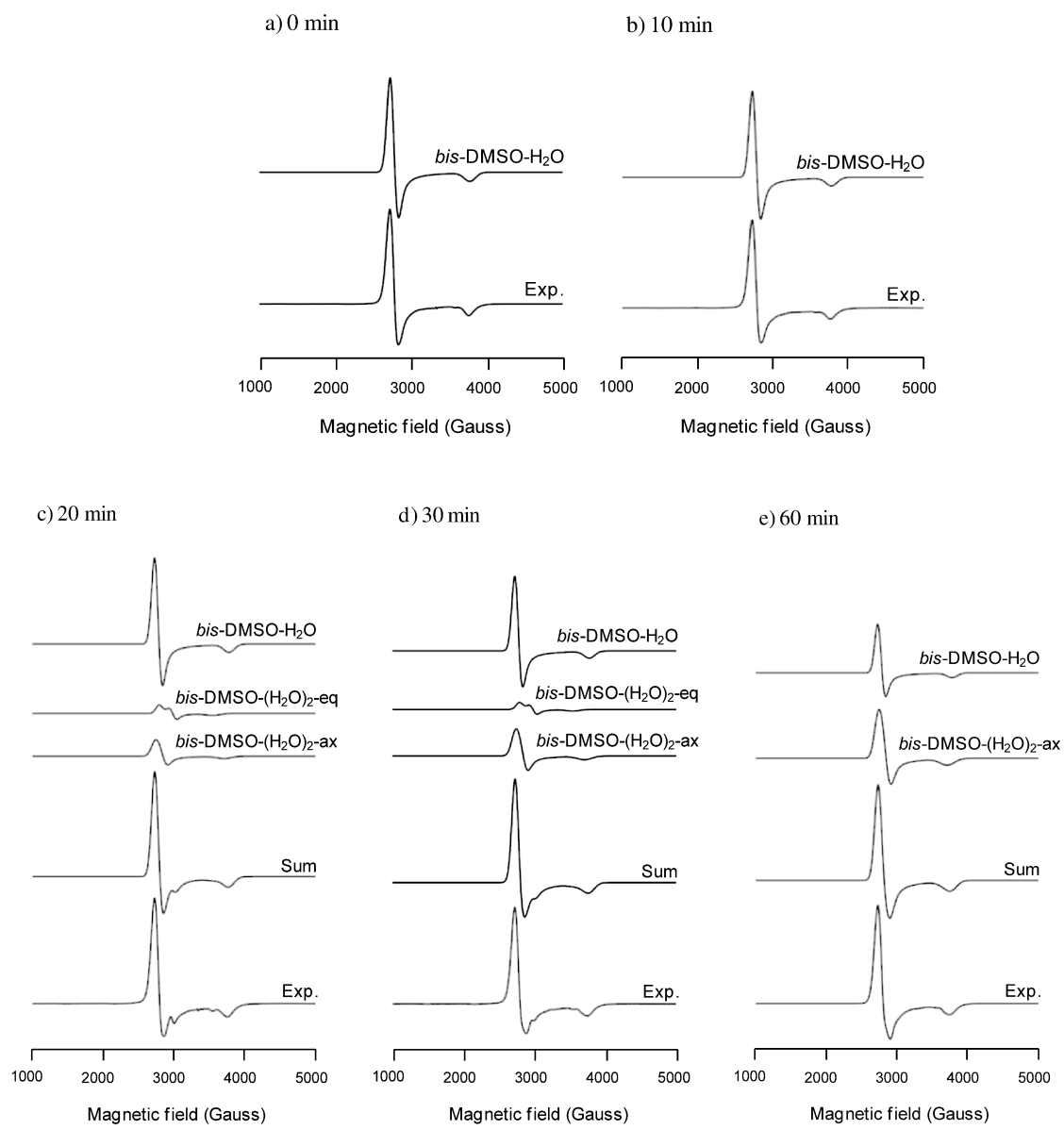


Figure F-3 (a-e) Deconvolution of EPR spectra from the *bis*-DMSO complex following incubation in PBS for 0, 10, 20, 30, and 60 minutes at 37 °C. Simulation parameters: For g values and linewidths, see **Table F-1**.

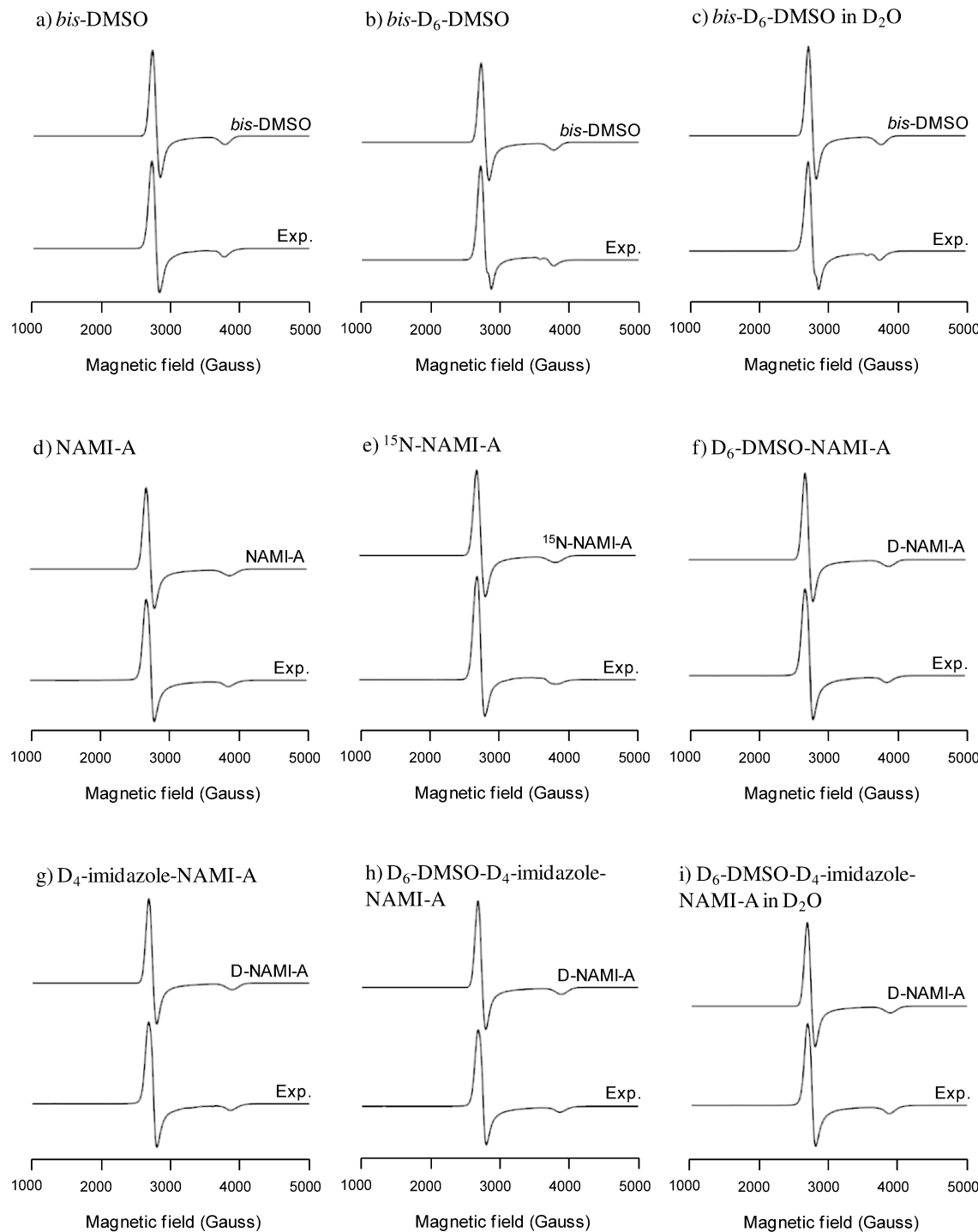


Figure F-4 (a-i) Deconvolution of EPR spectra from all “NAMI-A family” compounds and isotopically labelled derivatives used in ENDOR in PBS. Simulation parameters: For g values and linewidths, see **Table F-1**.

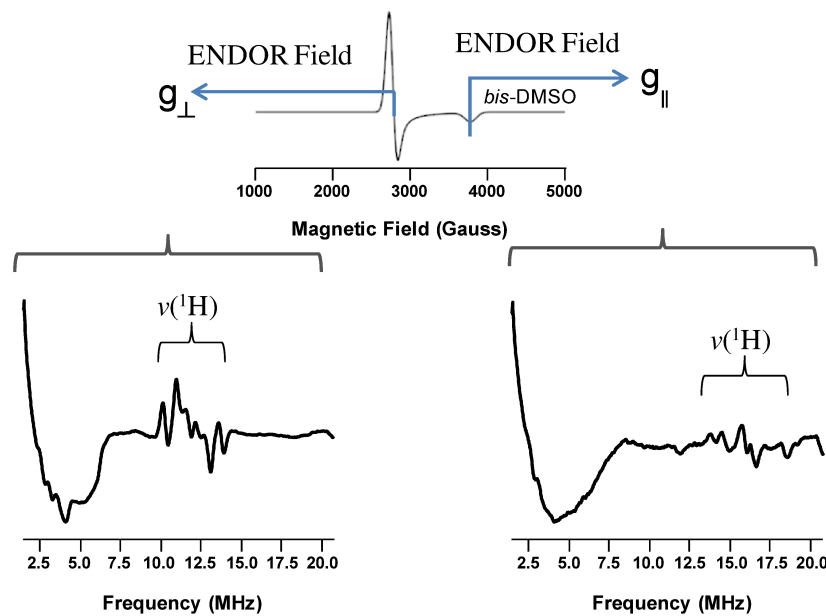


Figure F-5 EPR spectrum of the *bis*-DMSO complex in PBS and the resulting ENDOR spectra measured at g_{\perp} and g_{\parallel} .

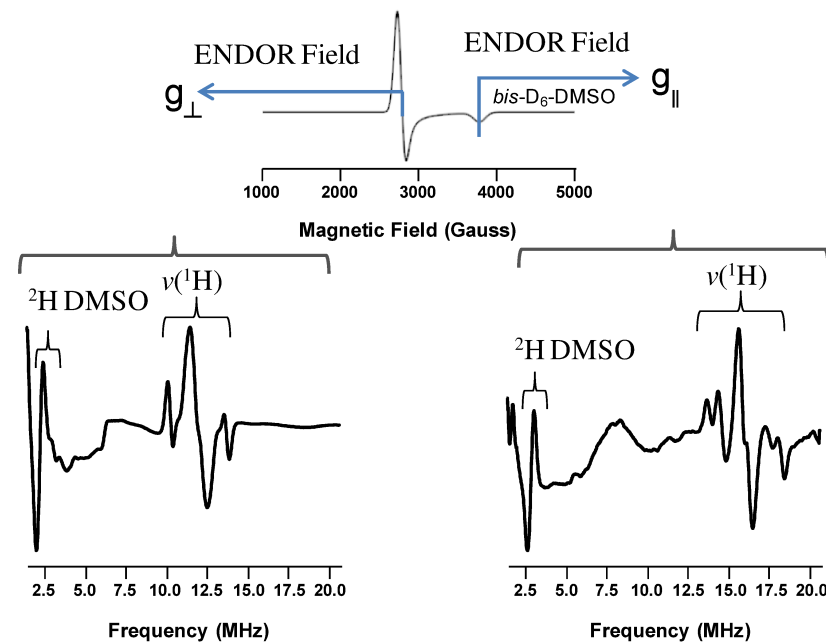


Figure F-6 EPR spectrum of the D_6 -DMSO labelled *bis*-DMSO complex in PBS and the resulting ENDOR spectra measured at g_{\perp} and g_{\parallel} .

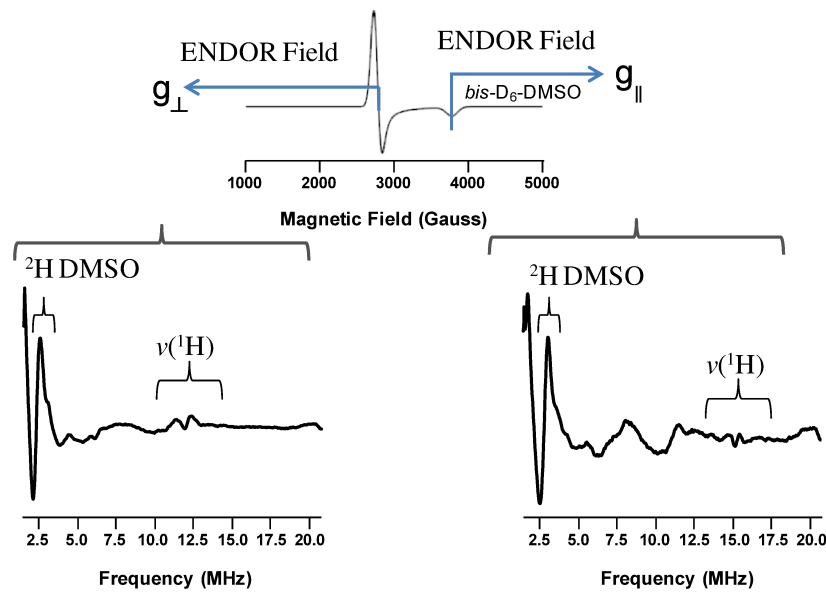


Figure F-7 EPR spectrum of the D_6 -DMSO labelled *bis*-DMSO complex in buffered D_2O and the resulting ENDOR spectra measured at g_{\perp} and g_{\parallel} .

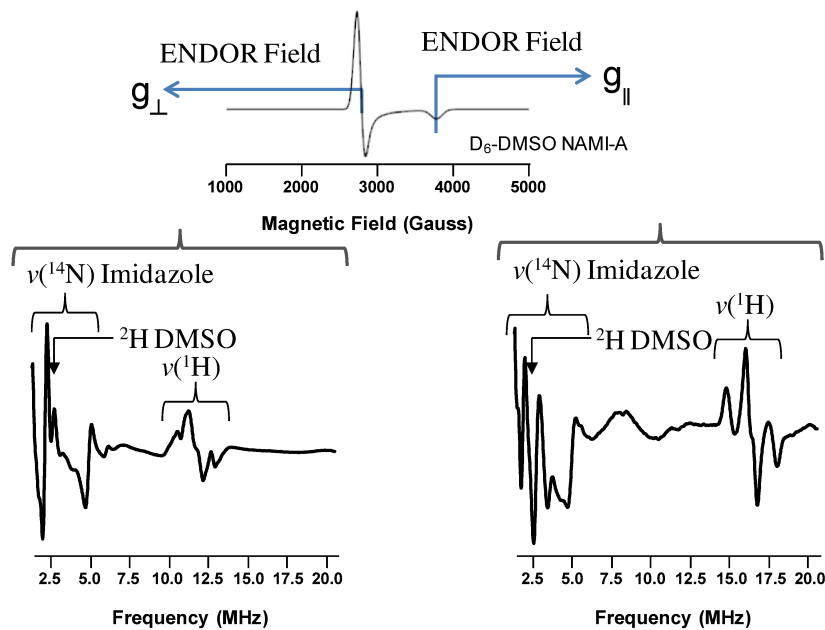


Figure F-8 EPR spectrum of D_6 -DMSO labelled NAMI-A in PBS and the resulting ENDOR spectra measured at g_{\perp} and g_{\parallel} .

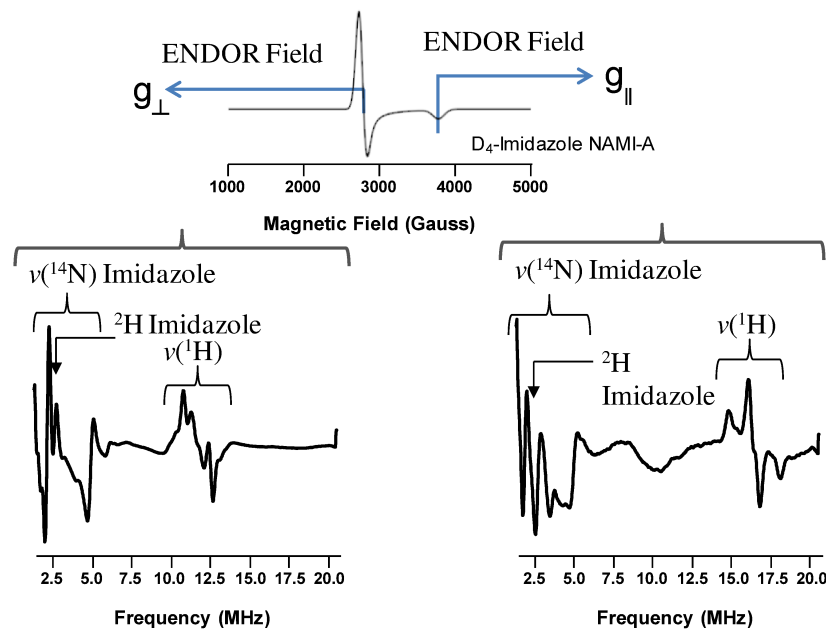


Figure F-9 EPR spectrum of D₄-imidazole labelled NAMI-A in PBS and the resulting ENDOR spectra measured at g_{\perp} and g_{\parallel} .

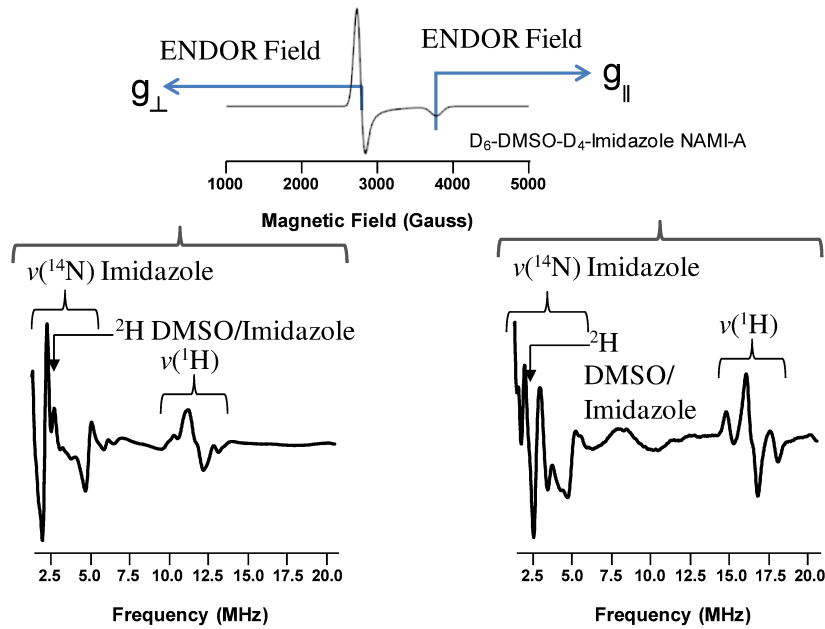


Figure F-10 EPR spectrum of D₆-DMSO and D₄-imidazole labelled NAMI-A in PBS and the resulting ENDOR spectra measured at g_{\perp} and g_{\parallel} .

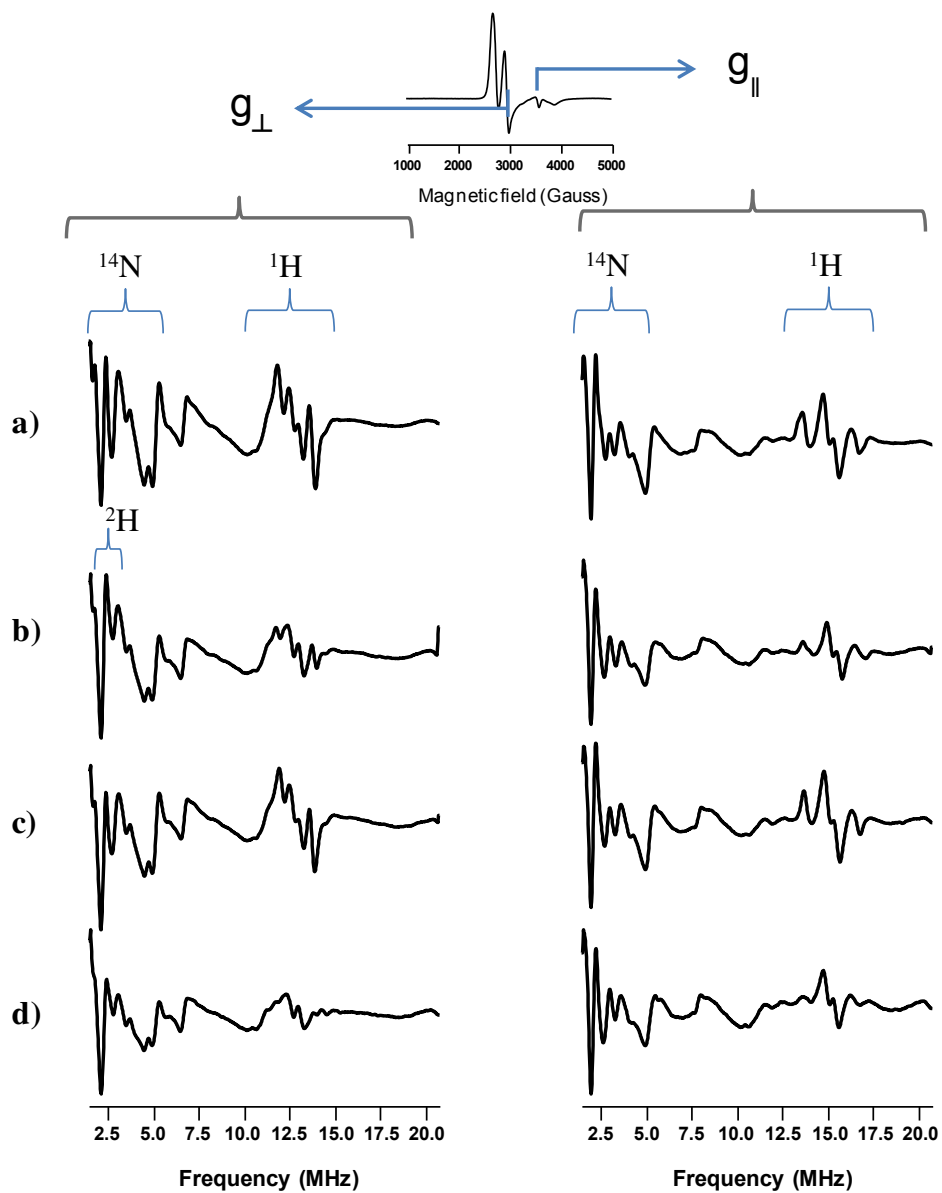


Figure F-11 EPR and ENDOR spectra measured at g_{\perp} and g_{\parallel} of: i) NAMI-A, ii) d^6 -DMSO-NAMI-A, iii) d^4 -Im-NAMI-A, and iv) d^6 -DMSO- d^4 -Im-NAMI-A following 20 minutes of incubation at 37 °C in PBS.

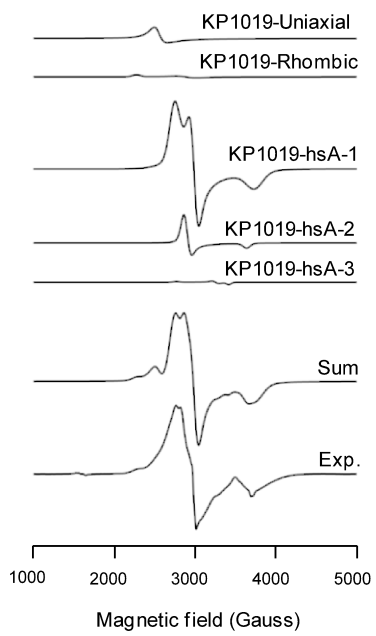


Figure F-12 Deconvolution of EPR spectra from KP1019 in PBS with hsA after incubation for 30 minutes at 37 °C. Simulation parameters: For g values and linewidths, see **Table F-1**.

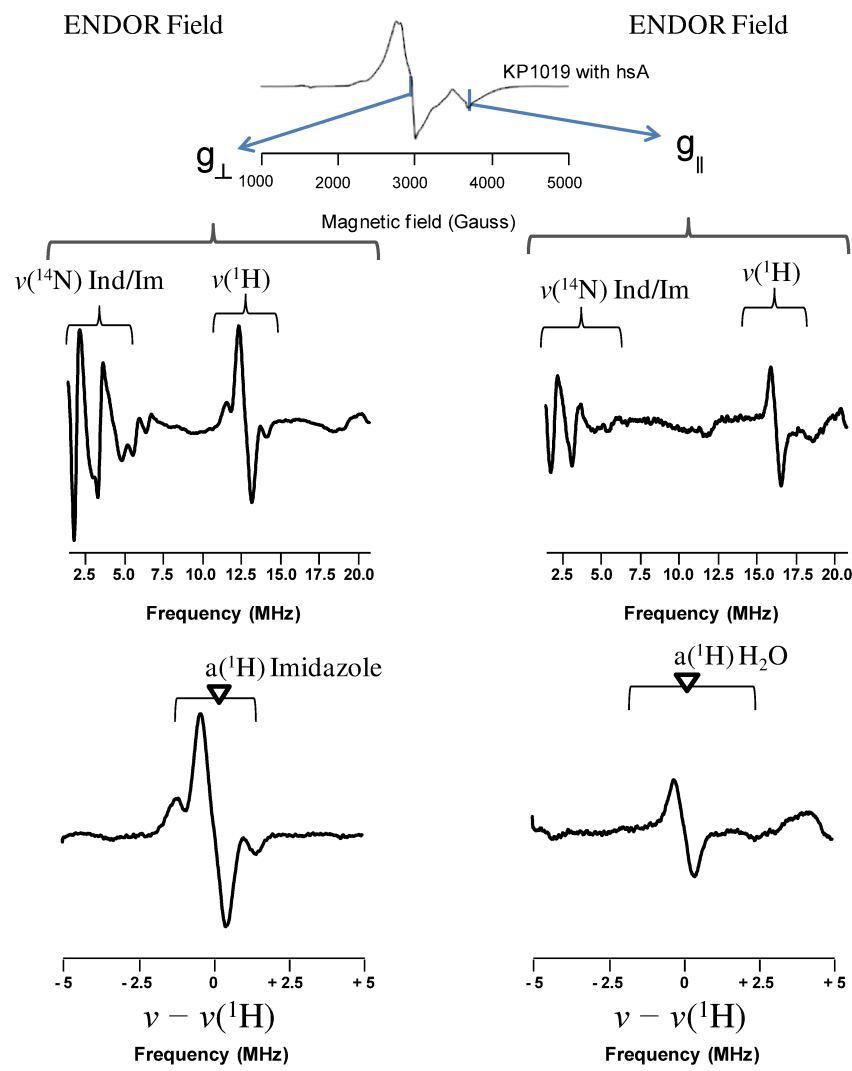
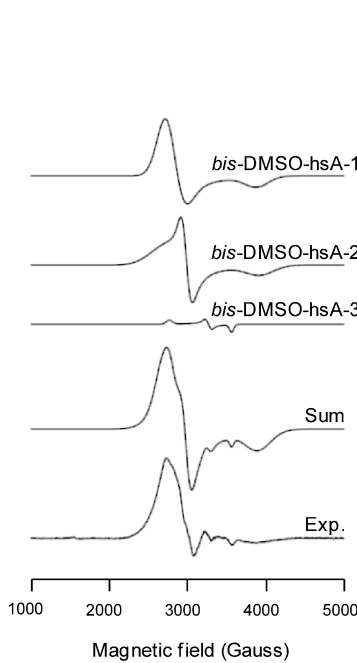
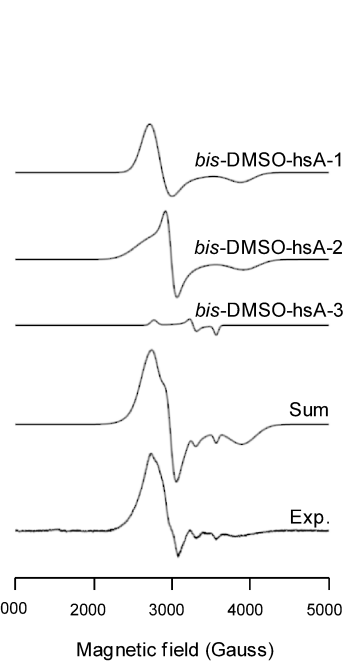


Figure F-13 EPR spectrum of KP1019 with hsA in PBS following incubation for 30 minutes at 37 °C and the resulting ENDOR spectra measured at g_{\perp} and g_{\parallel} , then expanded around the proton Larmor frequency.

a) *bis*-DMSOb) *bis*-D₆-DMSO

c) NAMI-A

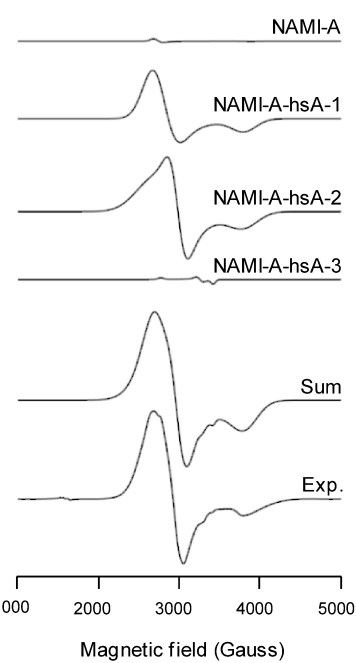


Figure F-14 (a-c) Deconvolution of EPR spectra from the “NAMI-A family” of compounds in PBS with hsA after incubation for 30 minutes at 37 °C. Simulation parameters: For g values and linewidths, see **Table F-1**.

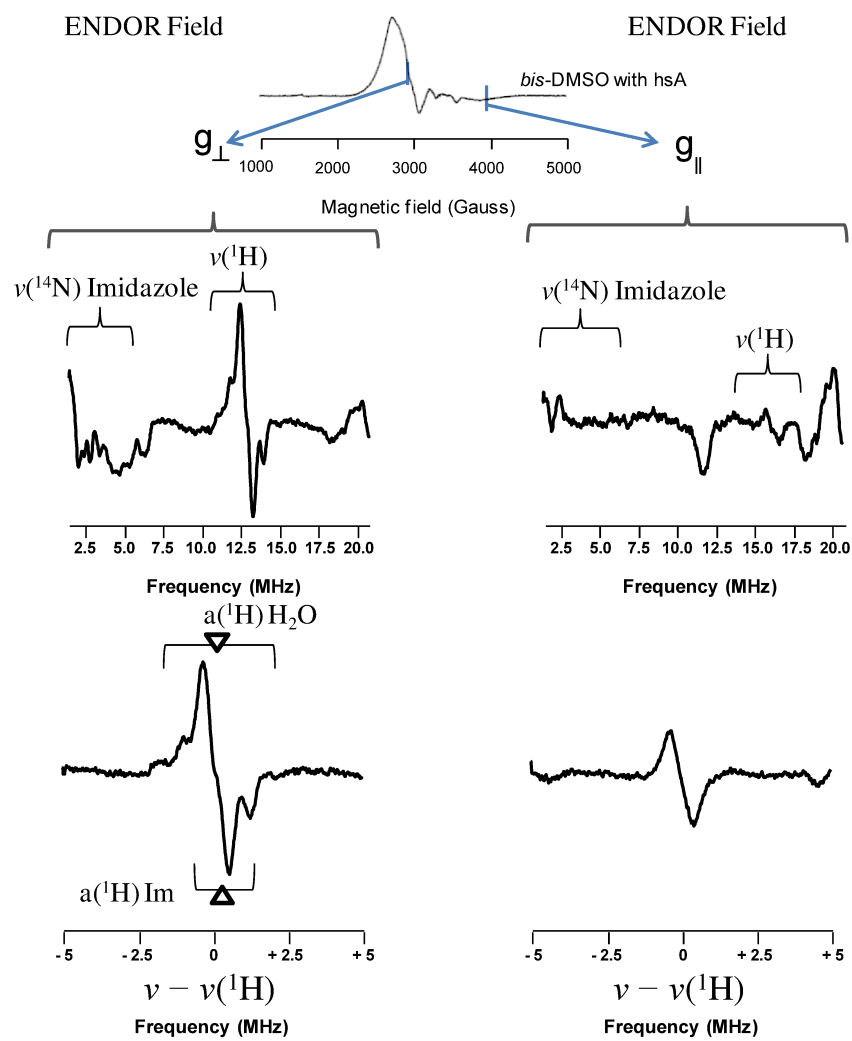


Figure F-15 EPR spectrum of the *bis*-DMSO complex with hSA in PBS following incubation for 30 minutes at 37 °C and the resulting ENDOR spectra measured at g_{\perp} and g_{\parallel} , then expanded around the proton Larmor frequency.

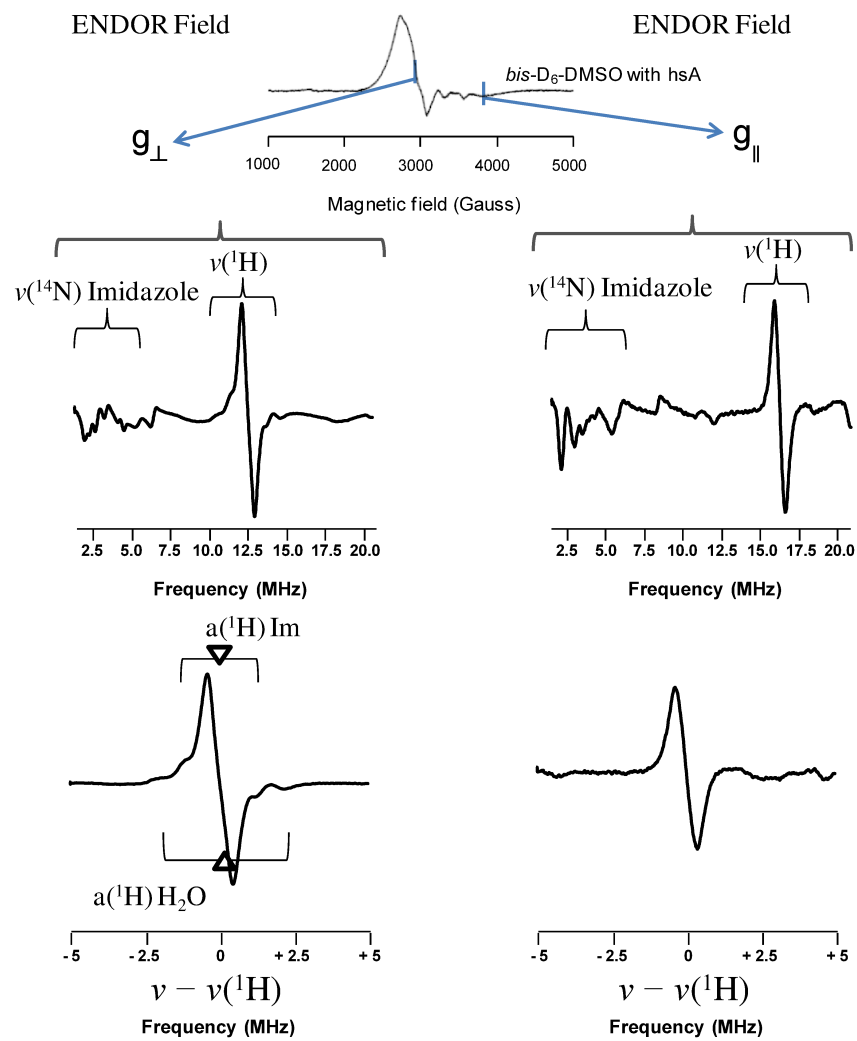


Figure F-16 EPR spectrum of the D₆-DMSO labelled *bis*-DMSO complex with hsA in PBS following incubation for 30 minutes at 37 °C and the resulting ENDOR spectra measured at g_{\perp} and g_{\parallel} , then expanded around the proton Larmor frequency.

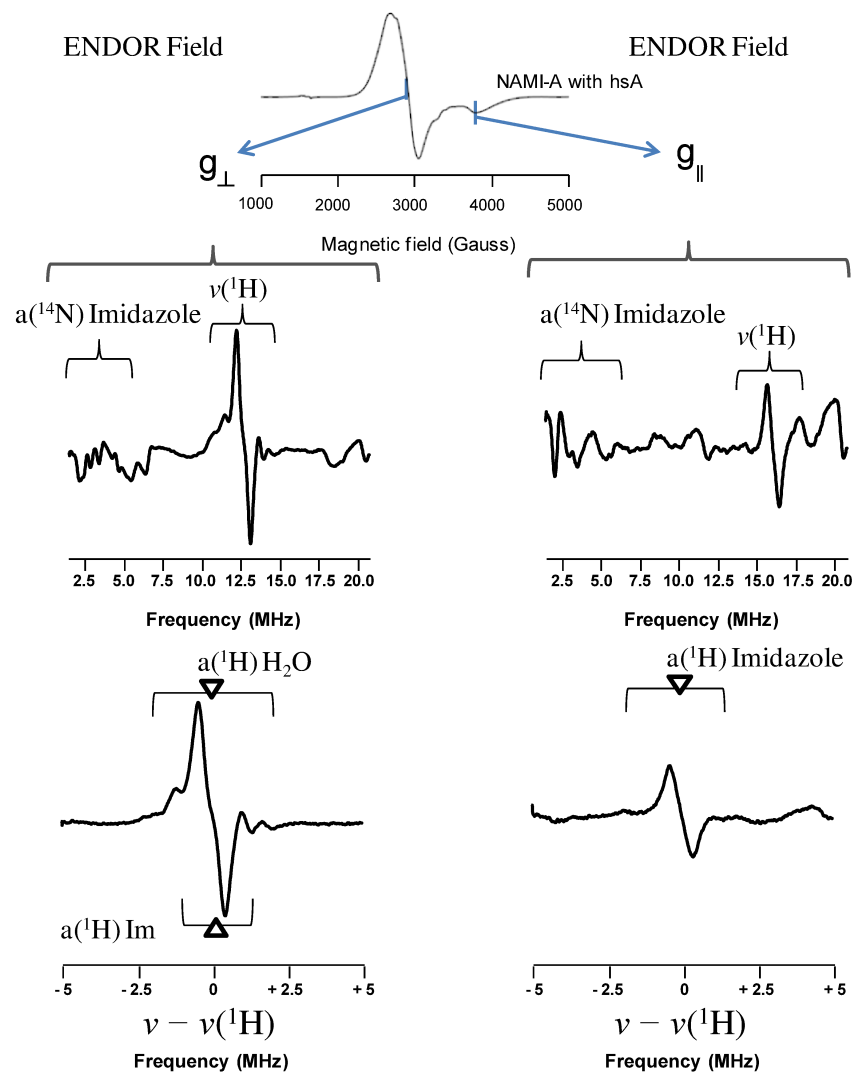


Figure F-17 EPR spectrum of NAMI-A with hsA in PBS following incubation for 30 minutes at 37 °C and the resulting ENDOR spectra measured at g_{\perp} and g_{\parallel} , then expanded around the proton Larmor frequency.

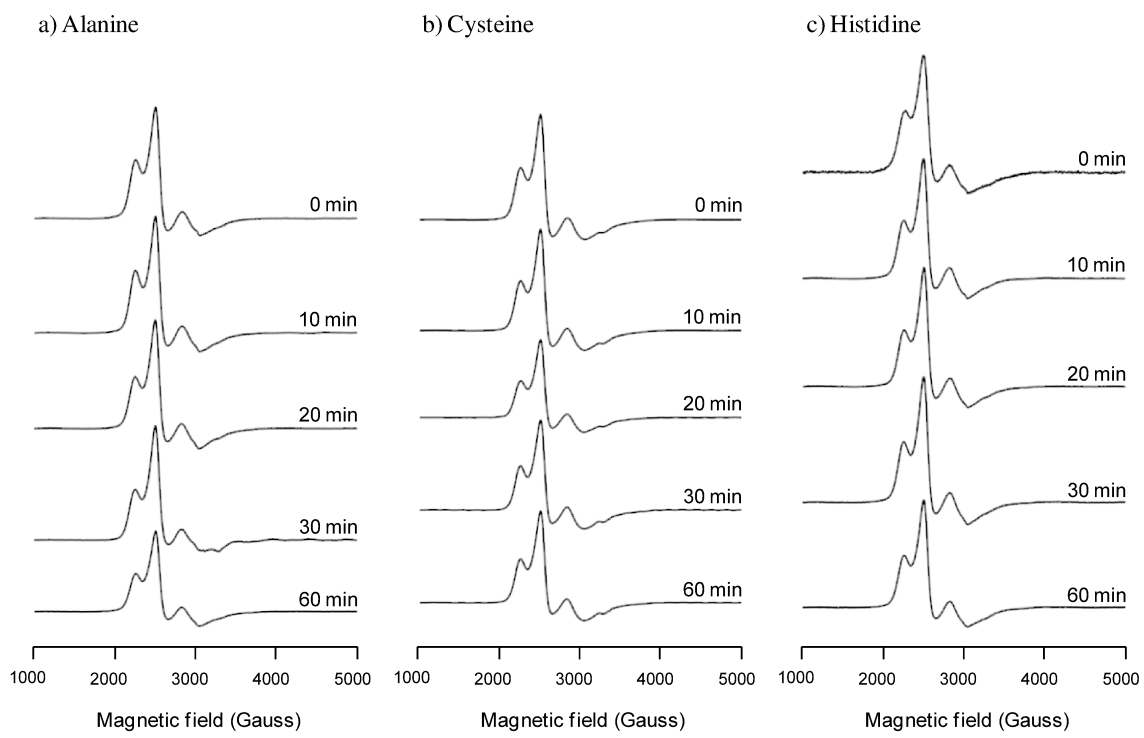


Figure F-18 (a-c) EPR spectra of KP1019 with alanine, cysteine, and histidine following incubation in PBS for 0 – 60 minutes at 37 °C.

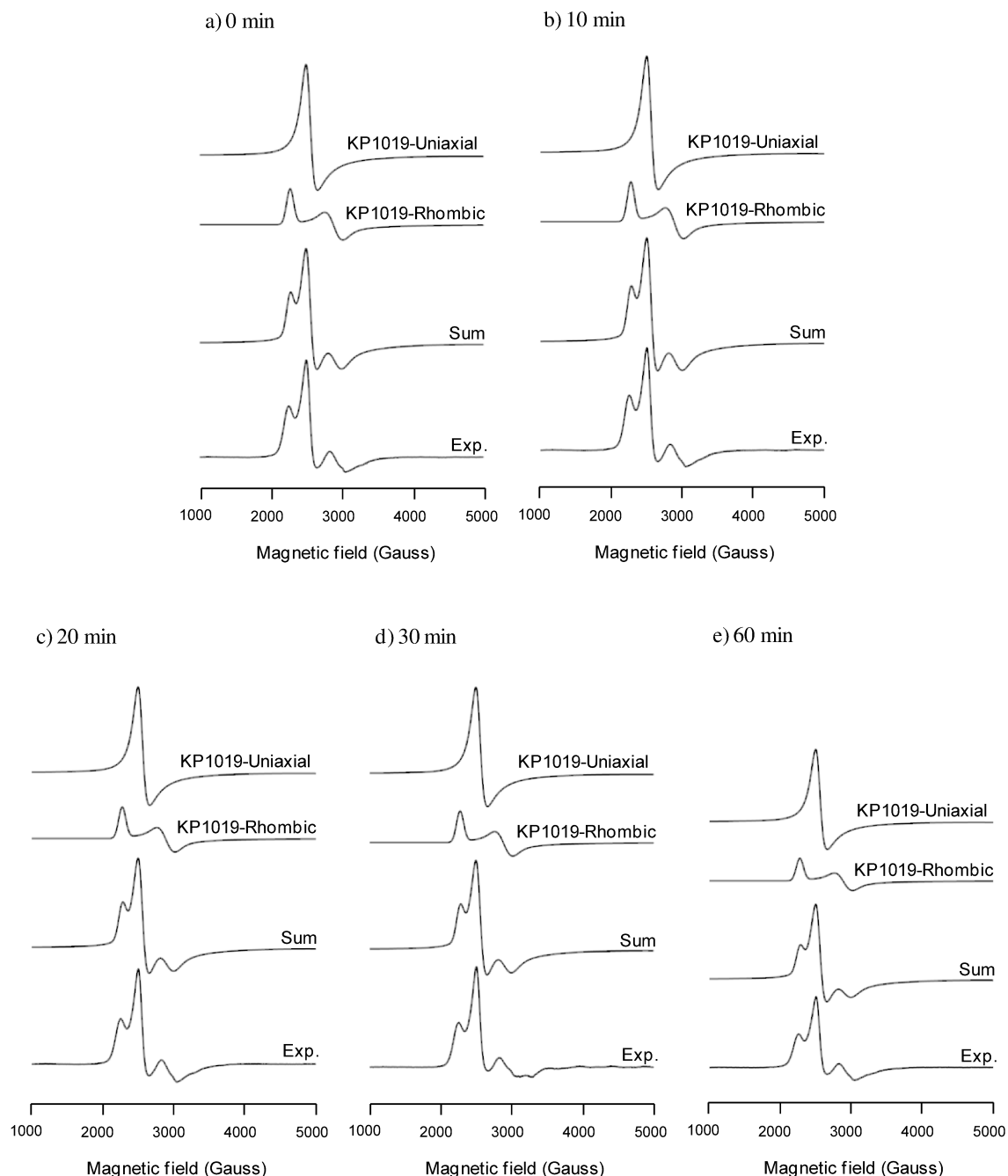


Figure F-19 (a-e) Deconvolution of EPR spectra from KP1019 with alanine following incubation in PBS for 0, 10, 20, 30, and 60 minutes at 37 °C. Simulation parameters: For g values and linewidths, see **Table F-1**.

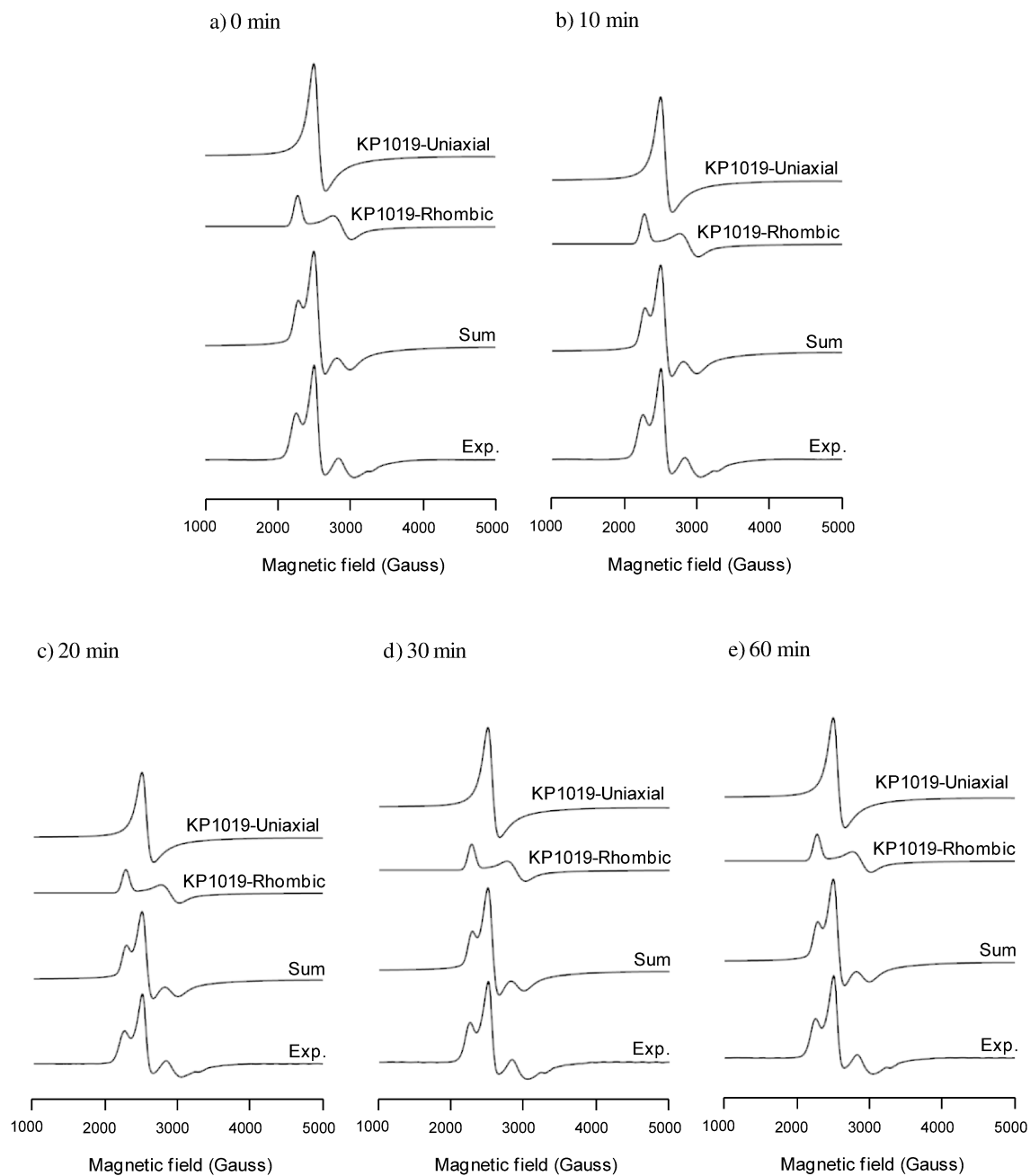


Figure F-20 (a-e) Deconvolution of EPR spectra from KP1019 with cysteine following incubation in PBS for 0, 10, 20, 30, and 60 minutes at 37 °C. Simulation parameters: For g values and linewidths, see **Table F-1**.

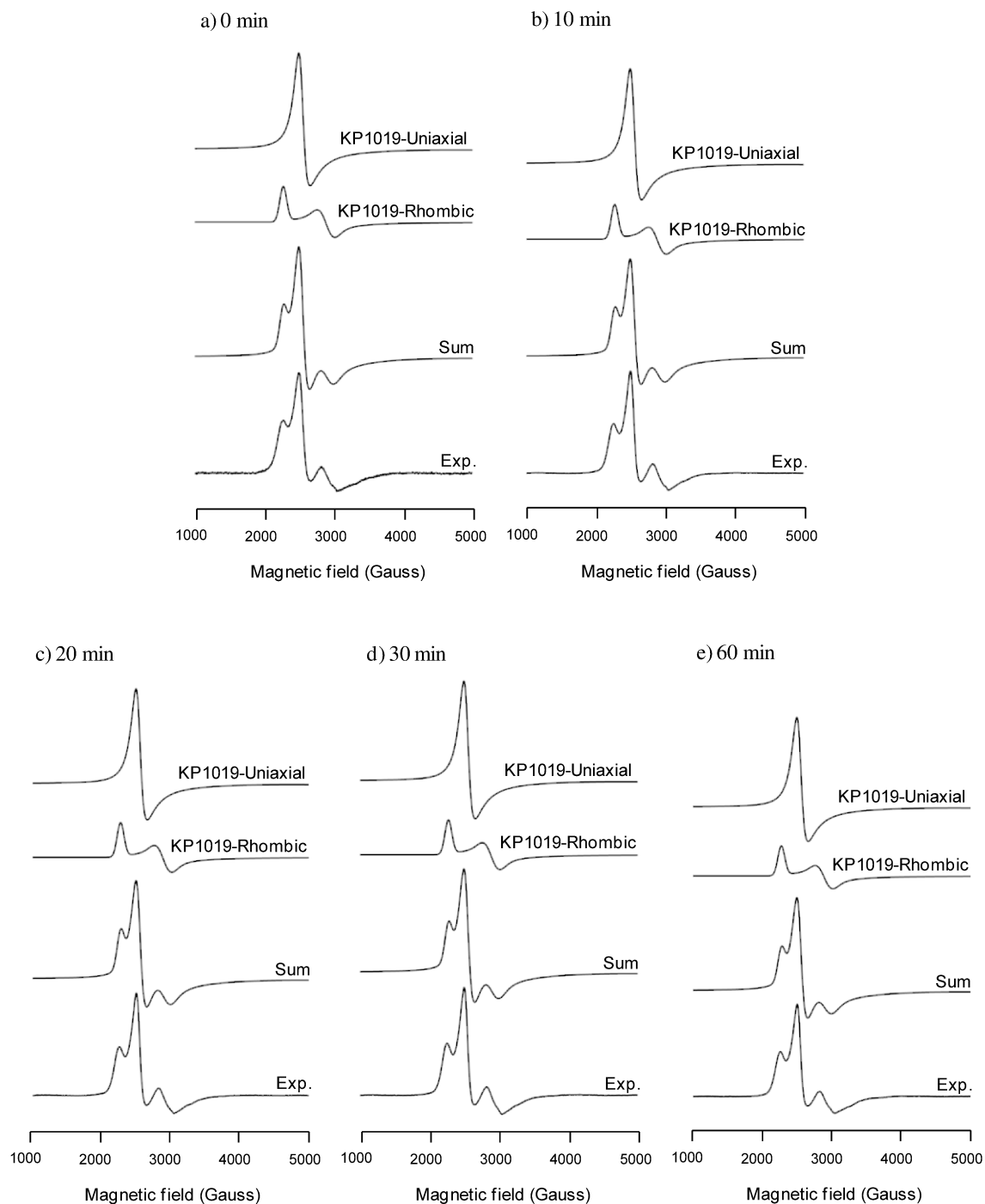


Figure F-21 (a-e) Deconvolution of EPR spectra from KP1019 with histidine following incubation in PBS for 0, 10, 20, 30, and 60 minutes at 37 °C. Simulation parameters: For g values and linewidths, see **Table F-1**.

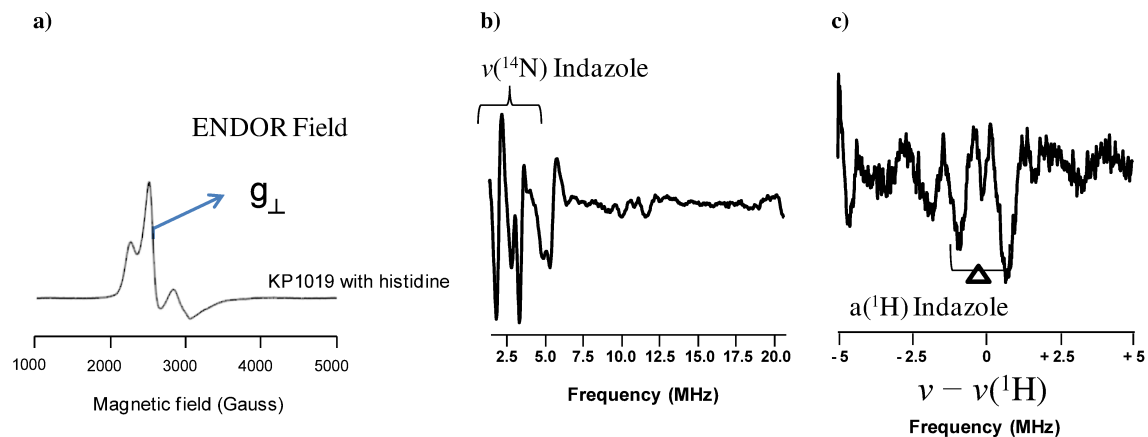


Figure F-22 a) EPR spectrum of KP1019 with histidine in PBS following incubation for 30 minutes at 37 °C and b) the resulting ENDOR spectra measured at g_{\perp} , then c) expanded around the proton Larmor frequency.

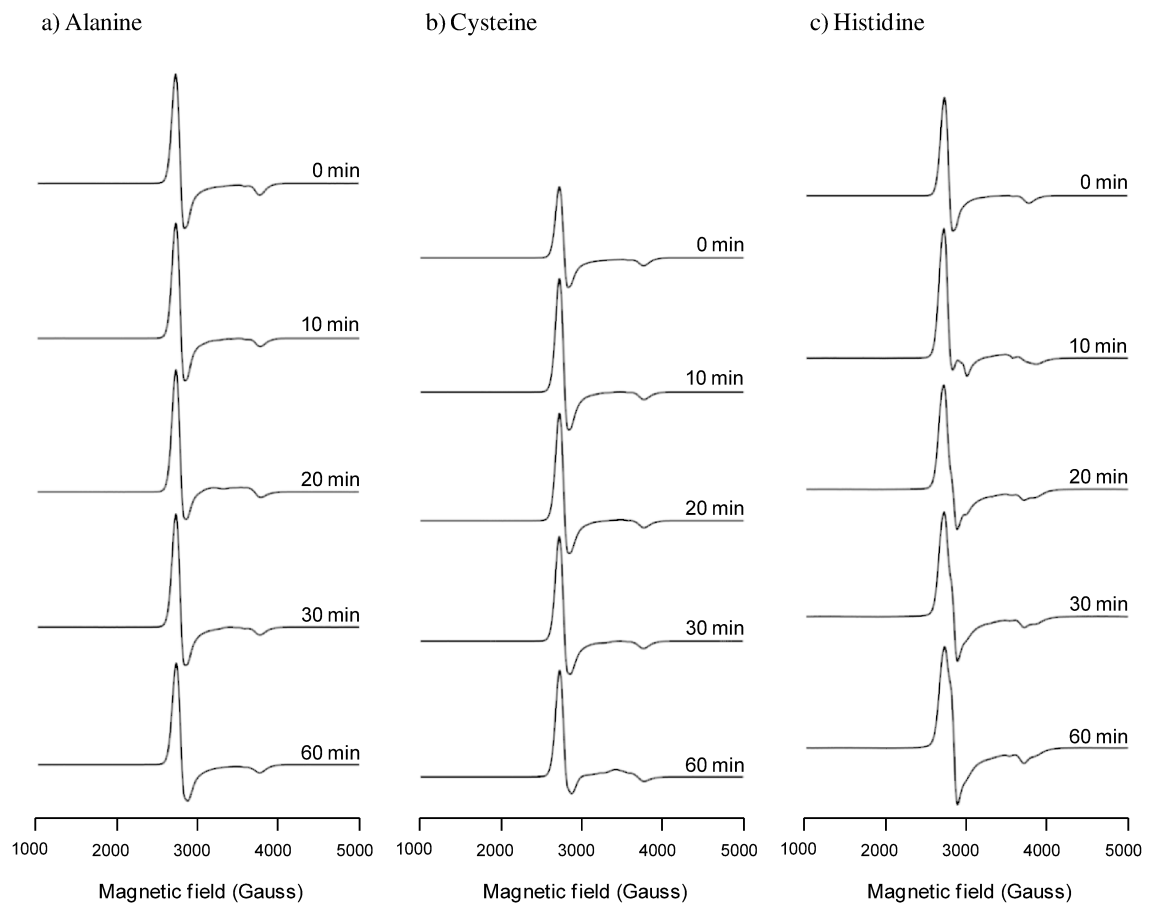


Figure F-23 (a-c) EPR spectra of the *bis*-DMSO complex with alanine, cysteine, and histidine following incubation in PBS for 0 – 60 minutes at 37 °C.

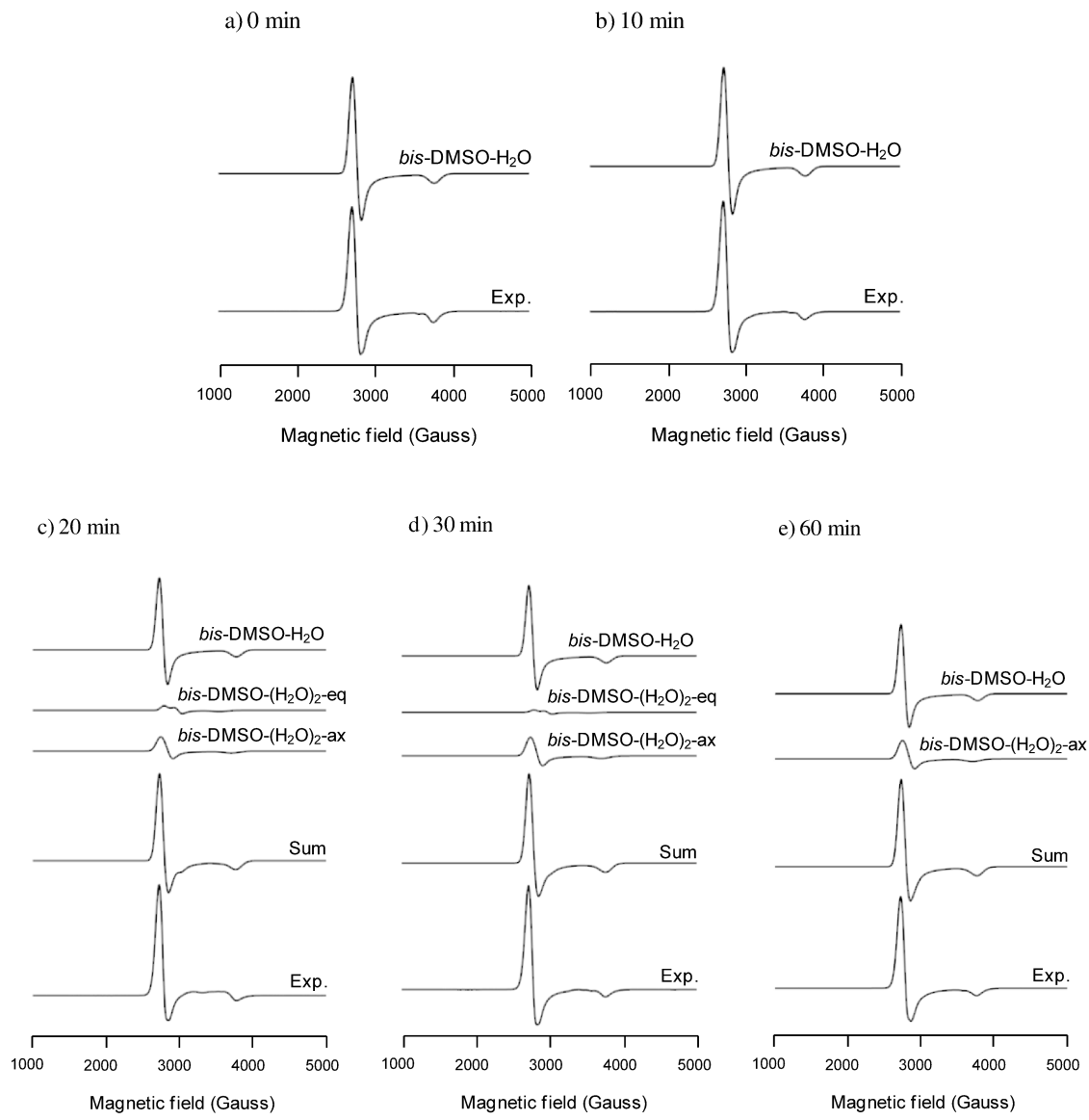


Figure F-24 (a-e) Deconvolution of EPR spectra from the *bis*-DMSO complex with alanine following incubation in PBS for 0, 10, 20, 30, and 60 minutes at 37 °C. Simulation parameters: For g values and linewidths, see **Table F-1**.

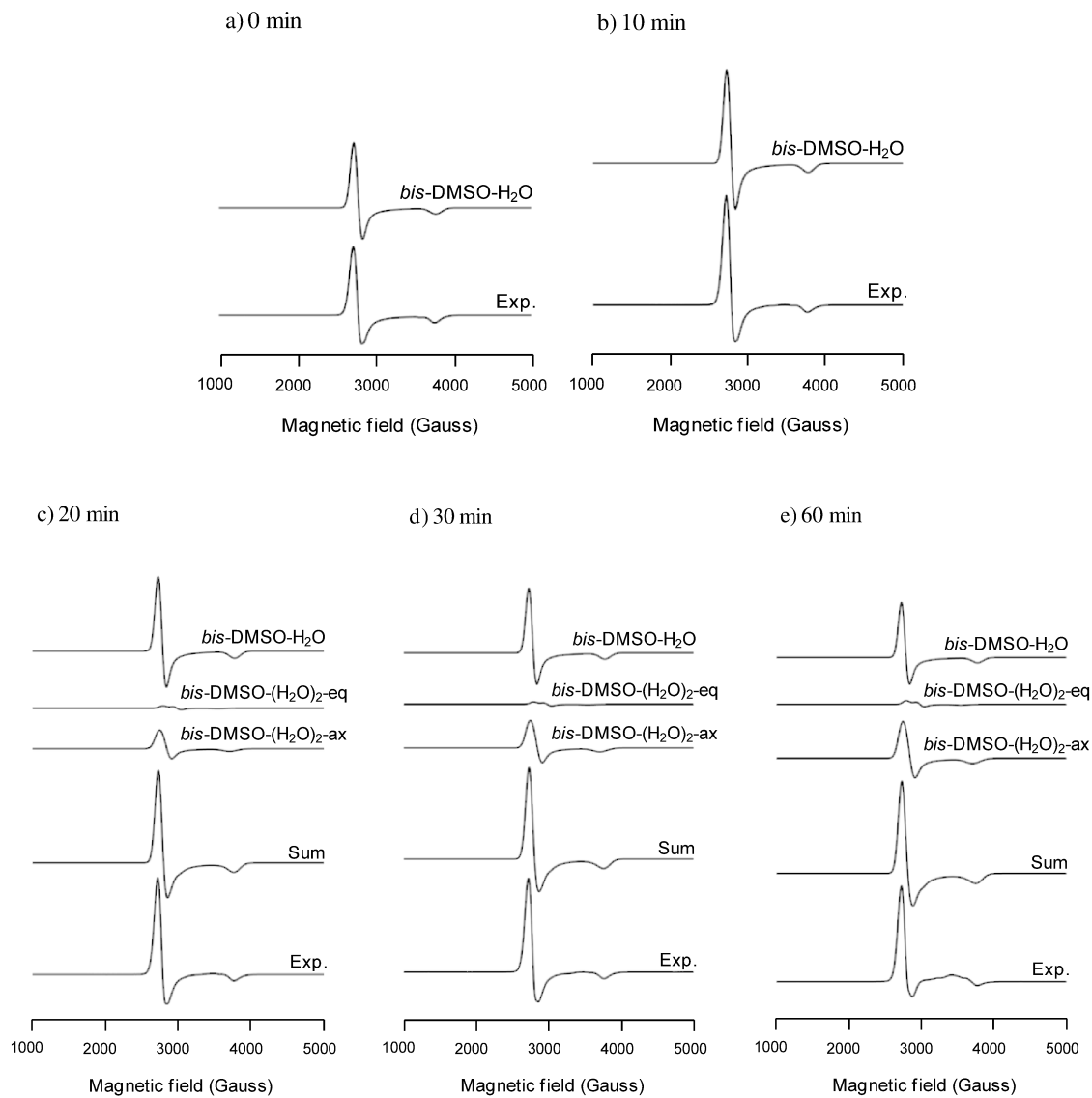


Figure F-25 (a-e) Deconvolution of EPR spectra from the *bis*-DMSO complex with cysteine following incubation in PBS for 0, 10, 20, 30, and 60 minutes at 37 °C. Simulation parameters: For g values and linewidths, see **Table F-1**.

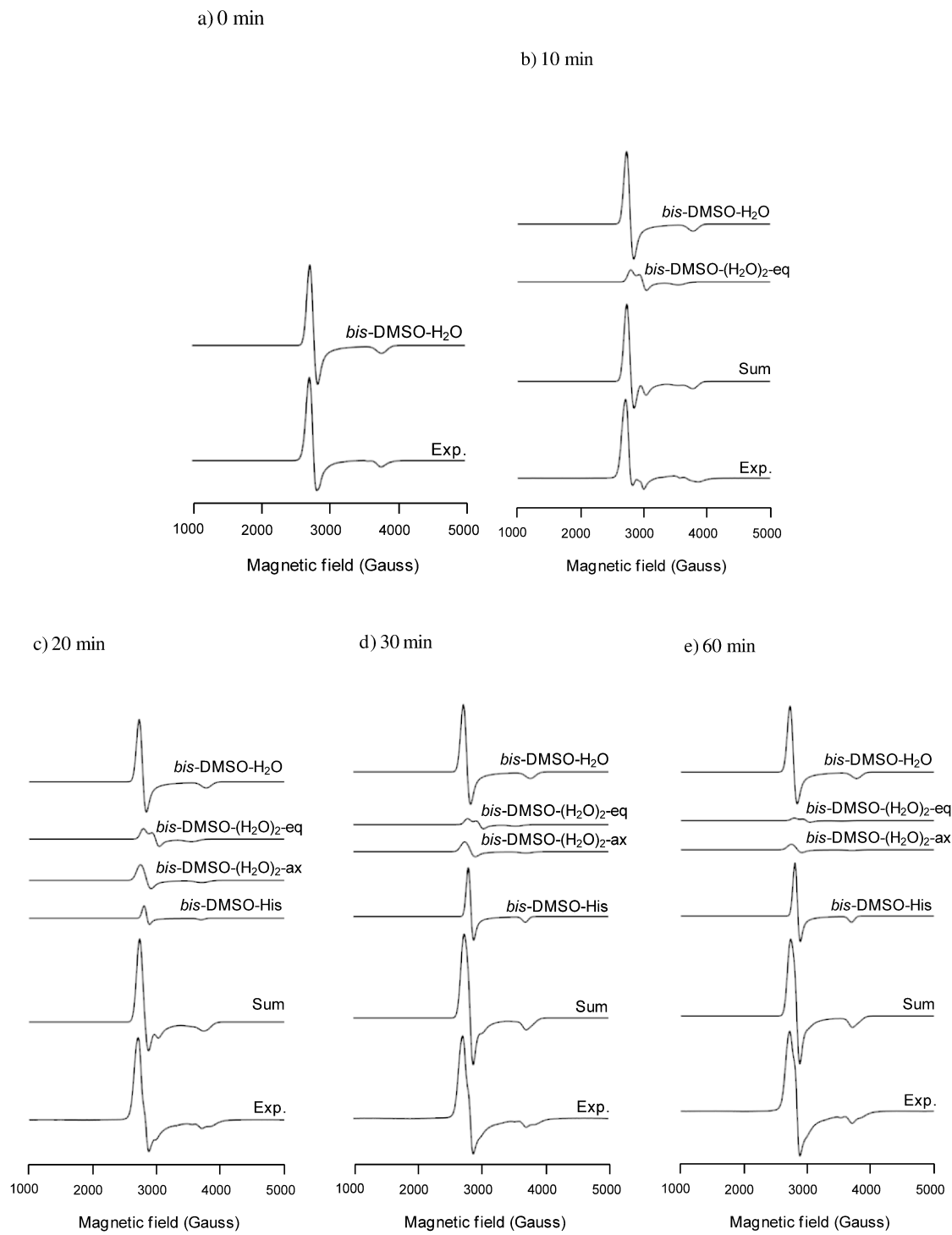


Figure F-26 (a-e) Deconvolution of EPR spectra from the *bis*-DMSO complex with histidine following incubation in PBS for 0, 10, 20, 30, and 60 minutes at 37 °C. Simulation parameters: For g values and linewidths, see **Table F-1**.

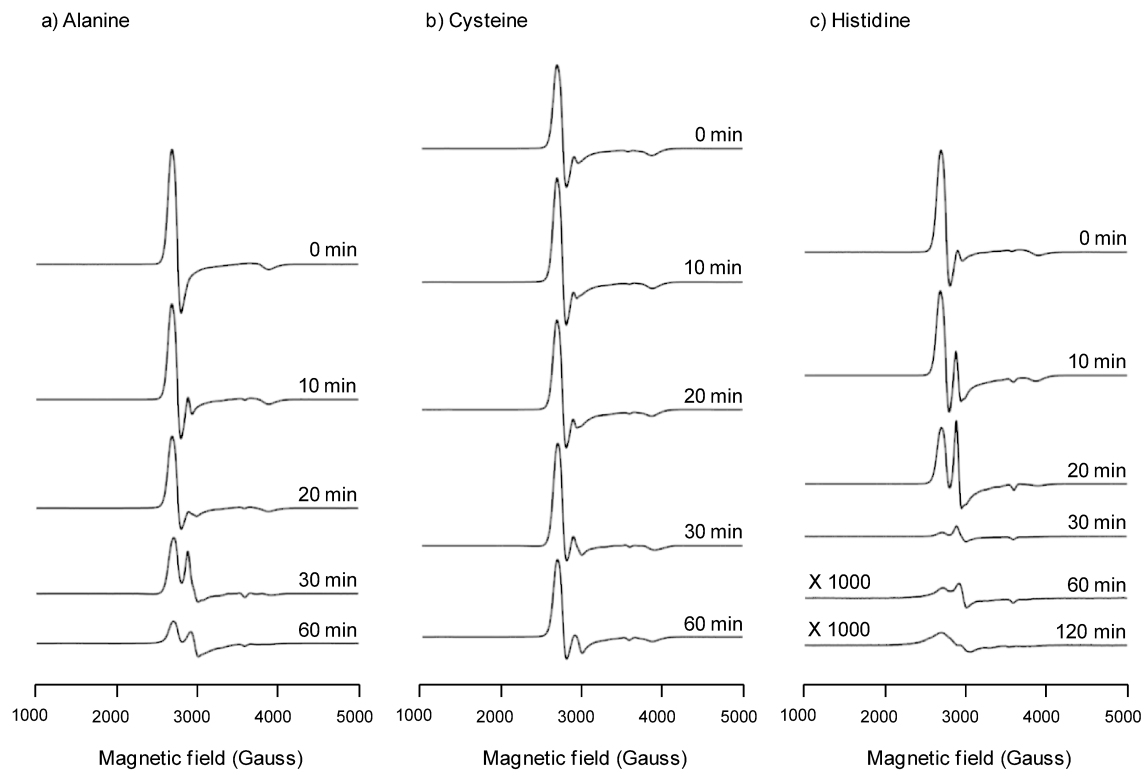


Figure F-27 (a-c) EPR spectra of NAMI-A with alanine, cysteine, and histidine following incubation in PBS for 0 – 60 minutes at 37 °C.

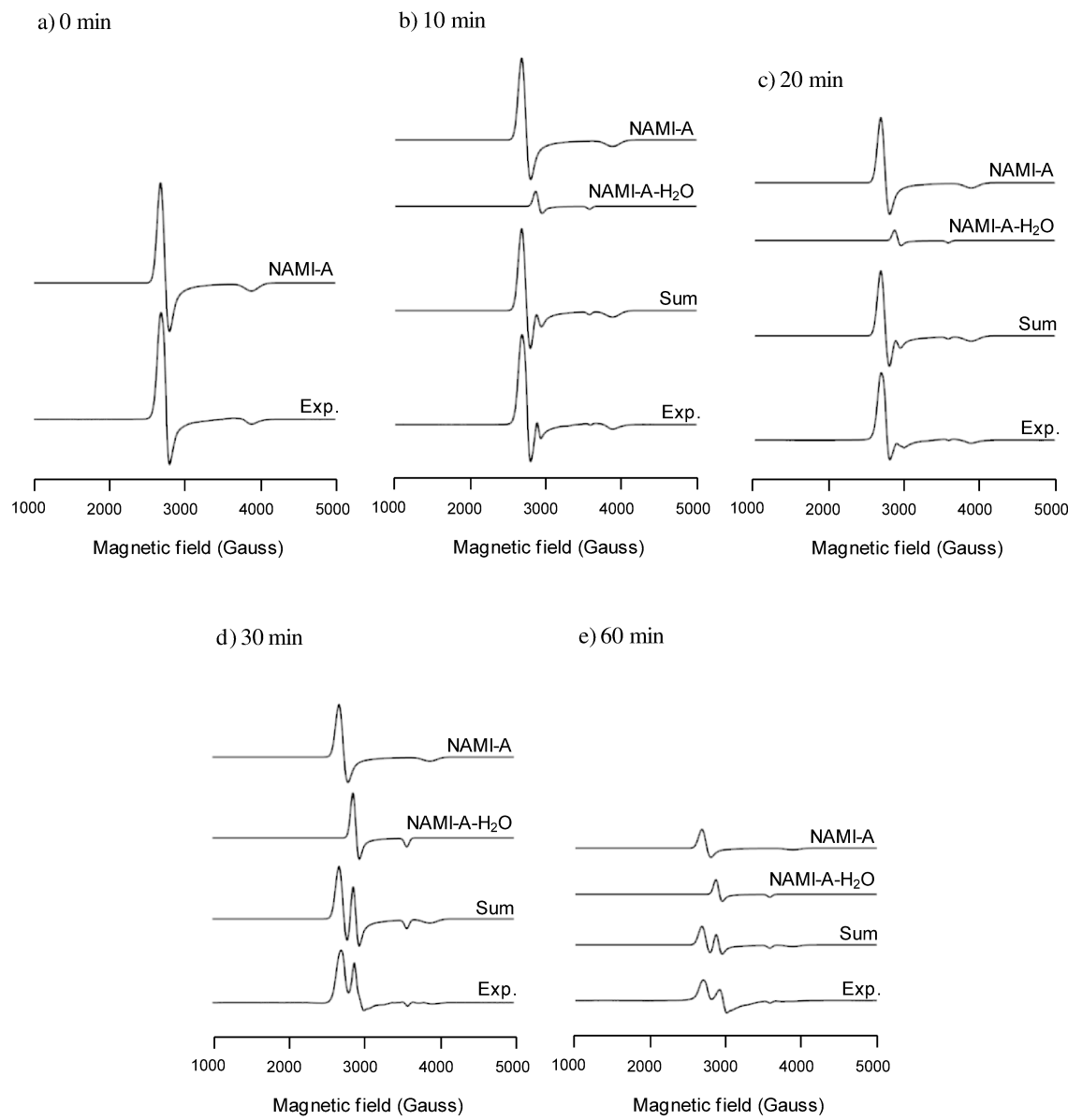


Figure F-28 (a-e) Deconvolution of EPR spectra from NAMI-A with alanine following incubation in PBS for 0, 10, 20, 30, and 60 minutes at 37 °C. Simulation parameters: For g values and linewidths, see **Table F-1**.

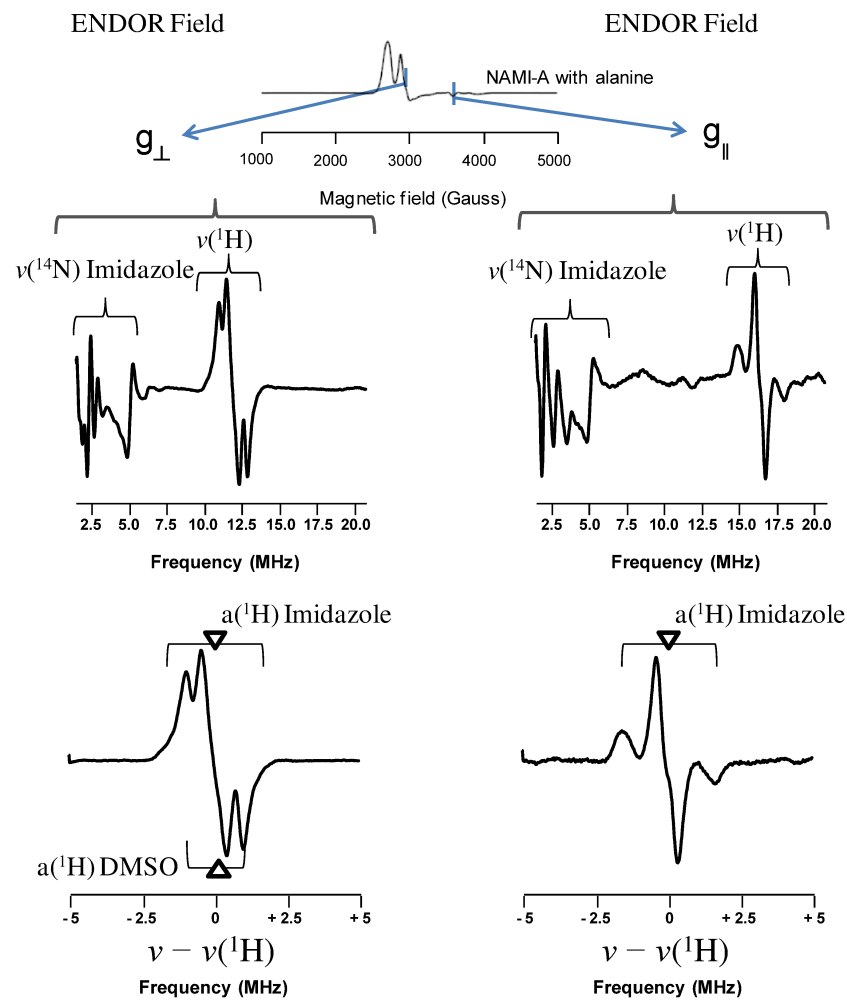


Figure F-29 EPR spectrum of NAMI-A with alanine in PBS following incubation for 30 minutes at 37 °C and the resulting ENDOR spectra measured at g_{\perp} and g_{\parallel} , then expanded around the proton Larmor frequency.

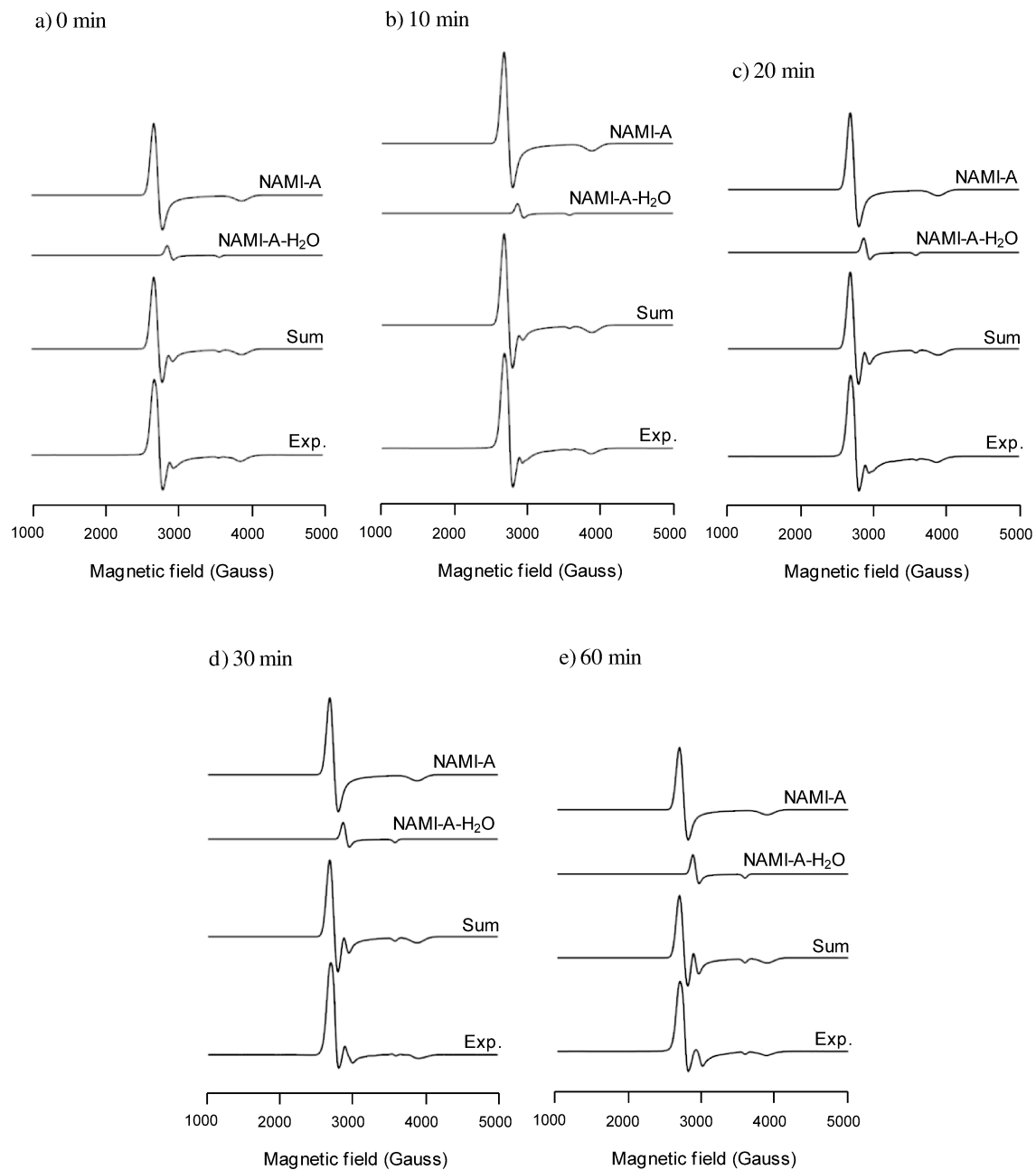


Figure F-30 (a-e) Deconvolution of EPR spectra from NAMI-A with cysteine following incubation in PBS for 0, 10, 20, 30, and 60 minutes at 37 °C. Simulation parameters: For g values and linewidths, see **Table F-1**.

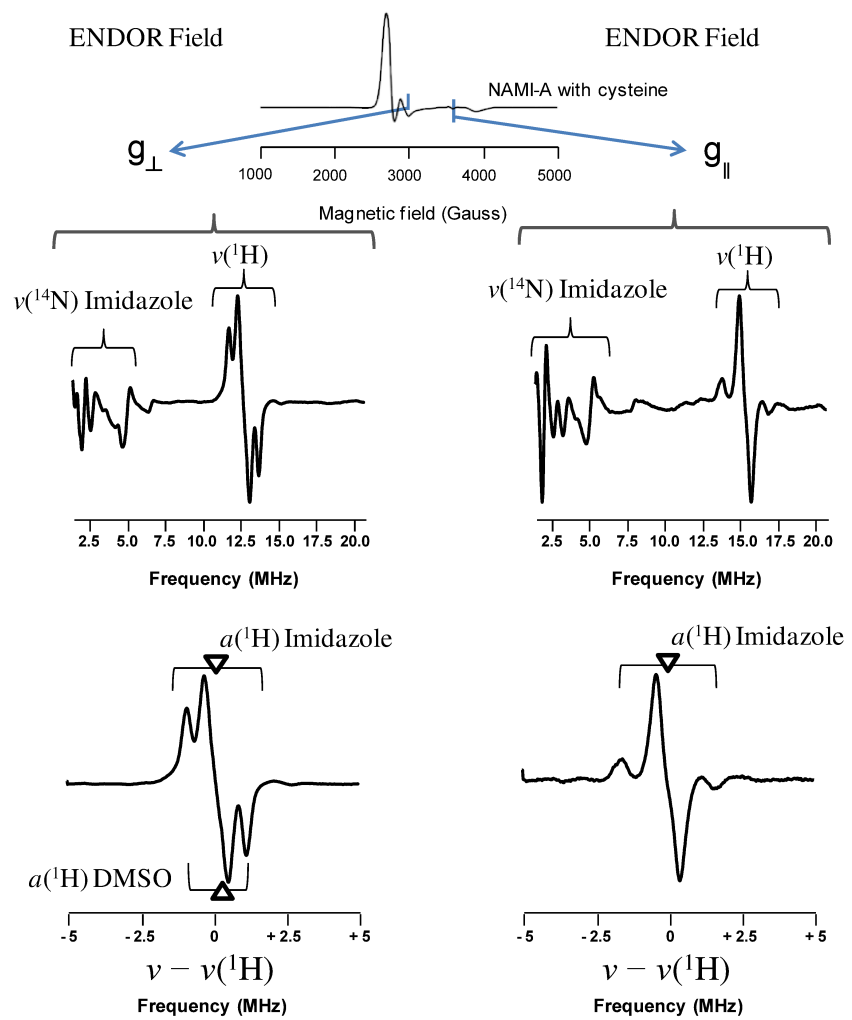


Figure F-31 EPR spectrum of NAMI-A with cysteine in PBS following incubation for 30 minutes at 37 °C and the resulting ENDOR spectra measured at g_{\perp} and $g_{||}$, then expanded around the proton Larmor frequency.

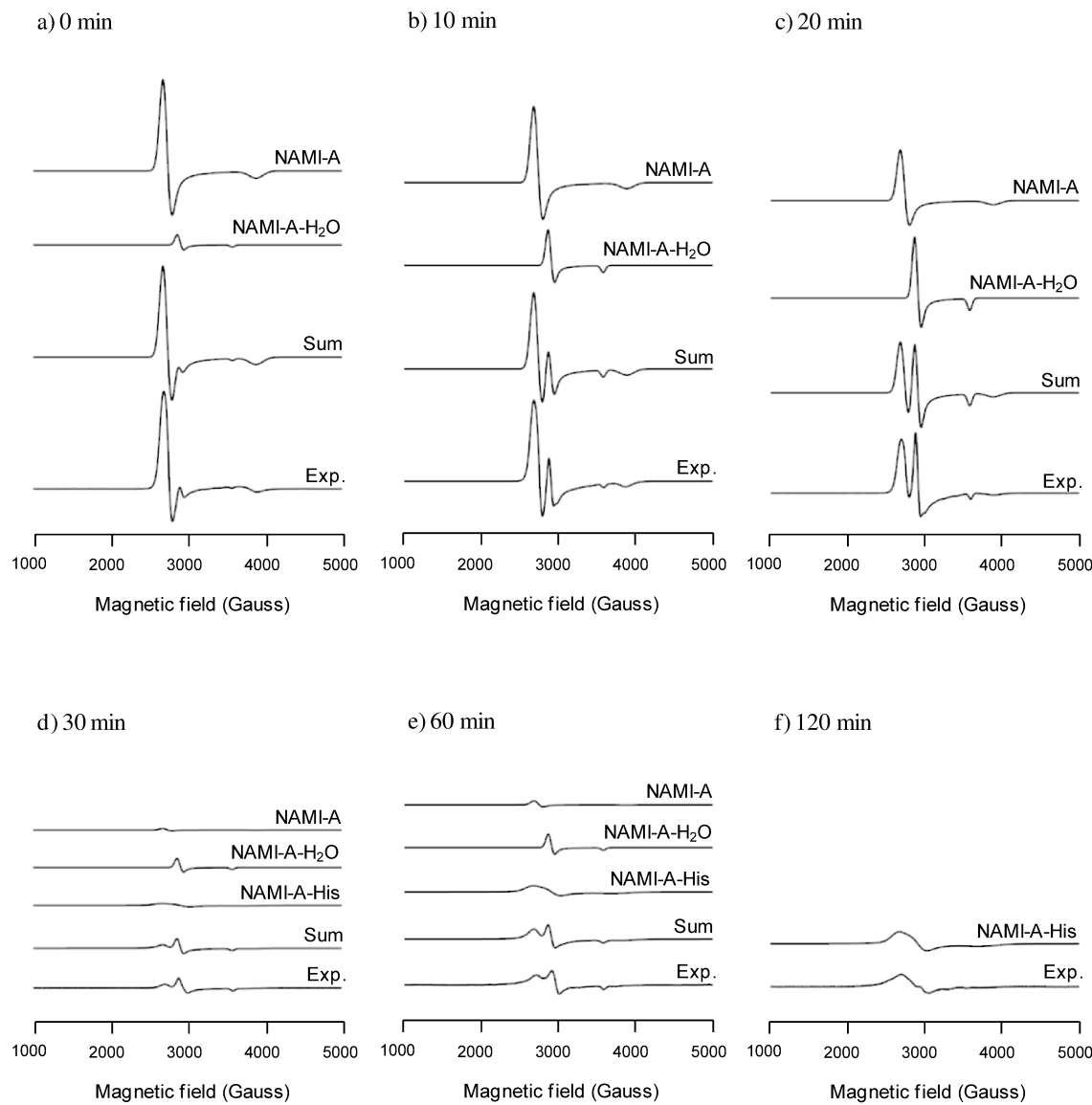


Figure F-32 (a-f) Deconvolution of EPR spectra from NAMI-A with histidine following incubation in PBS for 0, 10, 20, 30, and 60 minutes at 37 °C. Simulation parameters: For g values and linewidths, see **Table F-1**.

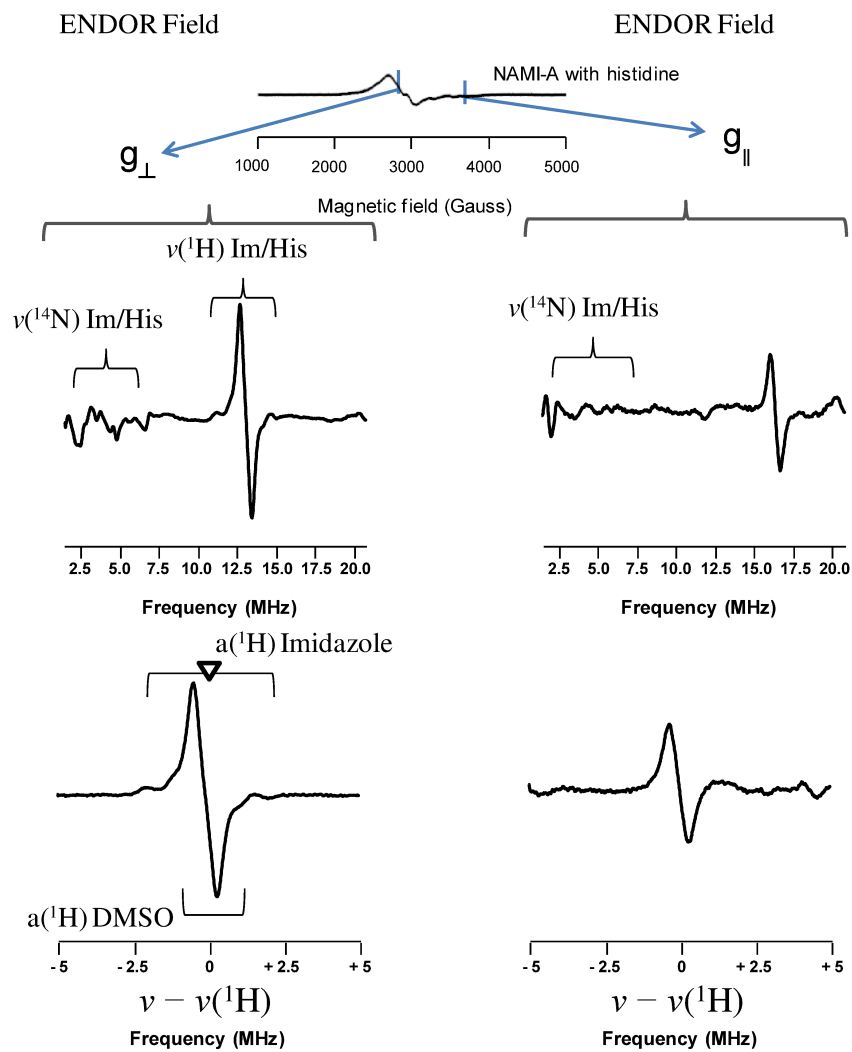


Figure F-33 EPR spectrum of NAMI-A with histidine in PBS following incubation for 120 minutes at 37 °C and the resulting ENDOR spectra measured at g_{\perp} and $g_{||}$, then expanded around the proton Larmor frequency.